

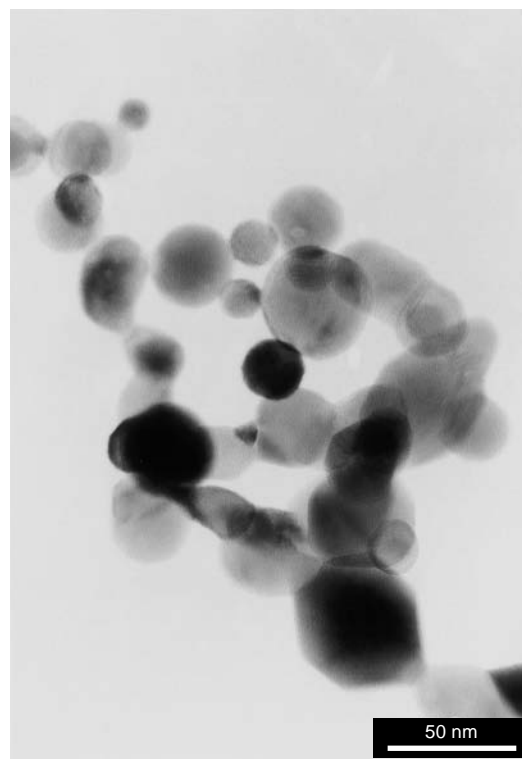
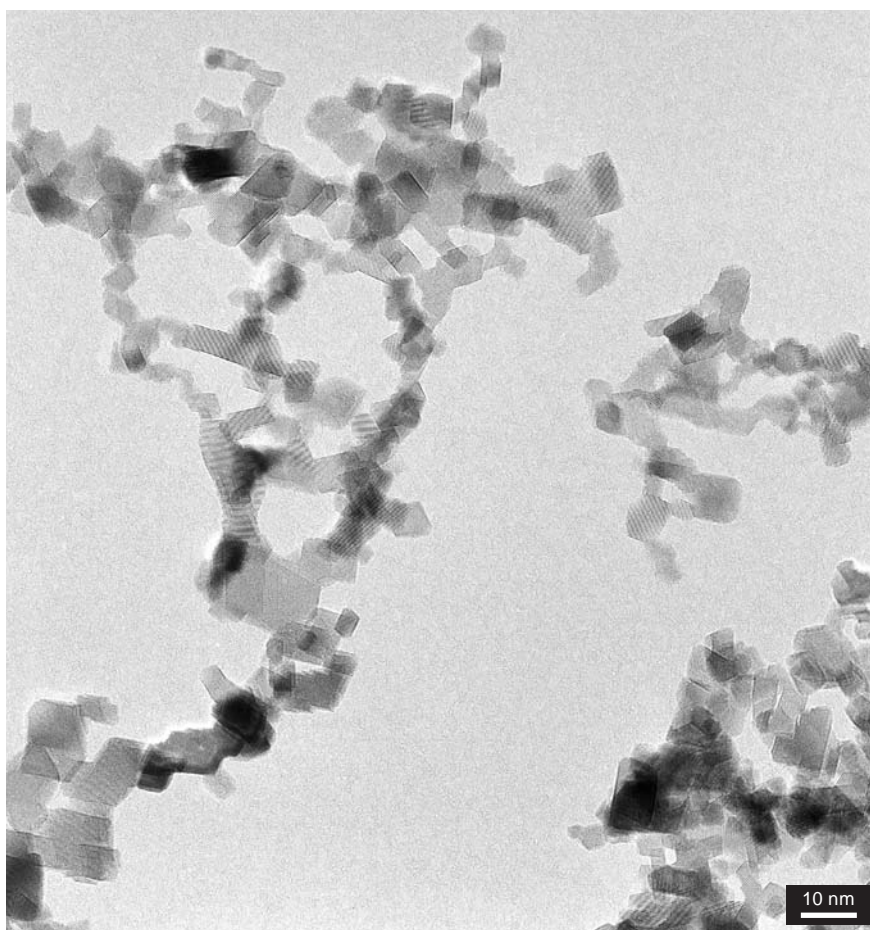


# KONA

## POWDER AND PARTICLE

# No.21 (2003)

Published by Hosokawa Powder Technology Foundation



Nanoparticles of Cerium Dioxide and Lanthanum Strontium Manganite produced by Nano Particle Reactor

now available online – [www.kona.or.jp](http://www.kona.or.jp)

# KONA

**POWDER AND PARTICLE**

<http://www.kona.or.jp>

KONA is a refereed scientific journal that publishes articles on powder and particle sciences and technology. KONA has been published annually since 1983 in Japan. KONA is distributed to researchers, members of the scientific community, universities and research libraries throughout the world.

## About the Cover of Journal "KONA"

The Chinese character “粉” is pronounced “KONA” in Japanese, and means “Powder”. The hand written “粉” is after the late Mr. Eiichi Hosokawa, founder of the Hosokawa Micron Corporation.



**Hosokawa Micron Corporation and its R&D Center**

## Editorial Board

**Y. Tsuji**

Editor in Chief  
(Osaka Univ., JAPAN)

## Asia/Oceania Editorial Board

**Y. Kousaka**

(Emeritus Professor of Osaka Prefecture Univ., JAPAN)

**Y. Morikawa**

(Emeritus Professor of Osaka Univ., JAPAN)

**K. Miyanami**

(Emeritus Professor of Osaka Prefecture Univ., JAPAN)

**H. Masuda**

(Kyoto Univ., JAPAN)

**H. Emi**

(Emeritus Professor of Kanazawa Univ., JAPAN)

**K. Higashitani**

(Kyoto Univ., JAPAN)

**K. Nogi**

(Osaka Univ., JAPAN)

**Y. Fukumori**

(Kobe Gakuin Univ., JAPAN)

**J. Hidaka**

(Doshisha Univ., JAPAN)

**M. Takahashi**

(Nagoya Institute of Technology, JAPAN)

**P. Arnold**

(Univ. of Wollongong, AUSTRALIA)

**S.H. Kang**

(Yeungnam Univ., KOREA)

**W. Tanthapani-chakoon**

(Chulalongkorn Univ., THAILAND)

**T. Yokoyama**

(Hosokawa Powder Technology Research Institute, JAPAN)

**K. Yoshida**

(Hosokawa Micron Corp., JAPAN)

## Secretariat

**T. Kawamura**

(Hosokawa Powder Technology Foundation, JAPAN)

## Europe/Africa Editorial Board

**E. Forssberg**

Chairman (Univ. Lulea, SWEDEN)

**J. Schwedes**

Vice Chairman (Univ. Braunschweig, GERMANY)

**K. Schönert**

(Technische Univ. Clausthal, GERMANY)

**H. Kalman**

(Ben Gurion Univ., ISRAEL)

**J.F. Large**

(Univ. de Tech. de Compiègne, FRANCE)

**N.Z. Lyakhov**

(Institute of Solid State Chemistry, RUSSIA)

**M. Ghadiri**

(Univ. of Leeds, UNITED KINGDOM)

## Secretariat

**P. van der Wel**

(Hosokawa Micron B.V. NETHERLANDS)

**P. Krubeck**

(Hosokawa Micron GmbH, GERMANY)

## Americas Editorial Board

**B.M. Moudgil**

Chairman (Univ. of Florida, U.S.A.)

**D.W. Fuerstenau**

Vice Chairman (Univ. of California, U.S.A.)

**R. Flagán**

(California Institute of Technology, U.S.A.)

**L. Augsburger**

(Univ. of Maryland School of Pharmacy, U.S.A.)

**P.S. Santos**

(Univ. of São Paulo, BRAZIL)

**R. Hogg**

(Pennsylvania State Univ., U.S.A.)

**D.J.W. Grant**

(Univ. of Minnesota, U.S.A.)

## Secretariat

**D.A. Scott**

(Hosokawa Micron Inter., U.S.A.)

## Publication Office

Hosokawa Powder Technology Foundation (Japan) in Hosokawa Micron Corporation

No. 9, 1-chome, Shoudai Tajika, Hirakata-shi, Osaka 573-1132 Japan

## Notes

- Hosokawa Powder Technology Foundation has entrusted the editorial duty to the editorial board organized by the Council of Powder Technology, Japan.

(Complimentary Copy)

Printed in Japan

## The Letter from the Editor



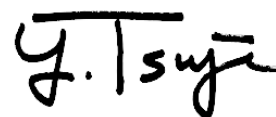
Yu Tsuji  
Editor-in-Chief

It is a great honor and pleasure for me to serve as the Editor-in-Chief of KONA, having taken over from Professor Kousaka. The number of technical journals is countless nowadays, but international journals specific to powder and particle technology are very few. KONA is unique amongst these, in that articles and papers published in KONA have been restricted to the highest quality. As a result, KONA has the reputation of truly internationally respected journal, I believe. KONA is issued by the Hosokawa Powder Technology Foundation, and all expenses for publication are covered by the Foundation. There is no need to make a profit, nor to keep subscribers. This is a great advantage of KONA over other journals, as editors can concentrate their efforts on maintaining the quality of articles and papers.

In the last ten years, our situation at KONA has changed in many respects. First, computer-based communication has become the norm. Responding to this change, it has been decided to provide KONA via internet. Anyone will now be able to visit the KONA website and download any articles and papers free of charge. Before starting web publication, 2000 copies per issue were distributed to specialists of powder and particle technology in the world. This level of circulation is outstanding. Owing to web publication, the circulation is expected to increase greatly to much more than 2000 copies. From now on, we will make web publication the norm. At the same time, printed versions of KONA will also be issued for organizations, but not for individuals. Needless to say, free download is possible thanks to the support of the Hosokawa Powder Technology Foundation.

Second, the range of powder and particle technology has greatly expanded in the last ten years. Several new research subjects have emerged from this field. Typical examples of such new areas are subjects related to nano technology with which many KONA readers are very familiar. KONA is always sensitive to new topics. However, we should not forget that conventional technology is also developing steadily and continue to play important roles in many industrial fields. As the editor-in-chief, it will be my responsibility to strike a good balance between current trends and conventional ones.

Finally, I must inform you of some sad news. Dr. Brian Kaye of Laurentian University has passed away. Dr. Kaye served on the KONA Board for more than 10 years before retiring two years ago. He was an excellent researcher and educator. With grateful appreciation for numerous services rendered by Dr. Kaye during his life time, we offer this token of our deepest sympathy.



# KONA

## GENERAL INFORMATION

### HISTORY OF THE JOURNAL

KONA journal has been published by the Council of Powder Technology, Japan. (CPT), from No.1 to No.12 issues, under the sponsorships of Hosokawa Micron Corporation (No.1 to No.9) and Hosokawa Powder Technology Foundation (No.10 to No.12).

The CPT has been established in 1969 as a non-profit organization to enhance the activities of research and development on powder science and technology in Japan under the sponsorship of Hosokawa Micron Corporation. In 1983, the CPT has decided to issue an international journal named "KONA", which publishes the excellent articles appeared in Japanese journals concerning powder science and technology, after translated into English, throughout the world. After the seventh volume issued in 1989, the CPT has changed its policy to internationalize the "KONA" from the 8th issue (1990) and on by incorporating the monographs originally written in English from the authors throughout the world. Immediately, the present editorial board including Asian, Americas' and European Blocks has been organized.

From the 13th issue and on, the Hosokawa Powder Technology Foundation has taken over the role of KONA publisher from the CPT in 1995 (No.13) and the Foundation has entrusted the editorial duty to the present KONA editorial board organized by the CPT without requesting any shift in our present editorial policies. This switching of publisher has been simply and only to make the aim and scope of the Foundation definite. Essentially no change has been observed in continuously editing and publishing this journal except in the designation on a part of the journal cover.

### AIMS AND SCOPE OF THE JOURNAL

KONA Journal is to publish the papers in a broad field of powder science and technology, ranging from fundamental principles to practical applications. The papers discussing technological experiences and critical reviews of existing knowledge in specialized areas will be welcome.

These papers will be published only when they are judged, by the Editor, to be suitable for the progress of powder science and technology, and are approved by any of the three Editorial Committees. The paper submitted to the Editorial Secretariat should not have been previously published except the translated papers which would be selected by the Editorial Committees.

### CATEGORY OF PAPERS

- Invited papers  
Original research and review papers invited by the KONA Editorial Committees.
- Contributed papers  
Original research and review papers submitted to the KONA Editorial Committees, and refereed by the Editors.
- Translated papers  
Papers translated into English, which were previously published in other languages, selected by the KONA Editorial Committees with the permission of the authors and / or the copyright holder.

### SUBMISSION OF PAPERS

Papers should be sent to each KONA Editorial Secretariat.

- Asia / Oceania Editorial Secretariat  
T. Kawamura  
Hosokawa Micron Corporation Micromeritics Laboratory 1-9,  
Shoudai Tajika, Hirakata 573-1132 JAPAN
- Europe / Africa Editorial Secretariat  
Dr. P. van der Wel or Mrs. P. Krubeck  
Hosokawa Micron GmbH  
Welsersstr. 9-11, 51149 Köln  
P.O. Box 920262, 51152 Köln  
GERMANY

- Americas Editorial Secretariat  
D.A. Scott  
Hosokawa Micron International Inc.  
10 Chatham Road, Summit, NJ 07901 USA

### PUBLICATION SCHEDULE

KONA is published once a year.

### SUBSCRIPTION

KONA is distributed free of charge to senior researchers at universities and laboratories as well as to institutions and libraries in the field throughout the world. The publisher is always glad to consider the addition of names of those who wish to obtain this journal regularly to the mailing list. Distribution of KONA is made by each Secretariat.

**Free electronic publication of KONA is available in**  
**<http://www.kona.or.jp>**

### INSTRUCTIONS TO AUTHORS

- (1) Manuscript format
  - Two copies should be submitted to the Editorial Secretariat, in double-spaces typing on pages of uniform size.
  - Authorship is to give author's names, and the mailing address where the work has been carried out on the title page.
  - Abstract of 100-180 words should be given at the beginning of the paper.
  - Nomenclature should appear at the end of each paper. Symbols and units are listed in alphabetical order with their definitions and dimensions in SI units.
  - Literature references should be numbered and listed together at the end of paper, not in footnotes. Please give information as in the following examples:
    - 1) Carslaw, H.C. and J.C. Jaeger: "Conduction of Heat in Solids", 2nd ed., Clarendon Press, Oxford, England (1960).
    - 2) Howell, P.A.: US Patent, 3,334,603 (1963).
    - 3) Rushton, J.H., S. Nagata and D.L. Engle: AIChEJ., 10. 294 (1964).
    - 4) Seborg, D.E.: Ph.D. Dissertation, Princeton Univ., N.J., U.S.A. (1969).
  - Original figures with each single copy should be submitted, on separate sheets. Authors' names and figure numbers are marked in the corner.
  - Figure numbers and captions are listed on a separate sheet.
  - Place of figure insertion is to be indicated in the margin of the manuscript.
  - Tables should be typed on separated sheets.
  - Author's short biography and photograph should be attached.
  - For data and text submissions we accept PC-format floppy and CD-ROM discs with unformatted text files in ASCII code. Files in Microsoft Word format are also acceptable. When submitting images, please insure that the files are compatible with Adobe Photoshop and have a resolution of at least 350 dpi.
- (2) Reprints
  - The authors shall receive 50 free reprints. Additional reprints will be furnished when ordered with return of galley proofs.
- (3) Publication policy
  - All papers submitted for publication become immediately the property of the CPT and remain so unless withdrawn by the author prior to acceptance for publication or unless released by the Editor. Papers are not to be reproduced or published in any form without the written permission of the CPT.



# KONA Powder and Particle No. 21 (2003)

## Contents

### < Review >

* Methods of Estimating the Dustiness of Industrial Powders – A Review	<i>F. Hamelmann and E. Schmidt</i> ..... 7
* Properties of Filter Cake in Cake Filtration and Membrane Filtration	<i>E. Iritani</i> ..... 19

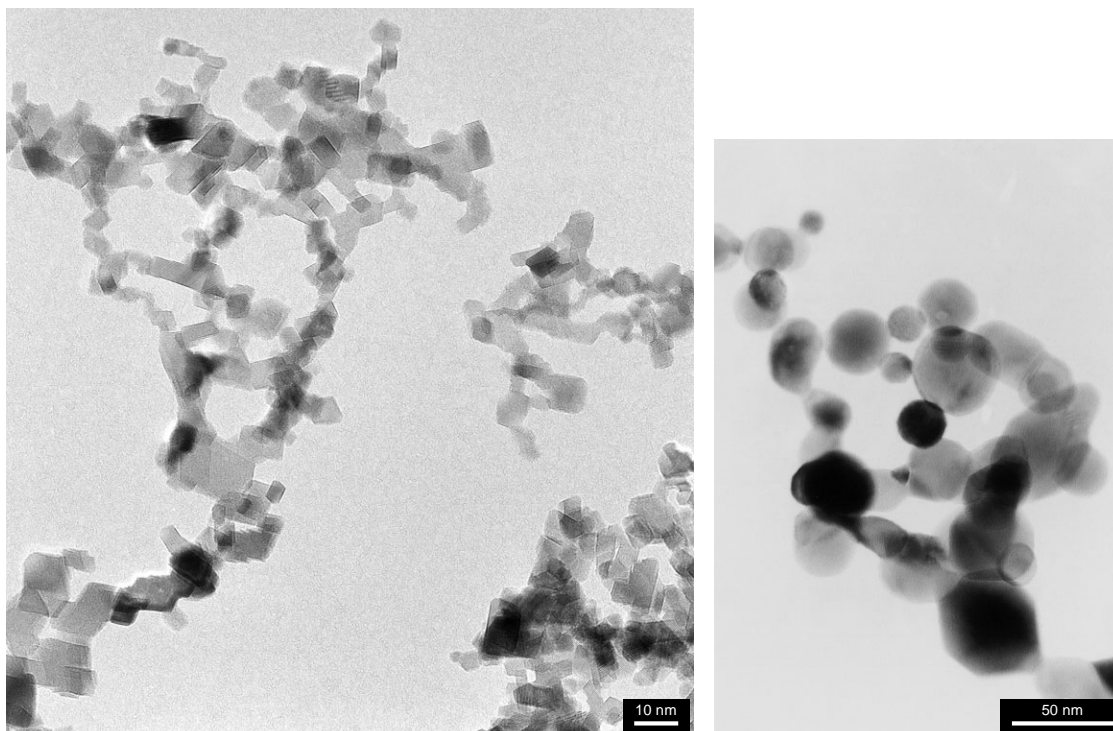
### < Original Research Paper >

* Developments in the Understanding and Modeling of the Agglomeration of Suspended Crystals in Crystallization from Solutions	<i>R. David, F. Espitalier, A. Cameirão</i> ..... 40 <i>and L. Rouleau</i>
* Aggregative Behavior of Cohesive Magnesium Carbonate Powders during Fluidization and Aerated Discharge	<i>G. Donsì, G. Ferrari, M. Poletto</i> ..... 54 <i>and P. Russo</i>
* Experimental Analysis of the Fluidization Process of Binary Mixtures of Solids	<i>B. Formisani and R. Girimonte</i> ..... 66
* Mechanochemical Grinding of Inorganic Oxides	<i>G.R. Karagedov and N.Z. Lyakhov</i> ..... 76
* Particle Impact Breakage in Particulate Processing	<i>A.D. Salman, G.K. Reynolds</i> ..... 88 <i>and M.J. Hounslow</i>
* Modelling of the gas fluidization of a mixture of cohesive and cohesionless particles by a combined continuum and discrete model	<i>B.H. Xu</i> ..... 100
* Modelling of Grinding in an Air Classifier Mill Based on a Fundamental Material Function	<i>L. Vogel and W. Peukert</i> ..... 109
* Modeling Breakage Kinetics in Various Dry Comminution Systems	<i>D.W. Fuerstenau, P.C. Kapur</i> ..... 121 <i>and A. De</i>
* Persistence of Granular Structure during Compaction Processes	<i>W.J. Walker</i> ..... 133
* Characterization of a Nanosized Iron Powder by Comparative Methods	<i>L.J. Kecskes, R.H. Woodman,</i> ..... 143 <i>S.F. Trevino, B.R. Klotz, S.G. Hirsch</i> <i>and B.L. Gersten</i>
* Development and Validation of a Constitutive Model for Size-Segregation during Percolation	<i>S.P. Duffy and V.M. Puri</i> ..... 151
* Vapor-Phase Synthesis of Fine Ag Powder and its Application to the Production of Fine Grained Sintered Ag-C Compacts	<i>H. Toku, O.W. Bender, A.C. Doring,</i> ..... 163 <i>A.C. da Cruz, P.K. Kiyohara</i> <i>and A.L. Silva</i>
* Slurry Design for Chemical Mechanical Polishing	<i>G.B. Basim and B.M. Moudgil</i> ..... 178

< **Translated Research Paper** >

* Separation of Automobile Shredder Residue by Gravity Separation Using a Gas-Solid Fluidized Bed	<i>J. Oshitani, T. Kajiwara, ..... 185</i> <i>K. Kiyoshima and Z. Tanaka</i>
* Feedback Control of Electrification in Powder Pneumatic Conveying Process	<i>S. Watano, S. Saito and T. Suzuki ..... 195</i>
* Improved Coal Pulverization Method Using the Embrittlement due to Cracks Generated in Pores of Coal	<i>T. Ono ..... 202</i>
* Particle Discharge Characteristics from the Nozzle of a Thin Tube Immersed in Liquid Subjected to Ultrasonic Wave Force	<i>K. Yamamoto, M. Shiokari, ..... 208</i> <i>T. Miyajima, M. Kawamura</i> <i>and M. Sugimoto</i>
* Sintering Mechanism of Two Spheres Forming a Homogeneous Solid Solubility Neck	<i>A. Shimosaka, Y. Ueda, ..... 219</i> <i>Y. Shirakawa and J. Hidaka</i>
* Mechanochemical Synthesis of Piezoelectric PLZT Powder	<i>K. Takagi, J.F. Li and R. Watanabe ..... 234</i>

# **Explanation of the Cover Photographs** **Nanoparticles of Cerium Dioxide and Lanthanum Strontium Manganite produced** **by Nano Particle Reactor**



The photographs show TEM images of cerium dioxide ( $\text{CeO}_2$ ) and lanthanum strontium manganite ( $\text{La}_{0.8}\text{Sr}_{0.2}\text{MnO}_3$ ) particles produced using a nano particle generator, named “Nano Particle Reactor (NPR)”.

The  $\text{CeO}_2$  particles are used for the three-way catalyst of car exhausts, Chemical-Mechanical Polishing (CMP) to treat semiconductor devices and various sensors. The  $\text{CeO}_2$  particles produced by NPR have single-nano size with an average particle size of 9 nm calculated from BET specific surface area. The single-nano sized particles are drawing much attention because of their high activity.

$\text{La}_{0.8}\text{Sr}_{0.2}\text{MnO}_3$  particles produced by NPR have a BET equivalent particle size of 63 nm. This material is used for the cathode of fuel cells.

NPR can produce various composite oxide nano particles including not only one element but also several kinds of elements in non-stoichiometric ratio.

# Methods of Estimating the Dustiness of Industrial Powders – A Review<sup>†</sup>

F. Hamelmann and E. Schmidt

Division of Safety Engineering/Environmental Protection, University of Wuppertal, Germany\*

## Abstract

*The industrial handling procedures for bulk materials, for example, to store, to convey, to mix, and to fill, etc. often lead to dust emissions. The generated dust is closely related to health hazards and environmental pollution, and is also a cause of fires and explosions. The particle size distribution and concentration determine the risks. The dust liberation property of disperse particle systems – so-called powders – depends on a multitude of variables and also on the method and intensity of stressing. The present paper describes practically all the dust measuring methods published in literature. It also presents related particle sizing and counting techniques and systematically summarises the integrated measurement methods.*

## 1. Introduction

The handling of materials, i.e. storing, conveying, filling, and mixing leads to dust liberation. This capability of generating dust is described as dustiness. Changing unit operations, including micro-encapsulations, masterbatches, and lost packages, have led to a reduced dustiness index of disperse goods [1, 2]. Because of necessary simplifications of the material stressing characteristics, the standardization of measurement methods did not prove suitable [3].

Two standardized methods for determining a dustiness index for pigments and fillers are described in DIN 55 992: the rotating drum apparatus and the single-drop dustiness apparatus [4]. To meet the requirements of occupational health, hygiene and safety, as well as those of fire and explosion prevention, the estimation of dustiness is becoming more and more important. Dustiness prevention by means of dustiness estimation even before a new method is installed or material is changed is the objective of process engineers et al. [5, 6]. One model for estimating the correlation between separation forces, binding forces and dustiness has been developed by Plinke [7]. Efforts are being made to develop standards for reproducible methods to achieve the dustiness index for bulk mate-

rials in context with occupational safety [8].

Excessively simple measurement methods fail because of two crucial reasons: On one hand, dustiness depends on the kind of stressing, i.e. the dustiness index during transfer can be below the index during mechanical stressing. And on the other hand, the special characteristics of the materials, for example the humidity, density, and morphology, differ over a wide range, turning the topic “dustiness” into an interdisciplinary subject including quality management for products, occupational safety, environmental protection, and fire and explosion prevention.

Consequently, one sole method will not be able to extensively simulate all important influences on dustiness capability. Many studies have proved the influence of inert powdery material on the human organism [9, 10]. Contact with these materials can lead to industrial diseases. According to Wichmann, particles < 1 µm have a particular effect on human health. Known occupational diseases are, for example, Byssinosis caused by cotton in the seed, the baker’s flour aversion, and metallic pneumoconiosis caused by the handling of metal (hard alloy or aluminum pneumoconiosis) [10-12].

The first studies on nano-sized particles and their increased importance showed significant effects on affected groups of persons based on correlations between emitted nano-sized particles during modern combustion processes and an increased number of allergy symptoms [10]. The studies also made evident

\* Rainer-Gruenter-Str. Geb. FF  
D-4211g Wuppertal

<sup>†</sup> Accepted: June, 2003



that nano-sized particles are emitted during most treatment processes [13].

Occupational safety as an example shows that the evaluation of the dustiness potential during the handling of disperse materials is of significant importance. If new materials are to be used, the expected dustiness will be an important judgment criterion.

## 2. Aims and requirements

The currently increased interest in dustiness estimation is based on the involved fields of occupational safety, health, hygiene, and fire and explosion prevention. The reduction of the airborne dust load as early as the planning phase of manufacturing processes through improved estimation models is the principal goal [5, 6]. This enables the reduction of secondary measures such as extraction systems, provided the technical requirements of the products are no obstacle.

Due to the integration nature of the total dust method, conclusions about particle size distribution are impossible. More appropriate methods will permit conclusions about particle size distribution. Corresponding requirements are, for example, standardized in DIN EN 481 [14], which classifies inhaled particles into 3 categories.

The penetration depth depends on the particles' aerodynamic diameter. **Fig. 1** displays the classifica-

tion of aerosols in the respiratory system, according to occupational health criteria.

The characteristics of materials, especially the physical ones, are often of increased interest. They are related to the dwell time of the particles in the air and their correlated particle mobility. Increasing particle mobility leads to a higher contamination risk.

The correlation between material stressing and the amount of emitted dust must be retraced by the measurement methods. Basically, the acceptance of the methods is increased through simple handling and high reliability. Additionally important for the economic aspects are versatility in use, easy handling, fast and reliable results, and easy cleaning. High efficiency leads to lower costs [16].

## 3. Historical methods of dustiness measurement

In the face of the variety of methods used for measuring the dustiness capacity of materials, the choice of appropriate apparatus is difficult.

Basic factors of choice are comparability to field conditions and the kind of output data (loaded filter or displayed results).

The comparability of results of different methods is often difficult because of the different time and kind of stressing, as well as the means of evaluation and sampling. By using modern particle measurement techniques, conclusions about the particle size fraction are possible.

Early studies were made in 1922. Andreassen et al. [17], for example, investigated the dustiness of 24 sample substances by using a single-drop apparatus (**Fig. 2**). Additionally, they described the influence of small particles on particle collectives and their capability of generating dust. Andreassen used a device consisting of a modular-design dust chamber and two fitted and sealed falling tubes. An iris is used as the shutter. The sample is placed on the iris and covered by a flat-turned tray to seal the sample against the influence of ambient air. Six metal slides are inserted successively from bottom to top into the dust chamber after the sample has been dropped.

The time interval of insertion is defined by a metronome. After the test, the slides are weighed. The height of the falling tube has not been documented.

ANSI/ATSM D547-41 standardized a modified method to investigate the index of dustiness of coal and coke. The initial method has been known since 1939 [18]. This method also uses the single-drop dustiness technique (**Fig. 3**). The dust chamber is

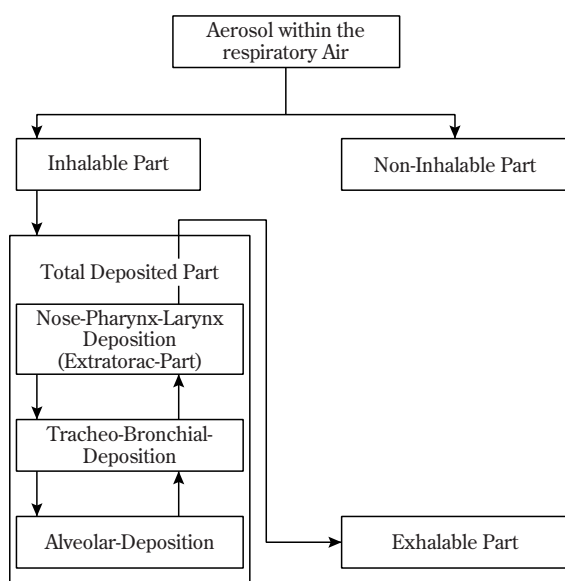


**Fig. 1** Classification of airborne aerosols according to occupational health criteria [15].

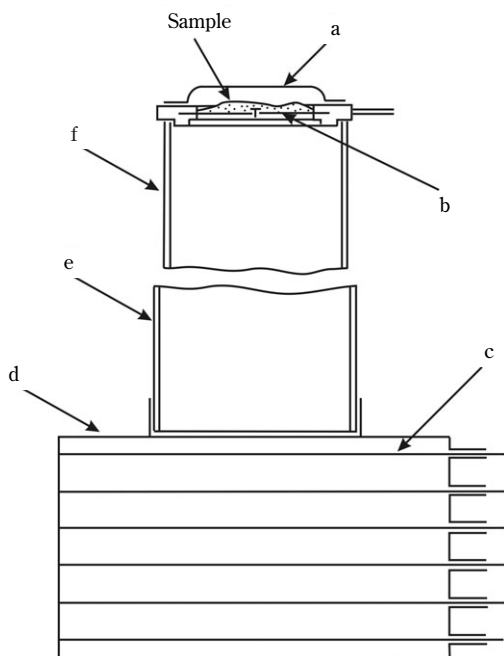


**Fig. 2** Single-drop dustiness apparatus used by Andreason. [17]  
a. cover, b. iris, c. slides, d. modular casing, e. falling tube part 1, f. falling tube part 2

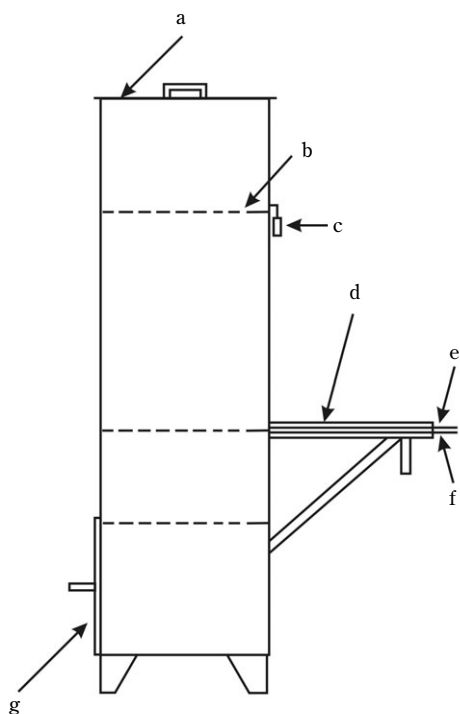


**Fig. 3** ANSI/ATSM D547-41 [18] standardized device to investigate the dustiness index of coal and coke, a. cover, b. upper slide (sample to be tested), c. stop watch, d. guides, e. slide for coarse dust, e. slide for float dust, f. drawer

sealed after the sample (22.7 kg) has been placed on the inserted upper slide. After drawing out the upper slide abruptly, the sample drops into the bottom drawer. Exactly 5 s later, both lower slides are inserted quickly. The top slide is pulled out after two minutes, the lower slide after 10 minutes. By weighing the two slides, a dust index is generated for coarse and float dust.

## 4. Characterization of airborne dust

### 4.1. Filter samplers

Filter samplers consisting of filter housing and filter are used as a standard measurement method. The whole airborne dust is collected in the filter, whereas conclusions about the particle size distribution are only possible by means of further measurement.

Fractional sampling units are used for the fields of occupational health and safety to deposit inhalable and respirable dust fractions [19]. With the aid of these techniques, non-conformity during further measurement can be avoided.

### 4.2. Foams

Metal and polymer foams with defined pore sizes are used alternatively [20]. The results are in accordance with the demands of DIN EN 481 (Fig. 4).

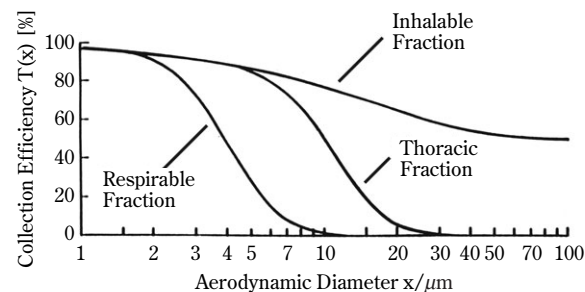


**Fig. 4** Classification of inhalable aerosols into health-related fractions according to DIN EN 481

### 4.3. Impactors

Impactors are often used to fractionally measure the dustiness. They can easily replace filter samplers in the test apparatus. Impactors can measure only low particle concentrations. Therefore the dust-laden air has to be diluted. The air velocity at the inlet has to be adequate to prevent particle sedimentation. Other-

wise, the particle size distribution alters. This problem is solved by isokinetic sampling combined with dilution. The disadvantage of this method is difficult handling, and time-consuming measurement and cleaning [20].

#### 4.4. Elutriators

These are rarely used units. Particle-laden air flows between several parallel plates. The distance between the plates and the air velocity define the deposited particle fraction [20].

#### 4.5. Optical measurement methods

These methods are commonly used in single-drop dustiness units. The dust concentration in the chamber is assessed by reducing the intensity of a laser beam. Additionally, some devices are able to analyse particle size distribution [16, 21].

Alternatively, counted particles can be assigned to equivalent defined particle sizes by analysing scattered light signals. This method is only able to handle low particle concentrations, causing inaccurate results and more difficult handling.

Easy handling, short cleaning periods and, in particular, the ability to draw mass-correlated conclusions, are the advantages of this method.

#### 4.6. Further methods

Due to the increasing importance of nano-sized particles, further studies in this field are absolutely necessary, thus requiring special techniques. During earlier studies, TEOM systems proved reliable. The implementation of otherwise approved methods such as SMPS or APS systems needs to be studied extensively (acronyms are explained in chapter 8).

### 5. Apparatus for measuring dustiness of disperse powders

#### 5.1. Single-drop dustiness apparatus

Usually, single-drop dustiness apparatus consists of a dust chamber and a falling tube sealed off with a shutter, as shown in **Fig. 5**. The sample is poured into the funnel above the falling tube. By opening the shutter briefly, the sample falls through the falling tube into the dust chamber and drops onto the bottom, thus generating dust. The dust concentration is assessed by the reduction of intensity of a laser beam. The reduction opacity is transformed into the dust index [22-43].

This concept using a dust chamber is not the only one: The method according to DIN 55992 [4] as-

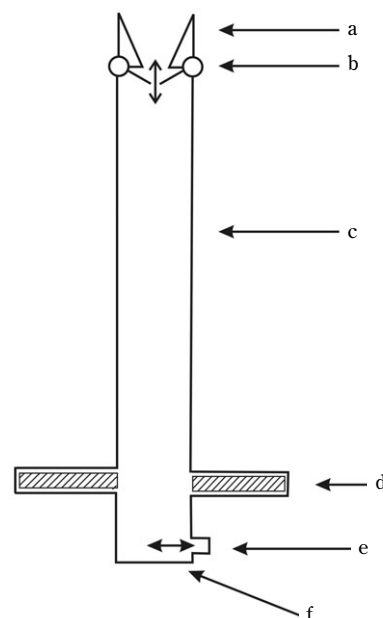


**Fig. 5** DIN 55992-2 [4] standardized single-drop dustiness apparatus to generate a dustiness index of fillers and pigments, a. funnel, b. shutter, c. falling tube, d. laser and detector, e. suction connector, f. base plate with ejector

sesses the dust index inside the falling tube itself. Another device marketed commercially in England draws the generated dust onto a filter [23]. In this case, the shutter is open to prevent low atmospheric pressure in the dust chamber. Single-drop dustiness units are laboratory devices which bring fast and reliable results. The measured dustiness index is usually below those assessed by other methods [23].

Due to low mechanical stressing of the sample, it can be assumed that the sample does not alter [20]. On the assumption that the particle movement during sedimentation has reached a steady state, a statement about the particle size distribution is possible.

The height of drop varies between 0.5 m and 1 m, some special devices going up to 3 m [24]. The sample mass varies between 5 g and 3 kg, usually between 30 g and 100 g. In most cases, the sample is dropped suddenly in one load, whereas in some special devices it is a continuous process, for example, by means of a conveyor belt.

For a single-drop dustiness apparatus, the variation of the results during one sample row is higher than with other methods [23].

During gravimetric measurement the amount of total dust is one possible result. Adjusted techniques allow conclusions to be made about certain fractions.

Optical measurement techniques enable the determination of the dustiness index function, allowing the reduction of airborne dust to be plotted over time in a graph and thus conclusions to be drawn about the particle size. The arrangement of measurement units has a considerable influence on the results. Higher values are to be expected if the light shines through the falling stream. By positioning the light beam to the side of the falling stream, only the generated dust is counted [26].

This measurement device has the advantage of easy handling, simple construction and fast measurement. Easy and fast cleaning, short time preparation for further tests, and self-clean fittings [16] are also an advantage.

### 5.2. Rotating drum apparatus

The stressing of the sample in the air-flow drum is similar to that of various rotating drum methods [44-63]. Dust generated from the sample is transferred to a measurement unit and collected by a filter or directly analysed. Lifter bars inside the drum prevent the sample from getting stuck on the drum. Filters, impactors and optical particle counters are used as measurement units. It must be taken into account that the air flow velocity is a determining factor for the particle size distribution and particle concentration. **Fig. 6** shows a typical test apparatus.

Related to the pressure ratio in the drum, two techniques can be distinguished, one with overpressure and the other below atmospheric pressure.

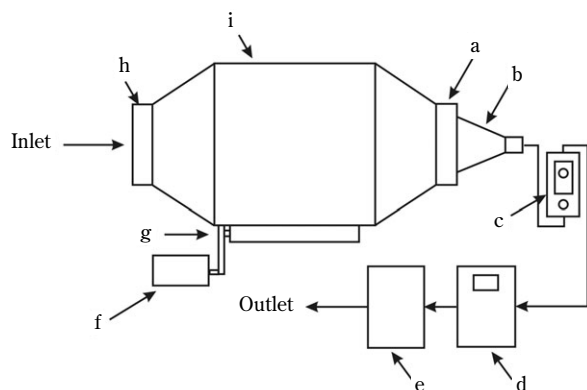


**Fig. 6** The Warren Spring Laboratory, U.K. [23] rotating drum tester, a. outlet, b. sampling unit, c. rotameter and air-flow controller, d. gauge, e. pump, f. drive motor, g. driven roller, h. inlet, i. drum

### 5.3. Inverse-flow drop apparatus

By charging the sample over a longer period of time, this method simulates continuous transfer [64, 74]. Sample transfer is possible via conveyor belt [64] or conveyor worm [65].

The MRI Tester [45] charges the sample by means of a tiltable beaker (**Fig. 7**). The filled beaker is tilted continuously, the sample drops from a height of 25 cm onto the aluminum-foil-covered foam pad of the dust chamber. The generated dust is transported by an air stream that enters the tester through two side baffles and exits it to the top. During this process, larger particles are sifted out due to their higher settling velocity. Depending on the aim of research, a filter or an impactor is used. The use of optical measurement units is not known in scientific literature. The smallest possible settling particle is defined by the air velocity.

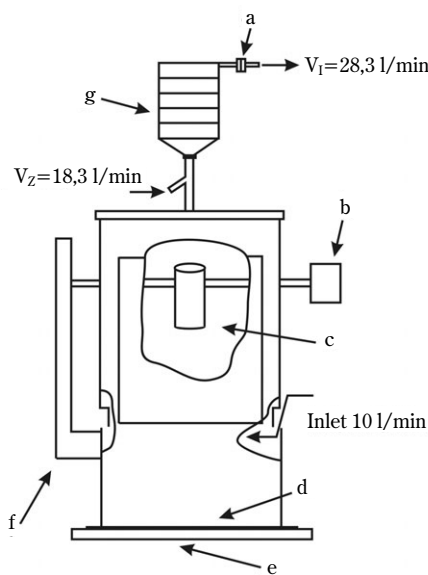


**Fig. 7** "MRI-Tester" developed by C. Cowherd [69], a. filter, b. vibrator, c. beaker, d. aluminum foil, e. foam pad, f. beaker rotating mechanism, g. impactor

### 5.4. Gas fluidization dustiness tester

The fourth class of method for testing dustiness, as schematically shown in **Fig. 8**, applies a gas fluidization dustiness tester [75, 77]. This device often consists of a vertical stainless steel cylinder and glass modules. The sample is placed onto the sintered plate



at the lower end of the tester, where it is continuously subjected to an upward air stream. Cohesive material needs an agent in order to perform homogeneous fluidization. Sand was chosen as the agent to perform a homogeneous fluidization [76].

Particles with a low settling velocity are carried to the upper outlet by an air stream. They are collected by a filter [3], measured by an optical particle counter, or analysed by a TEOM. Due to the high energy input, agglomerates or pellets are destroyed.

Therefore, gas fluidization dustiness testers are the most stressing class of method for dustiness tests. Due to collisions, inter-particle bonds between test materials are destroyed. This intensive stressing of the sample permits conclusions to be made about the ability of generating dust for only a limited range of application.

Additionally, the dustiness of a material depends on material properties such as the density of material, the form, and the particle size distribution [3, 78]. The dust index increases as the median diameter decreases, as stated in the Sethi investigation [75, 76], contradicting the model of Plinke [7].

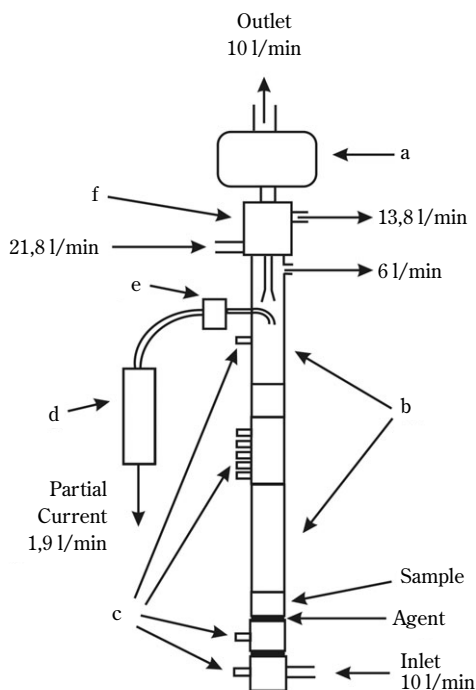


**Fig. 8** Gas fluidization tester designed by Sethi and Schneider [75,76], generated data of PM 1, PM 2.5, PM 10 by TEOM, a. optical particle counter, b. glass module, c. pressure measurement taps, d. TEOM, e. cyclone, f. diluter

## 5.5. Resuspension chamber

Visser [79, 80] studied the influence of air velocity and air humidity on coal by means of a resuspension chamber. The experimental set-up consisted of a conveyor belt, a rectangular wind tunnel and filter samplers (**Fig. 9**). The conveyor belt is positioned horizontally at 90 degrees to the main air stream.

The coal layer (0.08 m) is continuously supplied by the conveyor belt and dropped through the air stream into a container underneath the wind tunnel. The grille separating the container from the wind tunnel prevents the re-entry of dumped coal. A thin coal stream is dispersed by the air stream in the wind tunnel, the dust concentrations being measured downstream.

Nine equidistant squarely positioned samplers are installed downstream. While horizontal in-line samplers showed approximately equal dust concentration, vertical in-line samplers detected different concentrations. To permit visual evaluation, the tunnel consists of glass modules.

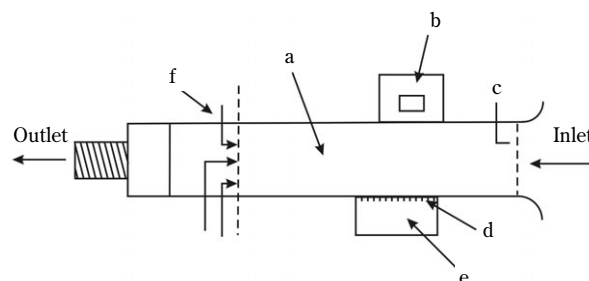


**Fig. 9** Visser used a resuspension chamber [79], a. wind funnel, b. covered conveyor belt, c. pitot tube, d. grille, e. dustiness chamber, f. sampler

## 5.6. Special designs

The methods of this group cannot be assigned definitively to any one of the preceding groups. Some of them are genuine special designs, others are combinations of preceding methods [81-84].

With the aid of two examples, these methods are described in greater detail. The method developed by the "Getreideforschungsinstitut Potsdam" characterizes the dustiness of flour and bread improvers. Especially in the baker's trade, these dusts are responsible for most occupational diseases.

The device used is placed on a base plate (2.5 m × 1 m), which is surrounded by 3 glass wall elements (height: 0.6 m). The device is not covered.

The gas-particle mixture is generated by a dust disperser. The dust disperser is positioned at the open

end of the device. The gas-particle mixture is injected at a height of 400 mm above the base plate. At a distance of 1.3 m from the dust disperser, samplers for respirable and inhalable fractions are installed which collect dust simultaneously, as shown in **Fig. 10** [82].

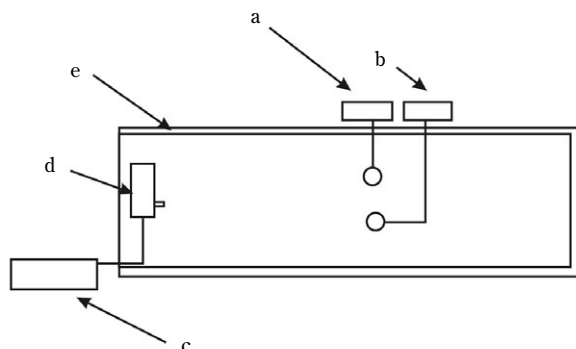


**Fig. 10** The dustiness tunnel [82] suggested in DIN 33897-3 a. sampler for inhalable dust fraction, b. sampler for respirable dust fraction, c. compressor, d. disperser, e. dust tunnel

In the course of a European research project, a combination of a single-drop dustiness apparatus and a rotating drum was developed [20]. This device consists of a two-part drum connected to the opposite sides of the chamber of a single-drop device (**Fig. 11**).

Due to the modular system, the device can be used

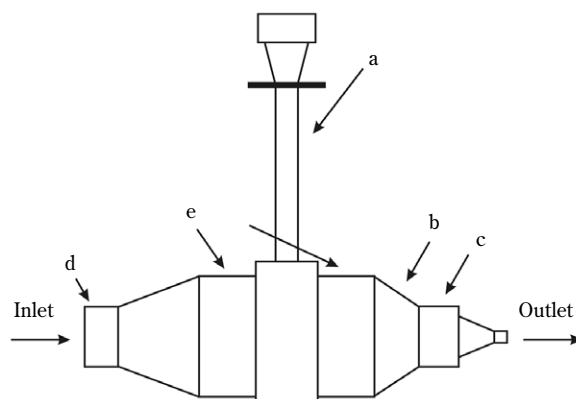


**Fig. 11** Combined HSL single-drop tester on the HSE/WSL MK2 rotating drum apparatus [20], a. falling tube with fitted funnel, b. outlet, c. sampling point, d. inlet, e. divided drum

as a single-drop tester, a rotating drum tester and as a combination of both. Both devices are proven designs. The inlet and outlet cones of the HSE/WSL MK2 [3] are modified in order to assure laminar flow.

The cone-shaped outlet causes the dust-laden air to accelerate up to 4 cm/s. At the outlet, a measurement unit is installed. The measurement unit consist of two porous polyurethane foams and one filter.

This unit leads to sampling according to DIN EN 481 [14]. The drop unit was developed to be similar to the Roaches dustiness drop tester [25]. This combination allows simulations of varying kinds of stressing, for example conveying or filling. Polyurethane foams are sensitive to moisture. Therefore, monitoring of the humidity is necessary [20].

## 6. Dustiness measurement systematics

The multitude of introduced methods and the possibility of combining them demonstrate the complexity involved in selecting an appropriate method for dustiness measurement.

Many manufacturers of powders and bulk materials as well as institutes use their own measurement methods. The results of those methods are not comparable or cannot be compared easily. Various fields of application do not allow a uniform apparatus.

For the future development of materials with reduced dustiness behavior, improved methods of simulation will be necessary, whereby the interaction of particulate matter and dustiness estimation needs to be investigated to counter dust generation. **Figure 12** displays a systematics about the methods used and their combinations.

In principle, a dustiness measurement of powders is subdivided into four areas: sample application, sample stressing, sampling, and analysis.

In the first three areas, the procedure can be discontinuous (e.g. single drop), continuous (e.g. continuous drop), and intermittent (e.g. periodic drop).

The selection depends on the kind of powder stressing, the amount of liberated dust and the dust fraction of interest.

To systematize all the methods needs more than a plain list. These methods can be summarized, e.g. by the kind of stressing, as done in this article, but it will not be of general use. This special kind of gradation does not permit reliable conclusions about the measurement units used such as impactors, filters, or TEOM [19, 55, 78, 85-101]. A useful systematic scheme of all methods (including all combinations and permutations) is still under construction.

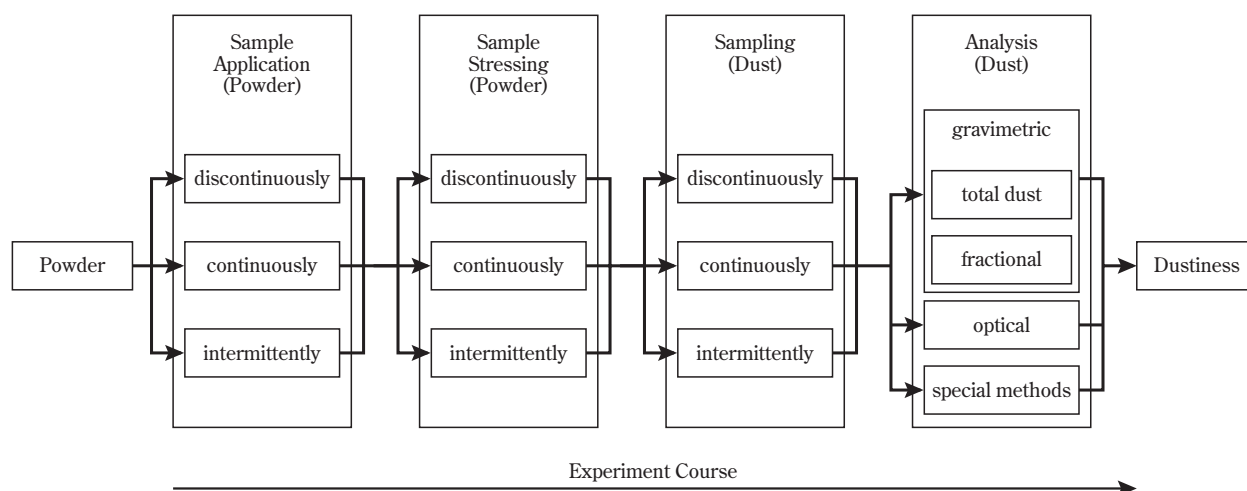


**Fig. 12** Systematics to classify apparatus for the determination of the dustiness of powders.

## 7. Conclusions

The present discussion on adequate measures to permit meeting the dust limits for workplaces was initiated by the realization of the harmful effects of dust as well as by the legal definitions for inhalable and respirable particles.

Initial monitoring of the building industry made it evident that about 40% of the samples taken were far above legal limits [15].

Although meeting the legal limits is sometimes hardly possible, further reduction of the limits is necessary in order to meet the requirements of occupational health. This causes a contradiction in terms. This conflict proves the importance of preventative measures against dust generation. The estimation of dustiness is directly correlated to these preventative measures.

Current methods permit the amount of liberated dust to be estimated. But it is impossible to prove direct correlations between the dustiness indices assessed during different kinds of stressing. The comparability of results of different methods is hardly possible. As a conclusion, it does not seem sensible to aim at one standardized method.

The future development of low-dustiness materials demands research on other characteristics. While the influence of the moisture content on dust generation has been scrutinized, other properties such as particle density and shape have not been considered sufficiently.

These stated problems will serve as a basis for future research.

## 8. Explanations

Masterbatch	For example, a coloring agent concentrate is called a masterbatch in granular, paste or liquid form to ink a natural-colored granulate.
Lost packages	A hazardous material added to the application by closed packing [102].
Inhalable dust	Inhalable dust fraction according to DIN EN 481 [102]
Respirable dust	Respirable dust fraction according to DIN EN 481 [102]
SMPS	A <u>S</u> canning <u>M</u> obility <u>P</u> article <u>S</u> izer measures particles with a mobility diameter from 3 to 1000 nm.
TEOM	A <u>T</u> apered <u>E</u> lement <u>O</u> scillating <u>M</u> icrobalance measures particle concentrations according to PM-10, PM-2.5, PM-1 and TSP in real time.
APS	An <u>A</u> erodynamic <u>P</u> article <u>S</u> izer is used to study particles with an aerodynamic diameter from 0.37 to 20 $\mu\text{m}$ in real time.
TSP PM	<u>T</u> otal <u>S</u> suspended <u>P</u> articulate Matter Particulate Matter

## 9. Literature

- [1] Eickelpasch, D.: Methodik zur Bestimmung diffuser Staubemissionen beim Schüttgutumschlag, Dissertation, Universität Dortmund, 1996.
- [2] Meyer, F., Eickelpasch, D.: Konstruktionsmethodik für minimale freie Oberflächen bei Verarbeitung,

- Transport und Lagerung von Schüttgütern, Forschungsbericht 832 der Bundesanstalt für Arbeitsschutz und Arbeitsmedizin, Dortmund, Berlin, **1999**.
- [3] Dustiness Estimation Methods for Dry Materials, British Occupational Hygiene Society, Technical Guide, No. 4, **1985**.
  - [4] DIN 55992, Bestimmung einer Maßzahl für die Staubentwicklung von Pigmenten und Füllstoffen, Beuth Verlag, Berlin, Teil 1: Rotationsverfahren, 1996, Teil 2: Fallmethode, **1999**.
  - [5] Blome, H.: Umgang mit partikelförmigen Schadstoffen, Sichere Arbeit, **2001**, 01, 19.
  - [6] Barig, A., Blome, H.: Allgemeiner Staubgrenzwert, Gefahrstoffe – Reinhaltung der Luft, **2002**, 62(1, 2), 37.
  - [7] Plinke, M.: Vorhersage der Staubentstehung bei der industriellen Handhabung von Pulvern, Fortschrittsberichte VDI, Reihe 3, Nr. 398, VDI-Verlag, Düsseldorf, **1995**.
  - [8] E DIN 33897-1, Arbeitsplatzatmosphäre – Bestimmung des Staubungsverhaltens, Teil 1: Grundsätze, Beuth Verlag, Berlin, **2002**.
  - [9] Vedral, P.C.: Health effects of inhalable Particles: Implications for British Columbia – Overview and Conclusions, <http://www.goc.bc.ca/air/particulates/heoipifb.html#2>, Vancouver, BC, **1985**.
  - [10] Wichmann, H.E. et al.: Gesundheitliche Wirkungen von Feinstaub, Fortschritte in der Umweltmedizin, Ecomed-Verlag, Landsberg/Lech, **2002**.
  - [11] Breum, N.O., Nielsen, E.M.: Dust content of cotton – quality control in terms of airborne dust and endotoxins: a pilot study, Gefahrstoffe – Reinhaltung der Luft, **1996**, 56(10), 389.
  - [12] Kniel, B. et al.: Bestimmung des Staubfreisetzungsvermögens pulverförmiger Schüttgüter für die Bäckerei, Getreide Mehl und Brot, **2001**, 55(6), 349.
  - [13] Riediger, G., Möhlmann, C.: Ultrafeine Aerosole an Arbeitsplätzen, Gefahrstoffe – Reinhaltung der Luft, **2001**, 61(10), 429.
  - [14] DIN EN 481, Festlegung der Teilchengrößenverteilung zur Messung luftgetragener Partikel, Beuth Verlag, Berlin, **1993**.
  - [15] Karsten, H., Schneider, W.: Möglichkeiten des technischen Arbeitsschutzes und der arbeitsmedizinischen Prävention bei Staubbelastung, Sicher ist Sicher, **2002**, 53(3), 100.
  - [16] Schünemann, J.W.: Den Staub in den Griff bekommen, Schüttgut, **1997**, 3(3), 323.
  - [17] Andreasen, A.H.M. et al.: Über das Staubungsvermögen der Stoffe, Kolloid-Zeitschrift, **1939**, 86(1), 70.
  - [18] ANSI/ASTM D 547-41 Standard Test Method for INDEX OF DUSTINESS OF COAL AND COKE (Reapproved **1980**).
  - [19] Storm, P.C.: Umweltrecht, Beck-Texte im dtv, **2002**, 14.
  - [20] Development of a Method for Dustiness Testing, Final Report, SMT4-CT96-2074, **2000**.
  - [21] Bürkholz, A.: Ein Verfahren zur Messung der Staubungsfähigkeit von pulverförmigen Produkten, Staub – Reinhaltung der Luft, **1989**, 49, 433.
  - [22] Hjemsted, K.: An Investigation of Dustiness with a Rotating Drum Method, PhD Thesis, University of Copenhagen, **1996**.
  - [23] Lyons, C.P., Mark, D.: An Evaluation of the Roaches Dust Particle Apparatus Dustiness Testing Equipment, HSE Contract, Research Report No. 40, **1992**.
  - [24] Trenker, C., Höflinger, W.: Entwicklung einer neuen Laborapparatur zur partikelgrößenabhängigen Messung diffuser Staubemissionen beim Schüttgutabwurf, Chem. Technik, **1999**, 51(5), 304.
  - [25] Dust Particle Analysis <http://www.roaches.co.uk/products/products.htm>, **2001**.
  - [26] BASF, Vorrichtung zur Bestimmung des Staubungsverhaltens von Substanzen, Deutsches Patentamt DE 296 18 510 U 1, **1996**.
  - [27] Jahresbericht, Institut für Verfahrens-, Brennstoff- und Umwelttechnik der TU Wien, **1999**.
  - [28] Trenker, C., Höflinger, W.: Experimentelle Untersuchung des Fallverhaltens von Schüttgütern mittels Laser-Doppler-Anemometrie, unveröffentlicht.
  - [29] Pieper, H.: Ein Verfahren zur Beurteilung der Staubentwicklung beim Umschlag von Schüttgütern, Staub – Reinhaltung der Luft, **1995**, 55, 25.
  - [30] Spivey, A.M.: Reduction of Dust in working Atmospheres by the use of improved Product Forms of Rubber Chemicals, Plastics and Rubber Processing and Applications, **1989**, 1, 201.
  - [31] Cooper, P., Arnold, C.: Air Entrainment and Dust Generation from a Falling Stream of Bulk Material, Kona, **1995**, 13, 125.
  - [32] Wells, A.B., Alexander, D.J.: A Method for Estimating the Dust Yield of Powders, Powder Technology, **1978**, 19, 271.
  - [33] Lundgren, D.A.: A Measurement Technique to Quantitate Fugitive Dust Emission from Handling of Granular Products, J. Aerosol Sci., **1986**, 17, 632.
  - [34] Herbener, R.: Staubarme Pulver durch Sprühtrocknen – Erfahrungen mit neueren Techniken, Chem.-Ing.-Tech., **1987**, 59, 112.
  - [35] Davies, K.M. et al.: Progress in Dustiness Estimation, Ann. occup. Hyg., **1988**, 32, 535.
  - [36] Heitbrink, W.A. et al.: An Investigation of Dust Generation by Free Falling Powders, AM. IND. HYG. ASSOC. J., **1992**, 53, 617.
  - [37] Vogl, A.: Verfahren zur Bestimmung der Staubungsneigung von Schüttgütern, Firmenschrift der FSA, **2001**.
  - [38] Authier-Martin, M.: Alumina Handling Dustiness, Edited by Paul G. Campbell, Light Metals, **1989**, 103.
  - [39] Hsieh, H.P.: Measurement of Flowability and Dustiness of Alumina, Proceedings of Sessions, American Institute of Mining, Metallurgical and Petroleum Engineers Annual Meeting, Light Metals, **1987**; Warrendale, PA, Metallurgical Society of AIME, **1989**, 139.
  - [40] Seewald, H. et al.: II. Kleintechnische Versuche zur



- Bestimmung des Einflusses von Zusatzmitteln zum Wasser auf die Staubentwicklung, Silikosebericht Nordrhein- Westfalen, **1981**, 12, 116.
- [41] Higman, R.W., Schofield, C., Taylor, M.: Bulk Materials Dustiness, an Important Material Property – Its Measurement and Control, 4th International Environment and Safety Conference, Barbican Centre London, **1984**.
- [42] Hammond, C.M.: Dust Control Concepts in Chemical Handling and Weighing, Ann. occup. Hyg., **1980**, 23, 95.
- [43] Chambers, A.J.: Assessment of Alumina Dustiness, Powder Handling & Processing, **1992**, 4(1), 47.
- [44] Chung, K.Y.K., Brammer, J., Chalmers, C.P.: Effects of Relative Humidity and Electrostatic Charge on the Dustiness of Powdery Material, International Symposium Toulouse (France), **2001**, 34.
- [45] Plinke, M. et al.: Experimental Examination of Factors that affect Dust Generation by using Heubach and MRI Testers, Am. Ind. Hyg. Assoc., **1992**, 53, 325.
- [46] Lyons, C.P., Mark, D.: Development and Testing of a Procedure to Evaluate the Dustiness of Powders and Dusts in Industrial Use, HSE Contract Research Report No. 62, **1994**.
- [47] Lyons, C.P. et al.: Further Development and Testing of the HSL/WSL Health-Related Dustiness Tester, HSE Contract Research Report No. 103, **1996**.
- [48] Upton, S.L., Hall, D.J., Marsland, G.W.: Some Experiments on Material Dustiness, Aerosol Society Annual Conference, University of Surrey, Guildford, Surrey, UK, **1990**.
- [49] Selck, S.: Die Entwicklung und Erprobung eines Laborverfahrens zur Bestimmung des Staubungsverhaltens von Schüttgütern, Diplomarbeit, Fachhochschule Bochum, **2000**.
- [50] Armbruster, L., Selck, S.: Neue Wirtschaft: NRW, Ergebnisse von Untersuchungen auf dem Gebiet der Staub- und Silikosebekämpfung im Steinkohlenbergbau für die Jahre 1997-1999, **2001**, 21.
- [51] Lyons, C.P., Mark, D., Chung, K.Y.K., Burdett, G.: The Application of Health-Related Size Fractions to Dustiness Measurement, J. Aerosol Sci., **1992**, 23(1), 607.
- [52] Westborg, S., Cortson, C.E.: Determination of Dustiness of Coal by the Rotating Drum Method, Journal of Coal Quality, **1990**, 9(3), 77.
- [53] Farrugia, T.R., Ahmed, N., Jameson, G.J.: A new Technique for Measuring Dustiness of Coal, Journal of Coal Quality, **1989**, 8(2), 51.
- [54] Breum, N.O., Schneider, T.: Rotating Drum Methods for Dustiness Testing of Materials, Gefahrstoffe – Reinhaltung der Luft, **2001**, 61(4), 155.
- [55] Kniel, B., Moser, M.A., Groebler, C.: Bestimmung des Staubbefreiungsvermögens pulverförmiger Schüttgüter für die Bäckerei, Getreide Mehl und Brot, **2001**, 55(6), 349.
- [56] Breum, N.O., Nielsen, E.M.: Dust content of cotton – quality control in terms of airborne dust and endotoxin: a pilot study, Gefahrstoffe – Reinhaltung der Luft, **1996**, 56, 389.
- [57] Breum, N.O.: The Rotating Drum Dustiness Tester: Variability in Dustiness in Relation to Sample Mass, Testing Time, and Surface Adhesion, Ann. occup. Hyg., **1999**, 43(8), 557.
- [58] Heitbrink, W.A.: Factors Affecting the Heubach and MRI Dustiness Tests, Am. Ind. Hyg. Assoc. J., **1990**, 51(4), 210.
- [59] Heitbrink, W.A., Todd, W.F., Cooper, T.C., O'Brien, D.M.: The Application of Dustiness Tests to the Prediction of Worker Dust Exposure, Am. Ind. Hyg. Assoc. J., **1990**, 51(4), 217.
- [60] Chung, K.Y.K., Burdett, G.J., Mark, D., Lyons, C.P.: Further Development and Testing of a Health-Related Dustiness Tester, World Congress on Particle Technology 3, **1998**.
- [61] Heitbrink, W.A., Todd, W.F., Fischbach, T.J.: Correlation of Tests for Material Dustiness with Worker Exposure from the Bagging of Powders, Appl. Ind. Hyg., **1998**, 4(1), 12.
- [62] Groebler, C.: Examination about Dust Generation of Powdery Bulk Goods in Bakeries and Determination of the Alpha-Amylase-Activity in Dusts Thereof, Diplomarbeit, Landwirtschaftliche Fakultät der Rheinischen Friedrich-Wilhelms-Universität, Bonn, **2001**.
- [63] Stauber, D., Beutel, R.: Determination and Control of the Dusting Potential of Feed Premixes, Fresenius Z Anal Chem, **1984**, 318, 522.
- [64] Plinke, M. et al.: Experimental Examination of Factors that Affect Dust Generation, Am. Ind. Hyg. Assoc. J., **1991**, 52, 521.
- [65] Dahmann, D., Hartfiel, G.-D., Möcklinghoff, K.: Ein Verfahren zur wirklichkeitsnahen Bestimmung der Staubungsneigung von Schüttgütern, Gefahrstoffe – Reinhaltung der Luft, **1997**, 57, 503.
- [66] IGF, Institut für Gefahrstoff-Forschung, Die Staubungsneigung von Schüttgütern wirklichkeitsnah ermitteln mit dem IGF – Gegenstrom – Fallrohr CDD (Continuous Drop Dust Pipe), Mitteilung von der A+A, Düsseldorf, **2001**.
- [67] Dahmann, D., Möcklinghoff, K.: Das Staubungsverhalten quarzfeinstaubhaltiger Produkte, Gefahrstoffe – Reinhaltung der Luft, **2000**, 60(5), 213.
- [68] E DIN 33897-2 Arbeitsplatzatmosphäre – Bestimmung des Staubungsverhaltens Teil 2: Kontinuierlicher Fall im Gegenstrom, Beuth Verlag, Berlin, **2002**.
- [69] Cowherd, C. et al.: An Apparatus and Methodology for Predicting the Dustiness of Materials, Am. Ind. Hyg. Assoc. J., **1989**, 50(3), 123.
- [70] Heitbrink, W.A., Baron, P.A., Willeke, K.: An Investigation of Dust Generation by Free Falling Powders, Am. Ind. Hyg. Assoc. J., **1989**, 53(10), 617.
- [71] Plinke, M. et al.: Particle Separation Mechanisms in Flow of Granular Material, Particulate Science and Technology, **1994**, 12, 71.
- [72] Cawley, B., Leith, D.: Bench-Top Apparatus to Examine Factors that Affect Dust Generation, Appl. Occup. Environ. Hyg., **1993**, 8(7), 624.

- [73] Plinke, M. et al.: Dust Generation from Handling Powders in Industry, *Am. Ind. Hyg. Assoc. J.*, **1995**, 56, 251.
- [74] Kahle, K., Schneider, D., Leib, G.: Zur Bestimmung der Staubneigung von Kalidüngemittel, *Neue Bergbautechnik*, **1978**, 8(6), 351.
- [75] Sethi, S.A.: Generation of Small Particles by Gas Fluidization, *J. Aerosol Sci.*, **1997**, 28(1), S539.
- [76] Sethi, S.A., Schneider, T.A.: A Gas Fluidization Dustiness Tester, *J. Aerosol Sci.*, **1996**, 27(1), S305.
- [77] Schofield, C.: Dust Generation and Control in Materials Handling, *Bulk Solids Handling*, **1981**, 1(3), 419.
- [78] Mörl, L.: Untersuchung des Zerfallsverhaltens von Partikeln in der Wirbelschicht mit der Zielsetzung, ein Standardverfahren zur Beurteilung des Partikelzerfalls zu entwickeln, *AiF-Vorhaben*, Nr. 11151 B, **1999**.
- [79] Visser, G.Th.: A Wind-Tunnel Study of the Dust Emissions from the Continuous Dumping of Coal, *Atmospheric Environment*, **1992**, 26A(8), 1453.
- [80] Chow, J.C. et al.: A Laboratory Resuspension Chamber to Measure Fugitive Dust Size Distribution and Chemical Compositions, *Atmospheric Environment*, **1994**, 28(21), 3463.
- [81] Page, S.J.: Relationships between Electrostatic Charging Characteristics, Moisture Content, and Airborne Dust Generation for Subbituminous and Bituminous Coals, *Aerosol Science and Technology*, **2000**, 32, 249.
- [82] Vorschlag DIN 33897-3 Arbeitsplatzatmosphäre – Bestimmung des Staubungsverhaltens Teil 3: Verstaubung im Staubkanal, **2002**.
- [83] Bachmann, M. et al.: Staubarme Streumehle, *Die Mühle und Futtermischtechnik*, **1999**, 136(9), 286.
- [84] Emmerichs, M., Armbruster, L.: Weiterentwicklung eines Vierstufenimpaktors zur Bestimmung der Kornverteilung von luftgetragenen Stäuben, *Silikose Bericht Nordrhein-Westfalen*, **1981**, 13, 111.
- [85] Carlson, K.H. et al.: A comparison of Two Dustiness Evaluation Methods, *Am. Ind. Hyg. Assoc. J.*, **1992**, 53, 448.
- [86] Stäube, Rauche und Nebel am Arbeitsplatz: Risiken und Prävention; Dust, Fumes and Mists in the workplace: Risk and their Prevention, *International Symposium, Toulouse (France)*, **2001**.
- [87] N.N., Development of Methods for Dustiness Testing, Proposal for Research on the Standards Measurement and Testing Programme 1994-1998, Theme II, **1998**.
- [88] N.N., Heubach-Dustmeter zur Bestimmung des Staubungsverhaltens von Pulvern, Tabletten und Granulaten, *Firmenschrift Heubach Engineering GmbH*, **2001**.
- [90] Plinke, M., Leith, D., Löffler, F.: Cohesion in Granular Materials, *Bulk Solids Handling*, **1994**, 14(1), 101.
- [91] Visser, J.: An Invited Review van-der-Waals and other Cohesive Forces Affecting Powder Fluidization, *Powder Technology*, **1989**, 58, 1.
- [92] Cowherd, C., Grellinger, M.A., Wong, K.F.: Dust Inhalation Exposures from the Handling of Small Volumes of Powders, *Am. Ind. Hyg. Assoc. J.*, **1989**, 50(3), 131.
- [93] Chung, K.Y.K., Aitken, R.J., Bradley, D.R.: Development and Testing of a New Sampler for Welding Fume, *Ann. occup. Hyg.*, **1997**, 41(3), 355.
- [94] Maynard, A.D., Kenny, L.C., Baldwin, P.E.J.: Development of a System to Rapidly Measure Sampler Penetration up to 20 µm Aerodynamic Diameter in Calm Air, using the Aerodynamic Particle Sizer, *J. Aerosol Sci.*, **1999**, 30(9), 1215.
- [95] Mark, D. et al.: Applications of closely graded Powders of Fused Alumina as Test Dusts for Aerosol Studies, *J. Aerosol Sci.*, **1985**, 16(2), 125.
- [96] Higman, R.W.: Dustiness testing: A useful Tool, *Ventilation'85 Proceedings of the 1st International Symposium on Ventilation for Contaminant Control*, Toronto, Canada, **1985**, 693.
- [97] N.N., The Control of Substances Hazardous to Health (COSHH) Guidance on Chemical Protective Clothing (Regulation 7), *Chemical Industries Association*, London, **1993**.
- [98] Vincent, J.H., Aitken, R.J., Mark, D.: Porous Plastic Foam Filtration media: Penetration Characteristics and Applications in Particle Size – Selective Sampling, *J. Aerosol Sci.*, **1993**, 24(7), 929.
- [99] Rupprecht, E., Meyer, M., Patashnick, H.: The tapered Element Oscillating Microbalance as a Tool for Measuring Ambient Particulate Concentrations in Real Time, *J. Aerosol Sci.*, **1992**, 23(1), S635.
- [100] Schneider, T. et al.: Design and Calibration of a Simple Instrument for Measuring Dust on Surfaces in the Indoor Environment, *Indoor Air*, **1996**, 6, 204.
- [101] Richter, M., Bley, W., Grimm, H.: Harmonisierung von Staubmessung in Europa, *ÖchemZ*, **1996**, 1, 4.
- [102] 92/32/EWG Abl. Nr. L 154, Anhang VII A zur RL 67/548/EWG, **1992**.

## Author's short biography



### **Eberhard Schmidt**

Eberhard Schmidt is full professor and head of the Division of Safety Engineering/Environmental Protection at the University of Wuppertal. He earned his scientific degrees at the University of Karlsruhe as a member of the Institute for Mechanical Process Engineering and Mechanics. As a visiting scientist at the Institute for Safety Technology at the Joint Research Centre in Ispra/Italy he gained international experience and as R&D engineer in Degussa's Department of Process Technology and Engineering in Wolfgang/Hanau he became acquainted with industrial processes. Current research in Wuppertal deals with gas-solid particle separation (emission control or product recovery), dust generation caused by powder handling, modelling and simulation of particulate systems, and water recovery by membrane processes.



### **Frank Hamelmann**

Frank Hamelmann is a scientific assistant at the Division of Safety Engineering and Environmental Protection of the University of Wuppertal, Germany, where he obtained his diploma degree in 1999. He is currently a lecturer at the division and involved in teaching and researching on the dustiness of bulk materials.

# Properties of Filter Cake in Cake Filtration and Membrane Filtration<sup>†</sup>

Eiji Iritani

Department of Chemical Engineering,  
Nagoya University\*

## Abstract

*Filtration of liquid suspensions is a widely practiced process in many industries. In recent years, membrane filtration of colloidal solutions has attracted a considerable amount of attention. The appropriate control of both the filtration rate and the rejection (or the transmission) of the particles and/or the macromolecules in the filtration process is of great interest in both industry and academia. Such filtration behaviors are strongly affected by the properties of the filter cake formed by the accumulation of the particles and/or the macromolecules on the surface of the filter medium or the membrane. This paper overviewed the author's own contributions on the recent developments on the behaviors of the filter cake in cake filtration and membrane filtration. The paper will mainly deal with measurements and analysis of the internal structures of the filter cake, the role of the solution environment in the properties of the filter cake, and filtration and fractionation mechanism of mixtures.*

## 1. Introduction

Filtration is the operation of separating a dispersed phase of solid particles from a fluid by means of a filter medium which permits the passage of the fluid but retains the particles. Filtration is probably one of the oldest unit operation. The old forms of filtration by straining through porous materials were described by the earliest Chinese writers. A gravity filter used in a chemical process industry was described in an Egyptian papyrus which has its origin in about the third century A. D.

In recent years, many developments have increased the application of filtration. Filtration steps are required in many important processes and in widely divergent industries. The importance of filtration techniques has been emphasized by the increased need for protection of the environment and by the increasingly critical need for larger supplies of energy. Recently, membrane filtration of colloids has become increasingly important in widely diversified fields.

The appropriate control of both the filtration rate and the rejection (or the transmission) of the particles and/or the macromolecules in the filtration process is of great interest in both industry and academia. While there exist many factors influencing the filtration behaviors [1], the underlying phenomena are currently not well understood.

The filtration behaviors are strongly affected by the properties of the filter cake formed by the accumulation of the particles and/or the macromolecules on the surface of the filter medium or the membrane [2]. Therefore, an understanding of the cake structure can serve as a basis for clarifying the real mechanism of cake filtration and membrane filtration. In this article, role of filter cake in cake filtration and membrane filtration is overviewed.

## 2. Experimental Testing Procedures

It is extremely important from both theoretical and industrial viewpoints to develop simple and precise filtration test methods. The most commonly used tests are classified into three groups: vacuum filtration tests, pressure filtration tests, and compression-permeability tests. Such overall filtration characteristics as the average specific filtration resistance  $\alpha_{av}$  and the average ratio  $m$  of wet to dry cake mass are mea-

\* Furo-cho, Chikusa-ku, Nagoya 464-8603, Japan  
Phone: +81-52-789-3374, Fax: +81-52-789-5300  
E-mail: iritani@nuce.nagoya-u.ac.jp

<sup>†</sup> Accepted: September 1, 2003



sured by conducting vacuum or pressure filtration experiments. In general,  $\alpha_{av}$  is calculated by using both the constant pressure filtration coefficient  $K_v$  determined from the slope of the Ruth plots [3] and the  $m$ -value. The value of  $m$  has almost invariably been determined by weighing the filter cake before and after the cake dries. However, visual determination of the end of filtration often leads to erroneous values for  $m$  and also  $\alpha_{av}$  because of the indistinct interface between the cake surface and the slurry.

The compression-permeability cell [4-6] is a device in which a mechanical load is applied through a piston to a cake resting on a filter medium. Both overall filtration characteristics and internal structures of the filter cake are analyzed on the basis of experimental data of the equilibrium porosity and the specific flow resistance of the compressed cake in the compression-permeability cell. However, this technique may be rather tedious and time-consuming for industrial practice.

A simple alternative procedure recently developed depends on measurement of the capillary suction time (CST), utilizing the very small suction pressure applied to the slurry by the capillary action of an absorbent filter paper [7]. However, little attempt has been made to determine filtration characteristics precisely and easily under relatively high filtration pressure conditions.

A method has been developed for evaluating rigorously the properties of the filter cake, such as the average porosity  $\varepsilon_{av}$  and the average specific filtration resistance  $\alpha_{av}$  [8]. It utilizes the sudden reduction in filtration area of the cake surface. The specially designed apparatus is schematically shown in **Fig. 1**. A close-fitting cylinder with an inner diameter  $D$  of 4 cm is inserted in the cylindrical brass filter. Inserted cylinders having heights  $h$  of 5, 10 and 15 mm are used. A disk with a hole having a diameter  $D_h$  of 6 mm is placed on top of the inserted cylinder, and the part below this constitutes the filter chamber.

Filter cake steadily builds up on the filter medium as soon as the filtration process starts. The surface area of the growing filter cake equals exactly the area of the filter medium. At this first stage, on the assumption of negligible medium resistance, the reciprocal filtration rate  $(d\theta/dv)$  is represented by the well-known Ruth equation for constant pressure filtration in the form [3]

$$\frac{dq}{dv} = \frac{2}{K_v} v \quad (1)$$

where  $\theta$  is the filtration time,  $v$  is the cumulative fil-

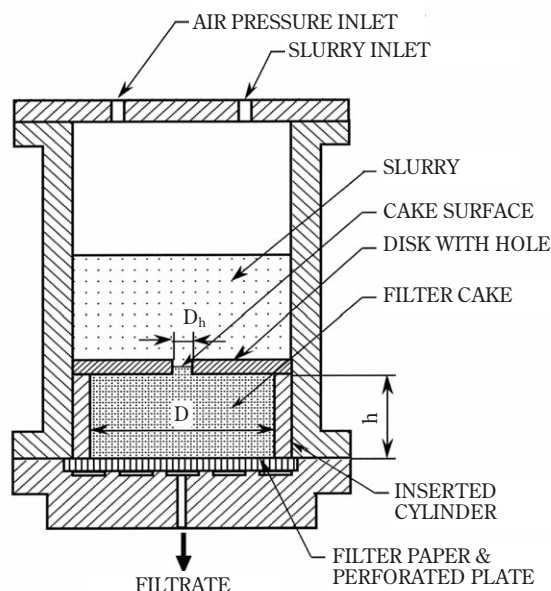


**Fig. 1** Schematic diagram of filtration apparatus having sudden reduction in its filtration area.

trate volume collected per unit effective medium area, and  $K_v$  is the Ruth coefficient of constant pressure filtration defined by

$$K_v = \frac{2p(1-ms)}{mr_s q_{av}} \quad (2)$$

where  $p$  is the applied filtration pressure,  $s$  is the mass fraction of solids in the slurry,  $\mu$  is the viscosity of the filtrate, and  $\rho$  is the density of the filtrate.

Once the filter cake builds up to the underside of the disk, the subsequent filter cake can form only inside the hole in the disk. Consequently, the filtration area of the cake surface is reduced suddenly, and the filtration rate decreases markedly in accord with the decrease in formation rate of the filter cake. After the filtrate volume  $v$  is beyond the critical volume  $v_t$  at the transition point, the reciprocal filtration rate  $(d\theta/dv)$  vs.  $v$  deviates remarkably from the relation represented by Eq. (1).

From the value of  $v_t$ , the average porosity  $\varepsilon_{av}$  of the filter cake can be calculated using an overall mass balance of dead-end filtration, to give

$$\varepsilon_{av} = \frac{r_s h(1-s) - r_s v_t}{r_s h(1-s) + r_s h} \quad (3)$$

where  $\rho_s$  is the true density of solids. The ratio  $m$  of wet to dry cake mass in Eq. (2) is related to the average porosity  $\varepsilon_{av}$  of the filter cake by

$$m = 1 + \frac{r e_{av}}{r_s (1 - e_{av})} \quad (4)$$

Thus, the average specific filtration resistance  $\alpha_{av}$  can be evaluated accurately from Eqs. (1), (2), and (4) by using the slope of the plot of  $d\theta/dv$  against  $v$  and the value of  $m$ .

The values of  $m$  and  $\alpha_{av}$  obtained by this method can be predicted by using the compression-permeability cell data. On the basis of the compressible cake filtration model [9, 10], the distributions of the local porosity  $\varepsilon$  and the local specific filtration resistance  $\alpha$  and the apparent liquid velocity  $u$  relative to solids in the filter cake can be estimated by using the compression-permeability cell data in the form of  $e$  and  $\alpha$  as functions of the local solid compressive pressure  $p_s$ . Consequently, the values of  $m$  and  $\alpha_{av}$  can be calculated from Eqs. (5) and (6), respectively.

$$m = 1 + \frac{r \int_0^1 e d\left(\frac{w}{w_0}\right)}{r_s \int_0^1 (1 - e) d\left(\frac{w}{w_0}\right)} \quad (5)$$

$$\alpha_{av} = \int_0^1 \left(\frac{u}{u_1}\right) d\left(\frac{w}{w_0}\right) \cdot \frac{p - p_m}{\int_0^{p-p_m} \frac{1}{\alpha} dp_s} \quad (6)$$

where  $w$  is the net solid volume per unit medium area lying from the medium up to an arbitrary position in the cake,  $w_0$  is the net solid volume of the entire cake per unit medium area, and  $u_1$  is the filtration velocity. The quantity  $p_m$  is the pressure loss through the filter medium, and can be neglected in this article.

In **Fig. 2**, the results obtained with the setup shown in **Fig. 1** are plotted in the form of the reciprocal flow rate ( $dq/dv$ ) vs. the filtrate volume  $v$  per unit medium area. In the first stage of the operation, each curve yields a straight line in accordance with Eq. (1). As soon as the cake builds up to the underside of the disk with the hole, the value of  $dq/dv$  increases remarkably.

The value of  $m$  can be calculated from Eqs. (3) and (4) by using the values of the thickness  $h$  of the filter chamber and the filtrate volume  $v_t$  at the transition point determined from **Fig. 2**. In **Fig. 3**,  $m$  is plotted with respect to the filtration pressure  $p$ . The value of  $m$  decreases with pressure. The experimental results are fairly consistent with the calculations based on the compression-permeability cell data. The discrepancy in the low-pressure region may be due to the influence of sedimentation, which becomes important in the case of small formation rate of the cake. For com-

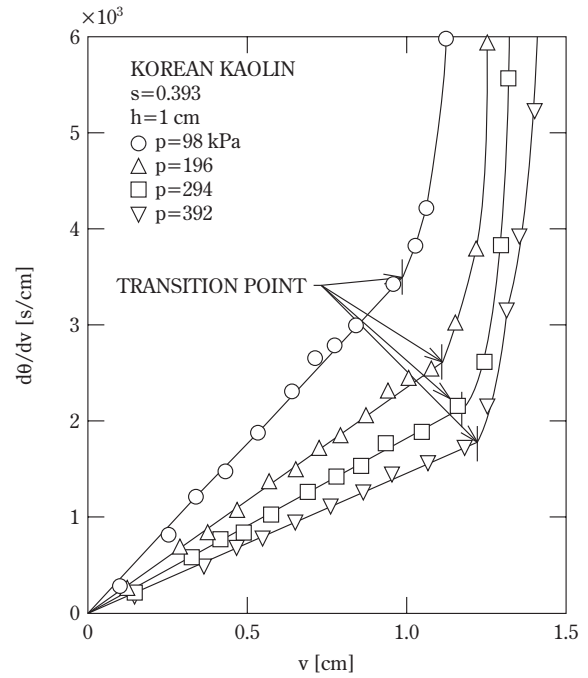


**Fig. 2** Relation between reciprocal filtration rate and filtrate volume per unit medium area for various applied filtration pressures.

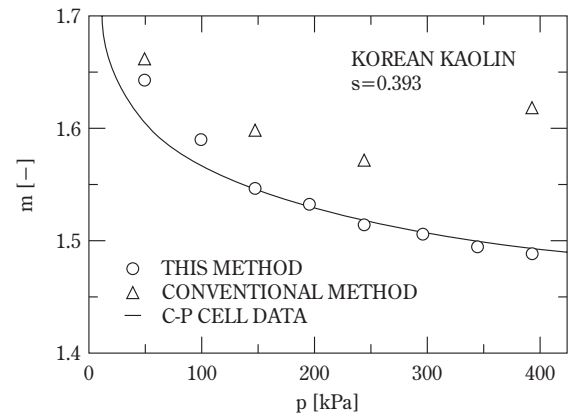


**Fig. 3** Relation between ratio of wet to dry cake mass and filtration pressure.

parison, the values of  $m$  determined by the conventional method of weighing the filter cake before and after being dried are also included in the same figure. The values thus obtained are rather large compared with the calculations because of the indistinct interface between the cake surface and the slurry. In **Fig. 4**,  $\alpha_{av}$  is plotted against pressure  $p$ . The resis-

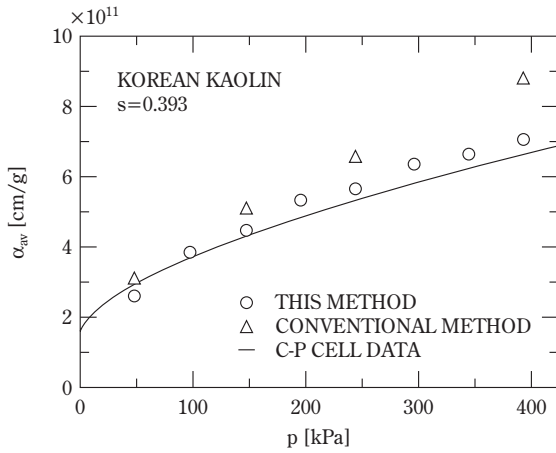


**Fig. 4** Relation between average specific filtration resistance and applied filtration pressure.

tance  $\alpha_{av}$  increases with pressure. The experimental results obtained by this method are fairly consistent with the calculations, whereas the results obtained by the conventional method show poor agreement because of incorrect values of  $m$ . It is demonstrated from the results of **Figs. 3** and **4** that this method is more accurate compared with the conventional one.

### 3. Compressible Cake Filtration Model

The compressible cake filtration model [9, 10] is used to evaluate such internal quantities as the solid concentration, the compressive pressure acting on the solids and the local specific filtration resistance within the filter cake exhibiting compressible behavior. The build-up of the filter cake increases the hydraulic resistance to flow, thereby reducing the filtration rate. Basically, the compressible cake filtration model can evaluate the reduction of the filtration rate due to the increase in the hydraulic resistance caused by the filter cake.

According to the compressible cake filtration model, the filtration rate  $J (=dv/dq)$  in dead-end filtration with negligible medium resistance compared with the resistance of the filter cake is represented by [3]

$$J = \frac{p}{m\alpha_{av}w} \quad (7)$$

where  $w_0$  is the net mass of deposited solids per unit effective medium area. By accounting for the effects of non-homogeneity and compressibility of the filter cake, the apparent solvent velocity  $J_w$  relative to solids at an arbitrary position  $w$  in the filter cake can be

described by [11]

$$J_w = -\frac{1}{mar_s} \cdot \frac{\partial p_s}{\partial w} \quad (8)$$

On the assumption that the solvent velocity  $J_w$  is constant throughout the entire cake, on the basis of Eqs. (7) and (8), one obtains [11]

$$\frac{w}{w_0} = 1 - \frac{\int_0^{p_s} \frac{dp_s}{a}}{\int_0^p \frac{dp_s}{a}} \quad (9)$$

$$a = \frac{\alpha_{av}}{1 - \frac{d(\ln \alpha_{av})}{d(\ln p)}} \quad (10)$$

$$e = e_{av} \left\{ 1 + \frac{\frac{d(\ln e_{av})}{d(\ln p)}}{1 - \frac{d(\ln \alpha_{av})}{d(\ln p)}} \right\} \quad (11)$$

where  $w_0 (=w_0/r_s)$  is the net solid volume of the entire filter cake per unit effective medium area, and  $e (=e/(1-e))$  is the local void ratio. Therefore, if the average specific filtration resistance  $\alpha_{av}$  and the average void ratio  $e_{av} (=e_{av}/(1-e_{av}))$  of the filter cake are represented as functions of the applied filtration pressure  $p$ , then the variations of the local solid compressive pressure  $p_s$ , the local specific filtration resistance  $a$  and the local void ratio  $e$  with  $w$  can be evaluated from Eqs. (9)–(11). Thus, the variation of the mass fraction  $c$  of the solid in the filter cake with the distance  $x$  from the medium surface can be also calculated from the result of  $e$  versus  $w$ .

For a practical standpoint, the following empirical functions of  $p_s$  may be convenient for simplified evaluations of filtration characteristic values [12, 13].

$$a = a_1 p_s^n \quad (12)$$

$$e = E_0 - C_c \ln p_s \quad (13)$$

where  $a_1$ ,  $n$ ,  $E_0$ , and  $C_c$  are the empirical constants. With the aid of Eqs. (12) and (13), Eqs. (9)–(11) can be written as [11]

$$\frac{p_s}{p} = \left( 1 - \frac{w}{w_0} \right)^{\frac{1}{1-n}} \quad (14)$$

$$\alpha_{av} = a_1 (1-n) p^n \quad (15)$$

$$e_{av} = E_0 + \frac{C_c}{1-n} - C_c \ln p \quad (16)$$

On the basis of the model of solutions in which the

macromolecules appear as solid particles [14], it is assumed that the model which has been employed in filtration of particulate suspensions can be applied to the flow of solvent through the filter cake in ultrafiltration of the solution. In **Fig. 5**, the average specific filtration resistance  $\alpha_{av}$  and the average void ratio  $e_{av}$  of the filter cake in protein ultrafiltration measured with a filter which has a sudden reduction in its filtration area are plotted as functions of the filtration pressure  $p$  [15]. The macrosolute used in the experiments was bovine serum albumin (BSA) with a molecular weight of 67,000 Da and with an isoelectric point of 4.9. Increasing the filtration pressure causes a reduction in the void ratio of the filter cake, leading to an increase of the specific filtration resistance. It is apparent that  $e_{av}$  around the isoelectric point (pH 4.9) is much smaller than that at pH 7.0. The two types of plots show a linear relationship over the entire range of data in accordance with Eqs. (15) and (16), respectively. The parameters  $\alpha_1$  and  $n$  in Eq. (12) can be calculated by fitting Eq. (15) to the logarithmic plot of  $\alpha_{av}$  vs.  $p$ . The value of  $E_0$  and  $C_c$  in Eq. (13) can be obtained from a plot of  $e_{av}$  vs.  $\ln p$  in accordance with Eq. (16), using the predetermined  $n$  value. The distributions of  $p_s$  within the filter cake can be obtained from Eq. (14). With the aid of Eq. (14), Eqs. (12) and (13) provide the distributions of  $\alpha$  and  $e$  within the filter cake, respectively.

The variations of the local solute compressive pressure  $p_s$  and the local specific filtration resistance  $\alpha$  across the filter cake for different values of the filtrate

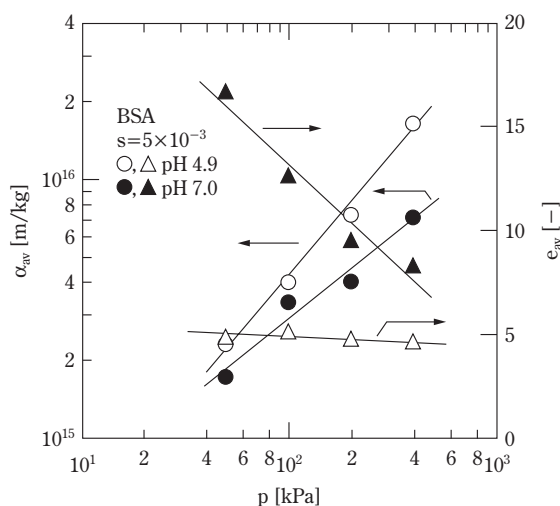


**Fig. 5** Effect of applied filtration pressure on average specific filtration resistance and average void ratio of filter cake for different values of pH.

volume  $v$  calculated from Eqs. (14) and (12) are illustrated in **Figs. 6** and **7**, respectively [16]. The distance  $x$  from the membrane surface in the figures may be calculated from  $w$  by

$$\frac{x}{L} = \frac{1 + e_{av,w}}{1 + e_{av}} \cdot \frac{w}{W_0} \quad (17)$$

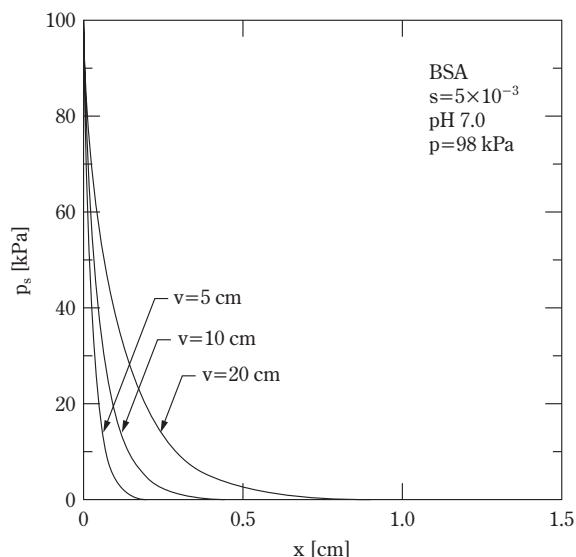


**Fig. 6** Distributions of local solute compressive pressure in filter cake for different filtrate volumes.

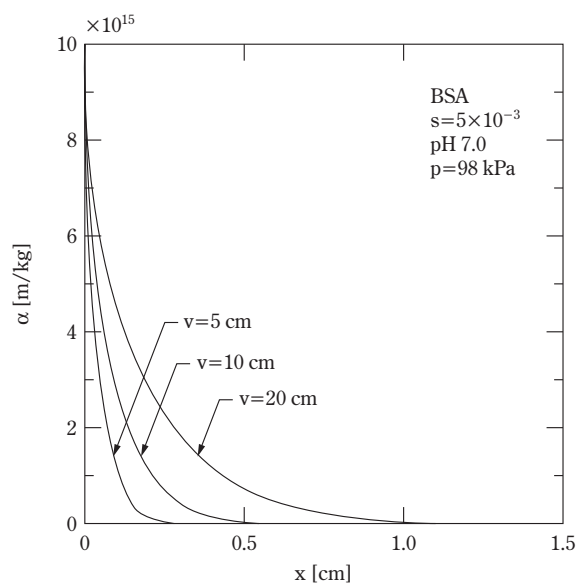


**Fig. 7** Distributions of local specific filtration resistance in filter cake for different filtrate volumes.

where  $e_{av,0}$  is the average void ratio from the membrane surface to the distance  $w$  from the membrane. The thickness  $L$  of the protein filter cake is expressed based on the material balance as

$$L = \frac{rs(1+e_{av})}{r_s(1-s) - rs e_{av}} v \quad (18)$$

As shown in the figure, high specific filtration resistance can be obtained although the porosity in the cake is not so small [2, 17]. The figure obviously demonstrates that both  $p_s$  and  $\alpha$  decrease with the distance  $x$ . As the filtrate volume  $v$  increases,  $p_s$  and  $\alpha$  increase. The solute compressive pressure at the surface of the protein filter cake is essentially zero as no drag on the solutes has developed. The frictional drag on each solute adds to the drag on the previous solutes as the solvent passes frictionally along the solutes in the compressible filter cake. Consequently, the net compressive pressure increases as the membrane surface is approached, resulting in the increasing resistance to flow. At the interface of the filter cake and the membrane,  $p_s$  has risen to its maximum value and is equal to the applied filtration pressure  $p$  for the negligible membrane resistance. Therefore, the protein filter cake tends to have a much more compact structure at the membrane exhibiting a large resistance to flow in comparison to a relatively loose condition at the surface because the cake is compressible. In the compressible filter cake formed by ultrafiltration of BSA solutions, it is demonstrated that a pronounced variation of characteristic values of the filter cake can be seen. This is in agreement with the results obtained for filtration of particulate suspensions [9, 18].

The local mass fraction  $c$  of the solute in the filter cake may be calculated from the local void ratio  $e$  in the form

$$c = \frac{r_s}{r_s + re} \quad (19)$$

Thus, the concentration distributions in the protein filter cake may be predicted from Eqs. (13), (14), (17)–(19).

#### 4. Analysis of Ultrafiltration Behaviors Based on Ultracentrifugation Experiment

The flux decline and the cake structure in ultrafiltration of protein solutions can be evaluated from analytical ultracentrifugation experiments [15, 19, 20]. The experiments were performed in a Hitachi Model 282 ultracentrifuge equipped with an optical system.

The rotor speed ranged from 45,000 to 60,000  $\text{min}^{-1}$ . The distributions of the concentration, the concentration gradient, and the refractive index gradient of the solutions in a 1.5 mm double-sector centerpiece were measured over time using both the ultraviolet scanner absorption system and Schlieren optics. In the sedimentation velocity experiment, the sedimentation velocity was determined from the displacement of the sedimentation boundary. In the high-speed sedimentation equilibrium experiment, the equilibrium thickness of the sediment of macromolecular solutes was measured after equilibrium was reached at a constant rotor speed.

At relatively high solution concentrations, there is an analogy between the sedimentation of a macromolecule in a solvent and the permeation of a solvent through the filter cake of macromolecules. The local specific flow resistance  $\alpha$  can be calculated as [15, 19]

$$\alpha = \frac{(r_s - r)r_i \Omega^2}{mr_s v_0} = \frac{r_s - r}{mr_s S} \quad (20)$$

where  $r_i$  is the radial distance of the sedimentation boundary from the center of rotation,  $\Omega$  is the angular velocity of the rotor,  $v_0$  is the sedimentation velocity, and  $S$  is the sedimentation coefficient.

Thus, the relation between  $\alpha$  and the volume fraction  $(1-e)$  of the solute may be written as [15, 19, 21]

$$(1/\alpha)^{1/4.65} = \left( \frac{r_s d_f^2}{18C_h} \right)^{1/4.65} \{1 - C_h(1-e)\} \quad (21)$$

where  $d_f$  is the average equivalent spherical diameter of solutes,  $C_h$  is the ratio of the volume of the hydrous protein molecule to volume of anhydrous protein molecule, and  $e$  is the porosity of the solution.

**Figure 8** shows the permeability data obtained by measuring the sedimentation velocities for a number of different solution concentrations. The plots are virtually linear as would be expected from Eq. (21). It is apparent that  $\alpha$  around the isoelectric point is much smaller than that at pH 7 with the same solution concentration. On the other hand, the average specific filtration resistance  $\alpha_{av}$  of the cake in the ultrafiltration of BSA solutions reaches a definite maximum around the isoelectric point [2]. In order to account for this discrepancy, a high-speed sedimentation equilibrium experiment was conducted.

If the local solute concentration of the cake formed in ultrafiltration is known, then the specific flow resistance  $\alpha$  of the cake can be evaluated by using the permeability data. Therefore, it is necessary to evaluate the local solute concentration of the cake. We thus determined the compression data representing the



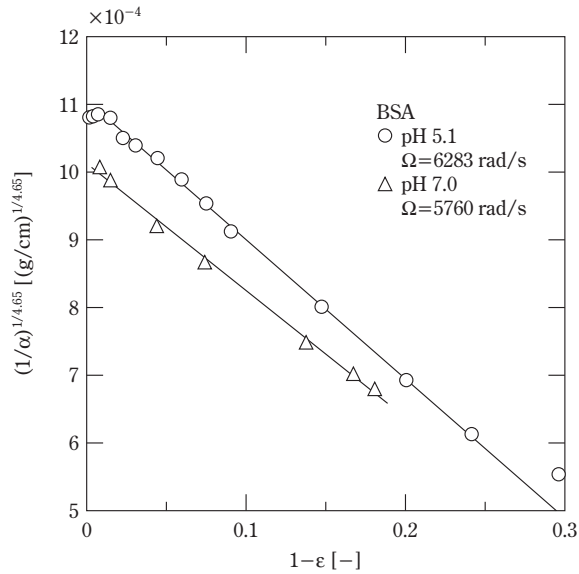


**Fig. 8** Relation between local specific flow resistance and porosity of solution.

relation between the local porosity  $e$  and the local solute compressive pressure  $p_s$  from high-speed sedimentation equilibrium experiments. If  $e$  is related to  $p_s$  by Eq. (22), the equilibrium thickness ( $R-r_s$ ) of the sediment is related to the centrifugal acceleration  $RW^2$  by Eq. (23) [15, 19, 22].

$$1-e = Ep_s^b \quad p_s \geq p_{si} \quad (22)$$

$$R-r_s = \frac{w_0^{1-b}}{E(1-b)} \{ (r_s-r) R \Omega^2 \}^{-b} \quad (23)$$

where  $R$  is the distance from the center of rotation to the bottom of the sediment,  $r_s$  is the distance from the center of rotation to the surface of the sediment,  $w_0$  is the net solute volume of the entire sediment per unit cross-sectional area, and  $E$  and  $b$  are the empirical constants. Below  $p_{si}$ ,  $e$  is assumed to be constant, and is equal to the porosity at pressure  $p_{si}$ .

**Figure 9** represents the logarithmic plot of the equilibrium thickness ( $R-r_s$ ) of the sediment against the centrifugal acceleration  $RW^2$ . The plot shows a linear relationship in accordance with Eq. (23). It is interesting to note that the sediment at the isoelectric point is much more compact than that at pH 7 because the BSA molecule carries no net charge at the isoelectric point. Therefore, it would be expected that in protein ultrafiltration a compact filter cake forms around the isoelectric point. The relation between  $e$  and  $p_s$  can be determined from the plot in the

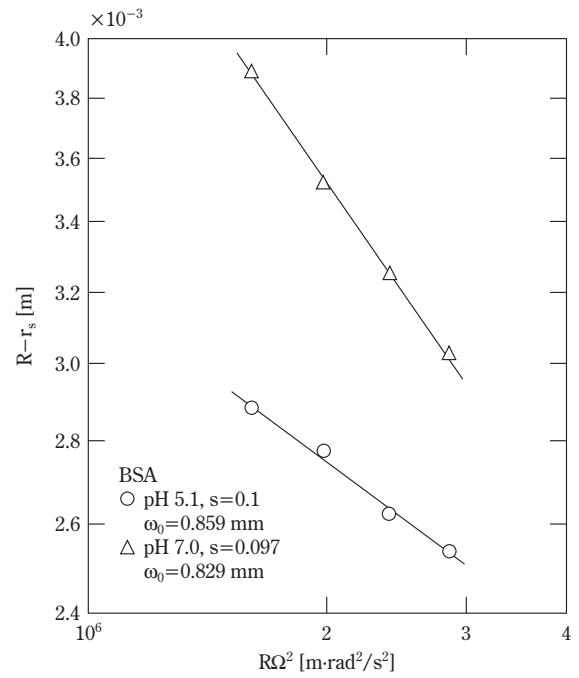


**Fig. 9** Relation between equilibrium thickness of sediment and centrifugal acceleration.

figure using Eqs. (22) and (23). On the basis of these relations, the variations of the filtration rate in ultrafiltration of protein solutions can be determined from the compressible cake filtration model [2, 9, 15].

In **Fig. 10**, the results of unstirred dead-end ultrafiltration are plotted in the form of the reciprocal filtration rate ( $dq/dv$ ) versus the filtrate volume  $v$  per unit membrane area. The filtration rate around the isoelectric point is much smaller than that at pH 7. The solid lines indicate the theoretical predictions based on the compression-permeability data obtained in analytical ultracentrifugation. The experimental data are in relatively good agreement with the theory, indicating that the compressible cake filtration model accurately describes the ultrafiltration behavior.

**Figure 11** shows the variations of the mass fraction  $c$  of the solute across the cake calculated on the basis of the ultracentrifugation data. In the compressible cake resistance model, the solutes deposited on the membrane are treated as the cake, and it is attributed to the hydraulic barrier. The cake tends to have a much more compact structure at the membrane in comparison to a relatively loose condition at the surface because the cake is compressible. Of considerable practical interest is that this result is in agreement with that obtained for cake filtration of par-

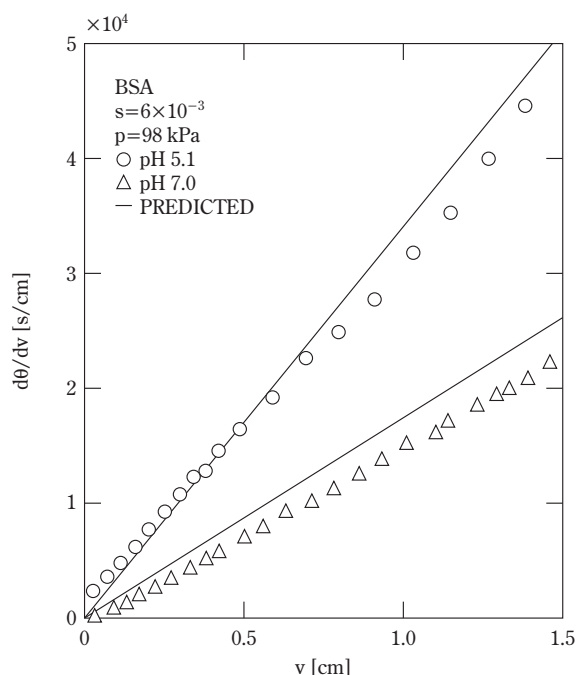


**Fig. 10** Evaluation of filtration rate based on ultracentrifugation data.

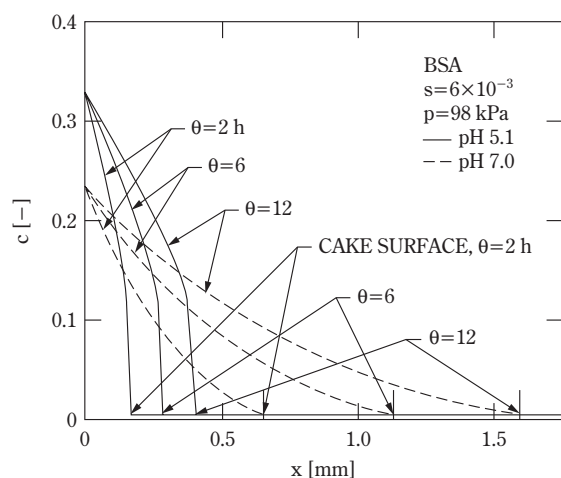


**Fig. 11** Evaluation of distributions of solute concentration in filter cake based on ultracentrifugation data.

ticulate suspensions [23]. A much more compact filter cake exhibiting a large resistance to flow may form around the isoelectric point than that which forms at pH 7. Consequently, the filtration rate at the isoelectric point becomes lower than that at pH 7.

## 5. Measurement of Concentration Distribution in Filter Cake of Ultrafiltration

A variety of theoretical models describing the fouling phenomenon during ultrafiltration quantitatively have been developed: the gel polarization model [24-26]; the osmotic pressure model [27-29]; the boundary layer model [30, 31]; and the cake filtration model [32-34]. Although a significant amount of research has been conducted to better understand the dynamics of ultrafiltration, the real mechanism of separation remains incompletely understood.

The compressible cake filtration model has been widely used to describe filtration behaviors of particulate suspensions [9]. Recently, some authors prefer to use the compressible cake filtration model to explain the mechanism of ultrafiltration [2, 15, 35], and it has the potential for analyzing the membrane fouling during ultrafiltration. The filtration flux rate during dead-end ultrafiltration of bovine serum albumin (BSA) solutions could be well evaluated by use of the ultracentrifugation data on the basis of the compressible cake filtration model [19]. The model regards a stagnant filter cake on the membrane as the structural assemblage of “particulate” solutes. In this model, highly resistant filter cake of excluded protein molecules accumulated in front of the membrane surface forms, and the filter cake acts as an additional hydraulic resistance to flow in conjunction with that provided by the membrane, thereby reducing the filtration flux rate. The model also takes the compressibility of the filter cake into account. Therefore, an understanding of the properties of the filter cake formed by the accumulation of the protein molecules on the membrane can serve as a basis for clarifying the real mechanism of ultrafiltration.

Several approaches have been developed for measuring the average value of the porosity in the filter cake formed on the membrane surface in ultrafiltration of protein solutions. Nakao et al. [36] measured the gel concentration by scraping a thin layer of deposited material from the surface of a tubular membrane in ovalbumin ultrafiltration. Iritani et al. [2] used a batchwise filter device which had a sudden reduction in its filtration area to determine the average porosity of the BSA cake. Also, in more recent work by Nakakura et al. [35], the porosity was obtained from the measurement of the electric conductivity within the filter cake during ultrafiltration of BSA solutions. It is, however, crucial to measure the porosity distribution since the filter cake formed on the membrane during ultrafiltration is extremely thin

in general.

Relatively few investigators have measured concentration distributions within the protein layer accumulated on the membrane during ultrafiltration. Vilker et al. [29] used an optical shadowgraph technique to measure the concentration gradient within the polarized layer on the membrane during unstirred dead-end ultrafiltration of BSA solutions. McDonogh et al. [37] reported the variation with time of concentration in the polarized layer on the membrane during ultrafiltration of BSA and Dextran Blue solutions using the electronic diode array microscope. Gowman and Ethier [38] used an automated, laser-based refractometric experimental technique for the measurement of concentration and concentration gradient in the concentration polarization layer during dead-end ultrafiltration of the biopolymer hyaluronan. Fernández-Torres et al. [39] obtained the evolution of concentration profiles during BSA ultrafiltration in an unstirred cell using the technique of holographic interferometry. Their results demonstrated that a filter cake was actually formed during BSA ultrafiltration. Although these non-destructive methods have the enormous advantage, they are technically complex and expensive.

A potential method has been explored for measuring the concentration distributions in the filter cake using the principle of the inclined ultrafiltration [40, 41], where the membrane was inclined and a large amount of filter cake was formed. The concentration distributions in the filter cake were measured after downward ultrafiltration was performed in the wake of inclined ultrafiltration. This destructive method is simple, and inexpensive.

The flowing behaviors of filter cake have been observed, as depicted in **Fig. 12** schematically. It was clarified that the filter cake formed mainly on the lower part of the membrane surface due to the effect of gravity during inclined ultrafiltration, as shown in **Fig. 12(a)** [40]. The same phenomenon cannot be observed in downward dead-end ultrafiltration. Once downward ultrafiltration was conducted after inclined ultrafiltration, the filter cake was spread over the membrane surface, as shown in **Fig. 12(b)** [41].

In **Fig. 13**, the flux decline behaviors in various filtration modes are plotted in the form of the reciprocal filtration rate  $1/J (=dq/dv)$  versus the cumulative filtrate volume  $v$  collected per unit effective membrane area, which is well known as the Ruth plot [3] in the ordinary cake filtration. For conventional downward dead-end ultrafiltration ( $y=0$ ), the filtration rate declines gradually due to the build-up of a BSA cake as filtration proceeds. The angle  $y$  represents the angle between the filtrate flow and the direction of gravity. The plot is virtually linear throughout the course of filtration in accordance with the Ruth filtration rate equation (1) [3] with negligible membrane resistance compared with the filter cake resistance. In contrast, in inclined ultrafiltration ( $y=p/3$  rad), the filtration rate becomes remarkably high because the filtrate passes through the upper part of the membrane which is less resistant. Furthermore, once downward ultrafiltration was conducted after inclined ultrafiltration, the filtration rate dramatically decreased because of the remarkable increase of the total filtration resistance. Surprisingly, the value of  $1/J$  in this case lies on the extension line in ordinary downward ultrafiltration, as shown in the figure. This

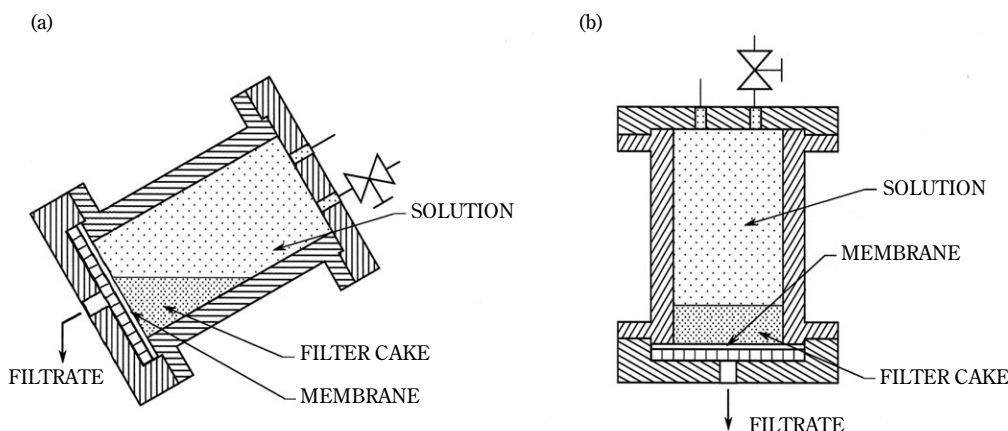


**Fig. 12** Schematic diagram of flowing filter cake: (a) inclined ultrafiltration, and (b) downward ultrafiltration.

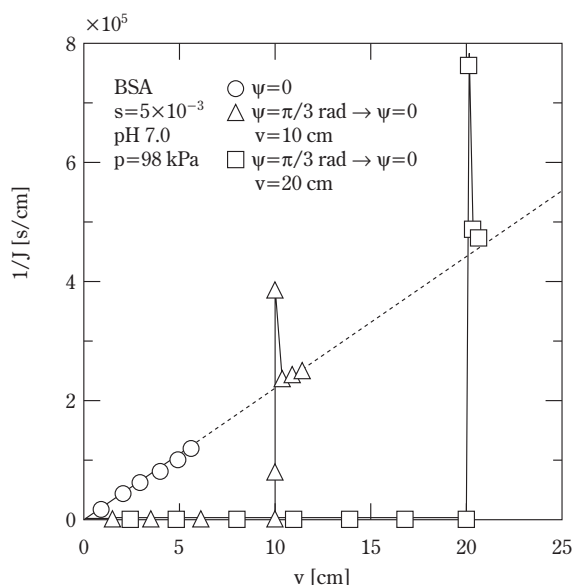


**Fig. 13** Relation between reciprocal filtration rate and filtrate volume per unit membrane area in various filtration modes.

result supports that the structure of the filter cake formed on the membrane such as the concentration distributions is almost the same between both operations.

In **Fig. 14**, the mass fraction  $c$  of BSA on the membrane measured after changing the angle  $\psi$  from  $\pi/3$  rad to zero is plotted against distance  $x$  from the mem-

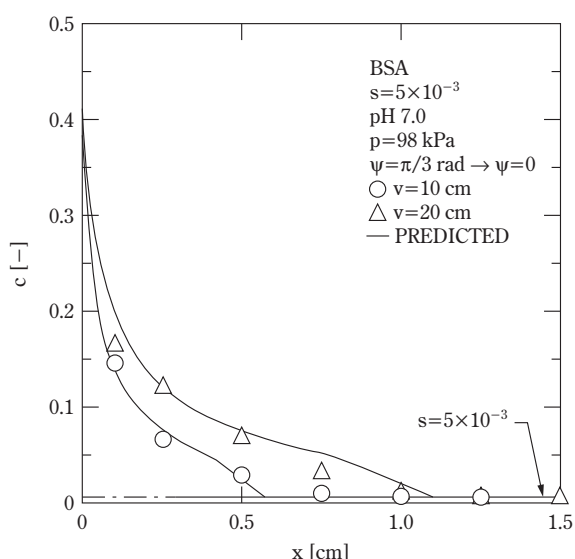


**Fig. 14** Distribution of solute concentration in filter cake for different filtrate volumes.

brane surface for the different values of the filtrate volume  $v$  collected until inclined ultrafiltration was switched to the downward mode. The profiles in this figure may be considered to be similar to those in ordinary downward ultrafiltration, as expected from the results of flux decline behaviors shown in **Fig. 13**. The filter cake which was thicker than 1 cm was formed at the filtrate volume of 20 cm. It is very difficult to obtain such a thick cake as this from downward dead-end ultrafiltration. The solid lines on the figure indicate the theoretical predictions based on a compressible cake filtration model. In the compressible cake filtration model, the concentration distributions of the solutes deposited on the membrane treated as the filter cake act as the hydraulic barrier. The pressure gradient on the liquid passing through the solute varies, and the porosity in the cake is not constant [42]. The figure distinctly demonstrates that there exists a concentration distribution within the filter cake formed on the membrane. The concentration  $c$  has a maximum at the membrane surface ( $x=0$ ) and decreases markedly with the increase of  $x$ , which shows the same trend as that observed for the cake filtration of particulate suspensions [9, 18]. It was verified that the solutes forming the cake are compact and dry at the membrane whereas the surface layer is in a wet and soupy condition. It was also found that the thickness of the filter cake formed on the membrane increases as filtration proceeds.

## 6. Role of Solution Environment in Properties of Filter Cake

Cake filtration of suspensions of solid particles in aqueous solutions is frequently encountered in widely diversified fields. In cake filtration, the nature of the cake formed upon the medium surface during filtration will govern the filtration rate of the remaining suspension. For fine particle suspensions, colloidal forces control the nature of the filter cake. Colloidal forces arise from interaction between the suspended particles. The two main colloidal forces are the attractive van der Waals forces which originate from fluctuating dipoles as a result of the motions of outer electrons on the interacting particles and the repulsive electrostatic forces due to the presence of like charges on the particles and a dielectric medium. Whilst for a given system the van der Waals forces are essentially constant, the electrostatic forces will vary with the surface charge of the suspended particles, which varies with the solution environment. Therefore, the filtration behaviors of the colloids are

affected significantly by the solution properties, including pH and electrolyte strength. Considerable work has been published on the effects of the solution environment on the filtration behaviors [43-52].

**Figure 15** shows the average specific filtration resistance  $\alpha_{av}$  and the average porosity  $e_{av}$  of the filter cake formed in particulate microfiltration at different values of pH under otherwise identical filtration conditions [53]. The particles used in the experiments was titanium dioxide of the rutile form with an original mean specific surface area size of  $0.47 \mu\text{m}$  and with an isoelectric point of 8.1. It should be noted that the resistance  $\alpha_{av}$  is a measure of the filtrability of the suspensions. A larger  $\alpha_{av}$  causes a smaller filtration rate. It can be seen that  $\alpha_{av}$  goes through a minimum around the isoelectric point. Thus, the largest filtration rate can be obtained when the particle carries no charge. Tarleton and Wakeman [49] reported similar results for crossflow microfiltration of anatase suspension. However, this result is in sharp contrast to that obtained in protein ultrafiltration [2, 54]. It is clear that  $e_{av}$  is much larger near the isoelectric pH. Since the titanium dioxide particles are hydrophobic colloids, they are destabilized around the isoelectric point where the van der Waals attraction is more dominant. Consequently, the particles will tend to come together, i.e. to flocculate, and the very porous flocs are then formed. Thus, it is speculated that the filter cake formed from such porous flocs has often loose and wet structures. On the other hand, the filter cake becomes compact and dry when the particle carries

the charge. Since the most loose filter cake forms around the isoelectric pH, the filter cake is most permeable. Thus  $\alpha_{av}$  is much smaller near the isoelectric point.

It is interesting to note that the results in protein ultrafiltration had a distinctly different behavior. In protein ultrafiltration of BSA solution, the filter cake is in its most compact state around the isoelectric point [2, 54], as shown in **Fig. 16**. Since the BSA molecules are hydrophilic colloids, their stability in the solution would appear to be influenced not only by the presence of a surface charge on the protein but also by hydration of the surface layers of the protein. The BSA molecules, because of hydrated layers surrounding them, are not destabilized by such considerations as depression of the electrical double layer. Thus, the BSA molecules have water bound to them even around the isoelectric point. The hydrophilic BSA molecules maintain a dispersed state in the solution due to hydration of the surface layers of the protein even around the isoelectric point. When a BSA molecule acquires a charge, the filter cake becomes loose and wet due to electrostatic repulsion between the charged BSA molecules. This contrasts to the compact filter cake around the isoelectric point. The average specific filtration resistance  $\alpha_{av}$  has a definite maximum around the isoelectric point since a compact filter cake provides a large hydraulic flow resistance.

Charge effects are weakened in the presence of solids. In **Fig. 17**, the average porosity  $e_{av}$  of the filter

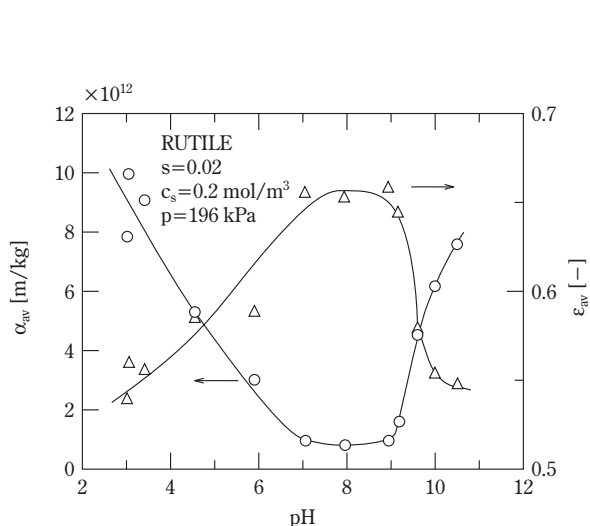


**Fig. 15** Effect of pH on average specific filtration resistance and average porosity of filter cake formed in microfiltration of titanium dioxide suspensions.

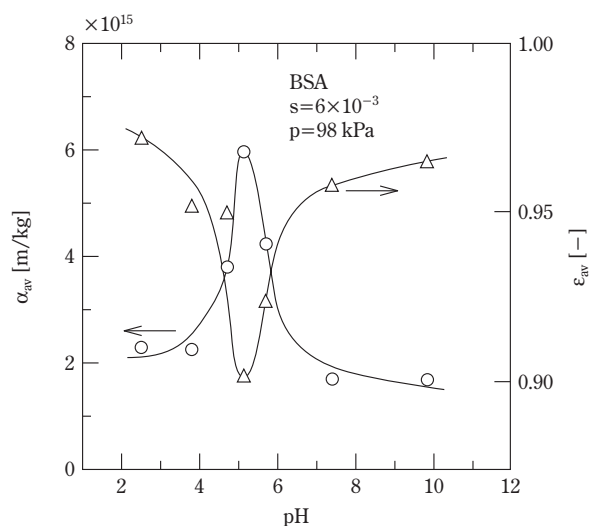


**Fig. 16** Effect of pH on average specific filtration resistance and average porosity of filter cake formed in ultrafiltration of BSA solutions.



cake formed in particulate microfiltration is plotted against absolute values of zeta potentials. This figure shows a close relation between  $e_{av}$  and the zeta potential. It is surprising that the plots can be represented by a unique curve irrespective of the sign of the zeta potential. The cake porosity increases with decreasing zeta potential. The porosity remains constant in the range of the zeta potential below ca. 20 mV. As the zeta potential decreases, the electrostatic repulsion decreases and thus the porous floc forms. Therefore, the average porosity of the filter cake increases. The repulsive force that stems from the overlapping of the electric double layers, depends on the presence or absence of ionized salt in suspension. The repulsive force is less effective at higher ion concentrations and cannot counteract the van der Waals attraction, and so the solution flocculates. Therefore, it is conceivable that the filtration rate is markedly influenced not only by the solution pH but also by the solution ionic strength. The result for the NaCl concentration of 200 mol/m<sup>3</sup> at pH 10.5 is shown in the figure. The magnitude of the zeta potential decreased remarkably as a result of the addition of NaCl compared with that for the NaCl concentration of 0.2 mol/m<sup>3</sup> at the same pH. The average porosity  $e_{av}$  of the filter cake is augmented markedly by the addition of salt. This is because the addition of salt destabilizes the suspension by reducing the double layer repulsion between rutile particles. It should be emphasized that the plot for the NaCl concentration of 200 mol/m<sup>3</sup> lies on the unique curve.

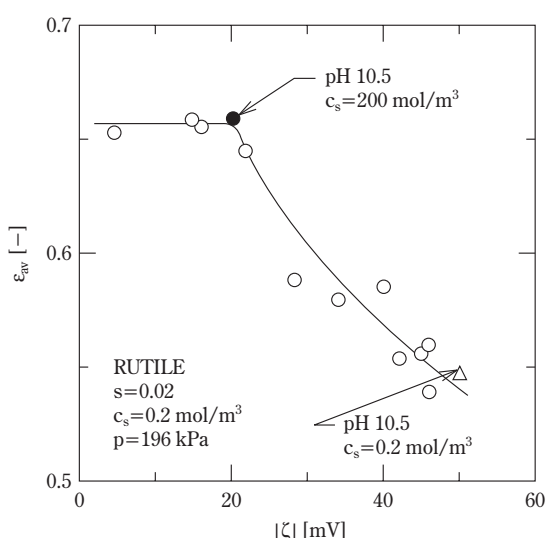


**Fig. 17** Relation between average porosity of filter cake and absolute value of zeta potential.

## 7. Properties of Filter Cake Composed of Mixtures

Especially when two types of particles which may be membrane foulants in combination are present in the feed fluid, the situation becomes more complex. The filtration behaviors can be strongly affected by the nature of the interaction between the dissimilar components.

The variations of the filtration rate with time and the properties of the filter cake were examined for microfiltration of binary mixtures of fine particles [55]. The average porosity in the filter cake of the binary particulate mixtures was explained well by the mixture packing model in which small particles fill the voids between large particles. Further, the average specific filtration resistance of the binary mixtures was well evaluated on the basis of the additive law of the effective specific surface area. However, in most of published works on filtration of binary particulate mixtures [56, 57], the effects of the physicochemical factors such as the pH and salt concentration on the filtration performance have received little or no attention.

Properties of a filter cake formed in dead-end microfiltration were examined using binary particulate mixtures of titanium dioxide and silicon dioxide having the different values of the isoelectric point for each material [58]. The original surface mean diameter of silicon dioxide is 0.92 μm. The silicon dioxide particle has negative charge because it contains only dissociable group of one type, the silanol groups SiOH. In **Fig. 18**, the average specific filtration resistance  $a_{av}$  and the average porosity  $e_{av}$  of the filter cake at pH 4.5 are shown against the mixing ratio ( $s_t/s$ ) of particles, where  $s_t$  is the mass fraction of titanium dioxide particles in the bulk suspension, and the total mass fraction  $s$  of particles is kept constant. It is immediately obvious that  $a_{av}$  tends to become smaller in a mixed system of two components in comparison with a single component system. A smaller specific filtration resistance was generally caused by a larger cake porosity. At this pH value, a titanium dioxide has a positive electrical charge, whilst a silicon dioxide is electronegative. For the single component suspension, the particles are likely to be well dispersed by repulsive electrostatic forces, and form cakes of higher resistance during filtration. However, the particles in mixed suspension come together due to heterocoagulation associated with a coulombic attractive force and the London-van der Waals force, and the very porous flocs are formed prior to deposi-

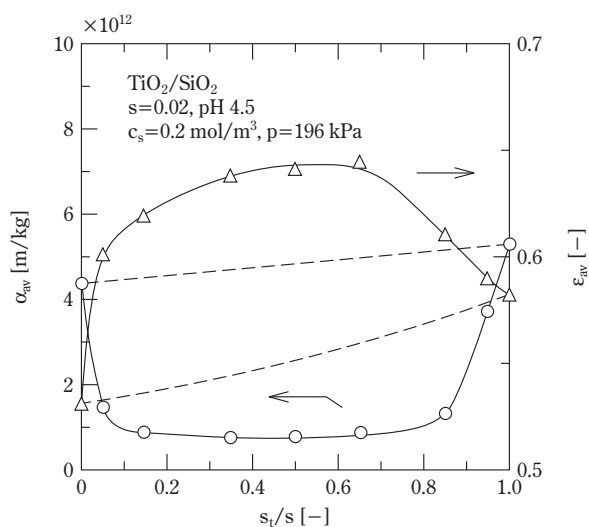


**Fig. 18** Effect of mixing ratio of particles on average specific filtration resistance and average porosity in microfiltration of binary particulate mixtures at pH 4.5.

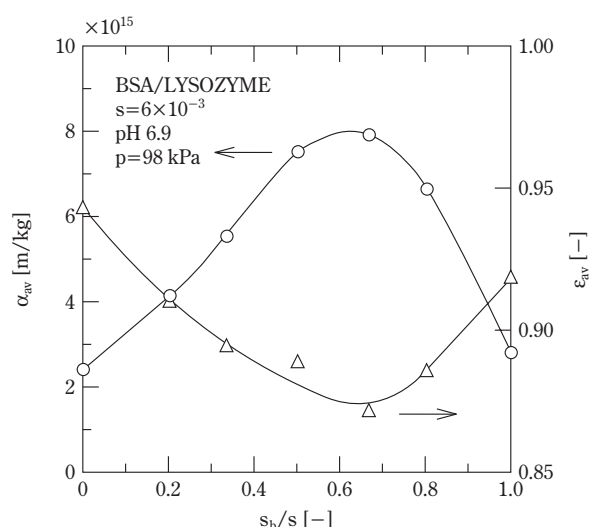


**Fig. 19** Effect of mixing ratio of proteins on average specific filtration resistance and average porosity in ultrafiltration of binary protein mixtures at pH 6.9.

tion. Thus, the coagulated colloids form highly permeable filter cakes, minimizing decreases in the filtration rate. For reference, the calculations based on the additive law on the specific volume and the effective specific surface area are shown as the dotted lines [56]. It is obvious that the effect of the surface charge of the particles on the cake properties should be considered.

It is of significance to compare the results with those obtained in dead-end ultrafiltration of the mixed protein solutions. It was observed that the results obtained with protein ultrafiltration were in sharp contrast to those with particulate microfiltration [17]. The properties of the cake formed on the retentive membranes in dead-end ultrafiltration of binary protein mixtures have been studied by using a mixture of the two proteins BSA and egg white lysozyme. The molecular weight and the isoelectric point of lysozyme are 14,300 Da and 11.0, respectively. In **Fig. 19**, the properties of the filter cake at pH 6.9 are shown against the mixture ratio of the proteins, where  $s_b$  is the mass fraction of BSA in the solution, and the total mass fraction  $s$  of solutes is kept constant. Of particular importance is the surprising result that the porosity  $e_{av}$  shows a distinct minimum. In the case of the single solute solutions, the average porosity is relatively large, since only an electrostatic repulsive force acts between the solutes. In contrast, in the mixed protein solutions, the BSA and lysozyme molecules are oppositely charged at pH 6.9. Therefore, the

average porosity of the cake decreases markedly by adding the other protein to the single protein solution because of a higher attraction between solutes. The decrease of the porosity  $e_{av}$  roughly corresponds to the increase of the resistance  $a_{av}$ . The resistance shows a definite maximum at the mixing ratio of about 0.6 because the most compact cake forms at that mixing ratio. Since the protein molecules are hydrophilic colloids, their stability in the solution is influenced not only by the presence of a surface charge on the protein but also by hydration of the surface layers of the protein. Even in the pH range where the two protein molecules have opposite electrical charges, protein molecules are well dispersed in the solution due to hydration of the protein. Consequently, the mixed protein cake becomes compact because of the attractive force associated with oppositely charged solutes.

In microfiltration of binary particulate mixtures, the effects of adding electrolyte on  $a_{av}$  and  $e_{av}$  at two different pH values are shown in **Fig. 20**. The addition of salts leads to a decrease of the zeta potential because of a less extensive electrical double layer. It is observed that at pH 4.5  $a_{av}$  increases and  $e_{av}$  decreases slightly, but discernibly with the increase of the salt concentration. The result is explained by assuming that the coulombic attractive force between the particles decreases due to a decrease of the zeta potential, and as a result the effect of heterocoagulation is weakened. At pH 9.6, it is found that  $a_{av}$

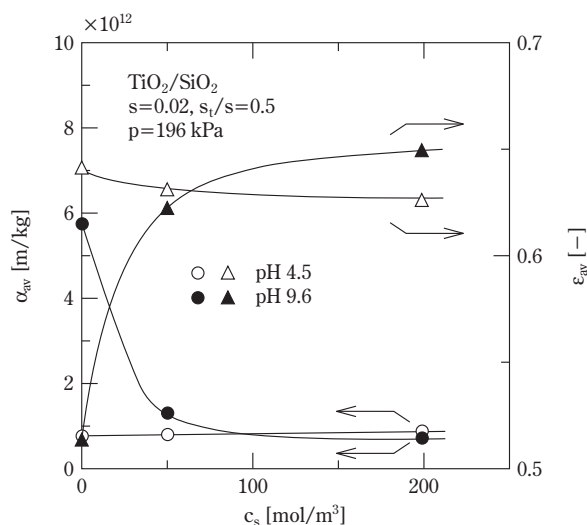


**Fig. 20** Effect of NaCl concentration on average specific filtration resistance and average porosity.

decreases and  $e_{av}$  increases markedly with increasing NaCl concentration. At this pH, the repulsive force that stems from the overlapping of the electric double layers, is reduced because of the charge-shielding due to the presence of salts, and consequently particles tend to aggregate [59]. Thus, the cakes formed are more open and have a lower resistance to flow.

In **Fig. 21**, the profiles of the average specific fil-

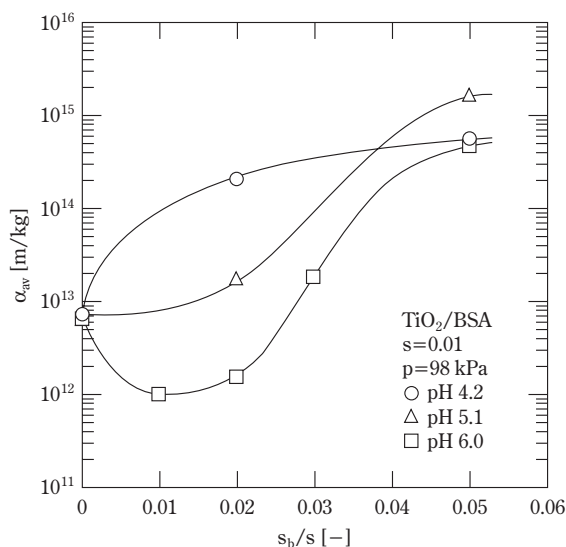


**Fig. 21** Effect of mixing ratio of proteins on average specific filtration resistance in ultrafiltration of particle/protein mixtures.

tration resistance  $a_{av}$  obtained in dead-end ultrafiltration of titanium dioxide suspensions containing BSA molecules using 10 kDa membranes are illustrated for various pH values against the mass ratio ( $s_b/s$ ) of BSA to the net colloids. At pH 4.2 and 5.1, the value of  $a_{av}$  increases with an increase of the mass fraction of BSA. This is because the specific resistance  $a_{av}$  of BSA is significantly larger than that of titanium dioxide. At pH 6.0, however, in the range of quite small BSA fractions  $a_{av}$  tends to become smaller than that of the cake composed of titanium dioxide alone ( $s_b/s = 0$ ). The result is perhaps surprising when one considers the high specific resistance of BSA. At pH 6.0 the positive charge of the titanium dioxide particle is cancelled by the adsorption of negatively charged BSA molecules. The flocculation of titanium dioxide therefore occurs due to a marked decrease of the zeta potential of the complex of titanium dioxide particles and BSA molecules. This brings about the specific behavior of  $a_{av}$  at pH 6.0.

The average specific filtration resistance  $a_{av}$  for different concentrations of sodium chloride is plotted in **Fig. 22** against the mass ratio of BSA to the net colloids. The value of  $a_{av}$  decreases markedly by the addition of an appropriate volume of sodium chloride and BSA. This is due to charge-shielding of both particles and proteins caused by the presence of the salts, thus reducing the electrostatic repulsion between titanium dioxide and BSA.

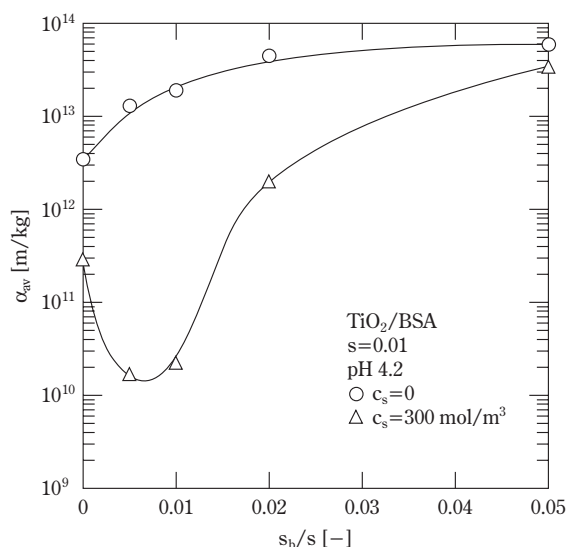


**Fig. 22** Effect of salt addition on average specific filtration resistance in ultrafiltration of particle/protein mixtures.

## 8. Fractionation of Mixtures by Filtration

Solute/solute interaction plays an important role in both the filtration rate and the solute rejection when two or more proteins are ultrafiltered [60-62]. It is generally accepted that solutes whose molecular dimensions are clearly small enough to permeate the membrane are substantially retained by that same membrane when larger solutes are present [63].

In **Fig. 23**, the solute rejection behavior following ultrafiltration of binary BSA/lysozyme mixtures containing equal amounts of each protein is shown in the form of the apparent rejection  $R_{\text{obs},l}$  of lysozyme versus the cumulative filtrate volume  $v$  per unit effective membrane area collected in the filtration time  $q$  [64]. Ultrafiltration experiments were carried out with the upward filtration mode, in which the filtrate flow was opposite to the direction of gravity, using hydrophobic, sorptive polysulfone membranes with a molecular weight cut off of 30,000 Da, making it essentially impermeable to BSA, but permeable to lysozyme. Solution pH was adjusted to 7, which is pH between the isoelectric points of both proteins, and the NaCl concentration  $c_s$  was varied. The apparent rejection  $R_{\text{obs},l}$  of lysozyme can be defined by

$$R_{\text{obs},l} = 1 - \frac{c_l}{s_l} \quad (24)$$

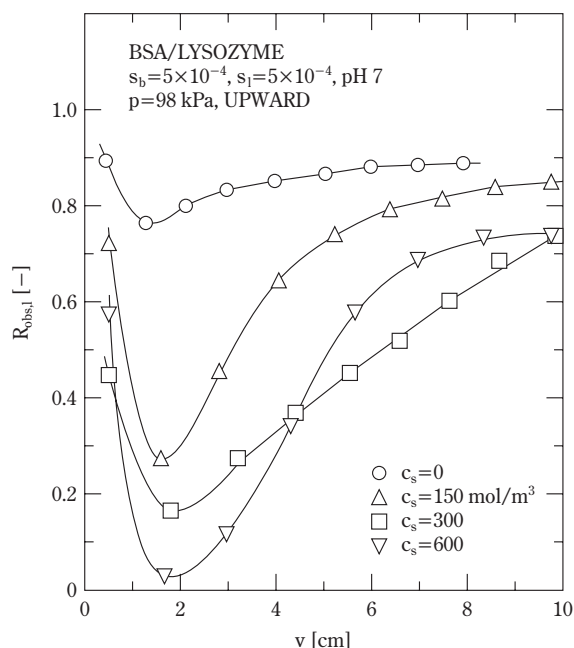


**Fig. 23** Effect of salt addition on apparent lysozyme rejection at pH 7.

where  $c_l$  and  $s_l$  are the mass fractions of lysozyme in the filtrate and bulk feed solution, respectively. Filtration of binary protein mixtures with this membrane resulted in nearly complete retention of BSA, but the variation in the lysozyme rejection with the filtrate volume. In the incipient stages of filtration, the membrane exhibits a high lysozyme rejection which may be attributed to adsorption of the lysozyme solutes on the hydrophobic surface of the membrane [65]. The rejection  $R_{\text{obs},l}$  is high during ultrafiltration in the absence of NaCl ( $c_s = 0$ ). The BSA molecule is negatively charged at pH 7, while the lysozyme molecule has a net positive charge at this pH value. The filter cake formed on the membrane surface consists of the admixture of two proteins very well packed to form a compact layer because the coulombic, attractive force associated with oppositely charged solutes, resulting in high rejection of lysozyme. It can be seen that the lysozyme rejection decreases with the increase of the NaCl concentration. In the case of a charge-stabilized colloid such as protein, solute interactions depend on the magnitude of the surface charge and/or on the extent of the electrical double layer, and this depends on the total electrolyte concentration. When salts are added, this leads to a less extensive electrical double layer. Such charge-shielding between the protein molecules resulting from the existence of salts would reduce electrostatic attraction between BSA and lysozyme molecules. Thus, the solute rejection at first declines to a minimum value. However, as filtration proceeds, the compressible filter cake of retained BSA solutes provides a barrier to transport of the smaller lysozyme solutes [66], and hence the rejection of the lysozyme solutes rises dramatically.

In **Fig. 24**, the flux behavior of the experiment described in **Fig. 23** is shown in the form of the reciprocal filtration rate ( $dq/dv$ ) versus  $v$ . This plot is well known as the Ruth plot [3] in the cake filtration of particulate suspensions. In principle, the value of  $dq/dv$  is directly proportional to the hydraulic resistance due to solute accumulation on or in the membrane. It would be expected that a rather dense, finely porous filter cake of retained BSA/lysozyme mixtures forms on the membrane surface during the early stages of filtration without added salt. Since the hydraulic resistance of this filter cake is remarkably large, the value of  $dq/dv$  rises rapidly to a near-asymptotic value with increasing filtrate volume. However, increase in the thickness of the filter cake is suppressed because the filter cake is exfoliated continuously by the effect of gravity with the progress of filtration, similar to upward ultrafiltration of single

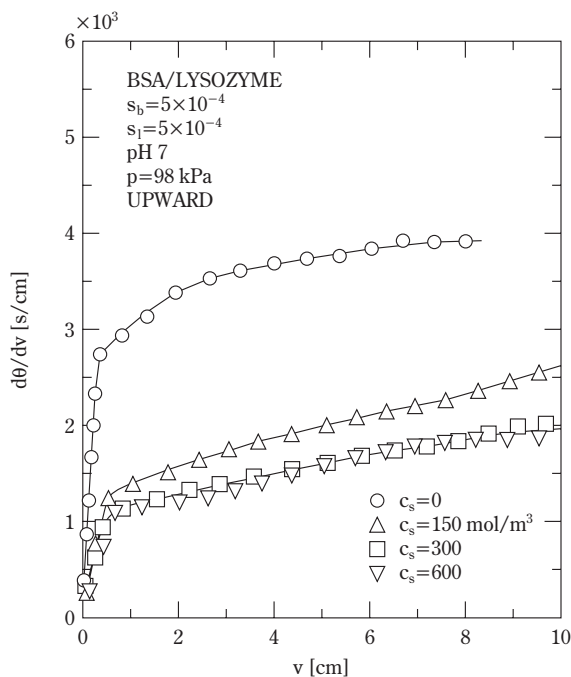


**Fig. 24** Effect of salt addition on filtration rate at pH 7.

protein solutions [40, 54]. The filtration rate increases markedly on addition of NaCl because of the formation of a filter cake which is substantially free from lysozyme molecules. However, as filtration proceeds, the filtration rate decreases gradually because the lysozyme molecules are trapped in the pores of the filter cake.

In **Fig. 25**, the reciprocal filtration rate ( $dq/dv$ ) in the unstirred downward and upward, and the stirred downward ultrafiltration of binary BSA/lysozyme mixtures is shown as a function of  $v$  [67]. For these experiments, ultrafiltration membranes with very low adsorptivity for proteins were used. Solution environment was set at pH 7 and the NaCl concentration of 300 mol/m³ where electrostatic interactions between BSA and lysozyme weakened comparatively as implied from **Figs. 23** and **24**. For conventional unstirred downward ultrafiltration, the plot is virtually linear throughout the course of filtration because of the continuous formation of the filter cake on the membrane in accordance with the compressible cake filtration model [2, 9, 15]. For unstirred upward ultrafiltration, the flux decline is suppressed, similar to the result of **Fig. 24**. The increase in the shear stress acting on the membrane surface by stirring leads to the suppression of the cake deposition, and consequently the marked increase in the filtration rate. Since the fil-

tration rate in upward ultrafiltration is slightly lower than that in stirred ultrafiltration with stirring of 5.2 rad/s, an effect of gravity acting on the filter cake in upward ultrafiltration corresponds to that of very low shear stress.

**Figure 26** shows the lysozyme rejection behavior of the experiment described in **Fig. 25**. The figure indicates that the lysozyme solutes pass almost completely through the membrane in unstirred downward

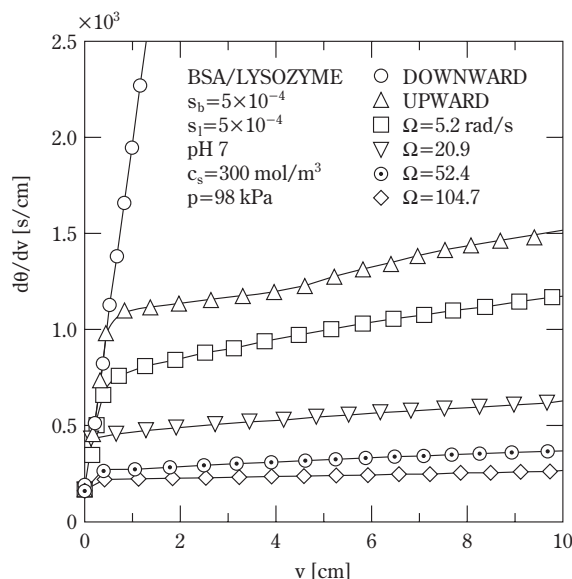


**Fig. 25** Effect of hydrodynamics above membrane on filtration rate.

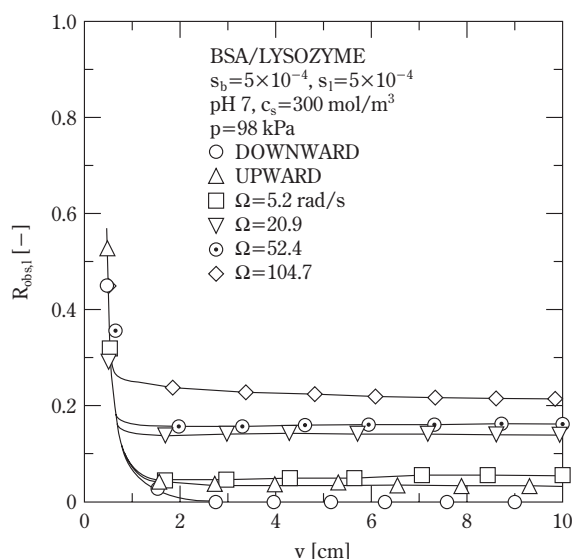


**Fig. 26** Effect of hydrodynamics above membrane on apparent lysozyme rejection.



ultrafiltration and are only a little retained by the membrane in upward ultrafiltration except that the high rejection appears in the incipient stages of filtration. It has been reported that in single protein solutions the stirring resulted in increasing the solute rejection [63]. It should be emphasized that also in binary protein mixtures the higher stirring speed causes the higher rejection of the solutes. This is because the concentration of lysozyme near the membrane decreases with increasing shear stress acting on the membrane.

**Figures 25 and 26** suggest that it is necessary to control the hydrodynamics above the membrane in order to obtain high lysozyme transmission simultaneously with high filtration rate. While hard stirred ultrafiltration, which produces the high filtration rate and solute rejection, is very effective for concentrating protein solutions, it is not suitable for fractionation of binary protein mixtures. It can be concluded from the figures that unstirred upward or mildly stirred ultrafiltration is more advantageous for the efficient fractionation of binary protein mixtures.

The effects of ultrasonic irradiation on the filtration rate and lysozyme rejection in upward ultrafiltration of binary BSA/lysozyme mixtures using the ultrafiltration membrane with very low adsorptivity for proteins at pH 7 and high salt concentration are shown in **Fig. 27** [67]. The whole of the filter was kept immersed in the ultrasonic cleaning bath full of water during the course of filtration. The filter was set up so that the membrane surface was perpendicular

to the propagation direction of the ultrasonic wave. The oscillating frequency and the output power of the ultrasonic irradiation were 25 kHz and 180 W, respectively. It is evident that the ultrasonic fields can contribute to the remarkable improvement in the filtration rate. As was shown in **Figs. 25 and 26**, although the observed filtration rate becomes high by increasing the shear stress on the membrane, the transmission of the lysozyme molecules becomes less. In contrast, of particular importance is the surprising observation that the ultrasonic irradiation does not lower the lysozyme transmission regardless of involving a marked increase in the filtration rate. One possible explanation for this result is that ultrasonic irradiation supplies vibrational energy to the filter cake to keep the solutes partly suspended, and therefore leaves more free channels for the filtrate flow.

To clarify the effects of the ultrasonic irradiation, the lysozyme rejections observed in the cases where the filtration rates with and without ultrasonic irradiation are very similar are compared in **Fig. 28**. The figure shows that the filtration rate in the ultrasonic upward ultrafiltration irradiated under output power of 180 W is substantially similar to that in downward ultrafiltration stirred with a rotational speed of 20.9 rad/s without ultrasonic irradiation. However, it is of importance to note that there is a marked difference in the lysozyme rejection. The lysozyme transmission in ultrasonic upward ultrafiltration is much higher than that in stirred ultrafiltration. Therefore, it is

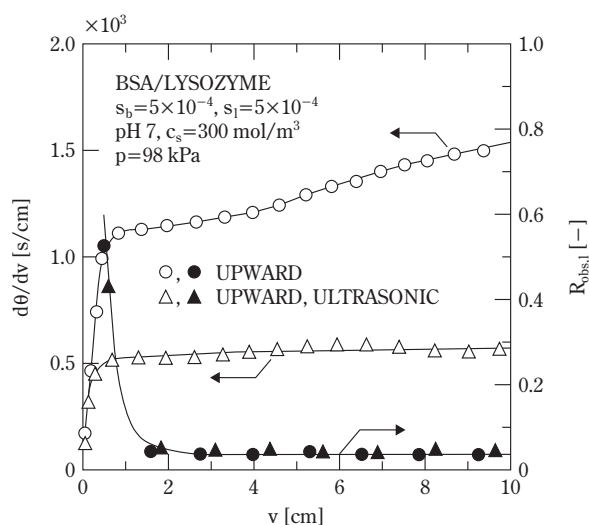


**Fig. 27** Effect of ultrasonic irradiation on filtration rate and apparent lysozyme rejection.

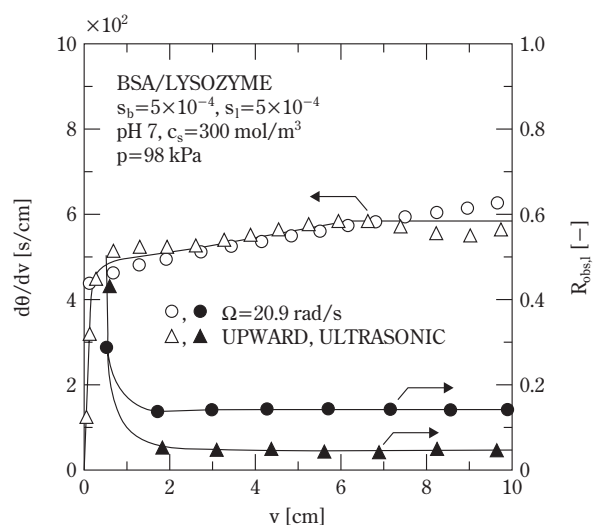


**Fig. 28** Comparison of apparent lysozyme rejection between cases with and without ultrasonic irradiation in which similar filtration rate are observed.

believed that the ultrasonic irradiation is quite effective not only for concentration of proteins by ultrafiltration [68] but also for fractionation of the binary protein mixtures by ultrafiltration.

## Conclusions

As was seen from this review, an understanding of the properties of the filter cake formed on the filter medium or the membrane can serve as a basis for clarifying the real mechanism of cake filtration and membrane filtration. In recent years, experimental testing procedures have been newly developed such as filtration experiments in which a filter was subjected to a sudden reduction in its filtration area and ultracentrifugation experiments. The compressible cake filtration model which explicitly took the non-homogeneity and the compressibility of the filter cake into consideration was used to describe the properties of the filter cake and the filtration behaviors. In protein ultrafiltration, the validity of the compressible cake filtration model was verified by the measurements of the concentration distributions in the filter cake using the principle of inclined filtration where a large amount of filter cake is formed. Moreover, it was shown that the solution properties (in particular, the solution pH and the electrolyte strength) play an important role in the filtration behaviors of colloids. The filtration behaviors of mixtures can be strongly affected by the nature of the interaction between the dissimilar components. Factors influencing fractionation behaviors by filtration were clarified. The author believes that many existing separation problems would have been avoided by the application of available scientific data although the random nature of most particulate dispersions has resulted in a difficult process problem.

## Acknowledgements

The author wishes to acknowledge the Ministry of Education, Culture, Sports, Science and Technology, Japan for the financial support and all university partners for the excellent cooperation.

## Nomenclature

$C_c$  empirical constant defined by Eq. (13)  
 $C_h$  ratio of volume of hydrous protein molecule to volume of anhydrous protein molecule  
 $c$  local mass fraction of solid or solute in filter cake

$c_l$  mass fraction of lysozyme in filtrate  
 $c_s$  NaCl concentration of solution (mol/m<sup>3</sup>)  
 $D$  inner diameter of inserted cylinder (m)  
 $D_h$  diameter of hole (m)  
 $d_f$  average equivalent spherical diameter of solute (m)  
 $E$  empirical constant defined by Eq. (22) (Pa<sup>-β</sup>)  
 $E_0$  empirical constant defined by Eq. (13)  
 $e$  local void ratio  
 $e_{av}$  average void ratio  
 $e_{av,w}$  average void ratio from filter medium surface to distance  $w$  from filter medium  
 $h$  height of filter chamber (m)  
 $J$  filtration rate (m/s)  
 $J_w$  apparent solvent velocity relative to solid at arbitrary position  $w$  (m/s)  
 $K_v$  Ruth coefficient of constant pressure filtration defined by Eq. (2) (m<sup>2</sup>/s)  
 $L$  thickness of filter cake (m)  
 $m$  ratio of wet to dry cake mass  
 $n$  empirical constant defined by Eq. (12)  
 $p$  applied filtration pressure (Pa)  
 $p_m$  pressure loss through filter medium (Pa)  
 $p_s$  local solid compressive pressure (Pa)  
 $p_{si}$  pressure below which  $e$  remains constant (Pa)  
 $R$  distance from center of rotation to bottom of sedimentation (m)  
 $R_{obs,l}$  apparent rejection of lysozyme defined by Eq. (24)  
 $r_i$  radial distance of sedimentation boundary from center of rotation (m)  
 $r_s$  distance from center of rotation to surface of sediment (m)  
 $S$  sedimentation coefficient (s/rad<sup>2</sup>)  
 $s$  mass fraction of solids in slurry, or mass fraction of solutes in bulk feed solution  
 $s_b$  mass fraction of BSA in bulk feed solution  
 $s_l$  mass fraction of lysozyme in bulk feed solution  
 $s_t$  mass fraction of titanium dioxide particles in slurry  
 $u$  apparent liquid velocity relative to solid (m/s)  
 $u_1$  filtration rate (m/s)  
 $v$  cumulative filtrate volume collected per unit effective medium area (m<sup>3</sup>/m<sup>2</sup>)  
 $v_t$  cumulative filtrate volume collected per unit effective medium area until cake surface reaches disk with hole (m<sup>3</sup>/m<sup>2</sup>)  
 $v_0$  sedimentation velocity (m/s)  
 $w_0$  net mass of solid per unit effective medium area (kg/m<sup>2</sup>)  
 $x$  distance from medium surface (m)  
 $\alpha$  local specific filtration resistance (m/kg)

$a_{av}$	average specific filtration resistance	(m/kg)
$a_1$	empirical constant defined by Eq. (12)	$(m^{n+1}s^{2n}/kg^{n+1})$
$b$	empirical constant defined by Eq. (22)	
$e$	local porosity	
$e_{av}$	average porosity	
$z$	zeta potential	(V)
$q$	filtration time	(s)
$m$	viscosity of filtrate	(Pa·s)
$r$	density of filtrate	(kg/m <sup>3</sup> )
$r_s$	true density of solid	(kg/m <sup>3</sup> )
$y$	angle between filtrate flow and direction of gravity	(rad)
$W$	angular velocity	(rad/s)
$w$	net solid volume per unit medium area lying from medium up to an arbitrary position in cake	(m)
$w_0$	net solid volume of entire cake per unit medium area	(m)

## References

- 1) Fane, A. G., "Ultrafiltration: Factors Influencing Flux and Rejection," Progress in Filtration and Separation, Wakeman, R. J. ed., Elsevier, Amsterdam, **4**, 134 (1986).
- 2) Iritani, E., Nakatsuka, S., Aoki, H. and Murase, T., "Effect of Solution Environment on Unstirred Dead-End Ultrafiltration Characteristics of Proteinaceous Solutions," *J. Chem. Eng. Japan*, **24**, 177 (1991).
- 3) Ruth, B. F., "Studies in Filtration. III. Derivation of General Filtration Equations," *Ind. Eng. Chem.*, **27**, 708-723 (1935).
- 4) Grace, H. P., "Resistance and Compressibility of Filter Cakes," *Chem. Eng. Progr.*, **49**, 303-318 (1953).
- 5) Shirato, M., Aragaki, T., Mori, R. and Sawamoto, K., "Predictions of Constant Pressure and Constant Rate Filtration Based upon an Approximate Correction for Side Wall Friction in Compression Permeability Cell Data," *J. Chem. Eng. Japan*, **1**, 86-90 (1968).
- 6) Tiller, F. M., Haynes, S. and W-M. Lu, "The Role of Porosity in Filtration: VII Effect of Side Wall Friction in Compression-Permeability Cells," *AIChE J.*, **18**, 13-20 (1972).
- 7) Gale, R. S., "Recent Research on Sludge Dewatering," *Filtr. & Sep.*, **8**, 531-538 (1971).
- 8) Murase, T., Iritani, E., Cho, J. H., Nakanomori, S. and Shirato, M., "Determination of Filtration Characteristics due to Sudden Reduction in Filtration Area of Filter Cake Surface," *J. Chem. Eng. Japan*, **20**, 246-251 (1987).
- 9) Shirato, M., Sambuichi, M., Kato, H. and Aragaki, T., "Internal Flow Mechanism in Filter Cakes," *AIChE J.*, **15**, 405-409 (1969).
- 10) Shirato, M., Aragaki, T. and Iritani, E., "Analysis of Constant Pressure Filtration of Power-Law Non-Newtonian Fluids," *J. Chem. Eng. Japan*, **13**, 61-66 (1980).
- 11) Murase, T., Iritani, E., Cho, J. H. and Shirato, M., "Determination of Filtration Characteristics Based upon Filtration Tests under Step-up Pressure Conditions," *J. Chem. Eng. Japan*, **22**, 373-378 (1989).
- 12) Terzaghi, K. and Peck, R. B., "Soil Mechanics in Engineering Practice," Wiley, New York, 65 (1948).
- 13) Tiller, F. M., "The Role of Porosity in Filtration. Part 2. Analytical Equations for Constant Rate Filtration," *Chem. Eng. Progr.*, **51**, 282-290 (1955).
- 14) Tanford, C., "Physical Chemistry of Macromolecules," Wiley, New York, 317 (1961).
- 15) Iritani, E., Hattori, K. and Murase, T., "Analysis of Dead-End Ultrafiltration Based on Ultracentrifugation Method," *J. Membrane Sci.*, **81**, 1-13 (1993).
- 16) Iritani, E., Mukai, Y. and Hagihara, E., "Measurements and Evaluation of Concentration Distributions in Filter Cake Formed in Dead-End Ultrafiltration of Protein Solutions," *Chem. Eng. Sci.*, **57**, 53-62 (2002).
- 17) Iritani, E., Mukai, Y. and Murase, T., "Properties of Filter Cake in Dead-End Ultrafiltration of Binary Protein Mixtures with Retentive Membranes," *Trans. IChemE, Part A, Chem. Eng. Res. Des.*, **73**, 551-558 (1995).
- 18) Tiller, F. M. and Cooper, H., "The Role of Porosity in Filtration. Part V. Porosity Variation in Filter Cakes," *AIChE J.*, **8**, 445-449 (1962).
- 19) Iritani, E., Hattori, K. and Murase, T., "Evaluation of Dead-End Ultrafiltration Properties by Ultracentrifugation Method," *J. Chem. Eng. Japan*, **27**, 357-362 (1994).
- 20) Iritani, E., Hattori, K., Akatsuka, S. and Murase, T., "Sedimentation Behavior of Protein Solutions in Ultracentrifugation Field," *J. Chem. Eng. Japan*, **29**, 352-358 (1996).
- 21) Michaels, A. S. and Bolger, J. C., "Settling Rates and Sedimentation Volumes of Flocculated Kaolin Suspensions," *Ind. Eng. Chem. Fundam.*, **1**, 24-33 (1962).
- 22) Murase, T., Iwata, M., Adachi, T., Gmachowski, L. and Shirato, M., "An Evaluation of Compression-Permeability Characteristic in the Intermediate Concentration Range by Use of Centrifugal and Constant-Rate Compression Techniques," *J. Chem. Eng. Japan*, **22**, 378-384 (1989).
- 23) Shirato, M., Aragaki, T., Ichimura, K. and Ootsuji, N., "Porosity Variation in Filter Cake under Constant-Pressure Filtration," *J. Chem. Eng. Japan*, **4**, 172-177 (1971).
- 24) Michaels, A. S., "New Separation Technique for the CPI," *Chem. Eng. Progr.*, **64**, 31-43 (1968).
- 25) Porter, M. C., "Concentration Polarization with Membrane Ultrafiltration," *Ind. Eng. Chem., Prod. Res. Dev.*, **11**, 234-248 (1972).
- 26) Trettin, D. R. and Doshi, M. R., "Ultrafiltration in an Unstirred Batch Cell," *Ind. Eng. Chem., Fundam.*, **19**, 189-194 (1980).
- 27) Kozinski, A. A. and Lightfoot, E. N., "Protein Ultrafiltration: A General Example of Boundary Layer Filtration," *AIChE J.*, **18**, 1030-1040 (1972).
- 28) Jonsson, G., "Boundary Layer Phenomena during Ultrafiltration of Dextran and Whey Protein Solutions," *Desalination*, **51**, 61-77 (1984).

- 29) Vilker, V. L., Colton, C. K. and Smith, K. A., "Concentration Polarization in Protein Ultrafiltration," *AIChE J.*, **27**, 632-645 (1981).
- 30) Wijmans, J. G., Nakao, S., van den Berg, J. W. A., Troelstra, F. R. and Smolders, C. A., "Hydrodynamic Resistance of Concentration Polarization Boundary Layers in Ultrafiltration," *J. Membrane Sci.*, **22**, 117-135 (1985).
- 31) van den Berg, G. B. and Smolders, C. A., "Flux Decline in Membrane Processes," *Filtr. & Sep.*, **25**, 115-121 (1988).
- 32) Reihanian, H., Robertson, C. R. and Michaels, A. S., "Mechanism of Polarization and Fouling of Ultrafiltration Membranes by Proteins," *J. Membrane Sci.*, **16**, 237-258 (1983).
- 33) Suki, A., Fane, A. G. and Fell, C. J. D., "Flux Decline in Protein Ultrafiltration," *J. Membrane Sci.*, **21**, 269-283 (1984).
- 34) Nakao, S., Wijmans, J. G. and Smolders, C. A., "Resistance to the Permeate Flux in Unstirred Ultrafiltration of Dissolved Macromolecular Solutions," *J. Membrane Sci.*, **26**, 165-178 (1986).
- 35) Nakakura, H., Yamashita, A., Sambuichi, M. and Osasa, K., "Electrical Conductivity Measurement of Filter Cake in Dead-End Ultrafiltration of Protein Solution," *J. Chem. Eng. Japan*, **30**, 1020-1025 (1997).
- 36) Nakao, S., Nomura, T. and Kimura, S., "Characteristics of Macromolecular Gel Layer Formed on Ultrafiltration Tubular Membrane," *AIChE J.*, **25**, 615-622 (1979).
- 37) McDonogh, R. M., Bauser, H., Stroh, N. and Grauschopf, U., "Experimental in situ Measurement of Concentration Polarization during Ultra- and Micro-filtration of Bovine Serum Albumin and Dextran Blue Solutions," *J. Membrane Sci.*, **104**, 51-63 (1995).
- 38) Gowman, L. M. and Ethier, C. R., "Concentration and Concentration Gradient Measurements in an Ultrafiltration Concentration Polarization Layer, Part I: A Laser-Based Refractometric Experimental Technique," *J. Membrane Sci.*, **131**, 95-105 (1997).
- 39) Fernández-Torres, M. J., Ruiz-Beviá, F., Fernández-Sempere, J. and López-Leiva, M., "Visualization of the UF Polarized Layer by Holographic Interferometry," *AIChE J.*, **44**, 1765-1776 (1998).
- 40) Iritani, E., Watanabe, T. and Murase, T., "Upward and Inclined Ultrafiltration under Constant Pressure by Use of Dead-End Filter," *Kagaku Kogaku Ronbunshu*, **17**, 206-209 (1991).
- 41) Zeng, W. P., Iritani, E. and Murase, T., "Dynamic Behavior of BSA Cake Layer Deposited on Membrane in Dead-End Inclined Ultrafiltration," *Kagaku Kogaku Ronbunshu*, **24**, 158-160 (1998).
- 42) Tiller, F. M., "The role of Porosity in Filtration, Numerical Methods for Constant Rate and Constant Pressure Filtration Based on Kozeny's Law," *Chem. Eng. Progr.*, **49**, 467-479 (1953).
- 43) Bacchin, P., Aimar, P. and Sanchez, V., "Model for Colloidal Fouling of Membranes," *AIChE J.*, **41**, 368-376 (1995).
- 44) Bacchin, P., Aimar, P. and Sanchez, V., "Influence of Surface Interaction on Transfer during Colloid Ultrafiltration," *J. Membrane Sci.*, **115**, 49-63 (1996).
- 45) Kawalec-Pietrenko, B. and Ruszel-Lichodziejewska, R., "The Influence of Physico-Chemical and Operating Parameters on the Filtration of Precipitate of Hydrated Zr(IV) Oxide," *J. Chem. Tech. Biotechnol.*, **35A**, 426-430 (1985).
- 46) McDonogh, R. M., Fell, C. J. D. and Fane, A. G., "Surface Charge and Permeability in the Ultrafiltration of Non-Flocculating Colloids," *J. Membrane Sci.*, **21**, 285-294 (1984).
- 47) McDonogh, R. M., Welsch, K., Fane, A. G. and Fell, C. J. D., "Incorporation of the Cake Pressure Profiles in the Calculation of the Effect of Particle Charge on the Permeability of Filter Cakes Obtained in the Filtration of Colloids and Particulates," *J. Membrane Sci.*, **72**, 197-204 (1992).
- 48) Schultz, J., Papirer, E. and Nardin, M., "Physicochemical Aspects of the Filtration of Aqueous Suspensions of Fibers and Cement. 4. Influence of the  $\zeta$  Potential of the Fibers on Filtration Efficiency," *Ind. Eng. Chem., Prod. Res. Dev.*, **22**, 102-105 (1983).
- 49) Tarleton, E. S. and Wakeman, R. J., "Understanding Flux Decline in Crossflow Microfiltration: Part II - Effects of Process Parameters," *Trans. IChemE, Part A, Chem. Eng. Res. Des.*, **72**, 431-440 (1994).
- 50) Ueshima, K., Iizuka, H. and Higashitani, K., "Ordered Structure of Monodispersed Particles Filtered at Constant Pressure," *J. Chem. Eng. Japan*, **24**, 647-652 (1991).
- 51) Welsch, K., McDonogh, R. M., Fane, A. G. and Fell, C. J. D., "Calculation of Limiting Fluxes in the Ultrafiltration of Colloids and Fine Particulates," *J. Membrane Sci.*, **99**, 229-239 (1995).
- 52) Willmer, S. A., Tarleton, E. S. and Holdich, R. G., "The Importance of Cake Compressibility in Deadend Pressure Filtration," *Proc. 7th World Filtration Congress, Vol. I*, p. 27-31, Hungarian Chemical Society, Budapest, Hungary (1996).
- 53) Iritani, E., Toyoda, Y. and Murase, T., "Effect of Solution Environment on Dead-End Microfiltration Characteristics of Rutile Suspensions," *J. Chem. Eng. Japan*, **30**, 614-619 (1997).
- 54) Iritani, E., Watanabe, T. and Murase, T., "Properties of Filter Cake in Dead-End Upward Ultrafiltration," *J. Membrane Sci.*, **69**, 87-97 (1992).
- 55) Iritani, E., Nagaoka, H. and Murase, T., "Filtration Characteristics and Cake Properties in Microfiltration of Binary Mixtures of Fine Particles," *Kagaku Kogaku Ronbunshu*, **22**, 648-654 (1996).
- 56) Shirato, M., Sambuichi, M. and Okamura, S., "Filtration Behavior of a Mixture of Two Slurries," *AIChE J.*, **9**, 599-605 (1963).
- 57) Abe, E., Hirose, H. and N. Yamada, "A Method for Predicting the Filtration Characteristics of Body Filtration," *J. Soc. Powder Technol. Japan*, **32**, 550-556 (1995).
- 58) Iritani, E., Mukai, Y. and Toyoda, Y., "Properties of a Filter Cake Formed in Dead-End Microfiltration of Binary

- Particulate Mixtures," *J. Chem. Eng. Japan*, **35**, 226-233 (2002).
- 59) Chang, D. J., Hsu, F. C. and Hwang, S. J., "Steady State Permeate Flux of Cross-Flow Microfiltration," *J. Membrane Sci.*, **98**, 97-106 (1995).
  - 60) Ingham, K. C., Busby, T. F., Sahlestrom, Y. and Castino, F., "Separation of Macromolecules by Ultrafiltration: Influence of Protein Adsorption, Protein-Protein Interactions, and Concentration Polarization," *Polymer Science and Technology, Ultrafiltration Membranes and Applications*, Cooper, A. R. ed., Plenum Press, New York, **13**, 141 (1980).
  - 61) Rodgers, V. G. J. and Sparks, R. E., "Reduction of Membrane Fouling in the Ultrafiltration of Binary Protein Mixtures," *AIChE J.*, **37**, 1517-1528 (1991).
  - 62) Zhang, L. and Spencer, H. G., "Selective Separation of Proteins by Microfiltration with Formed-in-Place Membranes," *Desalination*, **90**, 137-146 (1993).
  - 63) Nakatsuka, S. and Michaels, A. S., "Transport and Separation of Proteins by Ultrafiltration through Sorptive and Non-Sorptive Membranes," *J. Membrane Sci.*, **69**, 189-211 (1992).
  - 64) Iritani, E., Mukai, Y. and Murase, T., "Upward Dead-End Ultrafiltration of Binary Protein Mixtures," *Sep. Sci. Technol.*, **30**, 369-382 (1995).
  - 65) Iritani, E., Tachi, S. and Murase, T., "Influence of Protein Adsorption on Flow Resistance of Microfiltration Membrane," *Colloids Surfaces A: Physicochem. Eng. Aspects*, **89**, 15-22 (1994).
  - 66) Iritani, E., Itano, Y. and Murase, T., "Dead-End Inclined Ultrafiltration by Use of Dynamic Membranes," *Kagaku Kogaku Ronbunshu*, **19**, 536-539 (1993).
  - 67) Mukai, Y., Iritani, E. and Murase, T., "Fractionation Characteristics of Binary Protein Mixtures by Ultrafiltration," *Sep. Sci. Technol.*, **33**, 169-185 (1998).
  - 68) Kokugan, T., Kaseno, T., Fujiwara, S. and Shimizu, M., "Ultrasonic Effect on Ultrafiltration Properties of Ceramic Membrane," *Membrane*, **20**, 213-223 (1995).

### Author's short biography



#### Eiji Iritani

Dr. Eiji Iritani is Professor of the Department of Chemical Engineering at Nagoya University. He received his PhD from Nagoya University in 1981. He has worked extensively on most aspects of solid-liquid separation. These works now also include membrane separation, water treatment, and colloid engineering.



# Developments in the Understanding and Modeling of the Agglomeration of Suspended Crystals in Crystallization from Solutions<sup>†</sup>

René David<sup>1</sup>, Fabienne Espitalier<sup>1</sup>  
and Ana Cameirão<sup>1</sup>

Laboratory for Chemical Engineering of  
Particulate Solids

Loïc Rouleau<sup>2</sup>

Institut Français du Pétrole

## Abstract

*The paper deals with the modeling of the agglomeration of crystals during their crystallization. Crystal agglomeration actually consists of two steps, i.e. particle collision and agglomerate strengthening by crystal growth. The expression of agglomeration rates can be written in terms of a collision rate coupled with an efficiency factor. However, the mechanisms and rates of collision and disruption are related to the type of liquid flow that the mother crystals and the agglomerate experience, which in turn are dependent on their respective sizes. In particular, the influences of the absolute and relative sizes of mother particles, of the local energy dissipation and of the fluid viscosity differ according to the three types of motions, i.e. Brownian, laminar, turbulent. Besides this, the rapidity of the crystal growth, which in turn is a function of the supersaturation, plays a major role in the strengthening rate. The question of the limit cases between two regimes is also treated. The method takes into account and unifies previous expressions obtained by other authors in the various regimes. The model is also able to calculate the average agglomeration degrees.*

*The paper is illustrated by one example of crystal agglomeration from our recent work and introduces a general model.*

## 1. Introduction

The structure of many crystalline compounds obtained from suspension crystallization shows the presence of agglomerated crystallites or crystals. Solid bridges between the mother crystals bind the agglomerates. In some cases, the shape of the particles suggests a multistage agglomeration process with primary and secondary agglomerates (**Fig. 1a**). The sizes of the final agglomerates (1  $\mu\text{m}$  to 1 mm) and of their sub-units (a few tenths of nm to a few tenths of  $\mu\text{m}$ ) are widely spread out, depending on both the nature of the crystalline compound and the crystallization process. Among other materials, such structures have been observed for zeolites [1,21], adipic acid [2], calcium carbonate (calcite) and cal-

cium oxalate monohydrate [3,12], pseudo-boehmite [4], barium titanate [5].

Since the original paper of Schmoluchowski [20] one hundred years ago, many authors have tackled these mechanisms (see for instance [6,7]), and more recent progress [3,8,9] has been made in the simple and comprehensive modeling of agglomeration. In fact, crystal agglomeration consists of two steps, i.e. particle collision and agglomerate strengthening.

In the following paper, we intend to present a unified approach of the agglomeration in crystallization, which relies partly on published models that account for the different processes, which are applicable to the different size ranges and in agreement with experimental observations.

## 2. Efficiency of a binary agglomeration during crystallization

We suppose that all agglomerations result from a binary collision (**Fig. 1b**).

<sup>1</sup> CNRS-Ecole des Mines d'Albi-Carmaux, F-81013 Albi Cedex 9, France

<sup>2</sup> CEDI, BP 3, F-69390 Vernaison, France

<sup>†</sup> Accepted: June, 2003

Two particles of respective sizes  $S_i$  and  $S_j \leq S_i$  collide. An intermediate labile aggregate is formed. The collision of rate  $r_{col}$  is followed either by disruption into the two former mother particles or by consolidation by crystallization into an agglomerate, with respective rates  $r_d$  and  $r_{con}$ .

We suppose that the disruption and consolidation processes depend only on the concentration of the labile intermediate aggregate, which is assumed to be in a quasi-equilibrium state. Thus,

$$r_{col} = r_d + r_{con} \text{ with } r_{con} = k_{con} C_{int} \text{ and } r_d = k_d C_{int} \quad (1)$$

From the above set of equations (1), we derive the overall agglomeration rate

$$r_a = r_{con} = \eta r_{col} \quad (2)$$

Where  $\eta$  is the efficiency of the agglomeration, defined in terms of rate constants or characteristic times

$$\eta = 1 / (1 + k_d / k_{con}) = 1 / (1 + t_{cr} / t_d) \quad (3)$$

We assume that the consolidation process is crystallization: crystalline bridges are built by crystalline growth between the particles. Marchal et al [8] have shown that the crystallization time may be expressed as a function of the growth rate  $G$  of the crystal

$$t_{cr} = S_j f(S_j, S_j) / G \text{ and thus } \eta = 1 / (1 + S_j f(S_j, S_j) / G t_d) \quad (4)$$

The function  $f$  accounts for relative sizes and its

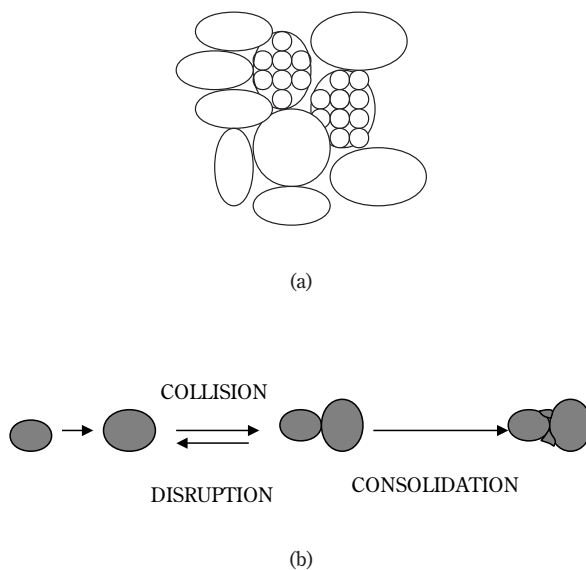


Fig. 1 Shape and creation of a two-stage agglomerate.

value always ranges between 10.5 and 12 from the expression of Marchal et al. [8]: It may be considered as a constant.

The variety of the sizes of the final agglomerates ( $1 \mu\text{m}$  to  $1 \text{mm}$ ) obtained in crystallization and of their sub-units (a few tenths of  $\text{nm}$  to a few tenths of  $\mu\text{m}$ ) is large. When compared with the characteristic sizes of fluid mechanics in the liquid phase (Taylor, Kolmogoroff, and Batchelor microscales [10]), it is clear that multiple collision and disruption mechanisms occur which are related to the type of liquid flow that the mother crystals and the intermediate aggregate experience. On the other hand, it is likely that the consolidation mechanism is crystalline growth. Its rate ranges between  $10^{-6}$  and  $10^{-11} \text{m/s}$  [11]. One difficulty is that the crystal growth rate varies during the process as a consequence of the depletion of the solute in the liquid phase.

### 3. Different regimes of particle motion

In the following paper, we assume that the agglomeration takes place under three different types of motion – Brownian, laminar, and turbulent – depending on the size of the colliding particles and of the resulting agglomerate. The collision between particles from size classes  $j$  and  $i \geq j$  is assumed to take place under motion  $k=b,l,t$  and the labile aggregate to be exposed to motion  $k'$ . Thus, the expressions of  $r_{col,k}$ ,  $t_{d,k'}$  and consequently  $\eta_{j,i,k'}$  will be different according to the types of fluid motions governing the collision and the disruption.

- Particles smaller than the Batchelor scale  $l_B$  experience Brownian motion: Particles collide as a result of a diffusion process. The random disruption competes with crystallization.
- Particles between  $l_B$  and the Kolmogoroff scale  $l_K$  are subjected to the laminar stretching and swirling process, also called engulfment [10]. The shear stress accounts for disruption, which competes with crystallization.
- Finally, particles larger than  $l_K$  collide under the influence of fluctuating velocities and are disrupted by the same phenomenon [8]. Crystallization is also here the agglomerating process.

If both mother particles and the agglomerate fall under one single regime, the values of  $k$  and  $k'$  are obvious.

The simplest exception is when the intermediate aggregate becomes larger than the upper limit of the regime governing collision of the mother particles. Then,  $k'$  switches over to the regime for larger parti-

cles.

This is not the case if the mother particles experience different regimes due to their very different sizes. Therefore, we have to make the following assumptions. The collision of particles in the Brownian and laminar regimes is governed by the diffusion of the smaller particle to the surface of the larger one ( $k=b$ ). The same approach holds for Brownian-turbulent collisions in the laminar boundary layer. The intermediate aggregate then evolves under a laminar disruption regime ( $k'=l$ ), the smaller particle being protected by the boundary layer of the larger one.

Collisions between particles in the laminar and in the turbulent ranges are consecutive to the turbulent motion ( $k=t$ ). The intermediate aggregate evolves like a turbulent agglomerate because its size exceeds  $l_K$  ( $k'=t$ ).

The different possibilities are summarized in **Fig. 2**.

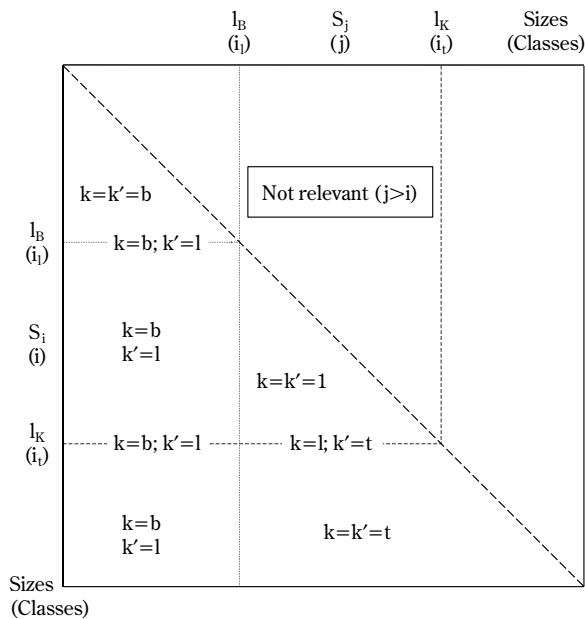


**Fig. 2** Different types of collisions and consolidation processes of agglomerates as a function of the sizes of the mother particles.

#### 4. Expressions of agglomeration kernels

The agglomeration rate in the collision regime  $k$  and in the disruption regime  $k'$  is expressed as

$$r_{a,j,i,k,k'} = \eta_{j,i,k'} r_{col,j,i,k} \quad (5)$$

It is generally accepted since the work of Schmoluchowski [20] that

$$r_{col,j,i,k} = \beta_{c,j,i,k} N_i N_j \quad (6)$$

where  $N_i$  and  $N_j$  are the respective concentrations of particles belonging to the classes  $i$  and  $j$ , respectively. Thus,

$$r_{a,j,i,k,k'} = \eta_{j,i,k'} \beta_{c,j,i,k} N_i N_j = \beta_{j,i,k,k'} N_i N_j \quad (7)$$

**Table 1** presents the expressions of  $\beta_{c,j,i,k}$  and  $\eta_{j,i,k'}$  for the different values of  $k$  and  $k'$  for either rapid or slow growth rates. In the case of a slow crystal growth rate, Eq. (4) simplifies to

$$\eta_{j,i,k'} \sim Gt_d/S_j \quad (8)$$

However, this simplification may not be correct for very small, i.e. nanometric sizes  $S_j$ . In this case, the entire expression (4) should be kept for  $\eta_{j,i,k'}$ .

The expressions for the Brownian and laminar collision kernels have been established and discussed since many years [6,7,9,24] (**Table 1**). In the Brownian range, when the particles are free of electric charges, Van der Waals forces ensure the cohesion of aggregates until crystallization takes place [22]; Otherwise, the DLVO theory [9] accounts for coagulation processes, but collisions with a third particle may lead to releases in the case of low crystalline growth.

Marchal [8] has proposed expressions for both collision rate and efficiency in the turbulent regime, which were validated on adipic acid. More recently, Hounslow and co-workers introduced several expressions for the laminar agglomeration efficiency [12]; among them we have retained the most recent one, which is in agreement with our general formulation of section 2. The disruption time is then expressed as [12]

$$t_d = \sigma^* L / [A_1 \rho_{susp} P X] \quad (9)$$

where  $X$  has the dimension of a length; Several expressions combining  $S_i$  and  $S_j$  have been tried for  $X$  and this will be discussed later.  $P$  is the dissipated energy per unit mass of suspension,  $\rho_{susp}$  is the density of the suspension,  $\sigma^*$  is the tensile strength of the solid,  $L$  a contact length between particles,  $A_1$  a dimensionless constant.

A first point is that the efficiency  $\eta_{j,i,k'}$  is close to 1 for the Brownian and laminar disruption regimes if the growth rate is high.

Now, let us have a closer look at the different types of collisions in **Fig. 2** under a low (**Table 2**) or high (**Table 3**) crystalline growth rate. In order to check the parameter sensitivity, we have examined three

**Table 1** Expressions of collision rate constant and consolidation efficiency for either low or high growth rates. Example of stirred tanks.

	LOW GROWTH RATE	HIGH GROWTH RATE
<b>k</b>	<b>Collision rate constant <math>\beta_{c,j,i,k}</math></b>	
b	$= \frac{2k_B T}{3\mu} \frac{(S_i + S_j)^2}{S_i S_j} \quad (1)$	
l	$= k'_{Al} \frac{(S_i + S_j)^3 P^{1/2}}{v^{1/2}} \text{ with } k'_{Al} \neq 0.16 \quad (2)$	
t	$= k'_{At} (S_i + S_j)^2 N D_A [8] \quad (3)$	
<b>k'</b>	<b>Efficiency <math>\eta_{j,i,k'}</math></b>	
b	$= 1 / (1 + A_b S_j / G) \quad (4)$	$= 1$
l	$= \frac{G \sigma^* L}{A_l P \rho_{\text{susp}} X S_j} \text{ with } L \sigma^* / A_l \approx 1 [12] \quad (5)$	$= 1$
t	$= \frac{G \left( 1 - \left( \frac{S_i + S_j}{\lambda_c} \right)^2 \right)}{A_t N S_j} [8] \quad (6)$	$= \frac{1}{1 + \frac{S_j}{G t_d}} \text{ with } t_d = \frac{\left( 1 - \left( \frac{S_i + S_j}{\lambda_c} \right)^2 \right)}{A_t N} [8] \quad (7)^*$

\*  $\lambda_c$  is the Taylor scale in the suspension, generally in the order of magnitude of a few mm and  $\sim P^{-1/2}$ .

**Table 2** Influence of stirring speed N or dissipated energy P, sizes of mother particles  $S_j$  and  $S_i$  on collision rate constant and efficiency for different size ranges of mother particles and agglomerate. Case of low growth rates.

$S_j$	$S_i$	$S_a$	k	k'	LOW GROWTH RATE	Collision rate constant $\beta_{c,j,i,k}$	Agglomeration efficiency $\eta_{j,i,k'}$	Overall agglomeration rate constant $\beta_{j,i,k,k'}$
$\leq l_B$	$\leq l_B$	$\leq l_B$	b	b	Expressions	(1)	(4)	(1) $\times$ (4)
					N or P increases	—	—	—
					$S_j = S_i$ increases	Constant $= 8kT/3\mu$	Decreases	Decreases
					$S_j$ increases with constant $S_i$	Decreases	Decreases $\sim S_j^{-1}$	Decreases
$\leq l_B$	Any size $\geq S_j$	$> l_B$	b	l	Expressions	(1)	(5)	(1) $\times$ (5)
					N or P increases	—	Decreases $\sim P^{-1}$	Decreases $\sim P^{-1}$
					$S_j = S_i$ increases	Constant $= 8kT/3\mu$	Decreases $\sim S_i^{-2}$	Decreases $\sim S_i^{-2}$
					$S_j$ increases with constant $S_i$	Decreases	Decreases $\sim S_j^{-2}$	Decreases
$> l_B$	$> l_B$	$> l_B$	l	l	Expressions	(2)	(5)	(2) $\times$ (5)
$\leq l_K$	$\leq l_K$	$\leq l_K$			N or P increases	Increases $\sim P^{1/2}$	Decreases $\sim P^{-1}$	Decreases $\sim P^{-1/2}$
					$S_j = S_i$ increases	Increases $\sim S_i^3$	Decreases $\sim S_i^{-2}$	Increases $\sim S_i$
					$S_j$ increases with constant $S_i$	Increases	Decreases $\sim S_j^{-2}$	Decreases
$> l_B$	$> l_B$	$> l_K$	l	t	Expressions	(2)	(6)	(2) $\times$ (6)
$\leq l_K$	$\leq l_K$				N or P increases	Increases $\sim P^{1/2}$	Decreases $\sim P^{-1/3}$	Increases $\sim P^{1/6}$
					$S_j = S_i$ increases	Increases $\sim S_i^3$	Decreases $\sim S_i^{-1}$	Increases $\sim S_i^2$
					$S_j$ increases with constant $S_i$	Increases	Decreases $\sim S_j^{-1}$	Minimum at $S_j = S_i/2$
$> l_K$	$> l_K$	$> l_K$	t	t	Expressions	(3)	(6)	(3) $\times$ (6)
					N or P increases	Increases $\sim P^{1/3}$	Decreases $\sim P^{-1/3}$	—, but decreases with sizes close to the Taylor scale
					$S_j = S_i$ increases	Increases $\sim S_i^2$	Decreases $\sim S_i^{-1}$	Increases $\sim S_i$ , until the Taylor scale is reached
					$S_j$ increases with constant $S_i$	Increases	Decreases $\sim S_j^{-1}$	Decreases

The relations numbered (1)-(7) correspond to those of **Table 1**.

**Table 3** Influence of stirring speed  $N$  or dissipated energy  $P$ , sizes of mother particles  $S_j$  and  $S_i$  on collision rate constant and efficiency for different size ranges of mother particles and agglomerate. Case of high growth rates.

$S_j$	$S_i$	$S_a$	$k$	$k'$	HIGH GROWTH RATE	Collision rate constant $\beta_{c,i,j,k}$	Agglomeration efficiency $\eta_{j,i,k'}$	Overall agglomeration rate constant $\beta_{j,i,k,k'}$
$\leq l_B$	$\leq l_B$	$\leq l_B$	$b$	$b$	Expressions	(1)	$=1$	(2)
					$N$ or $P$ increases	—		—
					$S_j=S_i$ increases	Constant= $8kT/3\mu$		Constant= $8kT/3\mu$
					$S_j$ increases with constant $S_i$	Decreases		Decreases
$\leq l_B$	Any size $\geq S_j$	$> l_B$	$b$	$l$	Expressions	(1)		(2)
					$N$ or $P$ increases	—		—
					$S_j=S_i$ increases	Constant= $8kT/3\mu$		Constant= $8kT/3\mu$
					$S_j$ increases with constant $S_i$	Decreases		Decreases
$> l_B$ $\leq l_K$	$> l_B$ $\leq l_K$	$> l_B$ $\leq l_K$	$l$	$l$	Expressions	(2)		(2)
					$N$ or $P$ increases	Increases $\sim P^{1/2}$		Increases $\sim P^{1/2}$
					$S_j=S_i$ increases	Increases $\sim S_i^3$		Increases $\sim S_i^3$
					$S_j$ increases with constant $S_i$	Increases		Increases
$\leq l_K$	$\leq l_K$	$> l_K$	$l$	$t$	Expressions	(2)	(7)	(2) $\times$ (7)
					$N$ or $P$ increases	Increases $\sim P^{1/2}$	Decreases	Increases
					$S_j=S_i$ increases	Increases $\sim S_i^3$	Decreases	Increases
					$S_j$ increases with constant $S_i$	Increases	Decreases	?
$> l_K$	$> l_K$	$> l_K$	$t$	$t$	Expressions	(3)	(7)	(3) $\times$ (7)
					$N$ or $P$ increases	Increases $\sim P^{1/3}$	Decreases	Increases, but diminishes when Taylor scale is reached
					$S_j=S_i$ increases	Increases $\sim S_i^2$	Decreases	Increases, but diminishes when Taylor scale is reached
					$S_j$ increases with constant $S_i$	Increases	Decreases	?

The relations numbered (1)-(7) correspond to those of **Table 1**.

influences: The increase of power dissipated in the suspension, the increase of size for the agglomeration of particles of the same size ( $S_i=S_j$ ), and the increase of smaller particle sizes  $S_j$  at a constant large particle size  $S_i$ . As far as the dissipated power  $P$  is concerned, note that (a) there is no influence of  $P$  on  $\beta_{i,i,k,k'}$  for mixing in the Brownian regime, (b) that high power is less favorable to laminar agglomeration at low growth rates, whereas (c) it has an enhancing factor at high growth rates. Finally, there is a miscellaneous influence of  $P$  on the agglomeration kernel in the turbulent regime.

The variation of the collision rate constant  $\beta_{c,i,i,k}$ , the efficiency  $\eta_{i,i,k'}$  and the agglomeration kernel  $\beta_{i,i,k,k'}$  in the case of colliding particles of equal sizes is particularly interesting (**Figs. 3** and **4**):  $\beta_{c,i,i,k}$  increases continuously with increasing size, whereas  $\eta_{i,i,k'}$  always decreases. The kernel is an increasing function of size for high growth rates and shows a mini-

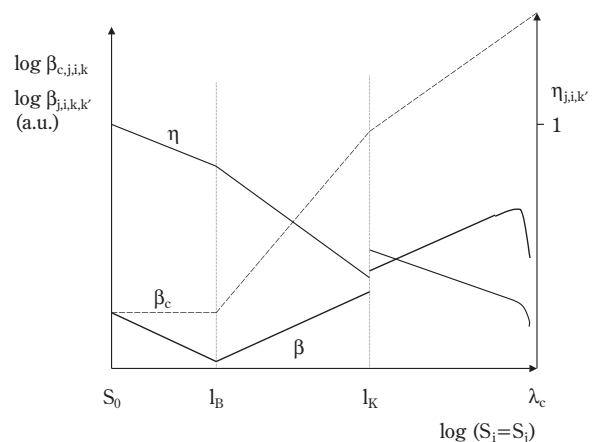


**Fig. 3** Collision and overall agglomeration rate constant against the common size of mother particles for collision of particles of the same size. Case of very low growth rates.



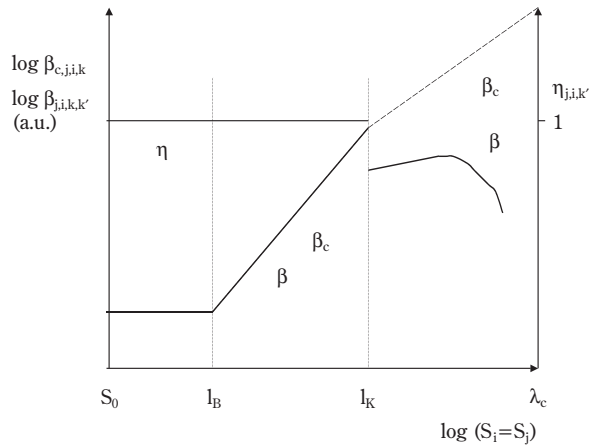


**Fig. 4** Collision and overall agglomeration rate constant against the common size of mother particles for collision of particles of the same size. Case of high growth rates.

num value at size  $l_B$  at low growth rates. In all cases, both  $\eta_{i,i,k'}$  and  $\beta_{i,i,k,k'}$  tend towards zero when the size reaches the turbulent Taylor scale  $\lambda_c$  [8].

Finally, looking at the influence of relative particle sizes, **Tables 2** and **3** show a major difference between the shapes of agglomerates generated by high and low growth rates in the different regimes. If the agglomeration kernel decreases with increasing  $S_j/S_i$  it means that the agglomeration between small and large particles is favored. Conversely, if the kernel increases it means that agglomeration between particles of similar sizes is enhanced. Thus, in the first case, agglomerates show the so-called “snowball” effect (compact agglomerates made from agglomerates and elementary smaller particles or agglomerates), while in the second case, the agglomerates will be made from equally sized mother agglomerates.

For high growth rates, the first case prevails until the Batchelor microscale is reached and the second case seems likely above this scale. At low growth rates, the kernel behaves differently: The limit between the two cases is about the Kolmogoroff microscale.

Generally, one should notice the different and sometimes opposite trends predicted by the model for the different couples of mother particles depending on their absolute and relative sizes and the intensity of the growth rate. This may explain the discrepancies observed in the literature [8,12,13] when trying to report and to model the variations of the agglomeration rate for several crystallizations or several crystal size ranges and varying the stirring power.

## 5. Transition between Brownian and laminar regimes

The transition occurs at the size limit  $l_B$ , which may be calculated as follows. The significance of the Batchelor scale is underlined by Baldyga and Bourne [10]. When a fluid portion undergoes laminar stretching, it reaches a reduced transversal size which is so small that the transportation length of a molecule by diffusion or of a particle due to Brownian motion during the stretching time is of the same order of magnitude as the thickness of the laminae. This length scale is called the Batchelor scale [10].

$$l_B = \left( \frac{\nu D^2}{P} \right)^{1/4} \quad (10)$$

where the diffusivity  $D$  of a particle of size  $S_j$ , the most mobile of the two, is [23]

$$D = \frac{k_B T}{3\pi\mu S_j} \quad (11)$$

$\mu$  and  $\nu$  are the dynamic and kinematic viscosities of the suspension, respectively;  $l_B$  is in the order of magnitude of a few hundred nm for particles from 10 to 100 nm in stirred tanks. Note that the collision rates calculated by (1) and (2) in **Table 1** are of the same order of magnitude when sizes of colliding particles both equal  $l_B$ . Therefore, since the collision rate increases strongly with the size of particles in the laminar regime, we assume that the representative curves cross at  $S_j = l_B$  (**Figs. 3** and **4**). For the low growth rates, we have no indication that the efficiencies are equal at the transition size. But, the physical continuity seems a fair assumption for the agglomeration process, as a change of slope (**Figs. 3** and **4**) will rapidly make the laminar agglomeration rate predominant with increasing sizes.

## 6. Transition between laminar and turbulent regimes

The Kolmogoroff microscale is expressed as [10]

$$l_K = (\nu^3/P)^{1/4} \quad (12)$$

If two particles are smaller than the Kolmogoroff microscale, they experience no velocity fluctuations for both collision and disruption. This scale is in the order of magnitude of some tenths of micrometers. An equality of the collision and agglomeration rate expressions seems likely at  $l_K$ , but the slope of the collision rate is reduced when switching to the turbulent regime (**Figs. 3** and **4**).

## 7. Particle size distribution

The modeling is based on the method of classes introduced by David et al. [2,8,14] where the size scale of particles is divided into  $n_c$  classes, and where the limits of these classes are in geometric progression with a factor of  $2^{1/3}$  [10], i.e. a factor of 2 for the volumes.  $n_c$  is chosen in order to verify  $L_{n_c} > \lambda_c$ . The actual continuous distribution is replaced by a virtual discrete distribution which works with classes of rank  $n$ , whose average size is  $S_n = (L_n + L_{n-1})/2$  and where the shape factor is volumetrically the same. Recently, Verkoeijen et al. [26] presented a generalized volume approach of population balances in the same manner which was applied to comminution, sintering and granulation. Here, the impact on class  $n$  of agglomerations between particles of classes  $j$  and  $i \geq j$  is represented by stoichiometric coefficients  $v_{n,ji}$  by analogy with a chemical reaction system. These coefficients have to be calculated in order

- to balance the solid volume, which is equivalent to the conservation of the 3<sup>rd</sup> moment of the distribution, and,
- to remove one single particle for each agglomeration (except for agglomeration (i,i) where only 1/2 a particle disappears due to symmetry) to permit compliance with the 0<sup>th</sup> moment equation of the PSD.

Three different schemes of agglomeration have to be differentiated with respect to the relative sizes of the particles. Hereafter, **(i)** represents the particle class  $i$  and so on

$$1/2 \text{ (i)} + 1/2 \text{ (i)} \rightarrow 1/2 \text{ (i+1)} \quad (13)$$

$$\text{(i-1)} + 1/2 \text{ (i)} \rightarrow 1/2 \text{ (i+1)} \quad (14)$$

$$v_i / (v_i - v_j) \text{ (j < i-1)} + \text{(i)} \rightarrow v_i / (v_i - v_j) \text{ (i)} \quad (15)$$

The corresponding stoichiometric coefficients that stand for the impact of agglomeration (i,j) on particle class  $n$  are

$$v_{n,ji} = \delta_{n,i+1}/2 - \delta_{n,i} \quad (16)$$

$$v_{n,i-1,i} = \delta_{n,i+1}/2 - \delta_{n,i}/2 - \delta_{n,i-1} \quad (17)$$

$$v_{n,ji} = v_j / (v_i - v_j) \delta_{n,i} - v_i / (v_i - v_j) \delta_{n,j} \quad (18)$$

$\delta_{n,i}$  is an element of the Kronecker matrix ( $\delta_{n,i} = 0$  if  $n \neq i$  and  $\delta_{n,i} = 1$  if  $n = i$ ). The resulting agglomeration rate for class  $n$  is

$$R_{A,k,k',n} = \sum_{i=1}^{n_c} \sum_{j=1}^i v_{n,ji} r_{a,j,i,k,k'} = \sum_{i=1}^{n_c} \sum_{j=1}^i v_{n,ji} \beta_{j,i,k,k'} N_j N_i \quad (19)$$

The particle size distribution (PSD)  $\Psi$  is integrated over class  $n$  between sizes  $L_{n-1}$  and  $L_n$  for  $n_c \geq n \geq 1$  in a batch stirred crystallizer with suspension volume  $V_{\text{susp}}$ , yielding the particle concentration in class  $n$ , i.e.  $N_n$

$$\frac{1}{V_{\text{susp}}} \frac{d(N_n V_{\text{susp}})}{dt} = G(L_{n-1}) \Psi(L_{n-1}) - G(L_n) \Psi(L_n) + \delta_{n,1} r_N + \sum_{k=b;1;t} \sum_{k'=b;1;t} R_{A,k,k',n} \quad (20)$$

with  $\Psi(L_{-1}) = \Psi(L_{n_c}) = 0$ . Note that  $r_N$  is the generation rate of crystalline particles. The nucleation term accounts for the generation of crystallites in class 1 only.

Classical characteristic length scales are derived from the discrete distribution; For instance

$$\overline{L_{43}} = \frac{\sum_{n=1}^{n_c} S_n^4 N_n}{\sum_{n=1}^{n_c} S_n^3 N_n} \quad (21)$$

The total number of particles per suspension volume unit which disappeared by an agglomeration through mechanism  $(k,k')$  is

$$R_{A,k,k',T} = \sum_{n=1}^{N_c} R_{A,k,k',n} \quad (22)$$

The rate of molar production of crystalline solid mass per unit volume of suspension is expressed as

$$\frac{dc_c}{dt} = \Phi_v \frac{\rho_s}{M_s} \left( 3G \sum_{n=1}^{n_c} L_n^2 N_n + S_0^3 r_N \right) \quad (23)$$

where  $\Phi_v$  is a volumetric shape factor,  $\rho_s$  and  $M_s$  are the density and molar mass of the solid, respectively, and  $r_N$  is the nucleation rate of the crystalline solid.

There may be other types of solids with concentration  $c_s$ , for instance amorphous solids, in the crystallizer. The concentration of the solute  $c_l$  can be derived from the solute plus solid mass balance

$$(c_{s0} + c_{c0}) V_{\text{susp}} + c_{l0} V_{l0} = (c_c + c_s) V_{\text{susp}} + c_l V_l \quad (24)$$

$$\text{With } V_l = V_{\text{susp}} (1 - M_s c_s / \rho_s + M_c c_c / \rho_c) \quad (25)$$

Finally, the growth rate is related to the supersaturation  $\sigma = c_l / C_c^* - 1$

$$G = G_0 \sigma^{k_1} \quad (26)$$

## 8. Implementation of other agglomerate properties

The description of agglomerates cannot simply be elucidated by means of a size distribution. The ag-

glomerate structure has to be characterized by other variables such as shape factors, porosity, fractality, or agglomeration degrees. The purpose of this section is to show how our method can give access to the average values of such additional properties, without introducing a 2-variable distribution function like that used by [15,16].

Therefore, we simply look at how each property is modified – or not – by every elementary agglomeration (i,j). In this section, we use the example of two different agglomeration degrees which we define as follows:

We call a primary agglomerate a structure made of crystallites with a minimum size  $L_{PA}$  which is approximated by the boundary between class  $n_{PA}$  and  $n_{PA}+1$ . The primary agglomeration degree (=average number of crystallites in the primary agglomerates) is

$$\overline{n_{PA}} = \frac{N_{CT} - \sum_{A=1}^{n_{PA}} N_n 2^{n-1}}{N_{PA}} \quad (27)$$

where  $N_{CT}$  and  $N_{PA}$  are the total concentration of crystallites and primary agglomerates, respectively.

In an earlier paper [14], we used another definition for the agglomeration degree. Starting from  $N_0$  particle concentration at time 0, and since every agglomeration removes one model particle from the suspension, we added the total number of agglomerations in the k regime for collision and the k' regime for consolidation

$$\overline{n_{PAI}} = \frac{1}{1 + \int_0^t R_{A,k,k',T} dt} \quad (28)$$

This relation encompasses all agglomerations in the regimes k and k' without any minimal size of the resulting agglomerate.

Similarly, the secondary agglomeration degree is the number of primary agglomerates embedded in a secondary agglomerate

$$\overline{n_{SA}} = \frac{(N_{PA} - N_{FPA})}{N_{SA}} \quad (29)$$

where  $N_{FPA}$  and  $N_{SA}$  are the total concentration of free primary agglomerates and secondary agglomerates, respectively.

Both definitions correspond to quantities which are easy to observe via image analysis with SEM or ESEM pictures.

**Table 4** shows the stoichiometric coefficients affecting  $N_{PA}$ ,  $N_{FPA}$  and  $N_{SA}$  for all elementary agglomeration processes between our classes of virtual particles.

Note that  $N_{CT}$  is not affected by any agglomeration. It only depends on the nucleation rate and is expressed in a batch crystallizer as

$$\frac{dN_{CT}}{dt} = r_N \quad (30)$$

Consequently, the equations describing the evolu-

**Table 4** Stoichiometric coefficients for primary agglomerates, free primary agglomerates, secondary agglomerates concentrations depending on the type of agglomeration: (i) represents the i<sup>th</sup>-class of particles. Free primary agglomerates are only encountered in class  $n_{PA}+1$ . The standard virtual agglomerate of class  $n \geq n_{PA}+1$  encompasses  $2n - n_{PA} - 1$  primary agglomerates.

Agglomerations	Stoichiometric coefficients for		
	$N_{PA}$	$N_{FPA}$	$N_{SA}$
$v_i / (v_i - v_j) (1 \leq j \leq i-2) + (1 \leq i \leq n_{PA}) \longrightarrow v_i / (v_i - v_j) (i \leq n_{PA})$	0	0	0
$(n_{PA}-1) + 1/2(n_{PA}) \longrightarrow 1/2(n_{PA}+1)$	1/2	1/2	0
$1/2(n_{PA}) + 1/2(n_{PA}) \longrightarrow 1/2(n_{PA}+1)$	1/2	1/2	0
$(n_{PA}) + 1/2(n_{PA}+1) \longrightarrow 1/2(n_{PA}+2)$	1/2	-1/2	1/2
$1/2(n_{PA}+1) + 1/2(n_{PA}+1) \longrightarrow 1/2(n_{PA}+2)$	0	-1	1/2
$(n_{PA}+1) + 1/2(n_{PA}+2) \longrightarrow 1/2(n_{PA}+3)$	0	-1	0
$v_i / (v_i - v_j) (j = n_{PA}+1) + (i \geq n_{PA}+3) \longrightarrow v_i / (v_i - v_j) (i)$	0	$-v_i / (v_i - v_j)$	$v_j / (v_i - v_j)$
$v_i / (v_i - v_j) (n_{PA}+2 \leq j \leq i-2) + (n_{PA}+4 \leq i \leq n_c) \longrightarrow v_i / (v_i - v_j) (i)$	0	0	-1
$(i-1) + 1/2 (i \geq n_{PA}+3) \longrightarrow 1/2(i+1)$	0	0	-1
$1/2(i \geq n_{PA}+2) + 1/2(i) \longrightarrow 1/2(i+1)$	0	0	-1/2

tions of  $N_{PA}$ ,  $N_{FPA}$  and  $N_{SA}$  against time are

$$\begin{aligned} \frac{dN_{FPA}}{dt} &= G(L_{PA})\Psi(L_{PA}) + \frac{1}{2} [r_{a,n_{PA}-1,n_{PA},k,k'} \\ &\quad + r_{a,n_{PA},n_{PA},k,k'} - r_{a,n_{PA},n_{PA}+1,k,k'} \\ &\quad - r_{a,n_{PA}+1,n_{PA}+1,k,k'} - r_{a,n_{PA}+1,n_{PA}+2,k,k'} \\ &\quad - \sum_{i=n_{PA}+3}^{n_c} \frac{v_i}{(v_i - v_{n_{PA}+1})} r_{a,n_{PA}+1,i,k,k'}] \\ \frac{dN_{PA}}{dt} &= G(L_{PA})\Psi(L_{PA}) + \frac{1}{2} [r_{a,n_{PA}-1,n_{PA},k,k'} \\ &\quad + r_{a,n_{PA},n_{PA},k,k'} + r_{a,n_{PA},n_{PA}+1,k,k'}] \\ \frac{dN_{SA}}{dt} &= \frac{1}{2} [r_{a,n_{PA},n_{PA}+1,k,k'} + r_{a,n_{PA}+1,n_{PA}+1,k,k'}] \\ &\quad - \sum_{i=n_{PA}+3}^{n_c} \frac{v_{n_{PA}+1}}{(v_i - v_{n_{PA}+1})} r_{a,n_{PA}+1,i,k,k'} \\ &\quad - \sum_{i=n_{PA}+3}^{n_c} \sum_{j=n_{PA}+2}^{i-1} r_{a,j,i,k,k'} - \frac{1}{2} \sum_{i=n_{PA}+2}^{n_c} r_{a,i,i,k,k'} \quad (31) \end{aligned}$$

The  $G\Psi$  term in differential equations for  $N_{PA}$  and  $N_{FPA}$  accounts for the growth of the agglomerate from class  $n_{PA}$  into class  $n_{PA}+1$ , thus leading to a free primary agglomerate according to our definition. Conversely, the quality of the agglomerate or free primary agglomerate is not lost by the growth from class  $n_{PA}+1$  into class  $n_{PA}+2$ . In the same manner, secondary agglomerates cannot be generated by simple growth from primary agglomerates, but only via an agglomeration of primary agglomerates: Therefore, there is no  $G\Psi$  term in the differential equation for  $N_{SA}$ .

Such sets of equations can be derived for other average properties such as, for instance, porosity: One simply has to express how far every agglomeration changes the porosity of the agglomerates.

## 9. Example of amorphous crystallization coupled with agglomeration of the crystalline form

The model is applied to the crystallization of zeolites. In this type of crystallization, an amorphous gel is formed immediately after mixing the reactants [1,17]. This gel is poured into a batch crystallizer and heated at temperatures ranging between 80 and 250°C, at which point the amorphous solid transforms into a less soluble, crystalline solid [25].

Experimental details are available in [23]. Samples were taken from the solid and the liquid phases in

order to determine the crystallinity by XRD, the PSD by laser diffractometry, and supersaturation by atomic absorption spectroscopy.

The following observations were made:

- The crystallizer is mechanically stirred (axial stirrer with a power number of 1 and diameter  $D_A=0.08$  m). At temperatures of around 200°C, the suspension behaves from a rheological point of view like a Newtonian fluid with a kinematic viscosity close to  $10^{-6} \text{ m}^2\text{s}^{-1}$ , and a suspension density of about  $10^3 \text{ kg.m}^{-3}$ .
- Amorphous particles in the suspension have an initial concentration of  $N_0$  and an initial size of  $L_0=65 \text{ nm}$  ( $S_0=57.5 \text{ nm}$ ).
- The suspension volume of  $10^{-2} \text{ m}^3$  is constant. Coupled with the following assumptions:
- The initial supersaturation in the liquid phase is

$$\sigma_0 = C_{am}^*/C_c^* - 1 \quad (32)$$

- The increase of the solid mass during the whole process due to crystal growth can be neglected.
- According to the literature [18], it is likely that the crystallites are nucleated by the surface transformation of the amorphous particles. Agglomeration starts as soon as the external surface is crystalline. Dissolution of the amorphous compound obeys a Gaussian rate law. This is consistent with our experimental XRD observations when monitoring the crystalline fraction of the solid [19]. The molar concentration of the amorphous compound  $am$  decreases according to

$$\frac{dc_s}{dt} = \frac{dc_{am}}{dt} = -\Phi_v \frac{\rho_s}{M_s} S_0^3 r_N \quad (33)$$

- The crystal growth is independent of crystal size. Its order is  $k_1=1$  with respect to supersaturation.
- An amorphous particle has the same density  $\rho_s$ , shape factor  $\Phi_v$ , and molecular weight  $M_s$  as a crystalline one. No agglomerate porosity was assumed.
- Agglomeration takes place via the mechanisms described above.
- The laminar to turbulent transition occurs at about 100 to 70  $\mu\text{m}$  (Kolmogorov microscale) and agglomeration stops at 3.5 to 2.5 mm (Taylor microscale) depending on the stirring speed ( $N=1.7-4.3 \text{ s}^{-1}$ ). As the observed agglomerates are smaller than 50  $\mu\text{m}$ , we assume that there is no turbulent agglomeration taking place.
- For the sake of simplicity, we will choose in the following  $L_{PA}=L_B$ , i.e.  $n_{PA}=m$ .

The above equation system is expressed in dimen-

sionless variables: time  $\theta = tG_0/L_0$  with  $G = G_0 \sigma^{k_1}$  ( $G$  is estimated from SEM micrographies of crystallites by taking samples at different times); reduced size  $\lambda = L/L_0$ ; reduced average class size  $s = S/L_0$ ; reduced particle concentration in class  $n$ :  $y_n = N_n/N_0$ ; reduced density distribution  $\Phi = \Psi L_0/N_0$ ; reduced concentration in the liquid phase  $x_l = c_l/C_c^*$ ; reduced supersaturation  $\sigma = c_l/C_c^* - 1$ ; reduced concentration of the amorphous solid phase  $x_a = c_a/C_c^*$ ; and reduced concentration of the crystalline solid phase  $x_c = c_c/C_c^*$ .

## 10. Results, parameter estimation and discussion

Then, the initial conditions of the differential equations are

$$y_n = 0 (n = 1, n_c); y_{CT} = y_{PA} = y_{FPA} = y_{SA} = 0; \\ x_a = x_{a0} = m_0/c^*; x_{c0} = 0 \quad (34)$$

Four dimensionless parameters remain: the initial fraction of the solid phase

$$m_0 = m_{tot}/(\rho_s V_{susp}) = \Phi_v S_0^3 N_0 \quad (35),$$

the initial supersaturation  $\sigma_0$ , the solubility

$$c^* = M_s C_c^* / \rho_s \quad (36)$$

and the Brownian agglomeration rate constant

$$K_{Ab} = 2k_B T L_0 N_0 / (3\mu G_0) = 2k_B T m_0 / (3\mu G_0 \Phi_v S_0^3 L_0^2) \quad (37)$$

Then, the dimensionless agglomeration rate from (36) and Eqs. (1) and (4) of **Table 1** is expressed as

$$r_{a,j,i,b,b} \frac{N_0 L_0}{G_0} = K_{Ab} \frac{(s_i + s_j)^2}{s_i s_j} \frac{1}{1 + \left( \frac{A_b L_0}{G_0} \right) \frac{s_j}{\sigma_0^{k_1}}} \quad (38)$$

$A_b$  was estimated at about  $10^{-6} \text{ s}^{-1}$  by equalizing the agglomeration rates in the laminar and in the Brownian regimes at  $l_B = S_i = S_j$ . The efficiency was always very close to 1 and, therefore, the simulations were not sensitive to  $A_b$ .

The reduced laminar collision rate constant  $K_{Al}$  can be deduced from  $k'_{Al}$  by

$$K_{Al} = k'_{Al} (P/v)^{1/2} L_0 / G_0 \quad (39)$$

Normally,  $k'_{Al}$  should be equal to 0.16 according to the literature [9].

The initial upper size  $L_0$  and the kinetic growth rate constant  $G_0$  were estimated from the SEM pictures of the crystallites, with the actual supersaturation known. However, such a determination for  $G_0$  is rather inaccurate. Therefore, it is checked by comparing the

reduced final time of complete supersaturation consumption  $\theta_F$  and the measured one  $t_F G_0 / L_0$ . The parameters  $m_0$ ,  $c^*$  and  $\sigma_0$  are deduced from the measured solid mass and the initial and final concentrations of the solute in the liquid phase. No indication could be found in the literature about the order  $k_1$  in the crystal growth rate expression for the type of zeolite studied. Therefore, the simplest way was to take  $k_1 = 1$ .

Finally, two parameters were fitted by trial and error. Several expressions of  $X$  were tried in the expression of the laminar efficiency factor (**Table 1**). The best fit with the experimental PSD was observed using  $X = S_i$ . In accordance with [12], the term  $\sigma^* L / A_1$  should be fixed at 1, which is the value for calcite, but  $\sigma^*$  and  $L$  may vary from species to species and from polymorph to polymorph. Finally, the best fit was obtained with  $\sigma^* L / A_1 = 0.0035$ .

Thus,

$$r_{a,j,i,l,l} \frac{N_0 L_0}{G_0} = K_{Al} \frac{m_0}{\Phi_v S_0^3} (s_i + s_j)^3 \frac{1}{1 + \left( \frac{A_1 P \rho_{susp} L_0^2}{G_0 \sigma^* L} \right) \frac{s_j s_i}{\sigma_0^{k_1}}} \quad (40)$$

A comparison between the final experimental and the calculated particle size distributions, both with the same geometrical progression for the class sizes on the abscissa scale, is represented in **Fig. 5**. The experimental PSD was obtained from samples taken by laser diffraction analysis. The agreement is fair with respect to the particular shape of the experimental PSD. The values of experimental parameters of the simulation are listed in **Table 5**. However, the main peak of the PSD is narrower for the simulation than

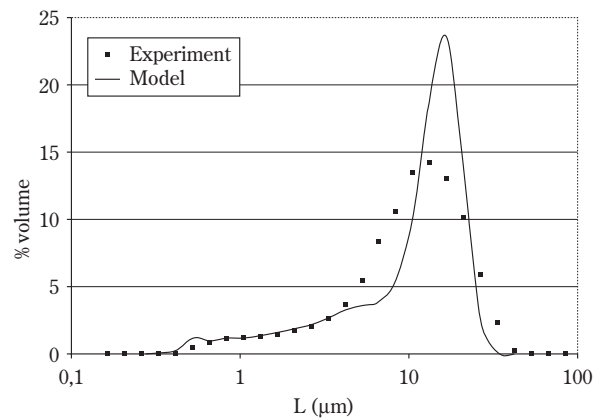


**Fig. 5** Comparison of experimental and calculated PSD. Experimental conditions:  $T = 180^\circ\text{C}$ ;  $N = 2.92 \text{ s}^{-1}$ ; stirrer power number = 1; stirrer diameter = 0.08 m; for other parametric values see **Table 5**.



**Table 5** Values of parameters of the simulation presented in Fig. 5.

$P=$	$8.16 \times 10^{-3} \text{ W/kg}$
$\nu=$	$10^{-6} \text{ m}^2 \cdot \text{s}^{-1}$
$V_{\text{susp}}=$	$10^{-2} \text{ m}^3$
$\rho_{\text{susp}}=$	$1000 \text{ kg} \cdot \text{m}^{-3}$
$\rho_{\text{sm}}=\rho_c$	$1800 \text{ kg} \cdot \text{m}^{-3}$
$M_{\text{sm}}=M_c$	$7.1 \text{ kg} \cdot \text{mol}^{-1}$
$k_1=$	1
$L_0=$	65 nm
$G_0=$	$2.5 \times 10^{-11} \text{ m} \cdot \text{s}^{-1}$
$m_0=$	$m_{\text{tot}}/(\rho_s V_{\text{susp}})=0.048$
$K_{\text{Ab}}=$	$2k_B T m_0 / (3\mu G_0 \Phi_v S_0^3 L_0^2) = 8.36 \times 10^6$
$K_{\text{Al}}=$	$k'_{\text{Al}}(P/\nu)^{1/2} L_0 m_0 / (\Phi_v S_0^3 G_0)$ with $k'_{\text{Al}}=0.16$
$c^*=$	$C^* M_c / \rho_c = 0.01$
$\sigma_0=$	$=0.55$
$A_b=$	$=10^{-4} \text{ s}^{-1}$
$A_l/\sigma^* L=$	$=0.0035 \text{ Pa}^{-1} \cdot \text{m}^{-1} [12]$

the experimental one. The porosity (0.35-0.5) shown by the secondary agglomerates (primary agglomerates appear non-porous) on SEM pictures may explain this difference: the agglomerates generated by laminar collision and consolidation processes, and whose size was measured by the laser diffraction, show an apparent volume larger than the actual solid volume. Due to the fractal nature of these agglomerates, an overall size dispersion is expected to be registered by the laser diffractometer.

## 11. Conclusions

The binary agglomeration of crystalline particles in a supersaturated solution has been shown to be the combination of two independent processes, i.e. particle collision and aggregate consolidation. Therefore, the overall agglomeration rate is expressed as the collision rate times an efficiency factor. This efficiency relies on a competition between crystallization and disruption.

When multiple agglomeration is evidenced, both collision and consolidation may take place in a Brownian, laminar or turbulent regime, depending on the size of the mother and daughter particles. In stirred tanks, the dependence on parameters such as stirring speed, liquid viscosity, or particle size differs according to the regimes involved. Boundary rules for limit cases have been established.

The method takes into account and unifies previous

expressions obtained by other authors in the various regimes and checked by them with respect to experimental results for several agglomerating products.

As far as the structure of agglomerates is concerned, the model using a reaction-like set of stoichiometric equations was able to calculate the average primary and secondary agglomeration degrees.

An example based on zeolite crystallization from the amorphous state has been developed. The particle size distribution was found to be in very good agreement with the experimental one.

We plan to extend the present work to other products that are subject to multiple agglomeration and other crystal properties.

## Acknowledgements

The authors thank the Institut Français du Pétrole for scientific and financial support of this work.

## Nomenclature

$A_b$	: Brownian efficiency constant	$[\text{s}^{-1}]$
$A_l$	: Laminar efficiency constant	$[-]$
$A_t$	: Turbulent efficiency constant	$[\text{m}^3 \cdot \text{s}^{-1}]$
$c, C$	: Concentrations	$[\text{mol} \cdot \text{m}^{-3}]$
$c^*$	: Reduced solubility	$[-]$
$C^*$	: Solubility	$[\text{mol} \cdot \text{m}^{-3}]$
$D_A$	: Stirrer diameter	$[\text{m}]$
$D$	: Diffusivity of a particle	$[\text{m}^2 \cdot \text{s}^{-1}]$
$f$	: Marchal's [8] function	$[-]$
$G$	: Growth rate of a crystal	$[\text{m} \cdot \text{s}^{-1}]$
$G_0$	: Growth rate constant	$[\text{m} \cdot \text{s}^{-1}]$
$k_B$	: Boltzmann Constant	$[\text{J} \cdot \text{molecule}^{-1} \cdot \text{K}^{-1}]$
$k'_{\text{Al}}$	: Constant of collision rate constant for laminar regime	$[-]$
$k'_{\text{At}}$	: Constant of collision rate constant for turbulent regime	$[-]$
$k_d$	: Disruption rate constant	$[-]$
$k_{\text{con}}$	: Consolidation rate constant	$[-]$
$k_l$	: Kinetic order of growth rate	$[-]$
$k_B$	: Boltzmann Constant	$[\text{J} \cdot \text{molecule}^{-1} \cdot \text{K}^{-1}]$
$K_{\text{Ak}}$	: Agglomeration rate constant of type $k$	$[-]$
$l_K$	: Kolmogorov microscale	$[\text{m}]$
$l_B$	: Batchelor scale	$[\text{m}]$
$L$	: Particle size	$[\text{m}]$
$L_0$	: Amorphous particle size	$[\text{m}]$
$\overline{L_{43}}$	: Average final particle size	$[\text{m}]$
$m_0$	: Initial fraction of solid phase	$[-]$
$m_{\text{tot}}$	: Initial particle mass	$[\text{kg}]$
$M_s$	: Solid molar mass	$[\text{kg} \cdot \text{mol}^{-1}]$
$N$	: Stirring speed	$[\text{s}^{-1}]$

$n_c$	: Total size class number	[–]	suspension	[kg.m <sup>-1</sup> s <sup>-1</sup> ]
$\overline{n_{PA}}$	: Primary agglomeration degree	[–]	$\nu$	: Kinematic viscosity of suspension [m <sup>2</sup> .s <sup>-1</sup> ]
$\overline{n_{PAI}}$	: Primary agglomeration degree	[–]	$\nu_{n,j,i}$	: Stoichiometric coefficient accounting for the impact of agglomeration ( $j,i$ ) on particle class $n$ [–]
$\overline{n_{SA}}$	: Secondary agglomeration degree	[–]	$\rho_c$	: Crystal density [kg.m <sup>-3</sup> ]
$N_0$	: Particle concentration at time 0	[m <sup>-3</sup> ]	$\rho_s$	: Solid density [kg.m <sup>-3</sup> ]
$N_{CT}$	: Total concentration of crystallites	[m <sup>-3</sup> ]	$\rho_{susp}$	: Suspension density [kg.m <sup>-3</sup> ]
$N_{FPA}$	: Total concentration of free primary agglomerates	[m <sup>-3</sup> ]	$\psi$	: Particle size density function (PSD) [m <sup>-4</sup> ]
$N_{PA}$	: Total concentration of primary agglomerates	[m <sup>-3</sup> ]	$\sigma$	: Supersaturation [–]
$N_n$	: Concentration of particles belonging to the class $n$	[m <sup>-3</sup> ]	$\sigma_0$	: Initial supersaturation [–]
$N_{SA}$	: Total concentration of secondary agglomerates	[m <sup>-3</sup> ]	$\sigma^*$	: Yield stress [Pa]
$P$	: Dissipated power per unit mass	[W.kg <sup>-1</sup> ]	$\theta$	: Reduced time [–]
$r_a$	: Overall agglomeration rate	[m <sup>-3</sup> .s <sup>-1</sup> ]	$\theta_F$	: Reduced final time of complete supersaturation consumption [–]
$r_d$	: Disruption rate for two particles $i$ and $j$	[m <sup>-3</sup> .s <sup>-1</sup> ]	<b>Subscripts and superscripts</b>	
$r_{col}$	: Collision rate for two particles $i$ and $j$	[m <sup>-3</sup> .s <sup>-1</sup> ]	$a/A$	: Agglomeration
$r_{con}$	: Consolidation rate for two particles $i$ and $j$	[m <sup>-3</sup> .s <sup>-1</sup> ]	$am$	: Amorphous
$r_N$	: Nucleation rate	[m <sup>-3</sup> .s <sup>-1</sup> ]	$c$	: Crystal
$R_{A,k,k',n}$	: Agglomeration rate of class $n$	[m <sup>-3</sup> .s <sup>-1</sup> ]	$col$	: Collision
$R_{A,k,k',T}$	: Global agglomeration rate for agglomeration of type $k,k'$	[m <sup>-3</sup> .s <sup>-1</sup> ]	$con$	: Consolidation
$s_i$	: Reduced average size	[–]	$cr$	: Growth
$S_i$	: Class average size = $(L_{i-1} + L_i)/2$	[m]	$CT$	: Total crystallites
$t$	: Time	[s]	$d$	: Disruption
$t_{cr}$	: Crystallisation time	[s]	$F$	: Final
$t_d$	: Disruption time	[s]	$FPA$	: Free primary agglomerates
$t_F$	: Measured final time of consumption	[s]	$i,j,n$	: Class
$T$	: Temperature	[K]	$l$	: Liquid
$V$	: Volume	[m <sup>3</sup> ]	$N$	: Nucleation
$V_{susp}$	: Suspension volume	[m <sup>3</sup> ]	$k$	: Regime for collision
$v$	: Particle volume	[m <sup>3</sup> ]	$k'$	: Regime for consolidation
$X$	: Length parameter (see Eq. (9))	[m]	$PA$	: Primary agglomerates
$x$	: Reduced concentration in the suspension	[–]	$s$	: Solid
$y_n$	: Reduced particle concentration in class $n$	[–]	$SA$	: Secondary agglomerates
$\beta_{c,j,i,k}$	: Collision rate constant for type $k$	[m <sup>3</sup> .s <sup>-1</sup> ]	$susp$	: Suspension
$\beta_{j,i,k,k'}$	: Agglomeration rate constant for type $k,k'$	[m <sup>3</sup> .s <sup>-1</sup> ]	$T$	: Total
$\delta_{n,i}$	: Element of the Kronecker matrix	[–]	$O$	: Initial
$\eta$	: Efficiency of the agglomeration	[–]	$*$	: Equilibrium
$\Phi$	: Reduced particle size density function (PSD)	[–]	<b>BIBLIOGRAPHY</b>	
$\Phi_v$	: Volumetric shape factor	[–]	[1]	Barrer, R.M.: Hydrothermal Chemistry of Zeolites, Academic Press, 1982, p 105
$\lambda$	: Reduced particle size	[–]	[2]	David, R.; Marchal, P.; Klein, J.P.; Villermaux, J.: Crystallization and Precipitation Engineering: IV – Kinetic model of adipic acid crystallization. Chem. Eng. Sci., vol. 46, 1991, 1129-1136
$\lambda_c$	: Taylor microscale	[m]	[3]	Hounsflow, M.J.; Mumtaz, H.S.; Collier, A.P.; Barrick, J.P.; Bramley, A.S.: A micro-mechanical model for the rate of aggregation during precipitation from solution, Chem. Eng. Sci., vol. 56, 2001, 2543-2552
$\mu$	: Dynamic viscosity of		[4]	Fauchadour, D.; Kolenda, F.; Rouleau, L.; Barré, L.;

- Normand, L.: Peptization mechanism of boehmites used as precursors in the alumina carrier synthesis, *Studies in Surf. Sci. and Catal.*, E. Gaigneaux eds, vol. 143, 2002, 453-461
- [5] Chen, H.J.; Chen, Y.W.: Hydrothermal synthesis of barium titanate, *Ind. Eng. Chem. Res.*, vol. 42, 2003, 473-483
- [6] Camp, T.R.; Stein, P.C.: Velocity gradients and integral work in fluid motion, *J. of Boston Society of Civil Engineers*, vol. 30, 1943, 219-230
- [7] Saffman, P.G.; Turner, J.S.: On the collision of drops in turbulent clouds, *J. Fluid Mech.*, vol. 1, 1956, 16-30
- [8] David, R.; Marchal, P.; Klein, J.P.; Villermaux, J.: Crystallization and Precipitation Engineering: III – A discrete formulation of the agglomeration rate of crystals in a crystallization process, *Chem. Eng. Sci.*, vol. 46, 1991, 205-213
- [9] Mersmann, A.; Braun, B.: Agglomeration, in *Crystallization Technology Handbook*, 2nd ed., M. Dekker, New York, 2001, 235-284
- [10] Baldyga, J.; Bourne, J.: *Turbulent Mixing and Chemical Reactions*, John Wiley, Chichester, UK, 1999, 74-85
- [11] Mersmann, A.: Crystal Growth, in *Crystallization Technology Handbook*, 2nd ed., M. Dekker, New York, 2001, 135-137
- [12] Liew, T.G.; Barrick, J.P.; Hounslow, M.J.: A micro-mechanical model for the rate of aggregation during precipitation from solution, *Chem. Eng. Technol.*, vol. 26, 2003, 282-285
- [13] Zauner, R.; Jones, A.G.: Determination of nucleation, growth, agglomeration and disruption kinetics from experimental precipitation data: the calcium oxalate system, *Chem. Eng. Sci.*, vol. 55, 2000, 4219-4232
- [14] David, R.; Paulaine, A.M.; Espitalier, F.; Rouleau, L.: Modelling of multiple-mechanism agglomeration in a crystallization process, *Powder Technology*, vol. 130 (1-3), 2003, 338-344
- [15] Wachi, S.; Jones, A.G.: Dynamic modelling of particle size distribution and degree of agglomeration during precipitation, *Chem. Eng. Sci.*, vol. 54, 1992, 3145-3147
- [16] Ilievski, D.; Hounslow, M.J.: Agglomeration during precipitation: II. Mechanism deduction from tracer data, *AIChE J.*, vol. 41, 1995, 525-535
- [17] Breck, D.W.: *Zeolite Molecular Sieves: Structure, chemistry and use*, Wiley-Interscience, 1974, 245
- [18] Koegler, J.H.; van Bekkum, H.; Jansen, J.C.: growth model of oriented crystals of zeolite Si-ZSM-5, *Zeolites*, vol. 19, 1997, 262-269
- [19] Cameirao, A.; Espitalier, F.; David, R.; Rouleau, L.: Analysis of the transformation rate from amorphous particles to crystalline zeolites Workshop on Nucleation, Saint-Etienne, France, June 17-18, 2003
- [20] Schmoluchowski, M.V.: Versuch einer mathematischen Theorie der Koagulationskinetik kolloider Loesungen, *Zeitschrift fuer Physikalische Chemie*, vol. 92, 1917, 129-168
- [21] Jacobs, P.A.; Martens, J.A.: Synthesis of high silica silico-aluminates zeolites, *Studies in Surf. Sci. And Catal.*, vol. 33, 1987
- [22] Adler, P.M.: Interaction of unequal spheres: I Hydrodynamic interaction: colloidal forces, *J. Coll. Interface Sci.*, vol. 84, 1989, 461-474
- [23] Hunter, R.J.: *Foundations of Colloid Science*, 2nd ed., Oxford University Press, Oxford, UK, 2001, 24-32
- [24] Higashitani, K.; Yamauchi, K.; Matsuno, Y.; Hosokawa, G.: Turbulent coagulation of particles dispersed in a viscous fluid, *J. of Chem. Eng. Japan*, vol. 16, 1983, 299-304
- [25] Paulaine, A.M.: Taille et agglomération des cristaux d'une zéolithe au cours de la synthèse: effet des paramètres expérimentaux et modélisation, PhD thesis (in french), Institut National Polytechnique de Lorraine, Nancy, France, 2002
- [26] Verkoeyen, D.; Pouw, G.A.; Meesters, G.M.H.; Scarlett, B.: Population balances for particulate processes – a volume approach, *Chem. Eng. Sci.*, vol. 57, 2002, pp 2287-2303

## Author's short biography



### René David

- 1949: Born in Pirmasens, Germany.
- 1968-71: Studied chemical engineering at the Ecole Nationale Supérieure des Industries Chimiques, Nancy, France.
- 1971-76: PhD at the Institut National Polytechnique de Lorraine, Nancy, France, on: Self-stirred reactors in the gas phase for the determination of reaction kinetics.
- 1976-79: Post-doc at Nancy, France, on micro-mixing effects in the liquid phase.
- 1979-82: Head of CNRS Office in Bonn, Germany.
- 1983-91: Assistant director of the Chemical Engineering Science Laboratory in Nancy, France.  
Research on crystallization and precipitation engineering.
- 1992-98: Scientific counsellor at the French Embassies in The Hague, Netherlands, and Bonn, Germany.
- Since 1998: Director of Chemical Engineering Laboratory for Particulate Solids at the Ecole des Mines d'Albi-Carmaux, France.
- 1999: Received the Bundesverdienstkreuz, Germany, First Class.

René David is the author of more than 80 articles in scientific journals and book chapters. He also was and still is a member of several expertise boards.



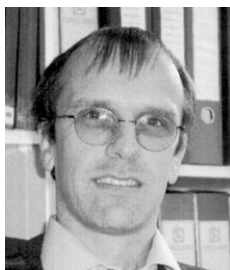
### Fabienne Espitalier

Received an engineering degree from the "Ecole Nationale Supérieure d'Ingénieurs de Génie Chimique" (Chemical Engineering Institute) of Toulouse in 1991 and a PhD degree from the "Institut National de Toulouse" on spherical crystallization in 1994. She is presently assistant professor in chemical engineering in the "Chemical Engineering Laboratory for Particulate Solids" (UMR CNRS) at the "Ecole des Mines d'Albi -Carmaux" at Albi, France. She focuses her work on crystallization and in particular on crystallization assisted by ultrasound and on spherical crystallization.



### Ana Cameirão

Ana Cameirão was born in Lisbon. She is a final-year student in chemical engineering at the Instituto Superior Tecnico of the Universidade Tecnica de Lisboa, Portugal. She is currently in her last year training at the Ecole de Mines d'Albi -Carmaux in the Centre Poudres et Procédés with Dr. R. David and Dr. Fabienne Espitalier. The subject of the training is "Improvement of mineral crystallites multiple agglomeration model in a stirred tank and computer simulation".



### Loïc Rouleau

Dr Loïc Rouleau is a research engineer in the Catalyst and Separation Division at Institut Français du Pétrole (IFP). He is in charge of zeolite development and of shaping techniques such as extrusion for refining-petrochemicals, catalysts and adsorbents. He has submitted several patents and written many articles in these fields.

Prior to joining IFP, Dr Loïc Rouleau graduated from the Engineering School in Materials Sciences in 1988 (ISITEM, Nantes) and obtained a PhD in catalysis in 1992 (Lyon).

# Aggregative Behavior of Cohesive Magnesium Carbonate Powders during Fluidization and Aerated Discharge<sup>†</sup>

G. Donsì, G. Ferrari, M. Poletto  
and P. Russo

Dipartimento di Ingegneria Chimica e  
Alimentare, Università degli Studi di Salerno\*

## Abstract

*In this paper we studied the aerated discharge of two magnesium carbonate powders differing in their average diameter and particle size distribution. These samples were characterized by means of fluidization experiments and rheology shear tests carried out in a rotating shear cell. In the hopper discharge experiments, besides the discharge rates and the mass of residual solids as a function of the aeration rate, the aggregative behavior was observed by means of photographic techniques. Solids aggregates were actually visible within the aerated beds of solids during the fluidization experiments and in the streams of the discharging solids. Experimental data on the powder flow properties and on fluidization were analysed in order to permit evaluation of the aggregate diameters. These values compared fairly well with the aggregate diameters observed and made it possible to evaluate the voidage values outside the aggregates. These results were used in a modified form of the De Jong and Hoelen [9] equation to predict the solids discharge rate with a reasonable degree of accuracy.*

## INTRODUCTION

The discharge of fine powders from hoppers is hindered by either fluid dynamic interactions (for example, see [1]) or cohesive interparticle interactions. The discharge rate of these powders is actually overestimated by the Beverloo *et al.* [2] equation:

$$W_s = 0.58(1 - \varepsilon_b) \rho_p g^{0.5} (d_o - 1.5d_p)^{2.5} \quad (1)$$

where  $W_s$  is the solids discharge rate,  $\varepsilon_b$  is the voidage of the bulk solids,  $\rho_s$  and  $d_p$  are the density and the mean diameter of the solid particles,  $d_o$  is the outlet diameter and  $g$  the acceleration due to gravity. The significance of fluid dynamic and cohesive interactions depends mainly on the particle diameter. Fluid dynamic interactions appear to set in for particle diameters which are somewhat larger than those for which cohesive interparticle forces appear to be effective. Geldart and Williams [3] extended the Geldart [4] classification of powders valid for fluidization to

the discharge behavior. Accordingly, Group A powders can be referred to as those for which fluid dynamic interactions affect the discharge, and Group C powders as those for which cohesive forces can produce irregular flow. This paper, in particular, regards the discharge of cohesive powders.

The effect of cohesive forces on the discharge behavior also depends on powder consolidation phenomena which appear as a consequence of compression forces acting on static and flowing solids. Such disturbing effects consist primarily in arching and ratholing phenomena. An evaluation of the storage conditions that can produce such phenomena was first given by Jenike [5].

The injection of air can produce favorable effects in the flow of fine powders. Air can be injected in different ways such as near the outlet of conical hoppers [6] or through the flat bottom of bins [7]. For Group C powders, the effect of aeration, regardless of how the air is injected, is that of promoting the flow which does not occur at zero air flow rate. Various attempts have been made to obtain valid equations for the correlation of the discharge rates of free-flowing solids at the different operating conditions which can be obtained at low, [1], intermediate [8], [9] and elevated

\* Via Ponte Don Melillo, I-84084 Fisciano (SA), Italy

<sup>†</sup> Accepted: August 22, 2003



[10] aeration rates. Some terms appearing in these equations such as the pressure gradient in the proximity of the hopper outlet or the air flux through the same orifice appear difficult to evaluate. Moreover, from experiments carried out in similar aerated discharging devices on freeflowing [11] and cohesive powders [12], it appears that a different discharge behavior is found in the two cases.

Experiments on a corn starch powder [13] demonstrated that the first effect of aeration is that of breaking up the arches at the outlet and preventing their subsequent formation. At low and increasing aeration levels, this powder shows rat-holing and core flow (funnel flow). The effect of solids flow promotion by increasing aeration is to mobilize the superficial layers of solids involved in the funnel flow mechanism. Only very high aeration rates are able to fluidize the solids and to produce flow fields similar to those found with aeratable powders at high aeration. In spite of such complex phenomenology, the corn starch discharge rate under aeration is roughly predicted by the above-mentioned equations. It is also possible to extend some simplifications to these solids that make the use of the De Jong and Hoelen [9] equation possible in a predictive way. Indeed, according to their equation, the discharge rate is expressed as the following:

$$W_s = 0.55 \rho_p (1 - \varepsilon_b) \left[ a \left( \frac{Q_{fo}}{\varepsilon_b} - \frac{Q_{so}}{1 - \varepsilon_b} \right)^2 + b \left( \frac{Q_{fo}}{\varepsilon_b} - \frac{Q_{so}}{1 - \varepsilon_b} \right) \right]^{0.5} \quad (2)$$

where

$$a = \frac{1.75}{12} \frac{\rho_f d_o}{\rho_p d_p \varepsilon_b} \left( 1 - 1.5 \frac{d_p}{d_o} \right)^4, \quad b = \frac{150}{8} \frac{\pi \mu_f d_o^3 (1 - \varepsilon_b)}{\rho_p (d_p \varepsilon_b)^2} \left( 1 - 1.5 \frac{d_p}{d_o} \right)^4,$$

$Q_{fo}$  and  $Q_{so}$  are the volumetric flow rates of the gas and of the solid through the outlet orifice,  $\rho_f$  and  $\mu_f$  are the gas density and viscosity. Some model evaluations based on gas pressure profiles allowed us to verify that, in the gas-mass balance during discharge, the amount of air percolating through the bed is negligible and, therefore, the gas rate through the orifice is equal to the sum of the aeration rate,  $Q_f$ , and of the interstitial air brought in by the solids, that is

$$Q_{fo} = Q_f + Q_{so} \varepsilon_b / (1 - \varepsilon_b) \quad (3)$$

Furthermore, no effect of gravity is included in equation (2) and, therefore, by comparison with equation (1) and use of equation (2), it can be modified into:

$$W_s = 0.55 \rho_p (1 - \varepsilon_b) [a (Q_f / \varepsilon_b)^2 + b Q_f / \varepsilon_b + g (d_o - 1.5 d_p)^5]^{0.5} \quad (4)$$

The comparison between equation (4) and the experi-

mental results obtained with corn starch is satisfactory. According to the general classification of powders as given by Schulze [14], however, the corn starch powder tested belongs to the easy flowing region as indicated by the flow function in **Figure 1**. In this figure, it is compared among others with the flow function of a free-flowing FCC powder for which equation (4) also gave satisfactory results. The above-discussed framework, therefore, might change if we use powders with poorer flow properties such as those found for the two magnesium carbonate powders reported in **Figure 1**.

From the standpoint of fluidization characteristics, according to Wang *et al.* [15], those of corn starch are among the most common for cohesive powders. This powder shows a velocity range of defluidized state at the lower aeration rates, above the minimum necessary to form a moving slug. Pacek and Nienow [16] associated this situation to the formation of aggregates whose fluidization starts at higher aeration rates. Pressure drops lower than the bed weight can also be found under agglomerate fluidization at decreasing aeration rates and were attributed to a partial adhesion of particle agglomerates to the column walls [17]. The hypothesis of agglomerate fluidization is frequent in the literature and has also been introduced to explain the effect of techniques inducing the homogeneous fluidization of cohesive powders (see, for example [18]).

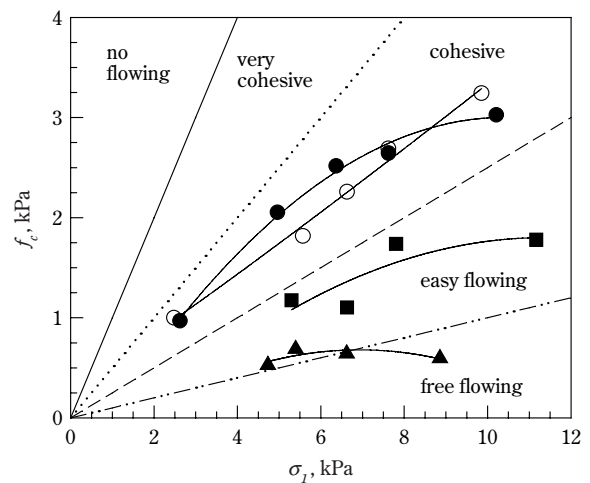


**Fig. 1** Flow functions of the two magnesium carbonate powders used in this work compared with those of the powders used by Donsi *et al.* [13] and with the powder classification as given by Schulze [14]:  $\blacktriangle$ , FCC 45  $\mu\text{m}$ ;  $\blacksquare$ , corn starch 19  $\mu\text{m}$ ;  $\bullet$ ,  $\text{MgCO}_3$  14  $\mu\text{m}$ ;  $\circ$ ,  $\text{MgCO}_3$  3  $\mu\text{m}$ .

The purpose of this work is to extend the discharge experiments to include two magnesium carbonate cohesive powders in order to verify whether the same mechanisms promoting the discharge of corn starch could apply or, instead, if some consideration should be given to the formation of powder agglomerates also in the description of solids discharge rates.

## EXPERIMENTAL

### Apparatus

A schematic of the aerated bin used is given in **Figure 2**. The bin had cylindrical walls of 3 mm in thickness made of transparent Perspex to allow a visual inspection of the interior. It was 520 mm high and 147 mm ID. At the bottom the bin was equipped with a gas distributor, D, consisting of 10-mm-thick sintered plate made of a 10- $\mu\text{m}$  brass powder. The wind-box, WB, below the distributor was made of stainless steel and was equipped in the middle with a vertical duct with increasing cross-section downwards to allow the solids to discharge. An interchangeable orifice, O, was mounted at the top of this duct, at the distributor level. This device created some space

between the discharging solids and the duct wall, thus allowing atmospheric pressure to set around the falling solids. At the exit of the duct, a pneumatically operated sliding valve, S, was used to close the outlet while loading the solids into the bin. The discharged solids were collected in a bin, DB, placed on a load cell, LC, based on a strain-gage bridge, operating in the range 0 – 50 N. The air flow rate through the distributor was regulated by a valve and measured with a rotameter, RM. Before entering the system, the air was dehumidified in a desiccator, E.

The fluidization curve of the powder was studied in a 50-mm-ID glass column fitted with a pressure tap located on the wall just above the sintered glass distributor.

The solids flow functions were studied in a rotating Peschl shear tester that was modified to extend the shear stress measurement to consolidation levels low enough to be compared with what might be experienced by the powder during the aerated discharge. To this purpose, a cinematic chain was designed and built to partially sustain the weight of the cell lid that, otherwise, is the minimum applicable load to the powder sample.

### Materials

In the experiments, two magnesium carbonate powders of 14 and 3  $\mu\text{m}$  average diameter were used. Scanning electron microscopy pictures of these powders at a magnification ratio of 1000 are given in **Figure 3**. For both powders, the particle density was  $2600 \text{ kg m}^{-3}$ . In contrast, the size distributions of the two powders were quite different. The size distribution of the 14- $\mu\text{m}$  powder was in the range 2-40  $\mu\text{m}$  for the 80% of the mass and it was bimodal with two peaks at 3 and 20  $\mu\text{m}$ . The size distribution of the 3- $\mu\text{m}$  powder was in the range 1 and 11  $\mu\text{m}$  for the 80% of the mass and it was unimodal. The powder bulk density seems to be strongly affected by the differences in particle size distributions, in fact, it was about  $950 \text{ kg m}^{-3}$  for the 14- $\mu\text{m}$  powder and about  $650 \text{ kg m}^{-3}$  for the 3- $\mu\text{m}$  powder. A possible interpretation for this can be found in **Figure 3a** which shows that, in the 14- $\mu\text{m}$  powder, the finer particles tend to stick to the larger ones (see, for example [19]). This can give rise in this powder to both a less porous (larger bulk density) and a less homogeneous structure than in the unimodal 3- $\mu\text{m}$  powder. The size distribution and fluidization behavior assign these powders to group C of the Geldart [4] classification. In addition, the flow functions of the two powders reported in **Figure 1** indicate that their flow behavior is in the

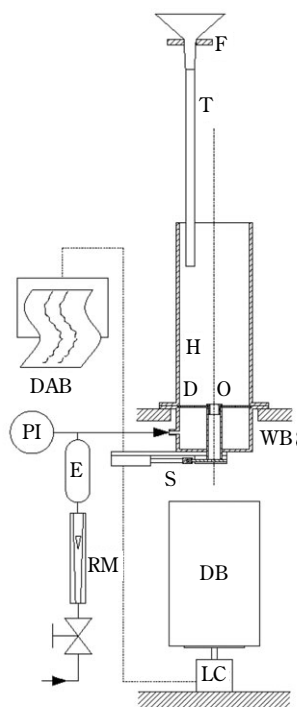


**Fig. 2** Experimental apparatus: D, gas distributor; DAB, data acquisition board or chart recorder; DB, discharge bin; E, desiccator; F, funnel; H, bin; LC, load cell; O, outlet orifice; PI, pressure indicator; RM, rotameter; S, slide lock; T, tube; WB, wind-box.

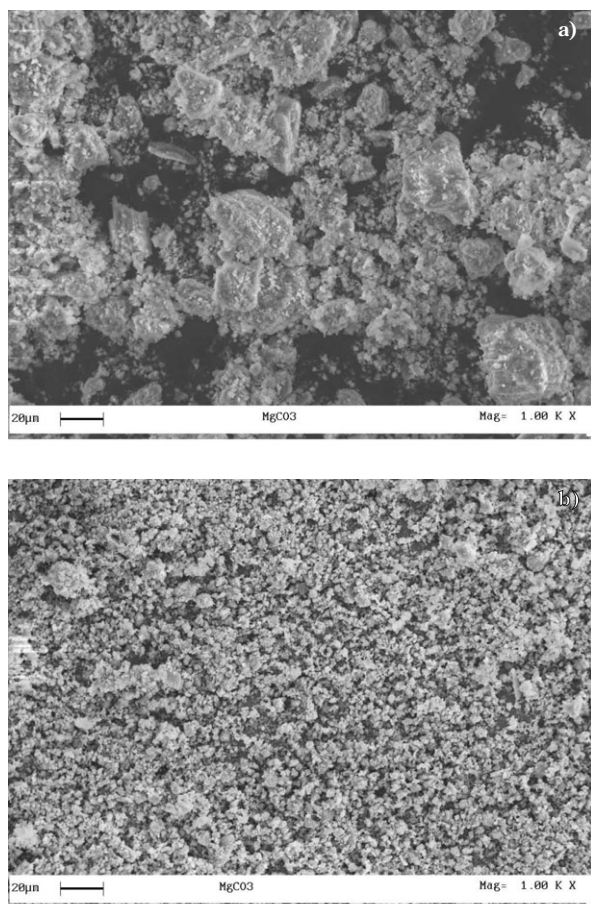


**Fig. 3** SEM images of the magnesium carbonate powders tested at 1000 magnifications: a), 14- $\mu\text{m}$  powder; b), 3- $\mu\text{m}$  powder.

range of significantly cohesive powders. In spite of the differences in particle size distributions and bulk density, it is possible to observe that the flow functions are very similar to each other. **Figure 4** shows the cohesion values and the internal friction angles found from the yield loci at increasing consolidation. The former of these two parameters increases with consolidation, while the latter seems almost unaffected by it.

### Procedures

The bin was loaded from the top through a funnel, F, in **Figure 2**, connected to a large Perspex tube, T, which plunged into the bin. The measurements were made by loading a fixed amount of solids of about 5.0 kg for the 14- $\mu\text{m}$  powder and of about 3.9 kg for the 3- $\mu\text{m}$  powder. The time series of the mass of solids discharged were acquired by a PC with a data acquisition board, DAB.

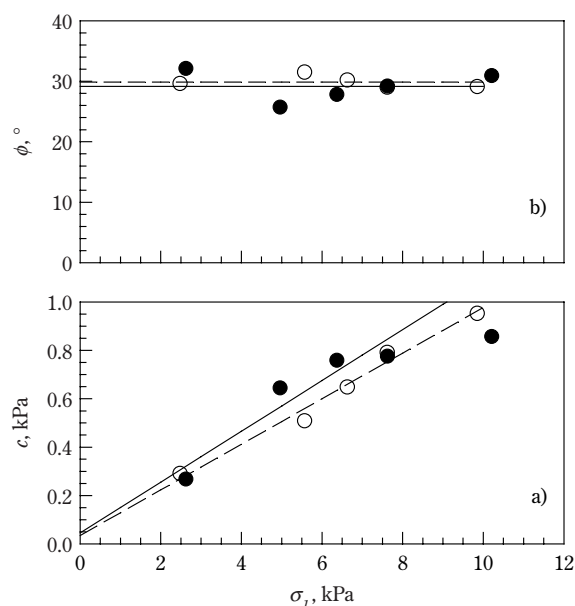


**Fig. 4** The cohesion, a), and the angle of internal friction, b), evaluated for the two magnesium carbonate powders at increasing consolidation: ●, experimental data 14- $\mu\text{m}$  powder; ○, experimental data 3- $\mu\text{m}$  powder; —, regression line 14- $\mu\text{m}$  powder; ---, regression line 3- $\mu\text{m}$  powder.

Images of the discharging streams of solids were obtained by means of a high-resolution Nikon Coolpix 990 digital camera and a stroboscopic light that, with its very short light pulses, can “freeze” the solids motion. To obtain a single light pulse during the exposure, the period between subsequent flashes of the stroboscopic light was set equal to the exposure time.

## RESULTS

### Fluidization curves

**Figure 5** shows the fluidization curves (**Figure 5a**) and the corresponding expansion curves (**Figure 5b**) of the two magnesium carbonate powders obtained in the 50-mm glass fluidization column with an initial bed height of about 140 mm. This height corresponds to a mass of 0.30 kg of the 14- $\mu\text{m}$  powder and to a mass of 0.21 kg of the 3- $\mu\text{m}$  powder and was coherent with the marked bulk density differences noted above in the shear test experiments. A double scale has been used to represent data at low and high aeration to improve visualization of the phenomena observed. The fluidization curves for the two powders tested show several similarities. At low aeration rates, pressure drops increase up to gas superficial velocities of about 7 mm s<sup>-1</sup> for the 14- $\mu\text{m}$  powder and of about 13

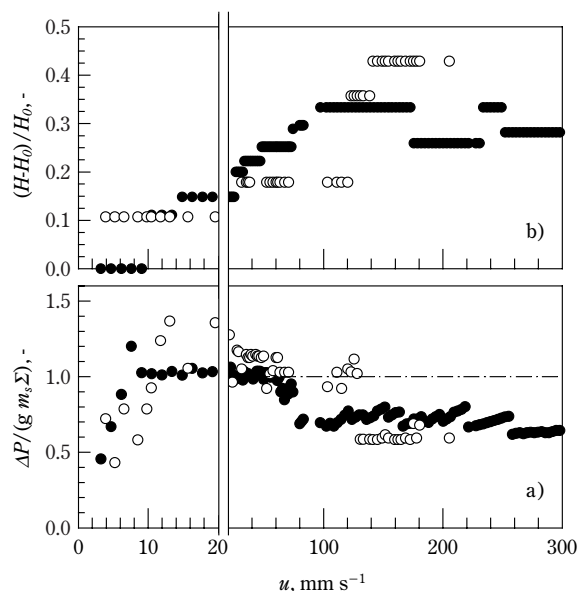


**Fig. 5** Fluidization and expansion curve for carbonate powders in 50-mm-ID fluidization column: ●, 14- $\mu$ m powder; ○, 3- $\mu$ m powder.

mm s<sup>-1</sup> for the 3- $\mu$ m powder. At these aeration velocities, a maximum of pressure is observed of about 1.2 and 1.4 times the bed weight value for the two powders, respectively. In the experiment, the pressure drops in excess of the bed weight corresponded to the formation of a rising slug that could only be kept within the column by breaking it. The slug was not a single piece but rather several horizontal cracks crossed its body at intervals of few centimeters. After the slug formation and breakage, the behavior of the two powders differed slightly. The 14- $\mu$ m powder bed immediately expanded to about 30% value in a fairly large velocity range up to 60 mm s<sup>-1</sup> and, correspondingly, the pressure drops kept constant at the bed weight value. In this velocity range, therefore, the powder could be considered fluidized in spite of the absence of evident powder motion. Closer inspection of the bed revealed an evident network of cracks defining aggregates of a few millimeters in diameter as shown in **Figure 6a**. In contrast, the 3- $\mu$ m powder, before expanding and being considered fluidized, showed a fairly wide range between 8 and 65 mm s<sup>-1</sup> in which unstable slugs formed and pressure drops fluctuated between values equal to the bed weight and 10% higher. Large horizontal cracks were still present as shown in **Figure 6c**. This powder expanded and could be considered fluidized in the gas superficial velocity range between 65 and 130 mm s<sup>-1</sup>. In

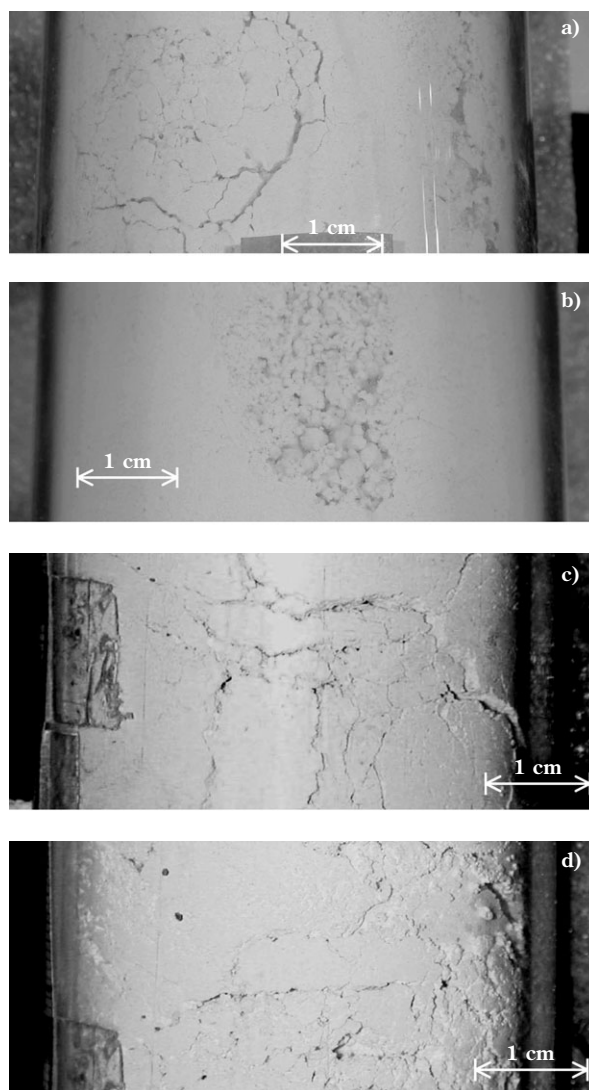


**Fig. 6** Aggregation during aeration for magnesium carbonate powder: a) 14- $\mu$ m powder,  $u=27.9$  mm s<sup>-1</sup>; b) 14- $\mu$ m powder,  $u=120$  mm s<sup>-1</sup>; c) 3- $\mu$ m powder,  $u=35$  mm s<sup>-1</sup>; d) 3- $\mu$ m powder,  $u=114$  mm s<sup>-1</sup>.

these conditions the cracks appeared more uniform, as shown in **Figure 6d**. For both powders, the pressure drops decreased at values of about 30-40% lower than the bed weight at the highest gas velocities, suggesting the onset of channeling phenomena. The bed also continued to expand in this aeration range. A typical channeling region at high aeration is shown in **Figure 6b**, where the high gas shear action smoothes the aggregates shapes.

### Discharge experiments

Several time series of the discharged mass of solids were obtained at different aeration rates for both magnesium carbonate powders. An example of these is



reported in **Figure 7**, which was obtained for the 14- $\mu\text{m}$  powder at a nominal aeration velocity of  $u=21\text{ mm s}^{-1}$ . Some common features of mass time series can be summarized. At the very beginning, it was possible to identify a peak in the load trace due to the impact in the collection bin of the solids contained in the diverging channel for the solids discharge before the slide lock opened. Following this, an almost stationary discharge rate, appearing as a linear section of the curve in **Figure 7**, was observed in the first part of the discharge experiment. Only in the latest part of the experiment was it possible to observe time variations of the solids discharge rate, appearing as a convex portion of the discharge curve in **Figure 7**. These variations can be attributed to the onset of a system sensitivity to the changing bed height. The width of the mass range for which stationary discharge rates were observed tends to increase with the aeration rate, and this range of data was used to evaluate solids discharge rates. As an example in **Figure 7**, the range adopted is that contained in the hatched area, and the dashed line derives from the linear interpolation of these data. At all aeration conditions, solids discharge rates were assumed to be the slopes of the interpolating lines in the constant discharge rate region. Solids discharge rates evaluated in this way are reported in **Figure 8a** as a function of aeration. The final values of the discharged mass in

**Figure 7** and in the other mass time series did not generally correspond to the loaded mass of solids due to a residual load within the bin. The values of these residual masses relative to the loaded mass are given in **Figure 8b** as a function of the aeration rate.

From **Figure 8**, it is possible to observe that aeration affected both the average solids discharge rate (**Figure 8a**), by increasing it, as well as the amount of the residual mass in the bin at the end of the discharge (**Figure 8b**), by decreasing it. At low rates, aeration was more effective on the 3- $\mu\text{m}$  powder, while at high rates, aeration was more effective on the 14- $\mu\text{m}$  powder both in terms of higher solids discharge rates and a smaller fraction of residual solids at the end of the discharge experiment. If compared with solids fluidization curves, it appears that the attainment of the maximum value of the solids discharge rate seems to be related to the effective solids fluidization rather than to the establishment of larger pressure drops through the aerated bed. This is in agreement with what has been found to date on the effects of aeration. In spite of the generally similar trends of these variables with those found previously with corn starch, it must be noted that magnesium carbonate never showed the formation of rat-holes. On the contrary, the solids surface during the discharge was always flat and never showed the formation of a central depression with the onset of the

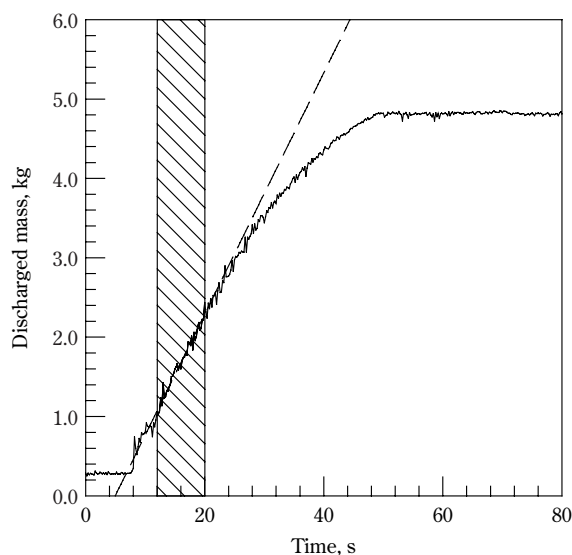


**Fig. 7** Mass of discharged solids as a function of time for 14- $\mu\text{m}$  powder at  $u=21\text{ mm s}^{-1}$ : —, experimental data; ---, linear interpolation of data in the constant discharge rate range within the dashed area.

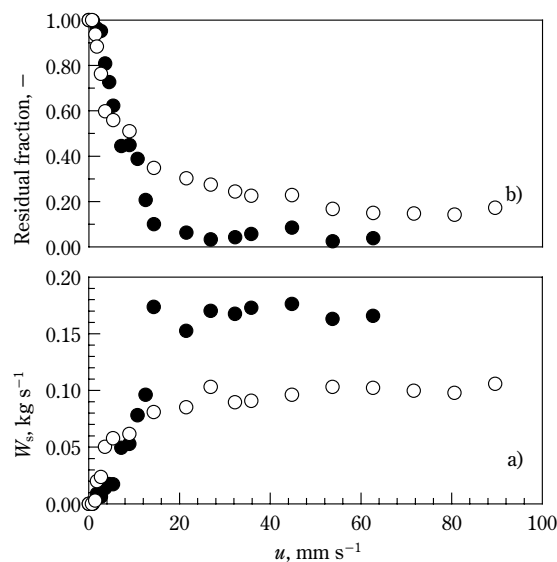


**Fig. 8** The solids discharge rate and the residual mass as a function of aeration: ●, 14- $\mu\text{m}$  powder; ○, 3- $\mu\text{m}$  powder.



centripetal motion which characterizes the funnel flow regime.

### Visualization of the discharging stream

Single high-resolution shots of the discharging solids were taken and are shown in **Figure 9** at different aeration velocities that span the entire aeration range tested for the discharge experiments. The

analysis of **Figure 9** indicates that aeration does not significantly affect the size of the discharging aggregates. Aggregates are very fragile and most of them break in the discharge process. However, the largest aggregates which are found in the discharging stream should be representative of the aggregates present in the bed of solids prior to discharge. All these aggregates showed sizes between 1 and 6 mm and accorded

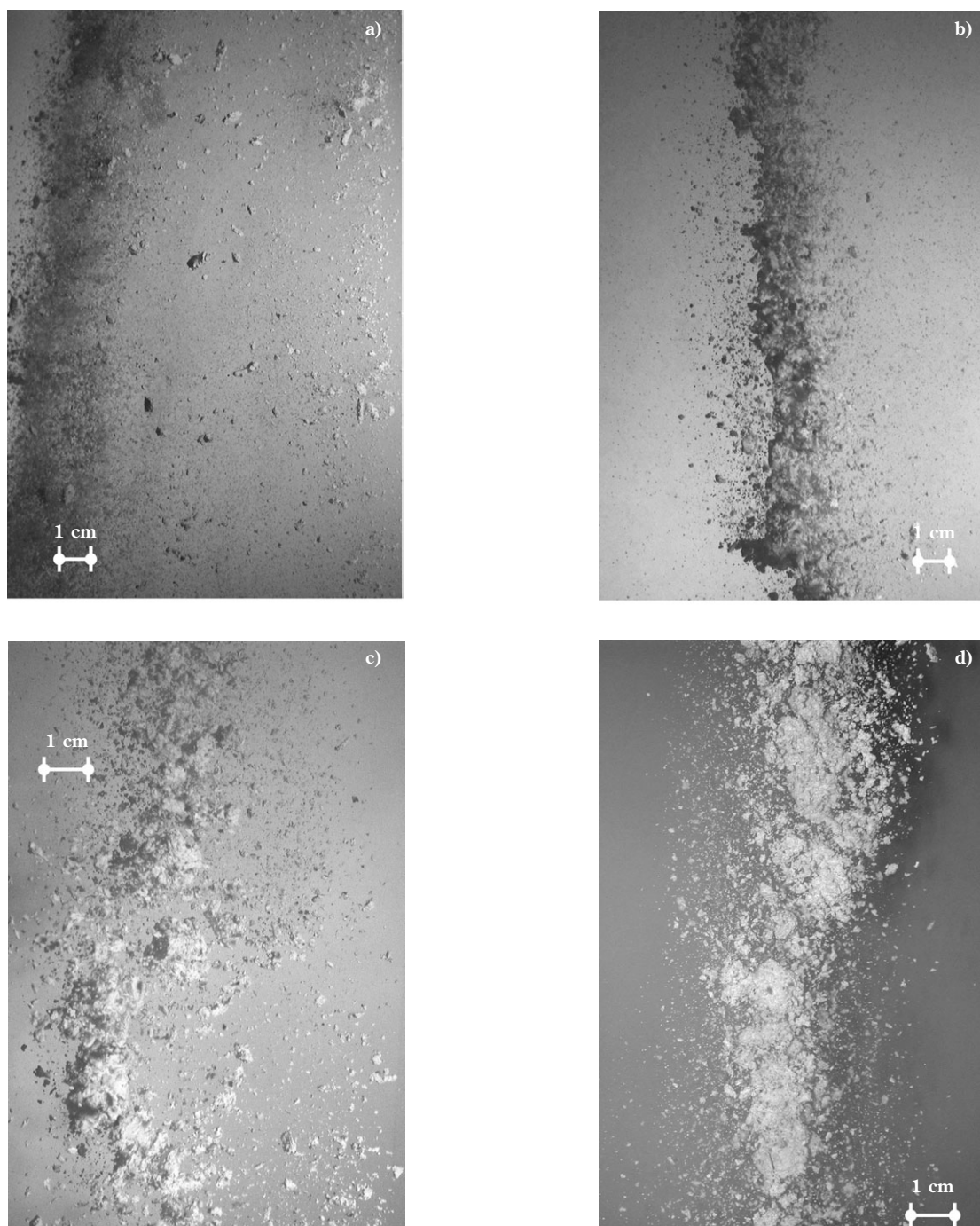


**Fig. 9** Aggregation during discharge of magnesium carbonate powder: a) 14- $\mu\text{m}$  powder,  $u=9.0 \text{ mm s}^{-1}$ ; b) 14- $\mu\text{m}$  powder,  $u=30 \text{ mm s}^{-1}$ ; c) 3- $\mu\text{m}$  powder,  $u=72 \text{ mm s}^{-1}$ ; d) 3- $\mu\text{m}$  powder,  $u=300 \text{ mm s}^{-1}$ .

with that which had been observed in **Figure 6**. It is worth noting that the discharge of aggregates also appeared at aeration rates at which their presence was not detected by direct observation of the fluidization column.

## DISCUSSION

All the fluidization and discharge features described above regarding the discharge of magnesium carbonate differ considerably from what had been previously observed by Donsi *et al.* [13] on corn starch and reported in the introduction. In particular, the fluidization behavior of magnesium carbonate shows an inversion in the sequence of fluidization and channeling. In this respect, the fluidization scheme is very similar to that found by Wang *et al.* [15] with limestone. In this case also, the size of aggregates was larger than 1 mm. In the solids discharge with the magnesium carbonate, we did not observe the changing behaviors found with corn starch. In particular with the 14- $\mu\text{m}$  powder, we observed an almost complete discharge of the loaded powders at all useful aeration rates. With the 3- $\mu\text{m}$  powder, in contrast, some solids residues tended to remain at all the aeration rates tested.

A possible interpretation of the aggregate formation could follow the hypothesis that the aggregates detach along surfaces of average weaker interactions when the beds starts to expand and, more precisely, when the first slug forms and horizontal cracks are visible in the bed. In these conditions, aggregates can form by detaching from the bulk in the lower portion of the slugs wherever the aggregate weight is greater than the attraction force,  $F_c$ , of the contact between the aggregate and upper lumps of the solids. The aggregate formation, therefore, should proceed by separating one by one towards the top of the bed. Assuming spherical aggregates, the force balance on the detaching aggregate is:

$$\frac{\rho d_a^3}{6} \rho_p (1 - \varepsilon_i) g = F_c \quad (5)$$

where  $d_a$  and  $\varepsilon_i$  are the aggregate diameter and its internal voidage. In principle, equation (5) should also include some other force contributions to account for the fluid dynamic forces. It is possible, however, that due to local voidage non homogeneities, this force might be lower or even higher than the particle weight according to the local gas velocity. In any case, being close to the fluidization condition, these forces are of the order of magnitude of the gravity force and,

therefore, equation (5) accounts correctly for the range of the forces involved in the aggregate formation. The value of  $F_c$  might be related to the bulk properties of the powder and, in particular, to the tensile strength of the powder. In fact, when the aggregates are compacted, the relationship between the tensile stress,  $\sigma_t$ , and  $F_c$  might be described by the force balance across a plane separating two aggregate layers:

$$\sigma_t = F_c n_c \quad (6)$$

where  $n_c$  is the contact density that, in turn, can be expressed as:

$$n_c = k d_a^{-2} \quad (7)$$

where  $k$  is the number of the effective contacts between an aggregate and its neighbors on another layer. Empirical functions  $k(\varepsilon)$  were developed by authors such as Rumpf [20] and Kendall *et al.* [21] in the case of packing of rigid spherical particles. In that case, the maximum value for  $k$  at the minimum allowed voidage was about 3. As this value is close to the maximum reasonable value, it was assumed also in the case of the aggregates. Combining equations (5) to (7), it is possible to correlate the aggregate size starting from the bulk tensile strength of the powder:

$$\frac{\rho d_a^3}{6} \rho_p (1 - \varepsilon_i) g = \frac{s_t d_a^2}{k} \quad (8)$$

Given an ideal Coulomb elastic-plastic solid, its yield will follow the equation:

$$t = s \tan f + c \quad (9)$$

where  $f$  is the angle of internal friction and  $c$  the cohesion. In this case the tensile strength,  $s_t$ , will be given by the following equation:

$$s_t = - \frac{2c \cos(f)}{(1 + \sin(f))} \quad (10)$$

Equation (10) is given by the intersection with the  $\sigma$ -axis of the Mohr circle representative of the stress state in the yielding powder subject to pure uniaxial tensile stress, which is the circle tangential to the yield locus on the tensile side and passing through the origin. Both cohesion  $c$  and the angle of internal friction  $f$  are a function of the powder consolidation and, assuming that this is very low inside an aerated powder, in equation (10) we used the extrapolation to zero consolidation of the parameter values given in **Figure 4**. Values of tensile strength of 45 and of 35 Pa were evaluated for the 14- and 3- $\mu\text{m}$  powders, respectively.

To evaluate the aggregate diameter and its internal voidage, it is possible to use the pressure drop evaluations found with the fluidization experiments. In this case the distribution of the solids mass,  $m_s$ , in the aggregates is:

$$m_s = \rho_p(1 - \varepsilon_i)(1 - \varepsilon_e)\Sigma H \quad (11)$$

where  $\varepsilon_i$  is the voidage within the aggregates and  $\varepsilon_e$  the voidage between the aggregates,  $\Sigma$  and  $H$  the bed cross-section and height. The mass balance of the gas is:

$$u = u_e \varepsilon_e + u_i \varepsilon_i (1 - \varepsilon_e) \quad (12)$$

where  $u$  is the gas superficial velocity,  $u_e$  is the gas velocity in the voidage external to the aggregates and  $u_i$  the gas velocity within the aggregates. The pressure drops through the aggregates and around them should be equal to the measured value of  $\Delta P$ . Therefore, within the aggregates and according to the Ergun equation for viscous regimes, we have:

$$\frac{\Delta P}{H} = 150 \frac{\mu_f u_i}{d_p^2} \frac{(1 - \varepsilon_i)^2}{\varepsilon_i^3} \quad (13)$$

while outside the aggregates, according to the Ergun equation for intermediate regimes, it is:

$$\frac{\Delta P}{H} = 150 \frac{\mu_f u_e}{d_a^2} \frac{(1 - \varepsilon_e)^2}{\varepsilon_e^3} + 1.75 \frac{\rho_f u_e^2}{d_a} \frac{1 - \varepsilon_e}{\varepsilon_e^3} \quad (14)$$

In principle, the set of 5 equations (8) and (11) to (14) can be solved for each fluidization condition independently to evaluate the five unknown variables  $d_a$ ,  $\varepsilon_i$ ,  $\varepsilon_e$ ,  $u_i$  and  $u_e$ . However, recognizing that the internal voidage of aggregate and the aggregate diameter are powder properties that should not depend on aeration, a different procedure was used. According to this procedure, the unique value of  $\varepsilon_i$  was found with a regression procedure on all fluidization/expansion data in which the bed appears completely fluidized. The regression objective in finding the best choice for  $\varepsilon_i$  was to minimize the sum of relative square deviations between diameters evaluated for each powder according to (8) and those evaluated for the same powder with equations (11) to (14) at each aeration condition in the fluidization range. Aggregate diameters of 2.9 and 3.1 mm and aggregate voidage values of 0.547 and 0.642 were obtained for the 14- $\mu$ m and 3- $\mu$ m powders, respectively. The standard deviation between the diameters calculated according to equation (8) and according to equation (11) to (14) is about 54% and 35%, which in absolute terms is very large, but not much in the order of magnitude evaluation pursued by our approach. In any case, the diame-

ter values appear satisfactorily close to the observed size of aggregates to sustain the proposed procedure. Internal voidage values of aggregates are in line with the different bulk densities of the two powders. External voidage values are given in **Figure 10a** as a function of the aeration rate. As it appears from the figure, most of these data are in the range between 0.2 and 0.3, and can be as low as 0.1 at low aeration rates. These voidage values represent the bed volume fraction occupied by voids between the aggregates and, therefore, they are not comparable with usual voidage values in beds of predominantly spherical particles. In the present case, these voids actually result from the gradual separation of aggregates and assume reticular low-voidage configurations such as those shown in the pictures of **Figure 6** and, in principle, it can be as low as 0 when the aggregates are compacted from an external load. Total bed voidage  $\varepsilon_b$  can be evaluated from internal and external voidages from equation (11) rewritten in the following way:

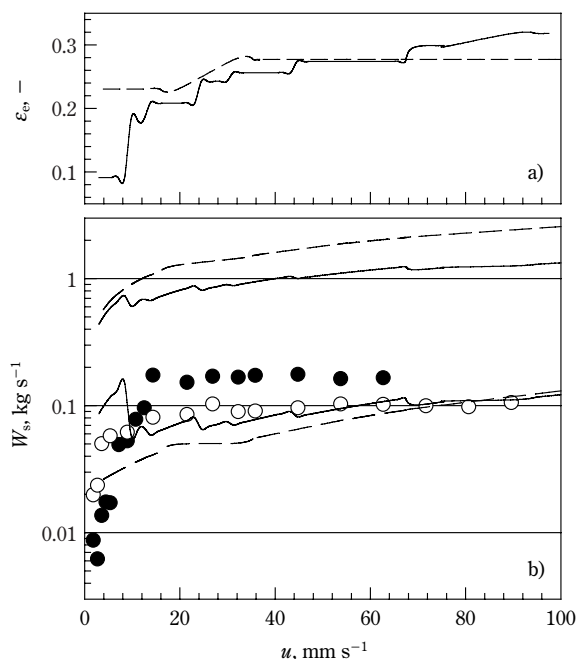


**Fig. 10** Voidage values, a), and solids discharge rates, b), as a function of the aeration rate. Voidage values in a) were evaluated according to equations (8) and (11) to (14) following the procedure given in the text: —, 14- $\mu$ m powder; ---, 3- $\mu$ m powder. Solids discharge rates in b) refer to the following: ●, 14- $\mu$ m powder experimental data; ○, 3- $\mu$ m powder experimental data; —, 14- $\mu$ m powder equation (4); ---, 3- $\mu$ m powder equation (4); —, 14- $\mu$ m powder equation (16); ---, 3- $\mu$ m powder equation (16).

$$\varepsilon_b = 1 - \frac{m_s}{\rho_p \Sigma H} = 1 - (1 - \varepsilon_i)(1 - \varepsilon_e) \quad (15)$$

To verify whether the aggregates play a significant role in the solids discharge, the solids discharge rate was compared with equation (4) and with the same equation in which the particle density and diameter and the average voidage are substituted with the aggregate density and diameter and the external voidage:

$$W_s = 0.55 \rho_p (1 - \varepsilon_i)(1 - \varepsilon_e) [a(Q_f/\varepsilon_e)^2 + bQ_f/\varepsilon_e + g d_o^5]^{0.5} \quad (16)$$

$$a = \frac{1.75}{12} \frac{\rho_f d_o}{\rho_p (1 - \varepsilon_i) d_a \varepsilon_e}, \quad b = \frac{150}{8} \frac{\pi \mu_f d_o^3 (1 - \varepsilon_e)}{\rho_p (1 - \varepsilon_i) (d_a \varepsilon_e)^2}$$

Should equation (16) describe the solids discharge data better than equation (4), this would imply that aggregates keep their own individuality in the phases of solids discharge significant for the rate determination. In equation (16), the interference between the aggregate diameter and the bin outlet as the base of the correction terms of the outlet diameter in equation (4) was neglected due to the relative fragility of aggregates that would break on the orifice edge rather than interfere with the solids flow. Both equations (16) and (4) are independent of the bed height. Therefore, the application of these equations finds a partial justification in the availability of solids discharge rate data that do not depend on the bin loading conditions. The comparison between the experimental results and those predicted by using equations (4) and (16) evaluated with the voidage values resulting from equation (11) is given in **Figure 10b**. Inspection of this figure reveals that equation (4) largely overpredicts the experimental results. Equation (16), on the other hand, somewhat underpredicts the experimental results, but the relative deviation between experimental results and equation (16) appears smaller than between the experimental results and equation (4). Furthermore, the relative variation of the solids discharge rates between the two powders is correctly accounted for in the aggregate discharge provided by equation (16), but not by the single particle discharge described by equation (4). It appears therefore that aggregation plays an important role in the determination of the solids discharge rate. The discrepancies between equation (16) and experimental results might possibly be attributed to the tendency of the discharging bed to internal movements, which might increase the bed homogeneity and produce somewhat larger flow rates.

## CONCLUSIONS

The following points summarize the main conclusions found in this work.

- Aeration was successfully used to improve the discharge of two cohesive magnesium carbonate powders differing in their particle size distribution. It appears that aeration is really effective in the promotion of solids discharge at aeration rates that can produce pressure drops through the bed comparable with the bed weight.
- The powders tested were characterized by means of fluidization experiments and by shear test experiments. The fluidization curves obtained are similar to those found by Wang *et al.* [15] for limestone. Similar to what was found by those authors, our direct observation of the fluidized solids evidenced the presence of clearly formed aggregates of a few millimeters in size. The presence of these aggregates was also detected in the discharging stream.
- By coupling data relative to the powder tensile strength and the pressure drops and mass balances through the fluidized bed, it was possible to correctly estimate the aggregate size by making simple hypotheses regarding the aggregate formation and their effects on aeration.
- The de Jong and Hoelen [9] equation was modified in order to evaluate the solids discharge rates as a function of the aeration rate. Also in this process aggregates seem to play an important role and, by accounting for their presence, corrections are obtained which tend towards a more accurate prediction of the solids discharge rates than what was obtained on the basis of a single particle discharge mechanism.

## ACKNOWLEDGEMENTS

The authors wish to thank Ms Sara Cardaropoli for her help with the discharge and shear test experiments, Dr Diego Barletta for his help with the shear test experiments, and Mr Gianluca Bovenzi of MiMac (Italy) for providing the magnesium carbonate powders.

## LIST OF SYMBOLS

$c$	cohesion	Pa
$F_c$	contact force	N
$d_a$	aggregate mean diameter	m
$d_p$	particle mean diameter	m
$d_o$	bin outlet diameter	m



$g$	acceleration due to gravity	$\text{m s}^{-2}$
$H$	bed height	$\text{m}$
$k$	number of the effective contacts between an aggregate and its neighbors on another layer	—
$m_s$	loaded mass of solids	$\text{kg}$
$n_c$	contact density	$\text{m}^{-2}$
$Q_f$	aeration rate	$\text{m}^3 \text{s}^{-1}$
$Q_{fo}$	gas volumetric flow rate through the orifice	$\text{m}^3 \text{s}^{-1}$
$Q_{so}$	solid volumetric flow rate	$\text{m}^3 \text{s}^{-1}$
$u$	gas superficial velocity	$\text{m s}^{-1}$
$u_e$	gas velocity in the voidage external to the aggregates	$\text{m s}^{-1}$
$u_i$	gas velocity within the aggregates	$\text{m s}^{-1}$
$W_s$	solids discharge rate	$\text{kg s}^{-1}$

### Greek symbols

$\Delta P$	pressure drops through the bed	$\text{Pa}$
$\varepsilon_b$	voidage of the bulk solids	—
$\varepsilon_i$	voidage within the aggregates	—
$\varepsilon_e$	voidage between aggregates	—
$\mu_f$	gas viscosity	$\text{Pa s}$
$\rho_p$	particle density	$\text{kg m}^{-3}$
$\rho_f$	gas density	$\text{kg m}^{-3}$
$\Sigma$	bed cross-section	$\text{m}^2$
$\sigma_t$	tensile strength	$\text{Pa}$
$\phi$	angle of internal friction	$\text{deg}$

### REFERENCES

- [1] Crewdson, B.J., Ormond, A.L. and Nedderman R.M.: Air-impeded discharge of fine particles from a hopper. *Powder Technol.*, 16, pp.197-207 (1977).
- [2] Beverloo, W.A., Leniger, H.A. and van de Velde, J.: The flow of granular material through orifices. *Chem. Eng. Sci.*, 15, pp.260-269 (1961).
- [3] Geldart, D. and Williams, J.C.: Flooding from hoppers: Identifying powders likely to give problems. *Powder Technol.*, 43, pp.181-183 (1985).
- [4] Geldart, D.: Types of gas fluidization. *Powder Technol.*, 7, pp.285-292 (1973).
- [5] Jenike, A.W.: *Gravity flow of bulk solids*. Bulletin n.108 of the Utah Engineering Experimental Station, University of Utah, Salt Lake City (UT), vol. 52(29) (1961).
- [6] Ouwerkerk, C.E.D., Molenaar, H.J. and Frank, M.J.W.: Aerated bunker discharge of fine dilating powders. *Powder Technol.*, 72, pp.241-253 (1992).
- [7] Ferrari, G., and Bell, T.A.: Effect of aeration on the discharge behavior of powders. *Powder Handling and Processing*, 10, pp.269-274 (1998).
- [8] Altiner, H.K.: Flow of solids from aerated hoppers: effect of aeration methods. *AIChE Symp. Ser.* 222, pp.55-59 (1983).
- [9] De Jong, J.A.H. and Hoelen, Q.E.J.J.M.: Cocurrent gas and particle flow during pneumatic discharge from a bunker through an orifice. *Powder Technol.*, 12, pp.201-208 (1975).
- [10] Massimilla, L., Betta, V. and Della Rocca, C.: A study of streams of solids flowing from solid-gas fluidized beds. *AIChE J.*, 7, pp.502-508 (1961).
- [11] Kurtz, H.P. and Rumpf, H.: Flow processes in aerated silos. *Powder Technol.*, 11, pp.147-156 (1975).
- [12] Jochem, K. and Schwedes, J.: Aeration discharge aid for silos. *Proceed. of 3<sup>rd</sup> World Congress on Particle Technology*, Brighton, UK, July 6-9, paper 322 (1998).
- [13] Donsi, G., Ferrari, G., Poletto, M. and Russo, P.: Gas pressure measurements inside an aerated hopper. In press on *IchemE Transactions* (2003).
- [14] Shulze, D.: Measurement of the flowability of bulk solids. In *Silos*, C.J. Brown and J. Nielsen Eds, pp.18-52 (1998).
- [15] Wang, Z., Kwauk, M. and Li, H.: Fluidization of fine particles. *Chem. Eng. Sci.*, 53, pp.377-395 (1998).
- [16] Pacek, A.W. and Nienow, A.W.: Fluidisation of very dense hard metal powders. *Powder Technol.*, 60, pp.145-158 (1990).
- [17] Mikami, T., Kamiya, H., Horio, M.: Numerical simulation of cohesive powder behavior in a fluidized bed. *Chem. Eng. Sci.*, 53, pp.1927-1940 (1998).
- [18] Russo, P., Chirone, R., Massimilla, L. and Russo, S.: The influence of the frequency of acoustic waves on sound-assisted fluidization of beds of fine particles. *Powder Technol.*, 82, pp.219-30 (1995).
- [19] Krupp, H.: Particle adhesion theory and experiment. *Advan. Colloid Interface Sci.*, 1, pp.111-239 (1967).
- [20] Rumpf, H.: *Agglomeration*. in W.A Knepper (ed.), Wiley, New York, pp.379-418 (1962).
- [21] Kendall, K., Alford, N. McN. and Birchall, J.D.: Elasticity of particle assemblies as a measure of the surface energy of solids. *Proc. R. Soc. Lond.*, A412, pp.269-283 (1987).



## Author's short biography



### Giorgio Donsi

Giorgio Donsi is professor of Chemical Engineering since 1980. He is at the University of Salerno since 1984 where he has acted as the Dean of the Faculty of Engineering in the period from 1986 to 1995. He was elected rector in 1995 and occupied this position until year 2001. His scientific activity is mainly concerned with fluid dynamics of heterogeneous systems, fluidisation, fundamentals of the design of apparatuses for the food industry. He is author of about 150 papers in these fields.



### Giovanna Ferrari

Giovanna Ferrari is professor of Chemical Engineering since 2000. She is at the University of Salerno since 1986. In the same University, she is responsible of the education programme in Chemical Engineering since 1998. Author of more than 100 papers in the field of powder technology and food process engineering, her research interests are focused on the following subjects: heat and mass transfer in particulate systems, characterisation of flow properties of powders, measurement and modelling of physical and transport properties of foods, design and characterisation novel technologies for food preservation.



### Massimo Poletto

Massimo Poletto is Associate Professor of Chemical Engineering at the Faculty of Engineering of the University of Salerno since 2001. He graduated in Chemical Engineering in 1989. In 1993 he obtained a Doctoral Degree in Chemical Engineering at the University of Naples "Federico II". From 1994 to 2001 he was Assistant Professor in the present Faculty. His scientific interests regard the fluid dynamics and mechanics of dense granular systems, in particular fluidisation and the gravity flow of powders with and without the use of aeration. In the past he also was involved in research projects on the extraction with supercritical fluids. His work appears in more than 60 papers and conference presentations.



### Paola Russo

Paola Russo works as research fellow at the Department of Chemical and Food Engineering of the University of Salerno. She graduated in Physics at the University of Naples and received a Doctorate Degree in Chemical Engineering at the same University with a thesis on the application of acoustic waves to fluidisation of cohesive powders. Her scientific interests mainly concern the gravity flow of cohesive powders from hoppers with and without the aid of aeration.

# Experimental Analysis of the Fluidization Process of Binary Mixtures of Solids<sup>†</sup>

B. Formisani and R. Girimonte

Dipartimento di Ingegneria Chimica e dei Materiali, Università della Calabria\*

## Abstract

*The simultaneous treatment of dissimilar solids is encountered in a number of processes that exploit fluidization technology (granulation, combustion, pyrolysis, etc.), but a satisfactory description of multicomponent fluidization dynamics is far from being achieved even for the relatively simple case of binary fluidization.*

*This paper discusses the fluidization properties of two-component beds of solids differing either in particle density or diameter. It is shown that although the minimum fluidization velocity of the mixture can be calculated by fully theoretical equations, it has very little meaning if referred to a two-component particle system. Experiments on both kinds of mixtures demonstrate that the binary fluidization process occurs within a characteristic velocity range whose boundaries coincide with the "initial" and the "final fluidization velocity" of the particle mixture. Substitution of the conventional concept of  $u_{mf}$  by these parameters allows us to recognize that the fluidization dynamics of any binary mixture is determined by the initial arrangement of the fixed bed, as well as by the system composition and size or density ratio of its components.*

## 1. Introduction

The fluidization dynamics of multicomponent particle beds has been the subject of a large number of experimental investigations in the last three decades. This persistent research effort is motivated by the technical and economic importance of the industrial processes which contemplate the simultaneous contact of a gaseous stream with two or more solids. These include fluidized bed combustors and gasifiers, waste incinerators, powder granulators, polymerization units and other types of reactors and contactors.

The variety of particle mixtures employed in these operations is fairly large. Based on the specific requirements of each application, the solid charge may be constituted by two or more types of materials. In turn, these may differ in one or more of their constitutive properties (particle size, density, shape, etc.), so that the mechanism through which a multi-

component particle bed enters into the fluidized state is not expected to be unique. Indeed, any given mixture exhibits a peculiar fluidization pattern whose characteristics are determined by the opposite tendencies of its components to mix or to segregate during suspension into the gaseous stream. Depending on the mixture properties as well as on the whole set of operating conditions, steady fluidization gives rise to a stable state of mixing of the solid components that may range from almost total segregation into distinct layers to practically complete mixing. In many practical situations, however, an intermediate component distribution is found, so that every component exhibits a particular concentration profile along the bed height. A major concern for these types of processes is therefore that of setting the operating conditions in a way that advantages associated with either mixing or segregation of the solid species can be exploited. The former regime is, for instance, the essential condition for ensuring uniform thermal properties and homogeneous product quality whenever required, whereas the latter can be exploited for conducting staged processes in distinct regions of the same bed.

At a lower degree of complexity, the equilibrium

\* I 87030 Arcavacata di Rende (Cosenza), Italy

<sup>†</sup> Accepted: April, 2003

between mixing and segregation phenomena is also the distinctive feature of the fluidization pattern of beds of only two solids. Because it should represent a relatively simple problem, investigating the fluidization behaviour of binary mixtures is considered an essential step towards the analysis of more complex systems. At the same time, two-component fluidization is normally considered a subject of practical interest on its own, due to its present uses in the area of coal processing, mineral solids handling, particle mixing and separation, etc. [1].

The intrinsic tendency of these systems to continuously change their component distribution while approaching the suspended state and the large number of factors that seem to influence the fluidization mechanism are the main sources of difficulty. Because of that, the currently available descriptions of two-solid fluidization are essentially empirical, whereas the extension of the basic principles of the fluidization theory to binary mixtures, as a preliminary condition for tackling more complex systems, has not yet been achieved. Based on experiments, this paper will discuss some points which are essential for analysing the behaviour of binary fluidized bed systems.

## 2. Experimental

All the experiments of this study were carried out in a transparent fluidization column of 10 cm ID, equipped with a 4-mm-thick plastic porous distributor, ensuring high head loss and good gas distribution. The fluidizing gas was compressed air, whose flow rate was monitored in the range 0-25000 Nl/h. Pressure drops across the whole particle bed were measured by a U-tube water manometer connected to a tap located 1 mm above the distributor plane, while three graduated scales spaced at 120° around the column wall were used to determine the bed height and the bed voidage:

$$\varepsilon_0 = 1 - \frac{m/\rho}{AH} \quad (1)$$

Because all the solids used in the experiments belong to group B of Geldart's classification and show no homogeneous expansion when fluidized, the fixed bed voidage  $\varepsilon_0$  was always considered equal to  $\varepsilon_{mf}$ .

Measurements were performed on three types of spherical solids: glass ballotini (GB), molecular sieves (MS), and steel shots (SS). The properties of each cut are listed in **Table 1**. The same table also reports the density and size ratios of the components of the four

**Table 1** Properties of solids and mixtures

Solid	$\rho$ [g/cm <sup>3</sup> ]	Sieve size [ $\mu$ m]	$d$ [ $\mu$ m]	Mixture	$\rho_i/\rho_f$	$d_i/d_f$
GB154	2.48	125-180	154	GB499-GB271	1	1.84
GB271		250-300	271			
GB428		400-500	428	GB612-GB154	1	3.97
GB499		350-600	499			
GB593		500-710	593	SS439-GB428	3.06	1.03
GB612		600-710	612			
MS624	1.46*	600-710	624	GB593-MS624	1.70	0.95
SS439	7.60	400-500	439			

\* envelope density

mixtures used throughout the experimental campaign. Two of them (GB593-MS624 and SS439-GB428), made of materials having approximately the same average diameter, are used to investigate the role of density difference on binary fluidization, whereas the other two (GB499-GB271 and GB612-GB154) were used to elucidate the role of size difference.

The fluidization behaviour of each mixture was studied with reference to two extreme states of mixing of the fixed bed. Thus, well-mixed and fully segregated beds were the object of a distinct series of measurements.

In each of these series, a bed ratio  $H/D$  close to 1.7 was maintained, so that the mixture concentration could vary by adjusting the solid concentration of each component.

## 3. The essential features of binary fluidization

From the experimental viewpoint, the minimum fluidization velocity of the bed is usually determined on a diagram  $\Delta p$  versus  $u$  similar to that of **Fig. 1**, at the intersection of the fixed bed curve with the horizontal line representing the suspended state.

When another solid of a different diameter is uniformly mixed, in any proportion, to the same material so as to form a binary mixture, the onset of fluidization throughout the bed becomes a gradual process. As sketched in **Fig. 2a**, at a certain velocity value a moving fluidization front establishes itself at the top of the bed. As the gas flow rate is increased, it moves across the bed down to the bottom of the column until, at a new characteristic velocity value, the whole bed is brought into a fully fluidized state. In the upper region of the bed, at its free surface, a bubbling layer builds up which contains almost exclusively one of

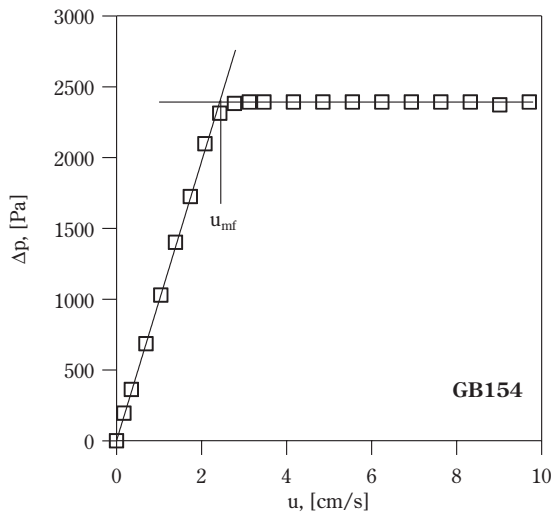


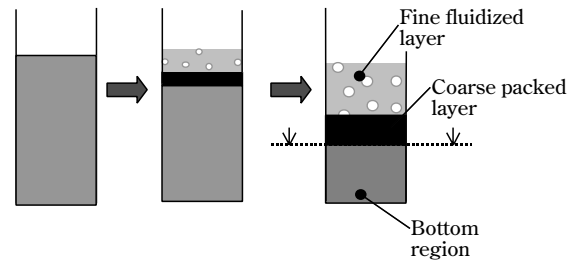
**Fig. 1** Fluidization of a monodisperse particle bed.

the two species (the ‘flotsam’, according to the terminology introduced by Rowe et al. [2]) whilst the other solid (the ‘jetsam’ component) sinks and forms a defluidized layer just behind the fluidization front. The fluidization process for the mixture is thus accompanied by solids segregation up to a new velocity threshold at which the bed is fully fluidized (both solids mix again and bubbles flow freely).

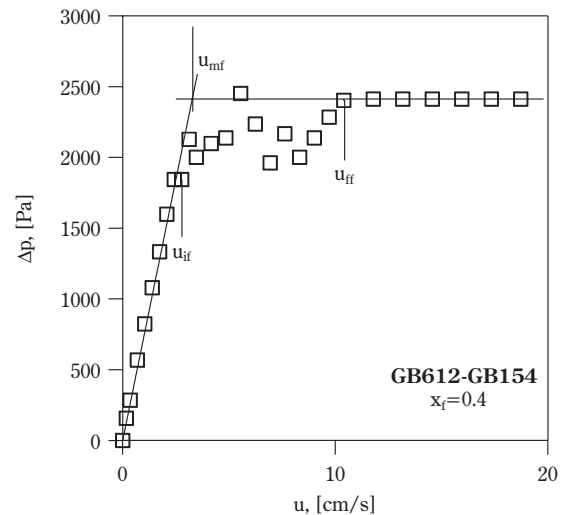
The peculiarities of this mechanism are fully reflected by the experimental pressure drop diagram of **Fig. 2b**, where two characteristic velocity thresholds can be recognized [3,4,5]. They are the “initial fluidization velocity”,  $u_{if}$ , at which  $\Delta p$  first deviates from the fixed bed curve, and the “final fluidization velocity”,  $u_{ff}$ , at which the ultimate value of  $\Delta p$  is first attained. Thus, these two limits identify the velocity range within which the entire particle collective undergoes suspension into the gaseous stream. Although it refers to a particular type of mixture (obtained by the complete mixing of spheres differing only in diameter), the diagram shows a common feature of any binary fluidization process, i.e. that their transition to the fluidized state is never instantaneous.

#### 4. Minimum fluidization velocity of a binary mixture

The fluidization of binary beds is generally analysed by defining a “minimum fluidization velocity”  $u_{mf}$  to be determined (as done with monosolid systems) at the intersection between the fixed bed  $\Delta p$  curve and the horizontal line relevant to the sus-



**(a) Fluidization phenomenology**



**(b) Pressure drop diagram**

**Fig. 2** Fluidization of a two-component mixture.

pended state (see **Fig. 2b**).

It has often been reported that, given the mixture composition,  $u_{mf}$  is not unique, as it can significantly change with the solids distribution within the fixed bed [6-9]. Moreover, different values of  $u_{mf}$  are obtained depending on whether it is measured at increasing or decreasing gas velocity. Such effects are due to the peculiarity of the mixing/segregation pattern which accompanies the fluidization process. As discussed in a previous work on size segregating mixtures [10], this pattern is determined by the arrangement of the fixed bed.

Therefore, the variables that affect the mixing/segregation dynamics are also the ones upon which the minimum fluidization velocity of the binary bed is expected to depend. The trends of  $u_{mf}$  as a function of the mixture composition (represented by the flotsam component volume fraction  $x_f$ ) were analysed in two

different cases pointing out the influence of the particle density and the particle size distribution on the fluidization pattern. This analysis was conducted on binary beds having opposite mixing states of their components, namely on perfectly mixed and thoroughly segregated systems.

For two-density beds, the results relevant to both homogeneous and segregated mixtures GB593-MS624 and SS439-GB428 are reported in **Fig. 3**. For these types of systems, the dependence of  $u_{mf}$  on  $x_f$  is always linear, so that the equation

$$u_{mf} = x_f u_{mf,f} + (1 - x_f) u_{mf,i} \quad (2)$$

proposed by Otero and Corella [11] applies. Irrespec-

tive of the component distribution, practically identical results are obtained with minor differences due to small variations in system voidage.

When, instead, mixture components are solids which differ only in diameter, as in the case of systems GB499-GB271 and GB612-GB154, the trends of  $u_{mf}$  versus  $x_f$  are quite different.

If the initial arrangement of the bed is such that the particles are well mixed, the relationship between the incipient fluidization threshold and the mixture composition is no longer linear. As observed also by other authors [12-14] and illustrated here in **Fig. 4**, experiments show a rapid fall of  $u_{mf}$  at increasing flotsam fraction, followed by a more gradual decrease at

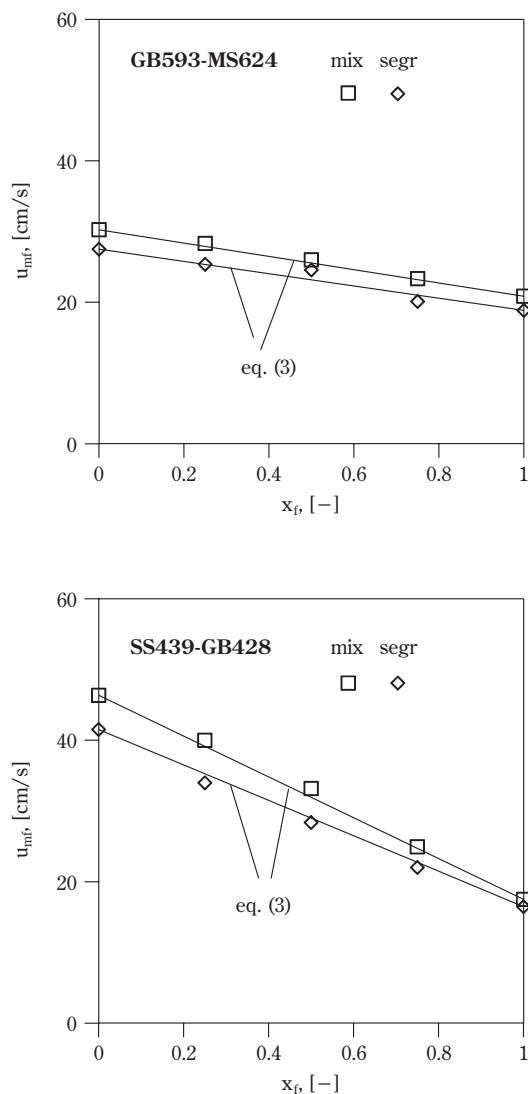


**Fig. 3** Density segregating mixtures. Dependence of the minimum fluidization velocity on composition.

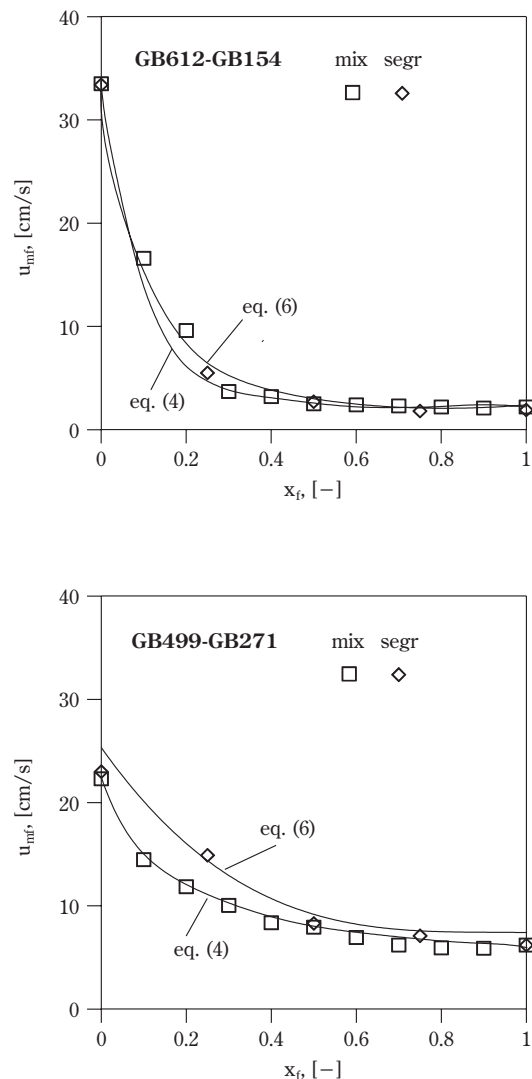


**Fig. 4** Size segregating mixtures. Dependence of the minimum fluidization velocity on composition.



higher values of  $x_f$ . Similar trends are shown also by flotsam-on-jetsam segregated beds, with higher values of  $u_{mf}$  at almost all  $x_f$ s.

Altogether, these data demonstrate that density and size differences between the two solids promote distinct mechanisms of fluidization in the mixture, so that the dependence of  $u_{mf}$  on either factor has to be analysed separately. In each case, a clear influence is exerted by the initial arrangement of the mixture: for a well-mixed bed, the transition to the fluidized state is associated with partial segregation of its components, while partial mixing is observed during the suspension process of an initially stratified particle system. Such almost opposite behaviour patterns cannot be represented by the conventional concept of minimum fluidization velocity, which does not capture their particular features.

## 5. Interpretation

A large number of empirical correlations, recently reviewed by Wu and Baeyens [15], have been proposed for calculating the minimum fluidization velocity of different kinds of binary mixtures. However, at least for the systems referred to in this paper, a fully theoretical analysis can be performed.

To this end, it must be remembered that when extended from monocomponent to binary beds of particles, the conventional definition of the minimum fluidization velocity provides a value of  $u_{mf}$  which is determined by equating the pressure drop across the fixed bed and the buoyant weight per unit section of the solid mass.

When dealing with mixtures of particles which differ only in density, it may be assumed that the incipient fluidization voidage of the bed is practically unaffected by both component composition and mixing state. Thus, both for mixed and segregated systems, it is possible to rewrite the Carman-Kozeny equation as follows:

$$180 \frac{\mu_g u_{mf}}{d^2} \frac{(1-\varepsilon_{mf})^2}{\varepsilon_{mf}^3} = [(\rho_f - \rho_g)x_f + (\rho_j - \rho_g)(1-x_f)]g(1-\varepsilon_{mf}) \quad (3)$$

It is easy to verify that Equation 3 is equivalent to Equation 2 and fully independent of the initial distribution of the two solid species. This explains why, as shown in **Fig. 3**, it provides identical and good predictions of  $u_{mf}$  both for homogeneous and segregated mixtures.

With regard to beds of different size distribution and initial mixing state, the bed voidage turns out to be strongly dependent on the composition [16] as

well as on the particle diameter ratio  $d_j/d_f$ . For the mixtures indicated as GB499-GB271 and GB612-GB154, experimental curves of  $\varepsilon_{mf}$  versus  $x_f$  are reported in **Fig. 5**.

As far as the  $\varepsilon_{mf}$  variation is concerned, the equation:

$$180 \frac{\mu_g}{d_{av}^2} u_{mf,M} \frac{(1-\varepsilon_{mf,M})^2}{\varepsilon_{mf,M}^3} = (\rho - \rho_g)g(1-\varepsilon_{mf,M}), \quad (4)$$

with the surface/volume average particle diameter being given by the relationship:

$$\frac{1}{d_{av}} = \frac{x_f}{d_f} + \frac{1-x_f}{d_j} \quad (5)$$

is capable, as shown in **Fig. 4**, to represent the experimental measurements.

When the same solids are initially arranged in the fixed bed as two segregated layers, with the fine component on top, the data of **Fig. 4** are well represented by the equation proposed by Chiba et al. [6]

$$180 \mu_g u_{mf,S} \left[ \frac{(1-\varepsilon_{mf,f})^2}{\varepsilon_{mf,f}^3} \frac{H_f}{d_f^2} + \frac{(1-\varepsilon_{mf,j})^2}{\varepsilon_{mf,j}^3} \frac{H_j}{d_j^2} \right] = (\rho - \rho_g)g[(1-\varepsilon_{mf,f})H_f + (1-\varepsilon_{mf,j})H_j], \quad (6)$$

with

$$x_f = \frac{H_f(1-\varepsilon_{mf,f})}{H_f(1-\varepsilon_{mf,f}) + H_j(1-\varepsilon_{mf,j})} \quad (7)$$

Equations 3, 4 and 6 make it possible to obtain, without introducing any adjustable parameter, good estimates of  $u_{mf}$  for any mixture composition provided

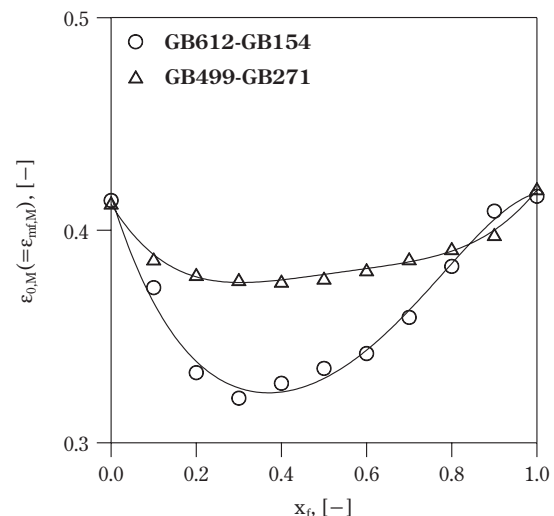


**Fig. 5** Voidage of the well-mixed beds versus flotsam component average fraction.

they are in one of the two extreme states of mixing represented by homogeneous and segregated beds.

## 6. A clearer approach to binary fluidization

Going by what prevails in the literature, devising predictive equations for  $u_{mf}$  should be considered a key result for a deeper analysis of binary fluidization. Indeed, when addressing the mechanism of solids segregation, most authors have agreed that it is driven by bubbles flowing through the bed. This interpretation is based on observations similar to those reported earlier by Rowe et al. [17], who showed that flotsam particles are able to migrate upwards in the wake of bubbles, thus accumulating in the upper region of the bed. At the same time, the tendency of jetsam particles to sink to the bottom of the column has been generally interpreted to be an effect of the displacement caused by bubbles within the dense phase.

It is not quite clear whether the action of bubbles determines the segregation equilibrium or is just dynamically superimposed to it. It has induced many authors to look for a relationship between segregation and bubble flow rate, and several empirical equations have been proposed to relate the degree of mixing of the bed components to the excess gas velocity  $u - u_{mf}$  [14,15,18].

However, quantifying the intensity of bubbling by this parameter, as is usually done with monocomponent beds, assumes that both  $u_{mf}$  and  $u - u_{mf}$  keep their physical meaning even when applied to two-component systems. This implicit assumption turns out to be wrong. Reverting to **Fig. 2b**, it can easily be observed that at  $u_{mf}$ , the upper region of the bed, which had begun to enter fluidization at  $u_{if}$ , is already bubbling, whereas the lower part of it is still packed. Even clearer is the case of segregated mixtures whose jetsam component initially forms the top layer. As shown in **Fig. 6** for the case of GB612-GB154, the experimental curve of  $\Delta p$ , related to an unstable mechanism of fluidisation analysed in detail elsewhere [19], shows that the total pressure drop increases over the buoyant weight per unit section of the particle mass, so that the conventional definition of the minimum fluidization velocity corresponds to a fluid dynamic condition at which the whole bed is still in the fixed state. These results demonstrate that in binary fluidisation, particle suspension and bubbling are simultaneous rather than sequential phenomena and that the parameter  $u_{mf}$  is not as significant as it is for monosolid beds. The excess gas velocity  $u - u_{mf}$

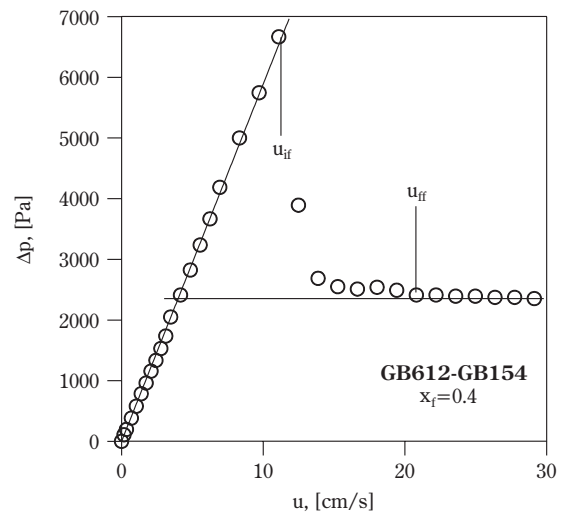


**Fig. 6** Pressure drop diagram of a jetsam-on-flotsam segregated binary mixture.

can therefore by no means be used for measuring the intensity of the bubbling regime and the controlling factor of segregation.

Addressing the real phenomenology of binary fluidization systems can be done by developing an approach based on the definition of the “initial” and “final fluidization velocity”. As mentioned in Section 3, these parameters constitute the lower and upper boundary of the interval of velocity along which any two-solid bed is crossed, from top to bottom, by the fluidization front.

Based on this, it is  $u_{ff}$ , rather than  $u_{mf}$ , that has to be viewed as the velocity at which the entire mixture attains the fluidized condition [3-5,9]. This velocity normally coincides with that of full mixing [10], while the difference between  $u_{ff}$  and  $u_{if}$  is the amplitude of the velocity range within which mixing/segregation phenomena occur [20]. A systematic investigation of the dependence of both the “initial” and “final fluidization velocity” on variables which characterize binary mixtures is therefore of great importance for an accurate description of their fluidization properties. Two of these variables that surely play a major role, namely solids concentration and particle size distribution, have been the object of a series of experiments performed separately on density and size segregating systems.

For the former types of beds, represented by the mixtures GB593-MS624 and SS439-GB428, the trends of  $u_{if}$  and  $u_{ff}$  at varying flotsam fraction  $x_f$  are reported in **Fig. 7** for the well-mixed arrangement, and in

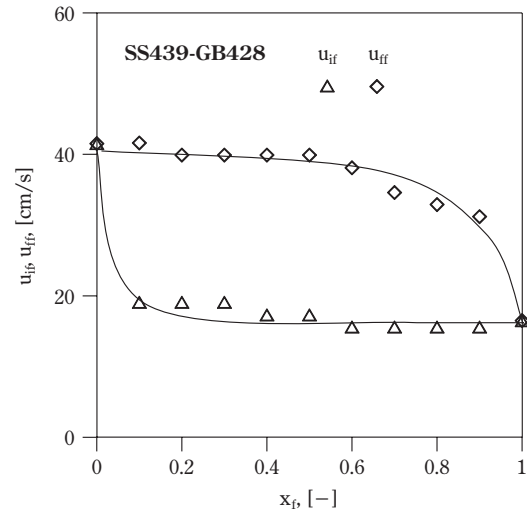
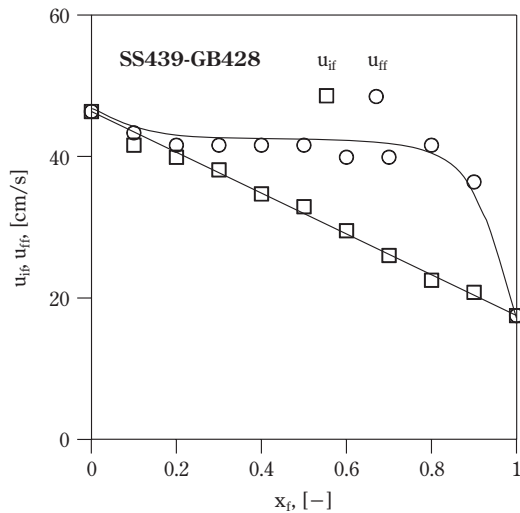
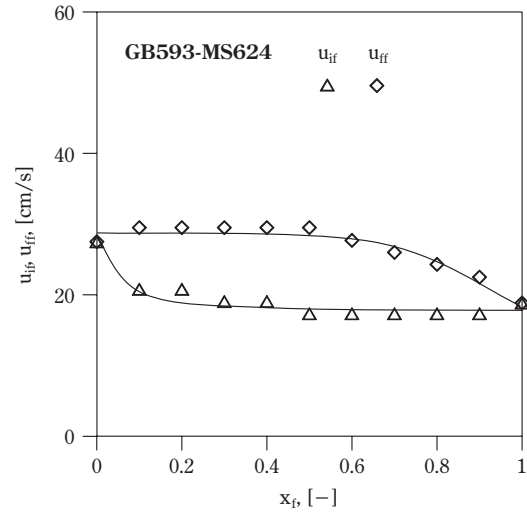
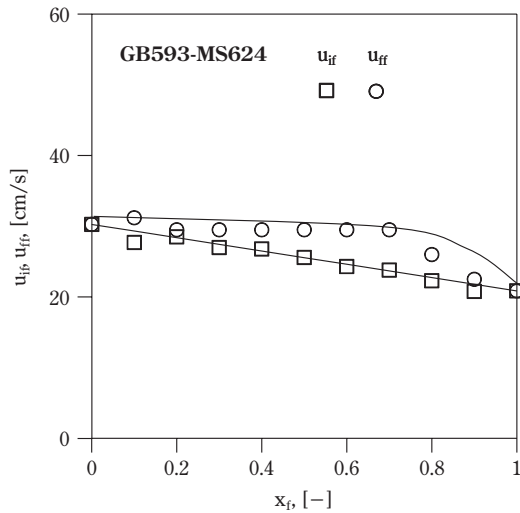


**Fig. 7** Fluidization velocity range of density segregating mixtures. Well-mixed beds.

**Fig. 8** Fluidization velocity range of density segregating mixtures. Segregated beds.

**Fig. 8** for the initially segregated one.

The comparison between the results obtained for each mixture in the two cases clearly shows that the dependence of  $u_{ff}$  on  $x_f$  is practically unaffected by the initial arrangement of the bed. For a wide range of compositions, its values are close to that of the minimum fluidization velocity of the jetsam component, with a visible decrease at high flotsam concentration. With regard to the dependence of  $u_{if}$  on  $x_f$ , when the initial mixture is homogeneously distributed (**Fig. 7**), the initial fluidization velocity of the bed is practically coincident with its  $u_{mf}$  (i.e. with the weighed average of the minimum fluidization velocities of the two solids). When the initial bed is segregated (**Fig. 8**),

fluidization starts in the upper bed layer where the flotsam components are, so that  $u_{if}$  is always practically equal to the minimum fluidization velocity of the flotsam. Such results demonstrate also that the value of the solid density ratio  $\rho_j/\rho_f$  does not alter the general dynamics of fluidization, although it determines the absolute amplitude of the velocity interval along which it takes place. Most important is that the analysis based on the two characteristic velocities shows that, for any density of segregating mixture, the fluidization pattern depends on the initial configuration of the fixed bed (**Fig. 3**).

The same analysis was performed on size segregating systems by examining the results reported in

**Figs. 9 and 10** for mixed and segregated beds, respectively.

As previously reported for two different density systems, the curve of  $u_{ff}$  is not related to the initial arrangement of the mixture components. On the contrary, for both GB499-GB271 and GB612-GB154, the initial fluidization velocity of the mixed bed is, particularly at low flotsam fractions, higher than that of the stratified one. Fluidization starts at the free surface of the bed so that when its upper layer is fluidized, the rapid fall of  $u_{if}$  observed in both diagrams of **Fig. 9** is mainly due to the voidage reduction accompanying the increase of the flotsam fraction. Beyond the value of  $x_f$  that corresponds to the minimum of each curve in **Fig. 5**, the mixture voidage increases again, but

the total weight of the particle mass per unit section keeps on decreasing, so that  $u_{if}$  approaches its ultimate value (i.e.  $u_{mf,f}$ , at  $x_f=1$ ) more gradually. In contrast, for the segregated systems,  $u_{if}$  coincides, at practically all  $x_f$ s, with the minimum fluidization velocity of the flotsam component, below which the jetsam layer acts as a passive gas distributor. That explains why the values of  $u_{if}$  in **Fig. 10** are practically unaffected by the mixture composition.

Given these trends of the characteristic velocities, the amplitude of the fluidization field is found to depend on the mixture composition as well as on the initial state of mixing of the two solids. With regard to the component size ratio  $d_i/d_f$ , the influence of this parameter on  $(u_{ff}-u_{if})$  is stronger than that exerted

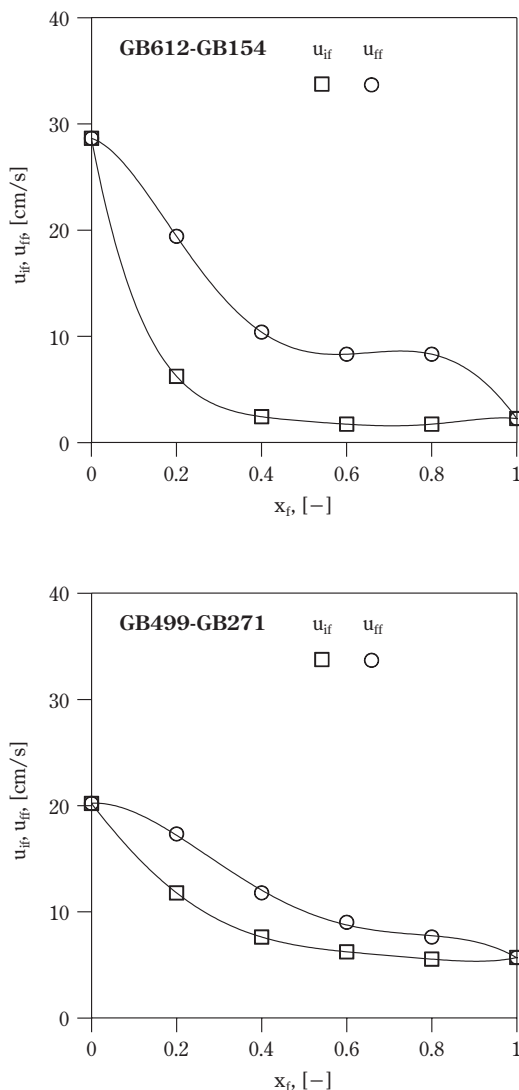


**Fig. 9** Fluidization velocity range of size segregating mixtures. Well-mixed beds.

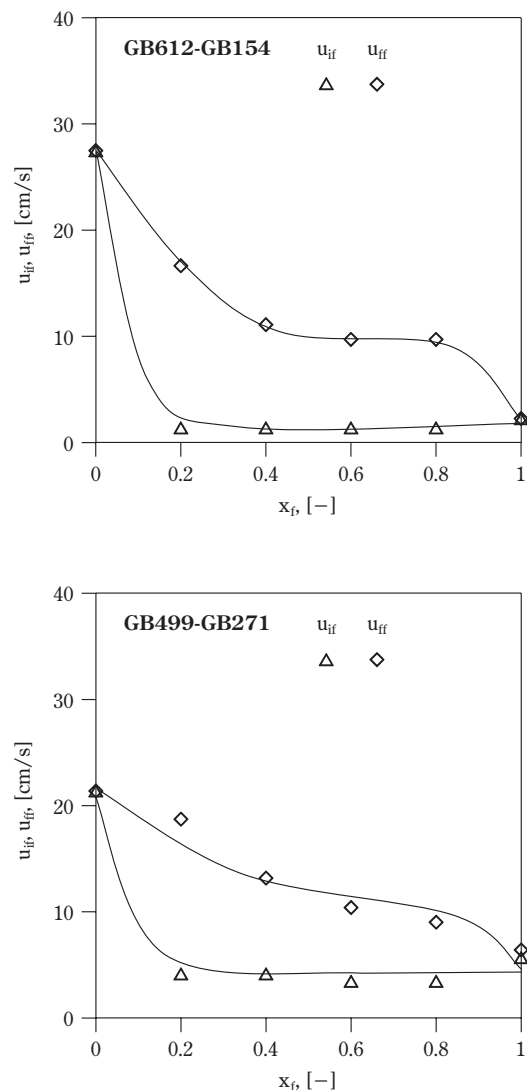


**Fig. 10** Fluidization velocity range of size segregating mixtures. Segregated beds.

on it by  $\rho_j/\rho_f$ . Indeed, as already shown in **Fig. 5**, as long as the two solids are not fully segregated, the size ratio determines the value of the bed voidage.

The strong relationship between  $d_j/d_f$  and  $\varepsilon_{mf}$  at any mixture composition is therefore the main element of difference between the mechanisms of size and density segregating fluidization.

## Conclusions

The fluidization of a two-solid mixture is a gradual process regulated by mixing/segregation phenomena that simultaneously change the component distribution of the bed.

The definition of a minimum fluidization velocity of the binary system, widely used in most literature studies, can result in a misleading analysis of its fluidization behaviour: although it can be calculated by rewriting theoretical equations such as Carman-Kozeny's in a form suitable for taking the specific nature of each mixture into account,  $u_{mf}$  does not represent the actual fluidization condition. As a consequence, it also constitutes a source of error for models which relate segregation to the bubble flow rate measured by the excess gas velocity  $u - u_{mf}$ .

It is possible to develop a clearer approach based on definition of the "initial" and "final fluidization velocity" of the binary mixture and closer to their actual phenomenology of fluidization. These parameters are the lower and upper boundary, respectively, of a characteristic fluidization velocity range whose amplitude, measured by the difference between  $u_{ff}$  and  $u_{if}$ , is mainly determined by the density or size ratio between the two components as well as by the mixture composition and component distribution within the fixed bed, whose influence is clearly highlighted.

## Acknowledgements

This work was partially supported by the Italian Ministry of University and Research (MIUR), within the scope of the "PRIN 2001" program.

The authors are grateful to Mr R. Mazzitelli for his careful work in sample preparation and granulometric analysis.

## List of symbols

$A$	column cross-section	[cm]
$D$	column diameter	[cm]
$d$	particle diameter	[ $\mu\text{m}$ ]

$d_{av}$	average particle diameter	[ $\mu\text{m}$ ]
$g$	gravity acceleration	[ $\text{cm/s}^2$ ]
$H$	height of the bed, of the layer	[cm]
$m$	solids mass	[g]
$\Delta p$	pressure drop	[Pa]
$u$	superficial gas velocity	[cm/s]
$u_{if}, u_{ff}$	initial, final fluidization velocity	[cm/s]
$u_{mf}$	minimum fluidization velocity	[cm/s]
$x_f$	volume fraction of the flotsam component	[-]
$\varepsilon_0$	fixed bed voidage	[-]
$\varepsilon_{mf}$	minimum fluidization voidage	[-]
$\mu_g$	gas viscosity	[g/cm s]
$\rho$	solids density	[g/cm <sup>3</sup> ]
$\rho_g$	gas density	[g/cm <sup>3</sup> ]

## Subscripts

$f, j$	of the flotsam, jetsam component
$M, S$	of the well-mixed, segregated bed

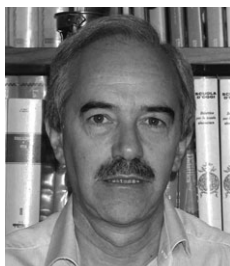
## References

- 1) Nienow, A. W. and Chiba, T.: "Fluidization of dissimilar solids", in J. F. Davidson, D. Harrison, and R. Clift (Eds.), *Fluidization*, Academic Press, London, England, pp.357-382 (1985).
- 2) Rowe, P. N., Nienow, A. W. and Agbim, A. J. (1972). The mechanism by which particles segregate in gas fluidised beds-binary systems of near-spherical particles. *Transactions of the Institution of Chemical Engineers*, 50, 310-323.
- 3) Chen, J. L.-P. and Keairns, D. L. (1975). Particle segregation in a fluidized bed. *The Canadian Journal of Chemical Engineering*, 53, 395-402.
- 4) Vaid, R. P. and Sen Gupta P. (1978). Minimum fluidization velocities in beds of mixed solids. *The Canadian Journal of Chemical Engineering*, 56, 292-296.
- 5) Carsky, M., Pata, J., Vesely, V. and Hartman, M. (1987). Binary system fluidized bed equilibrium. *Powder Technology*, 51, 237-242.
- 6) Chiba, S., Chiba, T., Nienow, A. W. and Kobayashi, H. (1979). The minimum fluidisation velocity, bed expansion and pressure-drop profile of binary particle mixtures. *Powder Technology*, 22, 255-269.
- 7) Yang, W.-C. and Keairns, D. L. (1982). Rate of particle separation in a gas fluidized bed. *Ind. Eng. Chem. Fundam.*, 21, 228-235.
- 8) Thonglimp, V., Hiquily, N. and Laguerie, C. (1984). Vitesse minimale de fluidisation et expansion des couches de mélanges de particules solides fluidisées par un gaz. *Powder Technology*, 39, 223-239.
- 9) Noda, K., Uchida, S., Makino, T. and Kamo, H. (1986). Minimum fluidization velocity of binary mixtures of particles with large size ratio. *Powder Technology*, 46, 149-154.
- 10) Formisani, B., De Cristofaro, G. and Girimonte, R. (2001). A fundamental approach to the phenomenology



- of fluidization of size segregating binary mixtures of solids. *Chemical Engineering Science*, 56, 1-11.
- 11) Otero, A. R. and Corella, J. (1971). *Anales de la RSEFQ*, 67, 1207-1219.
  - 12) Formisani, B. (1991). Packing and fluidization properties of binary mixtures of spherical particles. *Powder Technology*, 66, 259-264.
  - 13) Nienow, A. W., Rowe, P. N. and Cheung, L. Y.-L. (1978). A quantitative analysis of the mixing of two segregating powders of different density in a gas-fluidized bed. *Powder Technology*, 20, 89-97.
  - 14) Rice, R. W. and Brainovich, J. F. (1986). Mixing/segregation in two- and three-dimensional fluidized beds: binary systems of equidensity spherical particles. *A.I.Ch.E. Journal*, 32, 7-16.
  - 15) Wu, S. Y. and Baeyens, J. (1998). Segregation by size difference in gas fluidized beds. *Powder Technology*, 98, 139-150.
  - 16) Yu, A. B. and Standish, N. (1987). Porosity calculations of multi-component mixtures of spherical particles. *Powder Technology*, 52, 233-241.
  - 17) Rowe, P. N., Nienow, A. W. and Agbim, A. J. (1972). The mechanisms by which particles segregate in gas fluidized beds – binary systems of near-spherical particles. *Transactions of the Institution of Chemical Engineers*, 50, 310-323.
  - 18) Nienow, A. W., Rowe, P. N. and Cheung, L. Y.-L. (1978). A quantitative analysis of the mixing of two segregated powders of different density in a gas fluidized bed. *Powder Technology*, 20, 89-97.
  - 19) Formisani, B., Girimonte, R. and Guzzo, A. (2002). Unstable fluidization of size segregated binary mixtures with the coarser component initially on top. *Proc. "4<sup>th</sup> World Congress on Particle Technology"*, Sydney, Australia.
  - 20) Marzocchella, A., Salatino, P., Di Pastena, V. and Lirer, L. (2000). Transient fluidization and segregation by size difference of binary mixtures of particles. *A.I.Ch.E. Journal*, 46, 2175-2182.

### Author's short biography



#### Brunello Formisani

Brunello Formisani graduated in Chemical Engineering from the University of Naples, Italy, in 1979. In 1984, he joined the Department of Chemical and Materials Engineering at the University of Calabria, where he has been an associate professor since 1992. His teaching activity involves chemical plant design and solids processing. His research interests are in the field of particle fluidization, and include packed-fluidized beds, fluidization of solid mixtures, high-temperature fluidization, and interparticle forces.



#### Rossella Girimonte

Rossella Girimonte graduated in Chemical Engineering from the University of Calabria, Italy, in 1995 and received her Ph.D. in 1999. She is presently an assistant professor in the Department of Chemical and Materials Engineering at the same university, where she holds a course on unit operations. Her research activity is currently focused on high-temperature fluidization and fluidization of multicomponent particle beds.

# Mechanochemical Grinding of Inorganic Oxides<sup>†</sup>

G.R. Karagedov, N.Z. Lyakhov

*Institute of Solid State Chemistry and  
Mechanochemistry Russia\**

## Abstract

*A great deal of experimental data on the mechanochemical treatment of inorganic oxides and mixtures thereof falls into the simple scheme involving the concurrent manifestation of grinding, particle aggregation, and primary crystallite coalescence, respectively. The properties of resulting powders proved to be determined by the position of dynamic equilibrium among the processes taking place. Exerting an influence on the course of one or several processes makes it possible to shift the position of equilibrium and thus to obtain powders with different extents of aggregation, different particle sizes and size distribution curves, or to carry out the treatment under conditions favorable for mechanochemical synthesis. As a result, a weakly agglomerated 15-nm  $\alpha$ -Al<sub>2</sub>O<sub>3</sub> powder was prepared in one case, and either yttrium or calcium-stabilized zirconia formed directly in the mill in the other case.*

## Introduction

The progress in modern material science is mostly determined by the achievements made in science and the technology of super fine powder production. This evidence is mostly explained by the more stringent requirements imposed on powder substances in the submicron range on the one hand, and by the aroused interest in nanosized powders on the other hand. The development of nanostructured three-dimensional materials with unique parameters [1-5] is impossible without mastering the technology for producing weakly agglomerated powders with the mean size of 10-50 nm. However, the use of powders with particles of average size 10-100 nm instead of more coarsely dispersed powders offers rather promising and unexpected possibilities such as the coprocessing of ceramics with metals or the considerable reduction of energy costs due to low-temperature sintering [6].

All these factors brought about the rapid development of ultrafine powder production methods. Among them, the most successful results were obtained by the gas-phase method [7]. From our viewpoint, the method of ultrafine powder production by grinding

has largely escaped current attention. However, the mechanochemical grinding of oxides, for example, takes clear superiority over the other methods of fine powder production (above all during the mechanical treatment of the particles in the submicron range, the physical and chemical processes proceed simultaneously, in coordination, and to an inter-correlated pattern). The grinding method is (i) inexpensive, (ii) ecologically clean – since it does not require large volumes of solutions – and (iii) produces particles of the desired size [8]. It should be noted, however, that the oversimplified idea about the direct correlation between the average particle size and the intensity and/or duration of grinding that is valid for coarse grinding (i.e. the higher the intensity and duration of grinding, the smaller is the average size of the powder particles) became absolutely unsuitable in the submicron range [9]. The preparation of nanopowders by direct grinding without taking into account the particular characteristics of the nano-particle behavior under intensive mechanical treatment seems impossible.

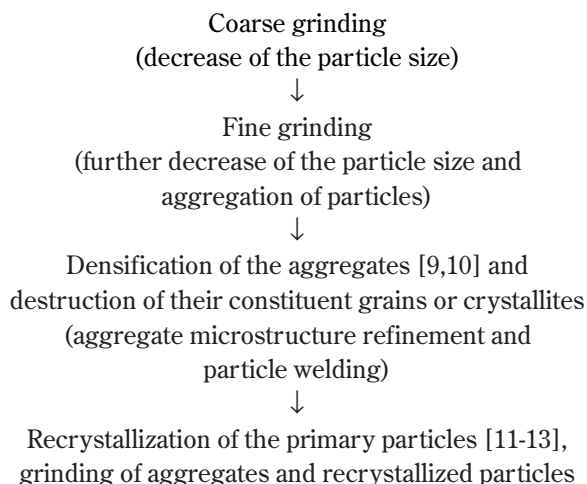
The goal of the present study is to describe the general process of intensive mechanochemical grinding, as well as to visualize how an understanding of the features of constituent physicochemical processes makes the task of producing nanopowders of inorganic oxides relatively simple.

\* Siberian Branch Russian Academy of Science Kutateladze  
18, Novosibirsk, 630128, Russia

<sup>†</sup> Accepted: June, 2003

## General Considerations

The present-day view on the processes occurring in the different types of grinding machines (i.e. ball, vibration, planetary mill, etc.), in which mechanical energy is transferred to the material by the grinding media is described by the following flow chart:



By increasing the intensity and/or the time of mechanical treatment of the powder, we can consequently transfer the system from one level to another. It should be noted that on the third or fourth level, the system inevitably achieves the dynamic equilibrium state, that is, the comminution and agglomeration or reduction of crystallites in size and their re-crystallization proceed at equal rates.

Under application of the curves plotted in **figure 1**, it was possible to obtain a qualitative representation of how the concurrent course of different physicochemical processes influences the size and properties of the treated material and, therefore, of how to predict the consequences of the deliberate alteration of experimental parameters. This figure demonstrates the variation of the powder particle size ( $R$ ) as a function of the parameter ( $I$ ), which could be described as the value of the treatment period under a fixed input of mechanical energy during a unit of time (intensity), or the intensity value during the fixed time. In any case, the curve mode is the same.

Curve 1 describes the decrease in the mean particle size if the particles do not aggregate. The fact that the energy needed to destroy the particles increases considerably with the decrease of particle size explains why the inclination of the curve tends towards zero with time if the intensity of the process is fixed. If we fix the time and increase the grinding intensity, then after achieving a particular particle size, the energy of brittle fracture exceeds that of its plastic

deformation (brittle-viscous transition), and the grinding terminates.

Curve 2 characterizes the process of agglomeration. It demonstrates the evident fact that under the given conditions, the particles of sizes smaller than the critical one are subjected to spontaneous aggregation. In this case, the higher the intensity of the action on the particle collective, the larger in size particles can be subjected to a plastic deformation that promotes aggregation and hence the more particles can be deformed simultaneously and form agglomerates. Curve 2 also tends towards a plateau, because gravitation forces considerably prevail over those of Van der Waals for the large particles and destroy agglomerates. Besides, the large particles and aggregates are preferably subjected to brittle fracture.

The resulting 1-2 curve determines the minimum particle size that could be achieved in the conditions given and points out the inevitability of dynamic equilibrium when the processes of comminution and aggregation counterbalance each other. It is important to note that after achieving the minimum point, a further increase in the intensity of the powder treatment (or increase in the duration of treatment) would only cause an increase of the particle size. Thus, if the system is located to the right of the minimal size, it is often sufficient to decrease the intensity of mechanical treatment in order to decrease the mean particle size. It is worth noting that the powders obtained under conditions when the system is located to the left of the minimum point are weakly aggregated and preferable for dense ceramic processing, whereas to

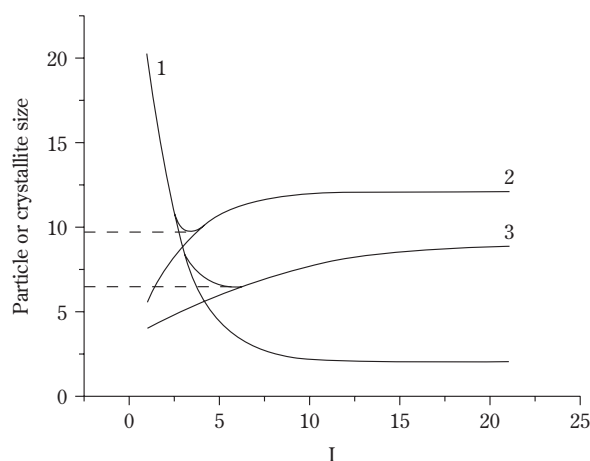


**Fig. 1** Schematic representation of particle (crystallite) size versus time (intensity) of mechanical treatment.

the right of the minimum, the powders are strongly aggregated and can be recommended for ultra-micropore materials.

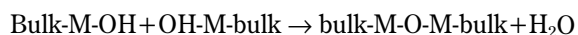
The fact that the system achieves the dynamic equilibrium state relative to the formation and decomposition of aggregates does not mean that the other characteristics will not alter. In particular, curve 3 demonstrates the growth of crystallites, whereas the minimum crystallite size is determined by the parabola composed by the curves 1 and 3. After stabilizing the size of the aggregates, their microstructure refinement can still take place and it terminates later.

It is important to note that the minimum crystallite size is achieved considerably earlier than the dynamic equilibrium state, which is characterized by continuous processes of coalescence and splitting of crystallites. These processes cause a considerable mass exchange between crystallites. Also the areas of local “overheating” with increased reactivity are constantly emerging. In this part of the diagram, the so-called mechanochemical reactions are most intensive. This fact is of the utmost importance for nanogrinding, because on the one hand, it helps to obtain the powder of the required chemical and phase composition, and on the other hand, it intensifies the processes causing contamination of the powder.

In order to achieve a particular goal and to determine the necessary alterations to the experimental conditions, it is of great importance to evaluate exactly what position the system – studied by means of specific equipment – occupies in the diagram shown in **Fig. 1**. Obviously, the decrease of the powder size to an extent less than the minimum size can only be achieved by displacement of the curves 1, 2, and 3 relative to each other. Thus, curve 1 can be moved to the left and curve 2 to the right by adding surface-active reagents. In this case, it was possible to markedly decrease the minimum possible size. Curve 3 can be shifted to the right (often with simultaneous shifting to the left of the curve 2) by adding an additive that is inert with respect to the powder to be ground and which covers the crystallites, thus preventing their coalescence to aggregates. The subsequent removal of the additives leads to the decomposition of aggregates and to the formation of a powder in the nanometer range.

It should be remembered that one and the same substance behaves in different ways under different modes of intensity or at different stages of mechanical treatment. For example, if organic surfactants are treated with significant intensity, they decompose. Also, minor amounts of water foster the formation of

very large aggregates with high bonding strengths (up to the formation of a stone mass) due to “welding” of the hydrated surfaces accompanied by the release of water in accordance with the following quasi-chemical equation:



Let us illustrate the considerations above by means of specific experimental examples.

## Experimental Details

Commercially available chemically pure alumina, zirconia and magnesia (>99.95%) were used. Prior to the experiments, the alumina was calcined at various temperatures (1150-1400°C) until X-ray diffraction patterns detect only the  $\alpha$ -phase. The mechanical treatment of the powder was performed using an AGO-2 planetary mill. Steel balls of 10 mm that ranged in effective density from 4 to 8 g/cm<sup>3</sup> were prepared by drilling reach-through holes. The density was then calculated as mass to enveloping sphere volume ratio.

The specific surface area of the powders was measured using the BET method after drying in the flow of argon gas at 200°C. The X-ray phase analysis and the determination of crystallite size using the line profile analysis was done with the DRON-4 diffractometer supplied with graphite monochromator. The instrumental line broadening as well as the contribution of lattice distortions were taken into account [14]. Electron microscopic studies were performed using the JEM-2000FX2 microscope.

In order to determine the particle size by means of auto-correlation spectroscopy, the powder was subjected to ultrasonic treatment in an aqueous solution of nitric acid (pH~4), and for the centrifuging process and scanning electron microscopy, in ethanol with 4-hydroxybenzoic acid as the dispersant.

## Preparation of superfine powders ( $\alpha$ -Al<sub>2</sub>O<sub>3</sub>)

The grinding of  $\alpha$ -Al<sub>2</sub>O<sub>3</sub> (acceleration 20g) gives evidence of the drastic decrease of the grinding effect with time (see **Table 1**). The powders treated for 10 and 20 minutes are considerably aggregated because the value of the particle size calculated from the specific surface area equals ~130 nm. This parameter is less significantly than the crystallite size shown in **Table 1**. From this, it was possible to draw logical deductions that the experimental points are located close to the minima of the curves 1-2 and 1-3 (**Fig. 1**),

and that a further increase in the duration of mechanical treatment will not lead to a further decrease of the size of the particles and crystallites.

**Table 1** Correlation between duration of mechanical treatment and the size of  $\text{Al}_2\text{O}_3$  particles (20g, balls and crushing cylinders are made of  $\text{Al}_2\text{O}_3$ )

Duration of grinding [min.]	Crystallite size [nm]	Specific surface area [ $\text{m}^2/\text{g}$ ]
0	195	6.4
5	100	—
10	65	12
20	63	11

**Figure 2** illustrates the change of the crystallite sizes of the alumina, magnesia, and ferric oxide by means of a relatively low-intensity grinding regime where the intensity is insufficient for a visible coalescence of particles and where the clearly detectable minimum is missing.

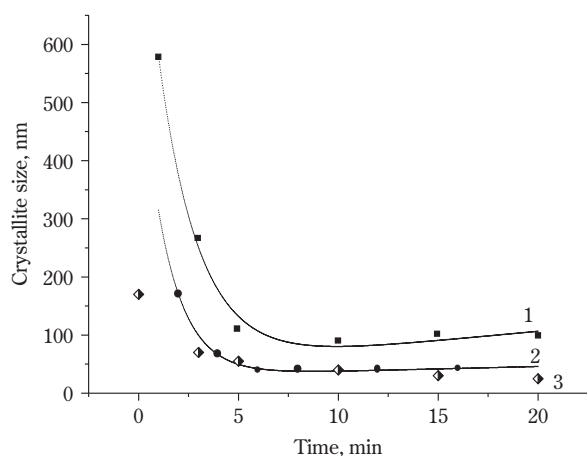


**Fig. 2** Crystallite size of  $\text{Al}_2\text{O}_3$ -1,  $\text{MgO}$ -2,  $\text{Fe}_2\text{O}_3$ -3 as a function of milling time

However, as we increase the intensity of grinding, in the plot showing the dependence of the particle size on the time (**Fig. 3**), both descending and ascending branches of curve 1-2 could be demonstrated (see **Fig. 1**). Curves of this type in coordinates “specific surface area – grinding time” could be observed under mechanical activation of numerous inorganic substances [15]. Such evidence is commonly accounted for the competition between the processes of

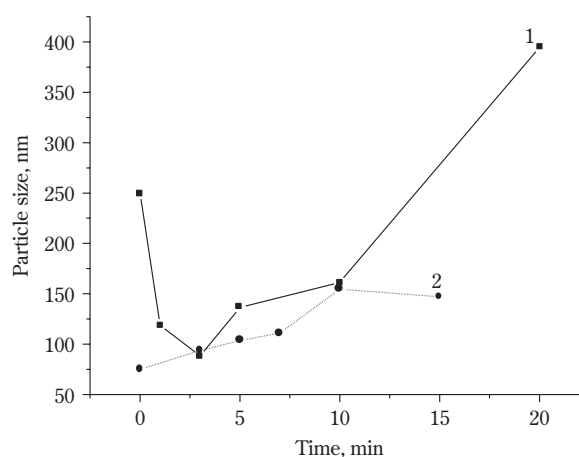


**Fig. 3** Particle size of coarse-1 and fine-2 aluminas calculated from the specific surface area versus time of milling

aggregation and grinding.

As was expected, if the initial powder is already represented by the particles with the mean size close to the minimum, then we can obtain only the ascending part of the curve (curve 2, **Figure 3**), by means of intensive mechanical treatment.

Obviously, similar curves can be obtained by varying the intensity of the mechanical treatment as well. For example, in **Table 2**, the influence of the density of the grinding media is shown that is proportional to the kinetic energy of the balls. The dependence of the specific surface area (from our viewpoint, it is exactly this value that reflects the size of the particles and dense aggregates) on the ball density is of an extreme character, which is predicted by the curve 1-2. Although with the increase of ball density, the energy of an impact also increases proportionally, the specific surface area of the powder achieves a particular value and then decreases.

**Table 2** Influence of the ball density on the  $\alpha\text{-Al}_2\text{O}_3$  grinding

Grinding time, 20g	Material of balls	Effective density of balls [ $\text{g}/\text{cm}^3$ ]	Specific surface area [ $\text{m}^2/\text{g}$ ]	Crystal size [nm]
20 min	$\text{Al}_2\text{O}_3$	3.9	12	63
15 min	Steel	3.9	11	51
15 min	Steel	5.4	17.5	
15 min	Steel	8	8	45
15 min	WC	16-17	—	66
15 min, 5%Al	WC	16-17	—	39.5



The brittleness of tungsten carbide balls brings about a greater contamination of the powder because of the associated wear. This leads to an ambiguity in the interpretation of the specific surface area values; hence, the latter was not measured. However, this fact does not interfere with determination of the crystallite size. The curve of type 1-3 becomes evident in this case as well.

It should be noted that the experimental data presented here were specially selected by the authors for the sole purpose of proving the evidence that (i) in order to decrease the powder particle size, it is not always rational to increase either the duration of treatment or the grinding intensity, and (ii) it is impossible to decrease the particle size to a value less than the minimum one without alteration of some other parameters. In practice, particular values obtained under different conditions depend on numerous factors, including those which in turn depend on the powder pre-treatment history (see **Table 3**). The suggestion that the temperature of alumina calcination effects the toughness through the perfectness of crystal structure seems natural.

**Table 3** Effect of  $\text{Al}_2\text{O}_3$  calcination temperature on specific surface area of mechanochemically treated powders subjected to successive acid leaching

Prehistory	Treatment time [min]	Acceleration [ $\text{m/s}^2$ ]	Ball diameter [mm]	Specific surface [ $\text{m}^2/\text{g}$ ]
1100°C	20	20	10	28
1300°C	20	20	10	22
1450°C	20	20	10	20
1100°C	20	20	5	23
1300°C	20	20	5	19
1450°C	20	20	5	12
1100°C	40	40	5	33
1300°C	40	40	5	30
1450°C	40	40	5	27

Treatment by commonly used surfactants that reduce the particle surface energy is not effective within the nanometer range, because they cannot prevent the fusion of crystallites.

On the contrary, the addition of a reagent with some adhesion to the powder in amounts sufficient to cover the surface of the particles may sterically pre-

vent crystallites from coalescence, thus reducing the achievable size [16], although the particles can aggregate better. The subsequent removal of the additive by dissolving or evaporation will destroy the aggregates and form a weakly agglomerated powder with very small particle sizes.

The additive should meet rigid and rather contradictory requirements. It should have good adhesion to the powder, but be chemically inert with it. It should be resistant to the high pressure and temperature generated in the area of ball impact; it should be easy to remove after grinding; and it should not be ductile in order to prevent slippage of powder particles relative to each other.

Among inorganic oxides, these requirements are often met by metals and carbon which do not react with many oxides and which can be removed by dissolving in acids or alkalis along with evaporation within the temperature range insufficient for the growth of oxide particles.

In **Table 4** (see also the bottom line in **Table 2**), one can see the sizes of crystallites obtained by grinding  $\text{Al}_2\text{O}_3$  for 15 minutes with the addition of Al as the most preferable from the viewpoint of purity, Fe as the metal with the strongest (except Pt) interaction with the alumina surface [17], and C that lacks lubricating properties. As a result, we obtained the mean particle size which is considerably less than that of the crystallites milled without additives (see **Fig. 2**, **Table 2**).

The treatment of the product obtained as above with hydrochloric acid removes the metal and, after careful drying, we obtained a weakly agglomerated

**Table 4** Crystallite size achieved after grinding for 15 min. with steel balls supplemented with various additives

Additive	Acceleration [ $\text{m/s}^2$ ]	Ball diameter [mm]	Additive amount [wt.%]	Crystallite size [nm]
Al	40	5	5	19
Al	40	5	10	24
Al	40	5	15	26
Al	40	5	20	33
Fe	40	5	10	32
Fe	40	10	10	22
Acetylene black	40	5	10	26
Acetylene black	20	5	10	38
Acetylene black	20	5	15	37
Acetylene black	20	5	20	34

powder. For example, in **Figure 4**, we illustrate the dependence of the mean size of the alumina powder particles calculated from the specific surface area on the milling time, after removal of the iron.

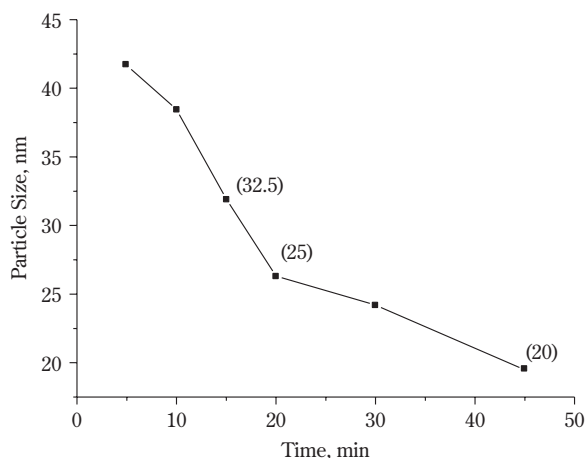


**Fig. 4** Particle size of alumina milled with 10% of Fe and leached with HCl as a function of the time of mechanical treatment

The crystallite sizes derived from the X-ray data are given in brackets. For a 25-nm powder, the particle size was additionally verified by laser autocorrelation spectroscopy, which demonstrates that approximately 80-90 mass% of the powder truly has this size.

However, electron microscopy images show some large (100-200 nm) particles, which are presumably the aggregates. The latter could have formed due to an incomplete coverage of the alumina crystallites by iron during the grinding process. If the conditions of mechanical treatment are to be optimized, additional studies are necessary, whereas a mere increase of the ductile metal (Fe, Al, Zn, Cr) content makes the efficiency of grinding deteriorate (**Table 4**).

In this study, the powder was redispersed in ethanol, treated by ultrasound with addition of 4-hydroxybenzoic acid [18]. The resultant suspension was centrifuged for 1 hour at 3000 rpm. The coarse (~30%) powder was isolated as the centrifugate. The electron microscopy image of the residual oxide (see **Fig. 5**) gives evidence of the lack of large particles and the resultant particle size distribution is rather narrow. After drying at 200°C, the powder had a specific surface area of 107 m<sup>2</sup>/g; crystallite size was 16 nm.

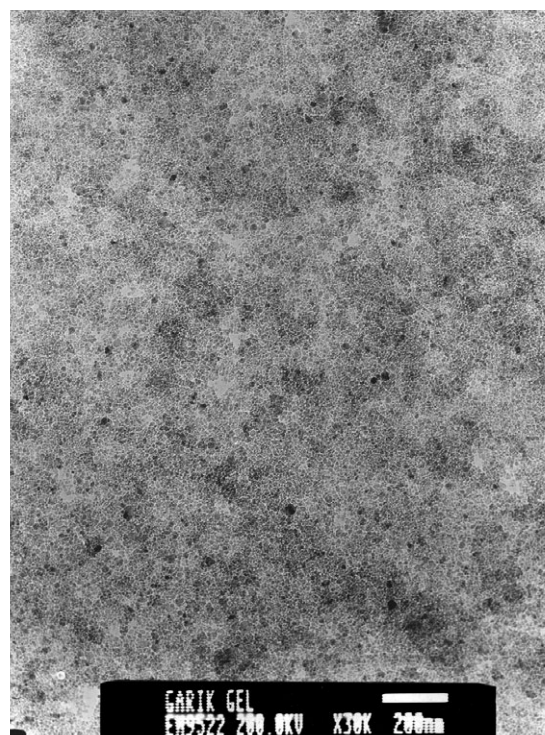


**Fig. 5** Electron micrograph of the fines of milled and washed-off alumina

### Contamination during Grinding

In all probability, the most serious disadvantage of using high-energy mills for grinding fine and ultrafine inorganic oxide powders is the inevitable contamination of the powdered material by the wear of the grinding media and, to a lesser extent, of the mill shell. As a first approximation, the level of contamination increases at the ratio  $t/r^2$ , where  $t$  is the grinding time, and  $r$  is the crystallite size of the oxide powder. In particular, 10 minutes of grinding Al<sub>2</sub>O<sub>3</sub> using balls made of ZrO<sub>2</sub> at an acceleration of 20g are sufficient to show up in the X-ray image as three peaks that correspond to the zirconium oxide. The kinetics of iron accumulation, if a steel shell and steel balls are used, is shown in **Figure 6**.

Although by optimizing the conditions of the mechanical treatment, in particular by increasing the quality of the grinding media, the wear can be considerably reduced, but the problem of obtaining fine powders cannot be solved by this method.

Previously [19], we already noted that long-term boiling of the Al<sub>2</sub>O<sub>3</sub> treated by steel balls in hydrochloric acid could not totally eliminate contamination. In the powder treated for 20 min. at an acceler-

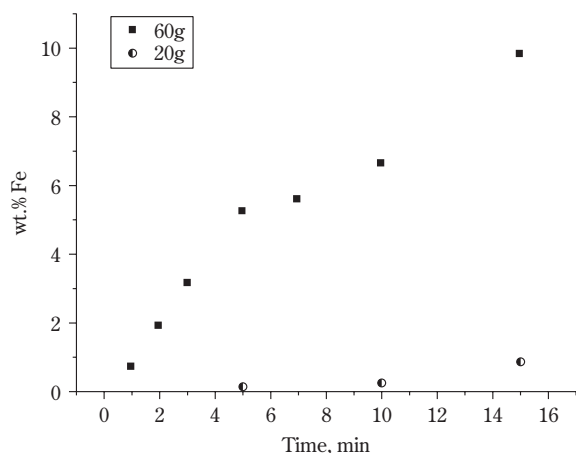
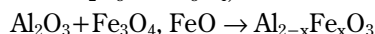
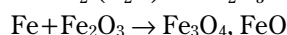
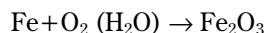


**Fig. 6** Percentage of iron contamination as a result of alumina grinding

ation of 40g, the residual iron was 1.5%, and residual chromium and silicon approximately 0.5% each. It was noted that Mössbauer spectra identify  $\text{Fe}^{3+}$  ions as being surrounded by oxygen.

Additional studies made by ESR spectroscopy have unambiguously supported the assumption on the formation of the  $\text{Al}_2\text{O}_3\text{-Fe}_2\text{O}_3$  solid solution under intense grinding. The logical conclusion is that the  $\alpha\text{-Al}_2\text{O}_3$  crystal lattice also contains Cr. So, after the intense grinding of alumina with steel balls, when the system falls into the range of plastic deformation (right branch of the curve 1-3 shown in **Fig. 1**), the following series of mechanochemical reactions takes place:



The first two reactions were proved by special experiments. It was shown that a durable grinding of alumina (or some other oxides) in the sealed shells causes a considerable pressure drop. When the rubber gasket is punctured by the syringe filled with liquid, the liquid penetrates the shell. So, it is natural to suppose that oxygen in the grinding chamber is consumed to produce ferric oxide. Besides this, it was shown that 30 minutes of grinding  $\text{Fe}_2\text{O}_3$  is sufficient for only FeO responses are being detectable on X-ray.

Since unoxidized metals are not able to react with alumina, we can consider grinding in a dry inert atmosphere as the first step for obtaining fine powders of alumina. In this case, a subsequent treatment by acid would help to obtain an extremely low contamination by iron and chromium residuals.

To this end, a specially constructed mill chamber was evacuated by heating ( $\sim 200^\circ\text{C}$ ) and then filled with Ar dried over sodium metal up to the pressure of  $2 \text{ kg/cm}^3$ .

The tests showed that the iron content in the samples subjected to acid leaching underwent an unexpectedly sharp increase. One may surmise in this case that encapsulation of tiny metal particles in the dense oxide aggregates occurs, thus reducing the efficiency of acid treatment. The lack of moisture and, hence, water adsorption layers covering the particles, facilitates the interaction between particles and their caking-up to form dense aggregates.

The data presented in **Figure 7** validate this hypothesis. Water layers between the particles decrease the friction and hinder the formation of dense aggregates. This phenomenon could be viewed visually in the form of a significant (immeasurable) rate of the powder lightening (its color changes from black to white) in the process of its washing off in acid.

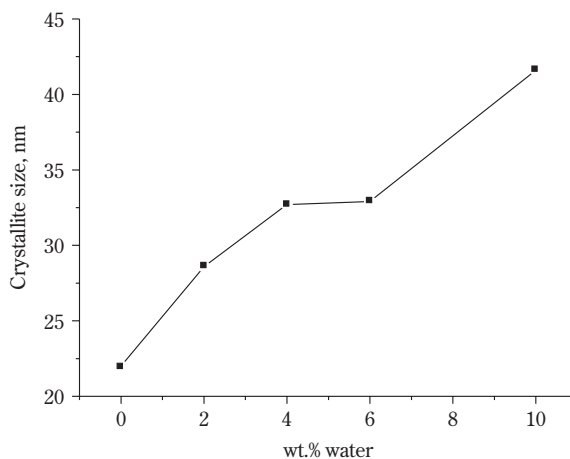


**Fig. 7** Crystallite size of ground alumina as a function of the amount of water added

It is obviously impossible to prevent the oxidation of iron by water and, hence, the contamination of  $\text{Al}_2\text{O}_3$  due to mechanochemical reaction with  $\text{Fe}_2\text{O}_3$ . But the experiments described above reveal one more mechanism of contamination of the oxide powder, that is, the encapsulation of fine metal particles, if the amount of the additive is insufficient for an effective decomposition of the particles in the aggregates.

The addition of metals may partially compensate the lack of a water layer by acquiring its functions. For example, the addition of 5-10% of Fe allowed us to obtain an  $\alpha\text{-Al}_2\text{O}_3$  powder with a mean particle size of

40 nm and a residual iron content of only 0.02%.

Remarkably, the starting alumina contained 0.035% of iron, so that in this case, we observe the phenomenon of “mechanochemical purification” of the powder. This effect seems rational, especially if we consider the possibility of segregation of the impurity atoms on the surface of the powder. During intense grinding, the surface of the powder multiplies many times. At the same time, the increased diffusion ability of the ions in the particles subjected to intense plastic deformation provides a rapid enrichment of the surface layer by the impurity. The subsequent treatment with an acid dissolves the strongly defective and even amorphous [20] surface layer.

In some cases, it was found promising to use an additive consisting of two substances, one aimed at separating the crystallites from the aggregates, whereas the other has an oxygen affinity and prevents oxidation or even has an ability to mechanochemically reduce the alien metal oxide. The latter reactions are well studied [21-24].

Thus, grinding the alumina with the mixture of Al and Fe at ambient atmosphere followed by acid treatment enables the production of powders with a specific surface area of 70 m<sup>2</sup>/g, crystallite sizes of 24 nm, and iron residues of less than 0.06.

### Grinding ZrO<sub>2</sub>

An intensive mechanical treatment of zirconium dioxide is characterized by a phase transformation [25,26] which is supposed to be due to the contribution of surface energy into the Gibbs potential value. The increase of the specific surface area converts the oxide into the tetragonal or cubic modification and becomes thermodynamically stable. For coarse powders, monoclinic zirconia is known as the stable one.

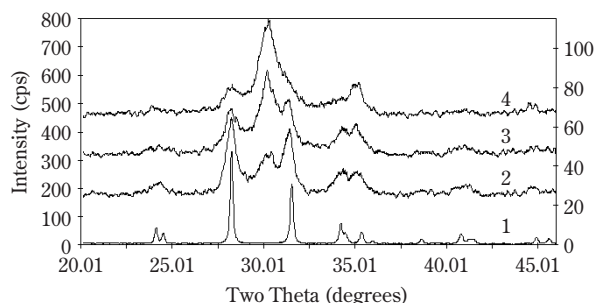


**Fig. 8** X-ray patterns of zirconia depending on milling time. 1- starting; 2- 5 min.; 3- 10 min; 4- 15 min.

**Figure 8** shows the X-ray patterns of zirconium dioxide powder samples that were initially represented by 100% monoclinic modification and that were mechanically treated at different periods of time. In **Figure 9**, one can see the alterations occurring during subsequent thermal annealing of one of the samples. As seen, even a short period of mechanochemical activation under these conditions is sufficient for around 50% phase transition of the monoclinic modification into a more symmetrical one. This fact was evidenced by the peak at approximately 30 degrees. Thermal treatment of the milled samples initially leads to a more pronounced phase change, but with further increase of temperature, this trend reverses.

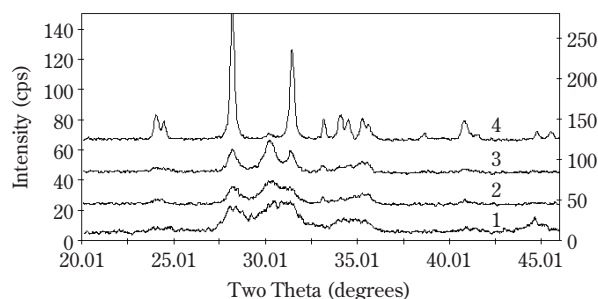


**Fig. 9** X-ray pattern of zirconia milled at 40g for 10 min. (1) and annealed for 1 hour at 700°C (2), 800°C (3) and 900°C (4).

A similar phenomenon was reported in [27], where the data were correlated with the crystallite size, namely that with the increase of crystallite size, the modification became monoclinic and vice versa.

Nevertheless, only the due consideration of the nature and the entirety of processes that take place during intensive mechanochemical grinding may be able to satisfactorily explain the total body of experimental evidence:

- mechanical treatment of the tetragonal ZrO<sub>2</sub> modification caused its rapid transformation into a monoclinic one [27];
- mechanical treatment of the monoclinic modification led to its transformation into a tetragonal one. In this case, the extent of transformation after grinding with tungsten carbide balls during a period of as much as 50 hours was only 45% [25], whereas intensive treatment with steel balls led to a 100% tetragonal modification after only ~20 min [26];



– thermal treatment of the mechanochemically synthesized tetragonal modification even at 800-900°C transformed it into a monoclinic one ([25,28], **Figure 9**), whereas by means of special experiments, we demonstrated that the onset of sintering of the milled zirconium dioxide was detected only at 1000-1050°C.

All these facts appear to be consistent only with the supposition that an intensive or durable mechanical treatment leads to the condition of a dynamic equilibrium between the processes of crystallite fracture and coalescence (curve 1-3, **Figure 1**). The crystallites of sizes larger than the threshold size and, hence in a phase of monoclinic modification, divide finely and transform to the tetragonal phase. The opposite process of coalescence of small particles causes a reverse change of phase. The rates of these processes in the equilibrium state are equal, which is why the authors [25] failed to obtain more than 45% transition, this result corresponds approximately to that shown in **Figure 8**.

In our opinion, a rather impressive result is given in **Figure 10**. After 10 minutes of grinding with steel balls at a relatively low intensity (20g), it can be seen that the X-ray lines are considerably broader, and tetragonal phase is clearly detectable. However, if this experiment is carried out with the shell cooling water switched off so that the background temperature in the shell increases to 50°C as determined in accordance with [29], then the phase transition does not take place and the X-ray lines are notably narrower.

Such significant alterations with only a slight change to the temperature can be explained only by

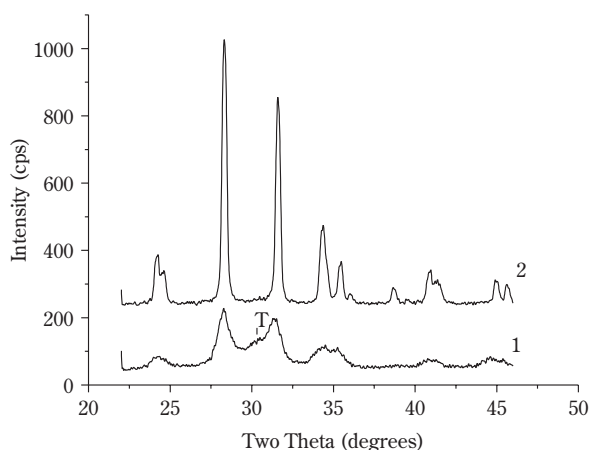


**Fig. 10** X-ray pattern of zirconia milled at 20g for 10 min with (1) and without (2) cooling of the shell

the growing plasticity of the particles with the rise of temperature, which in turn facilitates their coalescence and the crystallite growth, respectively. Therefore, the threshold size of transformation to tetragonal modification cannot be achieved and the monoclinic phase does not appear.

The contradiction with [26], where the authors were successful in running a complete mechanochemical phase transition is probably a result of the grinding media wear. In the course of intensive grinding with steel balls, fine metal particles will oxidize and the  $\text{Fe}^{3+}$  cation integrates into the oxide crystal lattice [30], by analogy to the  $\text{Ca}^{2+}$  and  $\text{Y}^{3+}$  cations (see below). Thus, the tetragonal phase becomes stabilized independent of the crystallite size. In its turn, the resulting solid solution decomposes at elevated temperatures [30].

Our experiments made under conditions where additives (balls and shell are ceramic) were excluded have demonstrated that even after 10 minutes of grinding (acceleration 20g), the phase transition of the  $\text{ZrO}_2$  monoclinic modification into the tetragonal one is about 30%. This value remains almost unaffected by the increase of the grinding time up to 1 hour or a rise of the intensity up to 40g.

Clearly, if the ultrafine tetragonal modification is mechanically treated, then this process will correspond to the conditions described by the left parts of curves 2 and 3 (**Figure 1**). In this case, even a weak mechanical action should cause the pronounced growth of the crystallite size followed by a transition into the monoclinic phase, as was observed in practice [25,27].

Following our concept, the addition of Al to  $\text{ZrO}_2$  should promote the intense grinding of the oxide. By restricting the growth of crystallites, this additive will prevent a reverse phase transition into the monoclinic modification, as shown in **Figure 11** (compare with curve 4, **Figure 9**), even at high temperatures.

Interestingly enough, the additive separating the crystallites from each other can fulfill its function even if it is present only at the grinding stage. In particular, instead of aluminum, we used polyvinyl alcohol that obviously evaporates from the powder long before 800-900°C. This procedure also prevents transition into the monoclinic phase under heating conditions. Clearly, the growth of crystallites in a non-aggregated powder is possible only if the temperature is higher than the sintering temperature, i.e. if it exceeds 1000°C.

From the above discussion, it is obvious that it is impossible to obtain fine-dispersed zirconia as well as



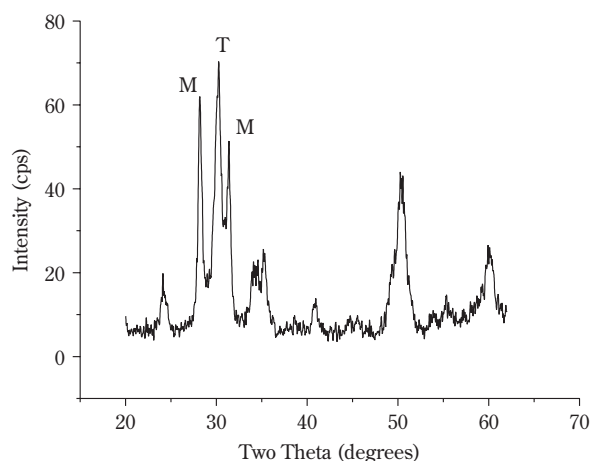


**Fig. 11** X-ray pattern of zirconia milled with 15% Al additive and annealed at 1000°C for 3 hours. (T-tetragonal, M-monoclinic modification.)

other metal oxides, only by intense grinding without additives and specially developed techniques. However, it was possible to make positive use of the same features of the mechanochemical grinding that prevent nanopowders from being obtained.

A problem of great concern in ceramics made of  $\text{ZrO}_2$  is that the path to obtaining yttrium- or calcium-stabilized phases is rather involved. The addition of proper compounds of yttrium or calcium zirconia followed by grinding under conditions favorable for mechanochemical reaction yields stabilized oxide directly in the mill without the need for any solutions.

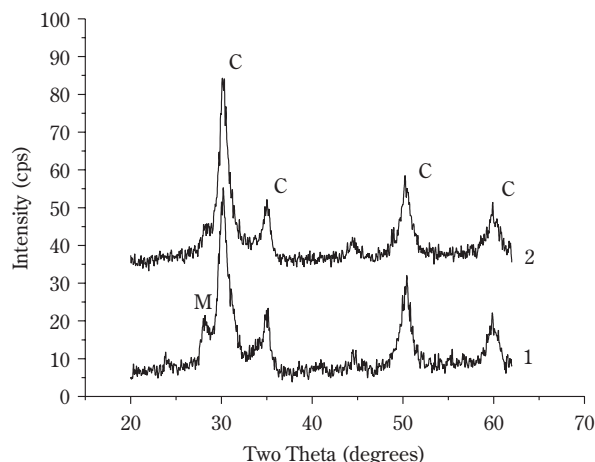


**Fig. 12** X-ray patterns of mechanically treated mixtures of  $\text{ZrO}_2+6\text{mol.}\% \text{Y}_2\text{O}_3$  (2) and  $\text{ZrO}_2+15\text{mol.}\% \text{CaO}$  (1). C – cubic phase, M – monoclinic

In **Figure 12**, one can see the results of such experiments (see also [31]). The above data cannot provide unambiguous evidence as to whether the tetragonal modification obtained is a result of grinding, where the role of an additive is played by the second oxide, or whether the process advances and we observe the product of a mechanochemical reaction. In either case, whether we obtain a stabilized oxide or only its highly reactive precursor, this product can be directly used in the ceramic production. The sintered samples are a dense 100% cubic  $\text{ZrO}_2$ .

## Conclusions

From our viewpoint, the results presented together with other experimental data cited in this publication can be successfully interpreted within the scope of a rather rough but very useful scheme. The entirety of processes that occur under intensive mechanical treatment of the powders in a planetary mill, vibratory mill, ball mill, etc. can be described by the counterbalance between reducing the size of the powder particles and crystallites and their agglomeration and coalescence under the action of the external factors of pressure and temperature. By aiming deliberately at this equilibrium by means of preventing or, on the contrary, by facilitating the coalescence of particles, it is possible to obtain nanocomposites or the products of mechanochemical reactions. Making provisions for the subsequent removal of the hindrance (additive), one can obtain quite finely dispersed powders. Moreover, by considering mechanochemical processes with various parameters, including those modified by additives or by the wear of the grinding media, it is possible to influence the general factors responsible for powder contamination, and thus to noticeably increase the purity of the powder.

## Literature

1. Karch, J.; Birringer, R.; Gleiter, H.: "Ceramics ductile at low temperature" *Nature*, 330, **1987**, 556-558.
2. Hahn, H.: "Microstructure and Properties of Nanostructured Oxides.", *Nanostructured Materials*, 2, **1993**, 251-265.
3. Siegel, R.W.: "Nanostructured Materials – Mind Over Matter", *NanoStructured Materials*, 4, **1994**, 121-138.
4. Kear, B.H.; Strutt, P.R.: "Nanostructures: The Next Generation of High-Performance Bulk Materials and Coatings", *Kona*, 13, **1995**, 45-55.
5. Gusev, A.I.: "Nanokristallicheskie materialy", Ekaterinburg, **1998**.
6. Weertman, J.R.; Farkas, D.; Hemker, K.; Kung, H.;

- Mayo, M.; Mitra, R.; Swygenhoven, H.: "Structure and Mechanical Behavior of Bulk Nanocrystalline Materials", *MRS Bulletin*, 24, **1999**, 44-50.
7. Gutsch, A.; Kramer, M.; Micael, G.; Muhlenberg, H.; Pridohl, M.; Zimmerman, G.: "Gas-Phase Production of Nanoparticles", *KONA*, 20, **2002**, 24-35.
8. Tsuzuki, T.; McCormick, P.G.: "Synthesis of Metal-Oxide Nanoparticles by Mechanochemical Processing", *Materials Science Forum*, 343-346, **2000**, 383-388.
9. Jimbo, G.; Zhao, O.O.; Yokoyama, T.; Taniyama, Y.: "The Grinding Limit and the Negative Grinding Phenomenon", *Proc. 2nd World Congress Particle Technology*, Kyoto, Japan, **1990**, pp.305-312.
10. Bokhonov, B.; Pavlukhin, Yu.; Rykov, A.I.; Paramzin, S.M.; Boldyrev, V.V.: "Crystal growth during mechanical activation of zinc ferrite.", *J. of Mater. Synth. and Process*, 1, **1993**, 341-346.
11. Alekseenko, V.V.; Karagedov, G.R.: "Interaction of Solids Subjected to Mechanical Stress", *Intern. J. Mechanochem. and Mechanical Alloying*, 1, **1994**, 1-6.
12. Bokhonov, B.B.; Konstanchuk, I.G.; Boldyrev, V.V.: "Structural and Morphological Changes during the Mechanical Activation of Nano-Size Particles.", *Materials Research Bulletin*, 30, **1995**, 1277-1284.
13. Alekseenko, V.V.; Karagedov, G.R.: "Interaction of Crystals under Conditions Modelling Mechanical Activation", *Neorganicheskie Materialy*, 33, **1997**, 817-821.
14. Rusakov, A.A: *Rentgenografia Metallov*, Moscow, Atomizdat, **1977**.
15. Avvakumov E.G.: *Mechanical Methods of Chemical Process Activation*, Novosibirsk, Nauka, **1986**.
16. G.R. Karagedov: "Mechanism of Mechanochemical Synthesis in Oxide Systems", *Proc. 4th Japan-Russia Symp. on Mechanochemistry*, Nagoya, **1992**, 137-147.
17. Fischmeister, H.F.: "Progress in the Understanding of Ceramic Microstructures and Interfaces since 1976", *Materials Science Research (Ceramic Microstructures '86)*, 21, 1-14, Plenum press.
18. Sumita S.; Rhine W.E.; Bowen H.K.: "Effects of Organic Dispersants on the Dispersion, Packing, and Sintering of Alumina", *J.Amer.Ceram.Soc.*, 74, **1991**, 2189-2196.
19. Karagedov, G.R.; Lyakhov, N.Z.: "Preparation and Sintering of Nanosized  $\alpha\text{-Al}_2\text{O}_3$  powder", *NanoStructured Materials*, 11, **1999**, 559-572.
20. Okada, K.; Kuriki, A.; Hayashi, S.; Yano, T.; Otsuka, N.: "Mechanochemical Effect for Some  $\text{Al}_2\text{O}_3$  Powders by Attrition Milling", *J.Mater.Sci.Letters*, 12, **1993**, 862-864.
21. Gaffet, E.; Bernard, F.; Niepce, J.-C.; Charlot, F.; Gras, C.; Caer, G.: "Some Recent Developments in Mechanical Activation and Mechanochemical Synthesis", *J. Materials Chemistry*, 9, **1999**, 305-314.
22. McCormic, P.G.: "Application of Mechanical Alloying to Chemical Refining", *Materials Transactions*, 36, **1995**, 161-169.
23. Takacs, L.: "Reduction of Magnetite by Aluminum: a Displacement Reaction Induced by Mechanical Alloying", *Mater. Letters*, 13, **1992**, 119-124.
24. Pardavi-Horvath, M.; Takacs, L.: "Iron-Alumina Nanocomposites Prepared by Ball Milling", *IEEE Transactions on Magnetics*, 28, **1992**, 3186-3188.
25. Bailey, J.E.; Lewis, D.; Librant, Z.M.; Porter, L.J.: "Phase Transformations in Milled Zirconia", *J.Brit.Ceram.Soc.*, 71, **1972**, 25-30.
26. Kuznetsov, P.N.; Zhizhaev, A.M.; Kuznetsova, L.I.: "Mechanochemical synthesis of nanosize metastable zirconium oxide", *RUSS J APPL CHEM ENG TR*, 75, **2002**, 171-176.
27. Whitney, E.D.: *Trans.Fraday Soc.*, 61, **1965**, 1991-1996.
28. Karagedov, G.R.; Ryzhikov, E.A.; Shazkaya, S.S.: "Peculiarities of  $\alpha\text{-Al}_2\text{O}_3$  and  $\text{ZrO}_2$  Nanogrinding", *Chemistry for Sustainable Development*, 10, **2002**, 89-98.
29. Kwon, Y.-S.; Gerasimov, K.B.; Yoon, S.K.: "Ball Temperatures during Mechanical Alloying in Planetary Mills", *J.Alloys and Compounds*, 346, **2002**, 276-281.
30. Cao, W.; Tan, O.K.; Zhu, W.; Jiang, B.: "Mechanical alloying and thermal decomposition of  $(\text{ZrO}_2)(0.8)\text{-(}\alpha\text{-Fe}_2\text{O}_3\text{)}(0.2)$  powder for gas sensing applications", *J SOLID STATE CHEM.*, 155, **2000**, 320-325.
31. Michel, D.; Faudot, F.; Gaffet, E.; Mazerolles, L.: "Stabilized Zirconias Prepared by Mechanical Alloying", *J.Amer.Ceram.Soc.*, 76, **1993**, 2884-2888.

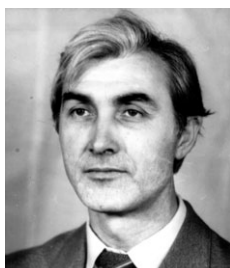
## Author's short biography



### Karagedov Garegin

Garegin Karagedov graduated from Novosibirsk State University as a chemist in 1977. He received his PhD (kandidate of science) in physical chemistry in 1986 in Institute of Solid State Chemistry Russian Academy of Sciences. His postdoctoral research included mechanochemical, sol-gel, and radiation-thermal synthesis of superfine powders of multicomponent inorganic oxides. In 1990 he has built up the separate research group aimed at preparation of nanopowders and sintering nanostructured ceramics. His activity in the field resulted in more than 40 publications in peer-reviewed journals.

Garegin Karagedov is currently heading the team for development the technology of advanced uranium oxide fuel rods at Novosibirsk Chemical Concentrates plant.



### Lyakhov Nikolai

Nikolai Lyakhov is Director of the Institute of Solid State Chemistry. He graduated from Novosibirsk State University (Physical Faculty) in 1969. He received his PhD from the Institute of Catalysis in 1976. The main scientific activity is connected with reactivity of solids, mechanochemistry, materials chemistry, synchrotron radiation.

N. Lyakhov is Professor at Novosibirsk State University, corresponding member of Russian Academy of Sci., Member of Asia-Pacific Academy of Materials, President of MRS-Russia, Vice-President of Mendeleev Russian Chemical Society.

# Particle Impact Breakage in Particulate Processing<sup>†</sup>

A.D. Salman, G.K. Reynolds  
and M.J. Hounslow

Department of Chemical and Process Engineering,  
University of Sheffield\*

## Abstract

*The study of particle breakage in particulate processing is presented at two principal scales. Single-particle impact results are shown to be useful in deducing and understanding process-scale particle breakage behaviour. Particulate breakage in fluidised bed granulation, high-shear granulation and pneumatic conveying systems are explored with a focus on presenting techniques and results connected with furthering understanding and modelling.*

## 1. Introduction

The processing and transport of particulate material, from raw material to final product, is of great importance to a wide range of industries. The role of particle breakage is significant in many cases in terms of yield and quality of product, whether the desire is to cause breakage or avoid it. However, the mechanisms and prediction of particle breakage are only understood to a limited extent. This paper seeks to review and present current research into the area of particulate breakage, from the individual particle scale to the process scale.

## 2. Single Particle Breakage

### 2.1 Impact Experiments

Single particle breakage has been studied to a limited extent in order to improve the understanding of ensemble breakage in particulate processing applications. Typical research has focussed on the impact or compression of spherical particles made from a range of materials. Single particle impact studies allow the isolation and prediction of breakage in systems where particulate transport leads to impacting conditions,

such as pneumatic conveying and high-shear granulation.

Bemrose and Bridgewater<sup>1</sup> state that multiple-impact studies can give empirical data that is useful for the direct application to realistic contexts, but do not generally reveal the basic failure mechanisms. Single-impact studies can be used to develop an understanding of failure processes and mechanisms, as well as providing useful statistical data that can be used for predictive analysis. Single-particle impact is typically achieved by propelling a particle from a pneumatic rifle at a rigid target in an arrangement similar to that depicted in **Figure 1**. This arrangement allows analysis of particle fracture mechanisms using high-speed imaging, and measurement of fragment size distribution.

The single particle impact of a large number of materials has been studied in the literature, in particular glass<sup>2-9</sup>, polymers<sup>10-13</sup>, ionic crystals<sup>14</sup>, sand-cement<sup>2</sup>, aluminium oxide<sup>7, 15</sup>, and agglomerates<sup>16-18</sup>.

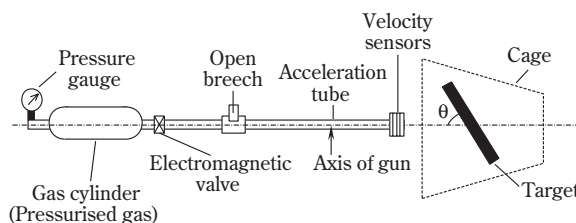


**Fig. 1** Typical arrangement for single-particle impact

\* Mappin Street Sheffield S1 3JD – United Kingdom  
Email: a.d.salman@shef.ac.uk

<sup>†</sup> Accepted: July, 2003

## 2.2 Failure pattern description

To demonstrate typical fracture pattern analysis, the failure patterns of spheres made from different materials will be discussed. The impact velocities are divided into three relative regimes at which failure can occur. A low-velocity regime is that at which the first signs of breakage occur with increasing impact velocity. The intermediate-velocity regime is a higher velocity at which a change in failure form occurs compared with the low-velocity regime. The high-velocity regime is again where a change in failure form is observed upon increasing impact velocity. Failure forms from these regimes are shown for a variety of spherical materials in **Figures 2, 3** and **4**, respectively<sup>19</sup>.

**Figure 2** shows low impact velocity regime fractures of several different materials. Typical Hertzian ring and cone cracks, which are usually the first failure patterns with increased normal impact velocity of glass spheres, can be seen in **Figure 2(a)**<sup>9</sup>. This failure is very similar to well-documented forms of failure under quasi-static indentation of a glass surface by a rigid sphere<sup>15</sup>. The principal Hertzian cone crack is labelled C1. Small, annular fragments of glass are removed when secondary cone cracks travel toward the free surface. It is expected that this section forms during the unloading post-impact phase, by analogy with similar cracks observed during slow indentation tests. Again by analogy with static indentation experiments, it has been proposed that additional cracks which form inside the main Hertzian ring are associated with inelastic deformation processes such as densification<sup>15</sup>. **Figure 2(b)** illustrates the low impact velocity regime failure of aluminium oxide. Local cracking and the development of a flat region over the contact area can be observed. Similar fracture patterns are also observed in tungsten carbide, solid granules, polystyrene, sapphire, zircon, steel, nylon, and fertiliser. The labelled compression failure is conical in shape. In aluminium oxide, fertiliser and solid granules, this conical region often disintegrates. Fractures can propagate from this region along meridian planes, producing hemispheres or quadrants (less the conical region). The low impact velocity regime failure of PMMA spheres (**Figure 2(c)**) reveals characteristic ‘angel wing’ radial cracks, sometimes joined by sections of circumferential crack and always associated with circumferential crazing. No observable deformation of the surface can be found. Wet granule deformation can be observed at very low velocities (**Figure 2(d)**) with flattening of the impact region into a relatively large contact area, but with no ob-

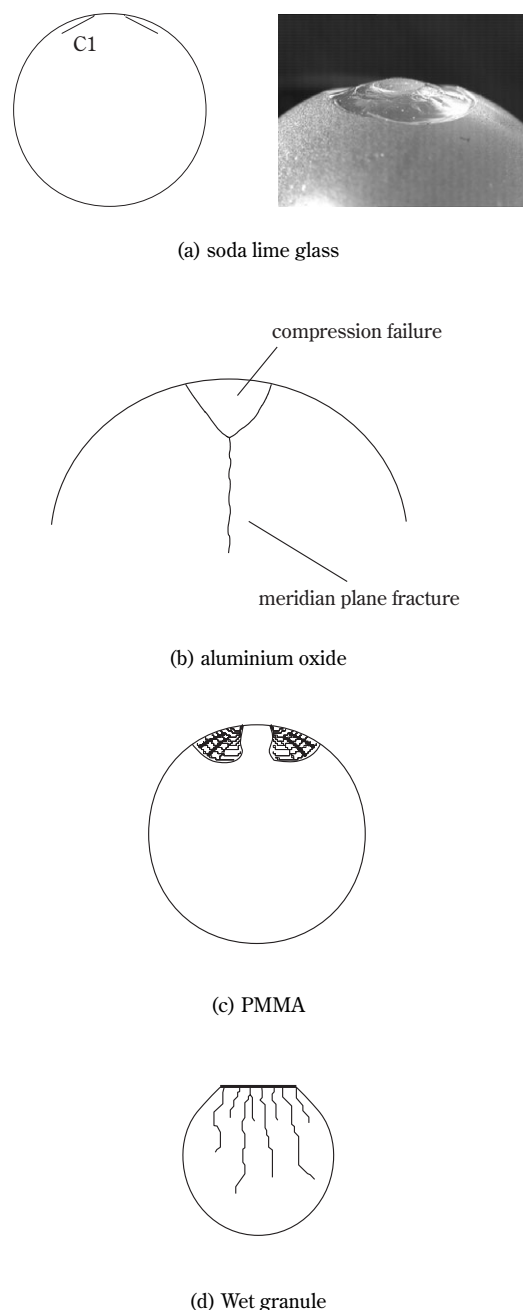


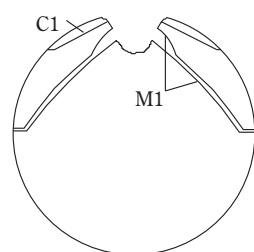
**Fig. 2** Normal low impact velocity regime failure patterns of several materials

servable cracking. There is a significant increase in the diameter parallel with the impacting surface and a reduction of diameter perpendicular to the impacting surface. A slight increase in impact velocity above this causes a number of small cracks to propagate from the deformed contact area parallel to the impact axis. The higher end of the low impact velocity regime for wet granules sees an increase in the number of these small cracks, but with the granule still

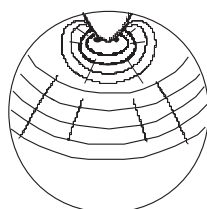


remaining a single entity. In the low impact velocity regime failure of binderless granules, a flattened impact zone is formed with small cracks propagating from this to the upper hemisphere of the granule. A small increase in impact velocity leads to the detachment of a small amount of material around the impact zone, and increased oblique cracks.

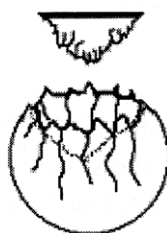
**Figure 3** shows intermediate impact velocity regime breakage patterns for (a) glass, (b) PMMA, (c) wet granules. The failure form of aluminium oxide, and the other materials similar to it, is very similar to the low velocity regime pattern (**Figure 2(b)**), except for the production of more segments from meridian plane cracks. Further failure forms become evident for the normal impact of glass spheres at increasing velocity, as illustrated in **Figure 3(a)**. Oblique cracks



(a) soda lime glass



(b) PMMA

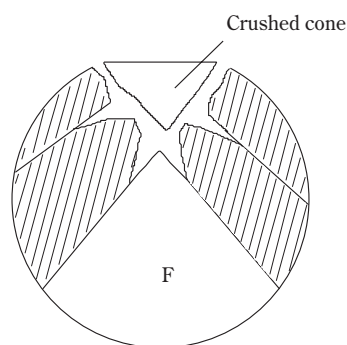


(c) Wet granule

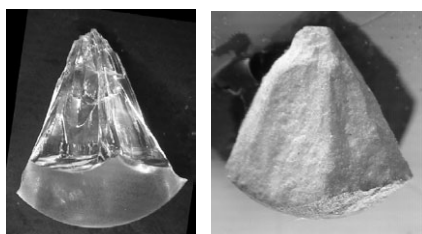
**Fig. 3** Intermediate impact velocity regime failure patterns of several materials

are observed to propagate from under the contact area, forming a large fragment and several smaller ones. The Hertzian cone crack (C1) is usually found inside one of the smaller fragments, and does not contribute to the size reduction process. A significant volume of material from under the contact area is pulverised by the impact, and hence is normally missing when the recovered fragments are reconstructed. The intermediate impact velocity failure of PMMA (**Figure 3(b)**) shows the sphere divided by a meridian plane crack. A roughly conical region below the contact area is defined by varying combinations of sections of surface ring cracks, cracks along the conical surfaces, or cracks across the conical region. However, the surface of the conical region seems to be undamaged. It has suffered no flattening and still remains transparent. Intermediate impact velocity failure forms of wet granules are shown in **Figure 3(c)**. A distinct cone-shaped fragment is formed at the contact area, with the remaining granules forming a mushroom-cup shape. A further increase in impact velocity leads to the mushroom cup fragmenting into several equal-sized pieces. The intermediate impact velocity failure of binderless granules leads to splitting into several equally-sized segmental fragments, leaving a compacted cone on the impact surface. A further increase in impact velocity leads to an increase in the size of the compacted zone, and an increase in the number of fragments, albeit of smaller size.

**Figure 4(a)** shows a generic high impact velocity failure pattern for a large number of materials, including glass, aluminium oxide, tungsten carbide, solid granules, polystyrene, sapphire, zircon, steel, nylon, fertiliser, and PMMA. A cone of crushed and compacted material and several oblique cracks can be observed. A large part of the sphere remains as a single characteristically shaped piece (marked F in the figure). Examples of this piece from a number of materials are presented in **Figure 4(b)**. Meridian plane cracks observed at lower velocities do not form part of this high impact velocity form. A further increase in impact velocity reduces most of the fragments to millimetre and submillimetre dimensions. However, the large central fragment (F) remains coherent the longest, gradually becoming narrower and shorter. At exceptionally high impact velocities, specimens can disintegrate into fine powder and leave no recognisable fragments at all, leaving a cone of compacted powder on the impact surface. The high impact velocity regime failure of wet granules shows a significant fragment size reduction. The contact



(a) generic high-velocity form



(b) segment F for soda lime glass and aluminium oxide, respectively

**Fig. 4** High impact velocity regime failure patterns of several materials

area cone size increases, and can even be larger than the initial diameter of the granule. The presence of wet binder allows significant plastic-like deformation to take place. Binderless granules completely disintegrate into a single compacted zone on the target at high impact velocities.

This type of analysis allows impact velocity regimes to be defined for different materials. Changes in failure form are often accompanied by a marked change in fragment size distribution. Coupled with knowledge of typical particle impact velocities in a given system, a certain level of qualitative prediction of particle breakage is possible. This allows more control in the design of comminution processes for the production of specific particle characteristics, or the reduction of particulate breakage in other systems.

### 2.3 Quantitative Modelling

Modelling the fragment size distribution mathematically allows the extent of fracture to be assessed quantitatively. Typical models have been reviewed as follows<sup>20</sup>. In comminution, the Rosin-Rammler model has been widely used to describe skewed particle size distributions<sup>21</sup>. This model is characterised by two

parameters, namely the mean size and the width of the distribution. An alternative two-parameter equation used in describing fragment size distribution was the Schuhmann equation<sup>22</sup>, which was defined by distribution and size parameters. According to Ryu and Saito<sup>23</sup>, no physical significance of the size parameter was given by Schuhmann. Gilvarry and Bergstrom<sup>24</sup> proposed a three-parameter distribution function to describe the fragment size distribution of brittle solids. This function was in good agreement with experimental results in the fine size region between 1  $\mu$ m and 1000  $\mu$ m. However, this idealised function was not satisfied outside the size interval specified due to the fact that the size of a real specimen was finite. Similarly, Arbiter et al.<sup>2</sup> found only reasonable agreement in the fine sizes when the Gaudin-Schuhmann double logarithmic plot was used to describe the overall size distribution of glass fragments produced in double-impact and slow compression tests. Ryu and Saito<sup>23</sup> found only a relatively good fit to both the coarse and fine fragments when reviewing the Gaudin-Meloy-Harris equation. This equation states that the volume (or weight) fraction,  $y'$ , passing fragment size of  $x$  takes the following form,

$$y' = 1 - \left[ 1 - \left( \frac{x}{x_0} \right)^\alpha \right]^\beta \quad (1)$$

where  $\alpha$ ,  $\beta$  and  $x_0$  are the empirical parameters. However, this equation was not favourable due to the large number of parameters required.

The impact of large numbers of single particles has also been modelled quantitatively by Salman et al.<sup>25</sup>. In a typical experiment, 100 particles are individually impacted at a constant velocity and the number of particles exhibiting failure is counted. A relationship between the number of unbroken particles ( $N_0$ ) and the impact velocity ( $v_p$ ) can be derived by a two-parameter cumulative Weibull distribution:

$$N_0 = 100 \exp \left[ - \left( \frac{v_p}{c} \right)^m \right] \quad (2)$$

In equation (2),  $c$  is the scale parameter and  $m$  is the Weibull modulus. The scale parameter  $c$  has no direct physical definition, but its value is equal to the impact velocity at which the number of unbroken particles is 36.8%. The Weibull modulus,  $m$ , corresponds to the standard deviation of the distribution. **Figure 5** illustrates a typical relationship between normal impact velocity and number of unbroken particles for fertilizer<sup>25</sup>. This analysis can also be used for particle impact under oblique angles. It allows particle breakage under impact conditions to be quantified through

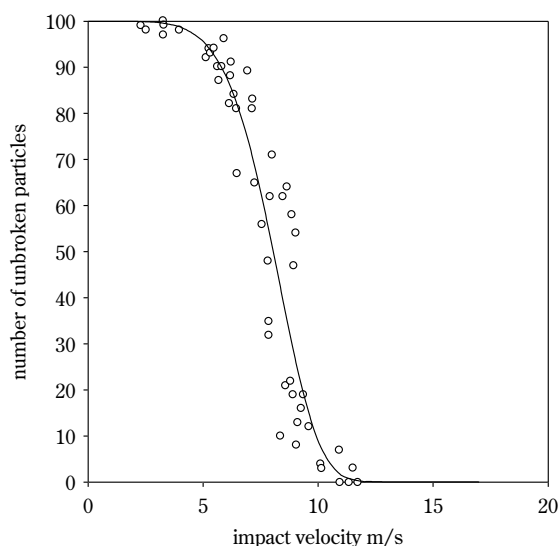


**Fig. 5** Typical relationship between particle impact velocity and number of unbroken particles (7-mm diameter spherical fertiliser particles under normal impact)

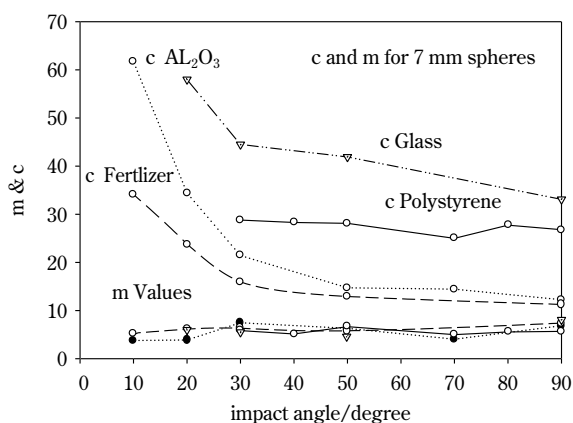


**Fig. 6** Weibull distribution parameters for 7-mm spheres from a range of materials

the use of two parameters,  $c$  and  $m$ . **Figure 6** shows these parameters for 7-mm spheres made from a range of materials. This data can be used to predict the extent of breakage at a range of impact velocities.

The short duration of particle impact breakage has meant that the physical experimental investigation has been replaced by the post-mortem examination of the fragments generated. However, advances in numerical simulations of single-particle and in particular single-agglomerate impact have allowed more detailed study of particle breakage during impact<sup>26-29</sup>.

Typical numerical simulations use the discrete element method (DEM) incorporated with autoadhesive interparticle interaction laws. The motion of each primary particle constituting the agglomerate is traced throughout the impact event using Newton's law of motion. A slightly different two-dimensional DEM approach was adopted by Potapov and Campbell<sup>26</sup> to simulate the breakage behaviour of homogeneous elastic solids impacting against a rigid wall. Instead of discrete particles, the elastic solid was divided into polygonal elements contacting with each other. The contacts were considered to be broken once the tensile force experienced was found to exceed a certain limit. Their simulation results indicated that a fan-like fracture pattern, with elongated fragments, existed over the range of solid material properties and impact velocities used. The formation of fan-like crack systems was accelerated when there was an increase in impact velocity. Potapov and Campbell also concluded that the impact kinetic energy was dissipated by elastic wave propagation through the elastic body under consideration.

The primary disadvantage with single-particle impact studies is that in a typical particulate system, particles do not exist as isolated entities, but rather discrete parts of an ensemble population. Interparticle interaction is likely to have a large effect on particle breakage forms and rates. However, it is only through study on the single particle, and even the intra-particle level that a mechanistic understanding of particulate breakage can be achieved.

### 3. Particulate Processing

Two specific areas of particulate processing are now discussed in order to present a range of research concerning particulate breakage on a process scale. In granulation, an understanding of particle breakage rates is fundamental to control of the final granular product. In pneumatic conveying, an understanding of particulate breakage is important to permit a design that minimises product loss.

#### 3.1 Granulation

Granulation has been widely used in the chemical, agricultural, pharmaceutical, foodstuff and mineral industries to consolidate fine powder into larger entities known as granules. Granules are formed by typically agitating fine powder together with a liquid binder, typically termed wet granulation. Agitation is achieved, for example, using unit operations such as a fluidised bed, high-shear mixer, rotating drum, or

spray dryer.

Traditionally, granulation behaviour has been described in terms of a number of different mechanisms such as nucleation or wetting, abrasion transfer, crushing and layering<sup>30</sup>. Recently, it was proposed that granulation could be considered as a combination of three sets of rate processes<sup>31-33</sup>. They are (1) wetting and nucleation, (2) consolidation and growth, and (3) attrition and breakage. However, there is still little understanding as to the sequence and importance of each mechanism<sup>34</sup>. During granulation, granules can interact with each other, and with solid walls, which can lead to deformation, attrition/breakage, rebounding, or sticking. The behaviour of the granules under impact loading is often very important. Granule breakage may also affect transportation processes by causing undesirable changes in the size, shape or appearance of the granular product.

On a process level, the modelling of breakage in granulation can be incorporated into a population balance model which allows prediction of the size distribution. For batch, well-mixed systems, with size being the only internal coordinate, a population balance equation can be expressed as<sup>35-38</sup>:

$$\frac{\partial n(v,t)}{\partial t} = B - D \quad (3)$$

with  $B$  and  $D$  representing sources of creation and destruction of granules of size  $v$ . Mechanisms that are often included in batch granulation population balance modelling for these terms are that of aggregation and breakage. Both aggregation and breakage mechanisms have associated birth ( $B$ ) and death ( $D$ ) functions. The aggregation of two granules of size  $u$  and  $v$  will lead to a loss of one granule each of size  $u$  and  $v$  and the creation of another granule of size  $u+v$ . Likewise, breakage of a granule of size  $v$  will lead to a loss of one granule of size  $v$  but the creation of a number of smaller granules dictated by the fragment size distribution. Source terms for breakage can be expressed as:

$$B_{\text{break}}(v,t) = \int_v^{\infty} b(v,u) D_{\text{break}}(u,t) du = \int_v^{\infty} b(v,u) S(u,t) n(u,t) du \quad (4a)$$

$$D_{\text{break}}(v,t) = S(v,t) n(v,t) \quad (4b)$$

Here,  $S$ , the selection rate constant, describes the rate of breakage of particles of a given size, and can also be considered time-dependent. This time dependence is related to the expected densification of granules during the granulation process, leading to stronger granules and hence a changing breakage

rate. In fact, the breakage rate should be a function of a number of granule properties, but as these are not taken into account in the single-dimensional population model, the term often becomes time-dependent. The breakage function,  $b$ , describes the sizes of the fragments from the breaking particle.

It was not until fairly recently that breakage was incorporated into the modelling of granulating processes. It is noted qualitatively by<sup>39</sup> that the modelling of aggregation terms only in batch granulation processes is not sufficient to describe the system.

### 3.1.1 Fluidised Bed Granulation

In fluidised bed granulation, a bed of primary particles are typically agitated by an air flow. Liquid binder is sprayed over the agitated bed, causing agglomeration between primary particles and leading to granule formation and growth. An understanding of the rates of agglomeration and breakage process within the system are fundamental to the successful control and prediction of the final granular product.

Only a limited amount of work has been conducted into the breakage of granules within fluidised beds. Pitchumani and Meesters<sup>40</sup> describe the breakage behaviour of different enzyme granules, manufactured using a fluidised bed, subjected to repeated impacts using a new instrument. The two types of granules used for the impact testing are produced from spray drying and fluidised bed granulation. The impact test involves bombarding the particles repeatedly against a flat target. The main feature of this new test is its ability to repeatedly impact a large number of particles against a flat target, and to generate extremely reproducible results. They have tested a large number of particles, yielding a statistically satisfactory result. The repeated impacts also provide information on the breakage behaviour of the particles based on their history. Their impact test allows the enzyme granules to undergo very low impact velocities of the order of 5m/s. These low impact velocities lead to attrition and chipping of the granules. However, although this test allows attrition and fragmentation to be quantified, it is also noted that it is still not possible to explain the concept of particle breakage for use in theoretical development, such as in a population balance model.

The inclusion of breakage in a population balance model of fluidised bed granulation has been presented by Biggs et al.<sup>41</sup>. They hypothesised that the breakage process was due to a reversal of the growth process, and hence able to be modelled using a negative aggregation rate. Breakage was observed experi-

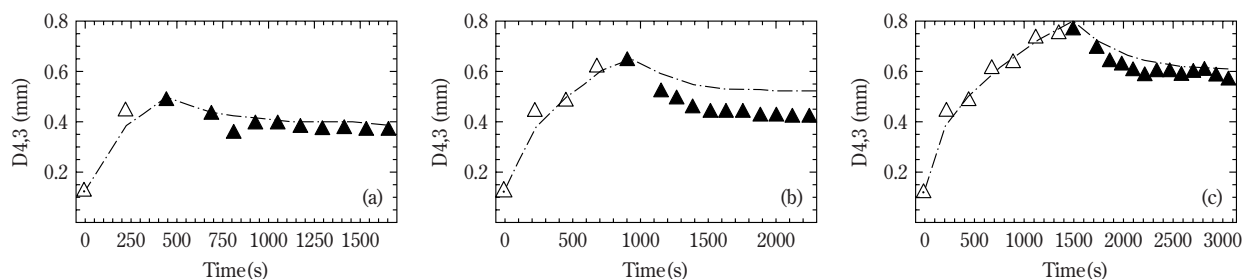


**Fig. 7** Comparison between model and experimental results for the change in mean size for liquid-to-solid ratios of (a) 0.05 (b), 0.1, and (c) 0.2 in fluidised bed granulation [35]

mentally by stopping the binder spray, and hence effectively terminating agglomeration in a system where the binder solidified once it had cooled to the fluidised bed temperature. **Figure 7** shows a comparison between their experimental and simulation work. A mean diameter, represented as the ratio of the fourth moment to the third moment of the granule size distribution, is plotted against operating time. The triangular points on the graph indicate experimental results, with the filled-in triangles representing data gathered after the spray of binder had been stopped. This shows that breakage becomes a dominant mechanism in this system when no further wet binder is introduced, due to solidification of the binder in the fluidised bed. The population balance model results are represented in **Figure 7** as the dashed line. It can be seen that during the spray- and agglomeration-dominant period, there is very good agreement. However, after spraying, during the breakage-dominant period, the model is observed to underpredict the rate of decrease in mean size. These results are a promising step towards including breakage kinetics in the population balance modelling of fluidised bed granulation, but some discrepancies between the experimental and modelling results indicate that further work is needed to include the description of faster breakage kinetics in their current model.

### 3.1.2 High-Shear Granulation

In high-shear granulation, a powder is typically agitated in a cylindrical bowl by a large impeller. Often an additional smaller impeller, termed a ‘chopper’, is used. Binder can be added by pouring or spraying onto the powder.

Sources of breakage exist within a high-shear granulator from particle-particle interaction, particle-wall collision, impeller, and the chopper where this is

used. Knight et al.<sup>42</sup> observed a lower extent of size enlargement relative to power input at high impeller speeds compared with lower ones. They concluded that the increased impeller speed contributed significantly to breakage that limited growth.

Tracer experiments on high-shear granulation have been conducted by Ramaker et al.<sup>43</sup>. They observed that the growth and destruction of granules from different sieve fractions could be measured with tracers. They derived conversion rate constants from the exponential decay of the colour concentration at different processing times for each sieve fraction. Compared to a dimensionless diameter, similar conversion rate constants were found between two high-shear processes (a coffee grinder and a Gral 10). The conversion rate constants of the smallest granules were higher (compared to the larger ones), which indicated faster growth of the smaller granules due to the destruction of the large pellets.

Clear evidence of breakage in wet high-shear granulation has also been shown by Pearson et al.<sup>44</sup>, through the use of coloured tracer granules. The system used calcium carbonate and polyethylene glycol (1500) as a binder. In the case of polyethylene glycol (1500) as a binder, the binder was added using a ‘melt in’ technique. The binder is solid at room temperature, and therefore the high-shear granulator is heated above the melting point (60°C). The binder is added as a solid at the start of the process, and melts as it reaches the operating temperature. Granules collected from this process are solid at room temperature, allowing easier handling for analysis. Granules were manufactured in a Fukae FS30, a 30-litre pilot-scale mixer, with a base-mounted impeller and a side-mounted chopper. The impeller and chopper had maximum speeds of 300 rpm and 3,000 rpm, respectively. A narrow sieve cut of coloured tracer granules was placed into placebo granulation batches in order



to observe the subsequent redistribution of coloured tracer. A multiple-phase discretised population balance model was constructed in order to extract breakage rates from the experimental data<sup>45</sup>. A bimodal breakage function was proposed. **Figure 8** shows a tracer distribution presented in the paper. Based on this, they proposed breakage to proceed as follows. When a granule breaks, it produces two kinds of fragments: many fine ones of mass-mean size near 150  $\mu\text{m}$ , and a few large pieces of mass-mean size somewhat less than that of the initial granule. In this way, on a mass basis, the breakage function is bimodal. The sum of two truncated log normal distributions was fitted to the tracer distribution shown in **Figure 8** (solid lines), giving a breakage function of:

$$b(x, l) = 0.484b_{f1}(x, l) + 0.516b_{f2}(x, l) \quad (5a)$$

where  $b_{f1}$  and  $b_{f2}$  are of the form given as follows with geometric volume-based averages of  $\bar{l}_{gv} = 160 \mu\text{m}$  (mode 1), and  $\bar{l}_{gv} = 3.8 \text{ mm}$  (mode 2); and geometric standard deviations of  $\sigma_g = 1.70$  (mode 1) and  $\sigma_g = 2.66$  (mode 2), respectively:

$$b_f(x, l) = \left(\frac{l}{x}\right)^3 \frac{\frac{1}{x\sqrt{\pi/2}\ln\sigma_g} \exp\left[-\left(\frac{\ln x/\bar{l}_{gv}}{\sqrt{2}\ln\sigma_g}\right)^2\right]}{1 + \text{erf}\left[\frac{\ln l/\bar{l}_{gv}}{\sqrt{2}\ln\sigma_g}\right]} \quad (5b)$$

This breakage function can then be incorporated into a population balance model (see equations 3a and 3b). It was shown by<sup>44</sup> that the selection rate constant was size-independent. They found that plots of the tracer-weighted mean-size suggested that the initial breakage rate was considerably greater immediately after the addition of tracer granules, rather than later. **Figure 9** was also found to support this hypothesis, as the rate of relegation of the tracer was considerably greater for the younger granules than it was for the older granules. Relegated tracer,  $\chi$ , is defined as the amount of dye over all sizes smaller than the initial tracer size. It was proposed that the breakage effectively ceased after the first minute or so subsequent to the addition of the tracer (which was introduced after 8 minutes of granulation), i.e. at  $t = 10 \text{ min}$ . An exponential decay was then chosen to represent the selection rate constant:

$$S(t, l) = S_A \exp\left(-\frac{t-480}{20}\right) \quad (5)$$

These choices of breakage function and selection rate constant were validated by a comparison between modelled and experimental data. A heterogeneous

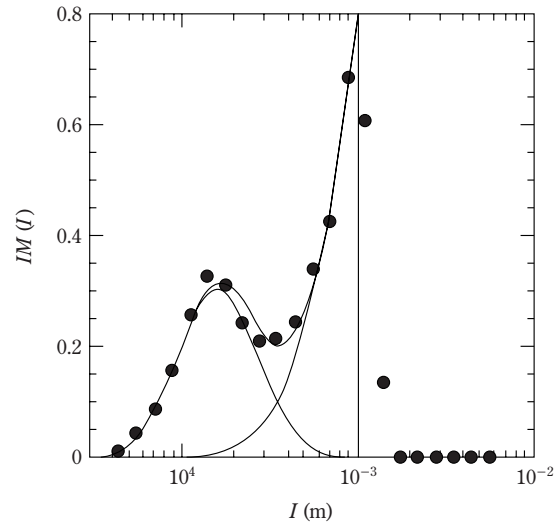


**Fig. 8** Normalised tracer distribution 1 min after adding tracer in the size range 1-1.18 mm [39]. Used for deduction of breakage function

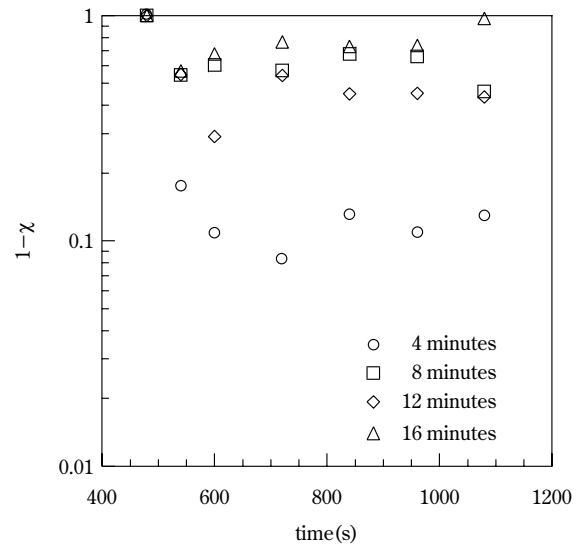


**Fig. 9** Fraction of tracer relegated for tracers of four different ages, but a constant size of 1.09 mm. All tracers were added after 8 minutes of granulation [38]

strength hypothesis was put forward as an attempt to explain the strong time-dependence on the selection rate constant. In this hypothesis, it is proposed that in each size class, a distribution of granule strengths exists. With the addition of tracer granules, the weaker granules rapidly break, leaving only a strong, nonbreaking residue and ultimately leading to a bimodal fragment size distribution and first-order selection rate constant decay. The proposed explana-

tion for the heterogeneous granule strength within any single size class is due to heterogeneity in liquid distribution. Good agreement was found between their modelled results and experimental findings, illustrating that breakage can be successfully incorporated into the population balance modelling of granulation processes.

### 3.2 Pneumatic Conveying

Pneumatic conveying systems are a key unit operation in the transport of particulate material. Typically, particles are transported along pipes using high-speed air flow. The breakage of particles in these systems, causing in some cases a change of size distribution and appearance, can lead to particulate products that no longer meet their required and designed specification. Fragmentation can lead to dust generation, handling and storage problems, in particular where breakage is so severe that aeration and flow characteristics are drastically changed<sup>46</sup>.

Extensive studies into the breakage of particles in dilute conveying systems have been presented by a number of authors<sup>47-53</sup>. Typical measurements are based on circulating the particles on a specific pneumatic conveying system. The change in particle size before and after circulation is observed and related to the air velocity and/or the number of circulations conducted. These studies have provided valuable general information concerning the minimisation of particle breakage during conveying. However, as there are so many variables involved in predicting the mechanisms of particle breakage, and it is difficult to isolate these variables, these studies are typically unique to one particular system. Therefore, they are largely unsuitable for predicting the breakage of particles in other systems.

Salman et al.<sup>46</sup> use a numerical model for calculating the particle trajectory in dilute-phase pipe transport. In their model, they consider a dilute system where inter-particle collisions are neglected and fragmentation is only considered upon impact with pipe walls. They use this model, coupled with single-particle impact studies, to predict particulate breakage in pneumatic conveying. The results are validated with experimental observations on a small-scale pneumatic conveying system consisting of a horizontal pipe with a 90° bend (see **Figure 10**). In this figure, model results are represented as lines, and experimental data as points. The figure shows that high velocities lead to a dramatic increase in particle breakage. Specifically, they found negligible breakage in the horizontal pipe due to a very low impact angle. This is

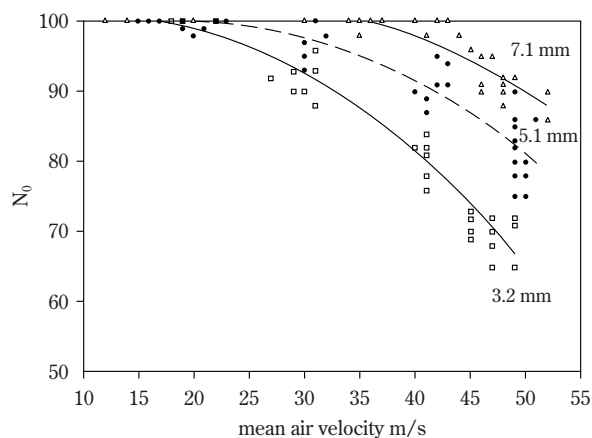


**Fig. 10** Relationship between the number of unbroken fertiliser particles and mean air velocity for 3.2-mm, 5.15-mm and 7.1-mm particles in a pneumatic conveying rig [40]

consistent with single-particle impact studies under different impact angles (e.g. **Figure 6**). Therefore, particle breakage at the bend can be reduced by decreasing the impact angle. This can be achieved by using long radius bends and by reducing the conveying velocity. This study shows that single-particle impact data can be used for predicting particulate breakage on a process level in dilute systems.

### 4. Conclusions

Analysis of the breakage of single particles and agglomerates is used to model and predict failure on a process level. Observation of failure forms shows that spherical particles of a wide range of materials can be classified into distinct failure regimes with respect to impact velocity. Specifically, many materials are observed to fail very similarly at a high impact velocity. Low- and medium-impact velocity forms contain some similarities and differences due to different material properties. The quantitative analysis of single-particle impact can be achieved by fitting breakage rates by a 2-parameter Weibull distribution. These two parameters can be used to successfully model the single-impact breakage rate under normal and oblique impact conditions. These single-impact studies can be used to explain breakage observations on a process level. For example, the amount of breakage in a pneumatic conveying system can be predicted using Weibull distribution parameters from single particle impact studies.

In granulation, breakage has been shown to exist. Specifically, in fluidised bed granulation by observing

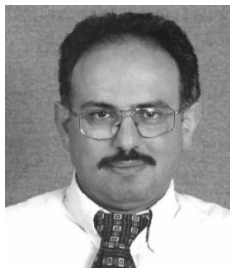
the changing mean size distribution after spraying, and in high-shear granulation by tracer and impeller speed studies. In both processes, breakage has been incorporated into population balance models in order to improve the evolving granule size distribution. More detailed information on breakage from tracer studies has enabled breakage functions to be deduced with the aim of improving model descriptions of the process.

## Bibliography

1. Bemrose, C.R, Bridgwater, J: A review of attrition and attrition test methods, *Powder Technology*, 49, 1987, 97-126.
2. Arbiter, N, Harris, C.C, Stamboltzis, G.A: Single fracture of brittle spheres, *Transactions of the AIME*, 244, 1969, 118-133.
3. Chaudhri, M.M. In: Kurkjian, CR Ed. *Strength of inorganic glass*. New York: Plenum, 1985.
4. Shipway, P.H, Hutchings, I.M: Fracture of brittle spheres under compression and impact loading I. Elastic stress distribution, *Philosophical magazine. A. Physics of condensed matter. Defects and mechanical properties*, 67, 1993, 1389-1404.
5. Shipway, P.H, Hutchings, I.M: Fracture of brittle spheres under compression and impact loading II. Results for lead-glass and sapphire sphere, *Philosophical magazine. A. Physics of condensed matter. Defects and mechanical properties*, 67, 1993, 1405-1421.
6. Shipway, P.H, Hutchings, I.M: Attrition of brittle spheres by fracture under compression and impact loading, *Powder Technology*, 76, 1993, 23-30.
7. Andrews, E.W, Kim, K-S: Threshold conditions for dynamic fragmentation of glass particles, *Mechanics of Materials*, 31, 1999, 689-703.
8. Salman, A.D, Gorham, D.A: The fracture of glass spheres under impact loading. Paper presented at *Powders & Grains 97*, Balkema, 1997.
9. Salman, A.D, Gorham, D.A: The fracture of glass spheres, *Powder Technology*, 107, 2000, 179-185.
10. Schoenert, K: Role of fracture physics in understanding comminution phenomena, *Transactions of the AIME*, 252, 1972, 21-26.
11. Schoenert, K: Aspects of the physics of breakage relevant to comminution. Paper presented at *Fourth Tewksbury Symposium*, Melbourne, 1979.
12. Papadopoulos, D.G, Ghadiri, M: Impact breakage of PMMA extrudates, *Advanced Powder Technology*, 7, 1996, 183-197.
13. Gorham, D.A, Salman, A.D: The failure of PMMA spheres under impact loading. Paper presented at *World Congress on Particle Technology*, Brighton, UK, 1998.
14. Yuregir, K.R, Ghadiri, M, Clift, M: Impact attrition of sodium chloride crystals, *Chemical Engineering Science*, 42, 1987, 843.
15. Salman, A.D, Gorham, D.A: Observation of blunt indentation at high loads, *Journal of Material Science Letters*, 16, 1997, 1099-1100.
16. Salman, A.D, Gorham, D.A: The failure of fertiliser particles under impact. Paper presented at *2nd Israel Conference on Conveying and Handling of Particulate Solids*, Jerusalem, 1997.
17. Subero, J, Ghadiri, M: Breakage patterns of agglomerates, *Powder Technology*, 120, 2001, 232.
18. Fu, J, Salman, A.D, Hounslow, M.J: Experimental study on impact deformation and rebound of wet granules. Paper presented at *World Congress on Particle Technology 4*, Sydney, Australia, 2002.
19. Salman, A.D, Reynolds, G.K, Fu, J.S, Cheong, Y.S, Biggs, C.A, Adams, M.J, Gorham, D.A, Hounslow, M.J: Descriptive classification summary of the impact failure form of spherical particles, submitted to *Powder Technology*, 2003.
20. Cheong, Y.S, Salman, A.D, Hounslow, M.J: The failure of glass particles under impact. Paper presented at *10th European Symposium on Comminution*, Heidelberg, 2002.
21. Djamrani, K.M, Clark, I.M: Characterization of particle size based on fine and coarse fractions, *Powder Technology*, 93, 1997, 101-108.
22. Schuhmann, R: *Transactions of the AIME*, 217, 1960, 22-25.
23. Ryu, H.J, Saito, F: Single particle crushing of nonmetallic inorganic brittle materials, *Solid State Ionics*, 47, 1991, 35-50.
24. Gilvarry, J.J, Bergstrom, B.H: *Transactions of the AIME*, 220, 1961, 380-389.
25. Salman, A.D, Biggs, C.A, Fu, J, Angyal, L, Szabo, M, Hounslow, M.J: An experimental investigation of particle fragmentation using single particle impact studies, *Powder Technology*, 128, 2002, 36-46.
26. Potapov, A.V, Campbell, C.S: Computer simulation of impact-induced particle breakage, *Powder Technology*, 81, 1994, 207-216.
27. Thornton, C, Ciomocos, M.T, Adams, M.J: Numerical simulations of agglomerate impact breakage, *Powder Technology*, 105, 1999, 74-82.
28. Subero, J, Ning, Z, Ghadiri, M, Thornton, C: Effect of interface energy on the impact strength of agglomerates, *Powder Technology*, 105, 1999, 66-73.
29. Mishra, B.K, Thornton, C: Impact breakage of particle agglomerates, *International Journal of Mineral Processing*, 61, 2001, 225-239.
30. Sastry, K.V.S, Panigraphy, S.C, Fuerstenau, D.W: Effect of wet grinding and dry grinding on the batch balling behaviour of particulate materials, *Transactions of the Society of Mining Engineers*, 262, 1977, 325-330.
31. Tardos, G, Irfan-Khan, M, Mort, P.R: Critical parameters and limiting conditions in binder granulation of fine powders, *Powder Technology*, 94, 1997, 245-258.
32. Mort, P.R, Tardos, G: Scale-up of agglomeration processes using transformations, *Kona*, 17, 1999, 64-75.

33. Ennis, B.J, Litster, J.D: Particle size enlargement. In: Perry, R, Green, D Eds. Perry's Chemical Engineers' Handbook. New York: McGraw-Hill, 1997:20-56 – 20-89.
34. Iveson, S.M, Litster, J.D, Hapgood, K, Ennis, B.J: Nucleation, growth and breakage phenomena in agitated wet granulation processes: a review, Powder Technology, 117, 2001, 3-39.
35. Randolph, A.D, Larson, M.A: Theory of particulate processes: Academic Press, 1971.
36. Hulbert, H.M, Katz, S: Some problems in particle technology, Chemical Engineering Science, 19, 1964, 555-574.
37. Ramkrishna, D: Population Balances: Theory and Applications to Particulate Systems in Engineering: Academic Press, 2000.
38. Hounslow, M.J: The population balance as a tool for understanding particle rate processes, Kona Powder and Particle, 16, 1998, 180-193.
39. Annappagada, A, Neilly, J: On the modeling of granulation processes: a short note, Powder Technology, 89, 1996, 83.
40. Pitchumani, R, Meesters, G.M.H, Scarlett, B: Breakage behaviour of enzyme granules in a repeated impact test, Powder Technology, 130, 2003, 421-427.
41. Biggs, C.A, Boerefijn, R, Buscan, M, Salman, A.D, Hounslow, M.J: Fluidised bed granulation: Modelling the growth and breakage kinetics using population balances. Paper presented at World Congress on Particle Technology 4, Sydney, Australia, 2002.
42. Knight, P.C, Johansen, A, Kristensen, H.G, Schaefer, T, Seville, J.P.K: An investigation of the effects on agglomeration of changing the speed of a mechanical mixer, Powder Technology, 110, 2000, 204-209.
43. Ramaker, J.S, Jelgersma, M.A, Vonk, P, Kossen, N.W.F: Scale-down of a high shear pelletisation process: flow profile and growth kinetics, International Journal of Pharmaceutics, 166, 1998, 89-97.
44. Pearson, J.M.K, Hounslow, M.J, Instone, T: Tracer studies of high-shear granulation: I. Experimental results, AIChE Journal, 47, 2001, 1978-1983.
45. Hounslow, M.J, Pearson, J.M.K, Instone, T: Tracer studies of high-shear granulation: II. Experimental results, AIChE Journal, 47, 2001, 1984-1999.
46. Salman, A.D, Hounslow, M.J, Verba, A: Particle fragmentation in dilute phase pneumatic conveying, Powder Technology, 126, 2002, 109-115.
47. Chen, C, Soo, S.L: Attrition and dehulling of grains in pneumatic conveying, Journal of Pipelines, 2, 1982, 103-109.
48. Zenz, F.A, Kelleher, E.G.J: Studies of attrition rates in fluid-particle systems via free fall, grid jets, and cyclone impact, Journal of Powder & Bulk Solids Technology, 4, 1980, 13-20.
49. Viswanathan, K, Mani, B.P: Attrition in a pneumatic conveying pipeline, Journal of Pipelines, 4, 1984, 251-258.
50. Kalman, H: Attrition control by pneumatic conveying, Powder Technology, 104, 1999, 214-220.
51. Taylor, T: Specific energy consumption and particle attrition in pneumatic conveying, Powder Technology, 95, 1998, 1-6.
52. McKee, S.L, Dyakowski, T, Williams, R.A, Bell, T.A, Allen, T: Solids flow imaging and attrition studies in a pneumatic conveyor, Powder Technology, 82, 1995, 105-113.
53. Theuerkauf, J.J, Schwedes, J, Feise, H.J: Two phase flow simulation and an application for comminution. Paper presented at World Congress on Particle Technology, Brighton, U.K., 1998.

## Author's short biography



### A.D. Salman

Agba Salman is a senior lecturer at the University of Sheffield, and a member of the Particle Products Group. He joined the university in 1999 after previous employment at the Open University. He has wide research experience in particle technology, and has published more than 50 papers on this subject. His main research expertise is in particle breakage, particle interaction with a solid wall, and particle movement. This research has involved a combination of experimental and numerical work.



### G.K. Reynolds

Gavin Reynolds graduated with an honours degree in chemical engineering with fuel technology from the University of Sheffield, UK, in 1998. Following this, he remained in the same department and spent three years completing a PhD on a technique to avoid slag accumulation around secondary air jets in incinerators. He is currently working as a post-doctoral research associate with the Particle Products Group in the Department of Chemical Engineering at the University of Sheffield, UK.



### M.J. Hounslow

Michael Hounslow holds Bachelors and Doctoral degrees from the University of Adelaide in South Australia. He has worked in industry for ICI Australia, and as an academic at the Universities of Adelaide, Cambridge and Sheffield. In Sheffield, he is head of the Department of Chemical and Process Engineering, and head of the Particle Products Group. His research interests are in the areas of crystallisation, granulation and population balance modelling.



# Modelling of the gas fluidization of a mixture of cohesive and cohesionless particles by a combined continuum and discrete model<sup>†</sup>

B.H. Xu

*Institute of Particle Science and Engineering,  
School of Process, Environmental and Materials  
Engineering, University of Leeds\**

## Abstract

*This paper presents a numerical study of the gas fluidization of a mixture of 45,000 cohesive and cohesionless particles ( $D=100\ \mu\text{m}$  and  $\rho=1,440\ \text{kgm}^{-3}$ ) using a Combined Continuum and Discrete Model (CCDM). In such a model, the motion of individual particles is obtained by solving Newton's second law of motion and flow of continuum fluid by the local averaged Navier-Stokes equations. In this work, the cohesion among particles is caused by van der Waals interactions. The Hamaker constants are used to distinguish the cohesivity among particles so that finite values are assigned to cohesive particles and zero values to cohesionless particles. It is shown that the presence of cohesionless particles in an assembly of cohesive particles can improve their flowability and that sustainable fluidization can be achieved if the amount of cohesionless particles is sufficient.*

## 1. Introduction

It has long been recognised that when fluidized by gas, particles show four distinct types of behaviour, i.e., cohesive, aeratable, sand-like and spoutable [1]. These effects are believed to be due to the variation in the relative importance of interparticle cohesive forces, such as van der Waals, capillary and electrostatic forces, compared with the fluid drag force exerted on particles by a fluidizing gas. However, such effects are difficult to quantify both analytically and experimentally due to difficulties in describing multibody interactions and in measuring interparticle forces in such a dynamic environment. With the recent development in numerical methods and computer technology, the effects of interparticle cohesive forces on gas fluidization can be evaluated by means of computer simulations.

Together with appropriate boundary and initial conditions, the solutions to Newton's second law of motion for discrete particles and the Navier-Stokes equations for continuum fluid will theoretically deter-

mine the solids and fluid mechanics in a gas-fluidized bed. In practice, however, there are usually a very large number of particles in such a bed. Consequently, this requires a very large number of governing equations to be solved for the motion of each particle, and the resolution of the fluid field has to be fine enough to resolve the flow of fluid through the gaps among closely spaced particles. The task is almost prohibitive with the current computing capacity. As a result, depending on the time and length scales of interest, simplifications have to be made when this theoretical approach is followed. This is reflected in the three models applied to the modelling of particle-fluid flow systems, i.e. Two-Fluid Model (TFM), Direct Numerical Simulation (DNS) and Combined Continuum and Discrete Model (CCDM).

In TFM, both solid and gas phases are treated as interpenetrating continuum media in a computational cell which is much larger than the individual particles but still small compared to the size of the process equipment, so that the number of governing equations is reduced significantly [2]. Two sets of local-averaged Navier-Stokes equations can be derived for both solid and fluid phases, which are then solved numerically. Since the first numerical simulation showing realistic bubbling in a gas-fluidized bed by Pritchett et al. [3], TFM has dominated the modelling

\* Leeds, West Yorkshire LS2 9JT, United Kingdom

<sup>†</sup> Accepted: July 18, 2003

of gas fluidization for decades, as summarized by Gidaspow [4]. However, successful applications of TFM depend on the establishment of constitutive laws governing the inter-phase transfer of momentum and energy for a given system, which cannot be derived from the continuum framework employed in TFM.

In DNS, the fluid field is resolved at a scale comparable with particle spacings while particles are treated as discrete moving boundaries [5]. DNS has great potential to produce detailed results of the hydrodynamic interactions between particles and fluid in a system [5, 6]. However, a major weakness of this model is its capacity in handling particle-particle interactions. In the earlier development of DNS [5], interactions among particles were not modelled at all: if the gap between two approaching particles was less than a preset small value, the simulation had to stop. In a recent development [7, 8], an arbitrary repulsive body force was introduced into the momentum equation to prevent possible collisions between particles. Therefore, DNS has mainly been applied to particle-liquid flow systems where either liquid is sufficiently viscous or the density difference between liquid and particles is small, so that the hydrodynamic interactions are dominant and particle-particle interactions are non-violent if they occur. This limits its applicability to gas fluidization where interactions among particles and hence interparticle forces are significant.

In CCDM, the motion of individual particles is determined by solving Newton's second law of motion, while the flow of continuum fluid is determined in the same way as TFM. As a result, two phases are modelled at two different length scales: with the solid phase at an individual particle level and the fluid phase at a computational cell level. Therefore, correct coupling between these two scales is important, and can be achieved by the principle of Newton's third law of motion as suggested by Xu and Yu [9, 10]. The major advantage of this model is its ability in handling detailed particle-particle and particle-wall interactions based on the Distinct Element Method (DEM) [11]. CCDM has been successfully applied to various particle-fluid flow systems [12-18]. Among those works, Horio and his co-workers [12] studied the effects of capillary forces on gas fluidization for a type D powder [1] whilst Rhodes and his co-workers [18] demonstrated the influence of an arbitrary attraction force, which is scalable to particle weight, on the fluidization of type B and D powders. Recently, Xu et al. [19, 20] studied the fluidization behaviour of a type A powder with van der Waals

interactions. In this work, the gas fluidization of a mixture of 45,000 cohesive and cohesionless particles ( $D=100\ \mu\text{m}$  and  $\rho=1,440\ \text{kgm}^{-3}$ ) is investigated. The aim of this study is to exploit possible ways of improving the flowability of cohesive powders in a gas-fluidized bed by adding cohesionless particles.

## 2. Combined continuum and discrete model

### 2.1. Discrete model

The translational and rotational motions of particle  $i$  at any time  $t$  in a bed are determined by Newton's second law of motion which can be written as

$$m_i \frac{d\mathbf{v}_i}{dt} = \mathbf{f}_{pf,i} + m_i \mathbf{g} + \sum_{j=1}^{k_i} \mathbf{f}_{pp,ij} \quad (1)$$

and

$$I_i \frac{d\boldsymbol{\omega}_i}{dt} = \sum_{j=1}^{k_i} \mathbf{T}_{pp,ij} \quad (2)$$

where  $m_i$ ,  $I_i$ ,  $\mathbf{v}_i$  and  $\boldsymbol{\omega}_i$  are, respectively, the mass, moment of inertia, translational and rotational velocities of particle  $i$ . The forces involved are: the particle-fluid interaction force,  $\mathbf{f}_{pf,i}$ , gravitational force,  $m_i \mathbf{g}$ , and interparticle forces,  $\mathbf{f}_{pp,ij}$ , between particles  $i$  and  $j$ .  $\mathbf{T}_{pp,ij}$  represents the interparticle torques. For multiple interactions, the interparticle forces and torques are summed for  $k_i$  particles interacting with particle  $i$ . Here, interparticle forces and torques also include possible contributions from particle-wall interactions.

#### 2.1.1. Interparticle forces

The interparticle forces result from particle-particle interactions. Generally speaking, these interactions include the forces due to direct or non-direct contacts between particles. In this work, the direct contact forces include the contact force and the viscous contact damping force, which are calculated based on the linear model given by Cundall and Strack [11]:

$$\mathbf{f}_{c,ij} = -\kappa_i \boldsymbol{\delta}_{ij} \quad (3)$$

and

$$\mathbf{f}_{d,ij} = -\eta_i \mathbf{v}_{ij} \quad (4)$$

where  $\kappa_i$  and  $\eta_i$  are, respectively, the spring constant and viscous contact damping coefficient of particle  $i$ ;  $\boldsymbol{\delta}_{ij}$  is the displacement vector between particles  $i$  and  $j$ , and  $\mathbf{v}_{ij}$  is the velocity vector of particle  $i$  relative to particle  $j$  at the point of contact, defined as  $\mathbf{v}_{ij} = \mathbf{v}_i - \mathbf{v}_j + (\boldsymbol{\omega}_i \times \mathbf{R}_i - \boldsymbol{\omega}_j \times \mathbf{R}_j)$ .  $\mathbf{R}_i$  is a vector running from the particle centre to the contact point with its magnitude equal to the radius of particle  $i$ ,  $R_i$ .

The increment of the displacement,  $\Delta\delta_{ij}$ , can be determined from the motion history of particles  $i$  and  $j$ , given by

$$\Delta\delta_{ij} = \mathbf{v}_{ij} \Delta t_{c,ij} \quad (5)$$

where  $\Delta t_{c,ij}$  represents the actual contact time between two colliding particles that can be determined based on the collision dynamics model developed by Xu and Yu [9]:

$$\Delta t_{c,ij} = \frac{-(\mathbf{r}_{ij} \cdot \mathbf{v}_r) + \sqrt{(\mathbf{r}_{ij} \cdot \mathbf{v}_r)^2 + |\mathbf{v}_r|^2 (R_{ij}^2 - |\mathbf{r}_{ij}|^2)}}{|\mathbf{v}_r|^2} \quad (6)$$

where  $\mathbf{r}_{ij} = \mathbf{r}_j - \mathbf{r}_i$ ,  $\mathbf{v}_r = \mathbf{v}_i - \mathbf{v}_j$ ,  $R_{ij} = R_i + R_j$ , and  $\mathbf{r}$  is the position vector of a particle at its mass centre.

Equations (3) and (4) are applicable to both normal and tangential directions. However, if  $|\mathbf{f}_{ct,ij}| > \gamma_{s,ij} |\mathbf{f}_{cn,ij}|$ , then sliding occurs, and  $|\mathbf{f}_{ct,ij}| = \gamma_{s,ij} |\mathbf{f}_{cn,ij}|$ .  $\gamma_{s,ij}$  is the sliding friction coefficient between particles  $i$  and  $j$ . The subscripts  $n$  and  $t$  represent, respectively, the normal and tangential components.

The non-direct contact forces that affect the gas fluidization comprise interparticle cohesive forces such as van der Waals, capillary and electrostatic forces. There is a general agreement in the literature that the interparticle cohesive forces encountered in the gas fluidization of fine powders are mainly attributed to van der Waals attractions [21, 22]. According to Israelachvili [23], the van der Waals force between two closely spaced spheres  $i$  and  $j$  is given by

$$\mathbf{f}_{v,ij} = \frac{H_{ij} d_{ij}}{6z^2} \frac{\mathbf{R}_i}{R_i} \quad (7)$$

where  $H_{ij}$  is the so-called Hamaker constant between two particles  $i$  and  $j$ ,  $z$  is the separation distance between two interacting surfaces, and  $d_{ij}$  is the radius of curvature at the point of contact which is equal to  $(R_i \times R_j) / (R_i + R_j)$  for particle-particle interactions and  $R_i$  for particle-wall interactions.

In practice, the estimation of the van der Waals force acting on real particles is complicated by factors such as the surface geometry of contacting particles, local deformation of contact areas, hardness of particle materials, and gas adsorption onto particle surfaces. These factors can change the magnitude of the van der Waals force significantly and are difficult to quantify. In this work,  $H_{ij} = \max(H_i, H_j)$ , so that there is still an attraction force if a cohesive particle  $i$  ( $H_i$ ) approaches a cohesionless particle  $j$  ( $H_j = 0$ ). To avoid the singularity in applying equation (7), a minimum separation distance,  $z_{min} = 1.0 \times 10^{-9}$  m [22], is used.

### 2.1.2. Interparticle torques

The tangential components of the forces due to the contact between particles  $i$  and  $j$  will generate a torque at the contact point, causing particle  $i$  to rotate. This interparticle torque can be calculated by

$$\mathbf{T}_{c,ij} = \mathbf{R}_i \times (\mathbf{f}_{ct,ij} + \mathbf{f}_{dt,ij}) \quad (8)$$

Moreover, the relative rotation among contacting particles will produce a rolling friction torque [24]. The effect of this rolling friction on the angle of repose of a sandpile has been demonstrated [25, 26] where a constant rolling friction coefficient was chosen. In this work, based on a simplified contact mechanics [19], the rolling friction torque is given by

$$|\mathbf{T}_{r,ij}| = \gamma_{r,ij} |\mathbf{f}_{cn,ij}| \quad (9)$$

where  $\gamma_{r,ij}$  is the dynamic rolling friction coefficient, defined as  $\sqrt{R_i^2 - (R_i - 0.5\delta_{ij})^2}$  for particle-particle contacts and  $\sqrt{R_i^2 - (R_i - \delta_{ij})^2}$  for particle-wall contacts, which are valid as  $\delta_{ij} < 2R_i$ . This interparticle torque is dissipative in nature, i.e.  $\mathbf{T}_{r,ij} = 0$  if  $\boldsymbol{\omega}_i = 0$ .

### 2.1.3. Fluid drag force

For gas fluidization, the particle-fluid interaction force is mainly attributed to the fluid drag, and the buoyancy force acting on a particle can be ignored as the density of particles is much larger than that of gas. The fluid drag force acting on individual particles depends not only on the relative velocity between particles and interstitial fluid, but also on the presence of other particles surrounding them. It is extremely difficult to determine this force analytically. On the other hand, empirical correlations have been established for the evaluation of this force in both fixed and fluidized beds over the full practical range of particle Reynolds numbers [27, 28]. According to Di Felice [28], the fluid drag force acting on a single particle in a fluid stream with the presence of other particles can be expressed as [10]

$$\mathbf{f}_{pf,i} = \mathbf{f}_{pf0,i} \varepsilon_i^{-(\chi_i+1)} \quad (10)$$

where  $\varepsilon_i$  is the porosity around particle  $i$ , taken as the porosity in a computational cell in which particle  $i$  is located. The fluid drag force acting on particle  $i$  in the absence of other particles,  $\mathbf{f}_{pf0,i}$ , and the equation coefficient,  $\chi_i$ , are respectively given by

$$\mathbf{f}_{pf0,i} = 0.5 c_{d0,i} \rho_f \pi R_i^2 \varepsilon_i^2 |\mathbf{u}_i - \mathbf{v}_i| (\mathbf{u}_i - \mathbf{v}_i) \quad (11)$$

and

$$\chi_i = 3.7 - 0.65 \exp \left[ -\frac{(1.5 - \log_{10} Re_{p,i})^2}{2} \right] \quad (12)$$

where  $\rho_f$  is the fluid density.  $c_{d0,i}$ , the fluid drag coefficient for an isolated particle, and the particle Reynolds number,  $Re_{p,i}$ , are given by

$$c_{d0,i} = \left( 0.63 + \frac{4.8}{Re_{p,i}^{0.5}} \right)^2 \quad (13)$$

and

$$Re_{p,i} = \frac{2\rho_f R_i \varepsilon_i |\mathbf{u}_i - \mathbf{v}_i|}{\mu_f} \quad (14)$$

where  $\mu_f$  is the fluid viscosity.

## 2.2. Continuum model

The continuum fluid field is calculated from the local-averaged continuity and the Navier-Stokes equations based on the mean variables over a computational cell. Under isothermal and incompressible conditions, these equations are given by

$$\frac{\partial e}{\partial t} + \nabla \cdot (\varepsilon \mathbf{u}) = 0 \quad (15)$$

and

$$\frac{\partial (\rho_f \varepsilon \mathbf{u})}{\partial t} + \nabla \cdot (\rho_f \varepsilon \mathbf{u} \mathbf{u}) = -\nabla p - \mathbf{F} + \nabla \cdot (\mathbb{T}) + \rho_f \varepsilon \mathbf{g} \quad (16)$$

where  $\mathbf{u}$ ,  $p$  and  $\mathbf{F}$  are, respectively, the fluid velocity, pressure and volumetric particle-fluid interaction force;  $\mathbb{T}$  and  $\varepsilon$  are the fluid viscous stress tensor and porosity in a computational cell which are given by

$$\mathbb{T} = \left[ \left( -\frac{2}{3} \mu_f \right) \nabla \cdot \mathbf{u} \right] \delta_K + \mu_f \left[ (\nabla \mathbf{u}) + (\nabla \mathbf{u})^{-1} \right] \quad (17)$$

and

$$\varepsilon = 1 - \frac{\sum_{i=1}^{k_c} V_i}{DV} \quad (18)$$

where  $\delta_K$  is the Kronecker delta.  $\Delta V$  and  $V_i$  are, respectively, the volume of a computational cell and the volume of particle  $i$  inside this cell.  $k_c$  is the number of particles in the cell. In the present work,

$\Delta V = 2\Delta x \Delta y R_i$  and  $\Delta x$  and  $\Delta y$  are, respectively, the lengths of a computational cell in  $x$  and  $y$  directions.

## 2.3. Coupling between continuum and discrete models

Mathematically, the coupling between continuum and discrete models is reflected by the calculation of the volumetric particle-fluid interaction force. This is realised by Newton's third law of motion so that the fluid drag force acting on individual particles will react on the fluid phase from the particles. As the fluid drag force is known for each particle, the volumetric particle-fluid interaction force in a computational cell can be determined by

$$\mathbf{F} = \frac{\sum_{i=1}^{k_c} \mathbf{f}_{pf,i}}{DV} \quad (19)$$

## 2.4. Solution schemes

The explicit time integration method is used to solve the translational and rotational motions of a system of particles in the discrete model. The interparticle force models are also applicable to interactions between a particle and a wall, with the corresponding wall properties used. However, the wall is assumed to be so rigid that no displacement and movement result from this interaction. The SIMPLE method [29] is used to solve the equations for the fluid phase in the continuum model. The second-order central difference scheme is used for the pressure gradient and divergence terms. A third-order upwind and bounded scheme [30] is used for the convection term, and a second-order Crank-Nicolson scheme is used for the time derivative. The no-slip boundary condition applies to the bed walls, and a uniform gas velocity is specified at the bottom of the bed. The zero normal gradient condition applies along the boundaries for the other parameters and at the top exit for the gas velocity.

**Table 1** lists the parameters used in the present

**Table 1** Parameters used for the present simulation\*

Solid phase			Gas phase		
Particle shape	spherical		Type of gas	air	
Number of particles	45,000		Viscosity, $\mu_f$	$1.8 \times 10^{-5}$	$\text{kgm}^{-1}\text{s}^{-1}$
Particle diameter	$1.0 \times 10^{-4}$	$m$	Density, $\rho_f$	1.205	$\text{kgm}^{-3}$
Particle density, $\rho_p$	1,440	$\text{kgm}^{-3}$	Bed width	$2.5 \times 10^{-2}$	$m$
Spring constant, $\kappa$	50	$\text{Nm}^{-1}$	Bed height	$6.0 \times 10^{-2}$	$m$
Sliding friction coefficient, $\gamma_s$	0.3		Bed thickness	$1.0 \times 10^{-4}$	$m$
Contact damping coefficient, $\eta$	$1.65 \times 10^{-5}$	$\text{kg s}^{-1}$	Cell width, $\Delta x$	$1.0 \times 10^{-3}$	$m$
Hamaker constant, $H$	$6.00 \times 10^{-19}, 0$	$\text{Nm}$	Cell height, $\Delta y$	$1.0 \times 10^{-3}$	$m$

\*. The wall properties such as  $\kappa$ ,  $\gamma$  and  $\eta$  are the same as those for particles.



simulations. The method suggested by Xu and Yu [9] is used to determine the computational time step and viscous contact damping coefficient, which are determined to be  $1.25 \times 10^{-6}$  s and  $1.65 \times 10^{-5}$  kgs $^{-1}$ , respectively. To generate an initial particle configuration in the calculation domain, the bed is divided into a set of square cells with its length equal to the diameter of particles. Along the height of the bed, each adjacent cell is offset by a distance of one particle radius. Then 45,000 particles are randomly positioned in these cells and allowed to settle to form a packing under gravity. The packed bed thus generated is then used as a base condition for the later simulations of fluidization where van der Waals forces are introduced in particle-particle and particle-wall interactions.

### 3. Results and Discussion

As demonstrated in the previous work [19, 20], the behaviour of fine particles in a gas-fluidized bed depends strongly on the ratio of the magnitude of interparticle cohesive forces to the particle weight. When this ratio is less than 30, smooth fluidization is achieved with bubbles of relatively small size rising through the bed. When the ratio is in the range of 40 to 100, although the bed is still fluidizable, the fluidization quality deteriorates significantly and severe channelling occurs, giving the so-called quasi-fluidization. When the ratio is greater than 250, fluidization is impossible by normal means to such an extent that the gas simply flows through gaps between solid blocks made from primary cohesive particles, and the bed is de-fluidized. The predicted trends agree with the experimental observations where the bed changes from smooth, quasi-, to de-fluidization state when the size of particles is decreased [21].

**Figure 1** shows the gas-solid flow patterns with

an initial two layers of 5,000 cohesionless particles placed alternatively in the bed of 40,000 cohesive particles. When the gas is introduced uniformly from the bottom of the bed, the particle assembly is lifted and detached from the bottom. During its upwards movement, the solid segments across the bed start to bend, which causes fractures at the interfaces along the layers of cohesionless particles. These fractures promote preferential gas flow and lead to the final breakage of solid segments into solid blocks. After the release of a large gas vortex, these solid blocks fall back to the bottom of the bed under gravity. A macroscopically stable de-fluidized bed is quickly established where gas simply flows through the gaps between the solid blocks. However, as highlighted in **Figure 2**, localised vigorous solids motion can still exist in such a bed: cohesionless particles trapped in the gaps between solid blocks can form a well-defined solid vortex. This localised solids motion is caused by the free flow of cohesionless particles under gravity and the strong underneath gas flow through the gap between the solid block and the side wall. This phenomenon is similar to the so-called raceway phenomenon in blast furnace iron making [16]. It is also noticed that there are layers of cohesive particles stuck onto the side wall, giving a very rough surface to the gas and solids flows.

From the above results, it is apparent that to facilitate the fluidization of a bed of cohesive particles, more cohesionless particles are needed. **Figure 3** shows the gas-solid flow patterns with an initial five layers of 12,500 cohesionless particles placed alternatively in the bed of 32,500 cohesive particles. Similar to the above two-layer case (see **Figure 1**), the preferential gas flow breaks the solid segments across the bed layer by layer along with the upward movement of the particle assembly. However, a segregated bed is established after initial disruption to the bed.

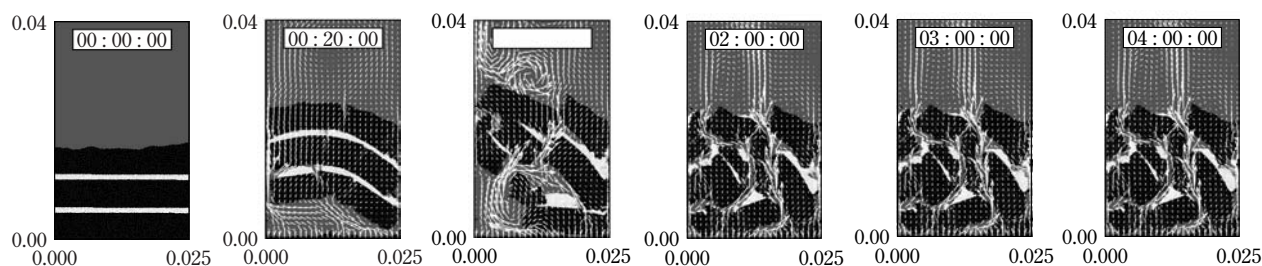


**Fig. 1** The gas-solid flow patterns with an initial two layers of 5,000 cohesionless (white) particles placed alternatively in the bed of 40,000 cohesive (black) particles at  $u/u_{mf}=4.8$ . The ratio of the maximum cohesive force at  $z_{min}$  to particle weight is 338.



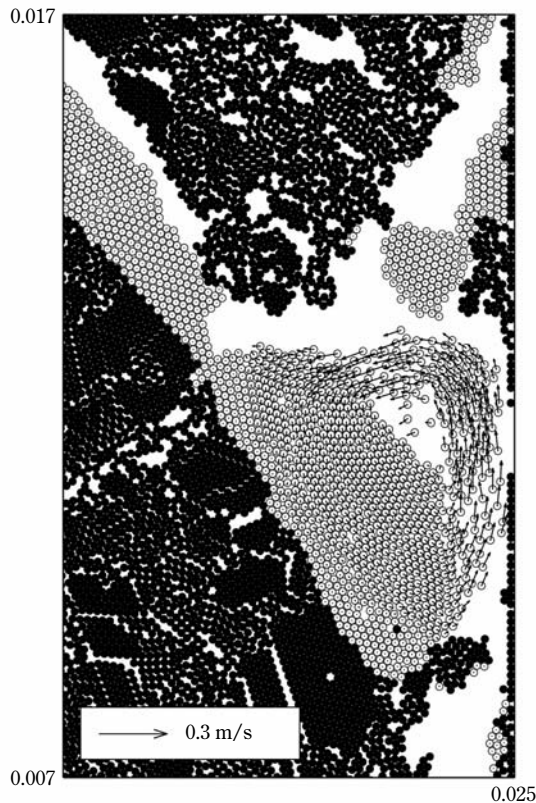


**Fig. 2** The localised solids motion in a macroscopically de-fluidized bed at  $t=4s$  and  $u/u_{mf}=4.8$ , showing the circulation of cohesionless (white) particles in the gap between blocks of cohesive (black) particles and side wall. The ratio of the maximum cohesive force at  $z_{min}$  to particle weight is 338.

The cohesionless particles are mainly found at the upper bed where they are fluidized, while the solid blocks are at the lower bed where they are de-fluidized. In the middle of the bed, there are some cohesionless particles trapped in the gaps among solid

blocks, they may be transported further upwards by the gas flow or downwards under gravity through these gaps. The simulated solid segregation patterns are comparable to the segregation experiments when particles of different sizes are fluidized [31]. However, after such an initial solid segregation, solid blocks at the upper bed are further migrated towards the side walls, leaving a V-shape zone at the centre for cohesionless particles where they are fluidized freely.

**Figure 4** shows the gas fluidization of a reversed particle configuration as shown in **Figure 1**. Two layers of 5,000 cohesive particles were placed alternatively in the bed of 40,000 cohesionless particles. A stable fluidized bed is established after these two layers of cohesive particles are broken into straw-like solid blocks by the strong gas flow. These straw-like solid blocks further reduce their size by shearing action from fluidizing cohesionless particles. This results in a wide size and shape distribution of solid blocks made from primary spherical cohesive particles. **Figure 5** shows the details of such a size reduction mechanism where the ‘tail’ of a solid block is about to be torn apart by the shearing action from fluidizing cohesionless particles. From **Figure 4**, it is noticed that the solid blocks with a high aspect ratio tend to settle to the bottom of the bed, while the solid blocks with a low aspect ratio are fluidized smoothly with the cohesionless particles. It is also found that solid blocks with a high aspect ratio can only be dragged into the upper bed when they are tilted on the bottom of the bed. However, they do not rise in the wake of the bubbles as for primary spherical particles, but in a series of jerks as successive bubbles pass through the bed. These results are in good agreement with experimental observations by Bilbao et al. [32] where straw and sand particles were fluidized.

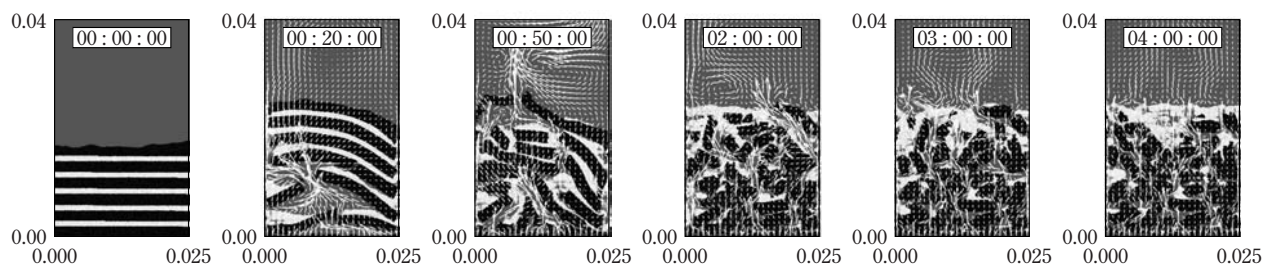


**Fig. 3** The gas-solid flow patterns with an initial five layers of 12,500 cohesionless (white) particles placed alternatively in the bed of 32,500 cohesive (black) particles at  $u/u_{mf}=4.8$ . The ratio of the maximum cohesive force at  $z_{min}$  to particle weight is 338.

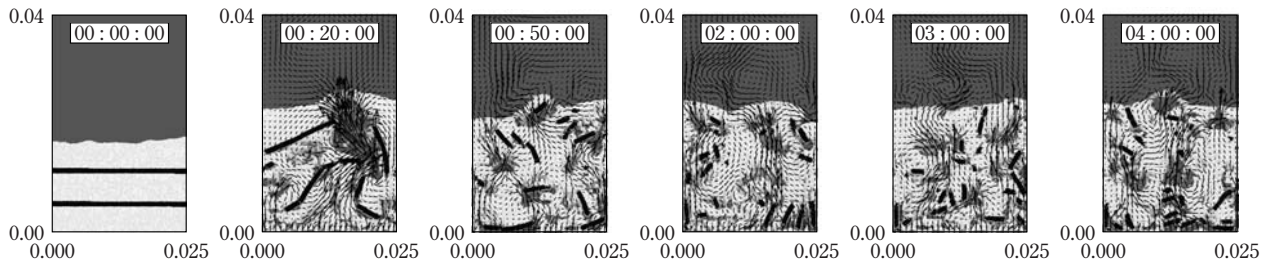


**Fig. 4** The gas-solid flow patterns with an initial two layers of 5,000 cohesive (black) particles placed alternatively in the bed of 40,000 cohesionless (white) particles at  $u/u_{mf}=4.8$ . The ratio of the maximum cohesive force at  $z_{min}$  to particle weight is 338.

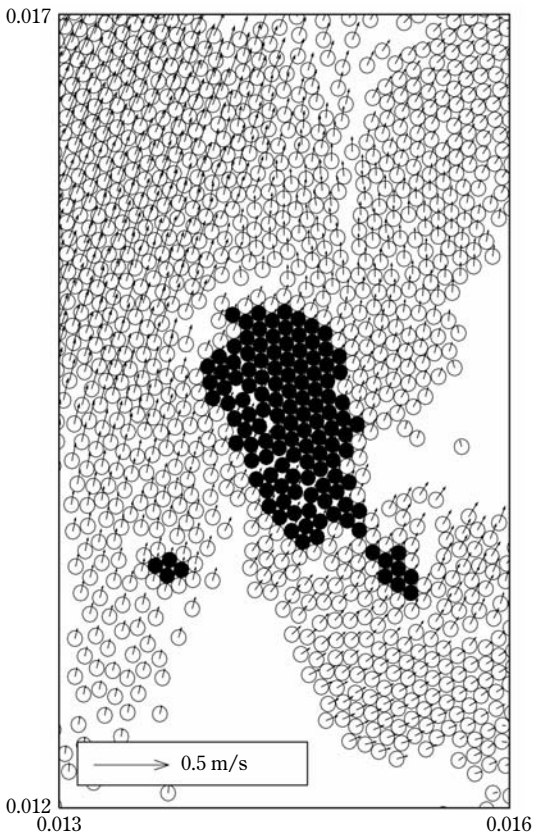


**Fig. 5** The details of a size reduction mechanism where the 'tail' of a solid block made from primary cohesive (black) particles is about to be torn apart by the fluidizing cohesionless (white) particles at  $t=4s$  and  $u/u_{mf}=4.8$ . The ratio of the maximum cohesive force at  $z_{min}$  to particle weight is 338.

#### 4. Conclusions

The work on cohesive particle flows has been extended to study the possible ways of improving the flowability of cohesive particles in a gas-fluidized bed.

It is shown that by adding a sufficient amount of cohesionless particles, sustainable fluidization can be achieved for cohesive particles which are difficult to fluidize by normal means. Further study is needed to find an optimised procedure for improving the flowability of cohesive particles.

#### Acknowledgments

The financial support from BNFL during the course of this research is greatly acknowledged. The code used in this work was originated by the author at the University of New South Wales.

#### Nomenclature

$c_{d0}$	coefficient of fluid drag for an isolated particle	<i>dimensionless</i>
$d$	radius of curvature at point of contact	<i>m</i>
$D$	diameter of a particle	<i>m</i>
$f$	force acting on a particle	<i>N</i>
$F$	volumetric particle-fluid interaction force	$Nm^{-3}$
$f_{pf0}$	fluid drag force acting on an isolated particle	<i>N</i>
$g$	gravitational acceleration	$ms^{-2}$
$H$	Hamaker constant	<i>Nm</i>
$I$	moment of inertia of a particle, defined as $I=2/5mR^2$	$kgm^2$
$k_c$	number of particles in a computational cell	<i>dimensionless</i>
$k_i$	number of particles interacting with particle $i$	<i>dimensionless</i>
$m$	mass of a particle	<i>kg</i>
$p$	pressure	<i>Pa</i>
$r$	position vector of a particle	<i>m</i>
$R$	radius of a particle	<i>m</i>
$Re$	Reynolds number	<i>dimensionless</i>
$t$	time	<i>s</i>
$T$	torque acting on a particle	<i>Nm</i>

$u$	fluid velocity	$ms^{-1}$
$v$	translational velocity of a particle	$ms^{-1}$
$V$	volume of a particle	$m^3$
$z$	separation distance between two interacting surfaces	$m$

### Greek letters

$\rho$	density	$kgm^{-3}$
$\delta$	displacement between two contacting particles	$m$
$\chi$	equation coefficient defined in Eq. (12)	<i>dimensionless</i>
$\mathbb{T}$	fluid viscous stress tensor	$kgm^{-1}s^{-2}$
$\varepsilon$	porosity	<i>dimensionless</i>
$\omega$	rotational velocity of a particle	$s^{-1}$
$\kappa$	spring constant of a particle	$Nm^{-1}$
$\mu$	viscosity	$kgm^{-1}s^{-1}$
$\eta$	viscous contact damping coefficient of a particle	$kgs^{-1}$
$\Delta t_c$	actual contact time between two colliding particles	$s$
$\delta_K$	Kronecker delta	<i>dimensionless</i>
$\Delta V$	volume of a computational cell	$m^3$
$\Delta x$	computational cell length in x direction	$m$
$\Delta y$	computational cell length in y direction	$m$
$\Delta \delta$	increment of displacement between two contacting particles	$m$
$\gamma_r$	rolling friction coefficient	$m$
$\gamma_s$	sliding friction coefficient	<i>dimensionless</i>

### Subscripts

$c$	contact
$d$	damping
$f$	fluid phase
$i$	particle $i$
$ij$	between particles $i$ and $j$
$j$	particle $j$
$mf$	minimum fluidization
$n$	normal component
$p$	particle phase
$pf$	particle-fluid
$pp$	particle-particle
$r$	rolling
$s$	sliding
$t$	tangential component
$v$	van der Waals

### References

- [1]. Geldart, D. (1973). Types of gas fluidization. *Powder Technology*, 7, 285-292.
- [2]. Anderson, T.B., & Jackson, R. (1967). A fluid mechan-

cal description of fluidized beds. Equations of motion. *Industrial & Engineering Chemistry Fundamentals*, 6, 527-539.

- [3]. Pritchett, J.W., Blake, T.R., & Garg, S.K. (1978). A numerical model of gas fluidized beds. *A.I.Ch.E. Symposium Series*, 176, 134-148.
- [4]. Gidaspow, D. (1994). *Multiphase flow and fluidization, continuum and kinetic theory descriptions*. San Diego: Academic Press.
- [5]. Hu, H.H. (1996). Direct simulation of flows of solid-liquid mixtures. *International Journal of Multiphase Flow*, 22, 335-352.
- [6]. Huang, P.Y., Hu, H.H., & Joseph, D.D. (1998). Direct simulation of the sedimentation of elliptic particles in Oldroyd-B fluids. *Journal of Fluid Mechanics*, 362, 297-325.
- [7]. Glowinski, R., Pan, T.-W., Hesla, T.I., Joseph, D.D., & Periaux, J. (2000). A distributed Lagrange multiplier/fictitious domain method for the simulation of flow around moving rigid bodies: application to particulate flow. *Computer Methods in Applied Mechanics and Engineering*, 184, 241-267.
- [8]. Singh, P., Joseph, D.D., Hesla, T.I., Glowinski, R., & Pan, T.-W. (2000). A distributed Lagrange multiplier/fictitious domain method for viscoelastic particulate flows. *Journal of Non-Newtonian Fluid Mechanics*, 91, 165-188.
- [9]. Xu, B.H., & Yu, A.B. (1997). Numerical simulation of the gas-solid flow in a fluidized bed by combining discrete particle method with computational fluid dynamics. *Chemical Engineering Science*, 52, 2785-2809.
- [10]. Xu, B.H., & Yu, A.B. (1998). Authors' reply to the comments of B.P.B. Hoomans, J.A.M. Kuipers, W.J. Briels, and W.P.M. van Swaaij. *Chemical Engineering Science*, 53, 2646-2647.
- [11]. Cundall, P.A., & Strack, O.D.L. (1979). A discrete numerical model for granular assemblies. *Géotechnique*, 29, 47-65.
- [12]. Mikami, T., Kamiya, H., & Horio, M. (1998). Numerical simulation of cohesive powder behavior in a fluidized bed. *Chemical Engineering Science*, 53, 1927-1940.
- [13]. Li, Y., Zhang, J., & Fan, L.-S. (1999). Numerical simulation of gas-liquid-solid fluidization systems using a combined CFD-VOF-DPM method: bubble wake behavior. *Chemical Engineering Science*, 54, 5101-5107.
- [14]. Kawaguchi, T., Sakamoto, M., Tanaka, T., & Tsuji, Y. (2000). Quasi-three-dimensional numerical simulation of spouted beds in cylinder. *Powder Technology*, 109, 3-12.
- [15]. Hoomans, B.P.B., Kuipers, J.A.M., & van Swaaij, W.P.M. (2000). Granular dynamics simulation of segregation phenomena in bubbling gas-fluidised beds. *Powder Technology*, 109, 41-48.
- [16]. Xu, B.H., Yu, A.B., Chew, S.J., & Zulli, P. (2000). Numerical simulation of the gas-solid flow in a bed with lateral gas blasting. *Powder Technology*, 109, 13-26.
- [17]. Yuu, S., Umekage, T., & Johno, Y. (2000). Numerical simulation of air and particle motions in bubbling flu-



- idized bed of small particles. *Powder Technology*, 110, 158-168.
- [18]. Rhodes, M.J., Wang, X.S., Nguyen, M., Stewart, P., & Liffman, K. (2001). Use of discrete element method simulation in studying fluidization characteristics: influence of interparticle force. *Chemical Engineering Science*, 56, 69-76.
- [19]. Xu, B.H., Yu, A.B., & Zulli, P. (2001). The effect of interparticle forces on powder fluidization behaviour. In Y. Kishino, *Powders and Grains 2001*, (p. 577). Lisse: A.A. Balkema Publishers.
- [20]. Yu, A.B. and Xu, B.H. (2003). Particle-scale modelling of gas-solid flow in fluidization. *Journal of Chemical Technology and Biotechnology*, 78, 111-121.
- [21]. Baerns, M. (1966). Effect of interparticle adhesive forces on fluidization of fine particles. *Industrial & Engineering Chemistry Fundamentals*, 5, 508-516.
- [22]. Visser, J. (1989). An invited review. van der Waals and other cohesive forces affecting powder fluidization. *Powder Technology*, 58, 1-10.
- [23]. Israelachvili, J.N. (1991). *Intermolecular and surface forces* (2nd ed.). London: Academic Press.
- [24]. Tabor, D. (1955). The mechanism of rolling friction. II. The elastic range. *Proceedings of the Royal Society of London, Series A. Mathematical and Physical Sciences*, 229, 198-220.
- [25]. Zhou, Y.C., Wright, B.D., Yang, R.Y., Xu, B.H., & Yu, A.B. (1999). Rolling friction in the dynamic simulation of sandpile formation. *Physica A*, 269, 536-553.
- [26]. Zhou, Y.C., Xu, B.H., Yu, A.B., & Zulli, P. (2001). Numerical investigation of the angle of repose of monosized spheres. *Physical Review E*, 64, 021301, 1-8.
- [27]. Ergun, S. (1952). Fluid flow through packed columns. *Chemical Engineering Progress*, 48, 89-94.
- [28]. Di Felice, R. (1994). The voidage function for fluid-particle interaction systems. *International Journal of Multiphase Flow*, 20, 153-159.
- [29]. Patankar, S.V. (1980). *Numerical heat transfer and fluid flow*. New York: Hemisphere.
- [30]. Gaskell, P.H., & Lau, A.K.C. (1988). Curvature-compensated convective transport: SMART, a new boundedness-preserving transport algorithm. *International Journal for Numerical Methods in Fluids*, 8, 617-641.
- [31]. Nienow, A.W. and Chiba, T. (1985). *Fluidization of dissimilar materials*. in *Fluidization* (Davidson, J.F., Clift, R. and Harrison, D., eds.), 2nd, ed., 357-382, Academic Press, London.
- [32]. Bilbao, R., Lezaun, J., Menendez, M. & Abanades, J. C. (1988). Model of mixing-segregation for straw/sand mixtures in fluidized beds. *Powder Technology*, 56, 149-155.

### Author's short biography



#### B.H. Xu

Dr B.H. Xu obtained his B.Eng in 1985 and M.Eng in 1988 from Xi'an Jiaotong University, Xi'an, China. After lecturing at Qingdao Institute of Architecture and Engineering, Qingdao, China for five years, he went to Australia to further his career in 1993. He completed his PhD in 1997 from the University of New South Wales, and then continued his association with the university as a research associate. He joined the University of Leeds as a lecturer in Particle Science and Engineering in 2002. His major research interest is modelling and simulation of particulate flow systems.

# Modelling of Grinding in an Air Classifier Mill Based on a Fundamental Material Function<sup>†</sup>

**Lutz Vogel**

*Degussa AG, Process Technology and Engineering\**

**Wolfgang Peukert**

*Institute of Particle Technology,  
University Erlangen-Nuremberg\*\**

## Abstract

*An approach to quantifying the impact grinding performance of different materials is presented. Based on a dimensional analysis and on fracture mechanical considerations, two material parameters,  $f_{Mat.}$  and  $W_{m,min}$ , are derived theoretically.  $f_{Mat.}$  characterises the resistance of particulate material against fracture during impact comminution.  $W_{m,min}$  gives the mass-specific energy which a particle can absorb without fracture. Using this approach, various materials over a wide size range, e.g. different polymers, crystalline substances, glass and limestone, can be characterised quantitatively. The derived material parameters are applied to the systematic modelling of grinding in impact mills. A population balance model is presented and the results of the simulation for an air classifier mill are shown. The developed model permits a clear separation of the influence of material properties, mill-specific features and operating conditions, thus enabling a deeper understanding of the impact grinding process.*

## 1. INTRODUCTION

Every material performs differently in the milling process and exhibits different grinding characteristics. A systematic and quantitative characterisation of the grinding performance of a powder is currently beyond scope because both the stressing of the particles in a mill and the breakage behaviour even under well-defined stressing conditions are not sufficiently understood, and the comparison of materials in a comminution process can therefore only be realised with the help of milling tests. These tests give results which are of value only for the type of mill under consideration. The possibility of transferring these results to other mills is debatable. This situation and the

lack of understanding of the influence of material properties on the comminution process is totally unacceptable. In this paper, an approach which describes the grinding performance of different products independent of the mill properties is introduced.

Furthermore, the modelling of impact grinding processes is addressed. In order to operate a modern and flexible process, it is essential to be able to at least estimate the effect of changes to the operational parameters or products on the process result. Even with a statistically optimised experimental strategy, the required effort in time and cost for this purpose is still considerable. A systematic and physically reliable computer simulation of the process would be a fast and cheap alternative to overcome these problems. Furthermore, a realistic model can help to understand the milling process and the interaction of single process steps. An approach to the simulation of grinding in mills based on a population balance model is presented. A simple model to describe the individual process steps inside the mill (i.e. grinding, classification and transport) was chosen. The main focus was

\* Rodenbacher Chaussee 4, 63457 Hanau, Germany  
Lutz.Vogel@degussa.com

\*\* Cauerstrasse 4, 91058 Erlangen/Germany  
W.Peukert@lfg.uni-erlangen.de

<sup>†</sup> Accepted: June, 2003



on a clear separation between material and operational parameters, respectively, in order to investigate their influence on the comminution result separately.

## 2. MATERIAL CHARACTERISATION

### 2.1 Similarity Considerations

The breakage probability and the breakage function quantify the result of particle fracture concerning the size distribution of the milling product. The breakage probability  $P_B$  describes the fraction of particles which is destroyed in an experiment. The breakage function  $B$  gives the size distribution of the fragments. The breakage of particles of different size, of different material and of different shape at various stressing conditions can be investigated with the help of similarity considerations. The following deduction is based on an approach first presented by Rumpf [1].

Analysing the parameters which have an influence on particle breakage leads to Eq. 1. It contains 13 parameters describing the particle stressing, the particle size and shape and bulk material properties. The single parameters of influence are combined to ten dimensionless groups, thus reducing the number of independent parameters and underlining combined influences. In Eq. 1,  $W_V$  denotes the volumetric, specific stressing energy,  $k$  the number of stressing events and  $v_d$  the velocity of the deformation, which together define the stressing conditions.  $x$  is the initial particle size and  $\psi$  a shape parameter, taking the effect of different particle shapes on fracture formally into account. The bulk material properties are quantified by the following parameters:  $\beta_{\max}$  denotes the crack extension energy per unit of created surface,  $E'$  the storage modulus of the particle material,  $E''$  the corresponding viscous loss modulus,  $H$  the hardness,  $\nu$  the Poisson ratio.  $v_{\text{fract}}$  is the velocity of the crack propagation,  $v_{\text{el}}$  the velocity of the propagation of elastic waves and  $l_i$  the inherent initial crack length or flaw size.

$$P_B, B = f \left\{ k, \frac{W_V \cdot x}{\beta_{\max}}, \frac{E' \cdot l_i}{\beta_{\max}}, \frac{H}{E'}, \frac{E''}{E'}, \frac{l_i}{x}, \frac{v_d}{v_{\text{el}}}, \frac{v_{\text{fract}}}{v_{\text{el}}}, \psi, \nu \right\} \quad (1)$$

Eq. 1 takes a large set of relevant parameters for particle fracture in general into account. For the case of impacting particles and the conditions considered here, it can be simplified. The velocity of propagating cracks is always significantly less than the velocity of elastic waves for brittle materials [2, 3]. The crack extension can be considered as quasi-static here and the ratio  $v_{\text{fract}}/v_{\text{el}}$  will not have an influence on particle breakage. The velocity of the propagation of elastic

waves is about 2400 m/s for brittle polymers such as PMMA and PS. For glass it even reaches values of 5800 m/s [3]. With impact velocities of up to 200 m/s, which is currently the technically realised maximum for hammer mills, the ratio  $v_d/v_{\text{el}}$  is far smaller than unity and the loading can be considered as quasi-static, too. The initial size of the particles under investigation in this work lies in the range of 95  $\mu\text{m}$  to 8 mm. It can be assumed that for these sizes, the initial flaw size of the particles is not yet influenced or limited by the initial particle size [3, 4]. Therefore, the parameter  $l_i/x$  in Eq. 1 will not have any influence on the comminution result for these coarse materials. The simplifications above lead to a reduced form of Eq. 1:

$$P_B, B = f \left\{ k, \frac{W_V \cdot x}{\beta_{\max}}, \frac{E' \cdot l_i}{\beta_{\max}}, \frac{H}{E'}, \frac{E''}{E'}, \Psi, \nu \right\} \quad (2)$$

### 2.2 Fracture Mechanic Model

Weichert [5] introduced the Weibull statistics [6] to the field of comminution. The following modified approach is based on his procedure. The Weibull statistics is based on the principle of the weakest link in a chain. It gives the probability  $P_B$  for the fracture of a chain which consists of  $z$  links of strength  $\sigma_s$  when the load  $\sigma$  is applied.  $m$  is a free parameter of the probability distribution which is not related to a physical property in Weibull's approach.

$$P_B = 1 - \exp \left\{ -z \cdot \left( \frac{\sigma}{\sigma_s} \right)^m \right\} \quad (3)$$

Crack initiation and particle breakage start at the circumference of the contact circle (simplifying Weichert's assumption of beginning breakage on the whole surface) [7, 8]. The highest tensile stresses occur at the circumference of the contact circle. Flaws and initial cracks in this area are subjected to these high stresses and are most likely to initiate particle failure. When a statistical distribution of flaws and micro-cracks is assumed, then the equivalent to the number of chain links needed for the application of Eq. 1 is the circumference or diameter  $a$  of the contact circle. It can be calculated from Hertz' theory according to Eq. 4. In Eq. 4,  $E$  and  $E_T$  denote Young's modulus of the particle and the target, respectively,  $\nu$  and  $\nu_T$  the Poisson ratio of the particle and the target, respectively,  $\rho$  the particle density and  $v$  the impact velocity.

$$a = 0,66 \cdot x \cdot \left[ 1 + \frac{E}{E_T} \cdot \frac{1 - \nu_T^2}{1 - \nu^2} \right]^{\frac{1}{5}} \cdot \left[ \frac{1 - \nu^2}{E} \cdot \rho \cdot v^2 \right]^{\frac{1}{5}} \quad (4)$$

For impacting elastic spheres, the Hertz theory [9]

also allows for the calculation of the pressure distribution within the contact circle (Eq. 5). Gildemeister [7] showed that for impacting spheres, the stress field  $\sigma$  within the sphere is similar for spheres of different diameters and proportional to the maximum pressure  $p_{\max}$  in the contact circle.

$$\sigma \sim p_{\max} = -0,84 \cdot \frac{E}{1-v^2} \cdot \left[ 1 + \frac{E}{E_T} \cdot \frac{1-v_T^2}{1-v^2} \right]^{-\frac{4}{5}} \cdot \left[ \frac{1-v^2}{E} \cdot \rho \cdot v^2 \right]^{\frac{1}{5}} \quad (5)$$

Interpreting the load in Eq. 1 as stress and applying Eq. 5 also to the strength  $\sigma_s$ , then the load term in Eq. 1 can be characterised by the equivalent velocities  $v$  and  $v_s$ :

$$\frac{\sigma}{\sigma_s} = \left( \frac{v^2}{v_s^2} \right)^{\frac{1}{5}} \quad (6)$$

Inserting the above three equations into Eq. 1 leads to Eq. 7. It theoretically describes the breakage probability of elastic spheres. Vervoorn and Austin [10] have shown that the Hertz equations not only describe the impact force well for spherical particles, but also for irregularly shaped ones. Therefore Eq. 4 and Eq. 5 can be used as an approximation for the loading of irregular-shaped particles in a grinding process.

$$P_B = 1 - \exp \left\{ -\text{const.} \cdot x \cdot \left[ 1 + \frac{E}{E_T} \cdot \frac{1-v_T^2}{1-v^2} \right]^{\frac{1}{5}} \cdot \left[ \frac{1-v^2}{E} \cdot \rho \cdot \frac{v_s^2}{2} \right]^{\frac{1}{5}} \cdot \left[ \frac{v^2/2}{v_s^2/2} \right]^{\frac{1+m}{5}} \right\} \quad (7)$$

Analogous to the principle of the weakest link in a chain, Eq. 1 can be applied to the repeated stressing of a particle taking into account the increase of the cumulated probability of particle breakage  $P_B$  due to  $k$  successive impacts. Furthermore, in Eq. 7, the particle breakage begins at very small impact intensities which lead to a very small, but not negligible, value for the breakage probability. In own experiments as well as data published in literature [11-14], a significant threshold value for the impact energy can be observed. Below this threshold value no particle breakage occurs. Therefore the energy threshold  $W_{m,\min}$  is introduced which finally leads to Eq. 8.

$$P_B = 1 - \exp \left\{ -\text{const.} \cdot k \cdot x \cdot \left[ 1 + \frac{E}{E_T} \cdot \frac{1-v_T^2}{1-v^2} \right]^{\frac{1}{5}} \cdot \left[ \frac{1-v^2}{E} \cdot \rho \cdot \frac{v_s^2}{2} \right]^{\frac{1}{5}} \cdot \left[ \frac{v^2/2 - W_{m,\min}}{v_s^2/2} \right]^{\frac{1+m}{5}} \right\} \quad (8)$$

The quantitative application of Eq. 8 is difficult because the relevant material parameters are seldom

known. Furthermore, it is not quite clear which material strength  $\sigma_s$  or equivalent velocity  $v_s$ , respectively, have to be used as most of the classic mechanical strength parameters such as tension or impact strength are strongly dependent on the test procedure. Further work will be carried out on this problem.

### 2.3 Derivation of Relevant Material Parameters

The two different approaches which lead to Eq. 2 and Eq. 8, respectively, can be united to form a single equation describing the breakage probability for particles of different materials. In Eq. 2,  $\beta_{\max}$ ,  $E'$ ,  $E''$ ,  $H$ ,  $l_i$  and  $v$  denote the fracture and deformation mechanical parameters which are appropriate, e.g. for geometrically well-defined problems. In the case of the comminution of particles, their quantitative application is difficult. Therefore, we will introduce two new parameters,  $f_{\text{Mat.}}^*$  and  $W_{v,i}$  here, which are related to  $\beta_{\max}$ ,  $E'$ ,  $E''$ ,  $H$ ,  $l_i$ ,  $v$  and  $\Psi$ , but which can be applied and determined directly by comminution experiments. They can be interpreted as mean particle properties which take the material properties of the particle and irregular particle shape fully into account.  $f_{\text{Mat.}}^*$  characterises the resistance of the particle material against the volume-specific external load energy.  $W_{v,i}$  is a measure for the volume-specific energy which is required to initiate fracture at an existing flaw of size  $l_i$ . Both parameters relate the external load during impact, characterised by the specific impact energy  $W_v$ , to the internal particle strength. Together with a rearrangement of the dimensionless variables this leads to a simplified form of Eq. 2:

$$P_B, B = f \{ f_{\text{Mat.}}^* \cdot (W_v \cdot x, W_{v,i} \cdot l_i) \} \quad \text{with} \quad (9)$$

$$f_{\text{Mat.}}^* \cdot \beta_{\max} = f_1 \left( \frac{E''}{E'}, \frac{H}{E'}, v, \Psi \right) \quad (9a)$$

$$\frac{W_{v,i} \cdot l_i}{E' \cdot l_i} = f_2 \left( \frac{E''}{E'}, \frac{H}{E'}, v, \Psi \right) \quad (9b)$$

Eq. 8 and Eq. 9 originate from different approaches but describe the same phenomenon: particle breakage. They can be united when the main influencing factors and dimensionless groups are compared. As the mass-specific impact energy  $W_{m,\text{kin}}$  and the volume-specific impact energy  $W_v$  are directly proportional to each other, Eq. 8 and 9 can only match if the free, adjustable exponent  $m$  of the Weibull distribution equals 4. Then, both equations show the same combined influence of the product of specific energy and particle size on the breakage probability. There-

fore  $m=4$  will be used in the following leading to:

$$P_B = 1 - \exp \left\{ -\text{const} \cdot k \cdot x \cdot \left[ 1 + \frac{E}{E_T} \cdot \frac{1 - v_T^2}{1 - v^2} \right]^{\frac{1}{5}} \cdot \left[ \frac{1 - v^2}{E} \cdot \rho \cdot \frac{v_S^2}{2} \right]^{\frac{1}{5}} \cdot \left[ \frac{W_{m,kin} - W_{m,min}}{v_S^2/2} \right] \right\} \quad (10)$$

Furthermore, comparing Eq. 9 with Eq. 10 shows that the threshold energy  $W_{m,min}$  has to be size-dependent. The product  $xW_{m,min}$  relates to  $l_i W_{Vi}$  and because both,  $l_i$  and  $W_{Vi}$ , are independent of the particle size,  $xW_{m,min}$  has to be a material constant, too.  $f_{Mat.}$  as well

as the factor  $\left[ 1 + \frac{E}{E_T} \cdot \frac{1 - v_T^2}{1 - v^2} \right]^{\frac{1}{5}} \cdot \left[ \frac{1 - v^2}{E} \cdot \rho \cdot \frac{v_S^2}{2} \right]^{\frac{1}{5}} \cdot \frac{1}{v_S^2/2}$  is

purely dependent on material properties and independent of the stressing conditions and particle size, thus again showing agreement between the two approaches. Finally, Eq. 10 can be written for  $k$  successive impacts with the single mass-specific impact energy  $W_{m,kin}$  and using the new material parameters  $f_{Mat.}$  (now mass-based) and  $W_{m,min}$  as follows (Eq. 11).  $f_{Mat.}$  denotes the resistance of the particle material against the external load  $W_{m,kin}$ , and  $W_{m,min}$  is a specific threshold energy for a particle of size  $x$ , which has to be exceeded by the specific impact energy in order to cause particle breakage. Below this threshold value, particle breakage does not occur.

$$P_B = 1 - \exp \{ -f_{Mat.} \cdot x \cdot k \cdot (W_{m,kin} - W_{m,min}) \} \quad (11)$$

Based on two different and independent approaches, the similarity considerations and the fracture mechanical model, an analytical function for the breakage probability is derived [24, 25]. Simplifying both approaches leads to the same main parameters determining particle breakage: the product of impact energy and initial particle size, the newly introduced material or particle parameter  $f_{Mat.}$  and the size-independent threshold value  $xW_{m,min}$ . According to the model assumption,  $f_{Mat.}$  and  $xW_{m,min}$  comprise all particle properties and should therefore describe the material influence on the comminution result.

### 3. SINGLE PARTICLE EXPERIMENTS

Single particle comminution experiments were carried out to validate the model and to determine the introduced material parameters. **Fig. 1** shows the single particle impact device used for the experiments. It was developed by Schönert [15]. A vibration feeder transports single particles from the feed chamber to the disc-shaped rotor. There, the particles are accelerated in radial channels by the centrifugal force. After

reaching the outer diameter of the rotor, they are ejected with a final velocity consisting of a radial and a tangential component, both equal to the circumferential speed of the rotor. As both feeder and grinding chamber are evacuated in order to avoid the disturbing influence of any air flows, the impact velocity  $v$  of the particles on the target ring is given by the ejecting velocity from the rotor, and because of its sawtooth shape, the particles impact at an angle of  $90^\circ$ . For the single particle tests shown here, impact velocities from 10 to 140 m/s were realised at an ambient temperature. At the end of a single test, the size distribution of the product particles was determined by sieve size analysis. After the analysis, the product particles were stressed again under the same conditions in order to simulate multiple impacts. This procedure was repeated up to five times. Five different polymers (polymethyl methacrylate: PMMA G55, G7 and G88 from BASF AG and Agomer GmbH, and polystyrene: PS 168N and 144C from BASF AG) with different molecular weight distributions which result in different mechanical properties were used. Furthermore, two crystalline materials (ammonia sulphate and potassium alum), limestone, two powder coatings (epoxy and polyester-based), and glass spheres were investigated. Narrow size fractions of the feed material were produced by sieving. In each experiment, approximately 2500 particles were stressed in order to obtain statistically reliable results.

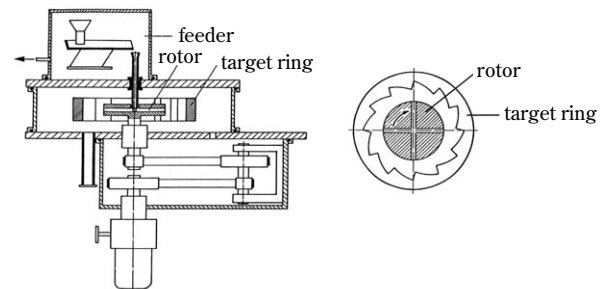


**Fig. 1** Single particle impact device [15]

### 4. EXPERIMENTAL RESULTS

Eq. 11 accounts for the influence of the initial particle size on fracture. **Fig. 2** shows the breakage probability  $P_B$  of glass spheres covering a size range of almost two decades. The data were taken from literature (open symbols and dashed lines [16], filled sym-

bols and solid lines [17]). The difference in breakage for the different sizes is obvious. For the same energy input smaller particles exhibit a smaller breakage probability. This can be explained by the fact that for smaller particles the circumference of the contact area is smaller and therefore fewer flaws are affected by the critical tensile stress.

If  $P_B$  is plotted versus  $x \cdot W_{m,kin}$  (**Fig. 3**), all curves overlap and show the predicted influence of impact energy and initial particle size in Eq. 11. Approximately, the energy threshold  $W_{m,min}$  is inversely proportional to the initial particle size, leading to a constant value for  $xW_{m,min}$  as predicted by the model. The threshold value can be determined in **Fig. 3** as the intercept of the curve with the abscissa. The lines in **Fig. 2** and **Fig. 3** are fits of Eq. 11 to the experimental data. They show good agreement between theory and experiment.

**Fig. 4** shows the breakage probability for two different polymers (PMMA G55 and G88). The initial particle size was a narrow sieve size fraction between 2.0 and 2.5 mm. The lines in **Fig. 4** are again fits of Eq. 11 to the experimental data. Both materials follow the model well. The results of the multiple impacts agree well with Eq. 11 when they are plotted as a function of the total net energy  $k \cdot (W_{m,kin} - W_{m,min})$ .

Fitting Eq. 11 to the breakage data of single particle impact tests gives the material parameter  $f_{Mat}$  and the size-independent threshold value  $xW_{m,min}$  for each material.  $f_{Mat}$  and  $xW_{m,min}$  are approximately inversely proportional to each other. Brittle materials are characterised by high values of  $f_{Mat}$ , more ductile materials show small values of  $f_{Mat}$ . For the investigated materials, these values are given in **Tab. 1**.

When the breakage data are plotted according to the probability distribution (Eq. 11) as a function of

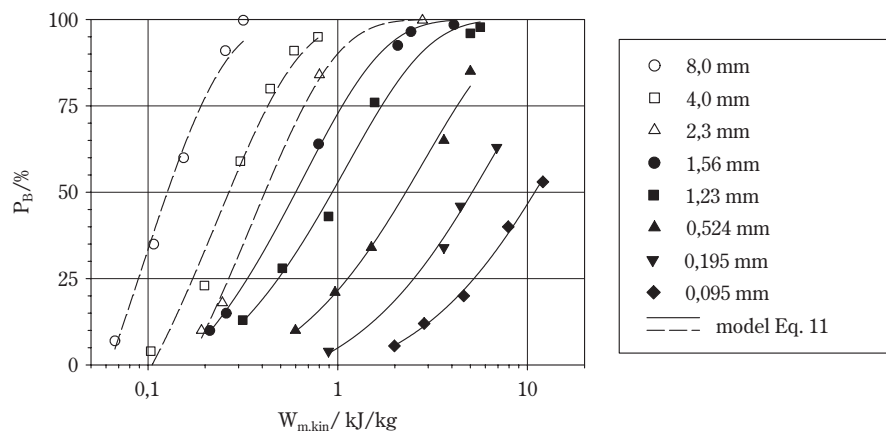


**Fig. 2** Breakage probability of glass spheres of different sizes [16, 17]

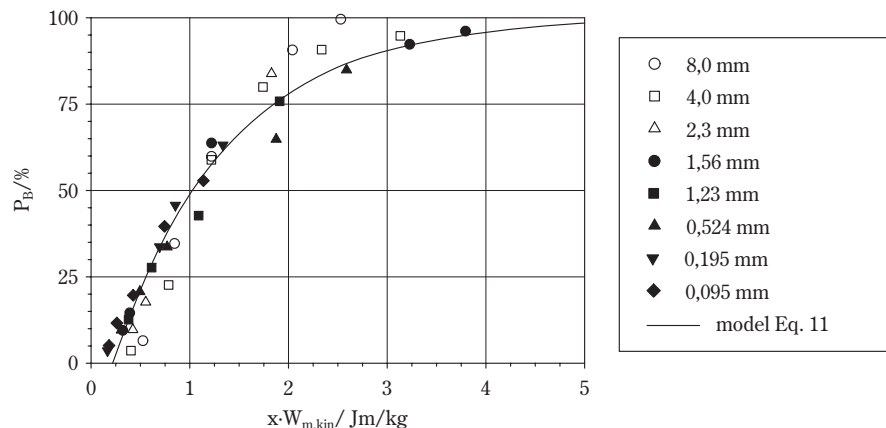


**Fig. 3** Breakage probability of glass spheres of different sizes [16, 17]

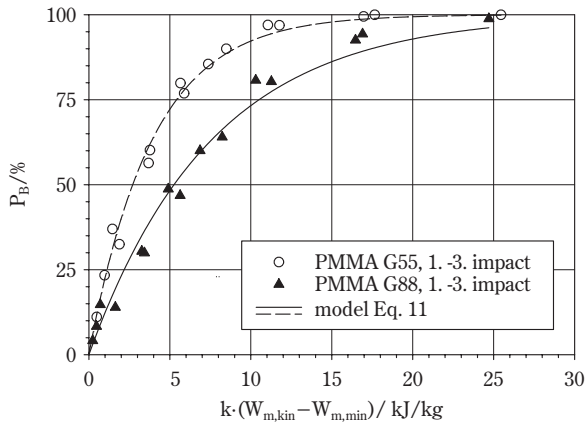


**Fig. 4** Breakage probability of PMMA as a function of the total net impact energy

**Table 1** Material parameters  $f_{Mat.}$  and  $xW_{m,min}$  determined from single particle tests

	$f_{Mat.}/\text{kg/Jm}$	$xW_{m,min}/\text{Jm/kg}$
PMMA G88	0.059	3.541
PMMA G7	0.095	5.898
PMMA G55	0.115	2.957
PS 168N	0.118	5.410
PS 144C	0.125	3.427
limestone	0.327	0.520
ammonia sulphate	0.884	0.126
glass spheres	0.944	0.297
potassium alum	1.491	0.147
powder coating (polyester)	2.299	0.018
powder coating (epoxy)	5.266	0.005

the product of total net impact energy  $k \cdot (W_{m,kin} - W_{m,min})$ , the initial particle size  $x$  and material parameter  $f_{Mat.}$  **Fig. 5** is obtained. For all materials under investigation, i.e. three PMMA, two PS, limestone, glass spheres, two crystalline materials and two powder coatings, a single curve describes the breakage probability. The experimental data is well within a deviation of  $\pm 15\%$  of Eq. 11. The main conclusion which can be drawn from these results is that the influence of the main parameters stress intensity (impact energy) and stress frequency (impact number), initial particle size and material properties are quantified correctly by the developed model. The plot in **Fig. 5** can be seen as a mastercurve describing the breakage probability of various materials. The product  $f_{Mat.} \cdot x \cdot k \cdot (W_{m,kin} - W_{m,min})$  can be interpreted as a dimensionless stressing parameter. For the first time, measurable material properties, i.e. the material parameter  $f_{Mat.}$  and the threshold value  $xW_{m,min}$  which describe the grinding performance of different materials quantitatively, can be determined and thus permit a systematic distinction to be made between different materials.

## 5. MODELLING OF GRINDING IN IMPACT MILLS

The main objective for the modelling of impact mills with population balances here was that of a clear separation of the different influences of material properties, machine-specific features and operating conditions in order to be able to interpret the results. It was therefore assumed that the grinding process can be described separately by a machine and a material

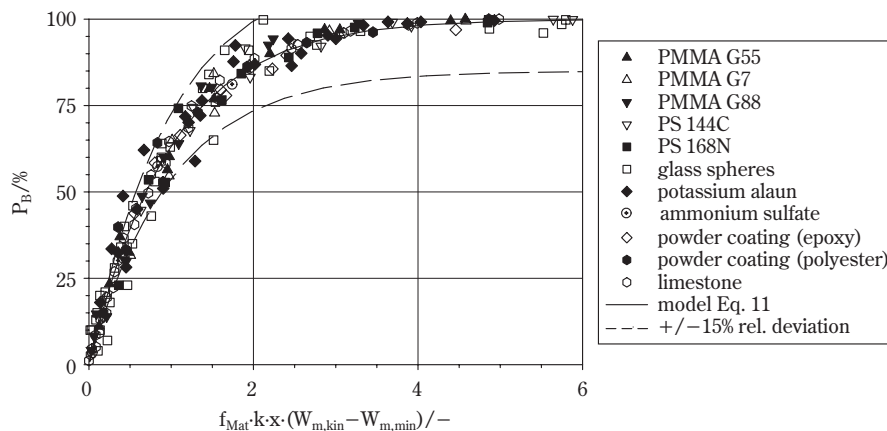


**Fig. 5** Mastercurve for the breakage probability of various materials



function [18, 25]. The machine function comprises the type of mill as well as all the operating conditions. By choosing the mill, the kind of particle stressing is defined. The operating conditions of the mill on the other hand determine the number of stress events, their intensity and the distribution of both. Operating conditions can be characterised, e.g. by the speed of revolutions, the air flow rate and the solids loading. For rotor impact mills, the speed of the hammers correlates with the stress intensity. The number of stress events depends on the residence time distribution of the particles in the mill. The experimental set-up, the structure of the model, the applied population balance and the material function is described below.

### 5.1 Experimental Set-Up

The experiments with the air classifier mill were carried out with a Hosokawa ACM 2 with a rotor diameter of 177 mm (Fig. 6) at Hosokawa Micron GmbH in Cologne, Germany. The particles are fed to the grinding zone by a rotary valve. There they are stressed by the grinding pins and then transported by the main air to the impeller wheel classifier. The shroud ring permits controlled transport by separating the grinding zone from the classifying zone. Material that is fine enough leaves the mill through the classifier with the main air, whereas coarse material is rejected and transported by the internal circulation back to the grinding zone. There it is stressed again. In the experiments, the revolution speed of the rotor (5787 to 10417 rpm, equivalent to circumferential velocities from 50 to 90 m/s), the revolution speed of the classifier (1270 to 6500 rpm) and the solids loading (0.056 to 0.1350 kg solids/kg of air) were varied. The air flow was monitored and kept at a constant value. The ground product was limestone.

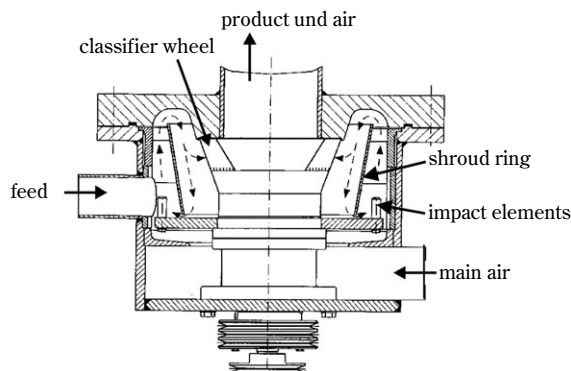


Fig. 6 Air classifier mill ACM 2

### 5.2 Structure of the Model

A simple structure for the model of the mill was chosen. It is shown in Fig. 7. The air classifier mill consists of a grinding zone and a classifying zone connected by a more or less defined particle transport. Grinding and classifying were transferred to two separate units in the model mill. A third unit, the hold-up, was added to mix the feed with the coarse material which was rejected by the classifier. Material leaving the grinding zone reaches the classifier and if small enough, is removed from the system or if too big, is recirculated to the hold-up. There it is mixed with the feed and again transported to the grinding zone. The recirculation flux is a free internal parameter of the model and not predetermined nor adjusted.

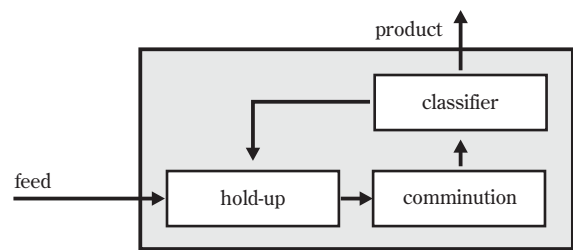


Fig. 7 Structure of the mill model

### 5.3 Population Balance

The change of the particle mass in a discrete size band during a discrete grinding step, e.g. after a single stressing event, is given by the mass leaving the size band as fragments and the mass entering the size band as fragments from larger sizes (Eq. 12, [19]). The mass leaving a size band  $i$  per unit of time is given by the product of the particle mass  $m_i$  in the size band multiplied by the breakage probability  $P_{B,i}$ . Entering class  $i$  from a bigger size  $j$  is the mass  $m_j$  inside class  $j$  multiplied with the breakage probability  $P_{B,j}$  and the mass transfer function  $b_{i,j}$ , which denotes the fraction of fragments breaking from class  $j$  into the size band  $i$ . Herein  $i=1$  denotes the largest and  $i=N$  the smallest particle size, respectively. The mass transfer function  $b_{i,j}$  can be calculated from the breakage function  $B_{i,j}$ .

$$\Delta m_i = \sum_{j=1}^{i-1} m_j \cdot b_{ij} \cdot P_{B,j} - m_i \cdot P_{B,i} \quad \text{with} \quad b_{i,j} = B_{i-1,j} - B_{i,j} \quad (12)$$

Taking into account not only a single size band  $m_i$  but all particle sizes leads to the particle size distribu-

tion vector  $\underline{m}$ . The particle size distribution  $\underline{m} + \Delta \underline{m}$  after a discrete grinding step can then be calculated from the particle size distribution before the interval  $\underline{m}$  when the balance according to Eq. 12 is calculated for all size intervals. This leads to a set of equations which can be written in vector form with  $\underline{Z}$  being the comminution matrix (Eq. 13).

$$\underline{m} + \Delta \underline{m} = \underline{Z} \cdot \underline{m}, \quad \underline{Z} = \begin{bmatrix} 1 - P_{B,1} & 0 & \dots & 0 \\ b_{21} \cdot P_{B,1} & 1 - P_{B,2} & 0 & 0 \\ \vdots & \vdots & \ddots & \vdots \\ b_{N1} \cdot P_{B,1} & b_{N2} \cdot P_{B,2} & \dots & 0 \end{bmatrix} \quad (13)$$

It can be shown [20, 21] that the comminution result after  $n$  multiple stressing events can be calculated by  $n$ -times multiplying the particle size vector  $\underline{m}(0)$  prior to the stressing with the comminution matrix  $\underline{Z}$ . This leads to the final form of the population balance which was implemented in the model:

$$\underline{m}(n) = \prod_{i=1}^n \underline{Z}_i \cdot \underline{m}(0) \quad (14)$$

The cut size of the air classifier mill was calculated by the equilibrium of drag and centrifugal force at the impeller wheel. The values were taken as values for the median size  $x_{50,t}$  of the separation curve. The sharpness of cut  $\kappa = x_{25,t}/x_{75,t}$  was assumed to be 0.5, as recommended for technical classifiers [22].

#### 5.4 Material Function

Eq. 11 was implemented in the model for the breakage probability. It allows for a clear separation between material properties and the stressing conditions. The fragment size distribution  $B$  was found to be in good agreement with an adjusted power law according to Eq. 15. Herein  $x$  denotes the size of the mother particles and  $y$  the fragment size. The parameter  $q$  denotes the power law exponent.

$$B = \left( \frac{x}{y} \right)^q \cdot \frac{1}{2} \cdot \left\{ 1 + \tanh \left( \frac{y - y'}{y'} \right) \right\} \quad \text{with } q = c \cdot v + d \quad (15)$$

As the power law fades only slowly to zero for small particle sizes, it always leads to a certain error by creating fines with unrealistically small sizes. The second factor forces the power law to fade more rapidly, reducing the effect of artificially created fines. The value  $y'$  is the fragment size from which point on the additional fading becomes significant. Logically, its value is chosen close to the minimal particle size expected by fragmentation, which can be estimated from [23]. It was possible to show from the results of single particle impact tests that the exponent  $q$  of the heuristic power law could be approximated well by a

linear function of the impact velocity  $v$ , which leads to a reduction in free model parameters. The linear function can be determined separately by single particle tests, thus again separating mill and material function. The parameters of the breakage function for the materials under investigation are given in **Tab. 2**.

**Table 2** Material parameters for the simulation

	$c / \text{s/m}$	$d / -$	$y' / \mu\text{m}$
limestone	-0.0050	0.70	1

## 6. EXPERIMENTAL AND SIMULATION RESULTS

**Fig. 8** shows typical results for the simulation of the air classifier mill. A good agreement between experimental results and simulation can be observed. Although no experimental data were available on the separation curve of the classifier, the calculated curve fits in well. Slight differences occur for the fines. The influence of the velocity of the grinding rotor and the speed of the impeller wheel classifier on the parameter  $n$  is given in **Fig. 9**. The model parameter  $n$ , a measure for the stressing frequency, decreases with increasing grinding rotor velocity. The parameter also decreases with increasing solids loading, whereas it is almost unaffected by the classifier wheel speed.

For the lower classifier speeds (1270 and 2540 rpm), the hold-up normalised by the corresponding mass of feed per unit of time is close to unity (**Table 3**). Most particles are small enough to leave the mill after the first passage through the grinding zone. In this range, the hold-up increases only slightly with increasing classifier speed. For higher classifier speeds, the hold-up increases significantly. Up to 2.6 times the amount of feed per unit of time is kept in the hold-up when the classifier operates at 6500 rpm. As expected, the finer cut size leads to a higher internal recirculation. The mill effectively operates with recirculation, which is in agreement with the structure of the mill shown in **Fig. 7**. There, the separation of grinding zone and classifying zone by the shroud ring can be seen.

The solids loading (mass flow of solids per mass flow of air) exhibits an influence that is similar to that of the classifier speed. Increasing the loading from small values, close to the conditions of single particle tests, up to 0.135 kg/kg and therefore approaching the conditions of production mills, leads to an

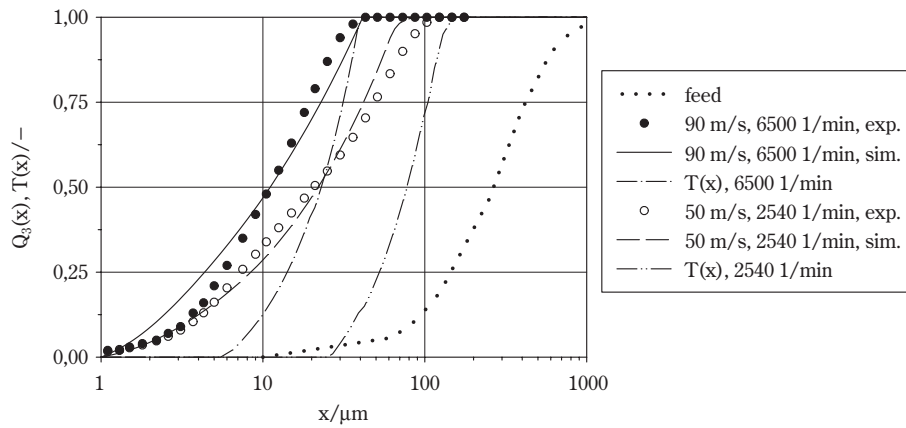


**Fig. 8** Representative simulation results for the air classifier mill

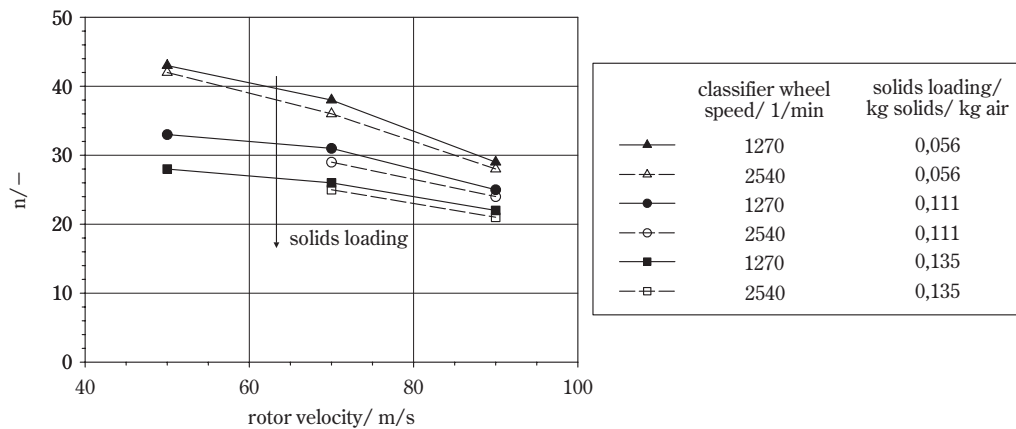


**Fig. 9** Influence of the grinding rotor velocity on model parameters

**Table 3** Hold-up as a function of the classifier wheel speed

classifier wheel speed [rpm]	1270	2540	3800	5075	6500
normalised hold-up / -	1.00	1.10	1.16	1.55	2.62

increase of the hold-up and reduces the parameter  $n$ . The agreement between simulation and experiment is still good and the simulation of even higher concentrations seems possible.

Similar investigations were carried out for sieve hammer mills. In this case, two types of PMMA were studied. We found a very good agreement again between our model and the experimental data.

## 7. CONCLUSIONS AND PERSPECTIVES

Two approaches describing the influence of material properties, particle size and external load on the result of impact comminution have been presented. It is shown that both lead to the same influencing parameters, namely the product of initial particle size, total mass-specific net impact energy and a newly introduced material strength parameter. The breakage probability is described by a single mastercurve comprising the breakage behaviour of different materials (polymers, limestone, crystals, glass) of various sizes (95  $\mu\text{m}$  to 8 mm) for multiple impacts. For the first time, measurable material properties describing the comminution performance of different materials have been derived and determined experimentally. These material parameters permit a quantitative dif-

ferentiation between various products and enable a comparison of different materials of different size.

These material parameters were applied to a simple model for the simulation of grinding different products in impact mills. A good agreement between simulation results and experiments was achieved while retaining a clear distinction between material and operating parameters. The material parameters were determined independent of the machine properties by single particle comminution tests. The free adjustable model parameter  $n$ , which correlates to the stressing frequency, showed systematic and reasonable trends with the operating parameters of the mills and could be explained by physical effects. Sieve hammer mills as well as air classifier mills can be simulated by the help of externally measured material functions using measurable operating parameters to describe the stressing conditions in the mill. A safe simulation of operating conditions within the range experimentally covered and a reasonably reliable extrapolation outside is possible. Because the material properties were determined independent of the mill, they can be utilised in similar applications for other types of impact mills.

In future work, it has to be examined whether experimental results for the breakage function can be explained by the product  $f_{\text{Mat}} \cdot x \cdot k \cdot (W_{\text{m,kin}} - W_{\text{m,min}})$ , too. A correlation of the comminution parameters to basic parameters from fracture mechanical considerations will be investigated. The population balance model presented here showed good agreement between simulation and experimental results, and the obtained model parameters could be explained reasonably, but no information based on experimental studies on the particle transport and the resulting stressing conditions is available so far. This shortcoming has to be overcome, and a more sophisticated and predictive modelling is aimed for.

## 8. ACKNOWLEDGEMENTS

This project is partly sponsored by the German Federal Ministry of Economics and Technology, grant number AiF-No. 12680 N. The authors appreciate the given support. The authors would like to thank Hosokawa Micron GmbH in Cologne, Germany, for carrying out the milling experiments. Furthermore, BASF AG strongly supported the simulation by providing the simulation tool. The authors greatly appreciate this support.

## 9. NOMENCLATURE

$a$	diameter of contact circle	[m]
$B$	cumulative breakage function	[–]
$b_{i,j}$	mass transfer coefficient	[–]
$c$	parameter	[s/m]
$d$	parameter	[–]
$E, E_T$	Young's modulus of particle and target material, respectively	[Pa]
$E', E''$	storage and loss modulus, respectively	[Pa]
$f, f_1, f_2$	function	
$f_{\text{Mat}}$	mass-based material strength parameter	[kg/Jm]
$f_{\text{Mat}}^*$	volume-based material strength parameter	[m <sup>3</sup> /Jm]
$H$	hardness	[Pa]
$k$	number of impacts	[–]
$l_i$	inherent flaw size	[m]
$m$	parameter of Weibull distribution	[–]
$m_i$	mass of particles in size band $i$	[kg]
$\underline{m}$	vector of particle size distribution	[kg]
$n$	model parameter correlating to stressing frequency	[–]
$P_B$	breakage probability	[–]
$p_{\text{max}}$	maximum pressure in contact circle	[Pa]
$q$	power law exponent	[–]
$Q_3(x)$	cumulative particle size distribution	[–]
$T(x)$	separation curve	[–]
$v$	impact velocity	[m/s]
$v_d$	deformation velocity	[m/s]
$v_{\text{el}}$	propagation velocity of elastic waves	[m/s]
$v_{\text{fract}}$	propagation velocity of cracks	[m/s]
$v_S$	strength	[m/s]
$W_{\text{m,kin}}$	mass-specific impact energy	[J/kg]
$W_{\text{m,min}}$	mass-specific threshold energy	[J/kg]
$W_V$	volume-specific stressing energy	[J/m <sup>3</sup> ]
$W_{V,i}$	volume-specific energy for activation of a inherent flaw	[J/m <sup>3</sup> ]
$x$	initial particle size	[m]
$y$	fragment size	[m]
$y'$	fragment size for additional fading	[m]
$z$	number of chain links	[–]
$\underline{Z}$	comminution matrix	[–]
$\beta_{\text{max}}$	crack extension energy	[J/m <sup>2</sup> ]
$v, v_T$	Poisson ratio of particle and target material, respectively	[–]
$\rho$	particle density	[kg/m <sup>3</sup> ]
$\sigma$	load	[Pa]
$\sigma_S$	strength	[Pa]
$\Psi$	shape factor	[–]

## 10. REFERENCES

- [1] Rumpf, H.: Physical aspects of comminution and a new formulation of a law of comminution, *Powder Technology*, 7, 1973, 145-159
- [2] Gross, D.; Seelig, Th.: *Bruchmechanik*, Springer-Verlag, Berlin 2001
- [3] Williams, J.: *Fracture mechanics of polymers*, Ellis Horwood, West Sussex 1984
- [4] Cahn, R.; Haasen, P.; Kramer, E.: Glasses and amorphous materials, in: *Materials science and technology*, Vol. 9, VCH Verlagsgesellschaft, Weinheim 1991
- [5] Weichert, R.: Anwendung von Fehlstellenstatistik und Bruchmechanik zur Beschreibung von Zerkleinerungsvorgängen, *Zement-Kalk-Gips*, 45, 1992, 1-8
- [6] Weibull, W.: A statistical distribution function of wide applicability, *Journal of Applied Mechanics*, 9, 1951, 293-297
- [7] Gildemeister, H.: Spannungszustände und Bruchphänomene in prallbeanspruchten Kugeln, PhD-Thesis Universität Karlsruhe 1976
- [8] Stieß, M.: Die Druckbeanspruchung von elastischen und inelastischen Kugeln bis zum Bruch, PhD-Thesis Universität Karlsruhe 1976
- [9] Hertz, H.: Über die Berührung fester elastischer Körper, *Journal für die reine und angewandte Mathematik*, 92, 1882, 156-171
- [10] Vervoorn, P.; Austin, L.: The analysis of repeated breakage events as an equivalent rate process, *Powder Technology*, 63, 1990, 141-147
- [11] Berthiaux, H.; Dodds, J.: Modeling fine grinding in a fluidized bed opposed jet mill – Part 1: Batch grinding kinetics, *Powder Technology*, 106, 1999, 78-87
- [12] Lecoq, O.; Guigon, P.; Pons, M.: A grindability test to study the influence of the material processing on the impact behaviour, *Powder Technology*, 105, 1999, 21-29
- [13] Subero, J.; Ning, Z.; Ghadiri, M.; Thornton, C.: Effect of interface energy on the impact strength of agglomerates, *Powder Technology*, 105, 1999, 66-73
- [14] Zverev, S.: Comminution of materials by free impact, *Russian Chemical Industry*, 25 (2), 1993, 31-36
- [15] Marktscheffel, M.; Schönert, K.: Liberation of composite particles by single particle compression, shear and impact loading, *Preprints of the 6. European Symposium Comminution*, Nürnberg 1986, 29-45
- [16] Priemer, J.: Untersuchungen zur Prallzerkleinerung von Einzelteilchen, PhD-Thesis Technische Hochschule Karlsruhe 1964
- [17] Behrens, D.: Über die Prallzerkleinerung von Glaskugeln und unregelmäßig geformten Teilchen aus Schwespat, Kalkstein und Quarzsand im Korngrößenbereich von 0,1 und 1,5 mm, PhD-Thesis Technische Hochschule Karlsruhe 1965
- [18] Peukert, W.; Vogel, L.: Comminution of Polymers – An Example of Product Engineering, *Chemical Engineering and Technology*, 24 (9), 2001, 945-950
- [19] Reid, K.: A Solution to the Batch Grinding Equation, *Chemical Engineering Science*, 20, 1965, 953-963
- [20] Müller, F.; Polke, R.; Schäfer, M.: Model-Based Evaluation of Grinding Experiments, *Powder Technology*, 105, 1999, 243-249
- [21] Berthiaux, H.: Analysis of Grinding Processes by Markov Chains, *Chemical Engineering Science*, 55, 2000, 4117-4127
- [22] Löffler, F.; Raasch, J.: *Grundlagen der Mechanischen Verfahrenstechnik*, Vieweg Verlag, Wiesbaden 1992
- [23] Schönert, K.: Size Reduction, in: *Ullmann's Encyclopedia of Industrial Chemistry*, VCH Verlagsgesellschaft, Weinheim 1998
- [24] Peukert, W.; Vogel, L.: Breakage behaviour of different materials – construction of a mastercurve for the breakage probability, *Powder Technology* 129, 2003, 101-110
- [25] Vogel, L.: Zur Bruchwahrscheinlichkeit prallbeanspruchter Partikeln, PhD-Thesis Technische Universität München, 2003



## Author's short biography



### Wolfgang Peukert

Wolfgang Peukert studied chemical engineering at the University of Karlsruhe. After receiving his diploma, he worked towards his PhD in the group of Prof. Loeffler at the Institute of Mechanical Process Engineering in Karlsruhe. His PhD-thesis is entitled "Combined collection of particles and gases in granular bed filters". In 1991, he joined Hosokawa Micron. He spent two years in Japan and then became the R&D Director of Hosokawa MikroPul in Cologne. In 1998 he left Hosokawa to accept a chair for Particle Technology at the Technical University of Munich. Since March 2003, W. Peukert heads the Institute of Particle Technology at the University of Erlangen-Nuremberg. His research activities cover a broad range of subjects in the field of particle technology with special emphasis on product engineering and interface science and technology. W. Peukert serves as a referee for various organisations and journals and is active in several working groups. He is a member of the editorial board of Powder Technology, Particuology, and editor-in-chief of Particle & Particle Systems Characterization. He has published more than 90 papers.



### Lutz Vogel

Lutz Vogel studied chemical engineering at the University of Karlsruhe (Germany) from 1992 to 1996, majoring in particle technology and combustion technology. He graduated with a diploma in chemical engineering in March 1998 and then joined the group of Prof. Dr.-Ing. Wolfgang Peukert at the new Institute of Particle Technology of the Technische Universität München as a research associate and co-worker. The characterisation and quantification of the grinding performance of different mills and the modelling of impact grinding processes are the main topics of his research work. He concluded his PhD thesis which is entitled "The Breakage Probability of Impacting Particles" in 2003. In May 2003, Lutz Vogel joined the Degussa AG at Hanau (Germany), where he continues to work in the field of particle technology.

# Modeling Breakage Kinetics in Various Dry Comminution Systems<sup>†</sup>

**D. W. Fuerstenau**

*Department of Materials Science and Engineering, University of California\**

**and P. C. Kapur**

*Department of Metallurgical Engineering, Indian Institute of Technology\*\**

**A. De**

*ABB. Inc*

## Abstract

*In modeling comminution systems, breakage rate (selection) functions are generally influenced more by the comminution machine than are breakage distribution functions, which are controlled by material properties. Linear grinding kinetics can be expressed either in terms of grinding time or specific energy consumption. Nonlinearities are caused by energy transfer mechanisms in the comminution machine whereby coarser particles might be ground preferentially or are protected by fines, by energy dissipation through interparticle friction in compressed bed comminution, and sometimes from heterogeneities produced in the feed particles. This paper discusses modifications of breakage rate functions in the grinding model for a number of situations and compares simulated and experimental results.*

## INTRODUCTION

The optimal design and control of comminution circuits require a mathematical model capable of depicting the size reduction behavior of every size fraction for grinding conditions of technological importance. This is particularly important for modeling closed-circuit comminution systems in which oversize material from a classifier or screen is recycled back to the comminution device. Comminution kinetics did not really have any practical application until a mathematical model of batch grinding was introduced – a model that incorporated both disappearance and production kinetics into one mathematical construct. A rigorous mathematical approach to comminution was published in 1954 by Bass [1] but the catalyst that led to worldwide utilization of this so-called population balance model (or batch grinding model) to the analysis of comminution in tumbling mills was perhaps the 1962 paper presented by Gardner and Austin [2] at the First European Comminution Symposium.

The batch-grinding model entails the formulation of a mathematical model which is phenomenological in nature in that it lumps together the entire spectrum of stress-application events which prevail in the system under a given set of operating conditions. The appropriately defined average of these individual events is considered to characterize the over-all breakage properties of the device and material. A single parameter is assumed to represent the resistance of particles of that size (or size fraction) to fracture, given the average grinding environment which exists in the mill. The isolation of such a parameter and a related set of quantities which constitute the breakage product size distribution for the average event in this size fraction allows the formulation of physically meaningful descriptive equations capable of yielding detailed information for simulation. The continuous-time, size-discretized solution of the batch grinding equation by Reid [3] provides a valuable practical simplification for data treatment since size distributions of comminuted products are usually determined in terms of a series of finite size intervals by sieving.

In dry batch ball milling, grinding kinetics follow a linear model. Linear breakage kinetics are said to prevail in a mill when neither the probability of breakage

---

\* Berkeley, CA 94720-1760, USA

\*\* Kanpur, India

<sup>†</sup> Accepted: September 9, 2003

of a particle (as measured by the breakage rate function) nor the distribution of fragments resulting from the primary breakage of that particle (as measured by the breakage distribution function) is influenced by the size consist in the mill. However, the rate of particle breakage may deviate from linearity due to changes in the nature of the comminution events or from changes in the heterogeneity of the particles being ground. For example, in some cases conditions may exist where the larger particles are ground preferentially or in other cases the larger particles may become protected after time. Under wet grinding conditions, at lower pulp densities suspension of the fine particles in the slurry may lead to an increase in the probability of coarser particles being ground, or at high pulp densities the slurry may become so viscous that grinding is retarded unless a grinding aid is added. In confined particle bed grinding, the product particles can be weakened through the generation of flaws and microcracks and consequently exhibit widely distributed strength behavior, which leads to nonlinearities in the regrinding of such particles. This paper discusses approaches taken to modify the model to describe that behavior.

## THE LINEAR BATCH GRINDING KINETIC MODEL

Consider the size range of a particulate assembly, characterized by a maximum size,  $x_1$ , and a minimum size  $x_{n+1}$  to be subdivided into  $n$  intervals (with  $n$  sieves). The  $i$ th size fraction is the interval bounded by  $x_i$  above and  $x_{i+1}$  below and denote the mass fraction of material in this size interval at time  $t$  by  $m_i(t)$ . If  $r$  is the geometric sieve ratio (which is generally  $\sqrt{2}$  for a series of sieves such as the Tyler sieve series), then  $x_i = rx_{i+1}$ .

The Reid solution to the size-discretized integrodifferential equation of grinding kinetics yields a mass balance for the material in the  $i$ th size interval in a batch ball mill at any time  $t$ :

$$\frac{dm_i(t)}{dt} = -k_i(t)m_i(t) + \sum_{j=1}^{i-1} k_j b_{i-j} m_j(t); \quad i=1, 2, \dots \quad (1)$$

where the parameter  $k_i$  is the breakage rate function (also called the selection function) for the solids in the  $i$ -th size interval which gives the fraction of material in size fraction  $i$  that is broken out in time  $t$  to  $t+dt$ , and  $b_{i-j}$  is the breakage distribution function and gives the fraction of progeny particles reporting to size  $i$  when unit mass fraction of particles of size  $j$  is broken.

If we consider the top size, first fraction only, then

$$\frac{dm_1(t)}{dt} = -k_1 m_1(t) \quad (2)$$

for first-order grinding kinetics where the breakage rate function is independent of time. Under these conditions, the behavior of the top fraction is predicted by the following relationship:

$$m_1(t) = m_1(0) \exp(-k_1 t) \quad (3)$$

Several different methods have been used to determine breakage rate and breakage distribution functions experimentally. For example, individual interior size fractions have been replaced by radioactively-labeled size fractions of the same feed material, a complicated technique that provides the greatest amount of information. In a simpler way, an insert fraction of a different material with some easily identifiable physical or chemical property has been used, such as using a quartz insert in a limestone bulk feed. Herbst and Fuerstenau [4] showed the mathematical and experimental basis for obtaining these parameters by batch grinding single-sized feed particles. The breakage distribution function is normalizable and can be considered invariant and will not be discussed further in this paper. However, there is a strong power law dependence of the breakage rate function on particle size,  $x$ :

$$k(x) = Ax^\alpha \quad (4)$$

where  $A$  is a constant depending on the material properties. In many of their simulations, Kelsall et al. [5] assumed  $\alpha=1.0$ . However, Herbst and Fuerstenau [4] showed that the value of  $\alpha$  has the same value as the distribution modulus of the Gaudin-Schuhmann size distribution of the comminuted product. To obtain the necessary data, a series of batch grinds should be carried out in a test mill to quantify not only the breakage rate but also the breakage distribution functions.

Using a 254-mm diameter instrumented ball mill, a series of batch grinding experiments was carried out dry by Herbst and Fuerstenau [4,5] with 7×9 mesh (2.8×2.0 mm) dolomite feed for various operating conditions: mill speeds  $N^*$ , ball loads  $M_b^*$ , and particle loads  $M_p^*$ . Details of the instrumented torque mill and experimental procedures can be found in these papers [4,6]. According to Eq. 3, a semilog plot of the fraction of feed material remaining in the top size vs. time in batch experiment will result in a straight line whose slope is proportional to the breakage rate function. **Figure 1**, which shows plots of batch data obtained for selected mill speeds, ball loads, and parti-

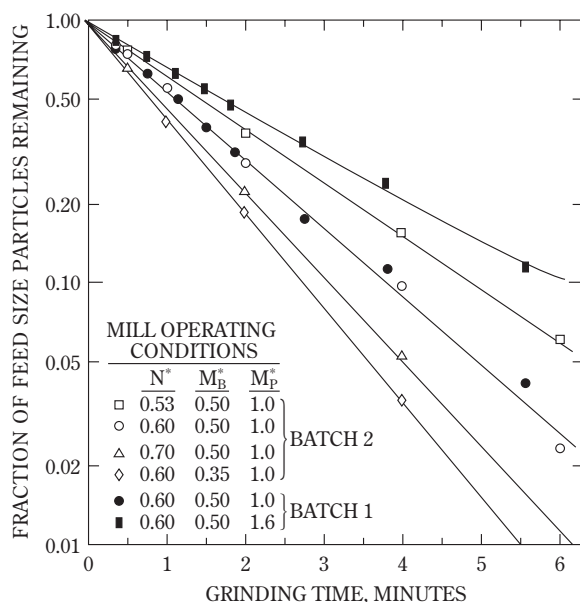


**Fig. 1** The influence of mill operating variables on the kinetics of disappearance of 7×9 mesh dolomite in dry batch ball milling.

cle loads (for two different batches of dolomite feed) illustrates the appropriateness of Eq. 2 for the range of operating variables tested. This figure also illustrates the strong dependence which feed disappearance kinetics have on mill operating conditions.

Herbst and Fuerstenau [4] experimentally ground a range of monosized dolomite feeds to obtain the dependence of breakage rate functions on particle size (and also found the cumulative breakage distribution function to be normalizable) and proved their predicted relation to zero order production kinetic phenomena. **Figure 7** given later, illustrates the dependence of breakage rate functions on particle size for dry ball mill grinding.

Using the values of breakage rate functions for particles of different size fractions and the normalized breakage distribution functions, the Reid solution to the batch grinding equation was programmed for a digital computer and the grinding behavior was simulated. **Figure 2** presents a comparison of the computed size distributions with the experimentally observed distributions. The simulation based on the linear batch grinding model indeed predicts the product size distribution over a wide range of grind times.

The very extensive experimental work carried out during the last four decades has proven the validity of the linear grinding model and the size-dependence of the breakage rate functions and the normalizability of

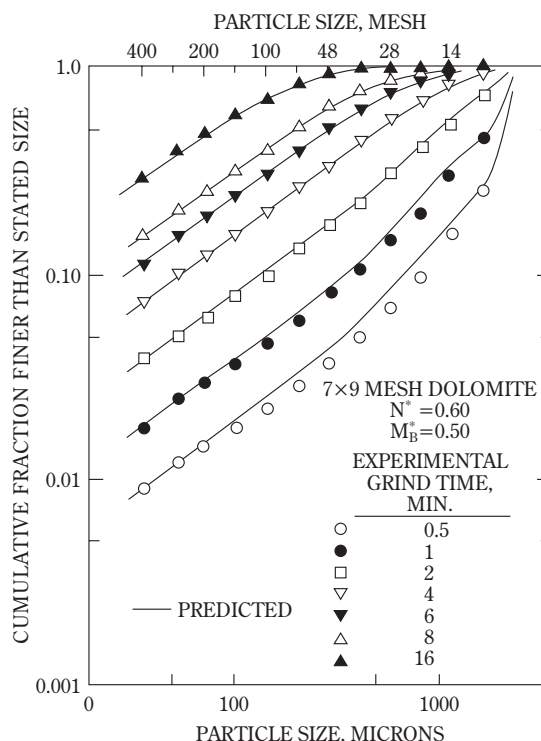


**Fig. 2** Simulation of the comminution of 7×9 mesh dolomite feed using the Batch grinding equation and the experimentally determined values of the breakage rate and breakage distribution functions.

breakage distribution functions. With confidence it, therefore, is possible to back calculate these parameters for simulation purposes.

## THE NONLINEAR KINETIC MODEL FOR ROD MILL GRINDING

Rod mill comminution represents a nonlinear grinding system, one in which the order is less than unity. In Eq. 1,  $k_1(t)$  represents the grinding rate function for monosized feed disappearance. There are two forms of  $k_1(t)$  which have physical meaning. The first is

$$k_1(t)m_1(t) = k_1(0)m_1(0) \quad (5)$$

which represents a “zero order” feed disappearance law where the feed grinding rate is constant for all time. This would occur if the grinding zones were saturated with respect to feed-size material and all comminution events are applied to feed-size particles. The second form of the breakage rate function is

$$k_1(t)m_1(t) = k_1(0)m_1(t) \quad (6)$$

or  $k_1(t) = \text{constant}$ . This “first order” feed disappearance occurs when statistically independent comminution events are applied to an infinite particle population in a completely mixed environment, as exemplified by dry batch ball mill grinding. Non-integer order grinding does not have physical meaning, except possibly for systems that can be represented by an arbitrary linear combination of zero and first order kinetics. Such is the case for rod milling where bridging of coarse particles between the rods decreases the proportion of comminution events applied to the fines.

Grandy and Fuerstenau [7] proposed that for comminution systems which have apparent grinding orders less than one, the system can be modeled by a convex linear combination of zero and first order kinetics:

$$\frac{dm_1(t)}{dt} = \phi_1 k_1(0) m_1(t) + (1 - \phi_1) k_1(0) m_1(t) \quad (7)$$

where  $\phi_1$  and  $(1 - \phi_1)$  give the respective fraction of first and zero order kinetics assumed. For rod mill grinding with kinetics that follow the foregoing relationship, the behavior of the top size material is predicted by Eq. 8:

$$m_1(t) = \frac{m_1(0) \exp[-\phi_1 k_1(0)t]}{\phi_1} + \frac{(1 - \phi_1)m_1(0)}{\phi_1} \quad (8)$$

functions are environment-dependent. Since the grinding order is between zero and one, it is appropriate to fit Eq. 8 to the data. A semilog plot of  $[m_1(t) + m_1(0)(1 - \phi_1)/\phi_1]$  vs. time should give a straight line with slope equal to  $-\phi_1 k_1(0)$ . For the foregoing rod mill grinding data, it was found by trial and error that a value of 0.91 for  $\phi_1$  gave the best straight line for feed loads.

To carry out computer simulations of these rod mill grinding tests, the mathematical representation of the environment dependence is given by

$$k_i(t_2) = k_i(t_2)\phi_i + (1 - \phi_i) \left( \frac{m_1(t_1)}{m_1(t_2)} \right) \text{ where } t_1 < t_2 \quad (9)$$

Using the technique of Herbst and Fuerstenau [4] to estimate the size dependence of all the breakage rate parameters and the fraction of first-order grinding given in **Figure 4**, the dry batch rod milling of the 7×9 mesh dolomite was accurately simulated. Since The simulated plots and experimental data fit exactly [7], those results are not presented here.

In a detailed investigation of the wet grinding of dolomite in the batch ball mill, Yang [8] found that plots of feed size breakage kinetics had the same

shape as those shown in **Figure 3** for rod mill grinding. This means that under the conditions of Yang’s experiments (60% solids), the fine product particles tended to be suspended in the slurry inside the mill

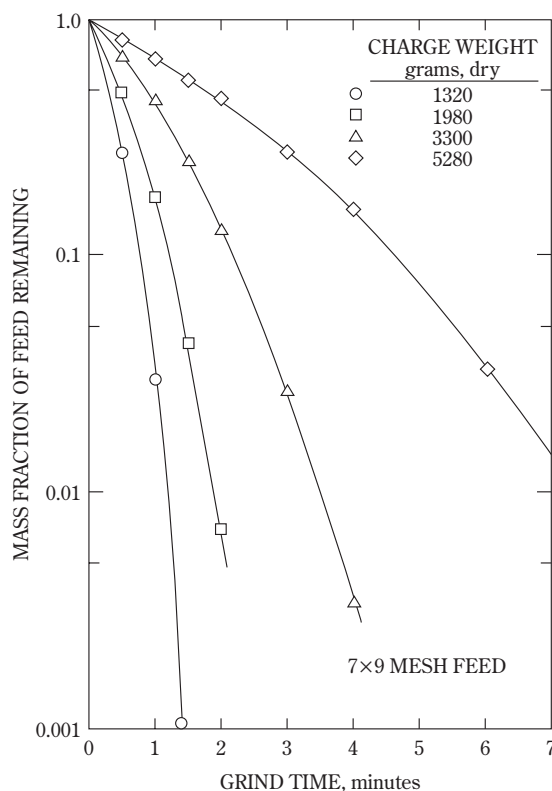


**Fig. 3** First order feed disappearance plot for rod mill grinding at several different feed loads in the batch mill.

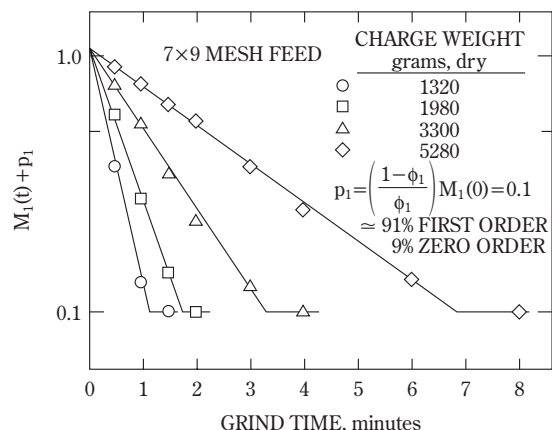


**Fig. 4** Linear combination of first order and zero feed disappearance kinetics in dry rod milling.



with the result that there was some preferential grinding of the coarser particles under those conditions. On the other hand, Klimpel [8] found that the disappearance kinetics plots for the fine wet grinding of coal at 57% solids density were first order but at 73% solids density became strongly concave as grinding progressed. Under these conditions the slurry inside the mill becomes increasingly viscous. As grinding progressed the rate of disappearance of feed size coal was significantly retarded. But by adding a polymeric grinding aid, which reduced the slurry viscosity markedly, Klimpel [8] was able to return the grinding kinetics to first order.

### LINEAR GRINDING KINETICS EXPRESSED IN TERMS OF SPECIFIC ENERGY

In conducting their batch grinding experiments with dolomite feed under a wide range of operating conditions, Herbst and Fuerstenau [6] also accurately measured the specific energy consumed by their mill. An analysis of the grinding kinetics in the dry ball mill revealed that the size-discretized breakage rate functions are proportional to the specific energy input to the mill and that the breakage distribution functions can be taken as invariant. Taking the experimental results used to prepare the plots given in **Figure 1** for a range of mill speeds, mass of solids in the mill, and the mass of grinding balls in the mill, the results are replotted and presented in **Figure 5** using spe-

cific energy as the independent variable instead of time.

Based on that extensive experimentation, Herbst and Fuerstenau [6] showed that over a fairly wide range of conditions the feed size breakage rate function can be approximated by

$$k_1 = k_1^E \left( \frac{P}{M_p} \right) \quad (10)$$

where  $P$  is the power input to the mill,  $M_p$  is the mass of feed material in the mill, and  $k_1^E$  is a constant. From Eq. 9, we can write the batch response for the first interval:

$$m_1(t) = m_1(0) \exp \left[ -k_1^E \left( \frac{P}{M_p} \right) t \right] \quad (11)$$

Since the product of specific power and time is equal to the net specific energy input to the mill,  $\bar{E}$ , Eq. 10 can be expressed alternatively as

$$m_1(\bar{E}) = m_1(0) \exp (-k_1^E \bar{E}) \quad (12)$$

The preceding analysis leads to expressing the batch grinding equation in terms of specific energy expended rather than in terms of grinding time as follows

$$\frac{dm_i(\bar{E})}{d\bar{E}} = -k_i^E m_i(\bar{E}) + \sum_{j=1}^{i-1} k_j^E b_{i-j} m_j(\bar{E}) \quad (13)$$

The fact that breakage kinetics can be accurately analyzed in terms of specific energy instead of time, has become very useful, with regard to mill scale-up and the analysis of other types of comminution systems, such as the roll mill.

Malghan and Fuerstenau [9] conducted a detailed study of the scale-up of ball mills using the population balance grinding model normalized through specific power input to the mills. In their investigation, they constructed three instrumented and scaled batch ball mills : 5-inch (12.7 cm) diameter, 10-inch (25.4 cm) diameter, and 20-inch (50.8 cm) diameter. They dry ground 8×10 mesh (2.4×1.7 mm) limestone. They found that the feed size breakage rate functions for all three different mill speeds, ball loads and feed loads in each mill fell on a single line when the feed size disappearance was plotted as a function of expended energy. Likewise, the breakage distribution function for all of the grinds were self-similar, completely independent of mill size and mill operating conditions. To illustrate the utility of the specific energy reduced breakage rate function concept, **Figure 6** presents the experimental size distributions obtained from grinding the 8×10 mesh limestone in the 20-inch mill

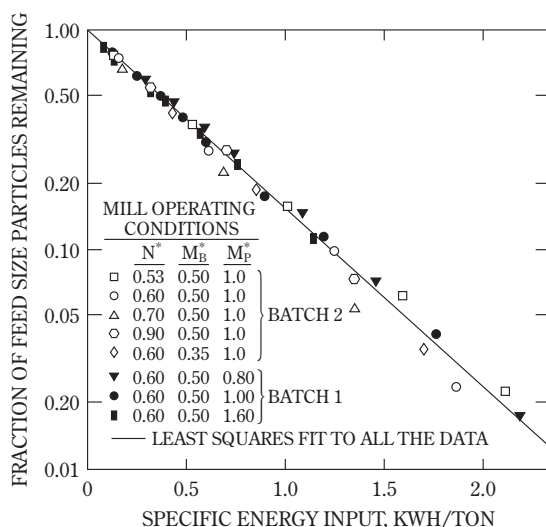


**Fig. 5** Feed disappearance kinetics normalized with respect to specific energy in kWh per ton of feed material.

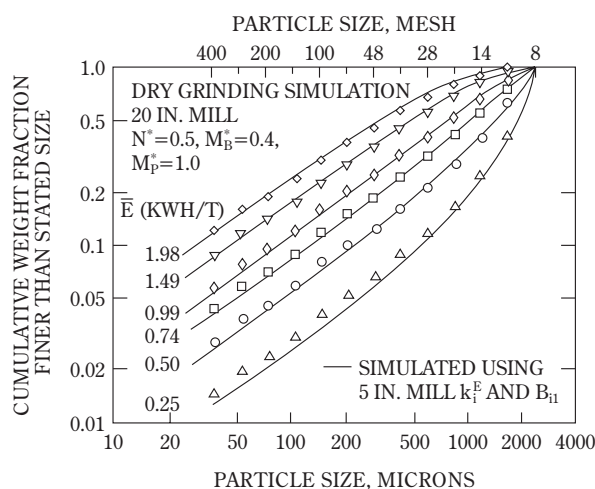


**Fig. 6** Comparison of experimentally determined size distributions and those Predicted for grinding 8×10 mesh limestone in a 20-inch (50.8 cm) diameter mill, using breakage rate and breakage distribution functions obtained from grinding the same material in the 5-inch (12.7-cm) mill.

and the simulation of grinding using the breakage parameters determined from grinds carried out in the 5-inch mill.

Malghan and Fuerstenau [9] also showed that if the breakage rate function were expressed in time rather than specific energy, for the range of mill speeds, ball loads, and feed loads, it would be proportional to  $D^{0.56}$  and proportional to  $(D - d_b)$  where  $D$  is the mill diameter and  $d_b$  is the ball diameter. The reduced breakage rate function simplifies analysis and design considerably since there would be no necessity for achieving kinematic and loading similarity. Scaling with time would require that the mills be compared at the same fraction of critical rotational speed.

Expressing grinding kinetics in terms of specific energy instead of grinding time also clarifies the complex behavior observed in wet grinding at high solids content [10].

## MODELING NONLINEAR HIGH-PRESSURE ROLL MILL COMMINUTION

After single-particle breakage, the next most efficient method of comminution is particle-bed comminution [11,12]. In this mode, comminution occurs primarily by very high localized interparticle stresses generated within the particle bed. No separate carrier is employed for the transport of energy to the solids, unlike in tumbling mills. Particle bed comminution is

carried out continuously in a device comprised of two counter-rotating rolls. As the feed particles pass through the roll gap, the particle bed is compressed and the coarser particles undergo an isostatic-like compression by the fine particles in which the coarser ones are embedded. Energy is lost in the high-pressure roll mill due to friction between the particles as they pass through the roll gap and due to the ineffectiveness of the isostatic loading phenomenon.

There really is no explicit running grinding time in the high-pressure roll mill, only a fixed time of passage of solids through the grinding zone of the rolls in a more or less plug flow manner. Therefore, in order to simulate roll-mill grinding, it is necessary to formulate the population balance model in terms of energy input to the mill. In addition, as the particle bed or column passes down through the rolls, it is compacted and densified and compacted more and more with an increasing rate of energy dissipation due to interparticle friction and incipient visco-plastic flow. Consequently, the energy component that actually goes into stressing the particle to fracture is progressively reduced. Kapur et al. [13] proposed that the increase in retardation of the breakage rate with energy input can be incorporated into the population balance model by defining a rescaled energy:

$$E' = \frac{1}{1-y} E^{1-y} \quad \text{where } 0 \leq y < 1 \quad (14)$$

For high-pressure roll mill grinding, the population balance equations for grinding kinetics can be formulated in terms on cumulative energy input, taking into account energy dissipation in accordance with Eq. 13, to yield the following relation:

$$\frac{dm_i(E)}{dE} = -\frac{k_1^0}{E^y} m_i(E) + \sum_{j=1}^{i-1} \frac{k_j^0}{E^y} b_{i-j} m_j(E) \quad (15)$$

Fuerstenau et al. [13] determined the product size distributions for grinding quartz, limestone and dolomite at various energy expenditures in a laboratory high-pressure roll mill (roll diameter of 200 mm) and from the results estimated the breakage rate and breakage distribution parameters. For each of these materials, the breakage distribution functions have essentially the same shape as those found for other comminution systems, such as the ball mill and rod mill. However, the breakage rate functions all remain quite high at all particle sizes, unlike in a ball mill where the specific rate constants drop sharply with particle size, especially in the medium and fine particle size range (the slope of a log-log plot of  $k$ -vs-size being the distribution modulus). **Figure 7** compares

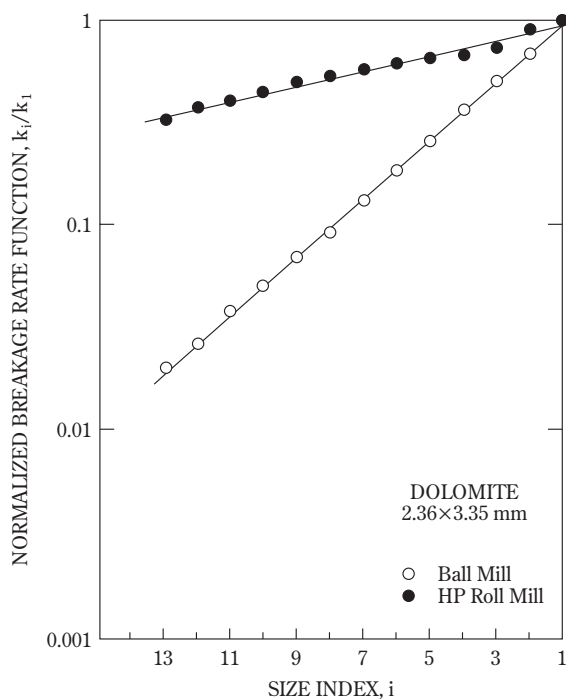


**Fig. 7** The effect of particle size on the estimated breakage rate functions for dolomite being ground in the high-pressure roll mill and a ball mill (size index 1=8×10 mesh here).

the effect of particle size on the breakage rate function for grinding dolomite in the high-pressure roll mill with grinding the material in a dry ball mill. As a consequence of this, the pressurized roll mill can perform size reduction much more efficient energy-wise than the ball mill. This probably explains the greater energy efficiency of the high-pressure roll mill at lower reduction ratios. The reason that the breakage rate functions for the high pressure roll mill appear to have only a small particle size effect must result from the energy transfer mechanism in the roll mill, namely that the high compression stresses are transferred from one particle to another as they pass through the roll gap, in contrast to the probabilistic nature of stress transfer in a ball mill. This apparently is the crucial difference between the two kinds of grinding mills. As a consequence, the pressurized roll mill can perform size reduction tasks much more efficiently energy-wise than the ball mill (at lower reduction ratios).

With the breakage rate parameters estimated from the high-pressure roll milling experiments, the size distributions of dolomite, limestone, and quartz were simulated with the population-balance grinding equation that had been suitably modified to account for

energy dissipation in the roll gap (Eq. 15). **Figure 8** shows the simulation of grinding quartz in the high-pressure roll mill at three different energy levels [13]. The simulations of the size distributions of the roll mill products are in good agreement with the experimentally determined size distributions.

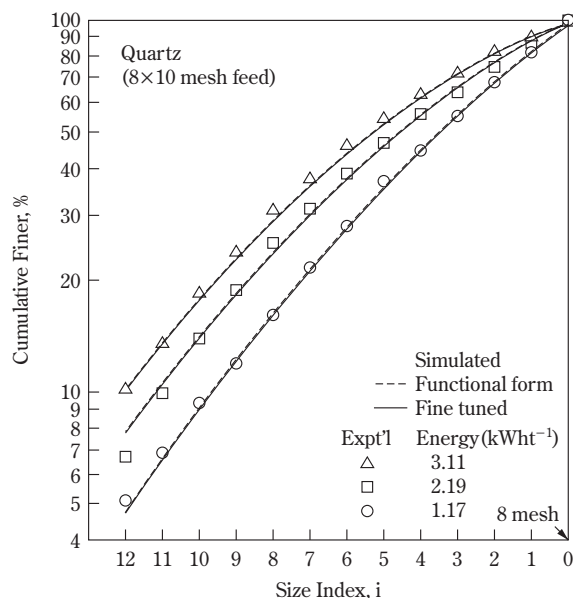


**Fig. 8** Experimental and simulated size distributions of quartz ground in a high-pressure roll mill at different energy levels.

## MODELING THE KINETICS OF GRINDING DAMAGED PARTICLES

Significant energy savings can be gained by using a two-stage grinding system which utilizes the efficiency of the high-pressure roll mill at low reduction ratios and the higher efficiency of ball mills at high reduction ratios [14]. As discussed in the foregoing section, particle breakage in the roll mill occurs through interparticle loading of the feed as it passes through the roll gap. Because the particles are not loaded by impact, as in ball milling, but by direct transmission of stresses from one particle to another, high-pressure roll mill grinding results in progeny particles that are broken, cracked, damaged or otherwise weakened. Consequently, the particles are distributed in strength which implies that the rate at which these particles will be ground in a ball mill will also be distributed. As already discussed, the linear population balance model used routinely for the simu-

lation of ball mill grinding of ordinary feeds assumes a single-valued rate parameter for particles of a given size fraction.

In order to successfully use the population balance approach to model the ball mill grinding of material that has first been ground in the high-pressure roll, we need to account for the pronounced heterogeneity in strength (or ease of grinding) of the high-pressure roll mill product particles [15]. We have noted earlier that the parameter  $A$  in Eq. 4 is a function of the material properties. In the simulation of batch ball milling of primary particles,  $A$  could be assumed to be constant, without affecting the quality of simulation. We can account for the heterogeneity in the strength of high-pressure roll-milled particles by letting  $A$  be variable. It is reasonable to say that  $A$  is a measure of the ease with which the particles could be broken, that is, a measure of the grindability. The larger the value of  $A$ , the easier it would be to break the particle. While primary particles are expected to be relatively uniform in strength, the particles in the high-pressure roll mill product are damaged and weakened to different extents, that is, that are distributed in  $A$ . We assume, however, that the distribution is independent of the particle size. In our analysis, we consider that the distribution in the grinding rate parameter,  $k$ , of the high-pressure roll mill product can be described by a modified gamma function:

$$m(A) = \frac{\lambda^\beta (A - A_0)^{\beta-1}}{\Gamma(\beta)} \exp[-\lambda(A - A_0)]; A_0 \leq A \leq \infty \quad (16)$$

where  $A_0$  is the minimum grinding rate constant encountered in the ball mill. And  $\beta$  and  $\lambda$  are the shape and scale parameters of the distribution. By incorporating Eq. 16 into Eq. 12, and integrating, we obtain the expression for the mass fraction retained on size  $x$  after an energy expenditure of  $E_b$  in ball milling the high-pressure roll mill product:

$$R(x, E_b) = R(x, 0) \frac{\exp(-A_0 x^\alpha E_b)}{(1 + x^\alpha E_b / \lambda)^\beta} \quad (17)$$

The shape and scale parameters are functions of the energy expenditure in the high-pressure roll milling stage.

These concepts were tested through a detailed study of the hybrid comminution of bituminous Pittsburgh No. 8 coal, that is for the open-circuit ball milling of coal that had first been ground in the high-pressure roll mill. **Figure 9** presents the experimental results of the mass fraction of ball mill product retained on a 200-mesh sieve ( $74 \mu\text{m}$ ) as a function of the energy expended for ball mill grinding the pres-

surized roll mill product, together with the computed results. In these experiments, the coal was first ground in the high-pressure roll mill (HPRM) at four different energy levels. **Figure 10** presents the experimental and computed size distributions of the ground coal after it had been comminuted in the ball mill at different expenditures of energy in the ball mill step after first being roll-milled at an energy expenditure of  $2 \text{ kWh/t}$ . The simulated results given in **Figure 10** are in excellent agreement with experiment.

The distribution in the grindability of coal particles

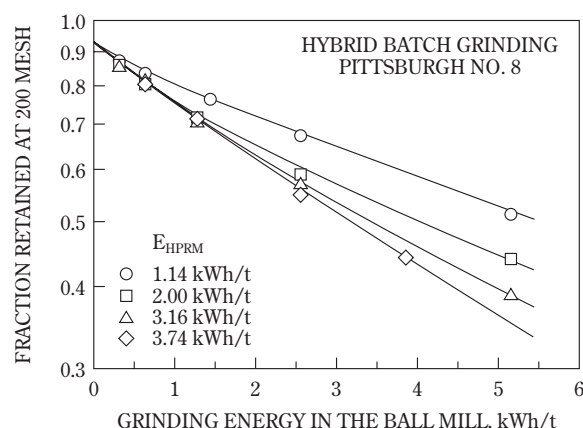


**Fig. 9** For the hybrid grinding of Pittsburgh No. 8 coal, the fraction retained on a 200-mesh sieve ( $74 \mu\text{m}$ ) sieve as a function of the energy expended in the ball mill on material that had been comminuted in the high-pressure roll mill at different HPRM energy levels: experimental data points and simulated curves.

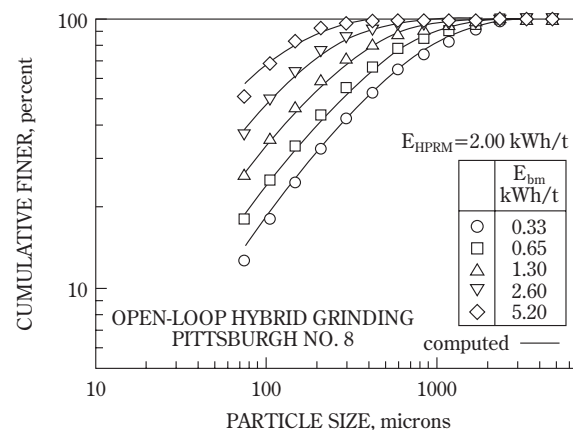


**Fig. 10** Experimental and computed size distributions of Pittsburgh No. 8 coal produced by open-circuit hybrid ball mill grinding of material that had first been ground at an energy expenditure of  $2 \text{ kWh/t}$  in the HPRM.

in the high-pressure roll mill product was assessed by fitting the mathematical model to the experimental data. **Figure 11** was constructed to show plots of the calculated density functions  $m(k)$  representing the distribution of breakage rate functions of 200-mesh particles of Pittsburgh No. 8 coal produced at energy consumptions of 1.14, 2.0, 3.16 and 3.74 kWh/t in the HPRM. Although the coal is discharged from the HPRM in a briquetted form, the individual particles are easily separated by stirring in aqueous methanol to determine their size distribution, if desired [15]. The fact that the mean of the distributions shifts towards higher grinding rate values with increasing energy input to the high-pressure roll mill strongly suggest that these results and concepts are phenomenologically meaningful.

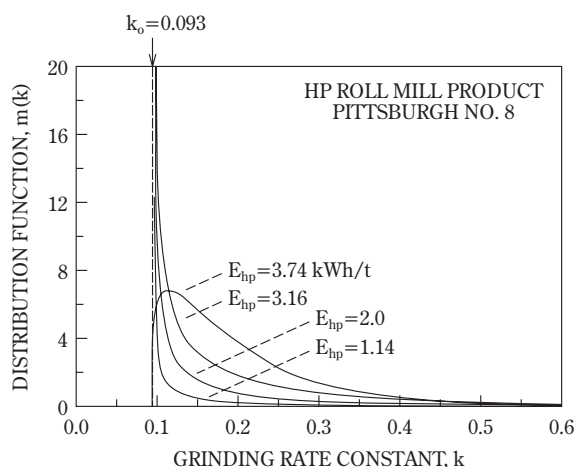


**Fig. 11** Density functions for the distribution of the specific ball mill grinding rates of Pittsburgh No. 8 coal produced in the high-pressure roll mill at different energy inputs.

## OPTIMIZATION OF OPEN-CIRCUIT HYBRID GRINDING SYSTEMS

The non-linearity of the kinetics of grinding primary particles in the high-pressure roll mill and the subsequent ball milling of the roll mill product present us with an interesting optimization problem. For open-circuit hybrid grinding, our goal would be to find the optimum energy expenditure in the high-pressure roll mill that would result in maximum particle damage at minimum energy dissipation, and the energy expenditure range in the ball mill where the energy is primarily spent in breaking the damaged

particles, that is the range where the ball mill grinding of damaged particles is essentially non-linear. **Figure 12** presents the simulated production of minus 200-mesh product and the specific energy expenditure per ton of product, as a function of the energy input in the high-pressure roll mill and the ball mill per tonne of feed for the open-circuit grinding of Pittsburgh No. 8 coal.

The specific grinding energy contours are shown as solid lines, and the contours of percent fines produced are presented as dashed lines. The simulation results indicate that the percentage of minus 200-mesh produced increases with the increase in grinding energy input in the ball mill for a given energy expenditure in the high-pressure roll mill. However, for a fixed energy input in the ball mill, the percentage of minus 200-mesh material produced goes through a maximum with increasing energy input in the high-pressure roll mill. As the production of minus 200-mesh particles increases, the high-pressure roll mill energy at which the maximum occurs shifts to higher energy values. The specific energy required to produce a unit weight of minus 200-mesh product, on the other hand, increases with the increase in energy input in both the ball mill and the high-pressure roll mill (except in the region defined by high-pressure roll mill energy between 1.75 kWh/t and 2.5 kWh/t and ball mill energy greater than 3.5 kWh/t). At a given specific energy consumption, particularly at higher percentage of fines production, an optimum partition exists between the energy input in the high-

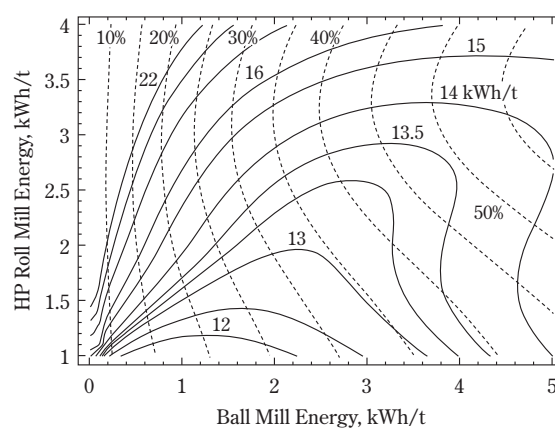


**Fig. 12** Relationship between specific grinding energy (solid lines) and the percentage of minus 200 mesh (74  $\mu$ m) fines produced (dashed lines) at different energy inputs in the high-pressure roll mill and the ball mill in open-circuit hybrid grinding of Pittsburgh No. 8 bituminous coal.



pressure roll mill and the ball mill in order to achieve a maximum percentage of minus 200-mesh product. For example, at a specific energy consumption of 13.25 kWh/t of minus 200-mesh product, the energy input should be 2.5 kWh/t of feed in the high-pressure roll mill and 3.2 kWh/t in the ball mill in order to produce a comminuted product with 43 percent of minus 200-mesh fines.

Because of the visco-plastic nature of coal, it is possible that the potential energy saving resulting from the fracturing and weakening of the particles as they are stressed in the HPRM could be more than offset by the increased briquetting at the high compressive stresses at higher energy expenditures in the pressurized roll mill step. Thus, a maximum benefit might be expected from the hybrid grinding of coal at an optimal energy expenditure in the high-pressure roll mill. In **Figure 13**, the percentage of energy saved through the hybrid grinding mode relative to the energy expended in ball mill grinding alone for the production of a fixed amount of fines is plotted against the energy expended in the HPRM step. These plots clearly show that not only is there an optimum for the energy input to the high-pressure roll mill but also the energy saving is negated if the energy expenditure in the high-pressure roll mill is higher than a threshold value, which would depend on the nature of the coal and the percentage of fines produced. There is a similar optimum for the hybrid grinding of minerals than can deform plastically, such as calcite and dolomite [14].

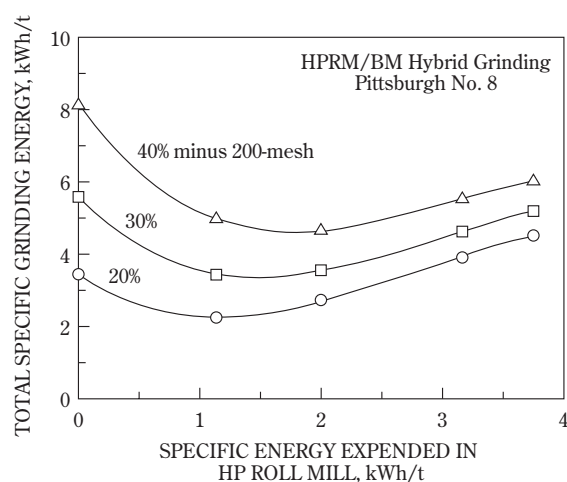


**Fig. 13** Relationship between the total specific comminution energy and the energy expenditure in the high-pressure roll mill for the production of minus 200-mesh fines in the hybrid grinding of Pittsburgh No. 8 coal.

## SUMMARY

Industrial comminution processes are inherently nonlinear. The extent of nonlinearity is governed by the mill characteristics, comminution environment, and the material properties. However, over a limited range of time or energy input, the processes could be treated as linear and modeled accordingly. For instance, in the initial stages of dry batch ball milling, grinding kinetics follow a linear model. Linear breakage kinetics prevail in the mill as neither the probability of breakage of a particle (as measured by the breakage rate function) nor the distribution of fragments resulting from the primary breakage of that particle (as measured by the breakage distribution function) is significantly influenced by the size consist in the mill. In the rod mill, on the other hand, where the larger particles are ground preferentially, the initial grinding behavior is significantly nonlinear. The nonlinearity can be modeled in such cases by suitably modifying the breakage probability function.

The change in the grinding environment in the media mills, over time, also leads to nonlinear comminution kinetics in these mills. This is primarily because of reduced energy utilization at larger grinding times due to particle shielding under dry grinding conditions, or increased slurry viscosity in wet grinding. Such nonlinearities can be easily resolved by recasting the grinding model equations in terms of energy input, instead of the grinding time. Expressing grinding kinetics in terms of energy instead of time also leads to simplifications in grinding mill scale up.

For confined particle bed grinding, as in high-pressure roll milling, due to the energy dissipation through interparticle friction and isostatic stresses at higher confining pressures, can only be modeled as a nonlinear process. A modified population balance model, that explicitly handles the retardation in energy utilization, has been presented. The modified model results in fairly accurate simulation of high-pressure roll mill grinding.

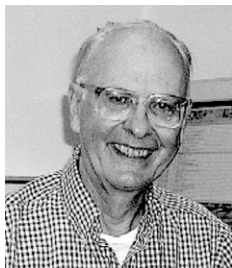
High pressure roll milling results in product particles that may become can be weakened though the generation of flaws and microcracks and consequently exhibit widely distributed strength behavior. This leads to nonlinearities in the regrinding of such particles in media mills. We have incorporated this distribution in particle strength into the batch ball mill grinding model and successfully simulated the open-circuit hybrid grinding of coal, where coal particles are first ground in the high-pressure roll mill and then in the ball mill. Experimental as well as simula-

tion results indicate that optimum specific energy per ton of product of desired fineness could be achieved by operating each of the mills in appropriate regimes. The optimal operating conditions and the energy partitioning would be dictated by the material properties and fineness of product.

## REFERENCES

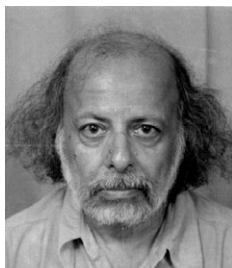
- [1] L. Bass (1954), *Zeits. Angew. Math. Phys.*, 5, 283-292.
- [2] R. P. Gardner and L. G. Austin (1962), Symposium Zerkleinern, 1st European Symposium on Comminution, ed. H. Rumpf and D. Behrens, Verlag Chemie, Weinheim, 217-248.
- [3] K. J. Reid (1965), *Chemical Engineering Science*, 20, 953-963.
- [4] J. A. Herbst and D. W. Fuerstenau (1968), *Trans. SME/AIME*, 241, 528-549.
- [5] D. F. Kelsall, K. J. Reid, and C. J. Stewart (1969-1970), *Powder Tech.*, 3, 170-179.
- [6] J. A. Herbst and D. W. Fuerstenau (1973), *Trans. SME/AIME*, 254, 343-347.
- [7] G. A. Grandy and D. W. Fuerstenau (1970), *Trans. SME/AIME*, 247, 348-354.
- [8] R. R. Klimpel (1982), *Powder Technology*, 32, 267-277.
- [9] S. Malghan and D. W. Fuerstenau (1976), in *Zerkleinern, Dechema-Monographien*, Verlag Chemie, GMBH, 613-630.
- [10] D. W. Fuerstenau, K. S. Venkataraman and B. V. Velamakanni (1985), *International Journal of Mineral Processing*, 15, 251-267.
- [11] K. Schoenert (1988), *International Journal of Mineral Processing*, 22, 401-412.
- [12] D. W. Fuerstenau and P. C. Kapur (1995) *Powder Technology*, 82, 51-57.
- [13] D. W. Fuerstenau, A. Shukla and P. C. Kapur (1991), *International Journal of Mineral Processing*, 32, 59-79.
- [14] A. De (1995), *Modeling and Optimization of Fine Grinding of Minerals in High-Pressure Roll Mill/Ball Mill Hybrid Comminution Circuits*, Ph.D. Thesis, University of California, Berkeley.
- [15] D. W. Fuerstenau and J. Vazquez-Favela (1997), *Minerals and Metallurgical Processing*, 13, 41-48.

## Author's short biography



### D. W. Fuerstenau

D. W. Fuerstenau received his Sc.D. degree in metallurgy (mineral engineering) from MIT in 1953. After a period in industry, he joined the faculty in the Department of Materials Science and Engineering of the University of California at Berkeley in 1959, where he continues as Professor in the Graduate School. He has been actively involved over the years in research on the processing of minerals and particulate materials, including extensive research on interfacial phenomena in these systems. Areas in which he has worked extensively include comminution, agglomeration, mixing, flotation and applied surface and colloid chemistry.



### P. C. Kapur

P. C. Kapur received his M. S. degree in 1964 and his Ph.D. degree in materials science and engineering in 1968 from the University of California at Berkeley. After working at the Colorado School of Mines Research Foundation, he returned to India as Professor of Metallurgical Engineering at the Indian Institute of Technology at Kanpur. Since retiring from IIT Kanpur in 1995, he has been on the staff of Tata Research Development and Design Centre as Consulting Advisor. He is widely recognized for his extensive research on the processing of particulate materials, mainly agglomeration, comminution and size distributions, and particularly the mathematical modeling and computer simulation of processing operations.



### A. De

A. De received his B. Tech. degree in 1981 and M. Tech. degree in 1983 in metallurgical engineering from the Indian Institute of Technology at Kanpur. In 1994, he received his Ph.D. in materials science and engineering from the University of California at Berkeley. At Berkeley his major research efforts were directed towards the comminution of coal, including experimental investigations and mathematical modeling. He currently is Senior Software Engineer with ABB, Inc.

# Persistence of Granular Structure during Compaction Processes<sup>†</sup>

William J. Walker, Jr.

New York State Center for Advanced Ceramic  
Technology at Alfred University\*

## Abstract

*Compaction of granulated powder is a common forming process used in the ceramics industry. Glass spheres were used as a model system to investigate granule failure during die compaction. Stresses within an assembly of spheres follow a network of pathways. Results demonstrate the statistical nature of granule failure during compaction, with some granules failing at very low applied pressures while a large fraction persist at even the highest applied loads. At high compaction pressures, size distributions of compacted spheres were seen to approach the Dinger-Funk distribution for maximum packing. In the limiting case of maximum density, the Dinger-Funk equation predicts 33% of the volume of granules will have sizes in the range of the initial size distribution.*

## 1. INTRODUCTION

Die compaction of granulated powder is a common forming process used in ceramics and other industries. Granulation of fine powder results in free flowing feed material with controlled composition and properties that can be easily used in high speed presses. In ceramic processes, application of pressure consolidates the granulated material into a green body, which is subsequently sintered. Artifacts of the granule structure may persist as pores and laminations after compaction, and remain as defects in the sintered microstructure. Such defects can be detrimental to the properties of the final part. Thus it is desirable to eliminate the granule structure during compaction. In this work, statistical analysis of the fragmentation of glass beads during die compaction was used as a model granular system to achieve a better understanding of persistent granular structures in compacts.

Compaction of granulated powder occurs in three pressure-dependent stages [1]. In Stage I, granule rearrangement at low pressures results in a small increase in density of the granular assembly. Above an apparent yield pressure  $P_y$ , which marks the onset of Stage II, the interstitial pores between granules

(intergranular pores) are reduced in size as the granules break down or deform, resulting in a linear increase in density with  $\log$  (compaction pressure). In Stage III, the intergranular pores are mostly eliminated, and particle rearrangement within the granules causes increased densification at high pressures. The types of granule-related defects that may persist after compaction include persistent intergranular pores and poorly joined interfaces between granules.

An assembly of granulated powder has a hierarchical structure consisting of packed granules, which are comprised of packed particles. The pore size distribution is bimodal; large intergranular pores are formed from the packing of the granules and small intragranular pores are formed from the packing of the primary particles. During compaction, the intergranular pores are reduced in size, and largely eliminated, as granules deform in response to applied pressure in Stage II and Stage III. The intragranular pores are eliminated during sintering. However, the size of persistent intergranular pores is sufficiently large that these pores cannot be removed by the sintering process. Consequently these pores can persist into the sintered part. Interfaces between granules may persist as well when the granule surfaces do not meld together. Uematsu [2] has developed an optical microscopy method that is useful for observing persistent granule structures. By immersing a thin section of sintered material in a liquid with refractive index similar to that of the ceramic powder, the per-

\* Alfred, NY 14802

<sup>†</sup> Accepted: September 9, 2003

sistent interfaces can be clearly observed. The results clearly reveal a granule structure that persists after sintering.

The coarse fraction of the granule size distribution has been shown to be responsible for the largest defects that persist after compaction. Strength testing is a very effective way to locate large defects. With  $10^9$  granules per  $\text{cm}^3$ , statistically there will be cases where the largest granules are positioned in such a way to create large triangular or tetrahedral pores. In unfired compacts of spray-dried alumina, Mosser [3] demonstrated that strength could be reduced through the introduction of oversized granules. Walker and Reed [4] found that, with a constant maximum granule size, the number of granules in the coarse end of the distribution was the dominating factor responsible for the formation of strength-limiting defects in sintered alumina, even when the total number of defects could be changed through changes in the strength and density of the granules. Fractography confirmed that the strength-limiting defects were granule related.

Stress transmission during compaction has been modeled by a number of researchers using a continuum approach [1]. This method provides a good macroscopic description of the pressure gradients that occur within compacts and the resulting density gradients that are observed. However, a discrete granule approach provides better insight into granule deformation and the origin of granule-related defects. Computer simulation [5] and a photoelastic disk method [6] have been used to model stress transmission through a packed bed of discrete granules. Stress distributions in photoelastic materials are easily observed as color changes when viewed under polarized light. Thus, stress distributions through a two-dimensional cell packed with photoelastic disks can be directly observed. Results from both computer simulations and photoelastic disk studies show that stress is transmitted through a granular material along a branched network of pathways which concentrate stress in some disks and bypass others. Flow occurs from sliding of block-like regions along slip planes. These methods are effective for modeling stress distributions below the elastic limit of the granules (Stage I). Yielding of granules due to brittle failure or plastic deformation, which occurs at approximately  $P_y$ , results in rearrangement of localized stress distributions.

In this work, glass beads were used to model granule breakdown during compaction. Previous studies using glass beads have been conducted by the author

[7-9] and by others [10]. The glass beads are spherical, as are spray-dried granules, and were selected to be of similar size distribution to granules commonly used for processing of ceramics. Glass beads are elastic, brittle, have low bulk compression and fail by brittle fracture. Granulated powder consists of porous agglomerates, which exhibit moderate bulk compression, and may only be elastic at low loads. While granules may be brittle they are often engineered to be plastic and thus deform rather than fracture under load.

## 2. EXPERIMENT

Glass beads (3M Company, St. Paul, MN) with a log normal size distribution (mean diameter  $85.5 \mu\text{m}$  and geometric standard deviation 1.25) were compacted in a steel die using a laboratory press (Laboratory Press Model M, Fred S. Carver, Inc., Menomonee Falls, WI.) at pressures ranging from 17.5 MPa to 1.05 GPa. The die had a cylindrical cavity with diameter 12.7 mm, and was fabricated in two halves that could be separated to facilitate removal of the specimens without an ejection step. Size distributions of the compacted beads were measured using laser scattering (Microtrac 9200, Leeds and Northrop, North Wales, PA) after dispersing the compacted material in water using ultrasound.

Compacts were vacuum infiltrated with epoxy and polished cross-sections were prepared and evaluated with a scanning electron microscope. For specimens pressed to low pressure, it was necessary to modify the die to allow a portion of one punch to be removed so the epoxy could be introduced while the compact was still constrained in the die.

## 3. RESULTS

**Figure 1** shows that the glass beads followed similar compaction behavior to that of granulated ceramic powders.  $P_y$  was 170 MPa, which is  $10^2$  to  $10^3$  that of typical spray-dried granules. This large difference is because of the much higher strength of the glass beads compared to that of a granulated powder. Just as in the case of granulated powder, a small increase in density was observed below the  $P_y$  from rearrangement of the spheres; and above  $P_y$ , density increased rapidly as spheres were fractured. Stage III, attributed to bulk compression of granules, was not observed in the case of the glass beads.

Some beads were observed to fracture at pressures as low as 53 MPa, as is shown in **Figure 2(a)**. As



pressure was increased, larger numbers of fragments were observed, but some large spheres remained intact at the highest compaction pressures tested, as is shown in **Figure 2(b)**. The internal structure of the compacts is seen by examining polished cross-

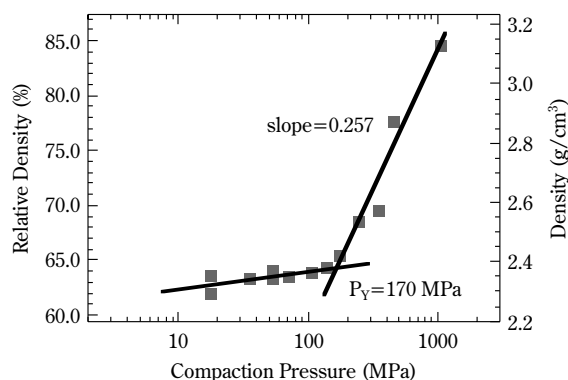
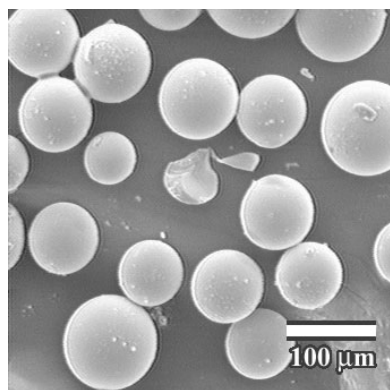
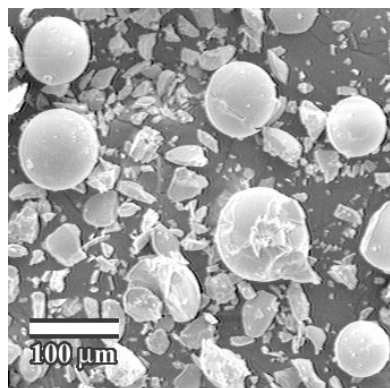


**Fig. 1** Compaction diagram of glass beads.



(a)

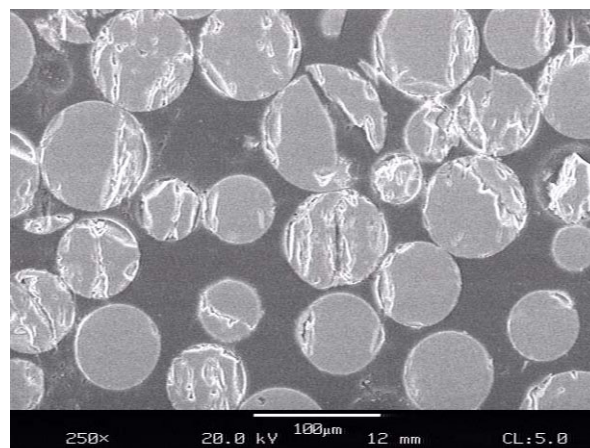


(b)

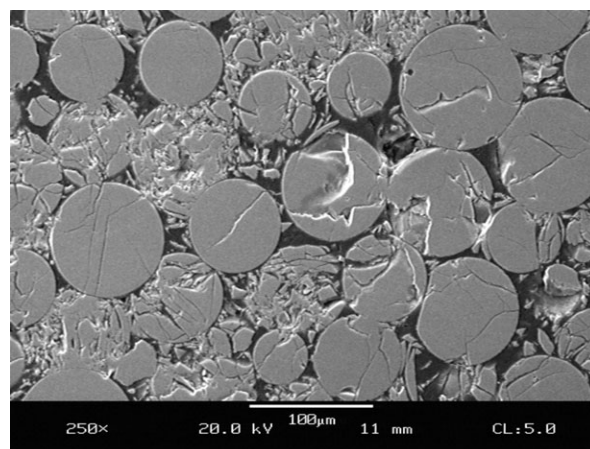
**Fig. 2** Glass beads compacted to (a) 53 MPa and (b) 420 MPa.

sections of compacts shown in **Figures 3(a)** and **3(b)**. Evidence of stress pathways through the assembly of spheres is evident even at low pressure. Large spheres persist intact at high pressures. Densification occurs as some spheres fracture and their fragments rearrange to fill packing voids between the spheres that persist intact.

With the large number of spheres ( $\sim 10^9/\text{cm}^3$ ) that are present in a single compact, simple observation does not give an accurate indication of trends involving so many particles. Particle size analysis provides a statistical method. **Figure 4** shows the change in particle size distribution of the glass beads at different compaction pressures. The particle size distribution of the uncompacted glass beads was log normal. As pressure was increased, the number of particles in



(a)



(b)

**Fig. 3** Polished cross sections of glass beads mounted in epoxy: (a) compaction pressure 170 MPa, relative density 64%, (b) compaction pressure 1.05 GPa, relative density 84.6%.

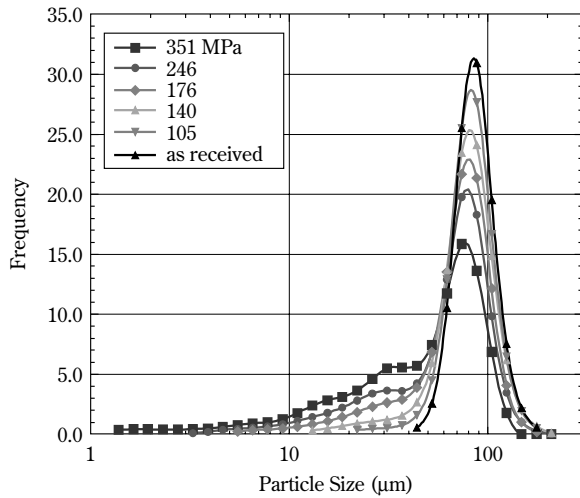


**Fig. 4** Change in particle size distribution of glass beads as a result of compaction.

the 70 to 110  $\mu\text{m}$  size range decreased and a tail of fine particles in the 10 to 60  $\mu\text{m}$  range increased as more beads became fractured.

## 4. DISCUSSION

### 4.1 LOW PRESSURE BEHAVIOR

A more accurate interpretation of the change in size distribution can be obtained by plotting 10<sup>th</sup>, 50<sup>th</sup> and 90<sup>th</sup> percentile sizes ( $a_{10}$ ,  $a_{50}$  and  $a_{90}$ , respectively) as a function of compaction pressure (see **Figure 5**). The size distribution remained constant at low pressures. At a compaction pressure of 60 MPa, which is about  $P_y/3$ , the size distribution began to change as glass beads fractured in response to the applied pressure. The median size and the fine end of size distribution both began to decrease at about 60 MPa ( $\sim P_y/3$ ). The coarse end of size distribution remained constant until a point near  $P_y$  ( $\sim 150$  MPa). As pressure was increased above  $P_y$ , the entire distribution shifted toward smaller sizes as more spheres became fractured. The increase in fines in the size distribution at compaction pressures below the point where the coarse end of the distribution begins to change indicates that smaller granules begin to fail at lower applied pressure, and that the larger spheres are more likely to remain intact at low compaction pressures. Similar behavior has been reported by Deis and Lannutti [11], who observed a tendency for small spray-dried alumina granules to yield at lower pressures than large granules. This behavior can be explained by considering Hertzian contact stresses

between spheres.

Granules will act as elastic spheres at low loads. Above some critical level of stress, yielding will occur as granules fracture or deform. Within an assembly of granules, yielding of any individual granule depends on the local loading conditions resulting from stresses transmitted from neighboring granules. Below the elastic limit, the level of stress in any individual granule will follow Hertzian behavior [12], and be dependent on the locally transmitted load  $P$ , the diameters of the two contacting spheres  $a_1$  and  $a_2$ , and the elastic modulus of the granules  $E$ . The maximum compressive stress  $\sigma_c$  occurs along the loading axis through the spheres and is given by

$$\sigma_c = 0.616 \sqrt[3]{\frac{PE^2}{K_a^2}} \quad (1)$$

where

$$K_a = \frac{a_1 a_2}{a_1 + a_2}. \quad (2)$$

The maximum tensile stress occurs radially at the edge of the contact area, and is given by

$$\sigma_t \approx 0.133 \sigma_c \quad (3)$$

and the maximum shear stress is given by

$$\tau_{\max} \approx \frac{1}{3} \sigma_c \quad (4)$$

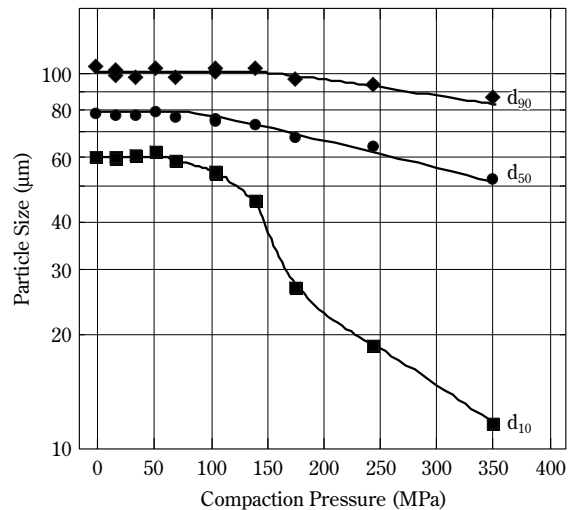


**Fig. 5** During compaction, the median size of the distribution ( $a_{50}$ ) and the fine end of size distribution ( $a_{10}$ ) begin to decrease in size at about 60 MPa ( $\sim P_y/3$ ). The coarse end of size distribution ( $a_{90}$ ) begins to change near  $P_y$  ( $\sim 150$  MPa).

and occurs along the loading axis at a distance of  $r/2$  below the contact surface, where  $r$  is the radius of the contact area, given by

$$r = 0.881 \sqrt[3]{\frac{PK_a}{E}} \quad (5)$$

Since the maximum tensile and shear stresses are equal to the maximum compressive stress multiplied by some constant, a generalized equation can be written

$$\sigma_i \propto \left( \frac{P}{K_a^2} \right)^{1/3} \quad (6)$$

where  $i$  is compression, tension or shear.

Since the force through an assembly of spheres is not uniformly transmitted, but instead follows a network of pathways, some spheres will experience much higher stresses than others. For spheres of non-uniform size, the maximum stress in each sphere will depend on the sizes of both spheres in a pair and the locally transmitted load.

**Figure 6** illustrates the range of stresses that might be observed in an idealized single chain of granules within an assembly. In this idealized example, the spheres are arranged in such a way that the load is transmitted along a single straight line which passes through the center of several granules, with none of the load being transmitted to neighboring granules. Since the magnitude of the stress resulting from a load being transmitted by the contact of two spheres is dependent on the diameters of both spheres, the highest stresses result from the contact of two small spheres and the lowest stresses result from the contact of two large spheres. Thus it would be expected that large spheres are less likely to experience the level of stress required for deformation or fracture to occur before smaller granules yield, rearranging the local distribution of stress pathways. The figure also shows that the level of stress at the contact between a granule and the die surface is very low. In the case of a sphere and a flat surface,  $a_2$  is infinite and  $K_a = a_1$ . Elimination of surface roughness caused by granule artifacts at the surfaces of pressed ceramic components is a common concern. Several researchers have achieved limited success in efforts to reduce surface roughness [3, 13].

The spray-dried granules used in the processing of ceramic material are themselves assemblies of fine particles and will thus fail in tension or shear. If the yield strength of the matrix comprising the granules is the same, regardless of the size of the spheres, failure would occur in each of the spheres. However,

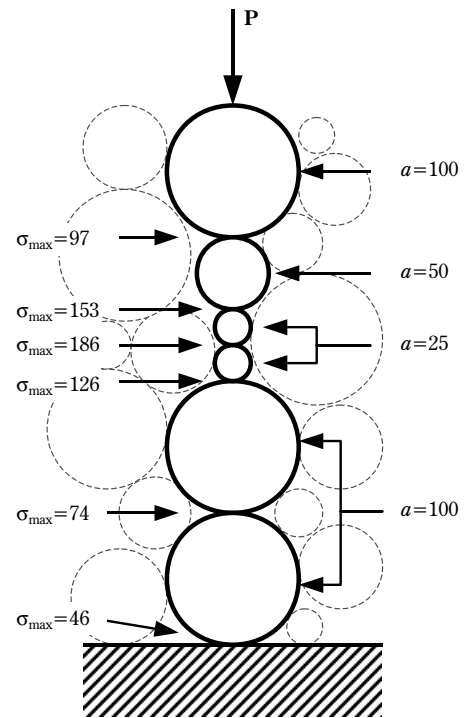


**Fig. 6** Schematic of a stress pathway in an assembly of granules. The load follows a chain of spheres of different sizes. The relative stress (in arbitrary units) in the contacting spheres is indicated.

since the volume where maxima occur in both shear and tensile stresses is related to the contact area (given in Eqn. 5), a larger relative volume of small granules is affected by the stress field, and small granules would be expected to experience more severe damage as a result.

The assumption that the strength of the matrix material is independent of granule size may not always be valid. Spray-dried ceramic powders are commonly processed using organic additives such as binders in order to impart lubricity during compaction and green strength after compaction. It has long been suspected, and recently been demonstrated [14] that some binders migrate to the granule surfaces during drying giving the granules hard shells. Larger granules, with more binder to migrate, might have thicker and thus harder shells than smaller granules, making the larger granules relatively stronger, and less prone to deformation. It has also been suggested that smaller granules might be subject to a different heating profile than large granules during drying [15]. If the trajectory and residence time of the drying droplets is constant with respect

to droplet size, the smaller droplets will dry more rapidly, and the protection from temperature of evaporative cooling on the organic binder will be shortened. Consequently, smaller granules may become harder due to temperature effects on the binder. Neither the temperature effect nor the binder-shell thickness effect has been experimentally verified as mechanisms that produce a size-dependence on granule strength.

## 4.2 HIGH PRESSURE BEHAVIOR

By recognizing that size distributions shown in **Figure 5** are bimodal with the coarse fraction consisting of largely unfractured beads and the fine fraction consisting of fractured fragments, it is possible to deconvolute the distribution curves (see **Figure 7**) into a log normal mode consisting of unfractured spheres, and an asymmetrical mode consisting of fragments. In **Figure 8**, the amount of material in each mode is plotted with respect to compaction pressure. The amount of material in each fraction changes rapidly between pressures of about 75 and 400 MPa. At higher pressures, the rate of change decreases. Above about 500 MPa the amount of material in each fraction becomes constant with respect to compaction pressure, with the size distribution consisting of about 40% coarse and 60% fine. Thus, the increase in density during compaction is a result of fragmentation of 60% of the material while about 40% of the volume of the compact consists of granules which are relatively unchanged from the precursor material. These results are consistent with the behavior observed using granulated alumina and other ceramic powders [2, 4,

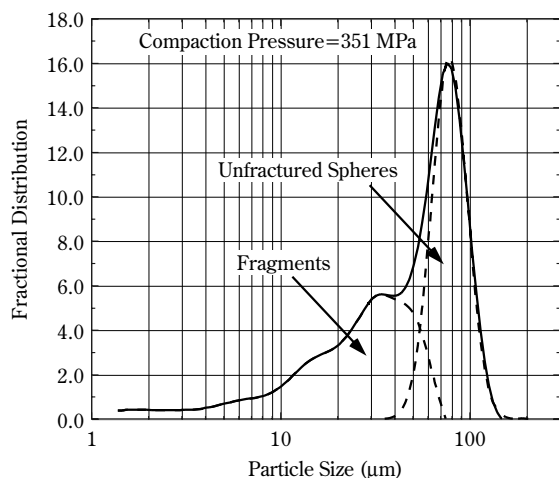


**Fig. 7** Bimodal size distribution of compacted glass spheres.

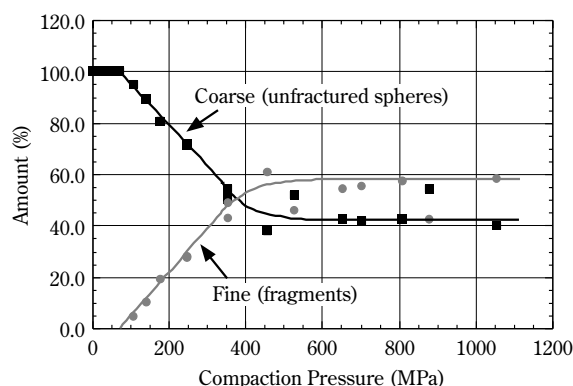


**Fig. 8** As compaction pressure is increased, the amount of unfractured spheres decreases as fragments are formed, but reaches a constant value of about 40% at high pressure.

8]. However, in the case of alumina, it was not possible to quantitatively describe the degree to which the precursor granular structure persisted after compaction.

As compact density increases with increasing applied pressure, the particle size distribution changes by continued fragmentation of the glass beads. The particle size distribution must necessarily change in the direction toward higher packing density. Therefore, predictions regarding the breakdown of granules during compaction can be made based on models for continuous size distributions that result in maximum packing.

Andreasen [16] postulated that maximum packing density would follow the distribution

$$F(a) = \left( \frac{a}{a_{\max}} \right)^m \quad (7)$$

where  $F(a)$  is the size cumulative distribution function,  $a$  is particle size,  $a_{\max}$  is the maximum particle size and the exponent  $m$  is in the range of 0.33 to 0.50. The basis for Andreasen's model was a fractal-like concept that in order to achieve maximum packing with a continuous size distribution, the relative sizes of neighboring particles would be the same for particles of any size. The range for the exponent was determined experimentally.

Dinger and Funk [17] recognized that any real size distribution must have a finite lower size limit  $a_{\min}$  and modified Andreasen's equation to

$$F(a) = \frac{a^m - a_{\min}^m}{a_{\max}^m - a_{\min}^m} \quad (8)$$

Computer simulation indicated that maximum pack-



ing of spheres would occur when the exponent  $m=0.37$ . Thus, it is expected that during compaction of brittle granules, the size distribution will approach Equation (8) with exponent  $m=0.37$  as the applied pressure increases.

**Figure 9** shows the size distribution of the glass beads along with calculated distributions from Eqn (8) using  $a_{\max}$  and  $a_{\min}$  from the experimental data, and various exponents. It can be seen that as pressure is increased, the slope of the distribution curve decreases. This change in slope corresponds to a decrease in the exponent  $m$  from Eqn. 8. At the highest compaction pressure that was tested, the data closely follows Eqn. 8 with exponent  $m=1$ . With further increase in compaction pressure, it is expected that the exponent  $m$  would continue to decrease until  $m=0.37$ , at which point maximum packing density would be achieved.

As previously discussed, the amount of material that remained largely unchanged from the initial size distribution was about 40% by weight over a range of the highest compaction pressures tested. In the limiting case of maximum packing density at  $m=0.37$ , the amount of material that would remain in this size range would be 33% by volume. Thus it can be concluded that in the case of brittle granules, 33% or more by volume of the granules will persist largely

intact, even at the highest compaction loads. The increase in packing density of the compact is a result of disruption and rearrangement of 67% or less of the mass of the granules.

Algebraic manipulation of an equation developed earlier by Furnas [18] results in an equation of the same form as Equation (8) with the exponent  $m=\log V^{(b/c)}$  where  $V$  is the pore volume of a single sieve fraction (with  $\sqrt{2}$  sieve size ratio) of particles,  $b$  and  $c$  are constants based on the width of the distribution. The values of  $b$  and  $c$  are based on experimental data, and can be determined from graphs presented in Ref 18. Based on  $a_{\min}$  and  $a_{\max}$  of the distribution obtained in the present work, the Furnas model predicts that maximum packing will occur with  $m=0.037$  (also shown in **Figure 9**). This would result in 18% of the volume of the particles remaining in the size range of the original distribution – a significant improvement over the prediction based on Dinger and Funk's  $m=0.37$ . However, since Furnas's work is based on experimental packing of fine particles, his results are subject to error due to factors that hinder packing, such as friction between particles and agglomeration of fines due to surface forces.

The analysis by Dinger and Funk was based on a continuous size distribution of spheres. In this experiment, the size distribution consists of spherical particles only at the coarse end of the distribution, and fragments of irregular shape throughout the medium to fine range. Dinger and Funk did not address the question of particle shape. Zheng [19] expanded on the work of Dinger and Funk and addressed the question of a size-dependence on particle shape. Their analysis considered the Dinger-Funk distribution as a mixture of an infinite number of discrete size fractions. The basic model for packing discrete size classes was also developed by Furnas [20]. Maximum packing occurs when the interstitial pores of a coarse fraction are filled by a finer fraction of size that can fill the pores without disrupting the packing of the coarser particles. The resulting pores are filled by a third even finer fraction, and so on. Zheng considered that a continuous size distribution following Equation 8 could be separated into an infinite number of Furnas packing sequences. He related the exponent  $m$  to the pore fraction  $\phi$  of packed monosized particles taken from the distribution:

$$m = - \left\{ \frac{\log \phi}{\log R} \right\} \quad (9)$$

where  $R$  is a constant related to the size ratio needed for unhindered packing of two discrete size classes.

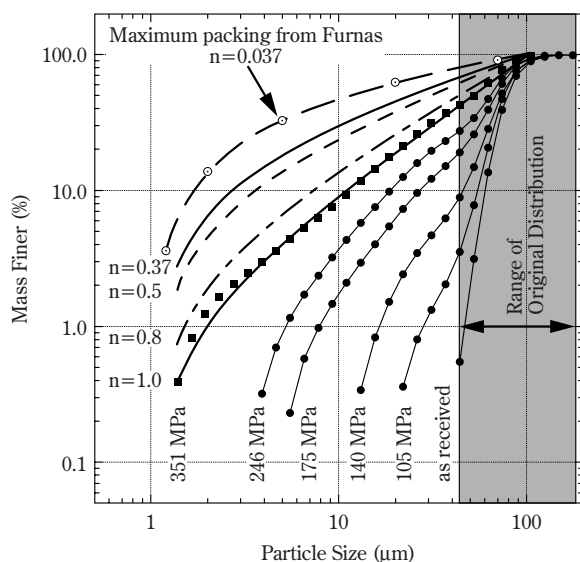


**Fig. 9** As pressure is increased, the size distribution of compacted spheres approaches the Dinger-Funk distribution (Eqn. 8) with exponent  $n=1$ . Maximum packing is predicted by Dinger and Funk when  $n=0.37$ . Maximum packing is predicted by Furnas when  $n=0.037$ .



When particle shape is constant across the entire size distribution,  $\phi$  is the same for each size class. Spherical particles have the highest packing factor, and thus the lowest  $\phi$ , and consequently, the highest value for  $m$  in the Dinger-Funk equation. As particle shape deviates from spherical, packing factor decreases and  $\phi$  increases, thus the exponent  $m$  would be expected to decrease following Equation 9. In the case where  $\phi$  is not constant across the distribution, They suggest that an average exponent for the different size classes will describe the conditions for maximum packing of the system. In the present work, the coarse end of the distribution consists of spheres, and thus has the highest packing factor. The coarse spheres will be surrounded by irregular medium and fine particles that pack to somewhat lower density, thus  $m$  would be less than 0.37 according to Zheng.

The work on particle packing by Andreasen and by Furnas is based in part on experimental data, and thus interparticle forces may have hindered rearrangement of particles and prevented maximum packing. Dinger and Funk utilized a computer simulation and thus were able to eliminate interparticle forces. They found that equivalent maximum packing could be obtained using a variety of packing algorithms. In the present work, changes in particle size distribution occur as a means of reducing bulk volume in response to an applied load. It is not known whether the same packing density would be obtained if the compacts were disrupted and the particles repacked, even if interparticle forces could be eliminated. However, the application of a load provides a driving force to achieve maximum packing density, by both particle rearrangement and by the fracture of particles into finer particles. By this path, a particle size distribution is obtained that will result in maximum packing for a given load. Such a size distribution will contain a significant fraction of coarse particles.

## SUMMARY AND CONCLUSIONS

During die compaction of granulated ceramic powders, the load is transmitted along a branched network of contacting granules, concentrating the stress in some granules while others are bypassed. As the applied load is increased, granules fail by deformation or fracture, the network of stress pathways rearranges to some extent, and the packing density of the granular assembly increases. However, evidence of the granular precursor material can be seen to persist in the microstructure of unfired and fired ceramics prepared by compaction. Glass spheres were used

as a model granular system to investigate the degree to which the granular structure persists during die compaction.

The state of stress within any individual granule depends on contact stresses from the locally transmitted load. The magnitude of the load, the diameter of the sphere, and the diameter of the neighboring spheres which transmit the load are all factors determining the state of stress within a sphere. Within a single chain of contacting spheres, those with smaller diameter experience higher levels of stress and will thus fail at lower loads. Within an assembly of a large number of spheres, a general trend observed is that smaller granules fail at lower compaction loads.

The size distribution of the glass spheres changed with applied compaction load as the spheres failed due to fracture. As the compaction load approached the apparent yield pressure of the granular assembly, a tail of fines was seen in the particle size distribution before any change is observed in the coarse fraction, indicating that fines are formed due to fragmentation of smaller spheres in the initial sample. As pressure was increased, the size distribution became bimodal, consisting of unfractured spheres in the coarse fraction, and fractured fragments in the fine fraction. The amount of material in each fraction changed rapidly during the early stages of compaction, but became constant at higher loads, with about 40% of the volume consisting of unfractured spheres. The size distribution approached that of a Dinger-Funk distribution with an exponent of  $m=1$ . In the limiting case of  $m=0.37$ , which Dinger and Funk determined to be the distribution with maximum packing density based on computer simulation, 33% of the granules would persist nearly intact.

## ACKNOWLEDGEMENTS

This work was supported in part by the New York State Office of Science, Technology and Academic Research through the New York State Center for Advanced Ceramic Technology at Alfred University.

## NOMENCLATURE

$a$	=granule or particle diameter	( $\mu\text{m}$ )
$a_{max}$	=maximum granule or particle size	( $\mu\text{m}$ )
$a_{min}$	=minimum granule or particle size	( $\mu\text{m}$ )
$b$	=constant related to width of size distribution	(—)
$c$	=constant related to width of size distribution	(—)

$E$	=elastic modulus	(Pa)
$F(a)$	=cumulative size distribution	(—)
$K_a$	=effective diameter of two spheres of unequal diameter	( $\mu\text{m}$ )
$m$	=exponent	(—)
$P$	=load	(N)
$P_y$	=apparent yield pressure	(Pa)
$R$	=size ratio needed for unhindered packing of fine particles into the interstices of a bed of packed large particles	(—)
$V$	=pore fraction of packed particles	(—)
$\phi$	=pore fraction of packed monosized particles	(—)
$\sigma$	=stress	(Pa)
$\tau$	=shear stress	(Pa)

## REFERENCES

- [1] J.S. Reed, *Principles of Ceramic Processing*, 2<sup>nd</sup> Ed., pp. 425-33, John Wiley and Sons, Inc., New York, 1995.
- [2] K. Uematsu, T. Sato, D. Shoji, N. Uchida, Z. Kato, S. Tanaka, M. Naito and T. Hotta, "Infrared Microscopy for Innovative Research in Ceramics;" pp. 157-171 in *Fractography of Glasses and Ceramics IV*, Ceramic Transactions, vol. 122. Edited by J.R. Varner and G.D. Quinn. The American Ceramic Society, Inc., Westerville, OH 2001.
- [3] B.D. Mosser III, "Processing Steps to Eliminate Green and Fired Defects in Dry Pressed Alumina Substrates;" M.S. Thesis, Alfred University, Alfred, New York, 1987.
- [4] W.J. Walker, Jr., J.S. Reed and S.K. Verma, "Influence of Granule Character on Strength and Weibull Modulus of Sintered Alumina," *Journal of the American Ceramic Society*, **82** [1] 50-56 (1999).
- [5] P.A. Cundall, A. Drescher and O.D.L. Strack, "Numerical Experiments on Granular Assemblies; Measurements and Observations," pp. 355-70 in *IUTAM Symposium on Deformation and Failure of Granular Materials*, Delft, Balkema, 1982.
- [6] A. Drescher and G. de Josselin de Jong, "Photoelastic Verification of a Mechanical Model for the Flow of a Granular Material," *Journal of the Mechanics and Physics of Solids*, **20** 337-51 (1972).
- [7] W.J. Walker, Jr. and J.S. Reed, "Granule Fracture During Powder Compaction," *American Ceramic Society Bulletin*, **78** [6] 53-57 (1999).
- [8] W.J. Walker, Jr., "Persistence of Granular Structure During Die Compaction of Ceramic Powders;" in *The Granular State*, Material Research Society Symposium Proceedings, vol. 627. The Materials Research Society, Warrendale, PA, 2001.
- [9] W.J. Walker, Jr., "Granule Structure Evolution During Powder Compaction of Ceramic Materials;" to be published in *Granular Materials Based Technologies*, Materials Research Society Symposium Proceedings, vol. 729. The Materials Research Society, Warrendale, PA, 2003.
- [10] S.J. Glass, "A Comparison of Pressure Compaction and Diametral Compression Tests for Determining Granule Strengths;" pp. 203-215 in *Science, Technology and Commercialization of Powder Synthesis and Shape Forming Processes*, Ceramic Transactions, vol. 62. Edited by J.J. Kingsley, C.H. Schilling and J.H. Adair. The American Ceramic Society, Westerville, OH, 1996.
- [11] T.A. Deis and J.J. Lannutti, "X-Ray Computed Tomography for Evaluation of Density Gradient Formation During the Compaction of Spray-Dried Granules," *Journal of the American Ceramic Society*, **81** [5] 1237-1247 (1998).
- [12] R.J. Roark and W.C. Young, *Formulas for Stress and Strain*, 5th ed. (McGraw-Hill Book Company, New York, 1975), pp. 513-29.
- [13] B.M. Schulz, U. Kim, H. Lee and W.M. Carty, "Evaluation of Surface Finish Quality from Various Dinnerware Forming Techniques," *Ceramic Engineering and Science Proceedings*, **23** [2] 19-27 (2002).
- [14] Y. Zhang, X.X. Tang, N. Uchida, and K. Uematsu, "Binder Surface Segregation During Spray Drying Of Ceramic Slurry," *Journal of Materials Research*, **13** [7] 1881-87 (1998).
- [15] J. Doran and W.M. Carty, "The Contribution of Moisture and Polymeric Additives to the Flow and Compaction of Spray-Dried Clay Bodies;" Paper #MEWW-26-96, presented at the 98<sup>th</sup> Annual Meeting of the American Ceramic Society, Indianapolis, IN, April 17, 1996.
- [16] A.H.M. Andreasen and J. Andersen, "Über die Beziehung zwischen Kornabstufung und Zwischenraum in Produkten aus losen Kornern," *Kolloid-Z*, **50** 217-228 (1930).
- [17] J.A. Funk and D.R. Dinger, *Predictive Process Control of Crowded Particulate Suspensions*, Klumar Academic Publishers, Norwell, Massachusetts, 1994.
- [18] C.C. Furnas, "Grading Aggregates, I, Mathematical Relations for Beds of Broken Solids of Maximum Density," *Industrial and Engineering Chemistry*, **23** [9] 1052-58 (1931).
- [19] J. Zheng, P.F. Johnson and J.S. Reed, "Improved Equation of the Continuous Particle Size Distribution for Dense Packing," *Journal of the American Ceramic Society*, **73** [5] 1392-98 (1990).
- [20] C.C. Furnas, "Relations Between Specific Volume, Voids and Size Composition in Systems of Broken Solids of Mixed Sizes," *U.S. Bureau of Mines Reports of Investigations*, No. 2894 (1928).

## Author's short biography



### **William J. Walker, Jr.**

Dr. William J. Walker, Jr. is Ceramic Research and Development Director at the Champion Ignition Products Division of Federal-Mogul Corporation, in Toledo, Ohio. Prior to his current position, Dr. Walker was an Assistant Director at the New York State Center for Advanced Ceramic Technology at Alfred University, in Alfred New York. His area of research specialization is ceramic powder processing, including colloidal behavior and rheology of crowded suspensions, spray-drying, powder compaction and near-net shape fabrication. Much of his research has focused on the use of organic processing additives in ceramic powder processing. He has over 50 presentations at international conferences to his name, and has authored over 20 publications. He holds one United States patent. Dr. Walker has a Ph.D. in Ceramics from the New York State College of Ceramics at Alfred University.

# Characterization of a Nanosized Iron Powder by Comparative Methods<sup>†</sup>

L.J. Kecskes, R.H. Woodman,  
S.F. Trevino, B.R. Klotz, S.G. Hirsch  
and B.L. Gersten\*

U.S. Army Research Laboratory  
Weapons and Materials Research Directorate  
Aberdeen Proving Ground\*\*

## Abstract

*Fe nanopowder, derived from microwave plasma synthesis (Materials Modifications Inc., Fairfax, VA), was obtained and characterized for particle size and size distribution. The methods used included dynamic light scattering (DLS), static laser scattering (SLS), surface area and size by Brunauer, Emmett, and Teller (BET) analysis, small angle neutron scattering (SANS), neutron diffraction (ND), x-ray diffraction (XRD), field emission scanning electron microscopy (FESEM), and transmission electron microscopy (TEM). Based on these methods, it was concluded that the Fe powder was composed of nanosized particles, but in micrometer-sized aggregates. DLS indicated a mean agglomerate size with a single mode distribution of  $70 \pm 6$  nm. In contrast, SLS revealed a wide bimodal distribution ranging from 0.5 to 20  $\mu$ m. The mean particle sizes that resulted from BET and XRD analyses were 60 nm and 20 nm, respectively. SANS, in combination with ND, determined that the powder had a bimodal distribution of mean size 24 and 64 nm. TEM and FESEM confirmed that the powder is composed of 50-80 nm particles that are found in large, dendritic particle agglomerates that are on the order of micrometers. The information derived from these results indicates that all of the selected methods were helpful in making an accurate and complete characterization of the powder.*

## 1. Introduction

Fe powders have many applications that may be enhanced with nanosized particles. These include the catalysis of carbon nanotubes with superior electronic properties [1] and magnetorheological fluids [2]. Also, nanosized feed material can lower the consolidation temperature and improve the structural properties of iron bodies prepared by powder metallurgical techniques [3]. However, in order to assess the contributions of nanopowders compared with larger-sized precursor powders, the particle morphology, size, and distribution must be evaluated. A number of books and articles address the topic of particle size measurement [4-6]. Only a few of these papers have dealt with the difficulties and limitations encountered in determining the particle size of nanopowders [7].

Many of the currently available particle size measurement techniques were designed for micrometer- and submicrometer-sized particles. While established off-the-shelf, canned methods offer ease of operation and minimal sample preparation, they still have limited applicability to nanopowders. For instance, field emission scanning electron microscopy (FESEM) and other electron or optical microscopy techniques analyze small samples that may not be representative of the powder. In gas adsorption methods such as Brunauer, Emmett, and Teller (BET) analysis, measurement can be done on a representative sample. However, adsorption of nitrogen or capillary condensation in interparticle voids can result in erroneous measurements [8].

Light scattering methods (e.g., dynamic light scattering [DLS] and static laser scattering [SLS]) have been developed for rapid measurement of particle size and size distributions of submicrometer-sized powders. Such methods measure either the spatial or the temporal variation of scattered light. In SLS, parti-

\* Now at Queen's College, Flushing, NY.

\*\*MD 21005-5069

<sup>†</sup> Accepted: September 9, 2003

cles suspended in a fluid are exposed to a laser, and the amount of light scattered and the scattering angle are measured. Once calibrations of the response coefficients of the scattering light and detectors are known, the measured intensity distribution of the scattered light can be converted into a particle size distribution. It may be noted that it is difficult to collect light at high scatter angles associated with nanoparticles. As a result, the static method is limited to a practical size range of 20 nm-1,000  $\mu\text{m}$ .

In contrast, DLS is used for finer particles with a range of 3 nm-6  $\mu\text{m}$ . In this method, the Brownian motion of the dispersed particles in the suspending fluid causes a Doppler shift of the incident beam. Consequently, the scattered light has a different temporal distribution than that of the incoming light. Iterative fitting operations of known frequency distribution functions (of particles with various known sizes) are applied to that of the unknown frequency distribution to obtain the unknown particle size.

Another challenge posed by nanosized powders is the preparation of dispersions. Such powders often do not wet or deagglomerate in the dispersing fluid medium. Pretreatment to deflocculate the nanopowder may require dispersants that need to be selected based on the surface chemistry of the powders. The powder suspension often requires a homogenization procedure (e.g., ultrasonics) to further break up aggregates. However, this process could also break up physically welded agglomerates, skewing the true particle size distribution of the sample.

Crystallography or diffraction-based techniques (e.g., x-ray diffraction [XRD] and neutron diffraction [ND]) determine crystallite size. If the nanopowder is polycrystalline, the result may be different than the apparent particle size [9]. Small angle neutron scattering (SANS) (or SAXS, small-angle x-ray scattering [7]) can theoretically provide information about aggregate size, particle morphology, size distribution, surface area, total pore volume, and the thickness of a surface layer. However, the size range is limited from 1 nm to about 300  $\mu\text{m}$  (1 nm-2  $\mu\text{m}$  for SAXS). This means that a prescreening for larger particles should be done. If the particles are very uniform in both size and shape, it is difficult to determine the size and shape of the powders from SANS alone.

The primary objective of this effort was to use FESEM, TEM, BET, DLS, SLS, XRD, and SANS/ND in conjunction with one another to determine the particle size and/or distributions of the nanosized Fe powder. Additionally, it was hoped that during the use of these methods, one or two would emerge as an

effective screening tool for the evaluation of nanopowders. In other words, one that requires the least amount of preparation and analysis but is most efficient in conveying an overall and accurate description of the sample.

## 2. Experimental Procedures

A representative sample of Fe nanopowder, derived from microwave plasma synthesis [3], was obtained from Materials Modification Inc., Fairfax, VA. Microwave synthesis of the nanopowder entailed the controlled decomposition of  $\text{Fe}(\text{CO})_5$  (iron pentacarbonyl) at 700°C. To prevent pyrophoric oxidation, freshly synthesized powder was quenched in liquid nitrogen ( $\text{LN}_2$ ).

### 2.1 BET

Nitrogen gas adsorption analysis was performed on a Micromeritics ASAP2010 Accelerated Surface Area and Porosimetry System (Norcross, GA). Samples were outgassed overnight at 200°C under vacuum. Two separate samples were subjected to six-point BET surface area analysis. Additionally, a full adsorption isotherm was collected from one of the samples.

The adsorption data offered no evidence of microporosity in the powder. Therefore, calculation of the equivalent area diameter yielded a meaningful value for particle size. Equation (1) depicts that  $S_{\text{BET}}$ , the surface area from the BET measurement, is inversely related to the particle radius:

$$r = 3[\rho(S_{\text{BET}})]^{-1}, \quad (1)$$

where  $r$  is the sphere radius and  $\rho$  is the density of Fe.

### 2.2 Light Scattering Methods

SLS was performed on a Horiba LA-910 using a flow cell. DLS was performed on a Horiba LB-500 (Irvine, CA) in a stationary quartz cell. Preliminary attempts to disperse Fe in  $\text{H}_2\text{O}$  with a microfluidizer (Microfluidics, Newton, MA) or titanium microtip ultrasonic probe for 10-60 s were unsuccessful. In a more effective dispersion method, 0.1 wt.% of sodium hexametaphosphate  $[(\text{Na}(\text{PO}_3))_6]$  was dissolved in deionized water. Approximately 0.023 g of nanosized Fe powder was dispersed in 20 ml of the base solution. The powder dispersion was sonicated for 10 min at 80 W, boiled for 5 min, and sonicated again for 10 min to break up the powder sample. Two SLS samples and one DLS sample were taken from this suspension.



## 2.3 X-ray Diffraction (XRD)

XRD analysis for determination of particle size was performed using Cu-K $\alpha$  radiation on a fixed optics, Philips APD1700 Automated Powder Diffractometer System (Natick, MA). Generator settings were 45 kV and 40 mA. For the Fe powder, the four most intense peaks, [(110), 44.67°], [(200), 65.02°], [(211), 82.33°] and [(220), 98.94°], were scanned. Preliminary scans were made to determine the dwell time, step size, and scan range such that the net peak height under each peak was at least 10,000 counts. All peaks were scanned with a step size of 0.010° and 2 $\Theta$  range of at least  $\pm 3^\circ$ . The instrumental broadening was determined by using both the -100 Mesh Fe and LaB $_6$  powders. Specifically, characteristic peaks of LaB $_6$  near the Fe peaks were scanned: [(200), 43.52°], [(220), 63.22°], [(320), 83.85°], and [(410), 99.64°]. Because of the narrowness of the LaB $_6$  peaks, a finer step size of 0.005° was used. After subtracting the instrumental broadening contribution from the nano Fe peaks, Scherrer's equation [9] was used to determine the particle size.

## 2.4 Electron Microscopy Techniques

FESEM was performed on a Hitachi S4700 F-SEM (Nissei Sangyo America, Gaithersburg, MD). Several attempts to obtain optimum imaging conditions resulted in selection of an electron energy of 5 kV. Lower kV settings did not have the required resolution; higher kV settings tended to penetrate into the particles too deeply, resulting in the loss of surface detail. Both lower SE(L) and upper SE(U) secondary electron detectors were used with a working distance ranging from 11.6 to 3 mm. The sample was prepared by sprinkling Fe onto a colloidal carbon covered aluminum stub. The loose, excess powder was blown off with an air gun.

The TEM used was a JEOL JEM-3010 (Japan Electron Optics Laboratory, Peabody, MA). Samples were prepared by placing a dash of powder in 2 ml of ethanol and sonicating for about 2 min, then just dipping a carbon-coated, standard 200-mesh copper grid into the suspension. The powder sample was examined in bright field imaging mode at an accelerating voltage of 150 kV.

## 2.5 Neutron-Based Methods

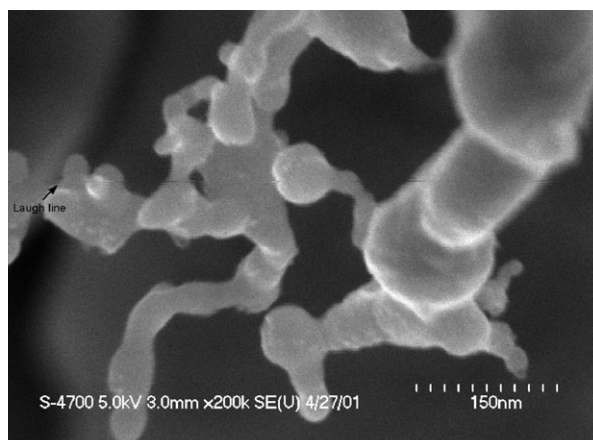
Both SANS and ND were performed at the Center for Neutron Research (CNR) at the National Institute of Standards and Technology (Gaithersburg, MD) on the 30-m SANS and BT1 powder diffractometer instruments, respectively. ND was performed on a

multidetector instrument where the neutrons are scattered by single crystal monochromators [Cu (311) and Si (531) with wavelengths,  $\lambda_{ND}$ , of 0.15405 and 0.15904 nm, respectively] at a fixed scattering angle. The neutron detector was composed of an array of 32 detectors separated by 5° in scattering angle. The width of the collimators before and after the monochromator and before the detectors are 7, 20, and 7 min of arc, respectively. The measurement was taken with 0.05° steps in 2 $\Theta$ . Measurements of particle size, local strain, and lattice strain distributions were obtained from the intensity,  $I_{ND}$ , versus  $Q_{ND}$  [ $4\pi\sin(\Theta)/\lambda$ ] data.

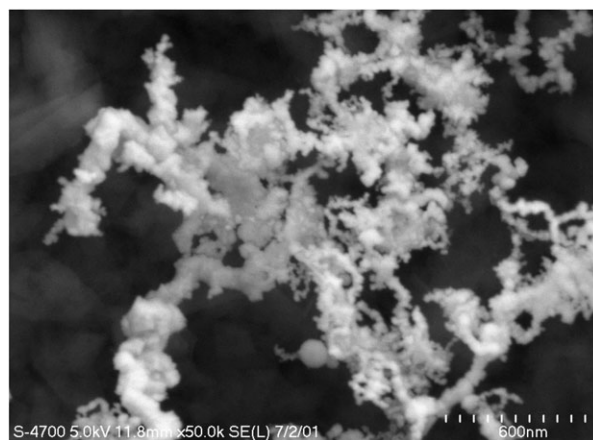
For SANS, a mechanical velocity selector rendered the "cold neutrons" from the source monochromatic and a monochromator provided wavelength resolution from 10-20% and wavelengths,  $\lambda_{SANS}$ , of 0.5-1.2 nm. The incident direction was defined by two circular pinholes. The scattered neutron direction was defined by a 5-mm spatial resolution, 2-D detector located perpendicular to the incident direction. The angular range available (and therefore the reciprocal wave vector range,  $Q$ ) was determined by the position of the detector with respect to the sample. The detector, placed at 1-15 m from the sample, could be laterally displaced by 25 cm. The distance between the incident pinholes was adjusted to match the resolution determined by the sample detector configuration. The sample was kept under vacuum so that the scattering length density of spheres was taken to be that of Fe ( $8.02 \times 10^{-4} \text{ nm}^{-2}$ ). The data were first analyzed using a uniform density sphere model. The data was then reanalyzed by a model of bimodal particle size distribution, as guided by the diffraction results. Each mode was represented by a Schulz distribution [10] whose parameters were a scale factor,  $I_{SANS}$ , a mean particle size,  $r$ , and a polydispersity,  $P$ . In the fitting process only  $I_{SANS}$  and  $P$  were allowed to vary. The value of the  $r$  used was obtained from the ND results.

## 3. Results

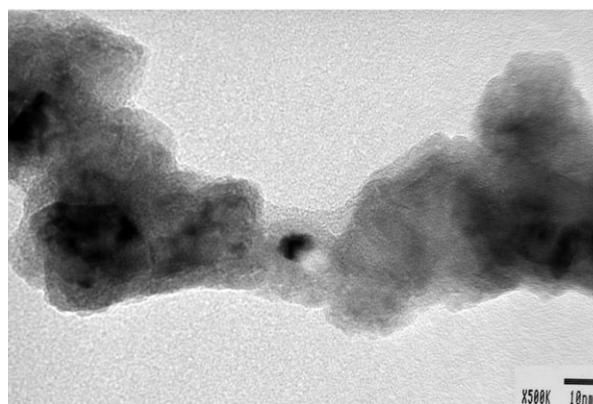
**Figures 1a** and **1b** depict FESEM images taken at 5 kV. The particle size appears to be 50-80 nm. It was difficult to locate any isolated Fe particles. Instead, the Fe grains appear to be fused to each other into chain-like tentacles that form dendritic agglomerates with sizes of 0.3 to 1  $\mu\text{m}$ . It is also worthwhile to note that the high contact angles seen in the particle-particle necks reflect late-stage particle-particle sintering. Despite the high transparency of the particle chains



(a)



(b)



(c)

**Fig. 1** Electron microscopy of the Fe nanopowder. FESEM images show in (a) the individual nanometer-sized particles, and in (b) the dendritic agglomerates. Bright field TEM image of the particle substructure is shown in (c).

(see **Figure 1c**), TEM examination of the powder was nevertheless able to discern a finer substructure within the apparently coarser 50-80 nm grains. The approximate size, or lower limit, of the subgrains was at least 20 nm.

**Figure 2** shows the BET plots for the two samples. Both are linear with least-squares correlation coefficients greater than 0.999. The linear BET plot corresponds to a BDTT Type II or Type IV isotherm. Microporous samples frequently exhibit a BDTT Type I isotherm also known as the Langmuir type [11]. Type I isotherms do not produce a linear fit in a BET plot. Furthermore, the value for the BET  $c$  constant was approximately 42 for each sample. If the powders were microporous, the value of this parameter would be higher (approximately 200 or greater), reflecting the higher apparent adsorption energy in a microporous solid [11]. The linear BET plots and the values of the  $c$  constant both indicate that the powders are free of fine pores and that the effective diameter calculated from  $S_{\text{BET}}$  is indicative of particle size.

Results of the BET surface area analysis were 13,870 and 15,080  $\text{m}^2/\text{kg}$ . Using a hard-sphere model and a 7,870  $\text{kg}/\text{m}^3$  density for Fe, the equivalent radius was found to be 28 and 25 nm, respectively, which corresponds to a diameter range of 50-60 nm. This particle size appears consistent with the FESEM results.

Frequency distributions of particle size for SLS and DLS are shown in **Figures 3a** and **3b**. From the various SLS measurements (see **Figure 3a**), Fe particles appear bimodal with particles sizes that are much larger than the size determined from the previous methods. Results of five consecutive DLS measurements spread over a 20-min time span indicated a single particle size distribution of a mean particle size of  $70 \pm 7$  nm.

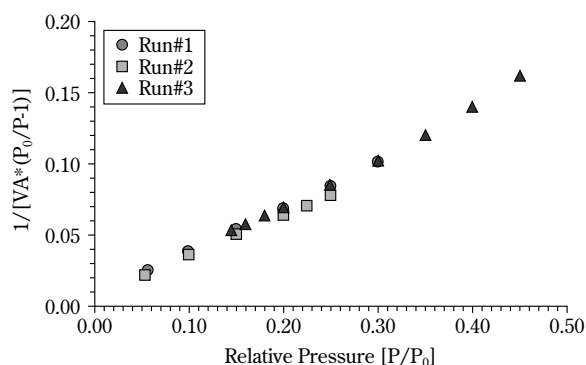
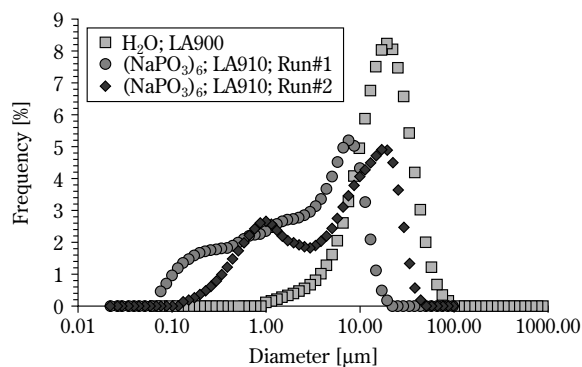
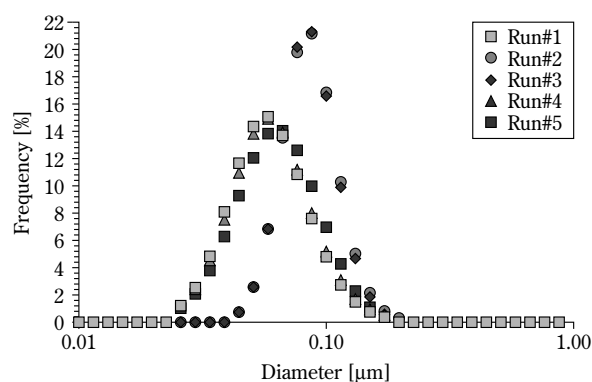


**Fig. 2** Type II BET surface area isotherm of the nanosized Fe.



(a)



(b)

**Fig. 3** Laser scattering results: (a) frequency distribution from SLS and (b) frequency distribution from DLS.

XRD line-broadening analysis of each of the 4 Fe peaks [10], using the Scherrer equation, yielded an average crystallite size of about  $20 \pm 3$  nm. Aside from the TEM results, this value was considerably less than those obtained by any of the other methods.

In the measured ND pattern obtained from the Fe sample with the Cu (311) monochromator, each peak consists of two components: a narrow and broad peak at the same positions as shown in **Figure 4** for the (110) Fe reflection. From ND, the narrow peak particle diameters were found to be 63 nm with a root mean square (RMS) strain of 0.028; the broad peak particle diameter was found to be 24 nm with an RMS strain of 0.165. The larger particles constituted 37% of the sample and comparatively did not have residual strain.

**Figure 5a** shows the SANS results of the fit to a

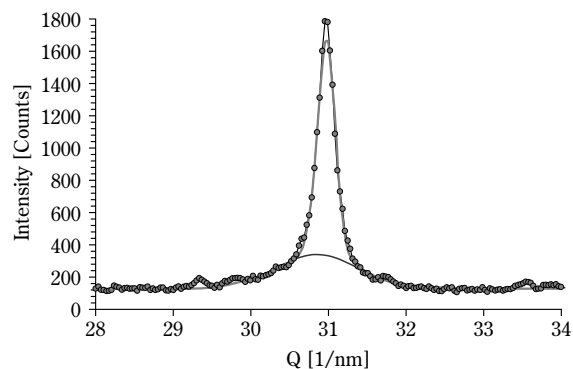
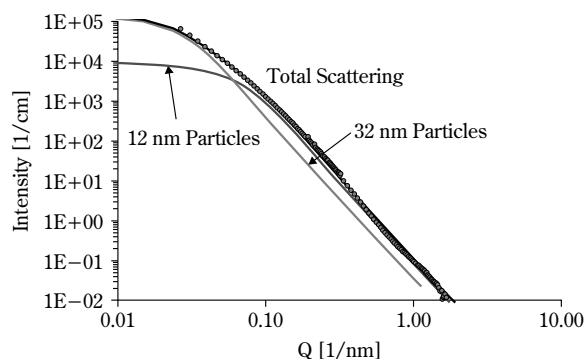
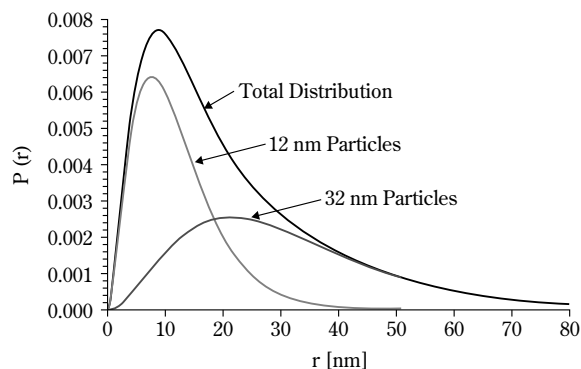


**Fig. 4** ND of the (110) Fe reflection. Note the presence of the two Gaussian fits under the peak.



(a)



(b)

**Fig. 5** SANS results confirming the existence of a bimodal distribution of crystallites in the nano Fe: (a) overall scattering data and (b) relative distributions of the particle sizes.

bimodal distribution model. In the figure, the data are shown as open circles and the fits as solid lines. The two distributions are found by the information represented by the broad concave curvature at  $Q \sim 0.001$  nm and a convex curvature at  $Q \sim 0.006$  nm. The particle size distributions,  $P$ , for each of these components are shown in **Figure 5b**. The total distribution is included as well. The scale factors indicate that the large component is 47% of the total rather than the ratio resulting from the ND. However, this is not considered important enough to assert that the two data sets (ND and SANS) are not consistent.

#### 4. Discussion

During the collection and evaluation of the particle size data it was quickly recognized that not all of the instruments provide first-hand or raw data output. Though statistically unsatisfactory, the electron optics-based observations instantaneously revealed the particle morphology and size information. In contrast, the BET and laser scattering techniques operate with factory-installed algorithms and geometrical models that require post-measurement interpretation related to the validity of the model. Lastly, the crystallographic methods required much more extensive user-based data fitting and analysis. Consequently, they do not readily lend themselves to the rapid assimilation and interpretation of the raw data.

**Table I** reports the summary of the mean particle sizes determined from all the methods. From the summary, it appears that the apparent, morphologically distinct Fe particle size is on the order of nanometers, ranging from roughly 25 to 80 nm. This is consistent with previous analyses of the powders [3]. However, the particles have a distinct fine structure and appear to cluster into much larger, micrometer-sized dendritic agglomerates. The evidence from

FESEM of particle-particle necks along the dendritic arms, indicative of near-late-stage sintering, was left unexplained in the previous article [3]. This is quite understandable, notwithstanding the size of the particles, the enhanced sinterability of nanopowders, and the excess heat available during the microwave sintering process. However, the available heat is limited because the internal crystal size within the particles appears to be smaller than their external dimensions. In other words, there is little or no indication of annealing within the grains.

As expected, FESEM yielded an adequate first-hand physical description of “typical” particle aggregates, though only semi-quantitative. The information gained with FESEM was more useful than that obtained with TEM because of the loss of surface detail in the latter. It may be noted that TEM also revealed a fine structure within the particles. Only, BET, the surface adsorption-based technique, identified the actual or functional particle size with a reasonable statistical variation. However, because BET is insensitive to the macroscopic morphological arrangement of the particles, it failed to indicate the nature of agglomeration.

Neither SLS nor DLS could correctly identify the size or nature of the agglomeration. In part, this was attributed to the intrinsic properties of the Fe nanopowder agglomerates, the limitations in preparing the powder suspension, and the inherent inability to interpret scattering data from an open agglomerate structure by the analysis software. Further discrepancies between the SLS and DLS results may also be likely accountable by the differences in sampling methods. In SLS, the sample dispersion is circulated during the measurement; whereas, in DLS, it is not. That is, while in the SLS the agglomerates remain suspended, in the stationary cell of the DLS, the heavier particles will settle out. As a result, DLS would not detect any of the larger agglomerates. Further experiments such as sedimentography may be needed to alleviate the disparity.

Both XRD and SANS/ND measurements, supported by TEM observations, resulted in a smaller particle size. This is most likely a measure of the crystal size within the particles. However, the ND/SANS with its greater resolution was able to identify at least two modes of crystallites within the sample.

#### 5. Summary and Conclusions

The size distribution of microwave-plasma-synthesized Fe nanopowder was evaluated by several analytical methods. The nanopowder was found to consist

**Table I** Summary of Methods and Results

Method	Particle Size [nm]	Comments
FESEM/TEM	50-80; 300-1,000	Bimodal
XRD	20	
SANS/ND	24 & 64	Bimodal, Gaussian
BET	60	Type II Isotherm
SLS	500-8,000	Bimodal
DLS	70	Gaussian

of dendritic agglomerates that were difficult to disperse. Individual grains within the dendrite structures were dense and spherical. Further scrutiny and analysis indicated the existence of a finer subgrain structure with a bimodal size distribution within the particles. The estimated average particle size was 60-80 nm with 20-nm subgrains, while the overall agglomerate size was about 0.3 to 1  $\mu\text{m}$ .

Consistent with many examples in larger-size powders, particle size determination in nanopowders was found to depend on the method used. Only FESEM and SLS provided information on the extent and morphology of agglomerates. Data from other methods were either complementary (BET and DLS) or provided detail (XRD and ND/SANS) beyond the required size and distribution information. Nevertheless, it is suggested that care be taken in making any of the measurements because, when viewed independently, the results may be misleading or erroneous.

## 6. Acknowledgements

This research was supported in part by an appointment to the research participation program at the U.S. Army Research Laboratory administered by the Oak Ridge Institute for Science and Education through an interagency agreement between the U.S. Department of Energy and the U.S. Army Research Laboratory.

## 7. References

- 1) A. Peigney, Ch. Laurent, O. Dumortier, and A. Rousset, "Carbon Nanotubes-Fe-Alumina Nanocomposites. Part I: Influence of the Fe Content on the Synthesis of Powders," *Journal of the European Ceramic Society* **18**, 1995-2004 (1998).
- 2) P.P. Phule, "Synthesis of Novel Magnetorheological Fluids," *MRS Bulletin* **23** [8], 23-25 (1998).
- 3) R. Kalyanaraman, S. Yoo, M.S. Krupashnkara, T.S. Sudarshan, and R.J. Dowding, "Synthesis and Consolidation of Iron Nanopowders," *Nanostructured Materials* **10** [8], 1379-1392 (1998).
- 4) T. Allen, "Particle Size Measurement," Chapman and Hall, New York (1997).
- 5) P.A. Webb and C. Orr, "Analytical Methods in Fine Particle Technology", Micromeritics Instrument Corporation, Norcross, GA (1997).
- 6) G. Geiger, "Selecting the Right Particle Size Analyzer," *The American Ceramic Society Bulletin* **75** [7], 44-48 (1996).
- 7) A. Singhal, G. Skandan, and R. Dowding, "A New Bench-Top Characterization Tool for Nanoparticulate Systems," *Scripta Metallurgica*, **44**, 2203-2207 (2001).
- 8) L. Jiqiao and H. Baiyun, "Particle Size Characterization of Ultrafine Tungsten Powder," *International Journal of Refractory Metals and Hard Materials*, **19**, 89-99 (2001).
- 9) H.P. Klug and L.E. Alexander, "X-Ray Diffraction Procedures," John Wiley and Sons, New York, NY, 655-656, 660-661 (1978).
- 10) B.D. Cullity, "Elements of X-Ray Diffraction," Addison Wesley, Reading, MA, 284 (1978).
- 11) S.J. Gregg and K.S.W. Sing, "Adsorption, Surface Area, and Porosity," 2<sup>nd</sup>. ed., Academic Press, New York, NY (1982).



## Author's short biography

**L.J. Kecskes**

Staff scientist, US ARL

**R.H. Woodman,**

Post-doctoral fellow, US ARL

**S.F. Trevino**

Staff scientist, US ARL

**B.R. Klotz**

Staff scientist, US ARL

**S.G. Hirsch**

Staff scientist, US ARL

**B.L. Gersten**

Assistant Professor, Queen's College, CUNY.

# Development and Validation of a Constitutive Model for Size-Segregation during Percolation<sup>†</sup>

S.P. Duffy and V.M. Puri<sup>1</sup>

Department of Agricultural and Biological Engineering  
The Pennsylvania State University\*

## Abstract

*Segregation is a widely occurring undesirable phenomenon in industries that store, handle and process particulate materials. Size-segregation induced by the percolation mechanism is observed in several important processes that negatively impacts the product quality and mixing. To quantify size-segregation, a constitutive model based on simultaneous convective and diffusive demixing was developed and validated. The primary segregation shear cell (PSSC) was used to measure the fundamental parameters and validate the convective-diffusive segregation model. Glass beads of size ratios of 10.9:1 (1250:115  $\mu\text{m}$ ), 8.7:1 (1000:115  $\mu\text{m}$ ), and 5.1:1 (1000:196  $\mu\text{m}$ ) were used for model parameter determination; whereas, size ratio of 6.4:1 (1250:196  $\mu\text{m}$ ) was used for model validation. As shown in a previous study, an effective segregation direction could be measured and used to validate the convective-diffusive segregation model for percolation. This justified the use of an effective segregation direction to model the percolation of fines. When compared to the normalized measured data for size ratios larger than 8.7:1, the convective-diffusive model resulted in standard deviations of 0.035. However, for size ratios smaller than 6.4:1, diffusive demixing was occurring during shear with the absence of a rapid initial discharge phase, i.e., minimal contribution due to convective component. Estimating the percolation for the 6.4:1 size ratio was accomplished by using the mean data of the 5.1:1 size ratio, which resulted in standard deviation of 0.055. The initial rapid discharge present in 10.9:1 and 8.7:1 size ratios suggests that a critical size ratio exists that differentiates free-fall discharge segregation from random mixing segregation. This can be critical to powder manufacturers that could use this critical limit to define size distribution recommendations during manufacturing.*

## 1. INTRODUCTION

In many particulate materials industries, the handling, storage, flow, and mixing represent important processing steps. During these and similar processing steps, product quality may be lowered by a phenomenon known as segregation. Accordingly, quantitative analysis of segregation plays a significant role in evaluating powder-related processing, manufacturing, storing, or conveying systems. Segregation is defined as a demixing process in which components

of a mixture separate as long as one component of the mixture is different than another. Of all the particle attributes, size is considered to be the most dominant variable (Williams, 1976, Duffy and Puri, 2002). Segregation has been measured using a coefficient, mechanism, and model (Rosato and Blackmore, 2000). The coefficient technique is by far the most common. However, it only describes the degree of segregation taking place for a particular set of operating conditions. The mechanism technique provides insight for processes that exhibit a dominating segregation mechanism. The most encompassing method is to model a particular process. It is neither possible nor practical to model every mechanism for a given process. However, if a specific mechanism is identified that explains the majority of segregation taking

---

\* 229 AG Engineering Building  
University Park, PA 16802

<sup>1</sup> Corresponding author

<sup>†</sup> Accepted: September 9, 2003

place; it would provide a powerful tool in understanding and minimizing segregation.

Percolation and sieving are two of the commonly observed mechanisms for segregation in industry. Percolation is similar to the sieving mechanism (**Figure 1**) that occurs during shear; however, a moving layer is absent. In the literature, percolation has been studied as a function of gravity and vibration (Tang et al., 2001). Vibration can cause a small individual particle to travel downward through the powder mass. Also, a smaller particle could travel through a larger granular mass due to gravity with diameter ratios less than 0.15. Due to the importance of percolation in industrial processing, a size-segregation mathematical model based on the convective-diffusive formulation for percolation is presented and validated in the paper.

All continuum theory-based constitutive models have material parameters that need to be measured for a specific powder under prescribed loading conditions. For this purpose, a primary segregation shear cell (PSSC) was developed. The details of the PSSC are given in Duffy and Puri (2002), which is a vertically oriented segregation shear cell of 101.6 mm (high)  $\times$  101.6 mm (wide)  $\times$  50.8 mm (deep). The overall schematic of the PSSC is shown in **Figure 2**. This shear cell can be used to test the time-dependent segregation response of binary mixtures over a large range of size ratios ( $>4:1$ ). In addition, the tester can be operated at strains ranging from 5% to 25% to provide different energy inputs. Also, the rate of loading, i.e., cycle speed or strain rate, can be varied from 0.75 Hz to 1.7 Hz to test the material over a range of energy input rates. The bed depth of coarse particles

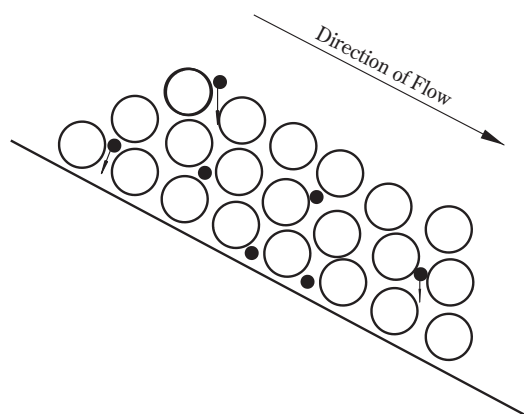


**Fig. 1** Segregation by sieving

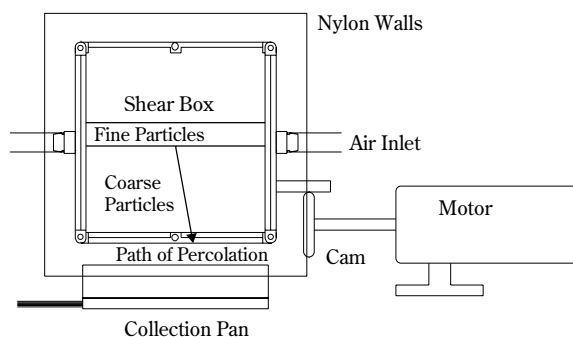


**Fig. 2** Overall schematic of primary segregation shear cell (PSSC)

can be preset ( $<90$  mm) to determine accurately the speed of movement of fines under different input energies, i.e., operating conditions. Additionally, the test material can be subjected to a constant confining pressure between 0 kPa (no confining pressure) to 10 kPa. In this study, the PSSC was used to measure the discharge of fine particles through a bed of coarse particles with the percolation parallel to the shear deformation and gravity directions.

## 2. LITERATURE REVIEW

Segregation, while important in every aspect of powder technology, remains to this date elusive in terms of the fundamental understanding and primary test devices for constitutive formulations (for example, see Rosato and Blackmore, 2000). Most researchers define a segregation coefficient and explore segregation for a particular process (Duffy and Puri, 2002). However, a shear apparatus has been developed by Duffy and Puri (2002) to measure the movement of fine particles through a bed of coarse particles. This apparatus was used to collect data for constitutive model development and validation.

Mixing and flow of particulate materials are important processes in powder industries such as agricultural and food, ceramic, chemical, mining, pharmaceutical, and powder metallurgy. Extensive work has been done in the flow of particulate materials especially out of hoppers. Most research on mixing has focused on determining a mixing efficiency. Sommer (1996) defined mixing as the blending of at least one solids component with another, where at least one property (such as size, shape, and density) of the two components is different. In this definition, segregation would be defined as demixing in which particles

with one similar property, usually size, accumulate together.

Sommer (1996) outlined four major models of powder mixing. A limited number of researchers have used stochastic formulation to describe segregation. Law and Kelton (1991) defined deterministic models as simulations that do not contain any probabilistic (random) components. A stochastic model contains at least one time-varying random component.

Model 1 – The Fokker-Planck Equation (1), similar to Fick's second law of diffusion, is used to describe mixing that arises from convective and random motions of particles.

$$\frac{\partial c(x, t)}{\partial t} = -u \frac{\partial c(x, t)}{\partial x} + D \frac{\partial^2 c(x, t)}{\partial x^2} \quad (1)$$

This equation is used to describe the concentration ( $c$ ) at a given position ( $x$ ) with respect to time ( $t$ ) in the mixer. Equation (1) contains two material parameters which are  $u$ , the transport coefficient, and  $D$ , the dispersion coefficient. The transport coefficient  $u$  (units of  $L/T$ ) describes the convective flow present in mixing, and the dispersion coefficient  $D$  (units of  $L^2/T$ ) is a measure of the random motion available in the mixer. This is referred to as the convective-diffusive model. A variation of this model with  $u=0$  was introduced by Bridgwater et al. (1978), which is the diffusion model.

Model 2 – The second type of mixing is batch mixing. The two sources of flow in Equation (1), convective and diffusion, can work against each other in a batch mixer, unlike random motion, resulting in demixing. The phenomena of demixing can also occur in the absence of convective transport, i.e.,  $-u \frac{\partial c(x, t)}{\partial x} = 0$ . Therefore, Equation (1) can be simplified to batch mixing:

$$\frac{\partial c(x, t)}{\partial t} = D \frac{\partial^2 c(x, t)}{\partial x^2} \quad (2)$$

This is the well-known form of Fick's second law of diffusion, where  $D$  is the dispersion coefficient ( $L^2/T$ ). Defining dimensionless variables  $\lambda = x/L$  and  $\tau = t/T$ , Equation (2) can be written in the following dimensionless form:

$$\frac{\partial c(\lambda)}{\partial \tau} = \frac{\partial^2 c(\lambda)}{\partial \lambda^2} \quad (3)$$

$T$  is a characteristic time ( $=L^2/D$ ) formed from a characteristic mixer length  $L$  and dispersion coefficient  $D$ . If rigid walls, i.e., there is no material flow at  $x=0$  and  $x=L$ , and a highly concentrated side ini-

tial condition are assumed, Equation (3) can be solved in closed form for a closed barrel of length  $L$ , given in Equation (4).

$$\frac{\sigma}{\mu} = \sqrt{2} e^{-\left(\frac{\pi}{L}\right)^2 D \cdot t} \quad (4)$$

Mixing efficiency is defined as the coefficient of variation,  $\sigma/\mu$  (standard deviation/mean). Sommer stated that this equation describes what is observed in practice, i.e., as the dispersion coefficient increases, mixing occurs more rapidly.

Model 3 – The third mixing model is the mixing of two (or more) material streams. If the two streams converge into a mixer so that no back flow occurs, each material stream can be described as:

$$\frac{\partial c_1(x, t)}{\partial t} = -u_1 \frac{\partial c_1(x, t)}{\partial x} + D_1 \frac{\partial^2 c_1(x, t)}{\partial x^2} \quad (5)$$

$$\frac{\partial c_2(x, t)}{\partial t} = -u_2 \frac{\partial c_2(x, t)}{\partial x} + D_2 \frac{\partial^2 c_2(x, t)}{\partial x^2}$$

This is simply the Fokker-Planck Equation (1) for each stream where  $c_1$ ,  $c_2$ , and  $u_1$ ,  $u_2$  and  $D_1$ ,  $D_2$  are concentrations, convective and diffusion parameters of components 1 and 2, respectively. Some work has been accomplished using Equation (5) to demonstrate that mixing efficiency was strongly dependent on the dispersion coefficient. However, simulations that varied the parameters showed the most influential parameter was the residence time (a parameter related to the characteristic fluctuation time  $T$  of the entrance streams).

Model 4 – The final mixing model described by Sommer was silo mixing. Silo (i.e., bin) mixing is described as various components mixed in a bin via external or internal blending and recirculation. This means different components introduced into the bin at the same time can leave the bin at different times. A cell/layer model was used to describe the time-dependent concentration distribution,  $c_k$ , given in Equation (6).

$$c_{k+1} = M \cdot c_k \quad (6)$$

where,  $M$  is the mixer matrix and contains the residence time spectrum data.

Williams (1986) outlined statistical calculations of random mixtures. A random mixture is defined as a mixture with the probability of finding a particular component of the mixture throughout the sample independent of sampling location and equal to the percentage of the component in the entire mixture. A random mixture composed of two sets of identical

particles was studied. Quantitative relationships for locating a component were developed. The models described herein and their variations have been applied to chute-flow (Vallance and Savage, 2000, Hwang, 1978), drum-flow (Khakhar et al., 2001), heap-flow (Shinohara and Golman, 2002), and constitutive model (Bridgwater, 1994).

The overall goal of this research was to develop and validate a percolation-induced segregation constitutive model to predict the movement of fines during shear of a binary, i.e., coarse-fine, mixture. In order to fulfill this goal, the specific objectives were:

1. To test several binary mixtures comprising varying size ratios at different boundary and loading conditions, i.e., strain, cycle speed, coarse particle bed depth, in the PSSC.
2. To quantify the fundamental parameters of the percolation constitutive model using experimental data from the PSSC.
3. To validate the constitutive model by performing tests with the PSSC under conditions different from the mechanism parameter determination and comparison with the results from the constitutive model.

### 3. EXPERIMENTAL METHODOLOGY

Four binary particulate material mixtures of glass beads were selected. Glass beads were used based on the availability of narrow cut sizes, sphericity, and non-hygroscopic properties under controlled ambient test conditions. All tests were conducted in an environment controlled laboratory with average temperature of  $21^{\circ}\text{C} \pm 3^{\circ}\text{C}$  and relative humidity less than 40% to minimize the effects of moisture on the test results. The glass spheres were considered dry (i.e., moisture content was equal to zero). A dehumidifier, placed near the shear apparatus, was used to reduce the ambient moisture in the environment.

Two size ranges of fines (106-125  $\mu\text{m}$  with  $d_{50}=115 \mu\text{m}$  and 180-212  $\mu\text{m}$  with  $d_{50}=196 \mu\text{m}$ ) and two size ranges of coarse particles (800-1200  $\mu\text{m}$  with  $d_{50}=1000 \mu\text{m}$  and 1000-1500  $\mu\text{m}$  with  $d_{50}=1250 \mu\text{m}$ ) were used to obtain the four size ratios (**Table 1**). Of these, three size ratios, 5.1:1 (1000:196), 8.7:1 (1000:115), and 10.9:1 (1250:196), were used for analysis and model development. A fourth size ratio of 6.4:1 (1250:196), obtained using the above size ranges, was used for validation purposes. The fourth size ratio of 6.4:1 was selected as the validation ratio because parameters could be interpolated to estimate the 6.4:1 data from the other size ranges.

Additional variables considered during data collection were strain, cycle speed and coarse particle bed depth. For determination of material parameters of the convective-diffusive constitutive model given in Equation (1), three strain values, two cycle speeds, and three beds depth shown in **Table 2** were used. Each combination was repeated four times for calculation of a representative mean response. This series of experiments is the same as those reported in Duffy and Puri (2002). They provide further information on the rationale for these variables and methodology of tests. To validate the segregation constitutive model, experiments given in **Table 3** were performed. The purpose of validation experiments was to provide a data set at an intermediate operating condition so that the effectiveness of the candidate segregation constitutive model could be evaluated.

**Table 1** Summary of size ratios of glass beads used for this study

Coarse Size, $d_{50}$	1000 and 1250 $\mu\text{m}$
Fine Size, $d_{50}$	115 and 196 $\mu\text{m}$
Size Ratios for Parameter Determination	1250:115 (10.9:1), 1000:115 (8.7:1), and 1000:196 (5.1:1)
Size Ratio for Validation	1250:196 (6.4:1)

**Table 2** Primary testing schedule for binary mixtures of spherical glass beads\*

<u>Parameter</u>	<u>Values</u>
Size Ratios	10.9:1, 8.7:1, and 5.1:1
Strains	5%, 10%, and 15%
Cycle Speeds	0.75 Hz and 1.33 Hz
Bed Depths	2.54 cm, 5.08 cm, and 7.68 cm

\*Each combination was repeated four times

**Table 3** Validation schedule for binary mixtures of spherical glass beads\*

<u>Parameter</u>	<u>Values</u>
Size Ratio	6.4:1
Strains	5% and 15%
Cycle Speeds	0.75 Hz and 1.33 Hz
Bed Depths	2.54 cm and 7.68 cm

\*Each combination was repeated four times

### 4. SEGREGATION CONSTITUTIVE MODEL

Based on literature review and its rational basis, the convective-diffusive segregation model (Equation 1) was selected. The convective-diffusive constitutive model can be used to describe one-, two-, or three-



dimensional analyses. A one-dimensional analysis was selected for the test conditions used in this study. This is an appropriate assumption based on the mechanism of shear. As discussed by Duffy and Puri (2002), the percolation of binary mixtures of glass beads is nearly spatially uniform. Furthermore, as shown by Duffy and Puri, an effective direction exists wherein any resultant anisotropies due to the loading conditions and test material can be fully addressed. This is shown as the  $\theta$ -direction in **Figure 3**. An effective percolation direction (one-dimensional) was identified by combining the mass versus time relationship from the six load measurement locations (**Figure 3**). The effective direction was a resultant mass discharge vector of the six load cell measurements (Duffy, 2001).

The convective-diffusive segregation model for percolation mechanism was rewritten in the  $\theta$ -direction as shown in Equation (7).

$$\frac{\partial m}{\partial t} = \bar{D}_\theta \frac{\partial^2 m}{\partial \theta^2} - \bar{u}_\theta \frac{\partial m}{\partial \theta} \quad \text{for } t > 0, 0 < \theta < \frac{h}{\cos(\theta)} \quad (7)$$

Equation (7) quantifies the mass of fines ( $m$ ) at any given time ( $t$ ) and location along the  $\theta$ -direction of the bed depth ( $h$ ) using the material parameters  $\bar{D}_\theta$  and  $\bar{u}_\theta$ , which are the fundamental material parameters

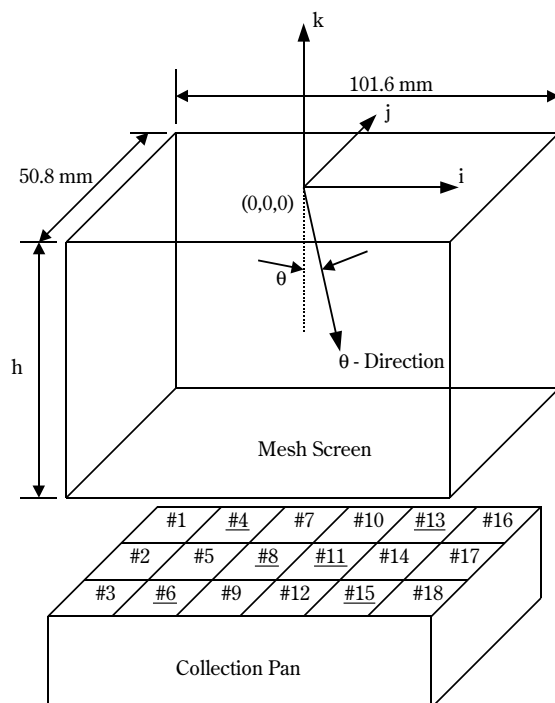
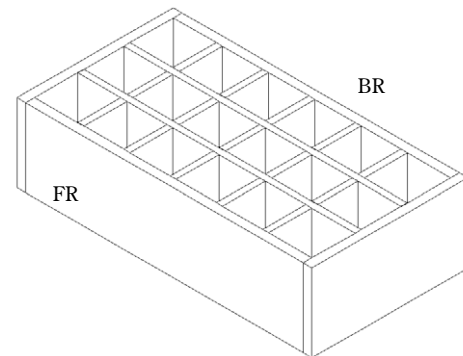


**Fig. 3** Schematic of global coordinates for the PSSC and the collection pan, underlined cell numbers are the measurement locations and  $h$  is the coarse material fill depth

and represent the diffusive and convective components, respectively. The units of  $\bar{D}_\theta$  and  $\bar{u}_\theta$  are  $L^2/T$  and  $L/T$ , respectively. The data collected from the six load cells (Cell #4 BR-LM, #6 FR-LM, #8 MR-LC, #11 MR-RC, #13 BR-RM, and #15 FR-RM) in **Figure 4** were used to get the mass versus time relationship in the  $\theta$ -direction by calculating a resultant percolation vector as a function of time. Geometrical distances from origin to the center of load cell grid in the mesh



(a)

	<div style="display: flex; justify-content: space-between; align-items: center;"> <span>Left</span> <span>Right</span> </div>					
Back Row	#1 BR-LL	#4 BR-LM	#7 BR-LC	#10 BR-RC	#13 BR-RM	#16 BR-RR
Middle Row	#2 MR-LL	#5 MR-LM	#8 MR-LC	#11 MR-RC	#14 MR-RM	#17 MR-RR
Front Row	#3 FR-LL	#6 FR-LM	#9 FR-LC	#12 FR-RC	#15 FR-RM	#18 FR-RR
	Left	Middle	Center	Center	Middle	Right

Cell Number  
 #10  
 BR-RC  
 Row Identification:  
 BR – Back Row  
 MR – Middle Row  
 FR – Front Row  
 Column Identification:  
 LL – Left Left  
 LM – Left Middle  
 LC – Left Center  
 RC – Right Center  
 RM – Right Middle  
 RR – Right Right

(b)

**Fig. 4** Schematic of load cell collection assembly (a) isometric view, (b) top view

screen plane, representing effective mean free paths, were used as the weight factors to obtain the effective mass values in the  $\theta$ -direction. Details of the calculation procedure are given in Duffy (2001).

The finite difference representation for Equation (7) and the associated boundary conditions are summarized in Equations (8) and (9). All values at the current time  $t$  are known. In addition, the subscript  $n$  denotes the  $n$ -th layer along the coarse bed depth.

$$m(\theta_n, t + \Delta t) = (\delta + \mu)m(\theta_{n-\Delta n}, t) + [1 - \mu - 2\delta]m(\theta_n, t) + \delta m(\theta_{n+\Delta n}, t) \quad (8)$$

$$m(\theta_0, t=0) = m_0 \quad (9a)$$

$$m(\theta_n, t=0) = 0, n=1, 2, \dots, r \quad (9b)$$

(i.e., initially, no fines in any  $r$  layer)

$$m(\theta_0, t + \Delta t) = m(\theta_0, t) - \sum_{n=1}^r m(\theta_n, t) \quad (9c)$$

$$m(\theta_r, t + \Delta t) = [\delta + \mu]m(\theta_{r-1}, t) + m(\theta_r, t) \quad (9d)$$

where,

$$\mu = \frac{\bar{u}_\theta \Delta t}{\Delta \theta}$$

$$\delta = \frac{\bar{D}_\theta \Delta t}{(\Delta \theta)^2}$$

The last term in Equation (8) represents a diffusive flux that is opposite to the direction of gravity. Based on physical observations at the top of the cell and the amount of time for the fines to reach the collection pan,  $\delta m(\theta_{n+\Delta n}, t) = 0$ . The process of fine particles dropping out of the test cell and into the collection pan gives minimal resistance in the direction of gravity. It should be noted that if the bottom of the test cell was blocked, this term could not be deleted. Therefore, the finite difference representation for the convective-diffusive model simplifies to Equation (10).

$$m(\theta_n, t + \Delta t) = (\delta + \mu)m(\theta_{n-\Delta n}, t) + [1 - \mu - 2\delta]m(\theta_n, t) \quad (10)$$

One of the two purposes of the finite difference formulation was to estimate the material specific parameters  $\mu$  and  $\delta$  in the convective-diffusive segregation constitutive model. The second purpose was to use the estimated  $\mu$  and  $\delta$  values to validate the segregation constitutive model. The parameters,  $\mu$  and  $\delta$ , were varied to minimize the cumulative squared error between the numerically solved and measured effective mass value  $m(\theta_n, t)$ . In order to determine  $\mu$  and  $\delta$ ,  $\Delta t = 1$  s and  $\Delta \theta * \cos \theta = 5.08$  mm, 10.16 mm, and 15.24 mm for bed depths of 25.4 mm, 50.8 mm, and 76.2 mm, respectively, were used. Considerations

such as convergence and number of cases were factored in the determination of  $\Delta t$  and  $\Delta \theta$  values.

The Solver utility in Microsoft Excel<sup>®</sup> was used to solve the finite difference equations in Equation (10) with the boundary and initial conditions shown in Equation (9). The precision of  $\mu$  and  $\delta$  was held to three decimal places (i.e., 0.000). Equation (11) defines the standard deviation between the actual and predicted data. The term,  $df$ , represents the degrees of freedom for the data. The values of  $\mu$  and  $\delta$  that produced the smallest error were taken as the material parameter for the given set of operating conditions. In Equation (11),  $M(t_i)$  represents the experimentally measured mass value at the exit, i.e., corresponding to  $\theta_r$ .

$$\text{Standard Deviation} = \sqrt{\frac{\sum_{i=1}^n (m(\theta_r, t_i) - M(t_i))^2}{n - df}} \quad (11)$$

## 5. RESULTS AND DISCUSSION

### 5.1 Convective-Diffusive Segregation Model Parameters

The convective-diffusive segregation model parameters,  $\mu$  and  $\delta$ , for strains of 15%, 10%, and 5% are given in **Tables 4** through **6**, respectively. In **Tables 4** through **6**, the convective term ( $\mu$ ) is reported first then the diffusive term ( $\delta$ ) separated by a slash. The standard deviation values between segregation model

**Table 4** Convective-diffusive segregation constitutive model parameter values ( $\mu/\delta$ ) at 15% strain with standard deviations between data and model in parentheses\*

Condition	Size Ratio 10.9:1	Size Ratio 8.7:1	Size Ratio 5.1:1
Cycle Speed 0.75 Hz Bed Depth 2.54 cm	0.293/0.458 (0.132)	0.135/0.539 (0.053)	0.000/0.255 (0.015)
Cycle Speed 0.75 Hz Bed Depth 5.08 cm	0.293/0.458 (0.097)	0.074/0.598 (0.102)	0.000/0.269 (0.009)
Cycle Speed 0.75 Hz Bed Depth 7.62 cm	0.417/0.344 (0.060)	0.318/0.414 (0.059)	0.000/0.243 (0.010)
Cycle Speed 1.33 Hz Bed Depth 2.54 cm	0.389/0.356 (0.050)	0.439/0.284 (0.031)	0.000/0.335 (0.015)
Cycle Speed 1.33 Hz Bed Depth 5.08 cm	0.139/0.532 (0.055)	0.330/0.389 (0.075)	0.063/0.099 (0.016)
Cycle Speed 1.33 Hz Bed Depth 7.62 cm	0.490/0.294 (0.057)	0.432/0.325 (0.067)	0.046/0.139 (0.015)

\* To convert  $\mu$  to  $u_\theta$ , multiply the entries by 1.969 (bed depth=2.54 cm), 0.984 (bed depth=5.08 cm), 0.656 (bed depth=7.62 cm) (units=cm/s), and  $\delta$  to  $D_\theta$ , multiply entries by 3.875 (bed depth=2.54 cm), 0.969 (bed depth=5.08 cm), 0.431 (bed depth=7.62 cm) (units=cm<sup>2</sup>/s)

**Table 5** Convective-diffusive segregation constitutive model parameter values ( $\mu/\delta$ ) at 10% strain with standard deviations between data and model in parentheses\*

Condition	Size Ratio 10.9:1	Size Ratio 8.7:1	Size Ratio 5.1:1
Cycle Speed 0.75 Hz Bed Depth 2.54 cm	0.038/0.586 (0.023)	0.172/0.431 (0.012)	0.000/0.133 (0.016)
Cycle Speed 0.75 Hz Bed Depth 5.08 cm	0.193/0.333 (0.019)	0.221/0.410 (0.035)	0.000/0.115 (0.005)
Cycle Speed 0.75 Hz Bed Depth 7.62 cm	0.034/0.542 (0.014)	0.144/0.214 (0.011)	0.000/0.088 (0.013)
Cycle Speed 1.33 Hz Bed Depth 2.54 cm	0.152/0.441 (0.025)	0.000/0.512 (0.037)	0.019/0.126 (0.026)
Cycle Speed 1.33 Hz Bed Depth 5.08 cm	0.228/0.382 (0.050)	0.198/0.249 (0.036)	0.000/0.141 (0.016)
Cycle Speed 1.33 Hz Bed Depth 7.62 cm	0.000/0.522 (0.038)	0.179/0.479 (0.035)	0.000/0.096 (0.008)

\* To convert  $\mu$  to  $u_0$ , multiply the entries by 1.969 (bed depth=2.54 cm), 0.984 (bed depth=5.08 cm), 0.656 (bed depth=7.62 cm) (units=cm/s), and  $\delta$  to  $D_0$ , multiply entries by 3.875 (bed depth=2.54 cm), 0.969 (bed depth=5.08 cm), 0.431 (bed depth=7.62 cm) (units=cm<sup>2</sup>/s)

**Table 6** Convective-diffusive segregation constitutive model parameter values ( $\mu/\delta$ ) at 5% strain with standard deviations between data and model in parentheses\*

Condition	Size Ratio 10.9:1	Size Ratio 8.7:1	Size Ratio 5.1:1
Cycle Speed 0.75 Hz Bed Depth 2.54 cm	0.000/0.140 (0.020)	0.000/0.512 (0.028)	0.000/0.116 (0.010)
Cycle Speed 0.75 Hz Bed Depth 5.08 cm	0.000/0.232 (0.014)	0.204/0.252 (0.018)	0.000/0.114 (0.015)
Cycle Speed 0.75 Hz Bed Depth 7.62 cm	0.000/0.242 (0.006)	0.000/0.479 (0.015)	0.000/0.107 (0.015)
Cycle Speed 1.33 Hz Bed Depth 2.54 cm	0.000/0.479 (0.031)	0.057/0.545 (0.015)	0.000/0.155 (0.018)
Cycle Speed 1.33 Hz Bed Depth 5.08 cm	0.087/0.558 (0.029)	0.176/0.440 (0.028)	0.000/0.117 (0.005)
Cycle Speed 1.33 Hz Bed Depth 7.62 cm	0.112/0.326 (0.009)	0.141/0.416 (0.022)	0.000/0.079 (0.010)

\* To convert  $\mu$  to  $u_0$ , multiply the entries by 1.969 (bed depth=2.54 cm), 0.984 (bed depth=5.08 cm), 0.656 (bed depth=7.62 cm) (units=cm/s), and  $\delta$  to  $D_0$ , multiply entries by 3.875 (bed depth=2.54 cm), 0.969 (bed depth=5.08 cm), 0.431 (bed depth=7.62 cm) (units=cm<sup>2</sup>/s)

calculated and measured values are given in parenthesis. The measured and model calculated normalized mass versus time relationships for three different treatments are given in **Figures 5** through **7**. Based on detailed analyses of experimental data by Duffy and Puri (2002), the normalized mass represents the preferred dependent variable rather than the absolute mass values. Therefore, normalized mass values are

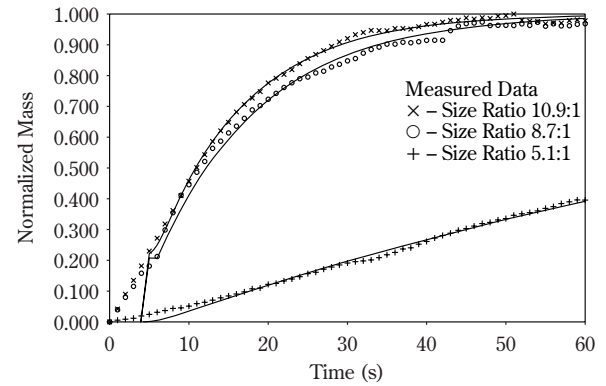


**Fig. 5** Measured ( $\times, \circ, +$ ) and convective-diffusive segregation constitutive model calculated (—) normalized mass versus time data – Strain=15%, Cycle Speed=0.75 Hz, Bed Depth=7.62 cm

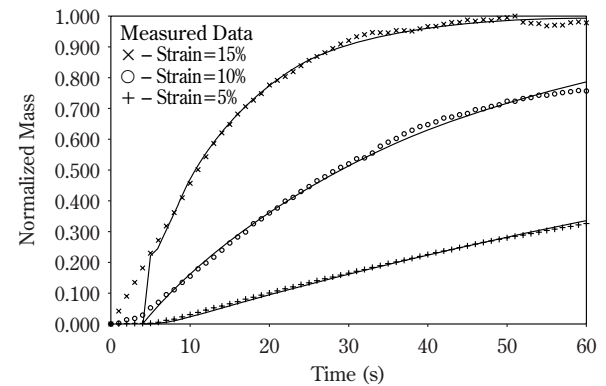


**Fig. 6** Measured ( $\times, \circ, +$ ) and convective-diffusive segregation constitutive model calculated (—) normalized mass versus time data – Size Ratio=10.9:1, Cycle Speed=0.75 Hz, Bed Depth=7.62 cm

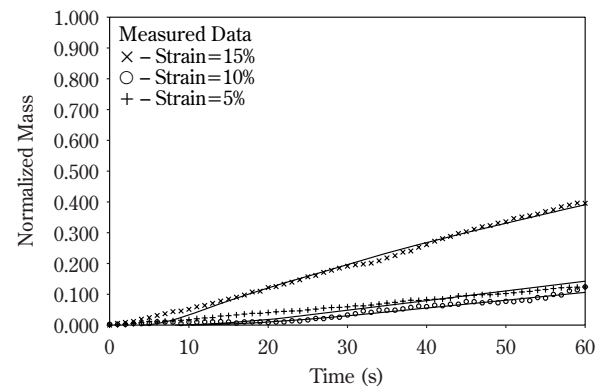


**Fig. 7** Measured ( $\times, \circ, +$ ) and convective-diffusive segregation constitutive model calculated (—) normalized mass versus time data – Size Ratio=5.1:1, Cycle Speed=0.75 Hz, Bed Depth=7.62 cm

used in the model development and validation studies. The normalized mass values were calculated by dividing the mass at any given location, i.e., cell locations as shown in **Figures 3 and 4**, with the measured mass of fines at that location at the end of data collection.

The average standard deviations in **Table 4** for 10.9:1, 8.7:1, and 5.1:1 are 0.075, 0.065, and 0.013, respectively. In addition, the convective model, without the diffusive terms was used. The average standard deviations for 10.9:1, 8.7:1 and 5.1:1 were 0.118, 0.146 and 0.071, respectively. At all strain values, the convective segregation model produced larger deviations between measured and predicted values as compared with the convective-diffusive segregation model. This suggests that random mixing is occurring which is characterized by the  $\delta$  parameter. The convective parameter characterizes the initial rapid discharge or free fall percolation occurring in the larger size ratios. As shown in **Tables 4 through 6**, the convective parameter of the 5.1:1 treatments is near zero. This suggests that the percolation of fines at the 5.1:1 treatments is dominated by the diffusive mixing mechanism. Average standard deviations in **Tables 5 and 6** are below 0.050 for all treatments with the standard deviations for 5.1:1 less than 0.030 for all strain levels.

Measured and modeled normalized mass versus time relationships for three different treatments are given in **Figures 5 through 7**. The first set of results, **Figure 5**, is for strain of 15%, cycle speed of 0.75 Hz, and bed depth of 7.62 cm. The three responses are for different size ratios. The measured data are represented by symbols and the predicted values are shown as solid lines. The convective-diffusive segregation constitutive model represents the measured data very well (standard deviations for 10.9:1, 8.7:1, and 5.1:1 are 0.060, 0.059, and 0.010, respectively). As shown in **Figure 5**, the majority of error in the standard deviation is within the first 5 seconds of the percolation profile. The model has a lag followed by a step which is not present in the measured data. This can be explained physically by assuming that some of the fine particles did migrate through the bed during deposition but did not fall out of the screen. The same trend is apparent in **Figure 6**, which is for the size ratio of 10.9:1 at a strain rate of 1.33 Hz and bed depth of 7.62 cm (standard deviations are 0.057, 0.038, and 0.009 for strains of 15%, 10%, and 5%, respectively). **Figure 7** is for the size ratio of 5.1:1 at cycle speed of 1.33 Hz and bed depth of 7.62 cm. For the size ratio of 5.1:1, the initial lag of fines in the collection pan dur-

ing data collection is present. Therefore, the model also predicts the initial lag very well (standard deviations are 0.015, 0.008, and 0.010 for strains of 15%, 10%, and 5%, respectively). The coefficient of variation for the convective term was large ( $>50\%$ ). This was influenced by the initial lag time. The coefficient of variation for the diffusive term ranged from 10 to 20%.

From this discussion it was concluded that the convective-diffusive segregation constitutive model describes the percolation of fines through a bed of coarse particles better than simply the convective segregation constitutive model. Generally, the standard deviations declined by a factor of three, and the calculated values follow the measured mass efflux trends. The validation of the convective-diffusive segregation model is presented in the next section.

## 5.2 Validation of Convective-Diffusive Segregation Constitutive Model

It was initially the goal to predict the normalized mass versus time relationship for the validation size ratio of 6.4:1. However, as discussed in the preceding section, the prediction is hindered by the presence or absence of an initial discharge of fines at the beginning of the test. As shown hereafter, the normalized mass versus time relationship for 6.4:1 is similar to the 5.1:1 ratio, i.e., does not exhibit an initial free fall discharge. Therefore, prediction attempts produced very large standard deviations when comparing the predicted values to the collected/calculated values of the 6.4:1 ratio. The convective and diffusive parameters were estimated using a linear interpolation based on the size ratio. For a size ratio of 6.4:1, the convective parameter ( $\mu$ ) and diffusive parameter ( $\delta$ ) were estimated as 0.137 and 0.263 for strain of 15% and 0.031 and 0.218 for strain of 5%, respectively. Graphical representations between the measured data and modeled data using the linear interpolation based on size are given in **Figures 8 and 9** for strains of 15% and 5%, respectively. The average standard deviations for 15% and 5% strain for the 6.4:1 size ratio using linear interpolation were 0.338 and 0.174, respectively. These deviations are much higher than the optimized models in the previous sections.

Since the 6.4:1 data were similar to the 5.1:1 data (i.e., no initial rapid discharge) and significantly different ( $p < 0.05$ ) than the data for the 8.7:1 and 10.9:1 size ratios (Duffy and Puri, 2002), the average convective and diffusive parameters at strains of 15% and 5% (of 5.1:1) were used to estimate the percolation of 6.4:1. For a size ratio of 6.4:1, the convective parameter ( $\mu$ ) and diffusive parameter ( $\delta$ ) were estimated as

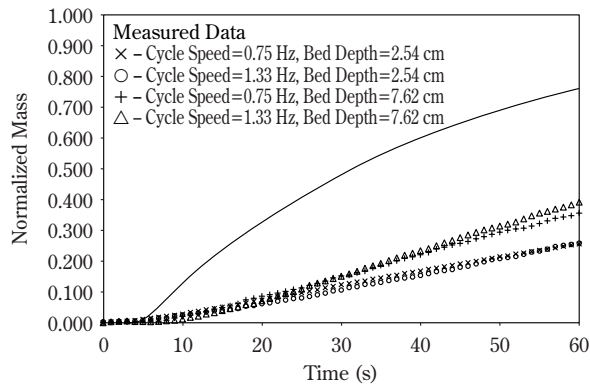


**Fig. 8** Calculated using linear interpolation (—) and measured data (×,○,+,Δ) for the 6.4:1 size ratio at strain of 15%

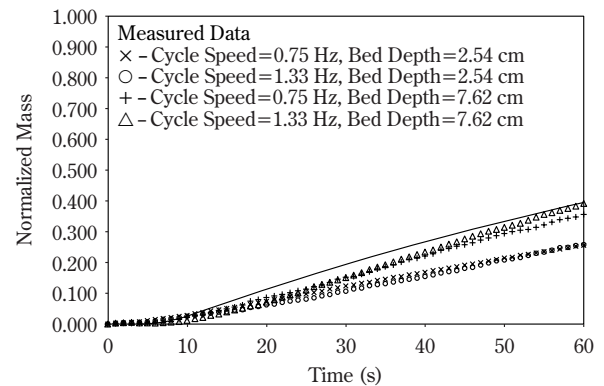


**Fig. 10** Calculated (—) using 5.1:1 data and measured data (×,○,+,Δ) for the 6.4:1 size ratio at strain of 15%

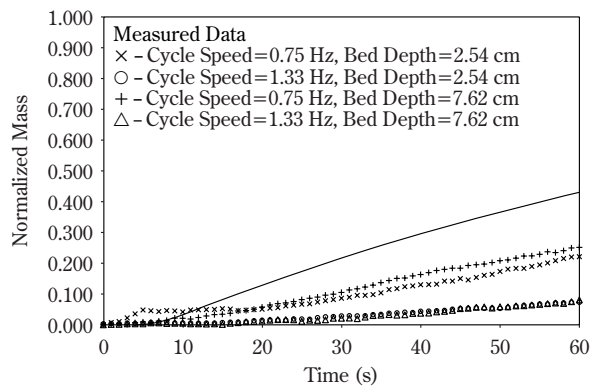


**Fig. 9** Calculated using linear interpolation (—) and measured data (×,○,+,Δ) for the 6.4:1 size ratio at strain of 5%

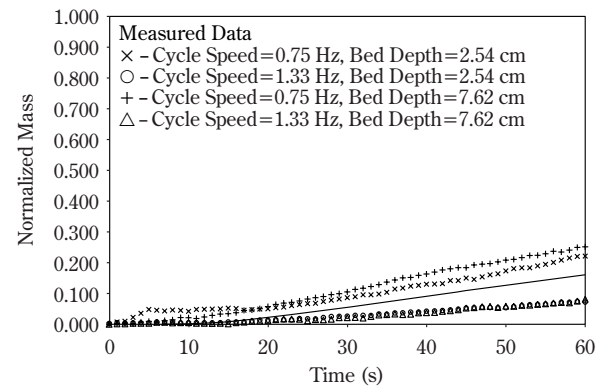


**Fig. 11** Calculated (—) using 5.1:1 data and measured data (×,○,+,Δ) for the 6.4:1 size ratio at strain of 5%

0.025 and 0.206 for a strain of 15% and 0.004 and 0.104 for a strain of 5%, respectively, using the average calculated parameters of 5.1:1. **Figures 10 and 11** compare the measured data and the calculated normalized mass discharge values for the size ratio of 5.1:1. The parameters averaged from the 5.1:1 data reduced the standard deviations to 0.061 and 0.048 for the 15% and 5% strains, respectively. This is an average reduction in standard deviation of 77% when compared with the linear interpolation values.

In addition, the convective and diffusive parameters of the segregation constitutive model were calculated by minimizing the standard deviation in the same manner as the other size ratios. The optimal solutions are given in **Tables 7 and 8**. The standard deviations from optimal solutions are comparable for this size ratio (6.4:1) to the three other ratios (10.9:1, 8.7:1, 5.1:1). The standard deviation values using 5.1:1 data to predicted 6.4:1 percolation profiles were 0.061 and 0.048 for strain of 15% and 5%, respectively. The corre-

sponding standard deviation values for optimal solutions are 0.009 and 0.007, respectively. While the magnitudes of standard deviation values when using 5.1:1

**Table 7** Convective-diffusive segregation constitutive model parameter values ( $\mu/\delta$ ) at 15% strain with standard deviations between model and data in parentheses\*

Condition	Size Ratio 6.4:1
Strain Rate 0.75 Hz Bed Depth 2.54 cm	0.000/0.177 (0.010)
Strain Rate 0.75 Hz Bed Depth 7.62 cm	0.000/0.167 (0.006)
Strain Rate 1.33 Hz Bed Depth 2.54 cm	0.035/0.141 (0.006)
Strain Rate 1.33 Hz Bed Depth 7.62 cm	0.057/0.086 (0.005)

\* To convert  $\mu$  to  $u_0$ , multiply the entries by 1.969 (bed depth=2.54 cm), 0.984 (bed depth=5.08 cm), 0.656 (bed depth=7.62 cm) (units=cm/s), and  $\delta$  to  $D_0$ , multiply entries by 3.875 (bed depth=2.54 cm), 0.969 (bed depth=5.08 cm), 0.431 (bed depth=7.62 cm) (units=cm<sup>2</sup>/s)



**Table 8** Convective-diffusive segregation constitutive model parameter values ( $\mu/\delta$ ) at 5% strain with standard deviations between model and data in parentheses\*

Condition	Size Ratio 6.4:1
Strain Rate 0.75 Hz Bed Depth 2.54 cm	0.000/0.146 (0.020)
Strain Rate 0.75 Hz Bed Depth 7.62 cm	0.000/0.068 (0.005)
Strain Rate 1.33 Hz Bed Depth 2.54 cm	0.000/0.169 (0.005)
Strain Rate 1.33 Hz Bed Depth 7.62 cm	0.000/0.068 (0.004)

\* To convert  $\mu$  to  $u_0$ , multiply the entries by 1.969 (bed depth=2.54 cm), 0.984 (bed depth=5.08 cm), 0.656 (bed depth=7.62 cm) (units=cm/s), and  $\delta$  to  $D_0$ , multiply entries by 3.875 (bed depth=2.54 cm), 0.969 (bed depth=5.08 cm), 0.431 (bed depth=7.62 cm) (units=cm<sup>2</sup>/s)

values is six-fold compared with optimal solutions, the absolute errors between measured and calculated values are approximately 5.5%. Such absolute errors are acceptable considering that no interpolation of parameter values was possible. Thus as a first approximation, 5.1:1 ratio parameters may be used to qualitatively assess the response of 6.4:1 size ratio mixtures.

## 6. CONCLUSIONS

A primary segregation shear cell (PSSC) was used to measure the material parameters of a convective-diffusive segregation constitutive model for percolation of fines through a bed of coarse particles. The effects of size ratio, strain, cycle speed, and bed depth on the percolation of fine particles in binary mixtures of glass spheres were modeled. Based on the tests conducted in this research, the following conclusions were made.

1. The convective-diffusive segregation constitutive model represented the normalized mass versus time relationships better than the convective model. On average, the range of standard deviation was 0.105 to 0.025, a 76% reduction, when comparing the PSSC convective model with the PSSC convective-diffusive model. This is due to the random mixing occurring during the diffusive behavior either during the entire duration of the test or after the initial discharge.
2. The convective-diffusive model was limited in predicting the percolation of the 6.4:1 ratio due to the absence of an initial discharge. Estimating the percolation for the 6.4:1 size ratio was accomplished by using the mean normalized mass vs.

time data of the 5.1:1 size ratio. The average data of the 5.1:1 size ratio reduced the standard deviation by 77% when comparing to size ratio linear interpolation using all three size ratios (10.9:1, 8.7:1, and 5.1:1). The initial rapid discharge present in 10.9:1 and 8.7:1 treatments increased the standard deviation of the prediction.

3. A region of size ratios that defines an initial rapid discharge for binary mixtures of spherical glass beads lies between 6.4:1 and 8.7:1.

## 7. ACKNOWLEDGEMENTS

This study was partially funded by the U.S. Department of Agriculture and Pennsylvania Agricultural Experiment Station.

## 8. NOMENCLATURE

c	concentration
df	degrees of freedom
D	dispersion coefficient
$\bar{D}$	diffusive component
h	bed depth
m	mass of fines
M	mixer matrix; mass of fines at the exit at a given time
n	number of data points at exit
t	time
u	transport speed
$\bar{u}$	convective transport component
x	position or location

## Greek symbols

$\delta$	dimensionless diffusive component
$\theta$	direction as shown in <b>Figure 3</b> ; position along this direction
$\lambda$	dimensionless length
$\mu$	mean; dimensionless convective transport component
$\sigma$	standard deviation
$\tau$	dimensionless time
$\Delta n$	increment (if positive) or decrement (if negative) refers to next or previous, respectively
$\Delta t$	time increment

## Subscripts

1	component 1
2	component 2
i	specified time value

- k cell or layer number
- n layer number
- r total number of layers
- $\theta$  along the direction shown in **Figure 3**

## 9. REFERENCES

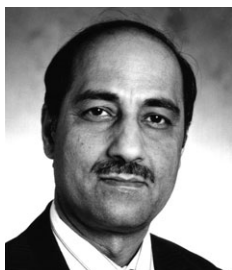
1. Bridgwater, J., M. H. Cooke, and A. M. Scott. 1978. Inter-particle percolation: equipment development and mean percolation velocities. *Trans IChemE*, Vol. 56: 157-167.
2. Bridgwater, J. 1994. Mixing and segregation mechanisms in particle flow. Ed.: Mehta, A. *Granular material-an interdisciplinary approach* 161-193. Springer-Verlag New York, Inc.
3. Duffy, S. P. and V. M. Puri. 2002. Primary segregation shear cell for size-segregation analysis of binary mixtures. *KONA (Powder and Particle)*, 20: (196-207).
4. Duffy, S. P. 2001. A Primary Tester for Size Segregation Analysis and Development and Validation of Two Mathematical Models for Percolation, Ph.D. Thesis. The Pennsylvania State University, University Park, PA.
5. Hwang, C. 1978. Mixing and segregation in flowing powders. Doctor of Philosophy Thesis. The Pennsylvania State University, University Park, PA.
6. Khakhar, D. V., A. V. Orpe, and J. M. Ottino. 2001. Continuum model of mixing and size segregation in a rotating cylinder: concentration-flow coupling and streak formation. *Powder Technology* 116: 232-245.
7. Law, A. M. and W. D. Kelton. 1991. Simulation modeling and analysis – 2nd edition. McGraw Hill, Inc. New York.
8. Rosato, A. D. and D. L. Blackmore. 2000. Segregation in granular flows. Proceedings of the IUTAM Symposium held in Cape May, NJ, June 5-10, 1999. Kluwer Academic Press, Boston, MA. Pp. 342.
9. Shinohara, K. and B. Golman. 2002. Particle segregation of binary mixture in a moving bed by penetration model. *Chemical Engineering Science* 57: 277-285.
10. Sommer, K. 1996. Mixing of particulate solids. *KONA* 14: 73-78.
11. Tang, P., V. M. Puri and P. H. Patterson. 2001. Size segregation analysis using a primary segregation shear cell. Eds.: Adair, J. H., V. M. Puri, K. S. Haris, and C. C. Huang. *Fine Powder Processing International Conference Proceedings*. Pp. 343-350. The Pennsylvania State University, University Park, Pennsylvania.
12. Vallance, J. W. and S. B. Savage. 2000. Particle segregation in granular flows down chutes. Eds: Rosato, A. D. and D. L. Blackmore. *IUTAM Symposium on Segregation in Granular Flows* 31-51. Kluwer academic Publishers.
13. Williams, J. C. 1976. The segregation of particulate materials – a review. *Powder Tech.* 15: 245-251.
14. Williams, J. C. 1986. Mixing of particulate solids – Chapter 16. In Uhl, V. W. and J. B. Gray. *Mixing – theory and practice*. Academic Press, Inc. New York.

## Author's short biography



**Shawn P. Duffy**

Dr. Shawn P. Duffy was a Graduate Research Fellow in the Department of Agricultural and Biological Engineering at the Pennsylvania State University. He received his BS, MS and PhD from Penn State specializing in Powder Mechanics. Dr. Duffy received numerous recognitions including US Department of Agriculture National Needs Fellowship and Particulate Materials Center's Research Fellowship. He served on American Society of Agricultural Engineers Bulks Solids Storage and Properties of Cohesive Materials Committees. The work reported in this paper is based on his PhD research. Currently, Dr. Duffy is employed by PPG Industries, Inc, as a Research Engineer.



**Virendra M. Puri**

Dr. Virendra M. Puri is Professor in the Department of Agricultural and Biological Engineering at the Pennsylvania State University. Professor Puri also served as the Acting Director of the Particulate Materials Center, a National Science Foundation's Industry/University Cooperative Research Center. He is also the research thrust leader of *Powder Mechanics* group of the Particulate Materials Center. Dr. Puri received his B.S. from Indian Institute of Technology and M.S. and Ph.D. from the University of Delaware in Mechanical Engineering. Professor Puri's research interests include: measurement of fundamental engineering properties of powders, development and validation of constitutive models, and use of numerical methods to model flow, segregation, and compaction behavior of powders. He has served as the chairperson of the Bulk Solids Storage Systems Committee of the American Society of Agricultural Engineers. Professor Puri is a Co-Editor-in-Chief of the *Particulate Science and Technology, An International Journal*. Dr. Puri regularly offers a postgraduate course in the area of powder mechanics and several hands-on industrial short courses. Professor Puri has received several teaching and research awards.

# Vapor-Phase Synthesis of Fine Ag Powder and its Application to the Production of Fine Grained Sintered Ag-C Compacts<sup>†</sup>

H. Toku, O.W. Bender, A.C. Doring  
and A.C. da Cruz

*Institute for Technological Research of  
the State of São Paulo—IPT  
Department of Mechanics and Electricity\**

P.K. Kiyohara

*University of São Paulo  
Institute of Physics\*\**

A.L. Silva

*Independent Consultant*

## Abstract

*An experimental investigation was carried out on the production of silver powder based on a vapor phase synthesis process. The main objective of the work was to investigate the feasibility of producing fine metal particles in a lab scale basis, which would lead to a fine grained microstructure of compacts produced from a mixture of these powders with graphite. Using a thermal plasma high temperature reactor, fine silver particles were produced at a rate of 500 g/h, with the thermal plasma power rated at 15 kW. The powders produced were characterized for particle size and size distribution by laser scattering technique, and particle size and morphology using scanning electron microscopy. Sintering experiments of compacted bodies obtained from a mixture of the powders produced and graphite powder demonstrated the feasibility of producing a material presenting a homogeneous microstructure suitable to the fabrication of high performance electrical switch contacts. Metallographic preparations of Ag/C compacts were used for the microstructure analysis using optical microscopy. The experimental apparatus involved the use of a transferred arc plasma evaporator coupled with a tubular cooling section in which the hot gases carrying the metal vapor are quenched to produce fine particles. A study was carried out to provide theoretical support to the experimental investigation. Applied to the tubular gas quenching section, a 2-D model was used to determine the temperature, velocity and species concentration fields. Fluid-dynamics was combined with a model for the nucleation and growth of particles based on the moments of particle size distribution.*

## 1. Introduction

The many methods employed in the preparation of metal and ceramics fine particles include gas-phase processes, laser ablation, sputtering techniques, and chemical methods. In the work of Kruis et al.<sup>1</sup> a comparison is made between two of these methods:

gas-phase and liquid based process. A number of advantages of the first are pointed out, including higher purity products, the potential to create complex chemical structures, better process and product control, economics, and less chemical segregation. Moreover, because the gas-phase method usually leads to continuous processing, it is better suited to large scale production.

The evaporation-condensation technique is one of the gas-phase methods used to produce fine particles. In order to achieve considerable evaporation rates, this method requires high temperatures and the use

\* P.O. Box 0141—CEP 01064-970—São Paulo, SP, Brazil  
E-mail: acarlos@ipt.br

\*\* P.O. Box 66318—CEP 05315-970—São Paulo, SP, Brazil

<sup>†</sup> Accepted: September 9, 2003

of intensive energy sources. In particular, the evaporation-condensation of materials using thermal plasmas has been largely studied<sup>2</sup>. A wide variety of different such plasma processes have been used to synthesize ultra-fine particles. Many different types of plasma generators including non-transferred arcs, transferred arcs, high frequency induction plasmas, and combinations of these have been applied in combination with both homogeneous and heterogeneous precursors. Usually very fine particles are produced, which may include pure metals, alloys, ceramics and composite materials<sup>3</sup>.

This paper reports a study on transferred-arc syntheses of silver (Ag) powder. Commercially available Ag powder is classified as microcrystalline, spheroidal, or lamellar, according to its particle shape<sup>4</sup>. All three types, which differ in method of manufacture, have specific areas of use. The most important method used for the production of microcrystalline Ag powder is precipitation by reducing agents. These powders were used almost entirely in sintering technology for a long time. Today, they are also used in stoving preparations (e.g., metallization of ceramics) and in pastes used in the manufacture of heated rear windows of motor vehicles. Spheroidal Ag powder is produced by atomization of molten silver by compressed air, inert gas, water jet, or a rapidly rotating knife. These powders are mainly used in sintering technology. Lamellar particles are obtained by ball milling microcrystalline silver powder and are mainly used as an additive to paints and adhesives to which they impart electrical conductivity as a result of the good particle-to-particle electrical contact.

The investigation has the main objective to produce Ag powder finer than the powders commercially available, particularly those produced by chemical precipitation intended for sintering of electrical contacts. To this respect we look at the production of sintering compacts with a refined microstructure, which can not be achieved with the commercially available powder.

In case of the present application, the main advantage of transferred-arc thermal plasma reactors is the unlimited temperature driving force for evaporation. Temperatures of more than 10000 K can easily be sustained either by striking the arc directly to the anode work piece, or by feeding raw material in the form of powders directly into the arc. Because transferred-arcs can be operated over a broad range of gas flow rates, including very low flow rates, operating costs can be kept low. Also, control over the concentration of the evaporated species in the exhaust gas (and con-

sequently over particle size) can be provided simply by adjusting the desired flow rate in face of a given evaporation rate. An additional advantage of transferred-arc systems is that the plasma evaporator may be scaled up over a broad range of powers simply by increasing the arc current (100–5000 A).

A modeling study concerning the nucleation and growth of fine particles from the transition of gas-to-condensed phase, adapted from a previous work involving both AlN and pure Al synthesis<sup>5</sup>, was carried out with the objective to provide theoretical support to the experimental investigation.

## 2. Experimental

A schematic diagram of the experimental apparatus is shown in **Figure 1**. The reactor mainly comprised an evaporation and a cooling chamber, according to the transferred-arc concept previously reported<sup>3</sup>. Inside the first chamber (270 mm i.d. × 300 mm high) Ag was evaporated from a molten bath (3 ~ 5 kg) contained in a graphite crucible that worked as the anode of a DC transferred-arc plasma. The plasma and cooling chamber were connected through a 40 mm i.d. × 175 mm long graphite tube. In all experiments argon (Ar) gas was used as plasma and Ag vapor carrier gas. Typical operating conditions are presented in **Table I**. Ar was fed in the arc chamber through the cathode assembly at 120 lpm flow rate. Ar or nitrogen (N<sub>2</sub>) were used as the cooling gas in three different assemblies of the cooling chamber, as shown in **Figure 2**. In Assembly #1, Ar was radially injected at a flow rate  $Q_A=80$  lpm through a 54 mm i.d. ring comprising 24 equally spaced holes of 1 mm

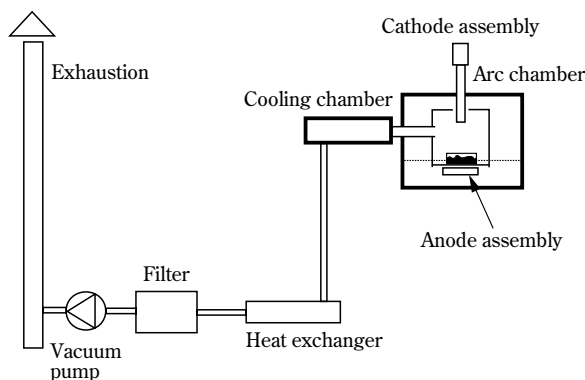


**Fig. 1** Schematic diagram of the plasma reactor applied for the vapor phase synthesis of Ag fine powder.



**Table I** Operating conditions applied in the plasma experiments for the preparation of fine Ag powders.

Starting material	Ag-99,9% min.		
Ar flow rate, cathode assembly (lpm <sup>(1)</sup> )	120		
Amount of Ag in the crucible (kg)	3,5 ~ 5,0		
Arc voltage (V)	60		
Arc current (A)	250		
Arc power (kW)	15		
Gas temperature at evaporation chamber outlet (K)	1500		
Cooling gas flow rate (lpm)	Exp. #1, Ass. #1	$Q_A=80^{(2)}$	—
	Exp. #3, Ass. #2	$Q_A=80^{(2)}$	$Q_B=60^{(2)}$
	Exp. #5, Ass. #3	$Q_A=160^{(3)}$	—

<sup>1</sup> Gas flow rates (lpm) referred to 298 K and 100 kPa; <sup>2</sup> Argon; <sup>3</sup> Nitrogen.

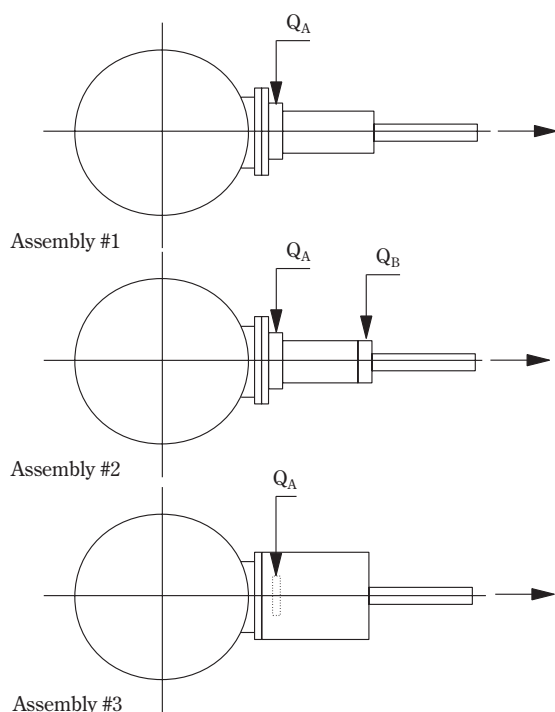


**Fig. 2** Schematic representation of the three cooling chamber geometries used for the vapor phase synthesis of Ag fine powder (top view of plasma and cooling chambers).

diameter each. The dimensions of the cooling chamber were 54 mm i.d. × 240 mm long. Using the same cooling chamber dimensions and radially fed Ar as in

Assembly #1, in Assembly #2 N<sub>2</sub> was additionally fed at the outlet port of the cooling chamber, at a flow rate  $Q_B=60$  lpm through an annular slit 2 mm wide. In Assembly #3 the dimensions of the cooling chamber were increased to 220 mm i.d. × 520 mm long. In this case only N<sub>2</sub> was radially injected at a flow rate  $Q_A=160$  lpm through a 80 mm i.d. ring comprising 18 equally spaced holes of 1.5 mm diameter each. The ring was placed on the center line of the cooling chamber, at a distance of 40 mm from its entrance.

Two experiments were carried out with each of the cooling chamber assemblies described above. Only the results for experiments #1, #3 and #5 are reported. Metal particles which formed in the cooling chamber were collected in a bag filter installed after a heat exchanger. The exhaustion line also included a vacuum pump used to keep constant pressure (close to 100 kPa) inside the evaporation chamber in spite of the head loss observed through the bag filter. Internally, the plasma chamber was heavily insulated in order to minimize heat losses. The external walls of reactor were water cooled to guarantee dimensional stability.

In all experiments, steady state condition at a plasma chamber off gas temperature of 1500 K was achieved after approximately 1 hr operation, with the DC transferred-arc plasma rated at 15 kW (60 V × 250 A). Using an optical pyrometer, bath temperatures of the order of 2400 K were measured right after shutting down the arc. At the given conditions, Ag powder was produced at a 500 g/h rate. An evaluation of the quenching conditions in terms of the average after-quenching-temperature for each of the experiments considered is shown in **Table II**.

The Ag powders produced were characterized for particle size distribution using laser scattering analysis and for particle size and morphology using scanning electron microscopy (SEM). In order to evaluate the degree of homogeneity of the microstructure

**Table II** Evaluation of quenching conditions for each of the experiments considered.

	Exp. #1	Exp. #3	Exp. #5
Carrier gas	Ar (1500 K) 120 lpm	Ar (1500 K) 120 lpm	Ar (1500 K) 120 lpm
Quenching gas	Ar (298 K) 80 lpm	Ar (298 K) 140 lpm	N <sub>2</sub> (298 K) 160 lpm
After quenching average temperature	1011 K	846 K	706 K

Ag melting point: 1234 K; boiling point: 2483 K.

resulting from the preparation of sintered compacts having electrical-contact characteristics, 1 kg of powder was produced from which mixtures with both graphite powder (Fisher mean diameter of 0.001 mm) and carbon black (Degussa Printex G) in a 95%Ag/5%C mass ratio were prepared. Typically, such compacts are prepared from the dry mixture of commercial Ag powder with graphite powder. Because this practice did not provide good results for the fine Ag powder we produced, its mixing with C was carried out using a suspension of the constituent powders in isopropyl alcohol. Compacts (15 mm dia.  $\times$  5 mm height) were prepared and sintered at 800°C in H<sub>2</sub>/N<sub>2</sub> atmosphere. Their microstructure was analyzed from metallographic preparations observed in an optical microscope. For the sake of comparison, the same microstructure analysis was also carried out with an Ag/C insert commercialized as electrical contact.

### 3. Numerical model

The cooling region is approximated to a tubular axis-symmetric section according to the geometry and dimensions shown in **Figure 3**. Hot gas containing Ag vapor enters a circular port of diameter 40 mm at a flow rate Q1. Room temperature Ar gas is fed through a circumferential gap 0.1 mm wide at 175 mm far from the entrance port at a flow rate Q2. The total length of the quenching section is taken as 435 mm.

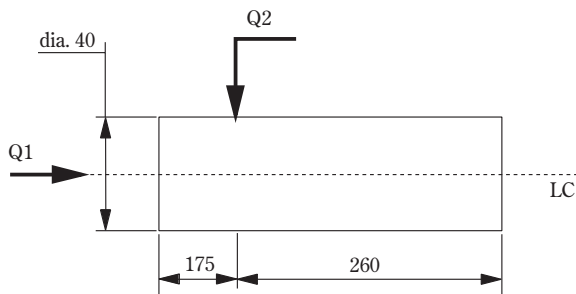


**Fig. 3** Schematic representation of the modeled region dimensions in mm.

The many conservation equations describing both fluid flow and phase transition phenomena are solved in two steps: (i) first, the fields for velocity, temperature, and chemical species concentration are calculated; (ii) following, the particle nucleation and growth

process arising from the mixing of a hot gas flux carrying Ag(v) and a radial jet of a cold Ar gas mixture is determined. The following conservation equations are solved in the first step, assuming laminar axis-symmetric flow:

Continuity:

$$\nabla \cdot (\rho u) = 0 \quad (1)$$

Moment conservation:

$$\nabla \cdot (\rho u u) = \nabla \cdot (\mu \nabla u) - \nabla p \quad (2)$$

Chemical species conservation:

$$\nabla \cdot (\rho u w_i) = \nabla \cdot (\rho D_{i,Ar} \nabla w_i) + S_i \quad (3)$$

Energy conservation:

$$\nabla \cdot (\rho u h) = \nabla \cdot \left( \frac{k}{C_p} \nabla h \right) + \nabla \cdot \left[ \sum_i h_i \left( \frac{k_i}{C_{p_i}} - \frac{k}{C_p} \right) \nabla w_i \right] + S_h \quad (4)$$

The particle nucleation and growth problem is solved using the method of moments of the PSD. It is assumed that: PSD can be represented by a single log-normal distribution at any location of the modeled region; particles are spherical and transported by convection, Brownian diffusion, and thermophoresis; and particles can grow by condensation and heterogeneous reaction and coagulation. The  $k^{\text{th}}$ -moment conservation is written as:

$$\frac{\partial M_k}{\partial t} + \nabla \cdot (u + u_{th}) M_k = \nabla \cdot (D_p \nabla M_k) + v_{cr}^k J - \int_0^\infty v^k \frac{\partial}{\partial v} (Gn) dv + (B - D)_k \quad (5)$$

The birth and death term (B-D) includes a nucleation equation that considers the effect of heterogeneous reaction in the AlN system<sup>6</sup>:

$$J = \frac{n(v_1) \beta s_1}{3 S_{Ag}} \sqrt{\frac{\theta}{\pi}} \exp \left[ -\frac{4}{27} \frac{\theta^3}{(\ln S_{Ag})^2} \right] \quad (6)$$

These two sets of conservation equations are written in the form of algebraic equations and solved using the SIMPLER computational method as developed by Patankar<sup>7</sup>.

## 4. Results and discussion

### 4.1. Ag powder synthesis

**Figure 4** shows the particle size distribution (PSD) of powders produced with the three different cooling

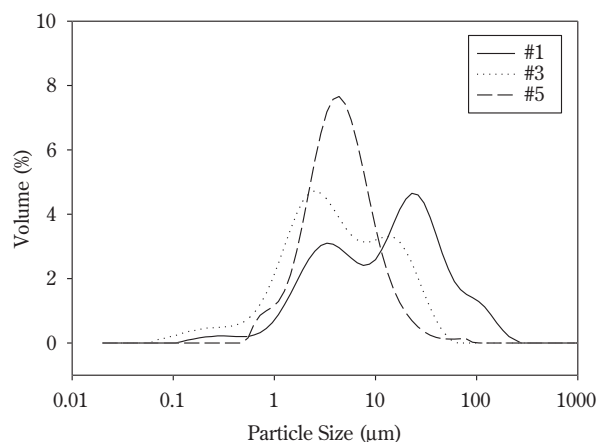
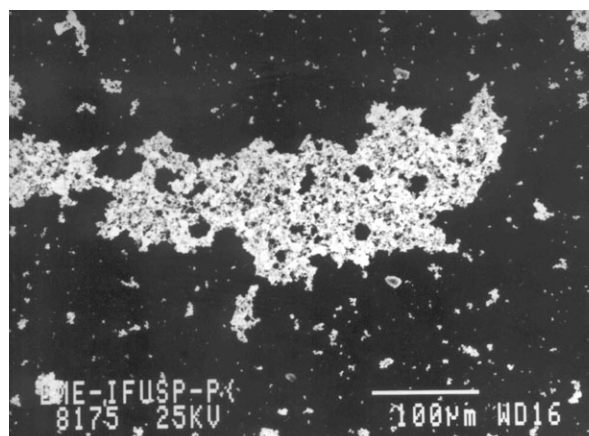


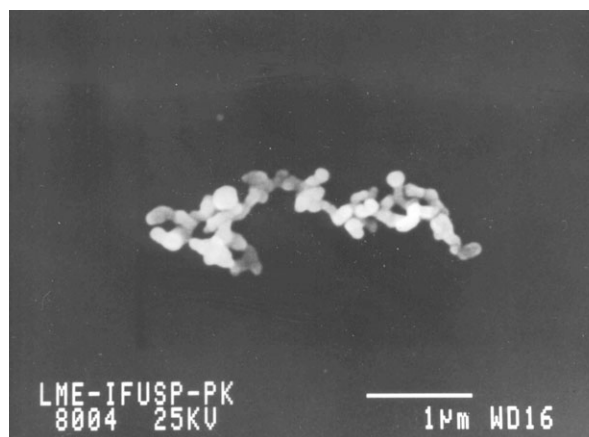
**Fig. 4** Particle size distribution of powders produced in different plasma synthesis experiments.

chamber assemblies. The transition which is observed between PSDs with many peaks (Exps. #1 and #3) and the practically log-normal PSD of the powder produced in Exp. #5 results from the different cooling conditions (cooling chamber geometry and gas flow rate) which were applied to the plasma chamber off-gas stream. As described before, each cooling chamber geometry was combined with a different set of cooling gas composition and flow rate. The different arrangements shown in **Figure 2** were progressively implemented aiming to increase cooling intensity and to prevent particle deposition on the cooling chamber walls that occurred with higher intensity in case of assemblies #1 and #3. SEM micrographs of typical agglomerates occurrences in Exp. #3 and Exp. #5 are shown in **Figure 5**. The large agglomerates observed in **Figure 5(a)** were also observed for the powder produced in Exp.#1. A more detailed analysis of primary particles shown in the SEM micrographs indicates that they are about the same size (100 ~ 200 nm).

Considering a plasma gas flow rate  $Q_1=20$  lpm at 2000 K entering the simplified quenching section shown in **Figure 3**, the Ag gas-to-condensed phase transition was analyzed using numerical simulation. At first a comparison was carried out between the nucleation and growth of Al, which was the subject of a previous study<sup>8</sup>, and Ag at a same set of operating parameters: radial quenching  $Q_2=7$  lpm of Ar at room temperature and pressure (298 K, 100 kPa). The corresponding temperature field is shown in



(a)



(b)

**Fig. 5** Typical particle agglomerates observed in different plasma synthesis experiments: a) Exp. #3); and b) Exp. #5.

#### Figure 6.

Assuming a metal vapor concentration at the entrance of the cooling section typically observed in Al evaporation/condensation experiments of the same sort<sup>8</sup>, conducted with a plasma chamber off-gas temperature of 2000 K, a metal vapor mole fraction 0.002 was considered in the phase transition simulation of both Al and Ag. The results for the nucleation rate field are presented in **Figure 7**. It is observed that for the above conditions the more intense Al nucleation (at a rate of  $10^{11}$   $1/m^3.s$  and above) occurs near the wall, before the region of stronger cooling and along the radial jet. The Ag nucleation on the other hand occurs only in the stronger cooling region along the radial jet and in a broader volume.

The vapor pressure and surface free energy of Al and Ag as a function of temperature are graphically

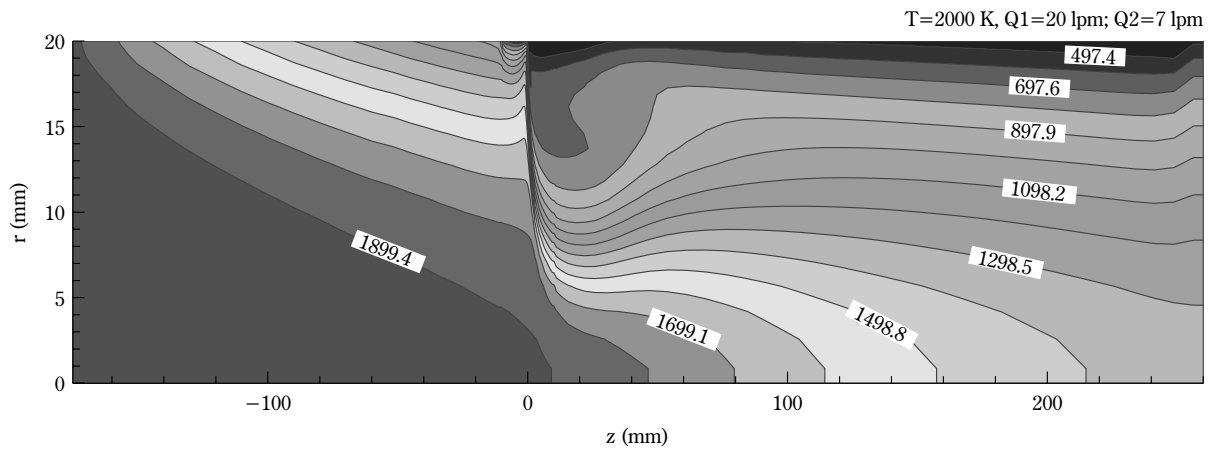


**Fig. 6** Temperature distribution inside the quenching section simulated for a tubular quenching section of 40 mm dia., Ar gas flow rate Q1=20 lpm at 2000 K, and quenching gas injection Q2=7 lpm.

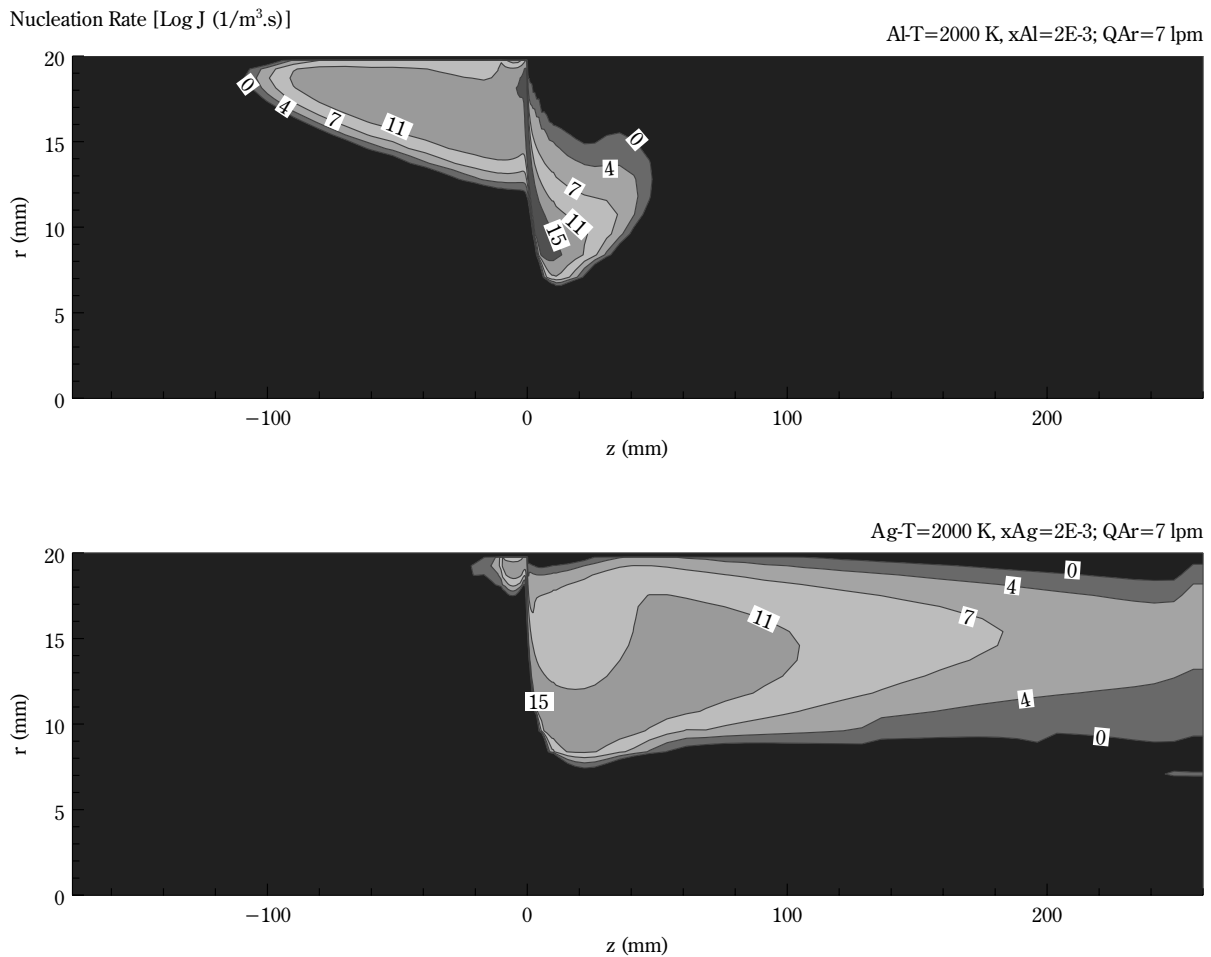


**Fig. 7** Distribution of the nucleation rates simulated for Al and Ag fine particle synthesis in a tubular quenching section of 40 mm dia., Ar gas flow rate Q1=20 lpm at 2000 K, quenching gas injection Q2=7 lpm, and metal vapor molar fraction of 0.002.

shown in **Figures 8** and **9**, respectively. The higher vapor pressures of Ag contributes to its easier evaporation when compared with Al. Accordingly, experimental data gathered along the present research point out to Ag vapor concentrations which are about one order of magnitude higher than could be obtained for Al evaporation experiments carried out at a higher temperature level<sup>9</sup> (1500 K in case of Ag vs. 2000 K in case of Al). With respect to the surface free energy, it is observed that its change associated with

the gas-to-condensed phase transition of Ag is greater than the corresponding change observed for Al. The Gibbs free energy change for such phase transition being given by:

$$\frac{\Delta G}{k_B T} = -(i-1)\ln S + i^{2/3}\theta \quad (7)$$

This fact explains the results shown in **Figure 7** according to which, for the metal vapor concentration considered, Ag vapor travels inside the cooling chamber longer than Al before critical conditions are achieved and particles nucleation is promoted. Considering these experimental and theoretical results, a new simulation of the Ag nucleation was carried out whose analysis is presented next.

The temperature distribution obtained for the simulation of Q1=100 lpm at 1500 K and Q2=60 lpm (Ar at room temperature) is shown in **Figure 10**. Compared with the graph of **Figure 6**, a sharper temperature gradient is observed in the present condition, with the influence of the radial jet reaching the center line of the tubular cooling chamber, very close to the cold gas injection axial coordinate. Two different Ag(v) concentrations were considered for the particle nucleation and growth simulation:  $x_{Ag_{in}}=0.002$  and 0.02. The results presented in **Figure 11** show that, analogous to the condition depicted in **Figure 7** for the Al nucleation, in case of the lower concentration situation some of the Ag particle nucleation occurs near the wall, before and along the quenching jet. On the other hand, the simulation with the higher concentration results in the predominant occurrence of nucleation at the very entrance of the quenching section. Accordingly, the distribution of the Ag(v) concentration presented in **Figure 12(b)** for  $x_{Ag_{in}}=0.02$

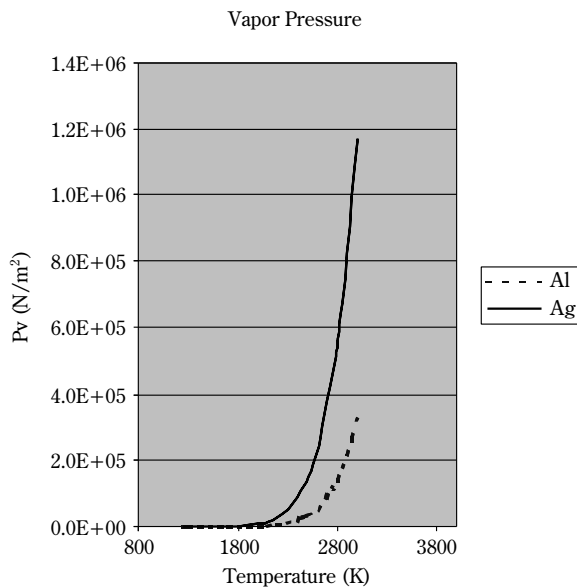


**Fig. 8** Change of the vapor pressure as a function of temperature for Al e Ag.

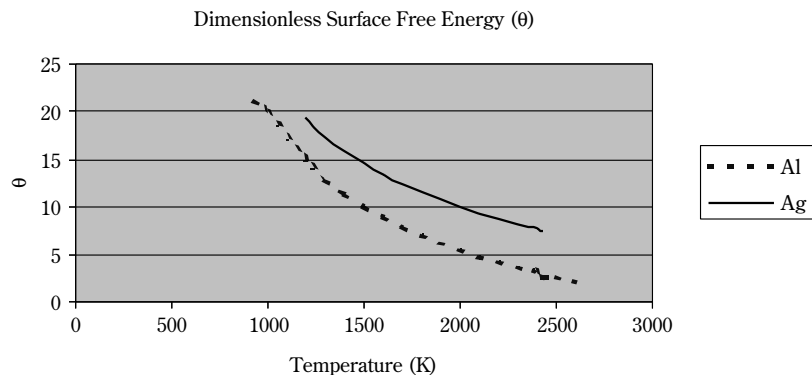


**Fig. 9** Change of the dimensionless surface free-energy as a function of temperature for Al e Ag.



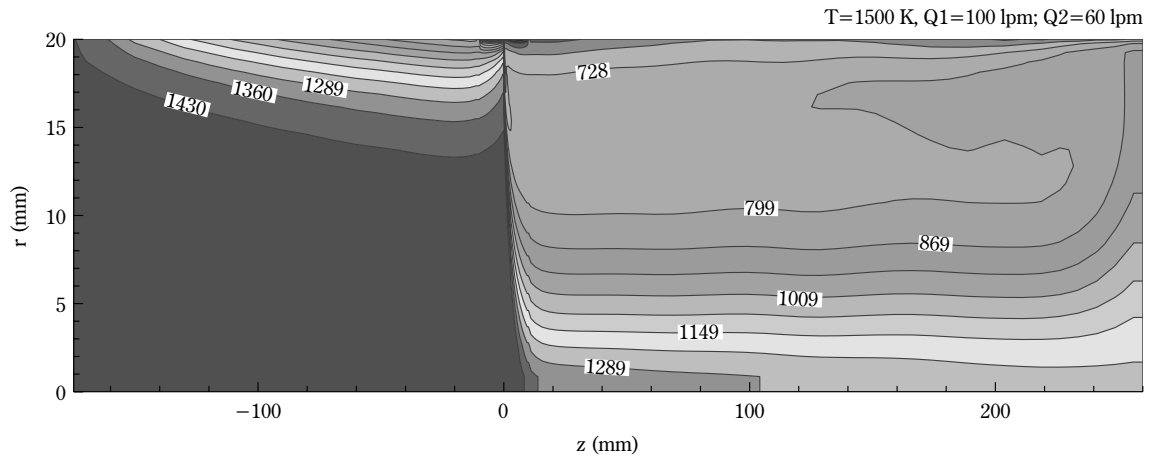


**Fig. 10** Temperature distribution inside the quenching section simulated for a tubular quenching section of 40 mm dia., Ar gas flow rate Q1=100 lpm at 1500 K, and quenching gas injection Q2=60 lpm.

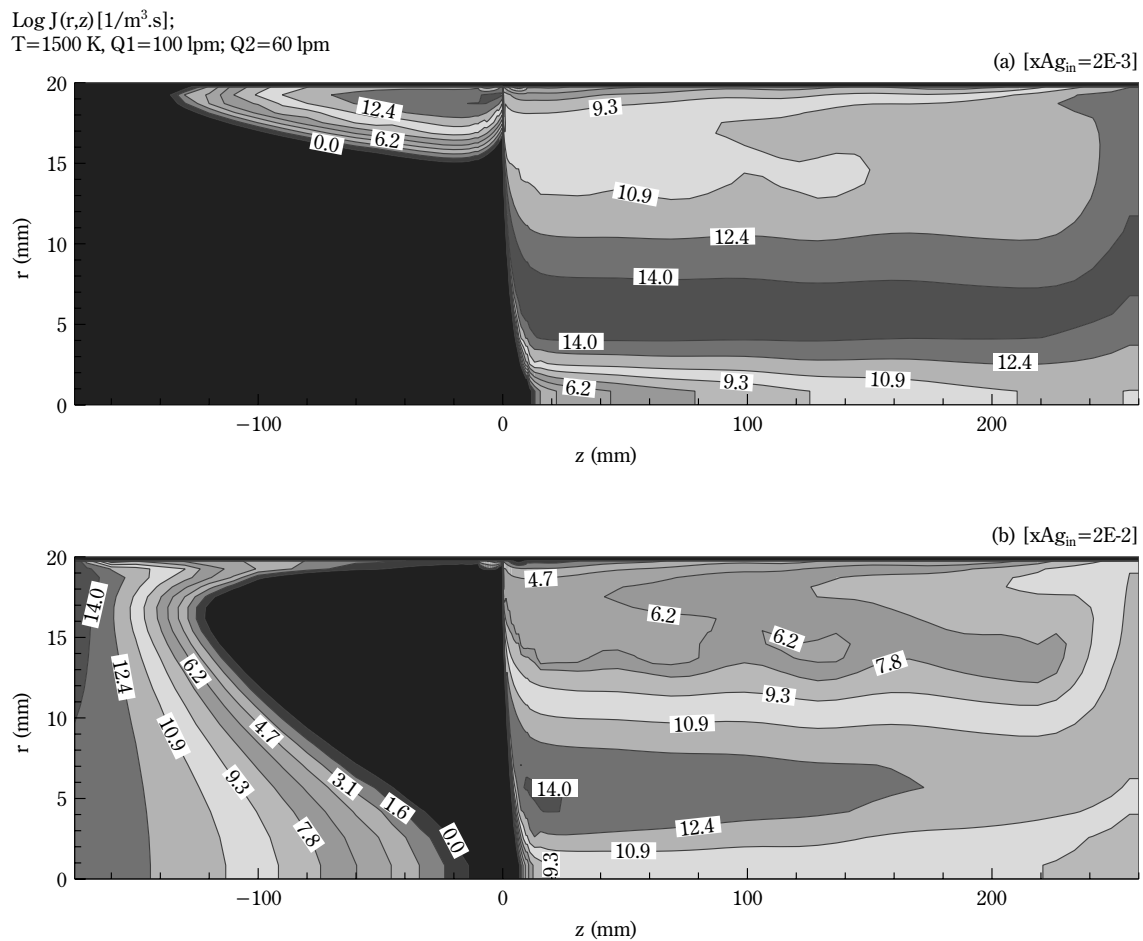


**Fig. 11** Distribution of the nucleation rates simulated for Ag fine particle synthesis in a tubular quenching section of 40 mm dia., Ar gas flow rate Q1=100 lpm at 1500 K, quenching gas injection Q2=60 lpm, and metal vapor molar fractions of 0.002 and 0.02.

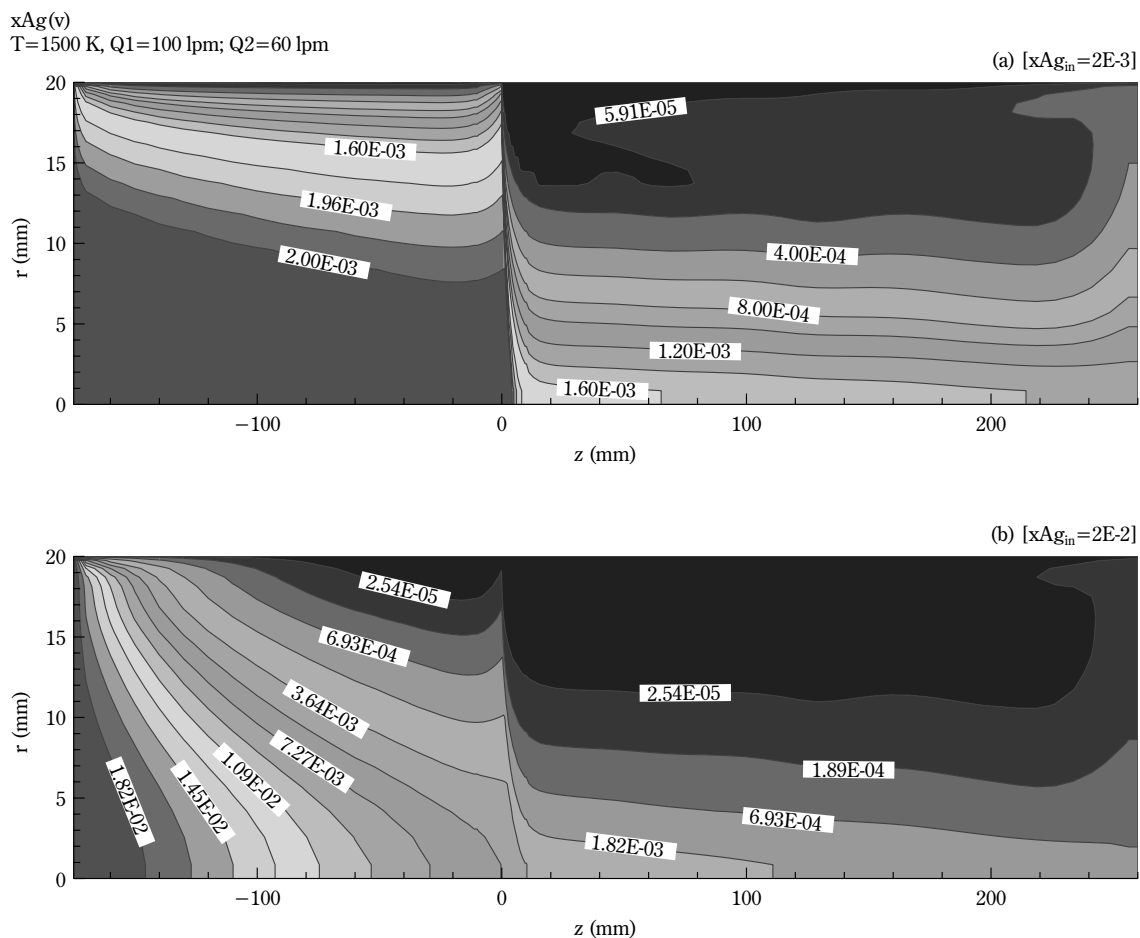


**Fig. 12** Distribution of vapor concentration simulated for Ag fine particle synthesis in a tubular quenching section of 40 mm i.d., Ar gas flow rate  $Q_1=100\text{ lpm}$  at 1500 K, quenching gas injection  $Q_2=60\text{ lpm}$ , and metal vapor molar fractions of 0.02.

shows that most of the metal vapor is consumed before the jet zone; at a same location after the quenching jet, the iso-contour lines depict vapor concentrations which are lower than the  $x_{Ag_{in}}=0.002$  case. As a consequence of the lower  $Ag(v)$  concentrations, the less intense particle nucleation that occurs in the jet dominated region when  $x_{Ag_{in}}=0.02$  results in a minor modification of average particle size, as shown in the distribution of particle diameter ( $d_{BET}$ ) evaluated in terms of the specific surface area of powder shown in **Figure 13** for both  $x_{Ag_{in}}$  considered. The use of the method of moments of PSD considerably simplifies the computational treatment of the problem. Nevertheless, because the method assumes that the PSD can be represented by a single log-normal PSD anywhere in the modeling region, multi-peaks PSD results as suggested from the two nucleation regions

exhibited in the plot of **Figure 11(b)** can not be exhibited in the computational work. The single peak PSD predicted by the model at the outlet of the cooling section for the higher vapor concentration condition is shown in **Figure 14**. In spite of the many simplifications, the fact that most of the Ag vapor condenses right at the entrance of the cooling section (when simulation is carried out with a  $x_{Ag_{in}}$  that corresponds to the Ag vapor concentration experimentally determined) is in good agreement with the experimental results according to which the primary particle size does not depend on the quenching conditions and cooling chamber geometry. Both experimental and modeling results suggest that the gas-to-condensed phase transition giving rise to the formation of primary particles started in the duct that connects the evaporation and cooling chambers,

$D_{BET}(nm)$ ;  
 $T=1500\text{ K}$ ,  $Q1=100\text{ lpm}$ ;  $Q2=60\text{ lpm}$

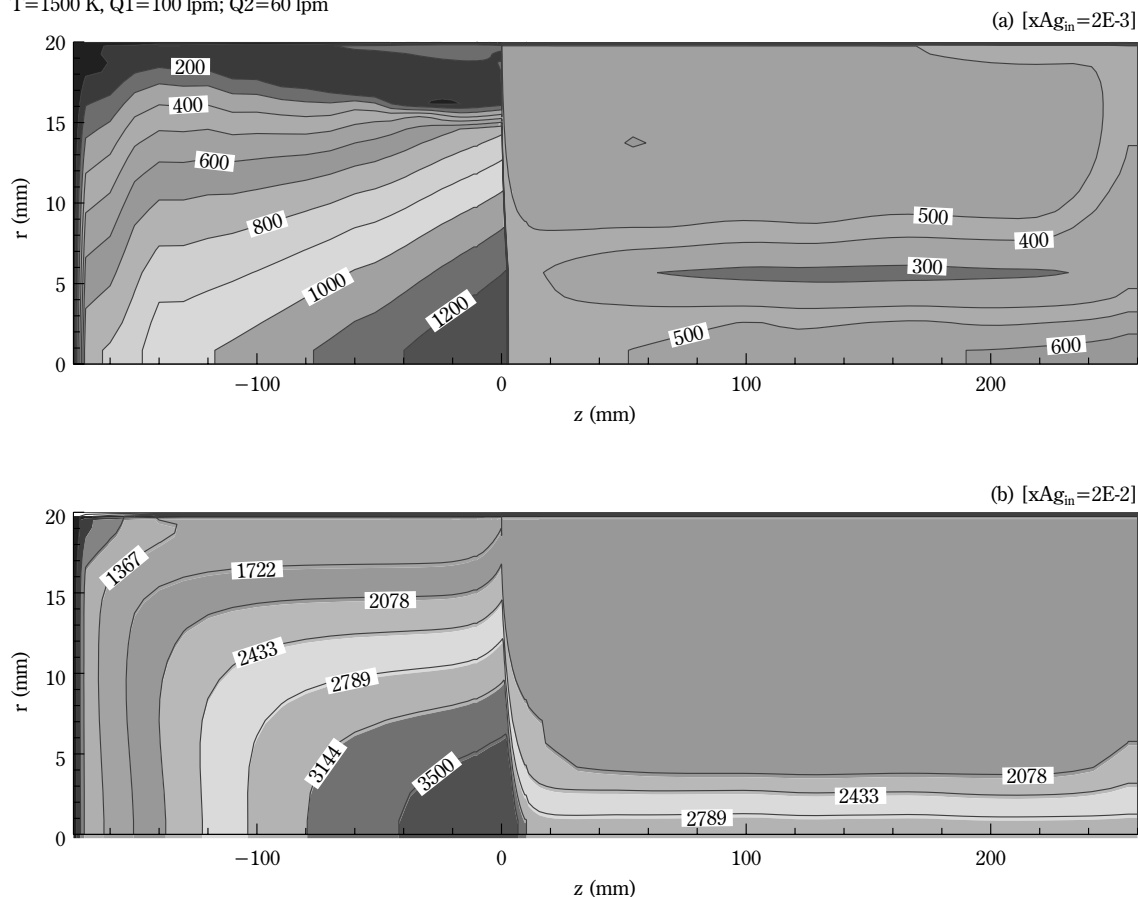


**Fig. 13** Distribution of the BET particle size diameter ( $d_{BET}$ ) simulated for Ag fine particle synthesis in a tubular quenching section of 40 mm i.d., Ar gas flow rate  $Q1=100\text{ lpm}$  at 1500 K, quenching gas injection  $Q2=60\text{ lpm}$ , and metal vapor molar fractions of 0.002 (a) and 0.02 (b).

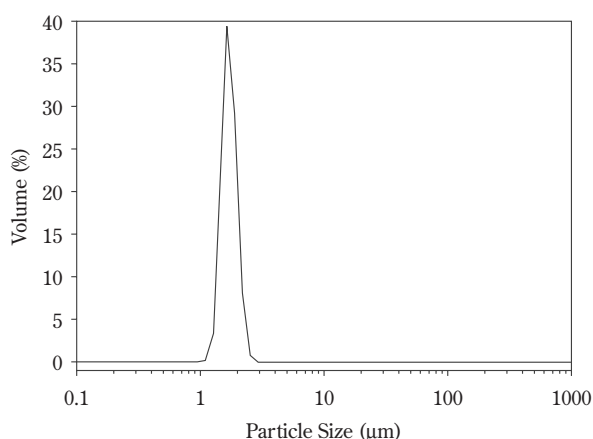


**Fig. 14** Log-normal particle size distribution of powder predicted at the outlet of the modelled region for Ag fine particle synthesis in a tubular quenching section of 40 mm i.d., Ar gas flow rate  $Q1=100\text{ lpm}$  at 1500 K, quenching gas injection  $Q2=60\text{ lpm}$ , and metal vapor molar fractions of 0.02.

before the hot gas stream could be quenched by the cold gas jets. Therefore, the definition of the primary particle size, which in principle can be controlled by quenching intensity, remained little affected by the amount and composition of the cold gas injected at the entrance of the cooling section and its geometry. Nevertheless, as can be observed from the micrographs shown in **Figure 5** changing the cooling variables was effective in preventing a stronger particle agglomeration.

#### 4.2. Ag/C compacts

Because of its well defined PSD and absence of large agglomerates, the powder produced on Exp. #5 conditions was chosen to carry 95Ag/5%C (Ag/5%C) mixture sintering experiments. For the sake of comparison, the PSDs of this powder and of a commercially available Ag powder are shown in **Figure 15**.

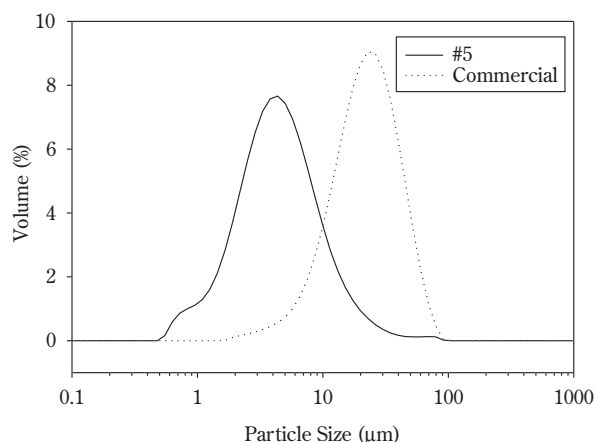
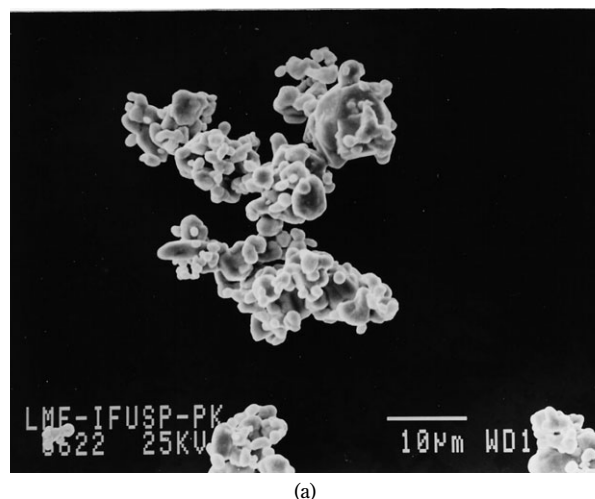


**Fig. 15** Comparison of PSD of plasma synthesized (Exp. #5) and commercial Ag powders.



(a)



(b)

**Fig. 16** Agglomerate morphology of commercial (a) and plasma synthesized [Exp. #5, (b)] Ag powders.

The morphology of particle agglomerates of both commercial and plasma synthesized powders are shown in the SEM micrographs of **Figure 16(a)** and **Figure 16(b)**, respectively. Commercial powder was produced by chemical precipitation. Both PSD and SEM analysis show that average agglomerate size of plasma synthesized powder is about one order of magnitude smaller than the commercial powder; primary particles on the other hand are in higher ratio (between one and two orders of magnitude).

A comparison between PSDs of graphite and carbon black powder which were used in the sintering preparation is shown in **Figure 17**. Particle morphology of these powders are shown in the SEM micrographs of **Figure 18**. The graphite particles have a flake like morphology, while the carbon black although agglomerated have a spherical primary particle morphology.

**Figure 19** shows the micrographs of potassium dichromate attacked metallographic preparations of the Ag/5C commercial electrical contact insert and a sintered compact produced with the plasma synthesized Ag powder. In both cases the graphite powder shown in **Figure 18(a)** was used as the C bearing material. Although the compact prepared with commercial Ag powder exhibits distinct large grains with better defined grain boundary, no relevant difference in terms of C dispersion in the Ag matrix can be noticed in both preparations. On the other hand, a considerable homogeneity improvement has been achieved with the preparation obtained with the powder of Exp. #5 mixed with the carbon black powder, whose micrograph is shown in **Figure 20**.

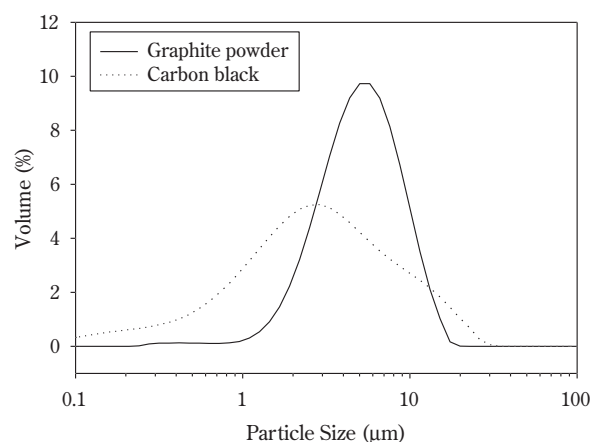
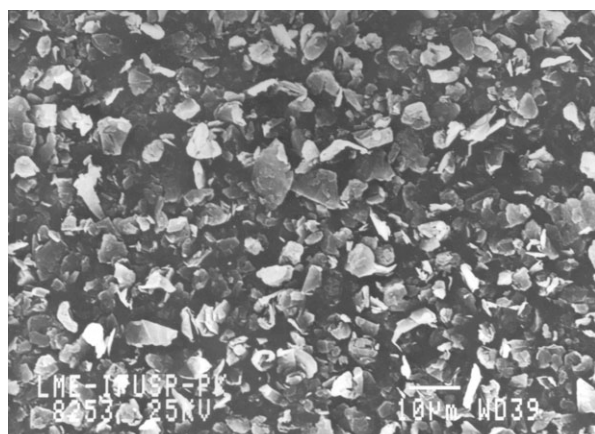
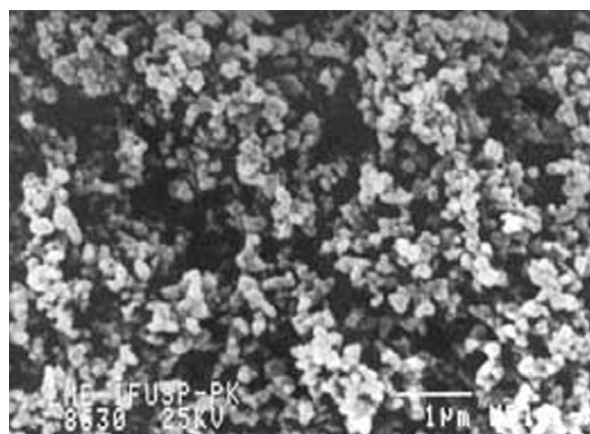


**Fig. 17** PSDs of graphite (Fisher size 0.001 mm) and carbon black (Degussa Printex G) powders used in the preparation of Ag/5C compacts.



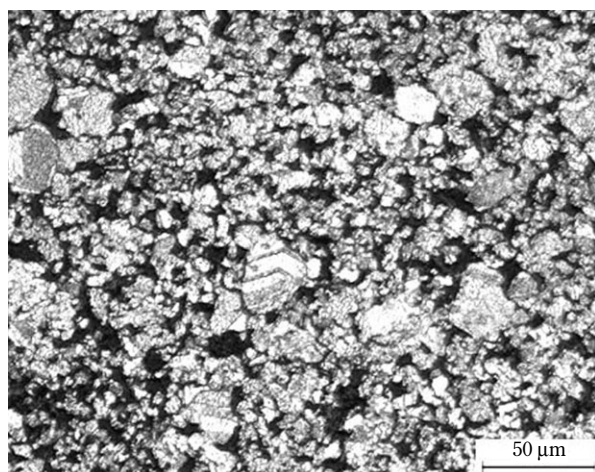


(a)

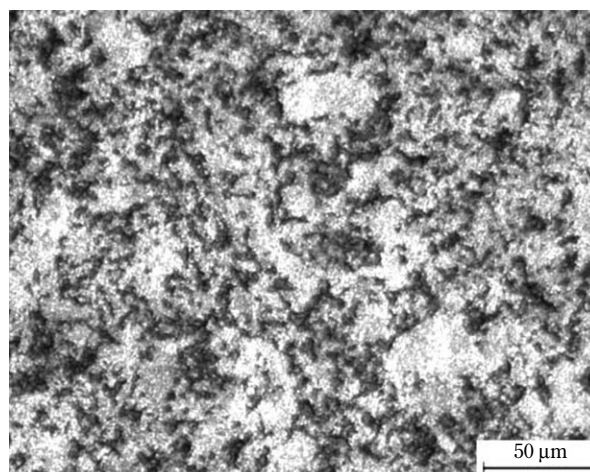


(b)

**Fig. 18** Graphite and Carbon Black powders used in the preparation of Ag/5%C compacts, respectively: (a) Fisher 0.001 mm; and (b) Degussa Printex G.



(a)



(b)

**Fig. 19** Metallographic preparation of Ag/5%C sintered compacts using graphite powder and: (a) commercial Ag powder; (b) plasma synthesized powder (Exp. #5).

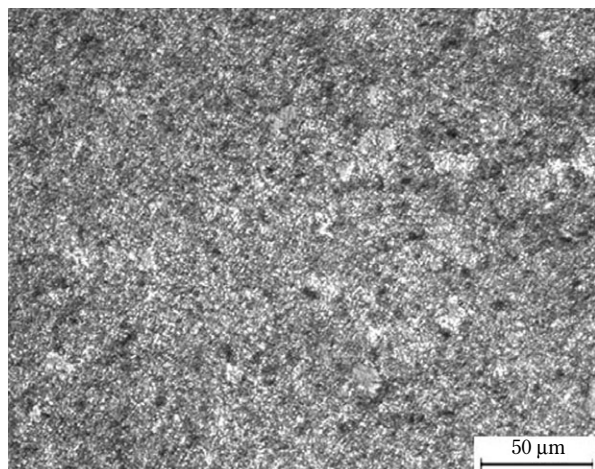


**Fig. 20** Metallographic preparation of Ag/5%C sintered compacts using plasma synthesized powder (Exp. #5) and carbon black.

## 5. Conclusion

Fine Ag powders were produced at a 500 kg/h rate using a transferred-arc thermal plasma synthesis reactor basically formed by evaporation and condensation separate chambers, with the plasma power rated at 15 kW. It is observed that the powders produced are formed by agglomerates which may vary in size depending upon cooling conditions and cooling chamber geometry, but are basically constituted of primary particles within about the same size range (100–200 nm). The expected influence of cooling conditions on primary particle size was not observed. Modeling analysis of this result suggests that gas-to-condensed phase transition possibly occurs inside the evaporation chamber and along the transition duct that exists between the two chambers. The primary



particle size of the plasma synthesized powder is considerably smaller than the one observed in the commercially available powders. Agglomerate size is about one order of magnitude smaller in case of plasma synthesized powder. Sintered compacts of 95%Ag/5%C mass ratio were prepared using the plasma Ag powder and both graphite and carbon black powders. The grain boundary of compacts prepared with commercial Ag powder (commercial electrical contact insert) are better defined, the C dispersion in the Ag matrix observed in both commercial and plasma synthesized Ag powder preparations using graphite powder is about the same. A considerably finer microstructure was observed for the plasma Ag powder when it was mixed with carbon black.

### Acknowledgment

The authors thankfully acknowledge the financial support given by Fundação de Amparo à Pesquisa do Estado de São Paulo–FAPESP, Brazil (Process No. 98/14864-5).

### Nomenclature

$B$	=birth term in the moment conservation equation	
$C_p$	=specific heat	(J/kg.K)
$D$	=death term in the moment conservation equation	
$D_{i,Ar}$	=mass diffusivity ( $m^2/s$ ) of species $i$ in argon;	
$D_p$	=particle diffusivity	( $m^2/s$ )
$G$	=surface growth rate ( $m^3/s$ ); Gibbs free energy	
$h$	=enthalpy	(J/kg)
$i$	=chemical species index (Ar, or Ag); nr. of monomers in a cluster in Eq. 7	
$J$	=nucleation rate	( $1/m^3.s$ )
$k$	=thermal conductivity	(W/m.K)
$M_k$	= $k^{th}$ -moment of particle size distribution ( $k=0, 1$ ou $2$ )	
$n$	=particle number density	( $1/m^3$ )
$p$	=pressure	(N/ $m^2$ )
$t$	=time	(s)
$T$	=temperature	(K)
$r$	=radius	(m)
$s_1$	=monomer surface area	( $m^2$ )
$S_h$	=energy conservation equation source term	
$S;S_{Ag}$	=supersaturation ratio; Ag supersaturation ratio	

$S_i$	=chemical species conservation equation source term	
$SSA$	=specific surface area	(g/ $m^2$ )
$u$	=velocity	(m/s)
$u_{th}$	=thermoforetic velocity	(m/s)
$w$	=mass fraction	
$v$	=particle volume	( $m^3$ )
$v_1$	=monomer volume	( $m^3$ )
$v_{cr}$	=critical particle volume	( $m^3$ )
$x_{Al}$	=Al mole fraction	
$x_{Ag}$	=Ag mole fraction	
$x_{Ag_{in}}$	=Ag mole fraction at the entrance of the cooling region	
$z$	=longitudinal coordinate	(m)

### Greek letters

$\beta$	=impingement (or condensation) rate	( $1/m^2/s$ )
$\theta$	=dimensionless surface energy	
$\mu$	=viscosity	(kg/m.s)
$\rho$	=gas density	(kg/ $m^3$ )

### References

- 1) Kruis, F.E and Fissan, H.: "Nano-process technology for synthesis and handling of nanoparticles", Kona Powder and Particle, Vol. 17, pp. 130-139, 1999.
- 2) Fauchais, P.; Boudrin, E.; Coudert, J.F.; and McPherson, R.: "High Pressure Plasmas and Their Application to Ceramic Technology", in Topics in Current Chemistry, Plasma Chemistry IV, Springer-Verlag, pp. 59-186, 1983.
- 3) Munz, R.J.; Addona, T.; and A.C. da Cruz, A.C.: "Application of transferred arcs to the production of nanoparticles", Pure Appl. Chem. 71, 10, pp. 1889-1897, 1999.
- 4) Ullmann's Encyclopedia of Industrial Chemistry, 6<sup>th</sup> Edition, 1998, Electronic Release.
- 5) Da Cruz, A.C.; Bender, O.W.; and Yoshimura, H.N., Modelling Study of the production of AlN nanoparticles in a new version of a Plasma Synthesis reactor, 15<sup>th</sup> Int. Symp. on Plasma Chemistry-ISPC 15, Vol. VII, pp. 2723-2728, Orléans, 2001.
- 6) Da Cruz, A.C. and Munz, R.J.: "Nucleation with simultaneous chemical reaction in the vapour phase synthesis of AlN ultrafine powders", Aerosol Science and Technology, Vol. 34(6), pp. 499-511, 2001.
- 7) S.V. Patankar: "Numerical Heat Transfer and Fluid Flow", McGraw Hill, 1980.
- 8) Da Cruz, A.C.; Bender, O.W.; Doring, A.C.; Thomas, O.; Coelho, K.C.; and Kiyohara, P.K.: "Produção de pó de alumínio ultrafino em nova versão de reator a plasma", 14<sup>o</sup>. CEBICMAT, São Pedro, SP, 2000.
- 9) Da Cruz, A.C.: "Experimental and Modelling Study of the Plasma Vapour-Synthesis of AlN Powders", Ph.D. Thesis, McGill University, Canada, 1997.

## Author's short biography



**H. Toku**

Helson Toku graduated in Mechanical Engineering from the São Paulo State University-UNESP, Brazil in 2001. Working at the Institute for Technological Researches of São Paulo State-IPT under a FAPESP's scholarship he has participated in the development of thermal plasma development of processes, particularly in the areas of ultra-fine particles synthesis and aluminum recycling. Currently he conducts his MSc program at the Metallurgy and Materials Science Department, Universidade de São Paulo-USP, focused on Ag ultrafine particle plasma synthesis and application in the production of electrical contacts.



**O.W. Bender**

Oskar Wessel Bender received his M.Sc. in Plasma Physics from University of São Paulo, Brazil. In 1986 he joined the Institute for Technological Researches of São Paulo State-IPT. His current interest includes the development and diagnostics of plasma torches, and the application of thermal plasma technology to materials processing.



**A.C. Doring**

Alex Clift Doring joined the Institute for Technological Researches of São Paulo State-IPT as a Mechanics Technician in 2000. Presently he conducts graduate studies on Environment Technology (SENAI College, Brazil). His current interest is the development of thermal plasma equipment and processes, particularly applied to the environment safe processing of materials and materials recycling.



**A.C. da Cruz**

Antonio Carlos da Cruz graduated in Mechanical Engineering and obtained his MSc degree in Chemical Engineering from Universidade de São Paulo, Brazil in 1978 and 1993, respectively. He earned his PhD degree in Chemical Engineering in 1997 from McGill University, Canada. In 1982 he joined the Institute for Technological Researches of São Paulo State-IPT. His main area of interest is the research and development of thermal plasma technology and its application to the processing of materials, particularly to the synthesis of nanosize particles.



**P.K. Kiyohara**

Pedro K. Kiyohara received his M.Sc (1984) and D.Sc (1991) in Chemical Engineering from Escola Politécnica, Universidade de São Paulo. Currently he is Associate Professor and Head of Electron Microscopy Laboratory at the Physics Institute, Universidade de São Paulo. His research interest involves utilizing electron microscopy-based imaging techniques in the study of advanced ceramics, particularly of aluminum oxide and hydroxide.

## Author's short biography



### A.L. Silva

Aurelindo Leme Silva is a Senior Engineer presently working with Tecumseh, Brazil. With an undergraduate background on Electronics and Electro-technique, he graduated in Industrial Engineering at Methodist University of Piracicaba, Brazil, and earned his master's degree in Industrial Marketing from College of Economy Sciences of São Paulo. He has more than 20 years experience in the application and reliability analysis of electrical contacts, working in several companies in the segment of electric and electronic components.

# Slurry Design for Chemical Mechanical Polishing<sup>†</sup>

G. Bahar Basim, Brij M. Moudgil\*

Department of Materials Science and Engineering\*\*

Particle Engineering Research Center

## Abstract

*Chemical Mechanical Polishing (CMP) process is widely used in the microelectronics industry for planarization of metal and dielectric layers to achieve multi layer metallization. For an effective polishing, it is necessary to minimize the surface defects while attaining a good planarity with optimal material removal rate. These requirements can be met by controlling the chemical and mechanical interactions during the polishing process, or in other words, by engineering the slurry chemistry, particulate properties and stability. This paper reviews the impact of chemical, inter-particle and pad-particle-substrate interactions on CMP performance. It is shown that for consistently high performing slurries, stability of abrasive particles must be achieved under the dynamic processing conditions by providing sufficient pad-particle-wafer interactions.*

**Key words:** Chemical Mechanical Polishing (CMP), chemically altered thin films, particle size, particle size distribution, slurry stability, interaction forces

## Introduction

Chemical mechanical polishing (CMP) is a surface smoothing and material removal process, made possible by combination of chemical and mechanical interactions. The wafer surface (on which microelectronic devices are to be built) is planarized by a slurry consisting of submicron sized abrasive particles and chemical reagents. The ultimate goal of CMP is to achieve an optimal material removal rate creating an atomically smooth surface with minimal number of defects, while maintaining global planarity. The chemical effect in CMP is provided by the addition of pH regulators, oxidizers or stabilizers depending on the process. The mechanical action on the other hand, is mostly provided by the submicron sized abrasive particles contained in the slurry, as they flow between

the polishing pad and the wafer surface.

As the rapid advances in the microelectronics industry demand a continuous decrease in the sizes of the microelectronic devices, minimal material removal with atomically flat and clean surface finish has to be achieved during manufacturing (1). This requires close monitoring of the CMP process that can be attained by controlling not only the operational variables (such as the applied head pressure and the relative pad velocity) but also the slurry particulate properties and chemistries. This paper focuses on the development of consistently high performing CMP slurries by selecting effective (i) chemistries, (ii) particulate properties and (iii) methods of stabilization.

## Design Criteria for Slurry Chemistries

Chemical reagents in the CMP slurry react with the wafer surface being polished, forming a chemically modified top layer with desirable properties compared to the initial wafer surface. In metal CMP, the modified layer has to be protective to achieve topographic selectivity. For example, passivation of tungsten by brittle tungsten-oxide film (2-3,8) prevents the metal etching in the low areas, while the high fea-

\* 205 Particle Science and Technology Building  
PO Box 116135, Gainesville, FL 32611-6135 USA  
Phone: (352) 846 3328 Fax: (352) 846 1196  
bmoudgil@erc.ufl.edu

\*\*University of Florida Gainesville, FL 32611, USA

<sup>†</sup> Accepted: September 9, 2003

tures are repeatedly oxidized by the chemicals and abraded by the slurry particles until the planarization is reached. Consequently, slurry oxidizers provide topographic selectivity in metal CMP. In silica polishing on the other hand, chemical effect is provided by increasing the slurry pH so that silica dissolution rate is very high (4) forming a soft hydrated surface layer due to the weakening of silica bonds (5-7,9). In both cases, material properties of the chemically modified layer are expected to be different than the film to be polished, which gives control over the CMP process. The absence of chemically modified layer was found to result in no material removal in tungsten polishing (10). Similarly, in silica CMP, material removal rate was observed to decrease with the decreasing slurry pH, where the chemical activity (dissolution of silica) is reduced (11). Polishing mainly by chemical means leaves an isotropically etched surface with no planarity, whereas polishing by only mechanical means a rough surface is obtained. As a result, the formation of a chemically altered film is necessary to achieve an optimal CMP performance and its properties must be tailored by the design of effective slurry chemistries.

### Effect of Slurry Particulate Properties

Abrasive CMP slurry particles provide the mechanical action during the polishing process. The chemically modified surface layer of the wafer is abraded continuously with the submicron size slurry abrasives resulting in material removal. To achieve an optimal polishing performance with minimal deformations and good planarity, it is necessary to optimize the rates of chemical modification and mechanical abrasions. The intensity of the mechanical abrasion also varies with the slurry particle size and concentration as these factors determine the load applied per particle. Furthermore, the frequency of abrasion depends on the number of slurry abrasives in contact with the wafer surface. Therefore, slurry particle size and concentration as well as the particle size distribution are very important factors in determining the polishing performance and should be studied carefully to understand the CMP process. A small variation in the slurry particle size distribution by oversize particle contamination or due to slurry destabilization may result in major changes in the particle-substrate interactions. Consequently, the material removal rate response may vary resulting in poor process control and the number of surface deformations may increase giving rise to defective microprocessors.

### Slurry Particle Size and Concentration

Effects of slurry particle size and concentration on CMP material removal rate response have been investigated by a number of researchers (5,12-17). The reported results however, are often contradictory in relating the material removal rate to the particle size. This discrepancy can be explained based on the type of the CMP process as well as the selected ranges of the particle size and concentration.

In a study on tungsten CMP (10), material removal rate was observed to increase with the increasing number of particle contacts, achieved by increasing the solids content of the slurry and decreasing the abrasive particle size. In silica CMP however, a maximum removal rate was reached for any given particle size at a particular solids concentration (11). These findings indicate that different polishing mechanisms may become predominant as a function of the type of CMP application as well as the slurry particulate properties for a given polishing system.

Two material removal mechanisms have been introduced to clarify the observed variations in the polishing rates, which can be explained on the basis of silica CMP explicitly (10). **Figure 1** illustrates the material removal rate obtained with 0.5 $\mu$ m particle size silica slurry as a function of the slurry solids concentration. At low solids loading of the slurries (0.2-5%wt.), material removal rate increases with the increasing solids concentration. The surface micrographs of the wafers obtained with the Atomic Force Microscopy (AFM) illustrates scratches on the polished wafer surface at these concentrations indicating that the abrasive particles were indenting and 'sliding' across the wafer surface resulting in mechanical removal. This type of material removal is defined as the indentation mecha-

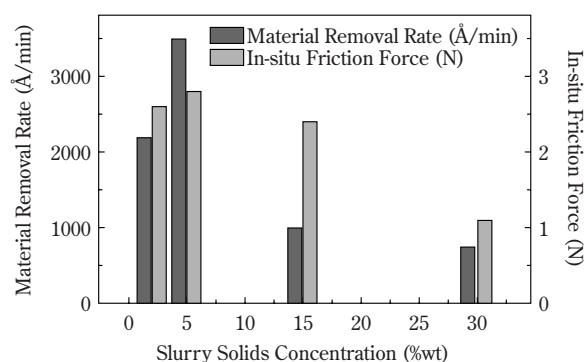


**Fig. 1** Material removal rate and friction force of silica as a function of solids loading of 0.5 $\mu$ m silica abrasives.



nism (10). A maximum was observed in the material removal rate at 5wt% solids concentration after which a significant decrease was detected. This transition occurs due to the change in the particle motion as the load per particle decreases with the increasing number of particles in contact with the wafer. More particles tend to start rolling rather than sliding across the wafer surface as the solids loading is increased from 5 to 15wt% (18). Consequently, total indent volume and the material removal rate decrease with the increasing solids concentration. AFM surface micrograph at 15wt% shows pitting type of deformation on the wafer surface rather than scratches, indicating that abrasives are in rolling motion. Hence, at these higher solids concentrations, mechanical indentation reduces significantly and material removal occurs predominantly due to chemical interactions. This type of material removal mechanism is defined as the contact area mechanism (10). In support of the proposed mechanisms, in-situ friction force measurements conducted on the same system have also shown similar trend in the total friction force as a function of the slurry solids loading for 0.5 $\mu$ m size slurry (**Figure 1**). In situ friction force measurements in CMP have been shown to correlate with the material removal rate response previously (19-20). As the indentation of the particles become negligible due to the decreasing load per particle with the increasing number concentration, particles start rolling resulting in decreased friction force. To reduce the number of surface deformations in CMP, it is necessary to operate in the contact area regime that requires the use of small size particles at high solids concentrations.

### Slurry Particle Size Distribution

In order to achieve an optimal polishing performance with minimal surface deformations, it is necessary to use monosized particles for the CMP slurries (5). In practical applications, however, there may be a few oversize particles in the slurries in the form of larger size particles (hard agglomerates) due to insufficient filtration, or the agglomerates of the primary slurry particles (soft agglomerates) due to poor stability. Presence of agglomerates in the CMP slurries result in unequal distribution of the applied head load on the abrasives, which may lead to surface deformations (21).

**Hard Agglomerates:** Although the presence of hard agglomerates was suspected to result in major surface deformations (5,21) their impact on polishing performance was only recently quantified in a systematic study (22). Polishing tests conducted in the

presence of hard agglomerates at the established detection limits verified significant degradation in the polishing performance. Surface analyses of the silica wafers polished with spiked slurries showed increased surface roughness, and more surface deformations relative to the baseline polishing as illustrated by the AFM images in **Figures 2a** and **b**. In addition, significant variations were detected in the material removal rate response in the presence of hard agglomerates indicating that they have to be removed from the slurries not only to protect the surface quality but also to achieve consistent material removal rate.

**Soft Agglomerates:** To remove coarser particles, filtration of CMP slurries is commonly practiced. Nevertheless, even after filtering the slurries, the defect counts on the polished surfaces are often observed to be higher than expected (26). It has been suspected that some of the defects may be created by the agglomerate formation during the CMP operations. A study conducted on silica-silica system by substituting a fraction of baseline slurry with dry aggregated, polymer flocculated and salt coagulated particulates have shown that even the agglomerates, which breakdown under the applied load can result in major surface deformations (**Figure 2c**) (27). These observa-

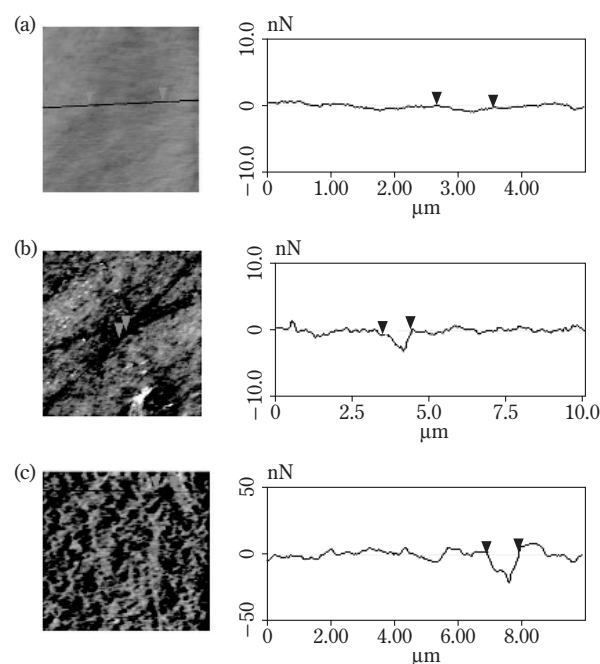


**Fig. 2** Surface response quality of the silica wafers polished with a) Baseline Rodel 1200 slurry, b) Rodel 1200 slurry spiked with 1%w 1.5 $\mu$ m size Geltech particles and c) Polymer flocculated 0.2 $\mu$ m size, 12%w Geltech slurry.

tions indicate that CMP slurries must remain stable during polishing to obtain optimal polishing performance.

There are several size analysis techniques available for detecting the larger size particles in the CMP slurries (23-25). Among these, the number counting techniques are the most promising in detecting the large size particles at the lowest concentrations (24). However, as the slurries are diluted for counting, some of the techniques may not be effective in detecting the soft agglomerates formed during slurry preparation. Therefore, combination of sizing techniques that can analyze both the dilute and concentrated (25) slurries must be used for effective detection of coarser size particulates.

### Stabilization of CMP Slurries

In CMP processes, polishing slurries have to be stabilized under extreme environments of pH, ionic strength, pressure and temperature, in the presence of reactive additives. Most of the commonly used stabilization techniques, such as, electrostatic stabilization, inorganic or polymeric dispersion may not perform adequately under these severe environments. An alternative is to use surfactant structures at the solid-liquid interface for the stabilization of particulate systems (28-33).

Self-assembled structures of  $C_{12}$ TAB (dodecyl trimethyl ammonium bromide), a cationic surfactant, have been shown to provide stability to silica suspensions at high ionic strengths and extreme pH by introducing a strong repulsive force barrier (33-34). This concept was utilized to stabilize the silica CMP slurry in the presence of 0.6M salt at pH 10.5.  $C_{12}$ TAB surfactant was used at 32mM concentration, which is two times the critical micelle concentration (CMC) in the absence of electrolyte (35). The baseline polishing slurry contained 12wt%, 0.2 $\mu$ m monodispersed silica particles at pH 10.5. Addition of 0.6 M salt coagulated the particles by screening the surface charge (36). At 8mM  $C_{12}$ TAB, a jump was reported in the repulsive force barrier due to the beginning of the formation of self-assembled surfactant aggregates (34) which led to increased slurry stability. At 32mM  $C_{12}$ TAB concentration, where a sufficient number of the surfactant aggregates form at the surface, the slurry became completely stable due to strong repulsive force barrier between particles.

Slurries stabilized with  $C_{12}$ TAB were used for polishing silica wafers. The surface quality response was observed to be optimal with minimal surface rough-

ness and deformation. However, material removal rate was only 70 Å/min. This observation highlighted the importance of particle-substrate interactions along with particle-particle interactions for optimal CMP operation.

Two reasons were suggested for the negligible material removal in the presence 32mM  $C_{12}$ TAB (35). First, it is known that the presence of surfactants can result in lubrication between the abrasive and the surface to be polished (37). This may decrease the frictional forces thus reducing material removal in the presence of surfactants. Alternatively, the high repulsive force barrier induced by the  $C_{12}$ TAB self-aggregated structures may be preventing the particle-surface engagement and, therefore, resulting in a very low material removal rate.

In order to isolate the effect of lubrication and the repulsive force barrier on material removal response, it was necessary to calculate the force applied on a single abrasive particle during polishing. Initially, this value was estimated to be 100-1000nN for a 0.2 $\mu$ m size particle based on the assumption of hexagonal close packed surface coverage of particles at  $2.7 \times 10^{-3}$  normalized pad area contact at 7psi head load. Furthermore, the exact value was calculated to be  $750 \pm 150$ nN for a 0.2 $\mu$ m size particle by determining the pad-substrate contact area at the applied head pressure and the particle concentration at the area of contact of the pad (18), which agreed with the modeling values in literature (38). Comparing the load applied per particle to the repulsive force barrier of a  $C_{12}$ TAB surfactant aggregate (6nN), it was clear that the repulsion introduced by the surfactant structures was overcome under the applied head load. Hence, it was more likely that the lubrication effects introduced by the surfactants controlled the material removal by varying the frictional forces between the abrasive particles and the wafer. Similar studies using  $C_{10}$ TAB and  $C_8$ TAB with added salt showed nonlinear behavior of lateral forces with respect to normal force (**Figure 3**). Though material removal rate values were low compared to the baseline, this approach opened a new venue of tailoring the friction forces encountered in CMP. Detailed studies of in-situ friction force response and single particle-substrate friction simulations with AFM for the surfactant mediated slurries have proved that the strength of surfactant adhesion and the chemistry of the slurries (pH, ionic strength and surfactant chain length) could be tailored to provide sufficient frictional force to achieve optimal polishing performance (35).

Palla has showed that in tungsten polishing the

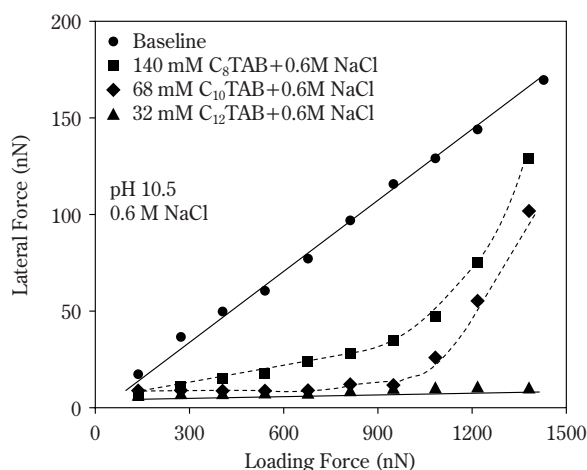


**Fig. 3** AFM friction force measurements on silica wafer with  $7\mu\text{m}$  size particle attached to the tip. (a) Solutions containing  $\text{C}_{12}\text{TAB}$ ,  $\text{C}_{10}\text{TAB}$  and  $\text{C}_8\text{TAB}$  surfactants at 32, 68 and 140mM concentrations without NaCl at pH 10.5 in the presence of 0.6 M salt in the solution. Reprinted from Basim et.al. (35) with permission from Elsevier.

addition of a mixture of ionic (SDS) and nonionic (Tween 80) surfactants over CMC concentrations could stabilize alumina particles in the presence of high concentrations of potassium ferricyanide by creating sufficiently high repulsive force barriers (39). The mechanism of stabilization in this system was explained by enhanced adsorption of nonionic surfactant using the strongly adsorbing ionic surfactant as a binding agent. The stabilizing ability of the surfactant system was also found to increase with increasing hydrophobicity of the nonionic surfactant and increasing hydrophobicity of the ionic surfactant. The effect of surfactant concentration on dispersion ability revealed an optimum concentration range for a given surfactant. When tungsten polishing was conducted using the slurries stabilized by the mixed surfactant system, 30% less material removal rate was obtained compared to the baseline slurry. However, a much better surface quality was obtained. Accordingly, surfactants can be used to modify the particle-particle and particle-substrate interactions during CMP to optimize the process performance based on the selected performance criteria.

## Conclusions

In CMP, slurry design has significant effect on the process performance and should be carefully monitored for optimal results. Slurry chemistry has to be tailored so that the slurry is free of any hard or soft

agglomerates (even in low concentration), which not only would deteriorate the surface quality but would also lead to inconsistent removal rates. The use of surfactants to stabilize the slurry in extreme environments can take advantage of the vast literature available for the solution behavior of surfactants.

## Acknowledgements

The authors acknowledge the financial support of the Particle Engineering Research Center (PERC) at the University of Florida, The National Science Foundation (NSF) (Grant EEC-94-02989), and the Industrial Partners of the ERC for support of this research. Any opinions, findings and conclusions or recommendations expressed in this material are those of the author(s) and do not necessarily reflect those of the National Science Foundation.

## References

- 1 S. P. Murarka in Chemical-Mechanical Polishing – Fundamentals and Challenges, edited by S. V. Babu, S. Danyluk, M. I. Krishnan, and M. Tsujimura, Mater. Res. Soc. Proc. 566 (2000), p. 3.
- 2 E. Paul, J. Electrochem. Soc., 148, p. G359 (2001).
- 3 F. B. Kaufman, D. B. Thomson, R. E. Broadie, M. A. Jaso, W. L. Guthrie, D. J. Pearson, M. B. Small, J. Electrochem. Soc., 138, p. 3460 (1991).
- 4 R. K. Iler, The Chemistry of Silica: Solubility, Polymerization, Colloid and Surface Properties, and Biochemistry, John Wiley & Sons Inc., New York (1979).
- 5 L. M. Cook, J. Non-Cryst. Solids, 120, p. 152 (1990).
- 6 J. A. Trogolo, K. Rajan, Journal of Materials Science, 29, p. 4554-4558 (1994).
- 7 J. J. Adler, Interaction of Non-ideal Surfaces in Particulate Systems, University of Florida Ph.D Thesis (2001).
- 8 D. F. Bahr, D. E. Kramer, W. W. Gerberich, Acta Mater. Res., 14, p. 2269 (1999).
- 9 T. A. Michalske, S. W. Freiman, Nature, 295, p.11 (1982).
- 10 M. Bielman, Chemical Mechanical Polishing of Tungsten, University of Florida Master Thesis (1998).
- 11 U. Mahajan, Fundamental Studies on Silicon Dioxide Chemical Mechanical Polishing, University of Florida Ph.D Thesis (2000).
- 12 N. J. Brown, P. C. Baker, R. T. Maney, Proc. SPIE 306, 42 (1981).
- 13 M. Tomozawa, K. Yang, H. Li, S. P. Murarka, in Advanced Metallization for Devices and Circuits-Science, Technology and Manufacturability, edited by S. P. Murarka, A. Katz, K. N. Tu and K. Maex, Mater. Res. Soc. Proc. 337, Pittsburgh, PA (1994), p. 89.
- 14 Y. Xie and B. Bhushan, Wear 200, p. 281 (1996).
- 15 R. Jairath, M. Desai, M. Stell, R. Tolles, and D. Scherber-Brewer, in Advanced Metallization for Devices

- and Circuits-Science, Technology and Manufacturability, edited by S. P. Murarka, A. Katz, K. N. Tu and K. Maex, Mater. Res. Soc. Proc. 337, Pittsburgh, PA (1994), p. 121.
- 16 S. Sivaram, M. H. M. Bath, E. Lee, R. Leggett, and R. Tolles, Proc. SRC Topical Research Conference on Chem-Mechanical Polishing for Planarization, SRC, Research Triangle Park, NC (1992), proc. Vol. #P92008.
- 17 T. Izumitani, in Treatise on Materials Science and Technology, Eds. M. Tomozawa and R. Doremus, Academic Press, New York (1979), p. 115.
- 18 Basim G. B., Vakarelski I. U., Brown S., Moudgil B. M., "Strategies for the Optimization of Chemical Mechanical Polishing (CMP) Slurries," The Journal of Dispersion Science and Technology (Forthcoming, 2003).
- 19 Bielman M., Mahajan U., Singh R. K., Shah D. O., Palla B. J., Electrochem. Solid-State Lett., 2, 46-48 (1999).
- 20 Bielman M., Mahajan U., Singh R. K., Shah D. O., Palla B. J., Electrochem. Solid-State Lett., 2, 80-82 (1999).
- 21 J. Schlueter, *presented at SemiCon Southwest 95* (1995).
- 22 Basim G. B., Adler J. J., Mahajan U., Singh R. K., Moudgil B. M., J. Electrochem. Soc., 147, 3523 (2000).
- 23 M. C. Pohl, D. A. Griffiths, J. Electron. Mater., 10, p. 1612 (1996).
- 24 R. Nagahara, S. K. Lee, H. M. You, publication by Particle Sizing Systems, VMIC Conference, p. 1, Jun. 18-20, 1996.
- 25 A. S. Dukhin, P. J. Goetz, Dispersion Technology Inc., Company Newsletter, December (1998).
- 26 Ewasiuk R., Hong S., Desai V., in "Chemical Mechanical Polishing in IC Device Manufacturing III", (Arimoto Y. A., Opila R. L., Simpson J. R., Sundaram K. B., Ali I., Homma Y., Eds.), p. 408, Electrochem. Soc. Proc. 99-37, Pennington, NJ, (1999).
- 27 Basim G. B., Moudgil B. M., Journal of Colloid and Interface Science, Vol. 256, No 1, p. 137, December (2002).
- 28 M. Colic, D. W. Fuerstenau, Langmuir, 13, 6644 (1997).
- 29 M. J. Solomon, T. Saeki, M. Wan, P. J. Scales, D. V. Boger, H. Usui, Langmuir, 15, 20 (1999).
- 30 L. K. Koopal, T. Goloub, A. deKaiser, M. P. Sidorova, Colloids Surf., 151, 15 (1999).
- 31 K. E. Bremmel, G. J. Jameson, S. Biggs, Colloids Surf., 146, 755 (1999).
- 32 C. R. Evanko, D. A. Dzombak, J. W. Novak, Colloids Surf., 110, 219 (1996).
- 33 J. J. Adler, P. K. Singh, A. Patist, Y. I. Rabinovich, D. O. Shah and B. M. Moudgil, Langmuir, 16, 7255-7262 (2000).
- 34 P. K. Singh, J. J. Adler, Y. I. Rabinovich and B. M. Moudgil, Langmuir, 17, 468-473 (2001).
- 35 Basim G. B., Vakarelski I. U., Moudgil B. M., Journal of Colloid and Interface Science (Forthcoming, 2003).
- 36 J. N. Israelachvili, "Intermolecular and Surface Forces", 2<sup>nd</sup> Ed., Academic Press, New York, (1992).
- 37 Y. L. Chen, S. Chen, C. Frank, J. N. Israelachvili, Journal of Colloid and Interface Science, 153, 244 (1992).
- 38 T. K. Yu, C. C. Yu and M. Orlowski, Proceedings of the 1993 International Electronic Devices Meeting, 4.1, 35 (1994).
- 39 B. Palla, Mixed surfactant systems to control dispersion stability in severe environments for enhancing chemical mechanical polishing (CMP) of metal surfaces, University of Florida Ph.D Thesis (2000).

## Author's short biography



### G. Bahar Basim

G. Bahar Basim is a senior process engineer working at Intel Corporation. She currently conducts research and development on semiconductor device manufacturing, including chemical mechanical planarization.

Basim received her PhD degree in materials science and engineering from the University of Florida in 2002 with specialties in electronic materials and particle science and technology. Her dissertation research focused on the design of engineering particulate systems for chemical-mechanical planarization applications. As a part of the research group at the Engineering Research Center for Particle Science and Technology, her graduate work led to 12 technical publications and a US patent application on the impact of slurry particulate properties on pad-particle-substrate interactions in CMP process. She obtained her MSc degree in mining and minerals engineering from the Virginia Polytechnic Institute and State University in 1997, and her BSc degree in Mining engineering from the Middle East Technical University in Ankara, Turkey in 1995. She has also worked as a Process/Product Development engineer for Engelhard Corporation.

Basim can be reached by e-mail at [gul.b.basim@intel.com](mailto:gul.b.basim@intel.com).



### B. Moudgil

Dr. B. Moudgil is a Professor of Materials Science and Engineering and Director of the ERC. His research interests are particulate processing, solid-solid/solid-liquid separations, fine particle packing, sol-gel processing, crystal modification, dispersion & aggregation of fine particles, polymer & surfactant adsorption, orientation of particles in slurries, and rheology of concentrated suspensions.



# Separation of Automobile Shredder Residue by Gravity Separation Using a Gas-Solid Fluidized Bed<sup>†</sup>

Jun OSHITANI\*, Tomoko KAJIWARA,  
Kouji KIYOSHIMA  
and Zennosuke TANAKA  
Department of Applied Chemistry,  
Okayama University\*\*

## Abstract

*The authors investigated the gravity separation of plastic, rubber, and wire harnesses in automobile shredder residue using a gas-solid fluidized bed. Uni-beads (barium silica titanate glass), zircon sand, and glass beads were employed as fluidized particles. Superficial air velocity was changed to see how the plastic, rubber, and wire harnesses floated and sank in the fluidized bed. Wire harnesses were almost completely separated from the other constituents by using uni-beads and zircon sand. Plastic can be separated from rubber by using glass beads, although separation efficiency is relatively low. Precise adjustment of superficial air velocity is essential for attaining high separation efficiency because particle flow and air bubbles in the fluidized bed affect how objects float and sink.*

**Key words:** Automobile shredder residue, fluidized bed, gravity separation, recycle

## 1. Introduction

Waste reuse and recycling are now considered important, and this also holds for automobile shredder residue. Most of the approximately 5 million end-of-life vehicles entering the waste stream each year are dismantled, with constituents including engines, tires, steel, and nonferrous metals being reused and recycled, bringing the recycling rate up to a high 75 to 80%. The remaining 20 to 25%, which is shredder residue, amounts to about 1 million tons annually and is nearly all disposed in controlled landfill sites. [1, 2] In response to the "End-of-Life Vehicle Recycling Initiative" released by the former Ministry of International Trade and Industry (now the Ministry of Economy, Trade and Industry) in 1997, the Japan Automobile Manufacturers Association (JAMA) un-

veiled a voluntary action plan with the numerical goals of raising the recycling rate to at least 95% and reducing landfilled waste to at least one-fifth the 1996 volume, both by 2015.

Automobile shredder residue comprises about 60% organic materials such as plastic, rubber, and urethane foam, and about 40% inorganic materials including glass, steel, wiring called harnesses, and nonferrous metals. JAMA and the automobile industry have developed a variety of technologies to separate these materials, such as sorting, volume reduction, and solidification; dry distillation; and pneumatic separation, and have shown it is quite possible to achieve the above numerical goals. [3-6] But these technologies have not found general use owing to high processing equipment costs. The authors explored a very simple pneumatic separation method in which air is blown into falling dust from the side to separate the plastic, rubber, urethane foam, wiring, and nonferrous metals in the dust. [7] But while the light urethane foam was separated with high efficiency because of its lightness, it was not easy to separate the other constituents.

\* Corresponding author

\*\*3-1-1, Tsushima-naka, Okayama 700-8530

TEL & FAX: +81-86-251-8086

E-mail: oshitani@cc.okayama-u.ac.jp

<sup>†</sup> Accepted: July 16, 2003

In this research we used gravity separation in a gas-solid fluidized bed to test separation of three shredder dust constituents: plastic, rubber, and wire harnesses. Because gas-solid fluidized beds fluidize powders with an air blast from below, therefore resembling liquids, [8, 9] objects lighter than their bulk density in a fluidized state float in the bed, while objects that are heavier sink. So far the authors have successfully used this method for coal cleaning [10] and for separating silica stone and pyrophyllite, which have a density difference of about  $250 \text{ kg m}^{-3}$ . [11] We have used uni-beads, zircon sand, and glass beads as fluidized powders to determine bulk densities and dispersion in a fluidized state based on how spheres with various densities float or sink. Densities of the three dust constituents in ascending order were plastic, rubber, and wiring. Only the wiring sank when using uni-beads and zircon sand, while we tried using glass beads to separate plastic and rubber by floating the former and sinking the latter. Because the constituents have small density differences, their floating and sinking are greatly affected by the particle flows and air bubbles in the bed, and hence their separation is likely difficult. To obtain high separation efficiency we therefore conducted a separation experiment that varied superficial air velocity.

## 2. Materials and Methods

### 2.1 Automobile Shredder Dust

We extracted the three constituents of plastic, rubber, and wire harnesses from automobile shredder dust we had obtained from a shredder operator, and used them in our separation experiment. **Table 1** gives the total weights and densities of the con-

**Table 1** Characteristics of each constituent of the automobile shredder residue

	Total weight (g)	Density ( $\text{kg m}^{-3}$ )
Plastic	21.4	$990 \pm 180$
Rubber	21.3	$1400 \pm 300$
Wire harnesses	20.9	$2800 \pm 500$

Note: An electronic balance (MC210S, Sartorius) was used to measure density.

stituents, and their photographs appear in **Fig. 1**. All constituents weighed about 21 g, and the pieces were 10 to 20 mm in size. Because average density differences were small, at  $400 \text{ kg m}^{-3}$  between plastic and rubber, and  $1,400 \text{ kg m}^{-3}$  between rubber and wiring, and because of the large density dispersion, we anticipated difficulty with gravity separation in a gas-solid fluidized bed.

### 2.2 Fluidized Powder

Our fluidized powders were uni-beads of barium silica titanate glass (Union Co., Ltd.), zircon sand (Lasa Co., Ltd.), and glass beads (Toshiba Barotini Co., Ltd.). For each powder **Table 2** shows particle size, true density, bulk density, shape, and the minimum fluidization velocity  $u_{mf}$  obtained in the method described below. Uni-beads and zircon sand were used to test the sinking and separation of wiring from the three constituents. Uni-beads are comparatively monodispersed and spherical, and are suited to obtaining basic data showing the tendencies of the three constituents to float or sink in the fluidized bed.

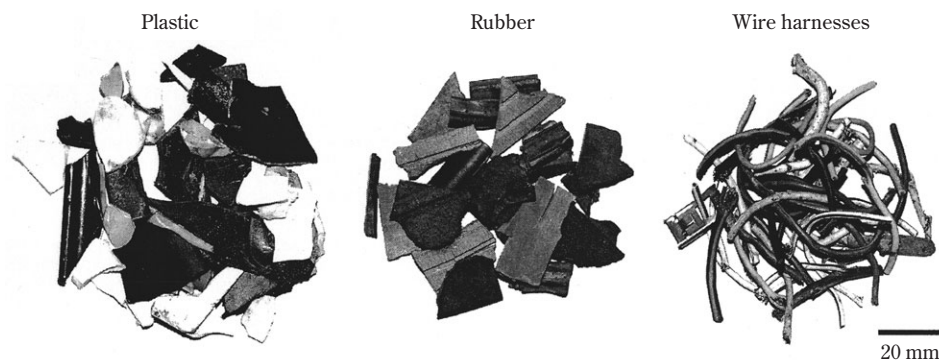


**Fig. 1** Photographs of each constituent of the approximately 21 g of automobile shredder residue

**Table 2** Powder characteristics

	Particle diameter ( $\mu\text{m}$ )	True density ( $\text{kg m}^{-3}$ )	Bulk density ( $\text{kg m}^{-3}$ )	Shape	Minimum fluidization velocity, $u_{\text{mf}}$ ( $\text{cm s}^{-1}$ )
Uni-beads	300-350	4200	2600	Spherical	$15.4 \pm 0.1$
Zircon sand	90-300	4650	3000	Non-spherical	$3.3 \pm 0.1$
Glass beads	250-300	2500	1500	Spherical	$5.6 \pm 0.2$

Note: Averaged values and standard deviations of  $u_{\text{mf}}$  were obtained from three measurements.

By contrast, zircon sand has a wide particle diameter range of 90 to 300  $\mu\text{m}$ , but is cheaper than uni-beads, and because the small  $u_{\text{mf}}$  presents advantages such as smaller blower power, it seems they are suited to practical use. We also tried separating plastic and rubber by using glass beads to float plastic and sink rubber.

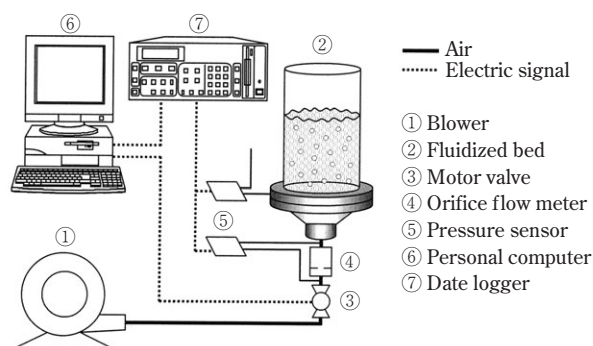
### 2.3 Experimental Apparatus

Our experimental apparatus, shown in **Fig. 2**, was the same as that in a previous report. [11] A fluidized bed was created in an acrylic cylinder 48 cm high with a 20.5-cm inside diameter and wall thickness of 0.5 cm, and an antistatic agent was applied inside to reduce the influence of static electricity. At the bed bottom was an air distributor made with cloth between two porous stainless steel plates having holes with 0.3-cm diameters, a pitch of 0.6 cm, and an opening ratio of 22.67%. Powder was prepared so that it would be at a height of 15 cm in the fluidized bed. Air was supplied by a blower to fluidize the powder, and superficial air velocity was fine-adjusted by opening and closing the motor valve. Superficial air velocity  $u_0$

and pressure drop  $\Delta P$  were calculated by first using pressure transducers to read, as voltages, the orifice flow meter pressure and the pressure difference between the bottom of the fluidized bed and the atmosphere, then using previously obtained relational equations for voltage/superficial air velocity and voltage/pressure drop.  $\Delta P$  was measured while gradually decreasing  $u_0$ , and the value of  $u_0$  at which  $\Delta P$  begins falling from a constant value was used for the minimum fluidization velocity  $u_{\text{mf}}$ .

### 2.4 Measuring Bulk Density and Its Dispersion in a Fluidized State

The bulk density  $\rho_{\text{fb}}$  of each powder in a fluidized state and its dispersion  $\Delta\rho_{\text{fb}}$  were determined by investigating the floating/sinking in a fluidized bed of 3.75-cm diameter spheres (table tennis balls containing a certain amount of steel shot) whose densities  $\rho_{\text{sp}}$  were adjusted for each  $10 \text{ kg m}^{-3}$ . We fluidized powders at prescribed superficial air velocity  $u_0/u_{\text{mf}}$ , put a sphere into the center of the top stratum, stopped the air after 5 min, and measured the distance from the bed bottom to the sphere's center of gravity,  $h_{\text{sp}}$ . When  $\rho_{\text{sp}} < \rho_{\text{fb}}$  the sphere floated, when  $\rho_{\text{sp}} \approx \rho_{\text{fb}}$  the sphere stayed in the middle of the bed without either rising or falling, and when  $\rho_{\text{sp}} > \rho_{\text{fb}}$  the sphere sank. We determined  $h_{\text{sp}}$  for each sphere's  $\rho_{\text{sp}}$ .  $\rho_{\text{sp}1}$  was used for the largest density sphere that floated, and  $\rho_{\text{sp}2}$  for the smallest density sphere that sank. These values were used in Eqs. 1 and 2 below to calculate  $\rho_{\text{fb}}$  and  $\Delta\rho_{\text{fb}}$ , respectively.  $\rho_{\text{fb}}$  is the average density of spheres that do not rise or fall, and  $\Delta\rho_{\text{fb}}$  is their density range.  $h_{\text{sp}}$  was measured three times at prescribed superficial air velocities in each powder. Averages and standard deviations of  $\rho_{\text{fb}}$  and  $\Delta\rho_{\text{fb}}$  were determined using the three measured values.


**Fig. 2** Schematic drawing of the experimental apparatus

$$\rho_{\text{fb}} = \frac{\rho_{\text{sp}2} + \rho_{\text{sp}1}}{2} \quad (1)$$

$$\Delta\rho_{fb} = \rho_{sp2} - \rho_{sp1} \quad (2)$$

## 2.5 Assessment of Residue Floating-Sinking and Separation

We fluidized powders at prescribed superficial air velocities  $u_0/u_{mf}$ . When using uni-beads we separately added plastic, rubber, and wiring; with zircon sand we added the three constituents together; and with glass beads we added plastic and rubber together. When using uni-beads we added the three constituents together at the  $u_0/u_{mf}$  at which plastic and rubber best floated, and wire harnesses best sank. We stopped the air one minute after adding the residue constituents, measured the distance from the bed bottom to each constituent's center of gravity  $i$ , and determined the weight percentage  $w_i$  of each constituent at each 3-cm stratum from the bed bottom.

To assess separation, we determined the purity  $x_p$  and recovery rate  $x_r$ , defined below. In uni-beads and zircon sand, plastic and rubber floated while wiring sank. Hence the values of  $x_p$  were the weight percentage of plastic and rubber in the dust that floated in the top stratum at  $i=12$  to 15, and the weight percentage of wiring in the dust that sank to the bottom stratum at  $i=0$  to 3. For  $x_r$  values we used the weight percentage of the portion of total plastic and rubber that floated in the top stratum at  $i=12$  to 15, and the weight percentage of the portion of total wiring that sank to the bottom stratum at  $i=0$  to 3. In glass beads plastic floated and rubber sank. Thus for their  $x_p$  values we used the weight percentage of dust plastic that floated in the top stratum at  $i=12$  to 15, and the weight percentage of dust rubber that sank to the bottom stratum at  $i=0$  to 3. For  $x_r$  values we used the weight percentage of the portion of total plastic that floated in the top stratum at  $i=12$  to 15, and the weight percentage of the portion of total rubber that sank to the bottom stratum at  $i=0$  to 3. The experiment was performed three times under each set of conditions, and the average and standard deviation of each value were determined.

## 3. Results and Discussion

### 3.1 Superficial Air Velocity and Pressure Drop

For each powder we measured pressure drop  $\Delta P$  while gradually decreasing superficial air velocity  $u_0$ . Results appear in **Fig. 3**. When  $u_0$  is big,  $\Delta P$  is constant, showing that all powders are fluidized, but under minimum fluidizing velocity  $u_{mf}$ ,  $\Delta P$  decreases linearly, showing that the powders are fixed. Uni-

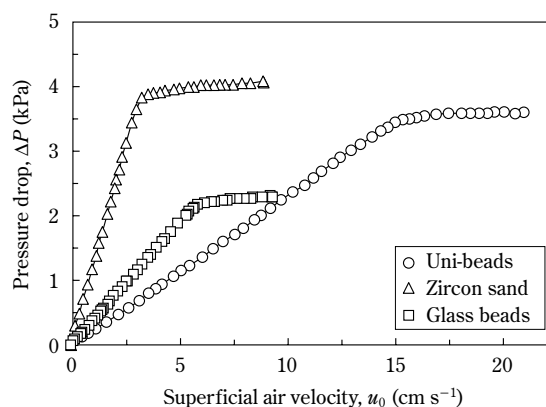


**Fig. 3** Dependence of pressure drop on superficial air velocity

beads and zircon sand have about the same bulk density, and they have about the same  $\Delta P$  values when in a fluidized state, but because zircon sand has many particles smaller than those in uni-beads, it has a smaller  $u_{mf}$  value than uni-beads, as shown in **Table 2**.

### 3.2 Bulk Density and Its Dispersion in a Fluidized State

We varied the superficial air velocity  $u_0/u_{mf}$  in each powder and checked the positions in the fluidized bed  $h_{sp}$  of spheres with various densities  $\rho_{sp}$ , then determined the bulk density  $\rho_{fb}$  and its dispersion  $\Delta\rho_{fd}$  in a fluidized state. **Figs. 4** and **5** show the  $h_{sp}$  at  $\rho_{sp}$  for various  $u_0/u_{mf}$ , and the  $\rho_{fb}$  and its  $\Delta\rho_{fb}$  for various  $u_0/u_{mf}$  when using uni-beads. At all  $u_0/u_{mf}$  there were spheres which floated at low density, but which, when their densities were larger, stayed in the middle stratum of the fluidized bed without either rising or falling, and which completely sank at still greater densities. The average density  $\rho_{fb}$  of spheres that stayed in the bed's midregion remained almost constant even if  $u_0/u_{mf}$  was changed, but its dispersion  $\Delta\rho_{fb}$  increased with  $u_0/u_{mf}$ . This is likely because powder fluidization becomes more intense as superficial air velocity increases, which destabilizes the floating and sinking of spheres. **Figs. 6** and **7** show the results for zircon sand.  $\Delta\rho_{fb}$  increased with  $u_0/u_{mf}$  just as with uni-beads, but  $\rho_{fb}$  tended to decline instead of remaining constant. Because the bulk volume of a fluidized powder generally increases as superficial air velocity increases,  $\rho_{fb}$  decreases. Using zircon sand we performed sphere float/sink experiments over a broader  $u_0/u_{mf}$  range than with uni-beads, and it seems this tendency appeared more salient. It is also possible

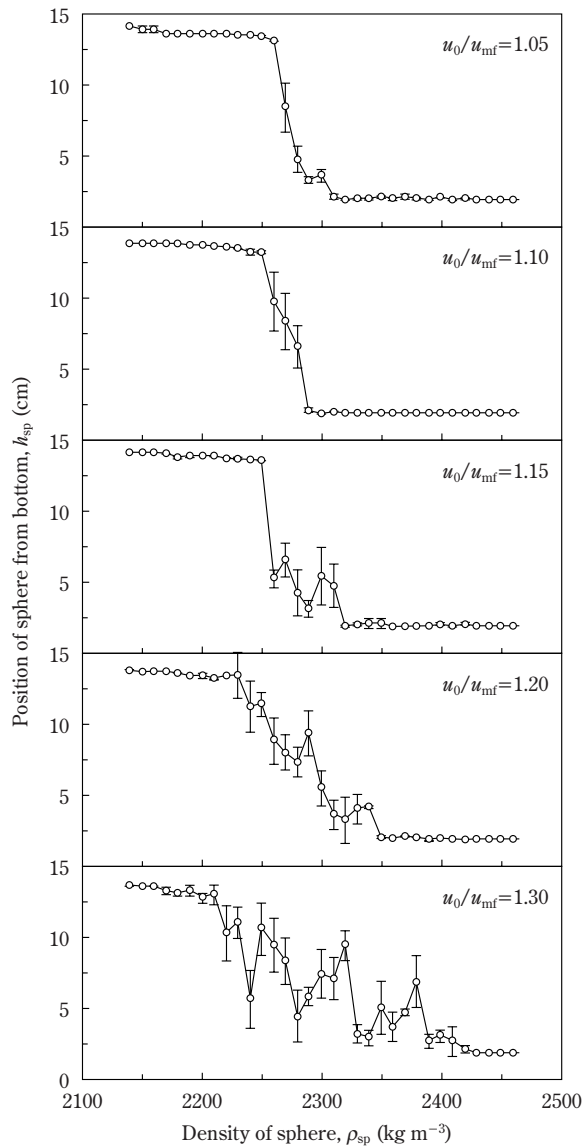


**Fig. 4** Dependence of sphere height on density at various superficial velocities. Powder is uni-beads.

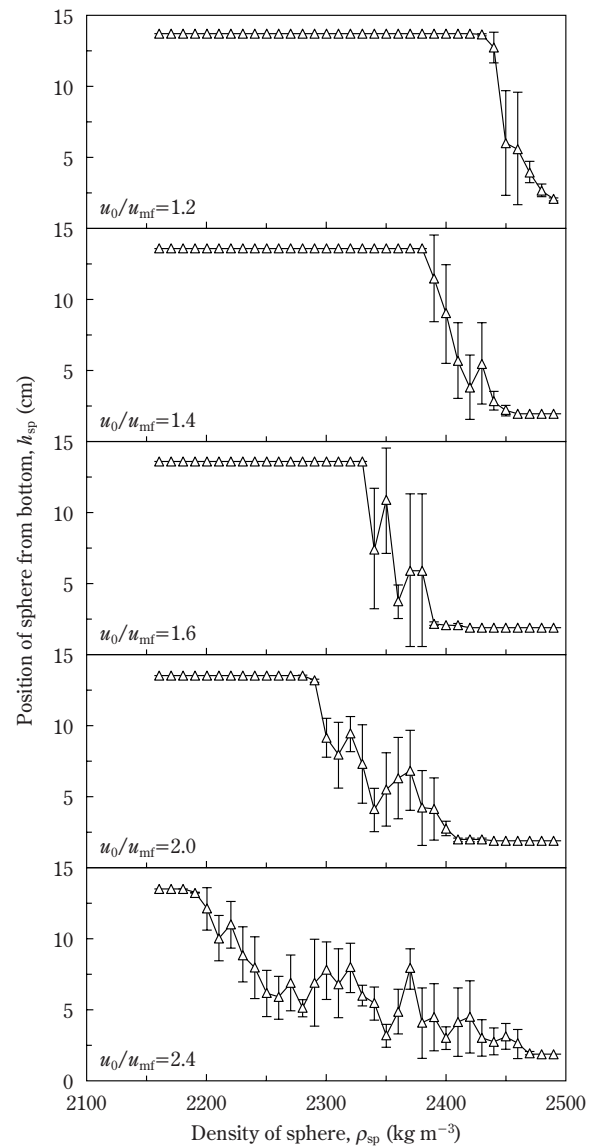


**Fig. 6** Dependence of sphere position on density at various superficial velocities. Powder is zircon sand.

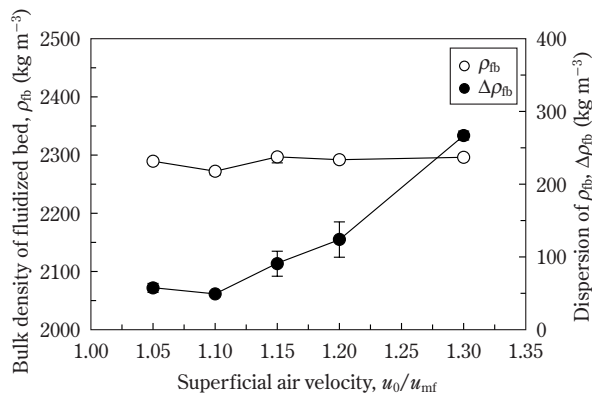


**Fig. 5** Dependence of fluidized bed bulk density and its dispersion on superficial air velocity. Powder is uni-beads.

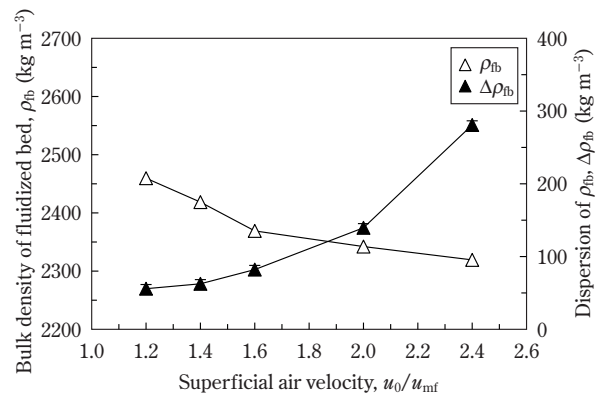


**Fig. 7** Dependence of fluidized bed bulk density and its dispersion on superficial air velocity. Powder is zircon sand.



that the wide range of zircon sand particle sizes and the non-spherical particle shape engendered porosity changes, and this is conceivably the reason for the difference observed in change tendencies between uni-beads and zircon sand. **Figs. 8** and **9** show the results for glass beads. Unlike uni-beads and zircon sand,  $\rho_{fb}$  and  $\Delta\rho_{fb}$  remain nearly constant even if  $u_0/u_{mf}$  is changed. A possible explanation is that glass beads have a lower density than uni-beads and zircon sand, but the reason is unclear.

These results show that uni-beads and zircon sand have bulk densities of  $\rho_{fb} \approx 2300$  to  $2400 \text{ kg m}^{-3}$  when

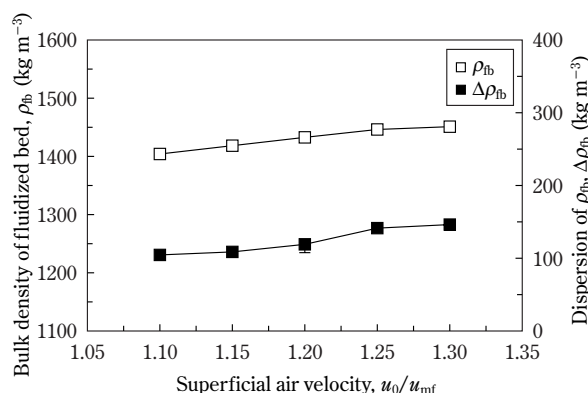


**Fig. 9** Dependence of fluidized bed bulk density and its dispersion on superficial air velocity. Powder is glass beads.

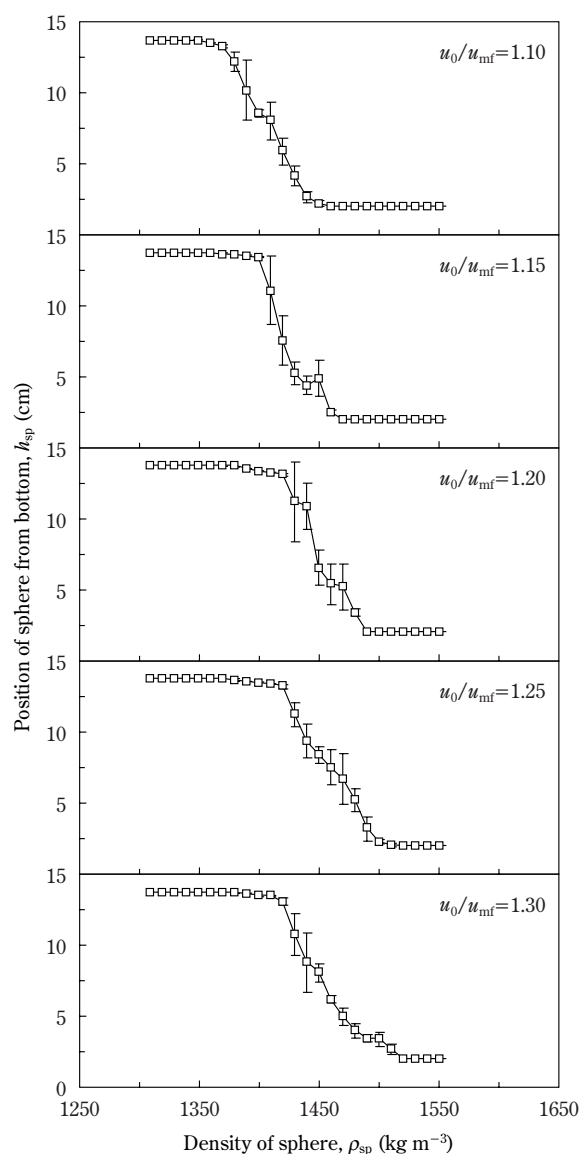


**Fig. 8** Dependence of sphere position on density at various superficial velocities. Powder is glass beads.

fluidized, which are between the average densities of rubber and wire harnesses. Glass beads, by contrast, have a bulk density of  $\rho_{fb} \approx 1400 \text{ kg m}^{-3}$  when fluidized, about the same as rubber's average density.

### 3.3 Residue Floating and Sinking

We performed float/sink experiments with plastic, rubber, and wire harnesses in several powder types while varying the superficial air velocity  $u_0/u_{mf}$ . **Fig. 10** shows the float/sink results when putting the three constituents into uni-beads separately. The vertical axis shows heights  $i$  in the fluidized bed at 3-cm strata, and the horizontal axis shows the weight percentage  $w_i$  of the three constituents in each stratum. When  $u_0/u_{mf} = 1.05$ , plastic and rubber were completely afloat, and wiring sank with difficulty. This is probably because superficial velocity was low and the powder was not very fluid. As  $u_0/u_{mf}$  increased, a growing percentage of the wiring sank, and when  $u_0/u_{mf} = 1.30$  the wiring almost completely sank, but plastic and rubber did not completely float. This could be because when superficial velocity is high, powder fluidization is intense, and especially because fluidized bed surface vibration is great. **Fig. 11** shows the purity  $x_p$  and recovery rate  $x_r$  obtained in the experiment for each constituent in relation to  $u_0/u_{mf}$ . The  $x_p$  of plastic and rubber increased as  $u_0/u_{mf}$  increased, and it was nearly 100% when  $u_0/u_{mf} \geq 1.15$ . Meanwhile, the wiring  $x_p$  was 100% when  $u_0/u_{mf} \leq 1.15$ , but it decreased when  $u_0/u_{mf} > 1.15$ . Change in  $x_r$  was the opposite from that of  $x_p$  because the  $x_r$  of plastic and rubber was 100% when  $u_0/u_{mf} \leq 1.15$ , but it decreased when  $u_0/u_{mf} >$

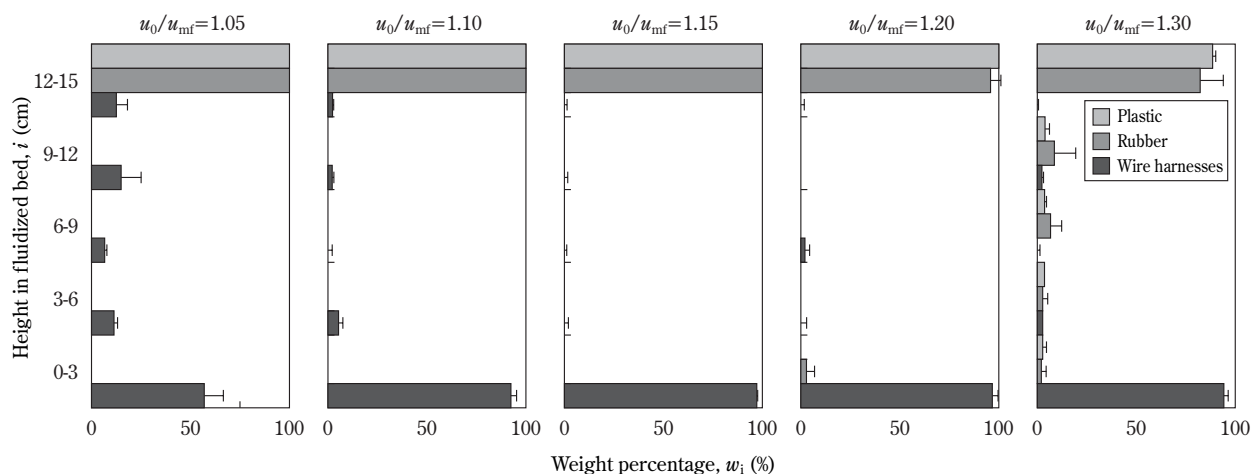


**Fig. 10** Weight percentages of plastic, rubber, and wire harnesses at each height in the fluidized bed at various air velocities

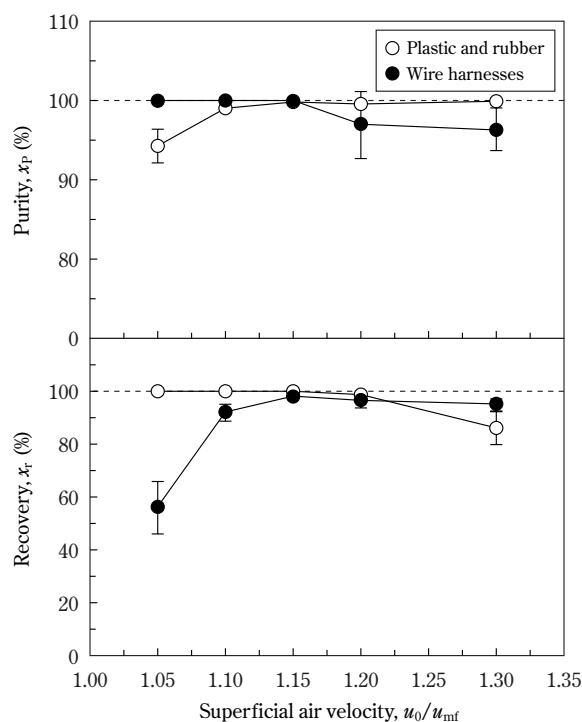


**Fig. 11** Dependence of purities and recovery rates of plastic, rubber, and wire harnesses on superficial air velocity. Powder is uni-beads.

1.15, while the  $x_r$  of wiring was nearly 100% when  $u_0/u_{mf} \geq 1.15$ , but was sharply reduced when  $u_0/u_{mf} < 1.15$ . As noted above, these factors are clear from the

connection to low powder fluidity and fluidization intensity. We performed a float/sink experiment by putting the three constituents together into the fluidized bed at  $u_0/u_{mf} = 1.15$ , which exhibited the best plastic and rubber floating and wire sinking. Results for plastic and rubber were  $x_p = 99.1 \pm 0.9$  and  $x_r = 100.0 \pm 0.0$ , and for wiring  $x_p = 98.8 \pm 1.7$  and  $x_r = 92.2 \pm 4.1$ . These results were about the same as when putting the constituents in separately, and showed that it is possible to separate wiring from the three constituents with high efficiency.

**Figs. 12 and 13** show, respectively, the float/sink results and the  $x_p$  and  $x_r$  according to  $u_0/u_{mf}$  when the three constituents were put in zircon sand together. The float/sink tendencies of the constituents were about the same as those for uni-beads. While the change trends of  $x_p$  and  $x_r$  too were about the same, the changes were more distinct in zircon sand. As observed in the previous section, conceivable reasons include the facts that zircon sand has a wider particle size distribution than uni-beads and is nonspherical, and that the  $u_0/u_{mf}$  is larger. When  $u_0/u_{mf} = 1.6$  the purity and recovery rate values of all constituents were about 100%, showing that zircon sand, which appears to be more suited to practical use than uni-beads, can also separate out wiring with high efficiency.

**Figs. 14 and 15** show, respectively, the float/sink results and the  $x_p$  and  $x_r$  according to  $u_0/u_{mf}$  when plastic and rubber were put in glass beads together. As  $u_0/u_{mf}$  increased, plastic floated with greater diffi-

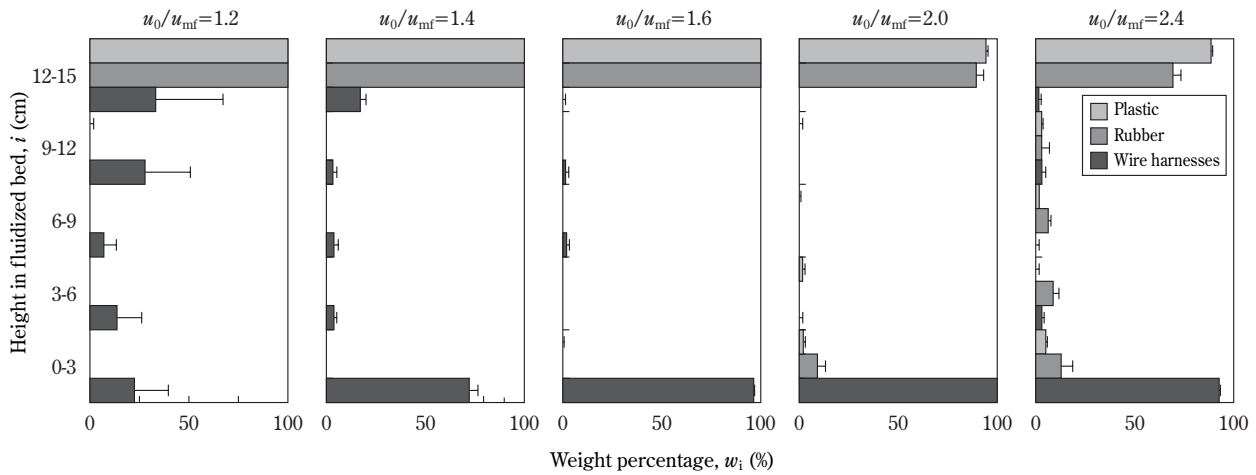


**Fig. 12** Weight percentages of plastic, rubber, and wire harnesses at each height in the fluidized bed at various air velocities

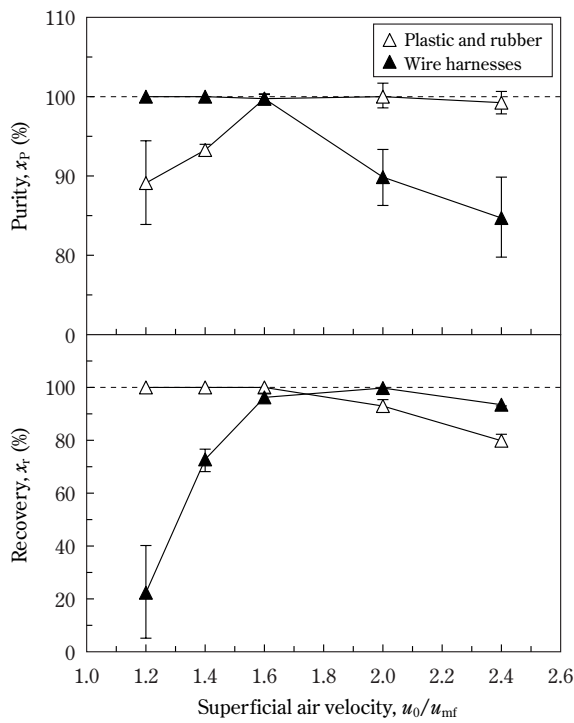


**Fig. 13** Dependence of purities and recovery rates of plastic, rubber, and wire harnesses on superficial air velocity. Powder is zircon sand.

culty and rubber sank more readily, and despite the use of different dust constituents, float/sink tendencies were about the same as in uni-beads and zircon

sand. The change tendencies of  $x_p$  and  $x_r$  also coincide qualitatively. The small difference between the average densities of plastic and rubber meant that items of about the same density were mixed, and thus the two were not completely separated in different strata, but when  $u_0/u_{mf}=1.20$  we obtained better-than-expected separation with a high  $x_p$  value of about 90 and  $x_r$  of 70 to 90.

When using uni-beads and zircon sand the  $\rho_{fb}$  falls between the average densities of rubber and wiring, suggesting that separating them is easy, but even though the  $\rho_{fb}$  of glass beads is about the same as rubber's average density, rubber almost completely sank especially when  $u_0/u_{mf}$  was large. Hence the above results likely do not represent floating and sinking in line with density differences. As described in another paper, [11] the probable reason is that because objects put into the fluidized bed are affected by the particle flows and air bubbles in the bed, whether they float or sink is not determined solely by density difference. Effects of the flow will be different depending on an object's size and shape, and therefore one expects that even among objects with the same density, some will sink and some will not. The  $\rho_{fb}$  values obtained in this research are based on the floating and sinking of spheres 3.75 cm in diameter. Because wire harnesses differ totally in size and shape from these spheres, and are accordingly affected differently by bed flows, it seems to follow that there are float/sink differences between spheres and wiring with the same density.

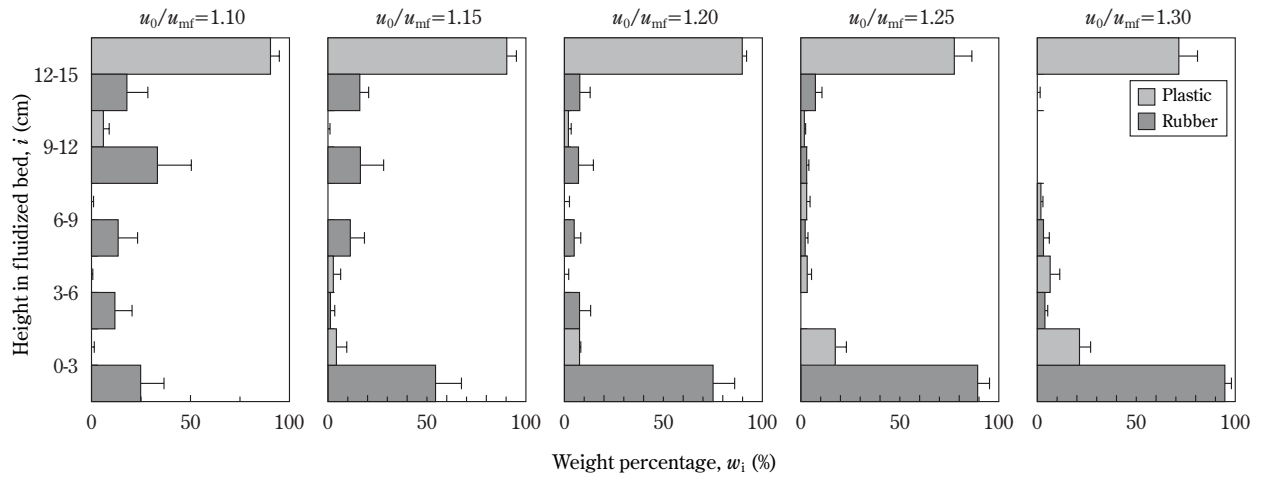


**Fig. 14** Weight percentages of plastic and rubber at each height in the fluidized bed at various air velocities

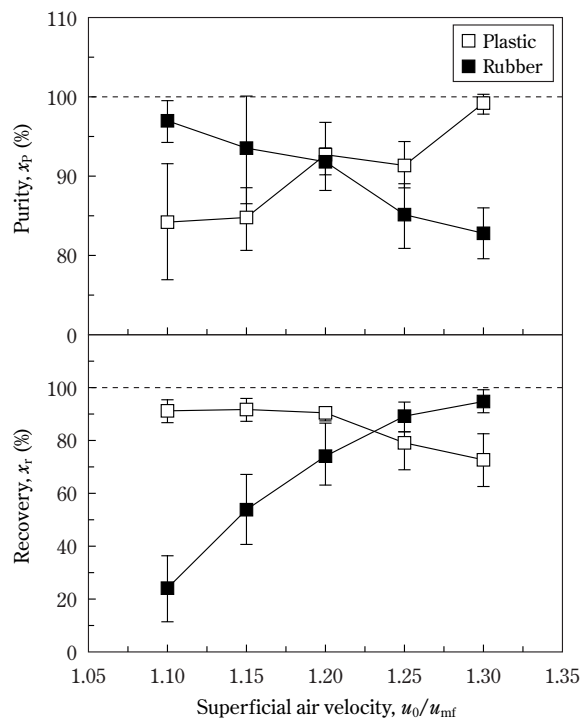


**Fig. 15** Dependence of purities and recovery rates of plastic and rubber on superficial air velocity. Powder is glass beads.

#### 4. Conclusion

We used gravity separation in a gas-solid fluidized bed to test the separation of wire harnesses from plas-

tic and rubber in automobile shredder residue. We investigated the separation of wiring from the three constituents in uni-beads and zircon sand, and the separation of plastic and rubber in glass beads. Results are as follows.

- 1) In uni-beads and zircon sand, plastic and rubber floated in the bed's top stratum, and wiring sank to the bottom stratum. It was thus possible to separate wiring from the three constituents with high purity and a high recovery rate. The difference between the average densities of plastic and rubber is not great, and we anticipated difficulty in separating these mixed items with similar densities, but by using glass beads we obtained better-than-expected separation with purity of about 90% and a recovery rate of 70 to 90%.
- 2) Floating and sinking of objects in the gas-solid fluidized bed depends not only on density differences, but also on the state of powder fluidization, the effect of bed flows on objects, and other factors, but we found that controlling superficial air velocity makes it possible to make objects float or sink according to density differences, and to attain high-efficiency separation.

#### Nomenclature

$h_{sp}$	position of sphere from bottom	(m)
$i$	height in fluidized bed	(m)
$\Delta P$	pressure drop	(Pa)
$u_0$	superficial air velocity	(m s <sup>-1</sup> )

$u_{mf}$	minimum fluidization velocity	( $\text{m s}^{-1}$ )
$w_i$	weight percentage at $i$	(%)
$x_p$	purity	(%)
$x_r$	recovery	(%)

## Greek

$\Delta\rho_{fb}$	dispersion of $\rho_{fb}$	( $\text{kg m}^{-3}$ )
$\rho_{fb}$	bulk density of fluidized bed	( $\text{kg m}^{-3}$ )
$\rho_{sp}$	sphere density	( $\text{kg m}^{-3}$ )
$\rho_{sp1}$	largest density of floating sphere	( $\text{kg m}^{-3}$ )
$\rho_{sp2}$	smallest density of sinking sphere	( $\text{kg m}^{-3}$ )

## References

- 1) Ito, H. "Current Situation and Problems Involved in Recycling (Car Dismantling and Shredding) of ELVs," *Jidosha-Kenkyu*, **19**, 399-403 (1997).
- 2) Iida, S. "Development of ASR (Automobile Shredder Residue) Recovery Technology by JAMA: Possibility to Achieve the ELV (End-of-Life Vehicle) Recycling Rate Target of 95% by 2015," *JARI Research Journal*, **21**, 695-698 (1999).
- 3) Kusaka, K. "Sorting, Volume Reduction and Solidification Technologies for Automobile Shredder Residue (ASR), Part 2," *JARI Research Journal*, **21**, 699-702 (1999).
- 4) Horii, H. and T. Kikushima. "Research and Development on Automobile Shredder Residue (ASR) Dry-Distillation/Gasification Technology, Part 2," *JARI Research Journal*, **21**, 702-706 (1999).
- 5) Toyota Motor Corporation, "Environmental Report 1999," pp. 50-59 (1999).
- 6) Nissan Motor Co., Ltd. "Environmental Report 2000," pp. 27-28 (2000).
- 7) Oshitani, J., K. Kiyoshima and Z. Tanaka. "Material Separation of Automobile Shredder Dust and Pneumatic Separation Method," *J. Soc. Powder Technol., Japan*, Submitted.
- 8) Association for Powder Process Industry & Engineering, Japan, ed. *Fluidization Handbook*, pp. 57-59, Bai-fuhkan (1999).
- 9) Bakhtiyarov, S. I. and R. A. Overfelt. "Fluidized Bed Viscosity Measurements in Reduced Gravity," *Powder Technology*, **99**, 53-59 (1998).
- 10) Tanaka, Z., J. Oshitani, T. Nakamura, T. Syouji and A. Horiuchi. "Development of Technology for Separating Low-Grade Coals from Raw Coals by Fluidized Bed of Dry Heavy Medium," *Kagaku Kougaku Ronbunshu*, **26**, 327-330 (2000).
- 11) Oshitani, J., M. Kondo, H. Nishi and Z. Tanaka. "Separation of Silicstone and Pyrophyllite by Gas-Solid Fluidized Bed Utilizing Slight Difference in Density," *J. Soc. Powder Technol., Japan*, **38**, 4-10 (2001).

## Author's short biography



### Jun Oshitani

Jun Oshitani is Research Associate of the Department of Applied Chemistry at Okayama University. He received his B.S. in 1994, M.S. in 1996, and D.Eng. in 1998 from the Department of Chemical Engineering at Kyoto University. He was a Visiting Researcher at University of Florida Engineering Research Center in 2001. He was awarded a Young Researcher's Award from The Society of Powder Technology, Japan in 2002. His research interests include fluidization technology and water chemistry.



# Feedback Control of Electrification in Powder Pneumatic Conveying Process<sup>†</sup>

S. Watano, S. Saito

Department of Chemical Engineering,  
Osaka Prefecture University\*

T. Suzuki

Kasuga Denki, Inc.

## Abstract

*In a powder pneumatic conveying process, powders are remarkably charged due to the collisions and frictions between themselves or against the conveying pipe, which sometimes causes explosion and fire. In order to prevent these troubles and hazards, development of a reliable system for monitoring and control of electrification (electrostatic charge) is strongly required.*

*In this study, an electrostatic charge control system composed of corona discharge neutralizer, electrostatic field strength sensor and computer control system was newly developed and applied to the powder pneumatic conveying process. Dynamic characteristics of electrostatic charge and its elimination by the corona discharge neutralizer were analyzed. Based on the characteristics, a simplified transfer function composed of first order lag element including dead time was proposed and optimal control parameters for the digital PID control was determined. Performance of the control system was also investigated experimentally under various control parameters. It was found that the electrostatic charge during powder pneumatic conveying process was favorably self-controlled by means of the newly developed control system.*

**Key words:** Control, Electrostatic charge, Pneumatic conveying, Corona discharge neutralizer, Electrostatic field strength sensor

## 1. Introduction

Recently, electrostatic disasters and troubles have become a serious problem in powder handling processes because they sometimes cause explosion and fire [1-3]. For example, in the process of powder pneumatic transportation, powders are tremendously charged due to their collisions between themselves and against transportation pipe. In the case such charged powders are fed into a silo directly, a lightning discharge (atmospheric discharge) in the upper space of the silo or cone discharge along with the accumulated powder surface are frequently observed, which sometimes induce explosion and fire [4-5].

In addition to the progress in the powder handling

technologies, size of powder becomes much smaller in order to increase the functionality. However, the minimum ignition energy also decreases awfully with a decrease in powder size. Among such fine powders, some of them have ignition energy smaller than 1mJ, which is as small as the flammable gas. The surface area also increases with a decrease in powder size, leading to increase the electrification. In order to prevent these hazards beforehand, development of continuous motoring and practical control system of powder electrification is strongly required.

So far, we have developed a novel electrostatic detecting system based on the measurement of electrostatic field strength, and tried to apply to fluidized bed drying and pneumatic conveying processes to continuously monitor the powder electrification [6-7]. We also have developed a corona-discharge type electrostatic neutralizer to remove electrostatic charge of powders during pneumatic conveying of powders into a silo [8]. However, it is impossible to remove electrostatic charge completely and sometimes electrifica-

\* 1-1, Gakuen-cho, Sakai, Osaka 599-8531, Japan  
Tel/Fax: +81-(0)72-258-3323

Email: watano@chemeng.osakafu-u.ac.jp

<sup>†</sup> Accepted: June 12, 2003

tion to the opposite pole due to the too much ion supply has been observed. In order to remove electrostatic charge completely without having the opposite electrification, accurate measurement and control of electrostatic charge is required.

In this study, we have tried to develop an electrostatic removal system composed of electrostatic field strength sensor, corona-discharge type neutralizer and computer control system. We also have applied this system to powder pneumatic conveying system and try to analyze the dynamic characteristics of electrification and its neutralization process. Base on the analysis, an optimum feedback control system of electrification has been developed and performance of the system was also confirmed.

## 2. Experimental

### 2.1 Equipment

**Figure 1** describes a schematic diagram of a pneumatic conveying system. The system consists of a transportation pipe (i.d.28mm×2m) made of stainless seamless pipe (SUS304), an electrostatic field strength sensor, a corona-discharge type neutralizer, and a Faraday cage. This Faraday cage is modified to have a stainless mesh at the bottom of the inner cylinder and a bag filter inside it, so that the only air passes through them and powders remain inside the bag filter. In the conveying experiment, powders are fed into the conveying pipe through a feeder and conveyed by air supplied from an induced blower. Powders are mainly charged due to their collisions with

conveying pipe and are continuously measured its electrostatic field strength by an developed electrostatic field strength sensor and finally measured its total charge by a Faraday cage. The air used for conveying powders were heated up to 333K to maintain its relative humidity around 45% R.H.

**Figure 2** illustrates measurement principle of a developed electrostatic field strength sensor [6,7]. The sensor is installed inside a stainless cylinder (i.d. 8mm) and measures electrostatic field strength as an alternating voltage, which is induced at an electrode by periodically chopping the electrostatic field.

Assuming that the chopping cycle is  $\omega$  ( $=500\text{Hz}$ ), area of the electrode where electrostatic field flows in is  $S_0$ , and the one which changes periodically due to the electrode vibrating is  $S_1$ , then the effective area of the electrode  $S$  can easily be written as:

$$S = S_0 + S_1 \sin \omega t \quad (1)$$

The Gauss's law calculates an electrical charge  $q$ , which is induced by the electrostatic field periodical change,

$$q = E S \epsilon_0 \quad (2)$$

where  $E$  shows an electrostatic field.

A current  $I_s$  running through an electric resistance  $R_s$  which connects the electrode and ground is calculated as,

$$\begin{aligned} I_s &= dq/dt \\ &= E \epsilon_0 \omega S_1 \cos \omega t \end{aligned} \quad (3)$$

The voltage of the electric resistance  $V_s$  is thus:

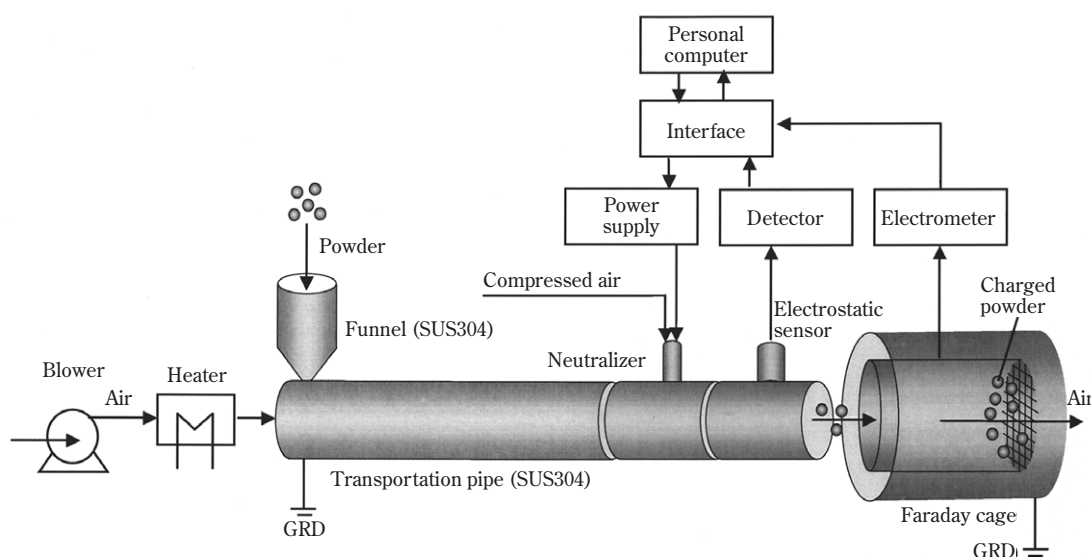


**Fig. 1** Schematic diagram of experimental apparatus used

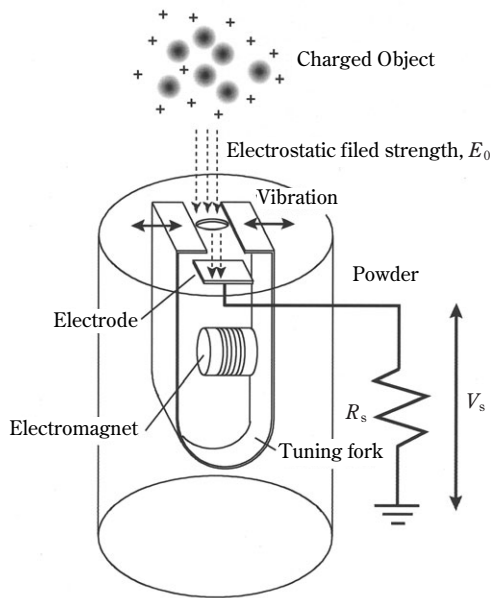


Fig. 2 Schematic diagram of electrostatic detecting sensor

$$\begin{aligned} V_s &= R_s I_s \\ &= R_s E \epsilon_0 \omega S_1 \cos \omega t \end{aligned} \quad (4)$$

Finally, the electrostatic field strength  $E$  can be detected by measuring the voltage  $V_s$  of the electric resistance  $R_s$ .

**Figure 3** describes a schematic diagram of a developed corona-discharge type neutralizer. The neutralizer composes of a needle electrode and nozzle electrode (grounded metal cover). Between the both electrodes, corona-discharge is occurred, leading to ionize the air supplied from a compressor. The ionized compressed air is then sprayed to charged powders to neutralize their charge. In this study, DC type is applied in order to increase the neutralize efficiency as much as possible. As shown in **Fig. 1**, the nozzle is installed perpendicular to the pipe and horizontal level of the nozzle extremity and the inside pipe surface is set at the same. For the needle material, Ni-Cr composite is used to prevent corrosion and erosion.

## 2.2 Powder sample

For powder sample, spherical PMMA particles, which had been sieved to have size range between 100 and 200 $\mu$ m were used. Before the experiment, the PMMA particles were sufficiently dried in a shelf drier and initial charge was removed by ground. The particle feed rate was 1kg/min and airflow velocity was set at 33m/s.

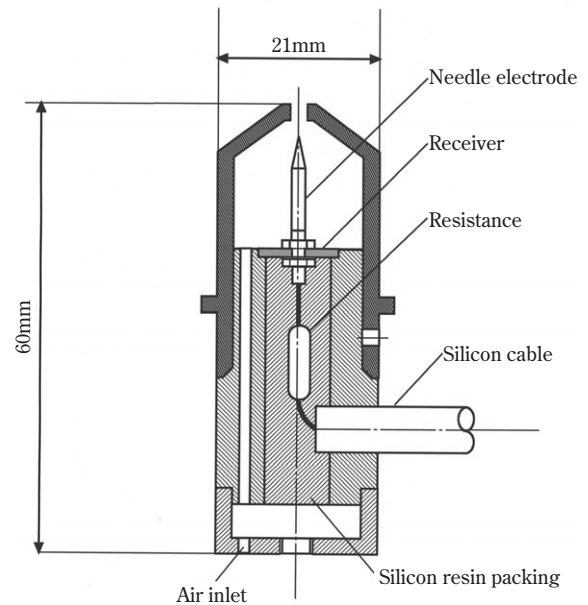


Fig. 3 Corona discharge type neutralizer

## 3. Results and discussion

### 3.1 Performance of the neutralizer

**Figure 4** investigates the relationship between supply current to the neutralizer and ion current generated by the neutralizer under various supplied air velocities. In this experiment, the ionized air was sprayed into the Faraday cage directly to measure the electric charge. Seen from the figure, the ion current increased with an increase in the supply current, and the larger ion current was observed when the supplied air velocity was larger for both negative and positive charge. This implies the possibility of practical control of neutralizing performance by means of the supply current.

### 3.2 Dynamic characteristics of the neutralizing process

In order to control the electrostatic charge in powder pneumatic conveying process, its dynamic characteristics should be intensively understood beforehand. Thus the step response of the neutralizing process was investigated by using developed equipment shown in **Fig. 5**. The equipment composes of two metal plates (0.2 $\times$ 0.2m) located at the opposite side having distance of 0.01m, electrostatic field strength sensor and corona-discharge type neutralizer. Stepwise input difference was generated by a personal computer then its output response was investigated. This equipment imitates the process in

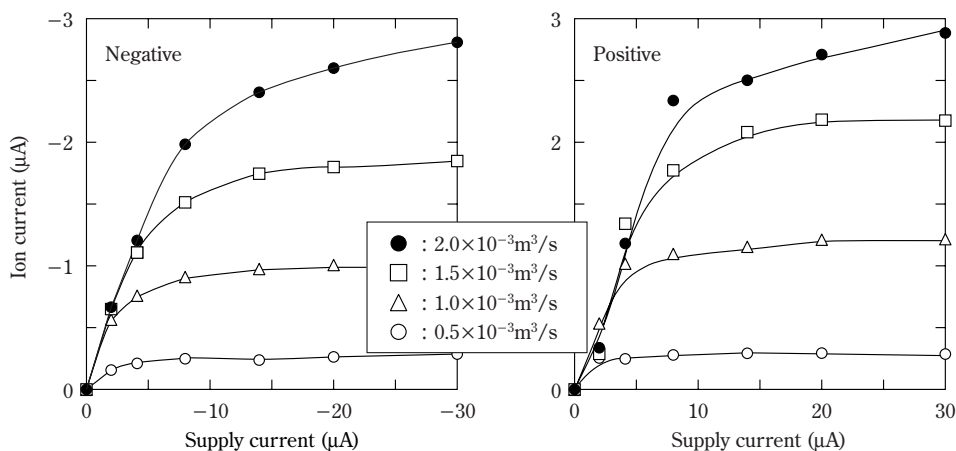


Fig. 4 Relationship between supply current and ion current generated by neutralizer under various supplied air velocities

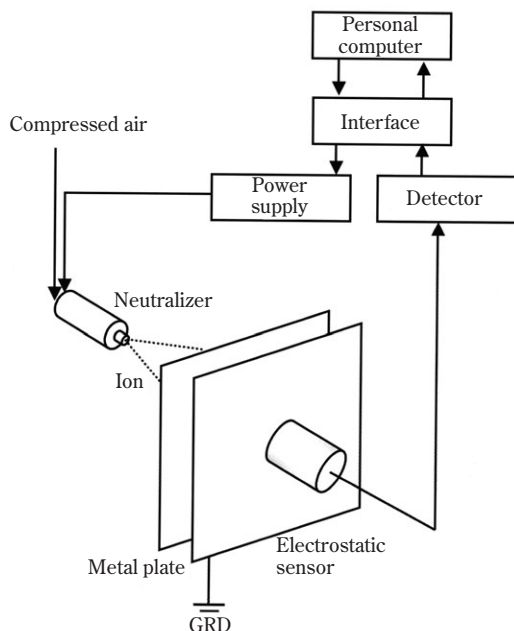


Fig. 5 Experimental set-up used for measurement of step response

which the electrostatic field strength sensor detects electrostatic field strength of the charged particles and then the corona-discharge neutralizer generates ionized air until the charged powders are completely neutralized.

Figures 6 and 7 illustrate the method for determination of step input response and result of output response against the unit step input, respectively. Seen from the figure, the output response converged to a constant value at  $t \rightarrow \infty$ . From this phenomena,

the dynamic characteristics of this process was assumed to be described by a simplified transfer function  $G(s)$  composed of first order lag element including dead time as Eq.(5).

$$G(s) = \frac{Ke^{-Ls}}{1+Ts} \quad (5)$$

where  $K$ ,  $L$  and  $T$  mean gain, dead time and time constant, respectively. By curve fitting, each parameters in Eq.(5) can be determined as  $K=1$ ,  $L=0.34s$  and  $T=0.95s$ . The inverse Laplace Transform gives the numerical output response against the unit step input, which is also described in the Fig. 7. Since adequate correlation was estimated between the both output responses, it is safe to assume that the dynamic characteristics of the neutralizing process is described by the Eq.(5). In the following, a feedback control of the powder charge is attempted by using the transfer function  $G(s)$ .

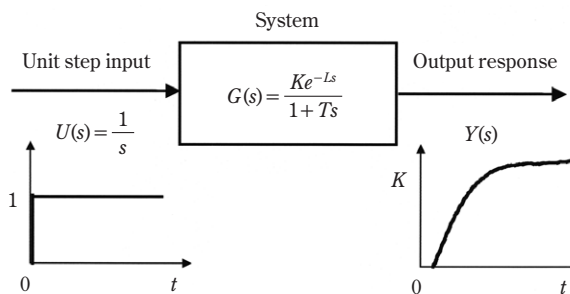
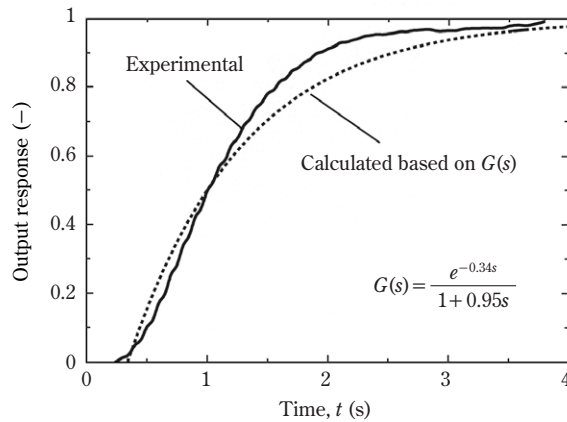


Fig. 6 Method for determination of transfer function



**Fig. 7** Output response against the unit step input

### 3.3 Feed-back control of powder charge in pneumatic conveying process

The PID controller has a transfer function composed of P (proportional), I (integral) and D (derivation) elements as,

$$G(s) = K_P \left( 1 + \frac{1}{sT_I} + sT_D \right) \quad (6)$$

where,  $K_P$ ,  $T_I$  and  $T_D$  indicate proportional gain, integration time and derivation time, respectively.

Assuming that the difference between the desired and output values is  $e(t)$ , the manipulated output value of the PID controller,  $u(t)$ , is described as Eq. (7).

$$u(t) = K_P \left\{ e(t) + \frac{1}{T_I} \int_0^t e(t) dt + T_D \frac{de(t)}{dt} \right\} \quad (7)$$

In the case that the transfer function is described by the first order lag element including the dead time, each parameters of PID controller can be determined by a method proposed by Ziegler and Nichols (**Table 1**) [10].

**Figure 8** shows the results of control by three different feedback control methods, P, PI and PID. Here, the desired value of each control was set at 0V/m and the sampling interval was 20Hz (0.05s).

From **Fig. 8**, it was confirmed that the powder charge was awfully decreased in each control

**Table 1** Optimal parameters for PID Control

Movement of Controller	$K_P$ (-)	$T_I$ (s)	$T_D$ (s)
(1) P	$T/L$	$\infty$	0
(2) PI	$0.9 T/L$	$3.3L$	0
(3) PID	$1.2 T/L$	$2L$	$0.5L$

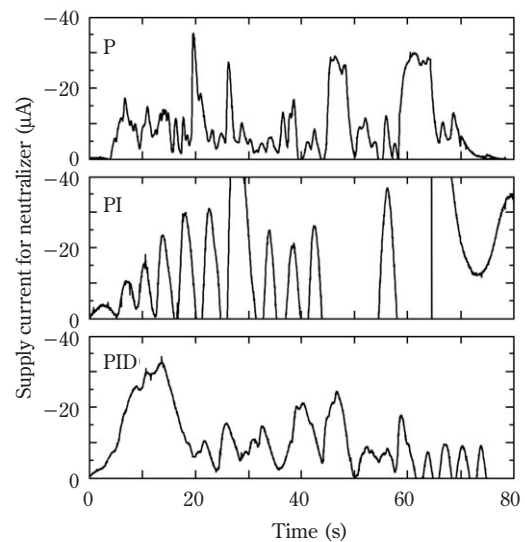
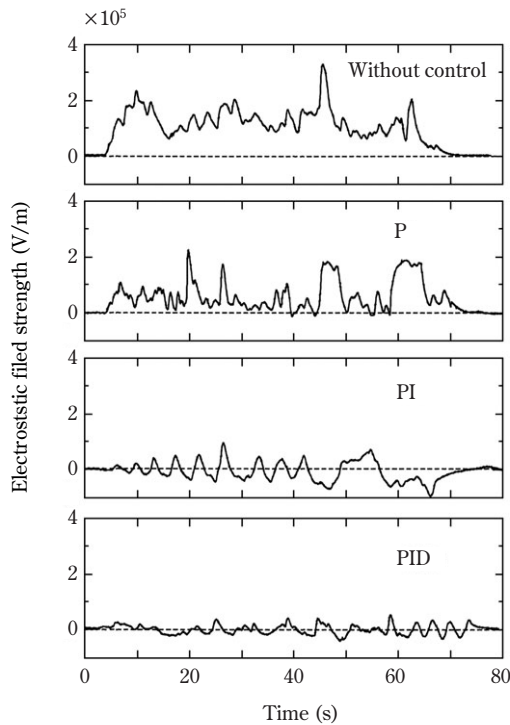


**Fig. 8** Results of control and behaviors of supply current for neutralizer under various control methods



method. However, in the P control, the powder charge did not converge to the desired value (0V/m) and offset was still remained. By contrast, PI control could remove the offset by introducing the integral (I) element. In addition, PID control could increase the response speed by applying the derivation (D) element.

**Figure 9** indicates the total charge of particle measured by the Faraday cage located at the downstream of the conveying pipe. By using the feedback control, the total charge could be greatly reduced. It was also found that the total charge of particles could be reduced almost 0 by using the optimized PID control.

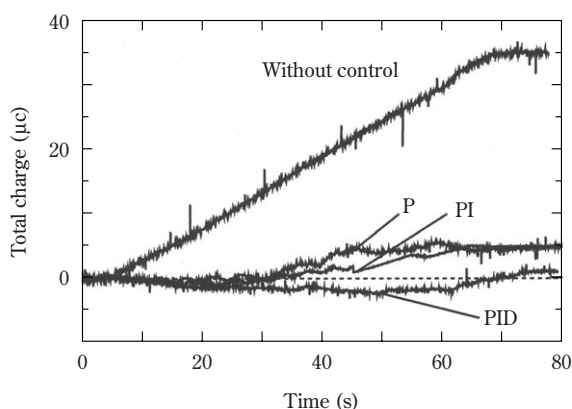


**Fig. 9** Total charge of particle measured by Faraday cage

## Conclusion

The electrostatic charge control system composed of corona discharge neutralizer, electrostatic field strength sensor and computer control system was newly developed and applied to the powder pneumatic conveying process. Dynamic characteristics of electrostatic charge and its elimination process through the corona discharge neutralizer were analyzed. Based on the characteristics, a simplified transfer function composed of first order lag element including dead time was proposed and the optimal control parameters for digital PID control was determined. Performance of the control was also investigated experimentally under various control parameters (P, PI and PID controls). It was found that

the electrostatic charge during the powder pneumatic conveying process was favorably self-controlled and powder charge was awfully reduced by each control. The optimum PID control was also found to reduce the powder charge almost completely without having any offset. This control method can be used to any kind of powder handling processes and is expected to be very useful and reliable device to prevent troubles originated by the electrostatic charge.

## Acknowledgement

The authors wish to acknowledge that this work is partially supported by Grants-in-Aid for Scientific Research 2002.

## References

- 1) Itagaki H.: "Specific Research Reports of the National Institute of Industrial Safety NIIS-SD-No.15", 10 (2001)
- 2) Seidenki Hand Book, The Institute of Electrostatics Japan, Ohmsha, Tokyo (1998)
- 3) Jones T.B and J. King: "Powder Handling and Electrostatics" Lewis Publisher (1991)
- 4) Glor, M. and B. Maurer: "Ignition Tests with Discharges from Bulk Polymer Granules in Silos (Cone Discharges)" *Journal of Electrostatics*, **30**, 123-134 (1993)
- 5) Asano K., T.B. Jones and Y. Matsubara: "Electrostatic Hazards in Industry – Their Recognition and Prevention –", Proc. of Second IUPAC-Workshop on Safety in Chemical Production Processing, pp.1-21, Yokohama, Japan (1993)
- 6) Watano S., Y. Ito, T. Suzuki and K. Miyanami: "The On-line Monitoring of the Electrostatic Field Strength in Fluidized Bed Granulation and Drying Using a Newly Developed Electrostatic Field Detecting System", *Journal of Powder Technology Japan*, **34** (10), 778-784 (1997)
- 7) Suzuki T., S. Watano, T. Numa, T. Taira and K. Miyanami: "On-line Monitoring of Electrostatic Field Strength in Powder Pneumatic Transportation Process Using Newly Developed Electrostatic Field Detecting System", *Journal of Powder Technology Japan*, **35** (12), 846-855 (1998)
- 8) Kodama T., T. Suzuki, K. Nishimura, S. Yagi and S. Watano: "Prevention of Incendiary Discharge in a Silo by Using a Newly Developed Electrostatic Eliminator", Proc. the 2000 IEEE Industry Application Conference, pp.652-656, Roma, Italy (2000)
- 9) The Institute of Electrostatics Japan: "Handbook of Electrostatics" Ohm Inc., Tokyo (1981).
- 10) Ziegler J.G. and N.B. Nichols, "Optimum Settings for Automatic Controllers", *Trans. ASME*, **64**, 759-768 (1942)

## Author's short biography



**Satoru Watano**

Prof. Satoru Watano has been at Chemical Engineering, Osaka Prefecture University, Japan since 1991. He is also a visiting professor at Particle Technology Center, New Jersey Institute of Technology, U.S.A. since 1997. His major research interest lies in measurement, control, optimization, computer simulation and scaling-up of powder handling processes, handling of nano-particles, and mechanism and control of electrostatic charge. Now, he is an editor of Journal of the Society of Powder Technology, Japan and Journal of Advanced Powder Technology.



**Seiji Saito**

Mr. Seiji Saito graduated from Department of Chemical Engineering, Osaka Prefecture University, Japan in 2000. He conducted fundamental research on measurement, control and computer simulation of electrostatic charge in powder handling processes under the guidance from Prof. Watano. Now, he is working at Engineering Department, Tyugai Pharmaceutical Industry.



**Teruo Suzuki**

Dr. Teruo Suzuki graduated from the Tokyo Denki University, Japan in 1979 with a B.E. in Electronics. He received Ph.D. from Osaka Prefecture University (Chemical Engineering) in 2000. He has been active in the field of electrostatics for the past 20 years. Currently, he is working at Kasuga Denki Inc. and responsible for the design and development of novel devices for detecting and eliminating electrostatics in powder handling processes. He is also an editor of the Journal of Electrostatics, Japan.

# Improved Coal Pulverization Method Using the Embrittlement due to Cracks Generated in Pores of Coal<sup>†</sup>

Tetsuo Ono

Department of Chemical Energy Engineering,  
Yokosuka Research Laboratory, Central Research  
Institute of Electric Power Industry (CRIEPI)\*

## Abstract

*Pulverized coals produced by a rounding method have a wide range of particle sizes. Even though the coals have the same Hardgrove Grindability Index (HGI), some coals are difficult to pulverize by the rounding method.*

*There are many pores in the coal. When pore pressure is rapidly reduced, cracks are generated in the pores by the expansion of air and the coal becomes brittle. The purpose of the present work is to investigate the performance of coal pulverization by an improved rounding method specifically by the embrittlement of coal due to the cracks generated in the pores.*

*The experimental results show that pulverized coals for CWM which have a wide range of particle size can be easily produced by the improved rounding method. Furthermore, a discharge pressure at the embrittlement treatment can control the particle size of the pulverized coals.*

**Key words:** Fine pulverization, Coal pore, Embrittlement, Rounding, Coal water mixture

## Introduction

When producing CWM (Coal Water Mixture) from pulverized coal, coal particle size distribution must be adjusted to a wider range consisting of a large quantity of finer particles. To this end, we developed a method for rounding pulverized coal particles to create large quantities of finer particles which will ease the necessary adjustment of particle size distribution. As stated in a previous report,<sup>1</sup> this technique makes it possible to produce a high quality CWM. However, another problem still remains, for even though certain brands of coal might have the same HGI (Hardgrove Grindability Index) value, some are more difficult than others to pulverize using this rounding method. Therefore, an improved pulverization technique must be developed in order to expand the number of coal types usable in making CWM.

To address this problem, we focused our attention

on the numerous pores present within coal and, on this basis, proposed a method for embrittling coal via the generation and propagation of cracks. First, coal powder is loaded into a pressure vessel and subjected to high pressure. Then, the pressure is rapidly released, causing the rapid expansion of the gases residing in the coal pores. In short, this method utilizes gas expansion pressure to trigger crack generation and propagation. If the coal powder embrittled in this manner is fine-pulverized using the rounding method, it becomes easier to adjust particle size distribution so it consists of large numbers of extremely fine particles that will be suitable for CWM. We report here that, through experimentation, we have investigated and been able to verify that, indeed, embrittled coal powder obtained by embrittling coal through a pressure release of 0.2-0.3 MPa is easily fine-pulverized to attain a particle size distribution suitable for CWM.

## 1. Coal Pores and Embrittlement of Coal

**Fig. 1** shows the particle size distributions of A coal (HGI=50) – which is difficult to fine-pulverize by rounding – before and after the rounding process,

\* 2-6-1 Nagasaka, Yokosuka-shi, Kanagawa-ken 240-0196, Japan

TEL: 046-856-2121, e-mail: ono@criepi.denken.or.jp

<sup>†</sup> Accepted: July 18, 2003

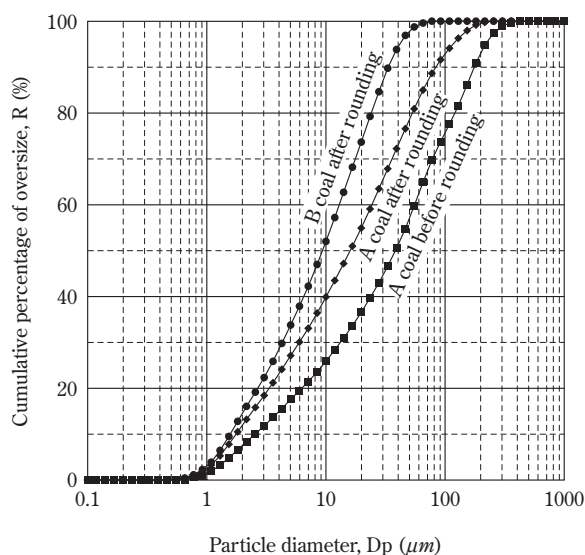


**Fig. 1** Particle size distribution of pulverized coal

analyzed using a Laser Micron Sizer (Seishin, LMS-30) particle size distribution analyzer. Included in the graph is an analysis of B coal (HGI=55) – which provides a high-quality CWM – after the rounding process.

In the graph, the post-rounding 10% diameter is approx. 1.6 mm for both A and B coal; the post-rounding 50% diameter for B coal is approx. 9 mm, while that for A coal is approx. 16 mm; and the post-rounding 90% diameter for B coal is 33 mm, while that for A coal is 88 mm. In sum, it is apparent that A and B coal differ in terms of the size of their larger particles. It is possible that A coal's tend to be larger due to the difficulty of fine-pulverizing its relatively large particles during the rounding process, despite the fact that fine particles are also generated.

Relatively large, less-pulverable particles can be pulverized but first must be transform into a ready-to-crack form. For this purpose, embrittlement of such particles via an embrittlement technique appears to be a promising solution.

Ordinarily, a very brittle solid substance will have numerous internal voids and cracks. When subjected to an external force, such a substance will fracture and break along these voids and cracks, leading to its pulverization. In some cases, pulverization will occur when the crystalline grain interfaces within a solid substance are subjected to a force which produces a shearing strain.

Coal is considered an amorphous substance. Therefore, to increase the brittleness of coal particles, it is

necessary to trigger cracks, etc., within them. As a means for triggering such cracks, we focused our attention on the pores present within coal particles. As shown in the SEM (Scanning Electron Microscope) photograph of a cross-section of a coal particle in **Fig. 2**, ordinarily both relatively wide and narrow cracks appear as striations inside the coal particle. Furthermore, numerous pores appear as black dots of various sizes. Founded on the porous nature of coal, our method relies on the generation and propagation of cracks. The preferred technique of crack generation and propagation is to utilize gas impact force by loading coal powder into a pressure vessel and, after subjecting it to high pressure, rapidly releasing the pressure to produce a rapid expansion of the gases within the coal pores. In this manner, the coal is embrittled by the generation of cracks started at the pores and by the cumulative force of the already started cracks. It is then possible, we believe, to obtain a particle size distribution suitable for CWM production by fine-pulverizing the embrittled coal using the rounding process.

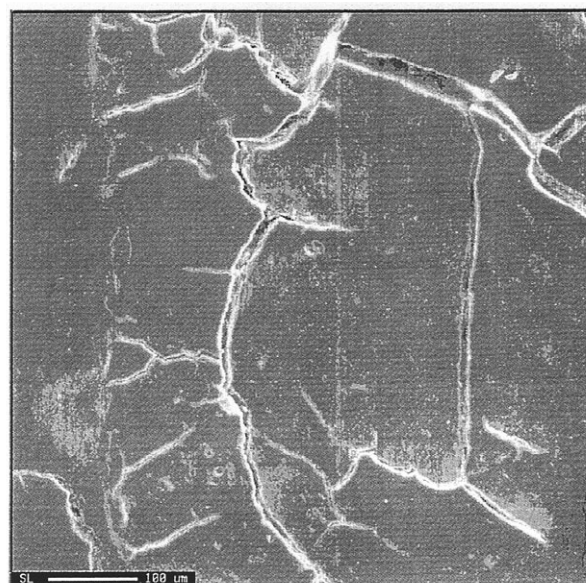


**Fig. 2** SEM photograph of cross-section of coal particle

## 2. Experiment

In our experiment, using a commercial cereal puffer to measure the effects, high pressure was exerted on coal powder then rapidly released, causing the gases in the coal pores to expand violently and, thereby, triggering the emanation of cracking from



the pores. The cereal puffer vessel itself, shown in **Fig. 3**, measures 250 mm×300 mm in diameter. One end of the vessel was fitted with a butterfly-shaped lid in order to effect the rapid release of pressure. The other end of the vessel was equipped with a gauge to monitor the internal pressure. In pastry-making, pressure is increased by heating with a burner. For our experiment, however, nitrogen gas was pressure-fed through pressure-gauge piping to increase the internal pressure, as shown in **Fig. 4**. Loaded with coal powder, the vessel's internal pressure was increased to a predetermined level with the pressurized nitrogen gas. Then, the lid was unlocked and opened, which caused the rapid release of pressure. As a result, the coal powder within the vessel was discharged and carried away by the outward flow of gas. To capture the discharged coal powder, a 250-liter polyethylene bag with a built-in lid was placed on the

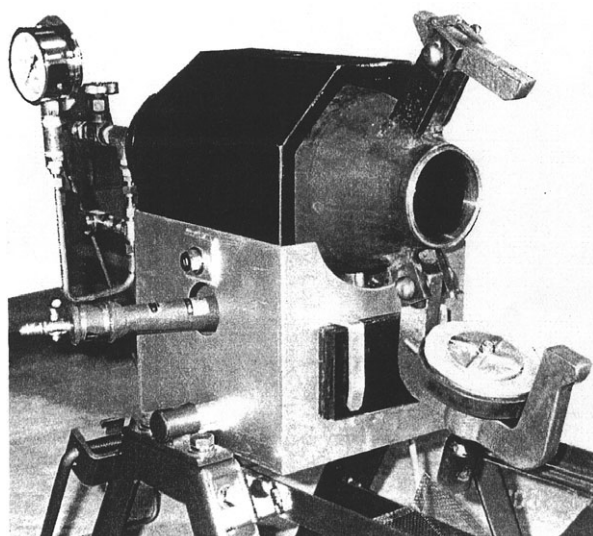


**Fig. 3** Cereal puffer

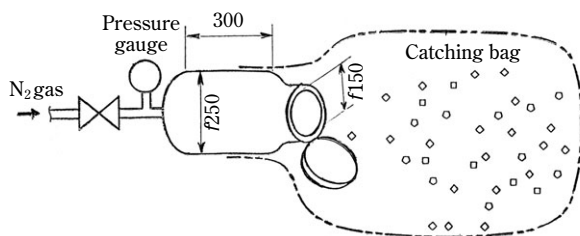


**Fig. 4** Experimental set-up of embrittlement

vessel as a collection bag. The amount of coal powder discharged per gas release cycle was set to approx. 400 ml. However, not all the coal powder was discharged from the vessel; a certain amount remained in the vessel in every discharge cycle because the discharge port measured only 150 mm in diameter.

Until a total of 2 liters of coal powder (an amount needed for the rounding stage of our experiment) had been embrittled, the above-mentioned sequence was repeated with our sample coal powder repeatedly filled into the vessel. As a result, coal powder accumulated in the vessel. Despite this fact, for our purposes, only the powder discharged from the vessel and captured in the collection bag was treated as embrittled coal powder because the discharged portion of powder was, we reasoned, subjected to the greatest expansion pressure. The experiment was repeated at each of four discharge pressures (0.2, 0.3, 0.5 and 0.7 MPa).

Next, in order to fine-pulverize the embrittled coal powder, the prototype rounding device shown in **Fig. 5** was employed.<sup>1</sup> The device consists of two disks (stationary disk and rotary disk) with meshing crusher teeth. The coal powder is fed through the center portion of the stationary disk. The coal particles sandwiched between the two crushing teeth are transported in circumferential, radial, and axial directions. During this process, the corners of our embrittled sample particles wore off by colliding with one another or through the friction of the crusher teeth, making the particles spherical and, at the same time, generating fine particles out of the shaved off corner portions.

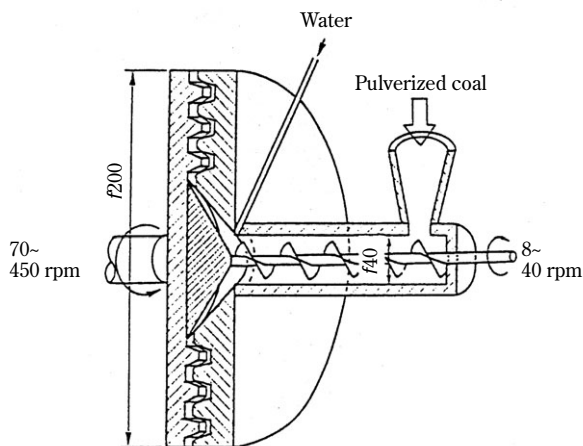


**Fig. 5** Rounding device



### 3. Results of Experiment, Observations

We evaluated the effectiveness of the embrittlement of the coal powder by verifying crack occurrence through the inspection of SEM photographs of cross-sections of the coal particles. In addition, after fine pulverization via the rounding process, we measured

the particle size distribution of the fine powder product.

#### 3.1 SEM Inspection

For comparison purposes, the cross-sectional SEM photographs of the coal particles both before and after embrittlement are shown in **Fig. 6**. Photos (a),

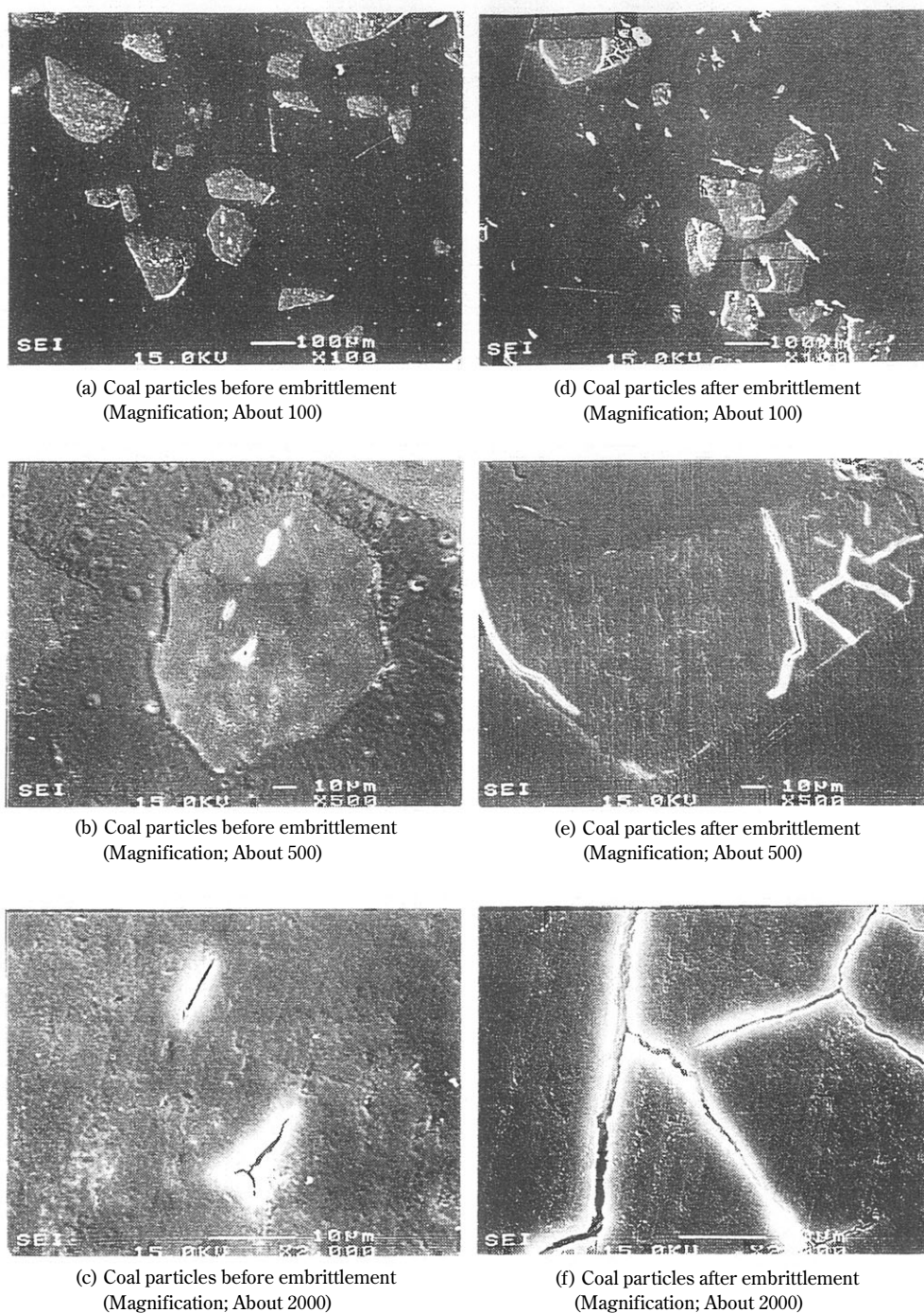


**Fig. 6** SEM photographs of cross-section of coal particles before and after embrittlement

(b), and (c) each represent a cross-sectional view of the coal particles before embrittlement, and photos (d), (e), and (f) each show a cross-sectional view of the coal particles after embrittlement. From these photos, each pre-embrittlement cross-sectional view exhibits innumerable pores as dots together with striated cracks. In contrast, each post-embrittlement cross-sectional view shows far fewer dots and an increased number of striated cracks. Moreover, the length of post-embrittlement striations is much longer and their width twice as large as the pre-embrittlement striations.

From these findings, it can be safely judged that subjecting coal powder to the rapid release of high pressure causes the gases residing in coal pores to expand violently, which results in the formation and spread of cracks.

### 3.2 Fine Pulverization by Rounding

Embrittled coal powder was fine-pulverized with the rounding device illustrated in **Fig. 5**. Then, the particle size of the fine-pulverized coal powder was again measured using the particle size distribution analyzer. The results of our analysis is graphed in **Fig. 7** and **Fig. 8**.

**Fig. 7** shows the particle size distributions of coal powders that were embrittled with discharge pressures of 0.2, 0.3, 0.5 and 0.7 MPa using the cereal puffer, and then were fine-pulverized using the previously mentioned rounding technique. For comparison purposes, this diagram also illustrates the particle

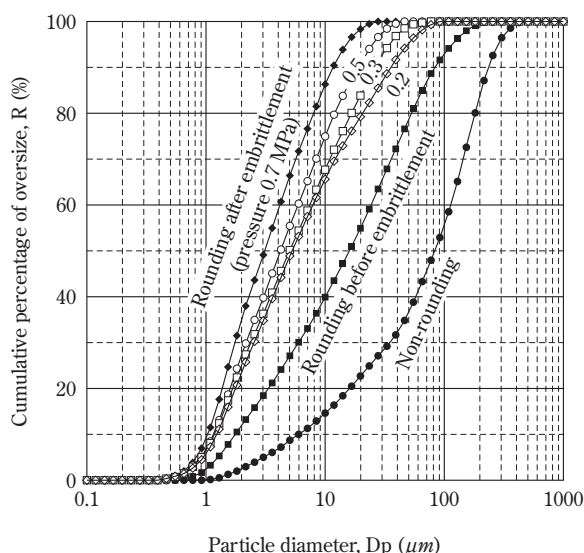


**Fig. 7** Particle size distributions of pulverized coal after embrittlement

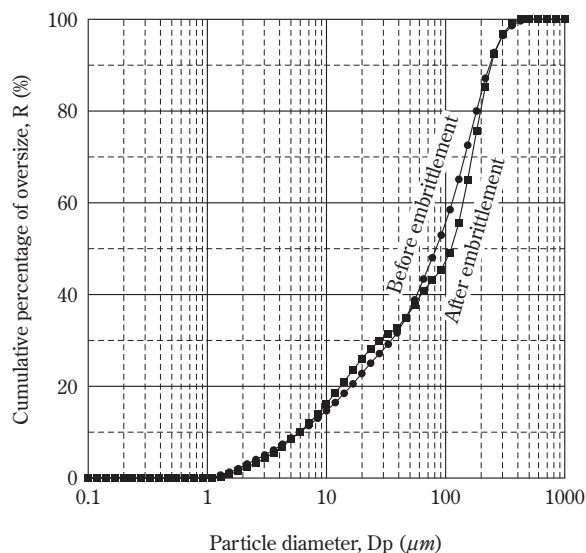


**Fig. 8** Transformation of particle size distribution by embrittlement

size distributions of a non-processed coal powder and a coal powder sample that was processed by rounding but was not embrittled. **Fig. 8** illustrates our investigation into possible changes in coal powder particle size based on whether or not crack propagation affects particle size during the embrittlement process. From these findings, it is apparent that the particle size of the coal powder exhibited virtually no change even when cracking was triggered by effecting the rapid expansion of the coal pore gases. Nevertheless, this coal powder was easily fine-pulverized via the rounding process. The particle size after fine-pulverization, for 90% diameter, was no greater than 35  $\mu\text{m}$  regardless of the level of pressure exerted in the embrittlement process. The particles at 50% diameter were 16  $\mu\text{m}$ , without having undergone the embrittlement process. Although results varied somewhat depending on the amount of pressure exerted, the coal powder sample at 50% diameter after having undergone the embrittlement process, fell into the much lower range of 3 to 5  $\mu\text{m}$ . Consequently, our method proved to be able to readily prepare coal powder that has a particle size distribution suitable for CWM formulation involving a large proportion of finer particles. Employing this method, a CWM of viscosity 1000 mPa-s at approx. 65% concentration was successfully produced with A coal, which otherwise would have been a material difficult to pulverize.

Additionally, **Fig. 9** illustrates the relationship between the pressure exerted and post-pulverization particle size – a greater discharge pressure led to a

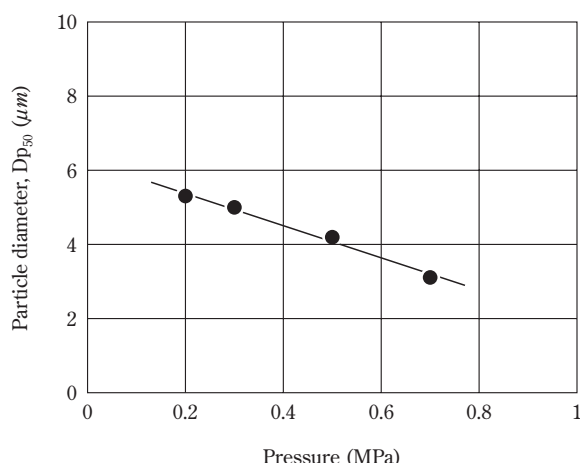


**Fig. 9** Relation between pressure and particle diameter

smaller 50% diameter. This means that by controlling the discharge pressure, the resultant post-rounding particle size can be controlled as required.

## Conclusion

We proposed a coal powder embrittlement method by which the gases in coal particle pores are compressed and then rapidly released, causing the violent expansion of the gases and, thereby, the generation of cracks emanating from the coal pores. We also proposed a grinding method for fine-pulverizing the coal particles thus embrittled, and demonstrated the effect of the combination of these methods in our experiment. The results clearly show that the particle size of coal powder, even after the embrittlement procedure, remains virtually unchanged while, in contrast, fine-pulverization is readily achieved by the

rounding procedure.

To sum up, by employing the method detailed herein, previously less pulverable coal brands that generate a lower amount of fine particles can be used to produce a large amount of finer particles. This method will contribute to the better production of high-quality CWM as well as to an increase in the range of coal brands usable in CWM manufacturing. In addition, the embrittlement method put forth here may make it possible to obtain the particle size needed for a given application, since controlling the discharge pressure during the embrittlement process changes the particle size produced in the rounding process.

## Acknowledgements

The author would like to thank the people at Kobe Steel, Ltd. for their generous cooperation in, among other things, supplying samples. Additionally, thanks are due to the author's colleagues who have helped make this research a success.

## Nomenclature

$D_p$	: particle diameter	(mm)
$D_{p50}$	: mass median diameter	(mm)
$R$	: cumulative percentage of oversize	(%)

## References

- 1) Ono, T. and Y. Yamasaki : "Particle Shape Control by Rounding Irregular Shaped Particles – Effects of Particle Shapes on Fluidity of Pulverized Coal in CWM and Fly-ash Particles –", *J. Soc. Powder Technol. Japan*, **35**, 655-661 (1998)

## Author's short biography



### Tetsuo Ono

Dr. Tetsuo Ono is a Research Scientist in the Department of Chemical Energy Engineering at the Central Research Institute of Electric Power Industry. His research interests include oxidation of coal in storage pile and coal spontaneous combustion, handling technology of pulverized coal, and producing of coal water mixture.



# Particle Discharge Characteristics from the Nozzle of a Thin Tube Immersed in Liquid Subjected to Ultrasonic Wave Force<sup>†</sup>

Kenichi Yamamoto\*, Mitsue Shiokari,  
Toshiaki Miyajima, Masateru Kawamura,  
Masunori Sugimoto

Department of Material Systems Engineering  
and Life Science, Toyama University

## Abstract

*A wet micro-feeder that utilizes ultrasonic wave force was designed and constructed to feed small particles into a container of wet particulate materials. The particle discharge characteristics from a nozzle with the inside diameter  $D_n$  were investigated using spherical and irregular particles of 80 to 180  $\mu\text{m}$  in diameter,  $d_p$ .*

*As a result, the critical ratio for particle blockage of the present feeder,  $(D_n/d_p)_c \approx 3.0$ , was found to be smaller than the values obtained previously ( $>4 \sim 5$ ) in the gravitational field for dry powders. The present feeder was able to achieve stable and continuous discharge of small amounts of particles. Multiple regression analysis proved that the discharge rate of particles, i.e. the number of particles discharged from the nozzle per unit of time,  $\bar{N}$ , depended on  $D_n$ ,  $d_p$ , the applied voltage  $V_0$ , and the median value of the particle shape index (surface roughness),  $y_{50}$ , and that  $\bar{N}$  was proportional to  $D_n^{2.29}$ . Therefore,  $\bar{N}$  could be controlled by  $V_0$  and  $D_n$  for given particles.*

**Key words:** Wet micro-feeder, particle discharge, ultrasonic field, nozzle aperture, particle shape

## 1. Introduction

When developing new materials, it is important to have the capability to feed small amounts of particles (i.e. “to microfeed particles”) of a uniform composition at a constant feed rate in air or liquid continuously into a container of particulate materials. In particular, wet microfeeders, in which raw materials are charged in a vessel filled with a liquid, are necessary for feeding wet materials into the device for particulate operation in liquid, and for feeding raw materials into a small-scale wet separator [6].

In air, the microfeeding of particles of smaller sizes becomes more difficult because it is easier for them to adhere to the wall of the feeder or to cohere with

each other. Matusaka et al. recently reported that capillary tubes vibrating at high frequency of less than 760Hz [1] or at an ultrasonic frequency of 20kHz [2] were effective for microfeeding fine powders in air.

On the other hand, liquid has an advantage of diminishing the particle adhesion and cohesion. It is expected that this advantage can be applied to the following wet microfeeding processes. (1) For “fine particles”, uniform-density suspension can be obtained because the settling velocity is very low. Wet microfeeders configured with a rotary pump and an elastic tube are now available to microfeed suspended fine particles. (2) For “small particles” which tend to deposit on the tube wall because the settling velocity is comparatively high, the above method (1) cannot be applied. Few reports concerning the wet microfeeding of “small particles” have been found.

In this paper, a wet microfeeder which utilizes ultrasonic force in liquid was designed and constructed on the basis that the dispersion and movement of small particles can be facilitated in the ultrasonic field in liquid. Discharge characteristics of small particles from

\* Corresponding author  
3190 Gofuku, Toyama 930-8555, Japan  
Tel.: +81 (0)76-445-6831  
Fax.: +81 (0)76-445-6831  
e-mail: kyamamot@eng.toyama-u.ac.jp

<sup>†</sup> Accepted: July 31, 2003

the nozzle of a thin glass tube were experimentally investigated in liquid subjected to ultrasonic force.

## 2. Experimental

### 2.1. Experimental materials

**Table 1** shows the properties of experimental materials used. Three couples of spherical (s) and irregular-shaped crushed (i) mullite particles (true density  $\rho_p=2920\text{kg/m}^3$ ) were prepared. Both the s- and i- particle groups in each couple had the same sieve opening range. The three couples had different average particle diameters ( $d_p=81, 127, 180\mu\text{m}$ ). Each spherical particle group consisted of many spherical particles, and some irregular-shaped ones with small protuberances as shown in the particle images of representative spherical groups (Mat-Ss) from **Table 1**. In this paper, the irregular-shaped particles in the spherical particle group are also referred to as “spherical particles” for convenience.

The shape index  $\psi$  defined by Eq. (1) presents the degree of surface roughness of the two dimensional particle image based on the circle of equivalent area:

$$\psi = \frac{4\pi A}{p^2} (\leq 1.0), \quad (1)$$

where  $A$  and  $p$  respectively denote the area and perimeter length of a particle image.

The  $\psi$  distributions in **Table 1** were measured in the vertical direction by an image analyzer (Luzex FS, Nireco, Hachioji, Japan) for about 300 particles randomly sampled from each group. The respective  $\psi_{50}$  values in **Table 1** denote the medians of  $\psi$  distribution concerned.

The volume shape factors  $f_n$  for groups of  $d_p=127, 180\mu\text{m}$  were obtained by the following equation:

$$f_n = \frac{M_n}{N_n \rho_p d_p^3}, \quad (2)$$

where  $M_n$  and  $N_n$  denote the mass and the number of 9,000 and 2,300 or more particles randomly sampled from 127 and  $180\mu\text{m}$  sized groups, respectively. The shape factors of the s- and i- particles in the smallest sized group ( $d_p=81\mu\text{m}$ ) were not shown in **Table 1** because reliable measurements of their  $M_n$ - and  $N_n$ -values were not obtained.

### 2.2. Experimental apparatus

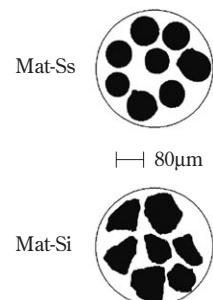
**Fig. 1** shows the schematic diagram of the wet microfeeder developed in this paper. Two ultrasonic transducers (1) (HEC-342445100, Langevin-type, Honda Electronics, Toyohashi, Japan) was fixed to the outer bottom of a rectangular vessel of stainless steel (2) (inner dimensions:  $117 \times 117 \times 117\text{mm}$ ). The transducers were driven by the sinusoidal power from an ultrasonic generator (W-113, including power amplifier, maximum output=100W, Honda Electronics, ibid.). The applied voltage  $V_0$  (V) (peak to peak value) to each transducer was controlled through a variable transformer (SLIDAC SK105, Toshiba, Tokyo, Japan).

A thin glass tube (3) (inside diameter=2mm, length=235mm) for charging and feeding particles was fastened with a joint (4) at the center of the rectangular-vessel top cover. The glass tube (3) had a cone-shaped nozzle of inside diameter  $D_n$  at the bottom from which particles could be discharged as shown in **Fig. 1**. This made it possible to observe the behavior of particles discharged from the nozzle, whose bottom was placed at  $-30\text{mm}$  in  $h$  which denotes the distance in the vertical direction from the inner bottom of the rectangular vessel.

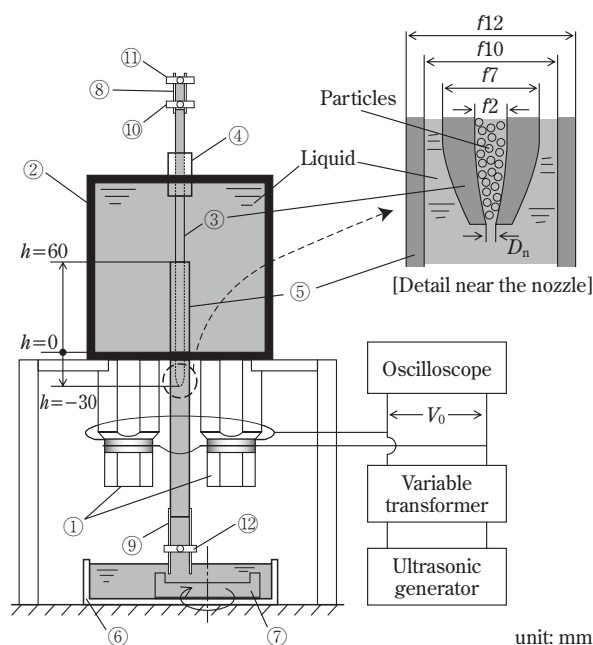
A dilute aqueous solution of a surfactant (Extran MA03, 0.2vol%, density=997kg/m<sup>3</sup>, viscosity=0.888 mPa·s at 25°C, Merck Japan, Tokyo) was added to fill the space of the apparatus drawn with grey-hatching as shown in **Fig. 1**.

**Table 1** Experimental materials used (mullite particles: density  $\rho_p=2,920\text{kg/m}^3$ )

Material	Size ( $\mu\text{m}$ ) Sieve opening range (Average diameter $d_p$ )	Shape	Shape index $\psi$ (-)		Volume shape factor $f_v$ (-)
			Min ~ Max	Median value $\psi_{50}$	
Mat-Ss Mat-Si	74 ~ 88 (81)	Spherical Irregular	0.780 ~ 0.988 0.333 ~ 0.900	0.961 0.625	— —
Mat-Ms Mat-Mi	105 ~ 149 (127)	Spherical Irregular	0.792 ~ 0.986 0.306 ~ 0.886	0.976 0.680	0.533 0.581
Mat-Ls Mat-Li	149 ~ 210 (180)	Spherical Irregular	0.770 ~ 0.991 0.321 ~ 0.818	0.968 0.599	0.677 0.744







- ① Ultrasonic transducer (Langevin-type)
- ② Rectangular stainless steel vessel  
(inner dimensions: 117×117×117)
- ③ Glass tube with a nozzle (ID=f2, OD=f7, length=235)
- ④ Joint
- ⑤ Particle collector of glass tube (ID=f10, OD=f12, length=167)
- ⑥ Glass dish                      ⑦ Sampler
- ⑧ Rubber tube (a)                ⑨ Rubber tube (b)
- ⑩ Pinchcock (a)                ⑪ Pinchcock (b)                ⑫ Pinchcock (c)

Fig. 1 Experimental apparatus

### 2.3. Experimental procedure

Particles were charged in the glass tube (3) and rubber tube-a (8) under the condition that both pinchcock-a (10) and pinchcock-b (11) were opened, while pinchcock-c (12) was closed. Then pinchcock-b (11) was closed so that the liquid in the glass and rubber tubes could not drain.

The ultrasonic power was supplied to transducers beginning 1 minute after pinchcock-c (12) had opened. The term  $t$  was defined as the time elapsed from the start of the ultrasonic power supply. The particles were sampled for 5 seconds at a sampler (7) from  $t=30$ s. The first sampling from  $t=30$ s was determined by considering the time required for particles to settle from the bottom of the nozzle to the sampler. Similar samplings of 5 seconds were repeated 15 times in 30-second intervals. Sixteen samples were obtained through a series of measurements for  $t=0-560$ s. The number of particles in each sample was counted through a light microscope. The corresponding number of particles discharged from the

nozzle per unit time,  $N_i$  ( $s^{-1}$ ) ( $i=1$  to  $n$ :  $n$  denotes the total number of samples, i.e., 16), was calculated respectively. Hereafter, the term  $N_i$  is referred to as the particle discharge rate.

The above experiments were carried out at room temperature (20–29°C) under the following conditions:

Oscillation frequency applied to the transducer:

$$f = 25, 45, \text{ and } 100 \text{ kHz}$$

Corresponding applied voltage:

$$V_0 = 0-900, 0-400, 0-400 V_{p-p}$$

Inside diameter of nozzle tip:

$$D_n = 0.16-0.67 \text{ mm}$$

The position of the upper surface of the particle bed charged in the glass tube (3) and rubber tube (8) changed in the range between the top and bottom of the rubber tube.

The behavior of particles near the nozzle was observed by visual observation using the naked eyes and/or a camera under the above experimental conditions. It was decided based on this observation whether or not the particles could be successfully discharged from the nozzle.

The ultrasonic power applied to the liquid in this experimental apparatus was measured under the condition of  $V_0$  and  $f$  by means of an ultrasonic sound pressure meter (SONIC SENSOR HUS-5, straight-typed probe, Honda Electronics, ibid.) using the following method. It was difficult to directly measure the ultrasonic power using the probe under the experimental conditions shown in Fig. 1. Therefore, the top cover of the rectangular vessel together with the set of parts affixed to the top cover, e.g., the glass and rubber tubes, was removed from the apparatus. The probe was inserted from the upper surface of the liquid, and the bottom of the probe was positioned at  $h=60$ mm, which corresponded to the top position of the particle collector of the glass tube (5). The indicated value of the ultrasonic sound pressure meter,  $V_{re}$  (mV), was read under the conditions of  $V_0$  and  $f$ , and was employed as a representative of ultrasonic power applied. Though the value of  $V_{re}$  doesn't present the sound pressure itself, the relative degree of ultrasonic power applied can be inferred.

## 3. Results

### 3.1. Qualitative particle discharge characteristics

Fig. 2 shows the *qualitative* discharge characteristics of particles from the nozzle obtained through a

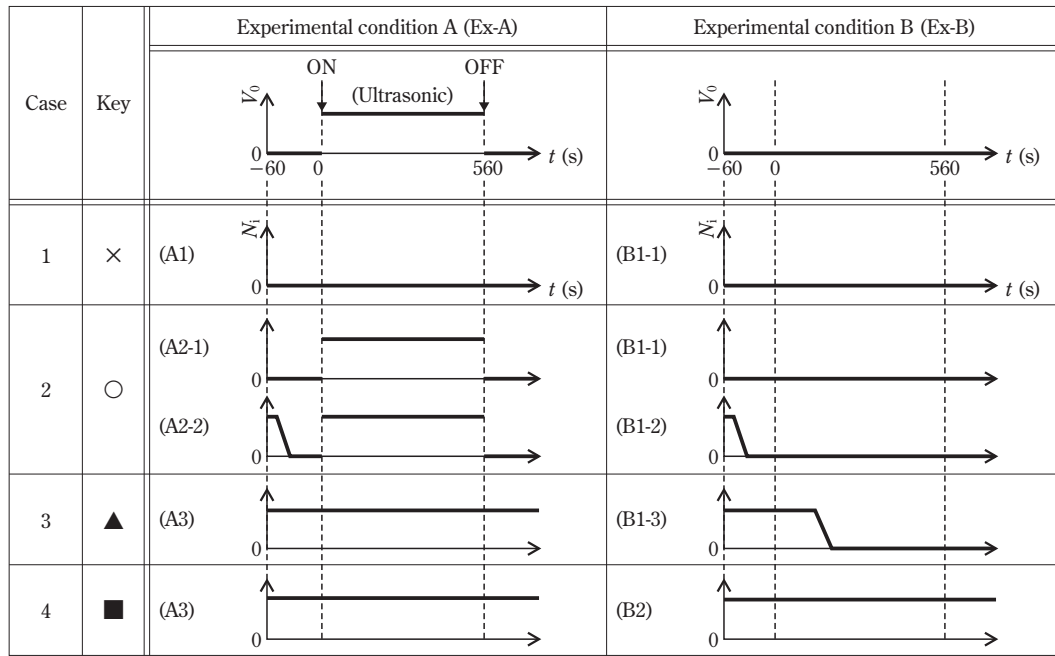


**Fig. 2** Particle discharge characteristics, Case-1 to Case-4, classified on the basis of the combination of respective  $N_i$  variations (A1-A3 vs. B1 and B2) obtained under the experimental conditions, Ex-A and Ex-B

series of observations of the particle behavior near the nozzle at  $t \geq -60$ s. When discharging and no discharging of particles could be confirmed, the corresponding values of  $N_i$  were presented in **Fig. 2** as  $N_i > 0$  and  $N_i = 0$ , respectively. Experimental conditions of A (Ex-A) and B (Ex-B) show the results obtained when ultrasonic power was applied at  $0 \leq t \leq 560$ s, and when ultrasonic power was not applied, i.e. only gravitational force was applied.

The qualitative discharge characteristics for Ex-A were classified into three cases of A1, A2, and A3, and those for Ex-B into two cases, B1 and B2, by considering  $N_i$  at  $t \geq 0$ , and  $t > 560$ s (= in a steady state). The cases in A2 were further classified into two sub-cases, A2-1 and A2-2, and those in B-1 were classified into three sub-cases, B1-1 to B1-3, based on  $N_i$  at  $t \geq -60$ s.

In this paper, the qualitative discharge characteristics were divided into 4 cases based on the combinations (A1-A3/B1, B2) of Ex-A at  $t \geq 0$  and Ex-B at  $t > 560$ s (= in a steady state): Case-1 (A1/B1), Case-2 (A2/B1), Case-3 (A3/B1), and Case-4 (A3/B2) as stated below.

- [Case-1]: no particles could be discharged from the nozzle under both conditions of Ex-A and Ex-B at  $t \geq -60$ s (A1, B1-1).
- [Case-2]: under the Ex-A conditions in the range of  $t < 0$ , no particles could be discharged (A2-1) or particles could be discharged only at  $t \approx -60$ s (A2-2);

in both cases of A2-1 and A2-2, however, particles could be discharged when the ultrasonic power was applied in the range of  $0 \leq t \leq 560$ s, while they stopped discharging after it was not applied ( $t > 560$ s).

On the other hand, under the Ex-B conditions, particles could not be discharged at  $t \geq -60$ s (B1-1), or particles could be discharged only at  $t \approx -60$ s in the range of  $t < 0$ . (B1-2)

- [Case-3]: under the Ex-A conditions, particles could always be discharged at  $t \geq -60$ s (A3); under the Ex-B conditions, particles could be discharged to the middle of  $0 \leq t \leq 560$ s, and subsequently could never be discharged (B1-3).

- [Case-4]: both under Ex-A and Ex-B conditions, particles could always be discharged at  $t \geq -60$ s (A3, B2).

**Figs. 3a** and **3b** show the qualitative discharge characteristics of spherical and irregular particles based on their corresponding cases, Case-1 to Case-4, at the oscillation frequency  $f = 25$ kHz for various particle diameters  $d_p$  and the nozzle inside diameters  $D_n$ , respectively. The discharge characteristics of particles belonging to Case-1 in the small range of  $D_n$  for any values of  $d_p$  and for both spherical and irregular particles were found to shift from Case-2 to Case-3 or Case-4 as  $D_n$  increases.

**Figs. 3c** and **3d** show the results obtained by converting  $D_n$  in the abscissa of **Figs. 3a** and **3b** into

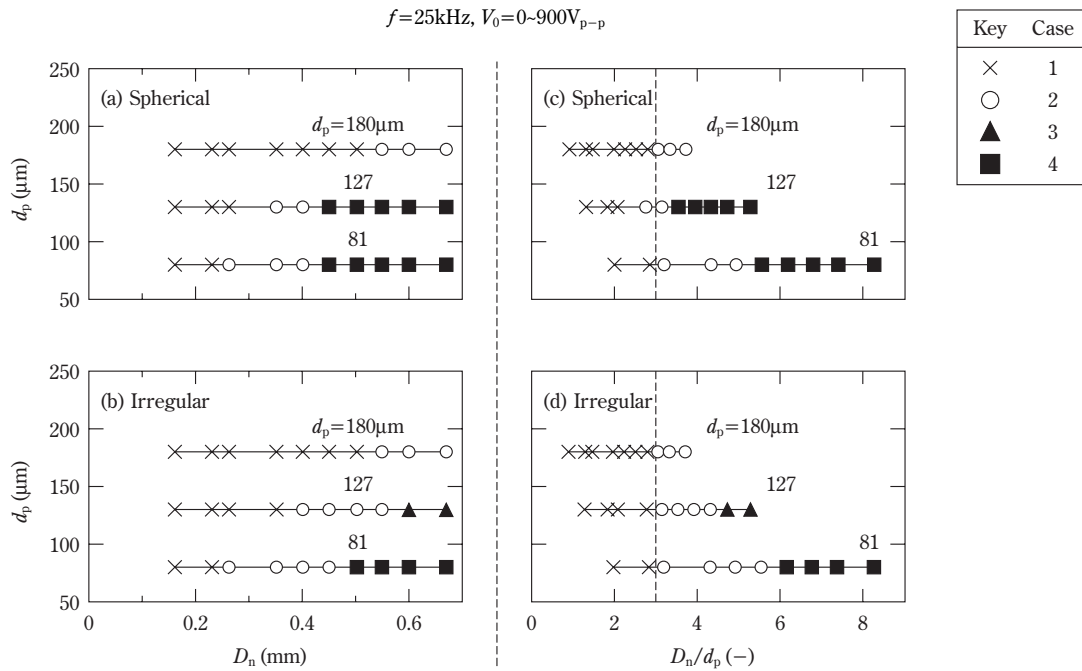


**Fig. 3** Particle discharge characteristics (Case-1 to Case-4) obtained for particle diameter  $d_p$  and nozzle inside diameter  $D_n$

$D_n/d_p$ , respectively. It was found that the boundary value of  $D_n/d_p$  between Case-1 and Case-2,  $(D_n/d_p)_c$ , was about 3.0, irrespective of  $d_p$  and the particle shape. The value of  $(D_n/d_p)_c=3.0$  obtained for the particles in the present apparatus was less than  $(D_n/d_p)_c \cong 4\sim 5$  for dry particles which were discharged in air from circular orifices under the gravitational field [3, 5]. This indicates that when  $d_p$  is constant, particles can be discharged through smaller- $D_n$  orifices under the ultrasonic field in liquid than under the gravitational field in air.

Hereafter, the experimental results are summarized only for Case-2 (A2-1, A2-2), Case-3 (A3), and Case-4 (A3, B2). In Case-2 (A2-1, A2-2), particles could be discharged by applying ultrasonic power ( $0 \leq t \leq 560\text{s}$ ), while they could not be discharged without applying it ( $t > 560\text{s}$ ), as described above. In Case-3 (A3) and Case-4 (A3, B2), particles could always be discharged both with and without ultrasonic power.

### 3.2. Effects of operating conditions on particle discharge rate

**Figs. 4a and 4b** show representative photographs taken by camera when the spherical particles, Mat-Ms, were settling through the liquid in the particle collector of the glass tube after they had been discharged from the nozzle when  $V_0=60$  and  $320V_{p-p}$ , respectively. It can be seen that the particles were dis-

charged from the nozzle somewhat intermittently, and that they tended to settle downwards while moving in the horizontal direction, and, therefore they were dis-

Mat-Ms ( $d_p=127\mu\text{m}$ , Spherical)  
 $D_n=0.40\text{mm}$ ,  $f=45\text{kHz}$ , Case-2 (Shutter speed=1/500s)

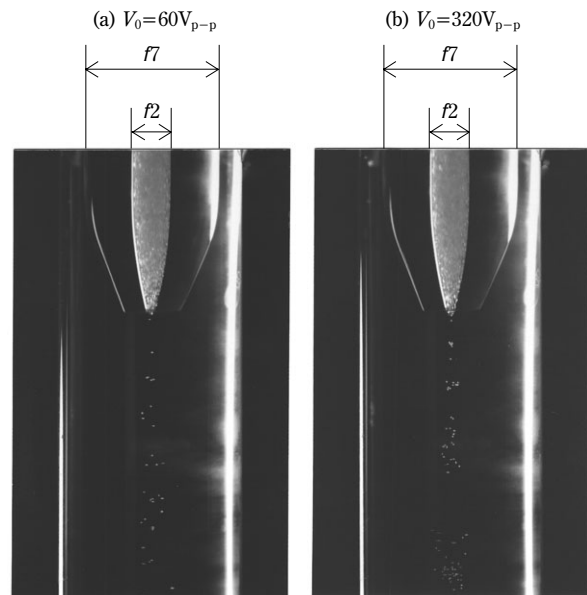


**Fig. 4** Representative photographs of particles (Mat-Ms) discharged from a nozzle in liquid with ultrasonic wave force

persed throughout a broader section of liquid. The number of particles discharged from the nozzle per unit time using the larger  $V_0$  ( $=320V_{p-p}$ ) was higher than the number discharged using the smaller one ( $=60V_{p-p}$ ) under these experimental conditions.

The behavior of particles near the inside wall of the nozzle was observed under the same conditions as in **Fig. 4**. The particles moved actively in the nozzle and were discharged from the nozzle. Consequently, the liquid under the nozzle flowed into the nozzle to replace the space of the particles higher up in the nozzle. The liquid flow resulted in the vertical circulation of particles in the nozzle.

**Fig. 5** shows the representative relationships between the particle discharge rate  $N_i$  ( $s^{-1}$ ) and the elapsed time  $t$  (s) with respect to spherical and irregular particles under two kinds of applied voltage  $V_0$ . Each broken line in **Fig. 5** show the average value of  $N_i$ , referred to as “average discharge rate  $\bar{N}$  ( $s^{-1}$ ),” which is derived using the following equation.

$$\bar{N} = \frac{1}{n} \sum_{i=1}^n N_i \quad (n=16) \quad (3)$$

The coefficient of variation  $CV$  (–) and the average mass discharge rate  $\bar{M}$  ( $kg \cdot s^{-1}$ ) in **Fig. 5**, and the

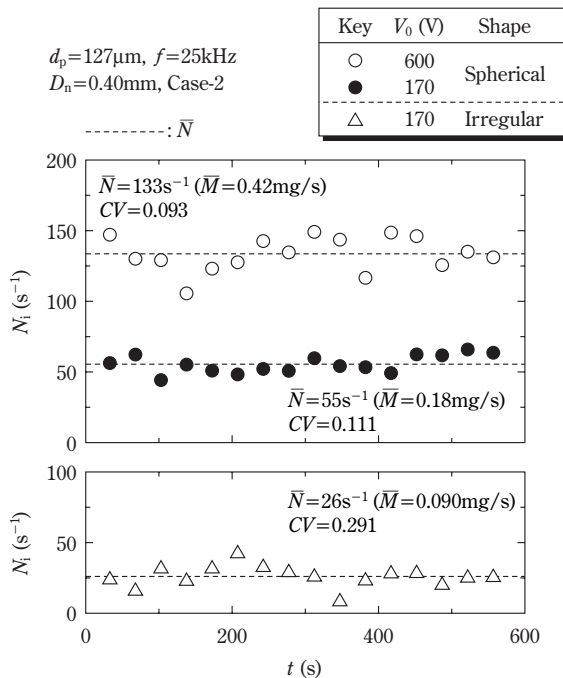


**Fig. 5** Representative results of discharge rate  $N_i$  through elapsed time  $t$

standard deviation of  $N_i$ -distribution,  $s$  ( $s^{-1}$ ), in Eq. (4), were calculated using the following equations.

$$CV = \frac{s}{\bar{N}} \quad (4)$$

$$\bar{M} = \rho_p f_v d_p^3 \bar{N} \quad (5)$$

$$s = \sqrt{\frac{1}{n-1} \sum_{i=1}^n (N_i - \bar{N})^2} \quad (n=16) \quad (6)$$

These results show that present apparatus was able to achieve a stable and continuous discharge of small amounts of particles, and that the  $\bar{N}$ -values varied for different applied voltages and particle shapes.

**Figs. 6a–6c** show the representative relationships

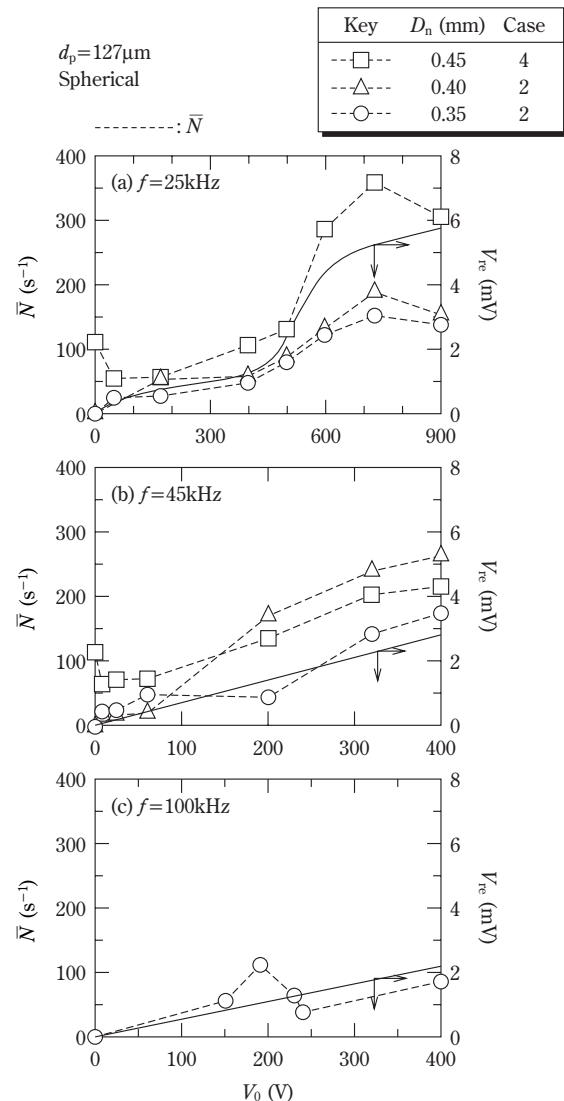


**Fig. 6** Relationships between average discharge rate  $\bar{N}$ , vs. applied voltage  $V_0$ , and calibration curves of  $V_{re}$  vs.  $V_0$  for each frequency  $f$

between the average discharge rate  $\bar{N}$  and the applied voltage  $V_0$  at frequencies of  $f=25, 45$ , and  $100\text{kHz}$ . The following tendencies can be observed. In **Fig. 6a** ( $f=25\text{kHz}$ ),  $\bar{N}$  increased with  $V_0$  in the range of  $50 \leq V_0 \leq 730V_{p-p}$ , and decreased with decreasing nozzle inside diameter  $D_n$ . In contrast, in **Fig. 6b** ( $f=45\text{kHz}$ ),  $\bar{N}$  became larger in the order of  $D_n=0.35, 0.45$ , and  $0.40\text{mm}$  at a given  $V_0$  in the range of  $V_0 \geq 200V_{p-p}$ . The relation between  $D_n$  and  $\bar{N}$  at  $f=45\text{kHz}$  differed from that at  $f=25\text{kHz}$ . In **Fig. 6c** ( $f=100\text{kHz}$ ), the relationship between  $\bar{N}$  and  $V_0$  was not linear, and the  $\bar{N}$ -values could not be controlled by  $V_0$ .

**Figs. 7a–7c** show the relations between the coefficient of variation  $CV$  and the applied voltage  $V_0$  with respect to the results in **Figs. 6a–6c**. At  $f=25\text{kHz}$  (in **Fig. 7a**), the  $CV$ -values at  $D_n=0.35\text{mm}$  were found to be larger than those at  $D_n=0.40$  and  $0.45\text{mm}$  on the whole. This indicates, for example, that the discharge of particles can be achieved more stably at  $D_n=0.40\text{mm}$  than at  $D_n=0.35\text{mm}$ . In contrast, at  $f=45\text{kHz}$  (in **Fig. 7b**), there were no significant variation in the  $CV$  among the three  $D_n$ -values when compared with  $f=25\text{kHz}$ .

As a result, it was confirmed that the effects of  $V_0$  and  $D_n$  on the discharge characteristic indices,  $\bar{N}$  or  $CV$ , depended on the frequency  $f$ . The cause of these results seems to be that the behavior of particles in the nozzle became complicated because of the simultaneous actions based on the effects of the particle dispersion by the ultrasonic force and of the liquid circulation as observed in **Fig. 4**.

Hereafter, the effects of various operating conditions on the particle discharge rates,  $\bar{N}$ , were investigated only at  $f=25\text{kHz}$  because it was considered that  $\bar{N}$  could be more easily controlled by  $V_0$  and  $D_n$  at  $f=25\text{kHz}$  than  $f=45$  or  $100\text{kHz}$ .

Each solid line in **Fig. 6** represents the calibration curve between the applied voltage  $V_0$  and the corresponding indicated value measured by the ultrasonic sound pressure meter,  $V_{re}$  (mV). It can be seen that  $V_{re}$  was proportional to  $V_0$  at  $f=45$  and  $100\text{kHz}$ , and was almost proportional to  $V_0$  at  $f=25\text{kHz}$  only in the range of  $0 \leq V_0 \leq 400V_{p-p}$ . The relations between  $\bar{N}$  and  $V_{re}$  at  $f=25\text{kHz}$  were determined based on the calibration curve in **Fig. 6a** and were used hereafter.

**Fig. 8** shows the discharge characteristics for spherical particles of  $81$  and  $127\mu\text{m}$  in particle size  $d_p$ . It can be seen in the range of smaller  $D_n$  ( $\leq 0.40\text{mm}$ : Case-2) that  $\bar{N}$  increased with  $V_{re}$  for both sizes of particles. In the range of larger  $D_n$  ( $\geq 0.50\text{mm}$ : Case-4), no obvious tendencies were found in the relation

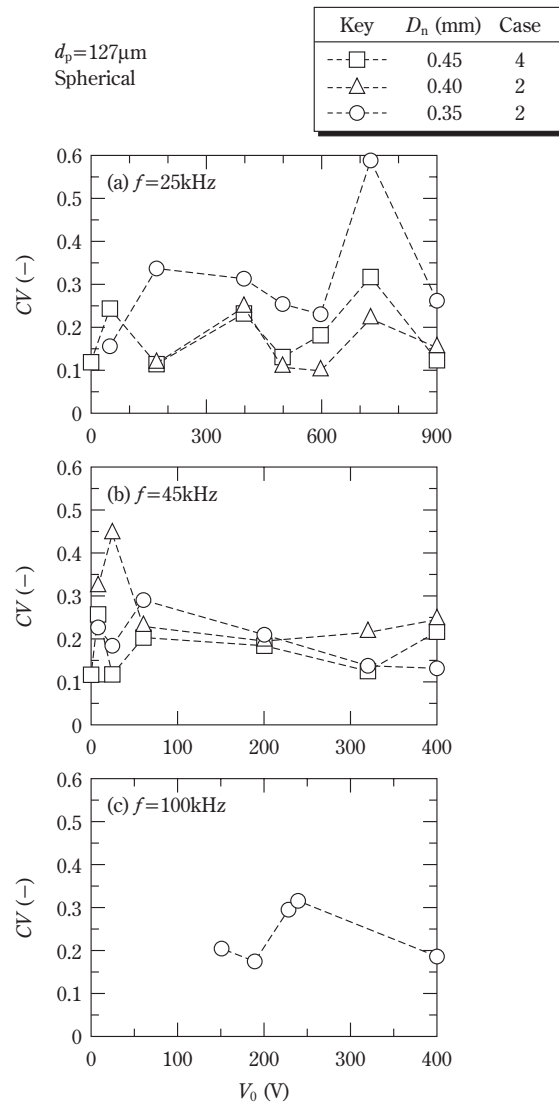


**Fig. 7** Relationships between coefficient of variation,  $CV$ , vs. applied voltage  $V_0$

between  $\bar{N}$  and  $V_{re}$ . A comparison of the results of  $D_n=0.40\text{mm}$  with these two particle sizes shows that the  $\bar{N}$ -values for  $81\mu\text{m}$ -sized particles were greater than those for  $127\mu\text{m}$ -sized ones.

**Fig. 9** represents the discharge characteristics for irregular particles. For the particles of  $d_p=81\mu\text{m}$  shown in **Fig. 9a**,  $\bar{N}$  increased along with  $V_{re}$  for the smaller  $D_n$  particles ( $\leq 0.40\text{mm}$ : Case-2). In contrast,  $\bar{N}$  decreased as  $V_{re}$  increased when  $D_n=0.55\text{mm}$  (Case-4). For the  $127\mu\text{m}$ -sized particles shown in **Fig. 9b**, the relationships of  $\bar{N}$  vs.  $V_{re}$  under the conditions of small  $D_n$  ( $\leq 0.45\text{mm}$ : Case-2) and large  $D_n$  ( $=0.67\text{mm}$ : Case-3) were similar to those for  $81\mu\text{m}$ -sized particles shown in **Fig. 9a**.

The results shown in **Figs. 8** and **9** indicate that



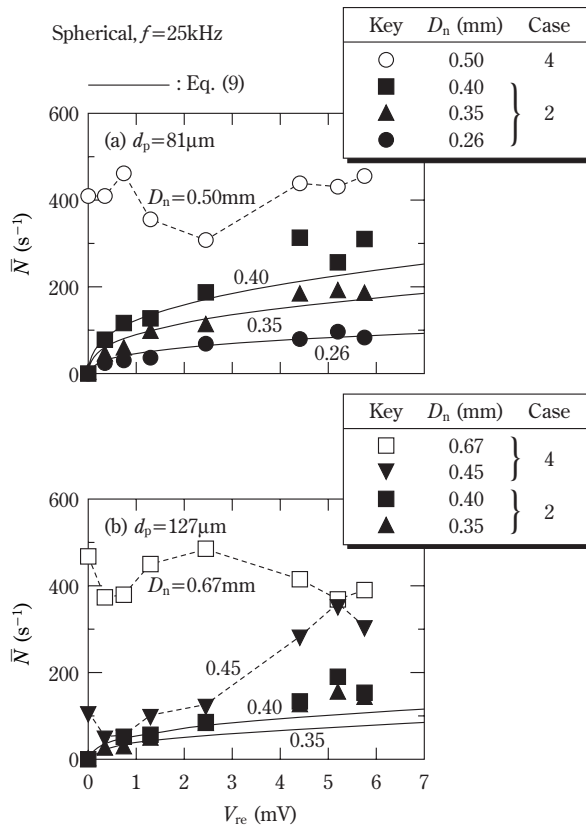


**Fig. 8** Average discharge rate of spherical particles,  $\bar{N}$ , under various operating conditions

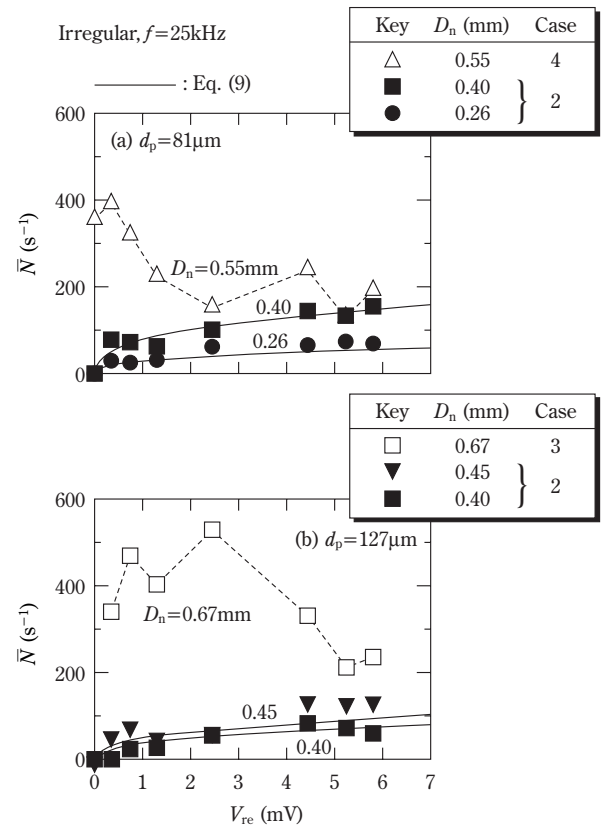


**Fig. 9** Average discharge rate of irregular particles,  $\bar{N}$ , under various operating conditions

the discharge characteristics of particles from the nozzle in the present apparatus is dependent on the strength of the ultrasonic wave force  $V_{re}$ , the particle size  $d_p$ , the nozzle inside diameter  $D_n$ , and the particle shape.

#### 4. Analysis

The effects of various factors on the average particle discharge rate  $\bar{N}$  were quantitatively investigated based on the multiple regression analysis [4] as follows. The analysis was restricted to the results of  $f=25\text{kHz}$  and Case-2 (see **Fig. 3**).

First, it was assumed that  $\bar{N}$  depends on the indicated value of the ultrasonic sound pressure meter,  $V_{re}$ , the nozzle inside diameter,  $D_n$ , the particle size  $d_p$ , and the representative value of particle shape index,  $\psi_{50}$ , and that the following equation holds true.

$$\bar{N} = a_0 V_{re}^{a_1} D_n^{a_2} d_p^{a_3} \psi_{50}^{a_4} \quad (7)$$

Taking logarithms of both sides yields the following linear equation,

$$\ln \bar{N} = \ln a_0 + a_1 \ln V_{re} + a_2 \ln D_n + a_3 \ln d_p + a_4 \ln \psi_{50} \quad (8)$$

where  $\ln a_0$  is the constant term, and  $a_1 - a_4$  are partial regression coefficients.

The values of  $\ln a_0$  and  $a_1 - a_4$  were estimated by multiple regression analysis on the basis of Eq. (8), and the following equation was obtained.

$$\bar{N} = 2.25 \times 10^6 V_{re}^{0.35} D_n^{2.29} d_p^{-1.74} \psi_{50}^{1.07} \quad (9)$$

The dimension of each variable in Eq. (9) corresponds to  $\bar{N}$  ( $\text{s}^{-1}$ ),  $V_{re}$  (mV),  $D_n$  (mm),  $d_p$  ( $\mu\text{m}$ ), and  $\psi_{50}$  (-).

**Table 2** shows the results of the above analysis in detail. Every partial- $F$  value for the corresponding partial coefficients satisfied the general criterion,  $F \geq 2.0$ . Therefore, it was statistically confirmed that the respective independent variables in Eq. (9) affected  $\bar{N}$ .

It was found that the power exponent, 2.29, of nozzle inside diameter  $D_n$  in Eq. (9) was greater than the known values of 2.5 to 3.0 [3] when dry powders were discharged from a circular orifice in air, and was

**Table 2** Results of multiple regression analysis ( $f=25\text{kHz}$ , Case-2)

	$\ln a_0$	$\ln V_{re}$	$\ln D_n$	$\ln d_p$	$\ln \psi_{50}$	Multiple correlation coefficient $R$
Partial regression coefficient, $a_1 \sim a_4$	(14.63)*	0.35	2.29	-1.74	1.07	0.828
Partial correlation coefficient, $\gamma$	—	0.71	0.70	-0.67	0.53	
Partial F-value, $F$	180.3	104.6	95.8	82.8	40.0	

\*) denotes the value of  $\ln a_0$

included in the range of 2.0 to 2.5 when dry powders were discharged from capillary tubes vibrating at high [1] or ultrasonic frequencies [2] in air.

**Fig. 10** shows the relationship between the estimated  $\bar{N}$ -values by Eq. (9),  $\bar{N}_{cal}$ , and the experimental ones,  $\bar{N}_{obs}$ . The multiple correlation coefficient  $R$  ( $=0.828$ ) was found to be comparatively large. The solid curves in **Figs. 8** and **9** present the relationships of  $\bar{N}$  vs.  $V_{re}$  as estimated by Eq. (9), and they are in agreement with the tendencies of the experimental ones.

The results estimated by Eq. (9) and the relationship between  $V_0$  and  $V_{re}$  in **Fig. 6a** (calibration curve) prove that the larger the applied voltage  $V_0$  and the nozzle inside diameter  $D_n$ , or the smaller the particle diameter  $d_p$ , the larger the average discharge rate  $\bar{N}$ . Furthermore, as the shape index  $\psi_{50}$  approaches unity, that is, as the roughness of the particle surface

declines, the  $\bar{N}$ -values increase.

Therefore, the present apparatus can be used as an effective wet microfeeder because it is possible to control the discharge rate  $\bar{N}$  for given particles of shape index  $\psi_{50}$  and size  $d_p$  by appropriate selection of the nozzle inside diameter  $D_n$  and the voltage that is applied to the ultrasonic transducers  $V_0$ .

## 5. Conclusion

A wet microfeeder that utilizes ultrasonic wave force in liquid was developed, and the discharge characteristics of small particles from a nozzle were experimentally investigated. As a result of these experiments, the following were confirmed.

(1) The critical ratio of particle blockage in the present wet microfeeder ( $(D_n/d_p)_c \doteq 3.0$ ), was smaller both for spherical and irregular particles than that previously obtained in the gravitational field for dry powders. The index  $(D_n/d_p)_c$  denotes the ratio of the nozzle inside diameter  $D_n$  to particle diameter  $d_p$  where particles begin to block up the nozzle.

(2) It was possible to continuously and stably discharge small particles of about 80 to 180  $\mu\text{m}$  in diameter using the present feeder.

(3) Multiple regression analysis at a frequency of  $f=25\text{kHz}$  proved the following facts. The average discharge rate, that is, the number of particles discharged from the nozzle per of unit time,  $\bar{N}$ , was dependent on the applied voltage to the ultrasonic transducers  $V_0$ , the nozzle inside diameter  $D_n$ , the median value of the particle shape index (surface roughness,  $\psi_{50}$ ), and the particle diameter  $d_p$ . The  $\bar{N}$ -value was proportional to  $D_n^{2.29}$ . Therefore, it was possible to control  $\bar{N}$  by adjusting the parameters  $V_0$  and  $D_n$ .

## Nomenclature

$A_p$	: area of a particle image	( $\text{m}^2$ )
$a_0$	: constant in Eq. (7)	(—)
$a_1 \sim a_4$	: partial regression coefficients defined in Eq. (8)	(—)

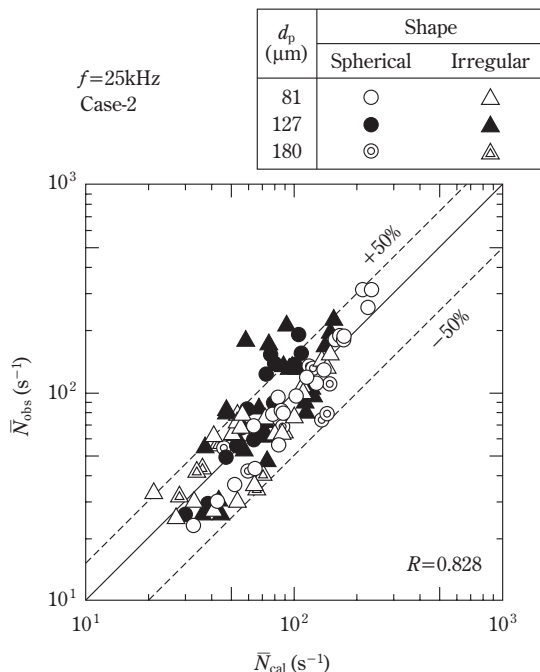


**Fig. 10** Average discharge rate ( $\bar{N}$ ) data obtained by calculation using Eq. (9) ( $\bar{N}_{cal}$ ) and experimental observation ( $\bar{N}_{obs}$ )

$CV$	: coefficient of variation (Eq. (4))	(—)	$\rho_p$	: true density of particles	( $\text{kg} \cdot \text{m}^{-3}$ )
$D_n$	: inside diameter of nozzle tip	(m)	$s$	: standard deviation of $N_i$ -distribution	(Eq. (6)) ( $\text{s}^{-1}$ )
$(D_n/d_p)_c$	: critical ratio of outlet diameter to particle diameter	(—)	$y$	: shape index defined as surface roughness (Eq. (1))	(—)
$d_p$	: average particle diameter	(m)	$y_{50}$	: median value of $y$ -distribution	(—)
$F$	: partial F-value	(—)	$f_v$	: volume shape factor (Eq. (2))	(—)
$f$	: oscillation frequency	(Hz)			
$h$	: vertical distance from the inner bottom of rectangular vessel (see Fig. 1)	(m)			
$M_v$	: mass of particles sampled for $f_v$ -measurement	(kg)			
$\bar{M}$	: mass of discharged particles per unit of time (Eq. (5))	( $\text{kg} \cdot \text{s}^{-1}$ )			
$N_i$	: discharge rate (number of discharged particles per unit of time) obtained from $i$ -sample	( $\text{s}^{-1}$ )			
$\bar{N}$	: average discharge rate (Eq. (3))	( $\text{s}^{-1}$ )			
$N_v$	: number of particles sampled for $f_v$ -measurement	(—)			
$n$	: number of samples	(—)			
$p$	: perimeter of a particle image	(m)			
$R$	: multiple correlation coefficient	(—)			
$t$	: elapsed time	(s)			
$V_0$	: voltage applied to ultrasonic transducer (peak to peak value)	(V)			
$V_{re}$	: indicated value of ultrasonic sound pressure meter	(mV)			
$\gamma$	: partial correlation coefficient	(—)			

## References

- 1) Matsusaka, S., K. Yamamoto and H. Masuda: "Micro Feeding of a Fine Powder Using a Vibrating Capillary Tube", *J. Soc. Powder Technol., Japan*, **32**, 83-88 (1995)
- 2) Matsusaka, S., U. Urakawa, M. Furutate and H. Masuda: "Micro-feeding of Fine Powders Using a Capillary Tube with Ultrasonic Vibration", Proc. of World Cong. on Particle Technol. 3, Paper No.343, CD-ROM Record No.25773-25861, Brighton (1998)
- 3) Miwa, S.: "Funtai Kougaku Tsuuron", pp.124-129, Nikkan Kogyo (1981)
- 4) Miyajima, T., K. Yamamoto and M. Sugimoto: "Effect of Particle Shape on Packing Properties during Tapping", *J. Soc. Powder Technol., Japan*, **37**, 10-18 (2000)
- 5) Soc. of Powder Technol., Japan: "Terminology Dictionary of Powder Technology", 2nd ed., p.325, Nikkan Kogyo (2000)
- 6) Yamamoto, K., N. Shimizu, M. Sugimoto and Y. Matsuoka: "Separation Characteristics of a Wet Shape Separator Developed for Fine Particles", *J. Soc. Powder Technol., Japan*, **35**, 630-638 (1998)

## Author's short biography



### Kenichi Yamamoto

Dr. Kenichi Yamamoto worked as an Associate Professor of the Department of Material Systems Engineering and Life Science at Toyama University from 1997 through 2002, and he has been a Professor at the same institution since 2002. He received his doctorate degree in 1994 from Osaka Prefecture University. His main fields of research are particle shape analysis, shape separation, solid mixing, and segregation. His current research activities are focused on the development of equipment such as a wet shape separator, a microfeeder, a useful resource separator, and a 3-D particle shape analyzer.



### Mitsue Shiokari

Mitsue Shiokari received her BE and ME degrees from the Department of Materials Science and Engineering at Toyama University in 2001. After graduating, she began working at Sugino Machine Limited as a research and design engineer. Her main interest is the research and development of machines for particle micronization.

## Author's short biography



### **Toshiaki Miyajima**

Dr. Toshiaki Miyajima has been working at the Department of Material Systems Engineering and Life Science at Toyama University since 1994, as a Research Assistant under the direction of Prof. M. Sugimoto and Prof. K. Yamamoto. He received his doctorate degree in 2002 from Toyama University. His main interests are particle shape analysis, particle shape characterization, and studying the effects that the shape of particles has on their behavior.



### **Masateru Kawamura**

Masateru Kawamura received his BE and ME degrees from the Department of Materials Science and Engineering at Toyama University in 1999. After graduating, he began working at Brother Industries, Ltd. as a research engineer. His main interest is the research and development of toner for laser beam printers.



### **Masunori Sugimoto**

Dr. Masunori Sugimoto was previously a Professor of the Chemical Engineering Department (1979-1990), and of the Materials Science and Engineering Department (1990-2002) at Toyama University. He received his doctorate degree in 1971 from Nagoya University. He is currently a Professor Emeritus at Toyama University. His major research interests are solid mixing and segregation, particle shape characterization and separation, and particle design with granulation. His current research activities are focused on the development of a continuous granulation process by simultaneous operation of granulation, grinding, and separation using the segregation behavior of particles passing through a rotating vessel, and the formation of small composite granules.

# Sintering Mechanism of Two Spheres Forming a Homogeneous Solid Solubility Neck<sup>†</sup>

Atsuko Shimosaka, Yasushi Ueda,  
Yoshiyuki Shirakawa and Jusuke Hidaka  
Department of Chemical Engineering and  
Materials Science, Doshisha University\*

## Abstract

*A simulation method for initial-stage sintering was proposed to understand the effect of sintering conditions on the sintering behavior of two particles of different sizes and compositions. This study employed a homogeneous solid solubility system of Cu-Ni. The sintering experiments were performed with two spherical Cu-Ni particles in contact, and the sintered particles were observed by SEM and EDX. It was confirmed that the sintered particles always form a curved neck and copper was the dominant component in the neck.*

*The proposed simulation method, in which the model for two particles of identical composition was modified, involves several mass transport mechanisms: surface diffusion, volume diffusion, grain-boundary diffusion, evaporation-condensation and, newly, grain growth. The sintering behavior of Cu-Ni particles was simulated using the proposed method and the results were highly similar to the experimental results. It was also found that grain growth was not negligible in initial-stage sintering, and that shrinkage and grain growth responded sensitively to sintering conditions. Consequently, by analysis of these simulation results, it is possible to understand the mechanism of sintering two spherical particles of different compositions and to determine the optimum sintering conditions.*

**Key words:** neck growth rate, grain growth, initial-stage, solid solution

## Introduction

Ceramics are in a certain sense composite materials comprised of grains, grain boundaries, and pores. Their functions are essentially governed not only by the characteristics of their constituents but also by their microstructure. To obtain a ceramic material that has the intended dynamic characteristics or energy conversion characteristics, it is therefore necessary to finely control the microstructure of the material. In a ceramic manufacturing process, the principal processes that create and develop the microstructure in the ceramic are the forming process and the sintering process. In the sintering

process, a series of phenomena occur which include the development of grains and grain boundaries, as well as the shrinking of pores; therefore, it has been a critical challenge to establish control technology that reliably achieves the targeted ceramic microstructure. However, the sintering process involves a large number of complicated parameters that mutually influence one another, such as the characteristics of the initial powder materials, the characteristics of the molding, the temperature field in the oven, and the sintering conditions. Therefore, it is not easy to determine the interrelationship between the microstructure formation behavior and the many associated parameters through experimentation. However, the progress in computer engineering in recent years has enabled simulation-based approaches to the aforementioned complicated phenomenon, and this has contributed to enhanced feasibility for engineering analysis of the sintering process.

\* Kyotanabe 610-0321

Tel: 0774-65-6648, e-mail: ashimosa@mail.doshisha.ac.jp

<sup>†</sup> Accepted:



To probe the feasibility of engineering analysis, the authors first simulated the neck growth behavior with two spherical grains having an identical composition, in the initial sintering stage, which is the elementary process of sintering. In this way, the authors clarified the interrelationship between the composite sintering behavior and sintering conditions where the surface diffusion, volume diffusion, grain boundary diffusion, and evaporation and condensation mechanisms are simultaneously involved (Shimosaka *et al.*, 1995). In a sintering process, two grain types of an identical composition are rarely used; usually, each of the two grain types used has a unique composition. The results from experimental studies on the sintering behavior with substances of dissimilar compositions have already been reported by W. A. Kaysser, F. J. Puckert, and others (Kaysser *et al.*, 1982, Puckert *et al.*, 1983). However, these studies lack evaluation of sintering speeds. The sintering behaviors of two sphere types having dissimilar compositions can vary depending on the solid solution formation status specific to each substance as well as the sintering conditions (Ueda *et al.*, 1996), and the two typical cases described below are observed: (1) the homogeneous solid solution type in which the sintering process progresses while a neck having a curvature is always being formed; and (2) the eutectic reaction type that is characterized by the two components having an identical eutectic point, and in which the sintering process progresses without the formation of a clearly defined neck at a temperature well below the eutectic point and that the sintering process develops at a temperature in the vicinity of and above the eutectic point with the formation of a neck having a curvature.

In this research, the authors focused their efforts on the system (1) above where a homogeneous solution is formed on the neck, and propose a novel simulation model that is an improvement over the previously reported simulation method for two spherical grains having an identical composition. Next, the authors studied the interrelationship between the simulation results and actual sintering behavior to clarify the effects of grain characteristics and sintering conditions on sintering behavior.

### 1. Simulation Method for Homogeneous Solid Solution Type Two-Sphere Sintering Process

As shown in the phase diagram (The Japan Institute of Metals ed.; 1993) in **Fig. 1**, over the entire range of compositions, the Cu-Ni two-sphere system forms a solid solution in which two dissimilar sub-

stances mutually dissolve into one another, and when subjected to a sintering process, the neck is formed between two dissimilar grains as illustrated in **Fig. 2**. This neck portion is Cu-rich as illustrated in the EDX analysis results in **Fig. 3**. For the previously mentioned simulation method for sintering two spherical grains having a common composition, the authors assumed that there is no mass transfer across the grain boundary across two spheres made of a common substance and therefore set the grain boundary

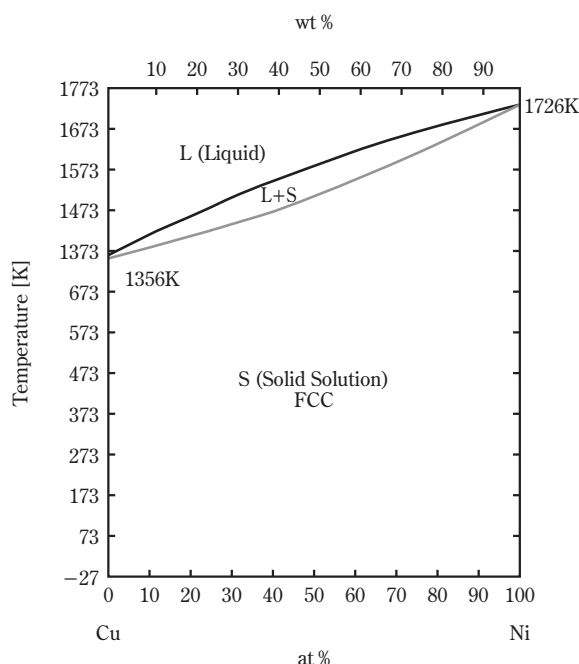


**Fig. 1** Phase diagram

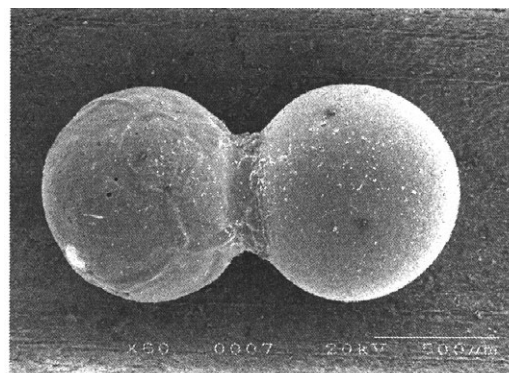


**Fig. 2** SEM photographs, Left-Cu, Right-Ni (Heating rate=300K/h, sintering temperature=1313K, isothermal sintering time =600min)

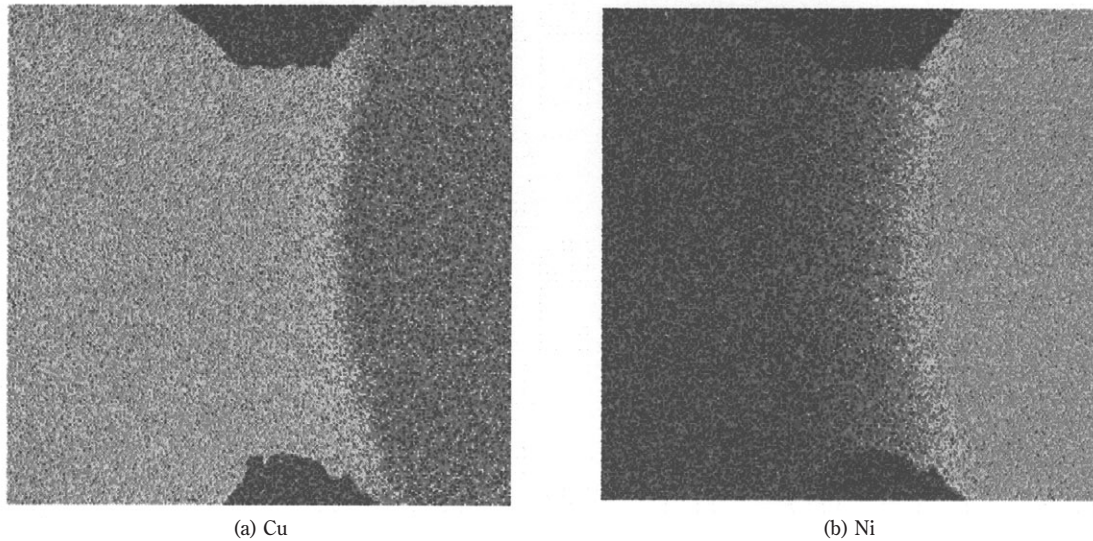


**Fig. 3** EDX analysis in the case of Fig. 2(b)

at the middle of the neck. In contrast, as can be understood from the EDX photos, the grain boundary in the Cu-Ni two-sphere system that forms a solid solution has a curvature and at the same time, the demarcation between Cu and Ni is not clear. For this reason, the authors made an arrangement in which the grain boundary at the middle of neck was removed to allow the substances from both spheres to transfer to the neck to form a solid solution. Next, the authors categorized the transfer of a plurality of substances that occurs in a sintering process into the adhesion process that does not involve sintering-triggered shrinkage and the densification process that involves shrinkage. Incidentally, if the difference in surface energy between two grains is large, mass transfer will occur, leading to the so-called “grain growth”. Thus, the authors propose a novel simulation method for homogeneous solid solution type two-sphere sintering behavior that incorporates the consideration for grain growth.

### 1.1 Adhesion Process

The authors focused their attention on the spherical grains 1 and 2 illustrated in **Fig. 4(a)**. In a system having a neck of a smaller curvature, and if the neck of an extremely high vacancy concentration and the grain surface of a lower concentration are present, a substance transfers along the vacancy concentration gradient on the path between the neck and the grain surface. In other words, the substance transfers from the grain surface to the neck, and, at the same time, the vacancy diffuses from the neck to the grain sur-

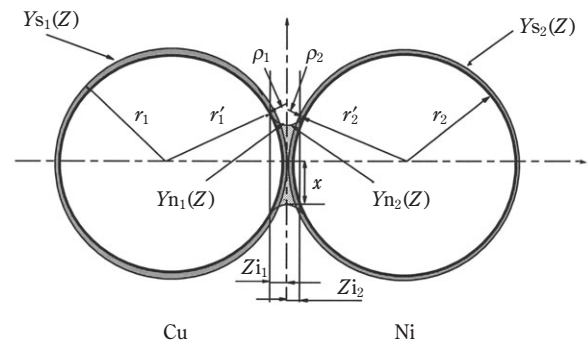


**Fig. 4(a)** Model of adhesion

face and dissipates. During this process, because the substance does not flow out from the contact area between the grains, the center-to-center dimension on the two grains does not change and no shrinkage takes place. This process that does not lead to shrinkage is regarded as the adhesion process. As a result of this process, the grain radii decrease from  $r_1$  to  $r'_1$  and from  $r_2$  to  $r'_2$ , respectively. The change in the volume of grains is retained as the increase in the volume of neck. Therefore, the following equation holds:

$$\begin{aligned} \frac{4}{3}\pi r_1^3 + \frac{4}{3}\pi r_2^3 &= \frac{4}{3}\pi r_1'^3 + \frac{4}{3}\pi r_2'^3 + \int_0^{Z_{i1}} \pi Y_{n1}^2(Z) dZ \\ &+ \int_0^{Z_{i2}} \pi Y_{n2}^2(Z) dZ - \int_{r_1-r'_1}^{Z_{i1}} \pi Y_{s1}^2(Z) dZ - \int_{r_2-r'_2}^{Z_{i2}} \pi Y_{s2}^2(Z) dZ \end{aligned} \quad (1)$$

Wherein the curved portion of radius of curvature  $\rho$  is the neck,  $Yn$  represents the curve of neck,  $Ys$  the curve of grain,  $Z_i$  is the distance from the center of two grains to a point of contact between the neck and grain surface, and the subscripts 1 and 2 represent the grain identification numbers. From the conditions according to which the neck surface smoothly comes into contact with the grain surface, the following equation is valid:

$$\frac{Z_{i1}}{r_1} = \frac{r_1}{r'_1 + r_1} \quad (2)$$

$$Yn_1(Z_{i1}) = Ys_1(Z_{i1}) \quad (3)$$

$$\frac{Z_{i2}}{r_2} = \frac{r_2}{r'_2 + r_2} \quad (4)$$

$$Yn_2(Z_{i2}) = Ys_2(Z_{i2}) \quad (5)$$

The unknowns  $\rho_1$ ,  $\rho_2$ ,  $Z_{i1}$ , and  $Z_{i2}$  in the equations above can be expressed by the following equations using the decreased grain radii  $r'_1$  and  $r'_2$ , and the corresponding neck radius  $x$ :

$$r_1 = \frac{r_1'^2 + x^2 - r_1'^2}{2(r'_1 - x)} \quad (6)$$

$$r_2 = \frac{r_2'^2 + x^2 - r_2'^2}{2(r'_2 - x)} \quad (7)$$

$$Z_{i1} = \frac{r_1(r_1'^2 + x^2 - r_1'^2)}{(r'_1 - x)^2 + r_1'^2} \quad (8)$$

$$Z_{i2} = \frac{r_2(r_2'^2 + x^2 - r_2'^2)}{(r'_2 - x)^2 + r_2'^2} \quad (9)$$

Now, the decreased grain radii  $r'_1$  and  $r'_2$  have to be determined with the volume retention equation (Eq. (1)). Since there are two unknowns, an approximation calculation is performed, that is, a value one step before is assigned to the decreased grain radii  $r'_2$ , and then  $r'_1$  is determined by a dichotomy. Then using the so-obtained  $r'_1$ ,  $r'_2$  is also determined by a dichotomy. Incidentally, the surface area of neck  $S_n$  is determined by the following equation:

$$S_n = \int_0^{Z_{i1}} 2\pi Yn_1(Z) \sqrt{1 + \left(\frac{dYn_1(Z)}{dZ}\right)^2} dZ + \int_0^{Z_{i2}} 2\pi Yn_2(Z) \sqrt{1 + \left(\frac{dYn_2(Z)}{dZ}\right)^2} dZ \quad (10)$$

Additionally, the increase in neck volume  $dVna/dx$  is determined by differentiating with the neck radius, the  $Vna$  that is defined by the third through sixth

terms in the right-hand member in Eq. (1) as well as by using a dichotomy that is based on the volume retention relation (Shimosaka *et al.*, 1995).

The mass transfer mechanism involved in the adhesion process consists of three mechanisms, that is, the surface diffusion from the grain surface to the neck, the volume diffusion from the vicinity of grain surface to the neck, and the evaporation from the grain surface and the condensation on the neck. To evaluate the neck growth in these modes, the equation of Kuczynski (Kuczynski, 1949) is modified for evaluation of the surface diffusion mechanism and the volume diffusion mechanism, and the equation of Kingery and Berg (Kingery and Berg, 1955) is modified for evaluation of evaporation to develop the following neck growth equations that can be applied to two spherical grains of different diameters:

$$\dot{x}_a = \dot{x}_{SS} + \dot{x}_{SV} + \dot{x}_{SE} \quad (11)$$

$$\dot{x}_{SS} = D_S \left( \frac{1}{r_1} + \frac{1}{r_2} - \frac{2}{x} + \frac{1}{r_1} + \frac{1}{r_2} \right) \left\{ \frac{2\pi\gamma s \delta^3 \delta_s}{(r_1 + r_2) k T \frac{dVna}{dx}} \right\} \quad (12)$$

$$\dot{x}_{SV} = D_V \left( \frac{1}{r_1} + \frac{1}{r_2} - \frac{2}{x} + \frac{1}{r_1} + \frac{1}{r_2} \right) \left\{ \frac{\gamma s \delta^3 S_n}{(r_1 + r_2) k T \frac{dVna}{dx}} \right\} \quad (13)$$

$$\dot{x}_{SE} = (P_{01} + P_{02}) \left( \frac{1}{r_1} + \frac{1}{r_2} - \frac{2}{x} + \frac{1}{r_1} + \frac{1}{r_2} \right) \left\{ \frac{\gamma s \delta^3 S_n \sqrt{M}}{(r_{p1} + r_{p2}) k T \sqrt{2\pi R T} \frac{dVna}{dx}} \right\} \quad (14)$$

The first subscript to  $\dot{x}$  represents the site of vacancy dissipation (S: surface), the second subscript stands for the type of mass transfer mechanism (S: surface diffusion, V: volume diffusion, E: evaporation & condensation),  $k$  is a Boltzman's constant,  $R$  is a gas constant, and  $T$  is a sintering temperature in the absolute temperature scale. Also,  $D_S$  means a surface diffusion coefficient;  $D_V$  a volume diffusion coefficient;  $P_0$  a vapor pressure;  $\gamma s$  a surface energy;  $d$  an interatomic distance;  $\delta_s$  a thickness of the region of enhanced diffusion at the surface;  $M$  a molecular weight;  $\rho_p$  a density of grain. Since the neck portion is in the form of a solid solution, the values of diffusion coefficients and surface energy were calculated from time to time in accordance with the concentration of each component (Kananovskii *et al.*, 1975). The neck growth speed in the adhesion process can be determined by substituting the so-determined values in the neck growth

speed equations Eqs. (11) through (14).

## 1.2 Densification Process

A substance is transferred along the vacancy concentration gradient from the neck (having a higher vacancy concentration) to the boundary and inside of grain (having a lower vacancy concentration). In other words, a substance migrates from the grain-to-grain contact area and inside the grains to the neck surface, and the vacancy diffuses from the neck surface to the grain-to-grain contact area and dissipates. As a result, the center-to-center dimension of the two grains decreases and shrinkage occurs (**Fig. 4(b)**). This shrinking phenomenon is referred to as the densification process. The change in the volume of grains is retained as the increase in the volume of the neck. Therefore, the following equation holds:

$$\frac{4}{3}\pi r_1^3 + \frac{4}{3}\pi r_2^3 = \frac{4}{3}\pi r_1'^3 + \frac{4}{3}\pi r_2'^3 + \int_0^{Z_{i1}} \pi Y n_1^2(Z) dZ + \int_{Z_{i1}}^{2r_1-\Delta L_1} \pi Y s_1^2(Z) dZ - \int_0^{Z_{i2}} \pi Y n_2^2(Z) dZ - \int_{Z_{i2}}^{2r_2-\Delta L_2} \pi Y s_2^2(Z) dZ \quad (15)$$

Additionally, as in the case of the adhesion process, the relation expressed by the following equations exists:

$$\frac{Z_{i1}}{r_1} = \frac{r_1 - \Delta L_1}{r_1 + r_1} \quad (16)$$

$$Y n_1(Z_{i1}) = Y s_1(Z_{i1}) \quad (17)$$

$$\frac{Z_{i2}}{r_2} = \frac{r_2 - \Delta L_2}{r_2 + r_2} \quad (18)$$

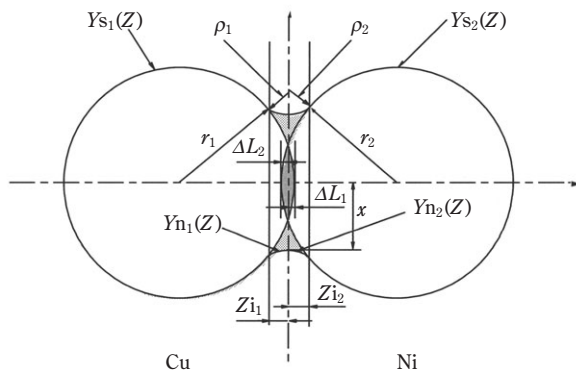


**Fig. 4(b)** Model of densification

$$Y n_2(Z_{i2}) = Y s_2(Z_{i2}) \quad (19)$$

The unknowns  $\rho_1$ ,  $\rho_2$ ,  $Z_{i1}$ , and  $Z_{i2}$  in the equations above can be expressed by the following equations as the function of the decrease in center-to-center dimension between two grains  $\Delta L_1$  and  $\Delta L_2$  and the corresponding neck radius:

$$r_1 = \frac{x^2 + \Delta L_1^2 - 2r_1'\Delta L_1}{2(r_1' - x)} \quad (20)$$

$$r_2 = \frac{x^2 + \Delta L_2^2 - 2r_2'\Delta L_2}{2(r_2' - x)} \quad (21)$$

$$Z_{i1} = \frac{(r_1' - \Delta L_1)(x^2 + \Delta L_1^2 - 2r_1'\Delta L_1)}{(\Delta L_1 - r_1')^2 + (r_1 - x)^2} \quad (22)$$

$$Z_{i2} = \frac{(r_2' - \Delta L_2)(x^2 + \Delta L_2^2 - 2r_2'\Delta L_2)}{(\Delta L_2 - r_2')^2 + (r_2 - x)^2} \quad (23)$$

The  $\Delta L_1$  and  $\Delta L_2$  in these equations can be determined by a dichotomy with Eq. (15). That is, in a manner identical to a one used to determine  $r_1'$  and  $r_2'$ , a value one step before is assigned to  $\Delta L_2$  to determine  $\Delta L_1$ , and then  $\Delta L_2$  is determined using the so-obtained  $\Delta L_1$ . Next, the increase in neck volume  $dV_{nd}/dx$  resulting from the densification process is determined by the previously mentioned method.

The mass transfer mechanism involved in the densification process consists of two mechanisms, that is, the grain boundary diffusion and the volume diffusion from the grain boundary to the neck surface. To evaluate the phenomenon resulting from these mechanisms, the equation of Johnson (Johnson, 1968) is modified to develop the following equations:

$$\dot{x}_d = \dot{x}_{GG} + \dot{x}_{GV} \quad (24)$$

$$\dot{x}_{GG} = 4D_B(x + r_1 + r_2) \left\{ \frac{\pi \gamma s \delta^3 \delta_B}{(r_1 + r_2) x k T \frac{dV_{nd}}{dx}} \right\} \quad (25)$$

$$\dot{x}_{GV} = 2D_V(x + r_1 + r_2) \left\{ \frac{\pi \gamma s \delta^3}{(r_1 + r_2) k T \frac{dV_{nd}}{dx}} \right\} \quad (26)$$

The first subscript to  $\dot{x}$  represents the site of vacancy dissipation (G: grain boundary), the second subscript stands for the type of mass transfer mechanism (G: grain boundary diffusion, V: volume diffusion),  $D_B$  and  $D_V$  respectively represent the grain boundary diffusion coefficient and the thickness of the region of enhanced diffusion at the grain-boundary. The neck growth speed in the densification process can be







$$\left(\frac{a_z}{\lambda_z}\right) = \frac{\int^{Particle1} dv}{\int^{Particle1} \frac{\lambda_z}{a_m(Z)} dv} = \frac{16\pi r_1}{R_{r1}^2 \{f(H_1) + f(Zi_1)\}} \quad (32)$$

$$f(H_1) = \frac{4^3 \sqrt{1-H_1} + 6H_1^2 \sqrt{1-H_1^2} + 6H_1 \sin^{-1} H_1 + 3\pi H_1}{\sqrt{1-H_1^2}} \quad (33)$$

$$f(Zi_1) = \pi(2r_1^2 + 2r_1 x + x^2 - 2r_1'' \Delta L_1 + \Delta L_1^2) Zi_1 - \pi(r_1'' - \Delta L_1) Zi_1^2 - \pi(r_1 + x) \{Zi_1 \sqrt{r_1^2 - Zi_1^2} + r_1^2 \sin^{-1}(Zi_1/r_1)\} \quad (34)$$

The transfer speed of substance  $dv_1/dt$  subjected to the above-mentioned grain growth model is defined as:

$$\frac{dv_1}{dt} = 4\pi r_1^2 \frac{dr_1}{dt} \quad (35)$$

Based on Eqs. (31) through (35), the grain growth rate  $dr_1''/dt$  is defined as follows:

$$\frac{dr_1''}{dt} = \frac{4D_{GG1}r_1}{r_1'^2 R_{r1}^2 \{f(H_1) + f(Zi_1)\}} \left( -\frac{\Delta G_g}{RT} \right) \quad (36)$$

Likewise, the growth rate of Ni grain is defined as follows:

$$\frac{dr_2''}{dt} = \frac{4D_{GG2}r_2}{r_2'^2 R_{r2}^2 f(H_2)} \left( -\frac{\Delta G_g}{RT} \right) \quad (37)$$

In these equations, it is assumed that  $R_{r2} = r_2''/r_2$  and  $H_2 = (r_2'' - \Delta L_2)/r_2''$ . Since being a diffusion coefficient for a grain growth process, the effective diffusion coefficient  $D_Z$  is superseded with the grain growth diffusion efficient  $D_{GG}$ . Since Cu and Ni are mutually diffused in the grain boundary area, the self-diffusion coefficient in **Table 1** (The Japan Institute of Metals ed.; 1993) is used as the  $D_{GG}$ .

**Table 1** Data for diffusion in pure metals

Solvent	Solute	$D_0$ [m <sup>2</sup> /s]	$Q$ [kJ/mol]
Cu	Ni	$2.70 \times 10^{-4}$	236
Ni	Cu	$5.70 \times 10^{-5}$	256

### [Calculation for simulation]

In the actual sintering operation, three processes – adhesion, densification and grain growth – simultaneously take place. Accordingly, in the authors' simu-

lation, the calculation for these three processes is performed as described below. First, the constants and sintering conditions are set up, and then the diffusion coefficient used for simulation of each process is determined by the equation below:

$$D = D_0 \exp(-Q/RT) \quad (38)$$

Wherein  $Q$  stands for the activation energy of self-diffusion and  $D_0$  represents the frequency factor.

However, the sequence in procedure may vary as needed. For example, first the above-mentioned neck growth rate  $\dot{x}_a$  in the adhesion process is determined, and then the neck radius  $x_a(i+1)$  in the adhesion process in the time span of  $t = t + \Delta t$  is calculated using a discrete time  $\Delta t = 1 \times 10^{-8}$ s:

$$x_a(i+1) = x_a(i) + \dot{x}_a \Delta t \quad (39)$$

Then, the so-obtained neck radius value  $x_a(i+1)$  as well as the grain radii  $r_1'$  and  $r_2'$  are used for the calculation for the densification process to determine the neck radius at the time  $t$  in the adhesion process:

$$x_d(i+1) = x_a(i+1) + \dot{x}_d \Delta t \quad (40)$$

Next, using the so-obtained  $r_1'$ ,  $r_2'$  and  $x_d(i+1)$ , the grain radii that vary during the grain growth process are calculated from the grain growth rate  $\dot{r}$  at the time  $t$ :

$$r_1''(i+1) = r_1' + \dot{r}_1 \Delta t \quad (41)$$

$$r_2''(i+1) = r_2' + \dot{r}_2 \Delta t \quad (42)$$

The so-determined neck radius and grain radii are taken as the neck radius  $x_a(i)$  and grain radii  $r_1(i)$  and  $r_2(i)$  for the adhesion process in the next step ( $i = i+1$ ). By repeating the above-mentioned calculation at intervals of  $\Delta t$ , the time-dependent change of the neck growth and grain shape during the two-sphere sintering process can be calculated. Incidentally, a value  $10^{-4}$  as large as the grain radius was used as the initial value for neck radius, and the discrete time was allowed to vary in accordance with the neck growth time (sintering time) to enable simulation for a long time period. As mentioned above, since the authors' simulation method is based on the consecutive calculation operation at intervals of  $\Delta t$ , it is possible to estimate the sintering behavior for the entire sintering process including the heating period, isothermal period, and cooling-off period that match the test conditions. The constants (Ashby, 1974; Wazzan, 1965) and conditions used for the simulation are listed in **Table 2**.

**Table 2** Physical constants, coefficients of sintering materials, and simulation conditions

	(Cu)	(Ni)	
Frequency factor, surface diffusion	$D_{0S}$	$2.0$	$3.0 \times 10^{-3}$ [m <sup>2</sup> /s]
Activation energy, surface diffusion	$Q_S$	$205$	[kJ/mol]
Frequency factor, volume diffusion	$D_{0V}$	$7.8 \times 10^{-5}$	$1.27 \times 10^{-4}$ [m <sup>2</sup> /s]
Activation energy, volume diffusion	$Q_V$	$211$	[kJ/mol]
Frequency factor, grain boundary diffusion	$D_{0B}$	$1.0 \times 10^{-5}$	$1.75 \times 10^{-6}$ [m <sup>2</sup> /s]
Activation energy, grain boundary diffusion	$Q_B$	$105$	[kJ/mol]
Frequency factor, grain growth	$D_{0GG}$	$5.70 \times 10^{-5}$	$2.7 \times 10^{-4}$ [m <sup>2</sup> /s]
Activation energy, grain growth	$Q_{GG}$	$258$	[kJ/mol]
Vaporization	$P_0$	$1.214 \times 10^6$	$1.214 \times 10^6$ [Pa]
Activation energy, vaporization	$Q_P$	$324$	[kJ/mol]
Surface energy	$\gamma_S$	$1.72$	[J/m <sup>2</sup> ]
Grain boundary energy	$\gamma_{gb}$	$0.325$	[J/m <sup>2</sup> ]
Atomic diameter	$\delta$	$2.48 \times 10^{-10}$	$2.491 \times 10^{-10}$ [m <sup>3</sup> ]
Density	$\rho_P$	$8.96 \times 10^3$	$8.845 \times 10^3$ [kg/m <sup>3</sup> ]
Molecular volume	$\zeta_M$	$7.1036 \times 10^{-6}$	$7.10 \times 10^{-5}$ [m <sup>3</sup> /mol]
Thickness of the region of enhanced diffusion at the grain boundary	$\delta_B$	$5.12 \times 10^{-10}$	$5.78 \times 10^{-10}$ [m]

## 2. Experimental Equipment and Methodology

The fine powders used as samples were Cu and Ni powders (each featuring purity of 99.999% or higher) whose grain diameter was adjusted to a range of 850 to 710  $\mu\text{m}$ . A 1000  $\mu\text{m}$  wide slot was formed on a stainless steel plate (SUS 304) that was used as a sintering stage, and Cu grains and Ni grains were alternately placed in a single line within this slot to bring Cu grains in contact with Ni grains. The sample grains were sintered in an Ar atmosphere at a predetermined heating rate (200 to 600 K/h) and a sintering temperature (1308, 1313, 1338K) for an isothermal period (1 to 1000 min), and then allowed to cool in an air atmosphere.

An entire image, including the two sintered grains as well as the neck formed between the grains, was photographed with a scanning electron microscope (SEM), and then the diameters of the sintered grains and neck were measured. The form of the sample grains used was not a true sphere. Therefore, the grain diameter was determined as follows. First, the photographic image obtained with the SEM was transferred to a computer, and the coordinates on the contours around the grain-to-grain contact area were read using image analysis software (NIH Image 1.55 (fpu)). Next, based on the resultant coordinates, a circle was drawn, and the diameter of a sphere having the radius of curvature of that circle was taken as the grain diameter. Furthermore, to examine the diffusion status of constituents in the neck, that is, of Cu and Ni atoms, the two sintered spherical grains embedded in an acrylic resin were cut along a plane that included the centers of the two grains, the cut

face was polished, and then the elements in the neck were analyzed with an energy-dispersive X-ray system (EDX).

## 3. Results and Discussion

### 3.1 Reliability of Authors' Simulation Method

In the initial stage of sintering with Cu and Ni grains, the sintering progresses while a well-defined neck is being formed between the Cu and Ni grains as shown in **Fig. 2**. **Figs. 5** and **6** illustrate the test results for the effect of sintering periods on the neck

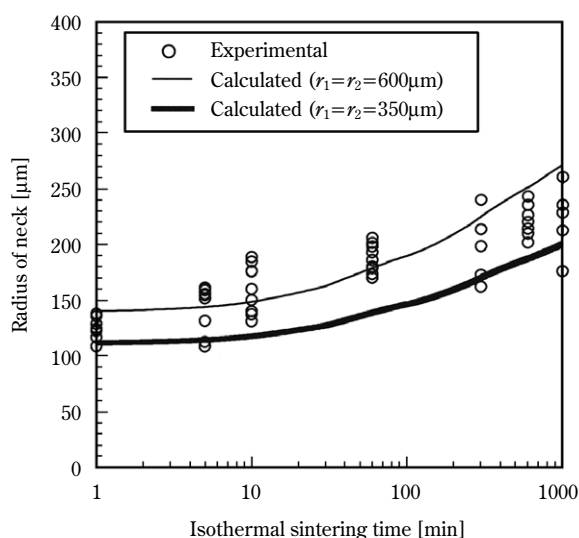


**Fig. 5** Relationship between radius of neck and isothermal sintering time  
(Heating rate=300K/h, sintering temperature=1313K)

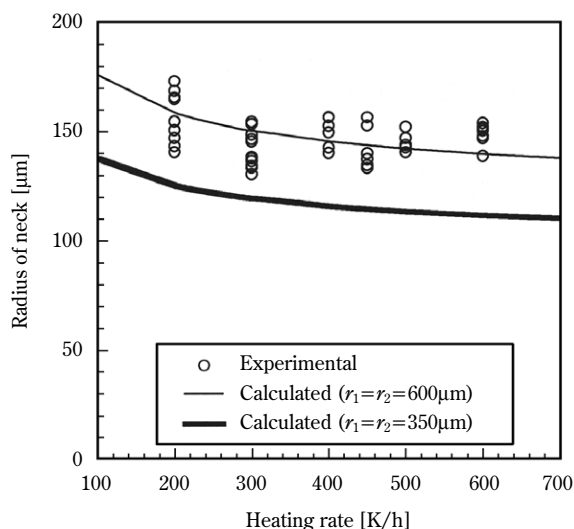


**Fig. 6** Relation between radius of neck and heating rate (Sintering temperature=1338K, isothermal sintering time =1min)

growth, the results of estimation about the effect of sintering periods according to the authors proposed simulation method, as well as the effects of the heating rate on the neck growth. The curvature radius at around the contact area between two sintered spherical grains was in the range of 600 to 350  $\mu\text{m}$ . Therefore, in the calculation for simulation, the neck radii for the maximum radius (600  $\mu\text{m}$ ) and minimum radius (350  $\mu\text{m}$ ) were determined and are shown in **Figs. 5** and **6**. The measurement values obtained from the experiment varied somewhat because the crystal orientation of the grain boundary varied among the grain-to-grain pairs tested and tended to be somewhat greater than the calculated values. The model grains applied to the calculation for simulation were true spheres and had smooth surfaces, whereas the grains used in the experiment were not true spheres and had uneven surfaces, as illustrated in **Fig. 2**. In particular, surface unevenness with a smaller curvature promotes mass transfer, possibly leading to a greater neck radius. A slight difference between the measurement values obtained from the experiment and the calculated values appears to have resulted from this surface unevenness and the fact that the grains were not true spheres.

Incidentally, it has been empirically known that since the total energy applied in the sintering process tends to be greater, a longer isothermal period at a sintering temperature and/or a smaller heating rate promote neck growth (Chu *et al.*, 1991). The results

of the authors' simulation match these facts about neck growth behavior.

The element analysis results on the neck by EDX illustrated in **Fig. 3** show that the neck is virtually composed of Cu atoms alone. **Fig. 7** provides examples of calculations for neck volumes and Cu atom volumes in the neck at various points in time during the sintering process. From this diagram, it is apparent that as was the case with element analysis by EDX, the results of calculation also show that the neck is virtually composed Cu atoms alone at any condition.

As discussed above, the simulation results from the initial stage of sintering behavior with two grains of dissimilar components clearly illustrate the sintering behavior that progresses while forming a homogeneous solid solution in the neck. Therefore, it is apparently possible that the authors' simulation method can be used to investigate to the interrelation between sintering behavior and sintering conditions.

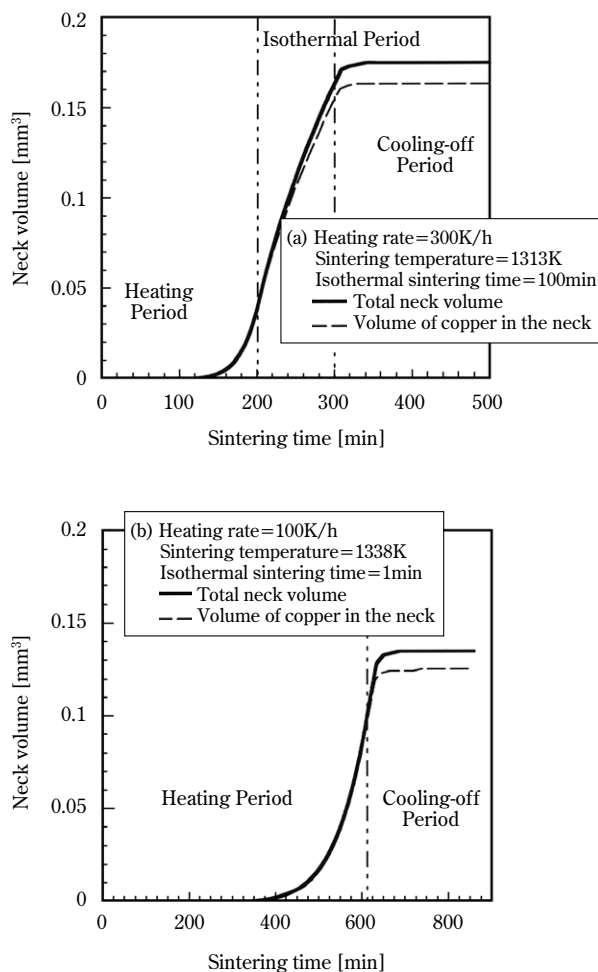


**Fig. 7** Change of neck volume during sintering process

### 3.2 Influence of Sintering Conditions on Sintering Behavior

The knowledge about the interrelationship between the mechanism of transfer of atoms and molecules to the neck between sintered grains and the sintering conditions is extremely important in controlling the microstructure of a ceramic material. The simulation for sintering behavior enables microscopic observation of neck growth behavior, making it possible to obtain detailed information about sintering conditions. **Fig. 8** summarizes the neck growth rates at various points in time during the sintering process that are estimated for each mass transfer mechanism. When a sintering process starts, the grain boundary diffusion quickly begins and the neck starts to grow. Next, as the temperature increases, the surface diffusion becomes active, and the volume diffusion also becomes active at the grain boundary. In solid solution type sintering where a clearly defined neck is formed, the associated substances transfer by the corresponding transfer mechanisms, but the dominant mechanism is determined by the sintering conditions. Because of disturbances in the atomic arrangement in the grain boundary and surface, the diffusion coefficient values in these areas are greater when compared with the values associated with volume diffusion (this phenomenon is known as “rapid diffusion”). Also, compared with a grain boundary coefficient

of a higher activation energy and a higher frequency factor, a grain boundary coefficient of a lower activation energy and a lower frequency factor features a greater value at a lower temperature range but its change associated with temperature increase is relatively slow. Furthermore, when a solid solution is formed in the neck, the surface diffusion actively progresses even at a lower temperature range owing to the mutual surface diffusion that results from the change in concentration of the solid solution. Based on these facts, it appears that grain boundary diffusion is dominant immediately after the start of sintering, and then as the temperature increases, mass transfer due to surface diffusion becomes particularly active. The factors that promote the densification of ceramic materials include grain boundary diffusion, and volume diffusion at the grain boundary. When the isometric period at the heating temperature starts after the heating period, the mass transfer mechanism is dominated by the surface diffusion that is disadvantageous in terms of densification. As a result, the microstructure formed is greatly influenced by the heating rate in sintering, the sintering temperature, and the duration of the isothermal period at the heating temperature. Therefore, the authors would like to discuss the interrelationship between these sintering conditions and sintering behavior.

The results of investigation into the effects of heating rate, isothermal period, and sintering temperature on the densification and grain growth are summarized in **Figs. 9** through **11**, respectively. **Fig. 9** shows the heating process alone where the effect of change in heating rate is illustrated with the sintering temperature and isothermal period where the sintering temperature is kept unchanged. With any heating rate, the shrinkage on the center-to-center dimension on the two grains greatly increases once the temperature of the grains reaches 800K. A lower heating rate contributes to greater shrinkage, thereby positively promoting densification. When the grain temperature reaches 1200K, a non-negligible grain growth occurs during heating even in the initial stage of sintering, and the volume of grain growth is greater at a lower heating rate. **Fig. 10** graphically illustrates the results of investigation into the effects of the isothermal period. A longer isothermal period contributes to the promotion of densification due to the volume diffusion from the grain boundary. At the same time, the grain growth is also rapidly promoted because of the neck growth. The proportion of densification during the cooling-off period is small, but the grain growth occurs at a non-negligible scale. The effect of the sin-

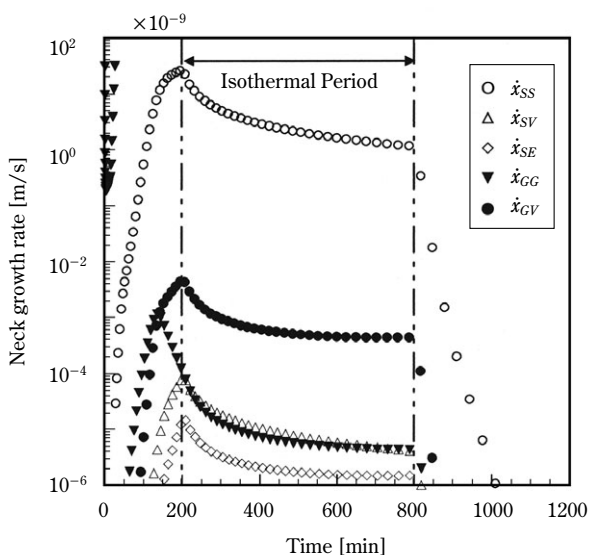


**Fig. 8** Neck growth rate on each mass transfer during sintering process  
(Heating rate=300K/h, sintering temperature=1313K, isothermal sintering time=600min)

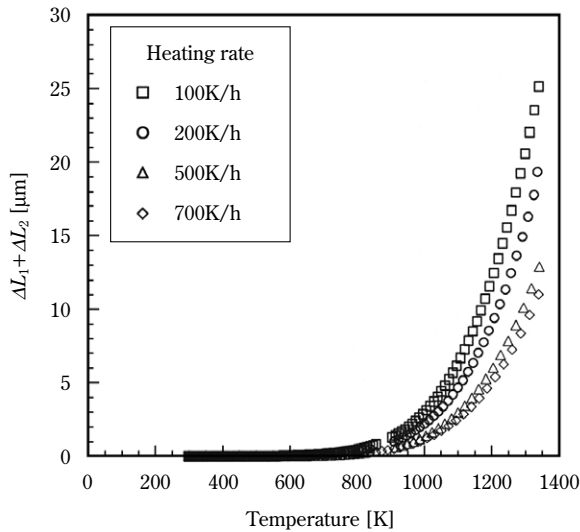


Fig. 9(a) Effect of heating rate on shrinkage

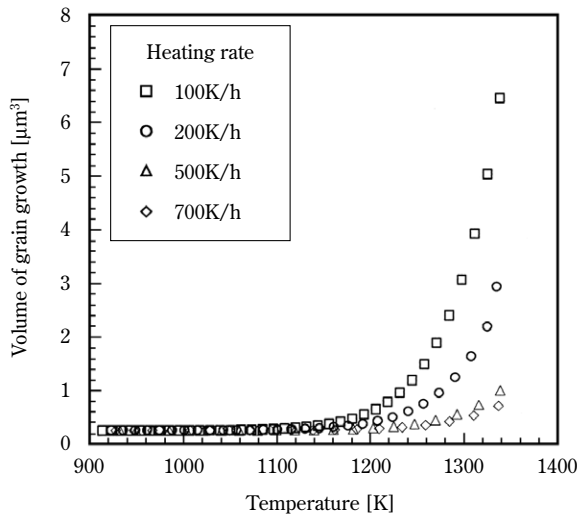


Fig. 9(b) Effect of heating rate on grain growth  
(Heating temperature=1338K, isothermal sintering time=1min)

tering temperature is illustrated in Fig. 11. The densification and grain growth are promoted as the sintering temperature increases. At a lower sintering temperature, the proportion of mass transfer owing to the surface diffusion during the isothermal period is small compared with that owing to the grain boundary diffusion. However, at the same time, the volume diffusion at the grain boundary is inhibited, resulting in inhibition of the densification of grain in spite of limited grain growth. As summarized above, it has been found that depending on the sintering condi-

tions, the grain growth in the initial stage of the sintering process cannot be neglected, and that the densification in the sintering process is promoted at a lower heating rate, with a longer isothermal period and a higher sintering temperature. However, excessive promotion of grain growth will lead to unevenness of the microstructure.

Therefore, to be able to promote the densification while inhibiting the grain growth, a relevant group of conditions must be set for the sintering of Cu and Ni. Therefore, the authors have investigated into the heating process that greatly influences the sintering behavior in the initial stage, as well as the conditions for the heating rate and sintering temperature. The

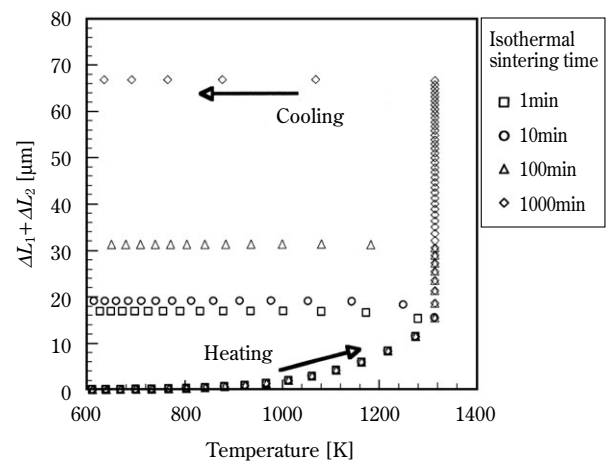


Fig. 10(a) Effect of isothermal sintering time on shrinkage

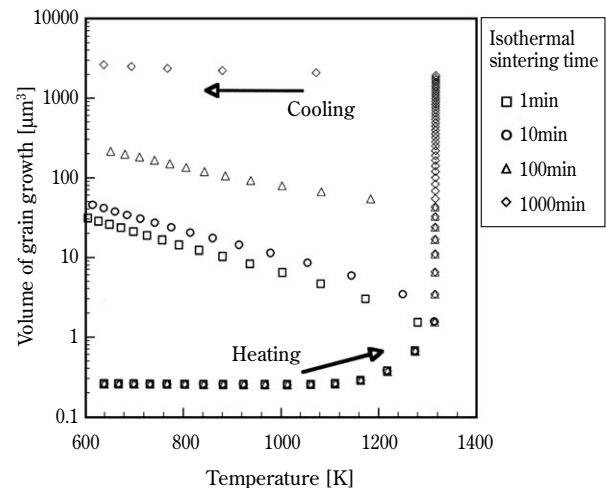
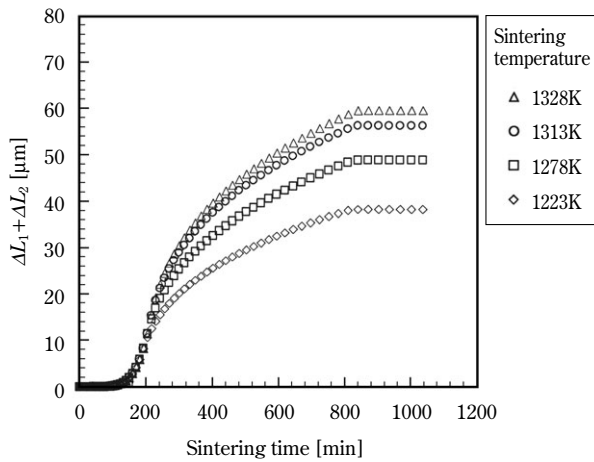
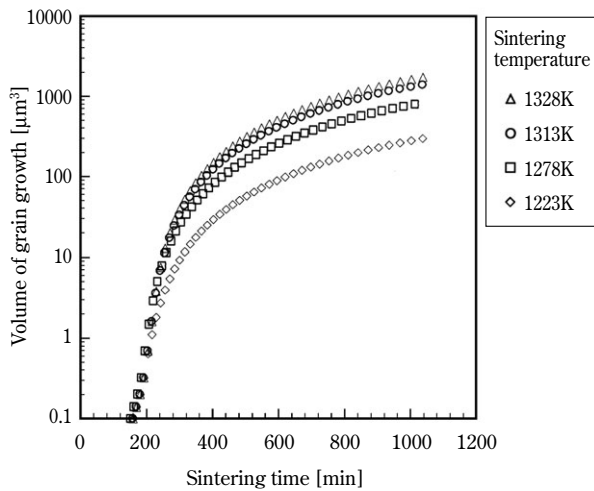


Fig. 10(b) Effect of isothermal sintering time on grain growth  
(Heating rate=300K/h, sintering temperature=1313K)





**Fig. 11(a)** Effect of sintering temperature on shrinkage



**Fig. 11(b)** Effect of sintering temperature on grain growth  
(Heating rate=300K/h, isothermal sintering time =600min)

results obtained are graphically illustrated in **Fig. 12**, where the values represent the grain growth-to-densification ratio ( $\Delta\bar{L} \times \bar{x} / \bar{v}$ ), wherein  $\Delta\bar{L}$  represents a normalized shrinkage of distance;  $\bar{v}$  normalized volume of grain growth; and  $\bar{x}$  a normalized neck radius. The normalization for this purpose was performed based on the following assumptions: a shrinkage of distance results from the densification process alone where the two grains were sintered to a neck radius of  $0.3 r$ ; at a heating rate of 1000 K/h. From this diagram, it should be understood that there is a range of sintering temperature effective for a heating rate, and that a higher heating rate results in a smaller sintering temperature range effective for the densification. Thus,

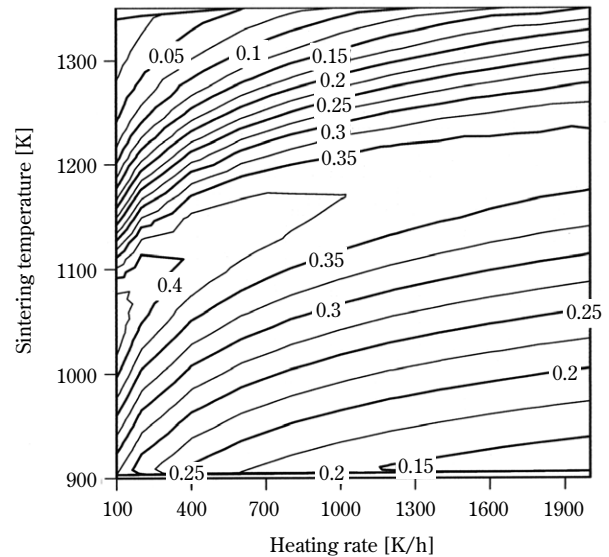


**Fig. 12** Map for the ratio of shrinkage to grain growth  
( $r_1=r_2=350\mu\text{m}$ )  
Numerals on the line denote  $\Delta\bar{L} \times \bar{x} / \bar{v}$   
 $\Delta\bar{L}$  ; Normalized shrinkage of distance  
 $\bar{x}$  ; Normalized radius of neck  
 $\bar{v}$  ; Normalized volume of grain growth

the authors have been able to determine the optimal sintering conditions for the initial stage of sintering.

## Conclusion

As a first step in engineering analysis for the sintering process that most greatly influences microstructure formation in ceramic manufacturing processes, the authors have performed a computer-aided simulation of the sintering behavior of two spherical grains having dissimilar compositions.

When the two spherical grains have dissimilar compositions, their sintering behavior can vary greatly depending on the characteristics of initial powder materials as well as the process parameters, including the sintering conditions. Therefore, an estimation model for each sintering behavior must be established. For this reason, in the authors' research, an experiment with the most rudimental two-grain sintering was first performed using a homogeneous solid solution type Cu-Ni system whose physical properties and characteristics values are well known, as a system that involves two grain types having dissimilar compositions. Next, the authors proposed a simulation model that can accommodate the sintering behavior learned through the results of experiments,

and performed a computer-aided simulation with this model. As a result of verification of the reliability of the proposed simulation method based on the above-mentioned results of experiments, the calculated value of neck growth volume closely matched the results of simulation. Based on these simulation results, the authors investigated into the sintering conditions, that is, the heating rate, sintering temperature, and isothermal period, and as a result learned that the grain growth, which previously had been considered not to occur during the initial stage of sintering, should not be neglected depending on the sintering conditions, and that the densification and grain growth are highly responsive to sintering conditions. Furthermore, the authors investigated the effect of the combination of heating rate and sintering temperature on densification and grain growth. The results of this investigation helped obtain the optimal design for the sintering conditions of the initial sintering process. The authors' research will constitute a first step for simulation activities in the near future that cover the entire continuous process for a multi-grain system, from the initial stage to the intermediate stage and the final sintering process.

This research was in part assisted by the RCAST, Doshisha University, and the authors would like to express their gratitude for assistance received.

## Nomenclature

$a_z$	=effective diffusion area	[m <sup>2</sup> ]
$D$	=diffusion coefficient	[m <sup>2</sup> /s]
$D_0$	=coefficient of holes diffusion	[m <sup>2</sup> /s]
$D_B$	=grain boundary diffusion coefficient	[m <sup>2</sup> /s]
$D_{GG}$	=grain growth coefficient	[m <sup>2</sup> /s]
$D_S$	=surface diffusion coefficient	[m <sup>2</sup> /s]
$D_V$	=volume diffusion coefficient	[m <sup>2</sup> /s]
$D_Z$	=effective diffusion coefficient	[m <sup>2</sup> /s]
$H$	=ratio of the distance from the grain boundary to the center of particle to radius of particle	[–]
$k$	=Boltzman's constant	[kJ/K]
$M$	=molecular weight	[g/mol]
$P_0$	=vapor pressure	[kg/m <sup>2</sup> ]
$Q$	=active energy of self diffusion	[kJ/mol]
$R$	=gas constant	[kJ/mol/K]
$R_r$	=ratio of radius of particle 1 to radius of initial particle 1	[–]
$r$	=radius of particle	[m]
$\dot{r}$	=grain growth rate	[m/s]
$r'$	=radius of particle after sintering densification process	[m]

$r''$	=radius of particle after grain growth	[m]
$S$	=surface area of particle	[m <sup>2</sup> ]
$S_{gb}$	=area of grain boundary	[m <sup>2</sup> ]
$S_n$	=surface area of neck	[m <sup>2</sup> ]
$T$	=sintering temperature	[K]
$t$	=time	[s]
$V_n$	=volume of neck	[m <sup>3</sup> ]
$v$	=volume of grain growth	[m <sup>3</sup> ]
$x$	=radius of neck	[m]
$\dot{x}_{SE}$	=neck growth rate by evaporation-condensation	[m/s]
$\dot{x}_{SS}$	=neck growth rate by surface diffusion	[m/s]
$\dot{x}_{SV}$	=neck growth rate by volume diffusion at particle surface	[m/s]
$\dot{x}_{GG}$	=neck growth rate by grain boundary diffusion	[m/s]
$\dot{x}_{GV}$	=neck growth rate by volume diffusion at grain boundary	[m/s]
$Y_n$	=curve equation of neck surface	[–]
$Y_s$	=curve equation of particle surface	[–]
$Z_i$	=distance from the center of two particles to a point of contact between neck and particle surface	[m]
$\gamma_s$	=surface energy	[kJ/m <sup>2</sup> ]
$\gamma_{gb}$	=interface (grain boundary) energy	[kJ/m <sup>2</sup> ]
$\Delta G_g$	=free energy translation by grain growth	[kJ/mol]
$\Delta L$	=shrinkage of the distance from the grain boundary to the center of the particle	[m]
$\Delta t$	=time step	[s]
$\Delta \phi$	=driving force of grain growth	[kJ/mol]
$d$	=interatomic distance	[m]
$d_B$	=thickness of the region of enhanced diffusion at the grain boundary	[m]
$d_s$	=thickness of the region of enhanced diffusion at the surface	[m]
$Z_M$	=molecular volume	[m <sup>3</sup> /mol]
$\lambda_z$	=effective diffusion length	[m]
$\rho$	=radius of curvature at neck	[m <sup>-1</sup> ]
$\rho_p$	=density of particle	[kg/m <sup>3</sup> ]

## Literature Cited

- Ashby, M.F.; "A First Report on Sintering Diagrams," *Acta Metallurgica*, **26**, 275 (1974)
- Chu, May-Ying, Mohamed N. Rahaman and Lutgard C. De Jonghe; "Effect of Heating Rate on Sintering and Coarsening," *J. Am. Ceram. Soc.*, **74**, 1217 (1991)
- Johnson, D.L.; "New Method of Obtaining Volume, Grain-boundary, and Surface Diffusion Coefficients from Sintering Data," *J. of Appl. Phys.*, **40**, 192 (1968)
- Kananovskii Yu. S. and Do Van Khai; "Diffuzionnyi Perenos Massy Po Poverkhosti Monokristallov Tverdykh

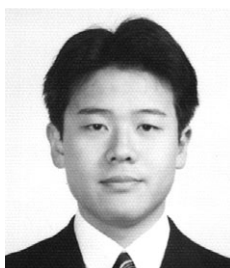
- Ractvorov Med-Nikel," *Fizika Metallov i Metallovedenie*, **39**, 828-836 (1975)
- Kaysser, W.A., S. Takajo and G. Petzow; "Low Energy Grain Boundaries in Liquid Phase Sintered Cu-Ag," *Z. Metallkde.*, **73**, 579-580 (1982)
- Kingery, W.D. and M. Berg; "Study of Initial Stages of Sintering, Solids by Viscous Flow, Evaporation-Condensation, and Self Diffusion," *J. of Appli. Phys.*, **26**, 1205 (1955)
- Kuczynski, G.C; "Diffusion in Sintering of Metallic Particles," *Metals Transactions*, **185**, 169 (1949)
- Nihonkinzokugakkai ed.; *Kinzoku Data Bukku*, 3<sup>rd</sup> Ed., PP21-23, P527, Marzen, Tokyo, Japan (1993)
- Puckert, F.J., W.A. Kaysser and G. Petzow; "Transient Liquid Phase Sintering of Ni-Cu," *Z. Metallkde.*, **74**, 737-743 (1983)
- Shimosaka, A., T. Sawai and J. Hidaka; "Computer Simulation of the Initial Stage Sintering of Particles," *J. Soc. Powder Technol Japan*, **32**, 668-674 (1995)
- Tanaka, H; "Normal and Abnormal Grain Growth Rates in Spherical Grain Matrix," *J. Ceram. Soc. Japan*, **104** [4], 253-258 (1996)
- Tanaka, H; "Simulation of Initial-Stage Sintering with Two-Sphere Model," *J. Ceram. Soc. Japan*, **105** [4], 294-298 (1997)
- Y. Ueda, A. Shimosaka and J. Hidaka; *Funtaikougakukai shunki kenkyu happyo koen ronbunshu*, 49-53 (1996)
- Wazzan, A.R.; "Lattice and Grain Boundary Self-Diffusion in Nickel," *J. of Appl. Phys.*, **36**, 3596 (1965)

## Author's short biography



### Atsuko Shimosaka

Atsuko Shimosaka has been a Lecturer at the Department of Chemical Engineering and Materials Science at Doshisha University since 1993. Her research interests are focused on the mechanical analysis of granular behavior and computer simulated design of ceramic materials. Currently, she is an editor of the Journal of The Society of Powder Technology, Japan.



### Yasushi Ueda

Yasushi Ueda received his B.S. (1996) and M.S. (1998) degrees from the Department of Chemical Engineering and Materials Science at Doshisha University. Since 1998, he has been working at Sumitomo Chemical Co., Ltd.



### Yoshiyuki Shirakawa

Y. Shirakawa graduated with a degree in Solid State Physics from Niigata University (1988), where he also received his Ph.D. (1993). He then took a position in post doctorate research, and studied the structure and electronic properties of non-crystalline materials for one year. He subsequently continued on at Niigata University as a research associate in Fundamental Science and Technology. Afterwards he became a research associate in Materials Science and Processing at Osaka University (1995-1998). Since 1998 he has been working in the Department of Chemical Engineering and Materials Science at Doshisha University, where he has been committed in understanding of the interface effects and development of nanoparticle composite materials.



### Jusuke Hidaka

Prof. Jusuke Hidaka has been at Doshisha University, Japan since 1976. His major research interests are focused on the mechanical analysis of powder flow using computer simulation, and the classification and instrumentation of powder industrial processes using acoustic emission. He is the vice president of The Society of Powder Technology, Japan.

# Mechanochemical Synthesis of Piezoelectric PLZT Powder<sup>†</sup>

Kenta Takagi<sup>1</sup>, Jing-Feng Li<sup>2</sup>,  
Ryuzo Watanabe<sup>2</sup>

<sup>1</sup> Graduate School, Tohoku University

<sup>2</sup> Department of Materials Processing, School of  
Engineering, Tohoku University

## Abstract

*The mechanochemical (MC) synthesis of La-modified lead zirconate titanate (PLZT) powder from its constituent oxides was conducted with planetary ball milling. A single-phase perovskite PLZT powder was synthesized by dry-milling the oxide mixture for a relatively short period (36 ks at 400 rpm). Dense PLZT bulk samples with fine-grained microstructures were obtained even from powders milled for a short time (3.6 ks) and at a lower sintering temperature than for the powders prepared by the conventional wet-mixing process. The present study suggests that the mechanochemical synthesis of PLZT comprises the following three stages: First, the pulverization, fine mixing, and granulation of the starting powders occur in the early stage. Second, the particles of the powders increasingly lost their crystallinity due to milling ball impact. Finally, the reaction between PbO and TiO<sub>2</sub> produced PbTiO<sub>3</sub>, whose reaction with the remaining oxides formed (Pb, La) (Zr, Ti)O<sub>3</sub> solid solutions.*

## 1. Introduction

There are expectations for the application of La-modified lead zirconate titanate (PLZT) in optical instruments because of its piezoelectric effect, electrooptical effect [1], bulk photovoltaic effect, [2] and the photostrictive effect that is manifested as a combination thereof. [3] When putting PLZT to work in optical instruments, the materials's light transmission is considered to be the main problem. Endowing ceramics with light transmission generally requires high density, few impurities, high homogeneity, and other qualities, and PLZT is no exception.

It is known that if one makes PLZT polycrystalline materials using a heat process, PbO volatilization that occurs under the high temperatures (1073 K and higher) in powder synthesis (calcination) and sintering will result in uneven structure formation and decreased sinterability, in turn lessening light transmission. [4] Because these problems are of significance when using PLZT in electrooptical switches and

other devices, researchers have long worked assiduously to develop ways to synthesize powders using the excess-Pb, [4] covering, [5] sol-gel, and other methods to obtain high-density sintered materials with good light transmission. Yet, these methods have many industrial drawbacks. For example, the covering method consumes much Pb-rich powder, while sol-gel powder is expensive. Researchers also believe that manifesting bulk electromotive force in particular requires not only light transmission, but also reducing the size of crystal grains to a certain extent, [6] but no one has reported an inexpensive synthesis process that can achieve both.

Mechanochemistry is a method that actively utilizes the physico-chemical changes and reactions that arise when applying mechanical energy to a substance and changing the atomic bonding state of its surface. Fine powder activated by mechanical milling is highly reactive, and it is known especially that composite substances are formed when processing mixed powders. This synthesis process is environmentally friendly because it is a nonthermal solid-state reaction. What is more, the powders yielded often have special properties that were unobtainable using conventional thermal action. Recently much work has been done on the synthesis of composite oxide

<sup>1,2</sup>Aramaki-aza-aoba Aoba-ku, Sendai 980-8579

<sup>†</sup> Accepted: May 26, 2003



ceramic powders created by the mechanochemical (MC) method, and there are reports on the various interesting phenomena that arise. [7] In particular Wang et al. [8, 9] performed MC synthesis of mostly Pb-based piezoelectric ceramics, and successfully obtained single-phase, high-density perovskite sintered materials with short milling time. There is also a report that sintered materials with sub-micrometer crystal grain sizes have been obtained from PLZT powder synthesized using the MC method. [10]

For these reasons the MC method offers promise as a method to synthesize PLZT powder with high sinterability, and judging by the fact that sintered products made with PLZT powder have a fine microstructure, this is also an effective means to achieve high bulk electromotive force. Further, PbO volatilization when synthesizing powder can be avoided because MC synthesis is nonthermal. However, there are still no detailed findings on the synthesized powder's high sinterability and the mechanism by which fine microstructures form.

In this research we therefore used MC synthesis to make PLZT powder with high sinterability, and investigated the synthesized powder's characteristics and sinterability. In particular we tried to elucidate the synthesis mechanism by focusing on powder characteristics in the initial stage of the MC synthesis process, which has not been studied very much.

## 2. Materials and Methods

Our starting powders were commercially available  $\beta$ -PbO (Wako Pure Chemical Industries, Ltd.; average particle size, 3  $\mu\text{m}$ ),  $\text{ZrO}_2$  (TOSOH; 100  $\mu\text{m}$ ; granulating powder), and  $\text{TiO}_2$  (Wako Pure Chemical Industries; 1  $\mu\text{m}$ ),  $\text{La}_2\text{O}_3$  (Japan Pure Chemical Co., Ltd.; 3  $\mu\text{m}$ ). Except for PbO, these powders are formed by the tight agglomeration of primary particles from 20 or 30 to several hundred nm in size. All the starting powders were weighed to yield the composition  $\text{Pb}_{0.92}\text{La}_{0.08}(\text{Zr}_{0.65}\text{Ti}_{0.35})\text{O}_3$ . The powders were then placed in a pot (100 mm inside diameter, 1-L volume) containing 1-kg balls (10 mm diameter), and then dry-milled for up to 144 ks at between 100 and 400 rpm with a planetary mill (FRITSCH Pulverisette 6) that yielded high energy. To avoid contamination with impurities during milling to the maximum extent, the balls and pot were made of  $\text{ZrO}_2$  ( $\text{ZrO}_2$  - 3 mass%  $\text{Y}_2\text{O}_3$ ), which is contained in the feedstock. For purposes of comparison, we also made powder mixtures with wet-milled powder and with calcined powder. To make the wet-milled powder, we started by

putting 20 g of the mixed feed powder and 100 ml of ethanol into a polyethylene pot containing  $\text{ZrO}_2$  balls (10 mm diameter), mixed slowly (80 rpm) in a ball mill for 90 ks to form a slurry, which is dried and pulverized in a mortar. A calcined powder was obtained by putting this powder in an  $\text{Al}_2\text{O}_3$  crucible and heat treating in air at 1173 K for 10.8 ks.

The dry-milled powder (below, "MC powder"), wet-milled powder (below, "mixed powder"), and calcined powder were subjected to phase identification by X-ray diffraction (RAD-C made by Rigaku Corporation), microstructure observation by SEM, and specific surface area measurement using the BET method (ADS-18 made by Shimadzu Corporation). Powder thermal characteristics were determined by heating DSC (DSC-404 made by NETZSCH) from room temperature to 973 K at a heating rate of 0.17  $\text{K s}^{-1}$ .

We sintered some synthesized powder to investigate sinterability. First we made some green compacts by using uniaxial compaction (100 MPa) and CIP (200 MPa) on MC powder, mixed powder, and calcined powder. These were put in a high-purity  $\text{Al}_2\text{O}_3$  crucible and heated to between 1273 and 1473 K at a heating rate of 0.17  $\text{K s}^{-1}$  using a tubular furnace, and sintered for 3.6 ks in air. To prevent as much as possible the volatilization of PbO from the sample, which occurs during sintering, a PbO atmosphere was maintained in the crucible by PbO- $\text{ZrO}_2$  powder. The sintered product's density was measured by the Archimedeian method, the product was examined by x-ray diffraction (XRD), and its structure subjected to SEM observation. We also used a dilatometer (TM1500H made by ULVAC-RIKO, Inc.) to investigate linear dilatation at a heating rate of 0.17  $\text{K s}^{-1}$ .

## 3. Results

**Fig. 1** shows changes over time in XRD patterns when conducting MC synthesis with a planetary mill at 100, 300, and 400 rpm. At 100 rpm we observed no change in the XRD pattern, which is probably because at low speed centrifugal force is not sufficient to keep the powder in between the milling balls, and the powder did not receive enough inter-ball collision energy. At 300 and 400 rpm diffraction patterns gradually changed over time, indicating gradual change in powder constituent phases. The 300 rpm results show that at the start of milling (0.9 ks) the XRD pattern merely smoothed overall, and the starting powder's peak positions are hardly changed. But the PbO peaks of  $2\theta=29.0$  and  $30.3^\circ$  in the mixed powder dis-

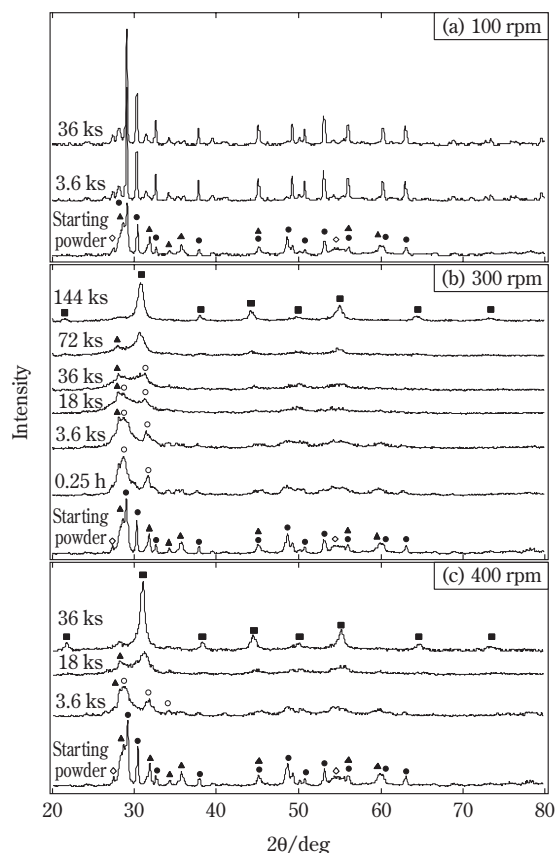


**Fig. 1** Changes in the XRD patterns of the powders MC-processed at (a) 100 rpm, (b) 300 rpm, and (c) 400 rpm.  
 $\beta$ -PbO,  $\alpha$ -PbO,  $\text{ZrO}_2$ ,  $\text{TiO}_2$ , perovskite PLZT

appeared, and new peaks appeared at  $28.7^\circ$  and  $31.7^\circ$ . This is because ball impact force transformed the rhombic crystal PbO ( $\beta$ -PbO, yellow PbO) used in the starting powder into tetragonal crystals ( $\alpha$ -PbO, red PbO), which is a low-temperature, low-pressure phase, [11] and for this reason powder color changed from yellow to orange. Hence at 0.9 ks we discerned no manifest reaction, and essentially there was no phase change from the starting powder. At 3.6 ks and above, starting powder peak intensity weakened over time, and especially the  $\alpha$ -PbO peak of  $2\theta=29.0^\circ$  rapidly weakened and all but disappeared by 72 ks. In its place the perovskite PLZT peak ( $30.9^\circ$ ) appeared. In the diffraction pattern after 72 ks the peaks for  $\alpha$ -PbO and  $\text{TiO}_2$  are all but gone, but the  $28^\circ$   $\text{ZrO}_2$  peak remains slightly. Finally, after 144 ks have elapsed, all starting powder peaks have vanished. The result was a single-phase perovskite powder, and the color changed from orange to milky white. At 400 rpm we observed the same phenomena occurring about four times faster. These results demonstrate that it is possible to synthesize a single-phase PLZT powder by applying at least a certain amount of mechanical energy to the starting mixed powder.

**Fig. 2** shows SEM photomicrographs of the mixed powder and the MC-synthesized powder, as well as chemically etched cross sections of the powder particles. XRD phase identification performed on the

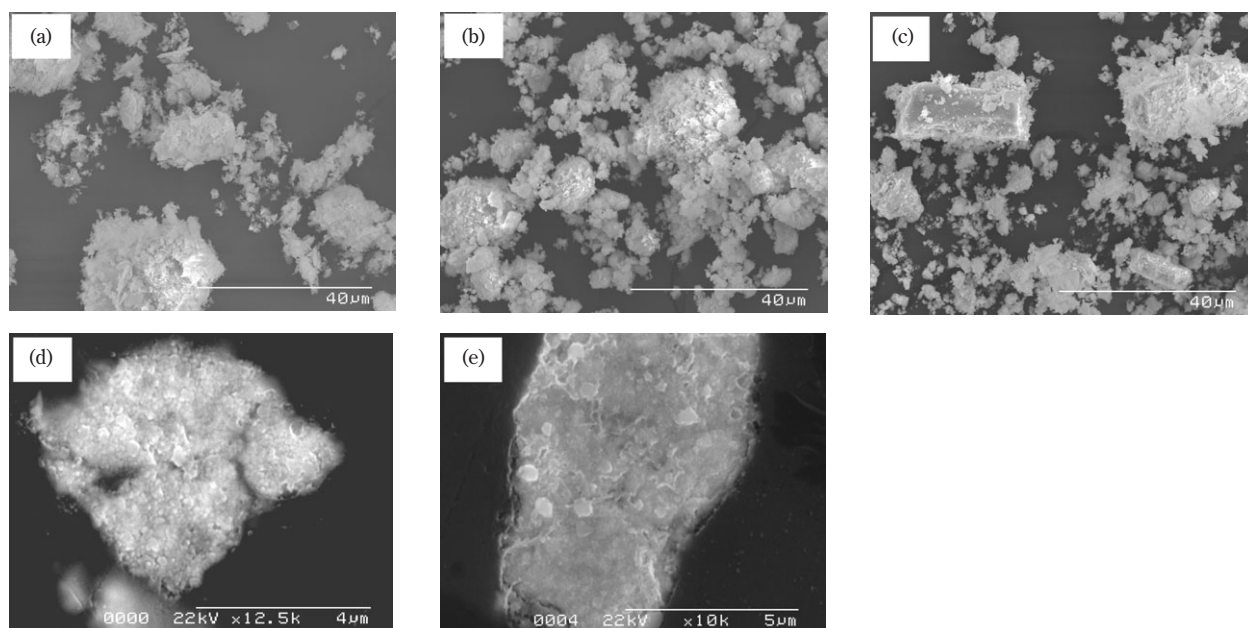


**Fig. 2** SEM photomicrographs of milled powders.  
 (a) wet-milled, (b) MC 3.6 ks at 300 rpm, (c) MC 144 ks at 300 rpm, and (d, e) chemically etched cross sections of the powders shown in (b) and (c)

mixed powder revealed no phase change from the starting mixed powder. The photomicrograph shows that the mixed powder consists of agglomerates several  $\mu\text{m}$  up to 20 to 30  $\mu\text{m}$  in size, which are formed by loosely agglomerated particles 20 to 30 nm in size. In **Fig. 2(b)** it appears that the MC 3.6-ks powder is loosely agglomerated like the mixed powder, but in **Fig. 2(d)** one can see that particles 20 to 30 nm large are tightly packed and form a single agglomerate. The MC 144-ks powder, which is single-phase PLZT, consists of angular coarse and fine particles, and the cross section in **Fig. 2(e)** reveals that the coarse powder particles have hardly any void, and are closer to being single particle than an agglomerate.

**Fig. 3** shows the XRD patterns obtained after heat treatment of mixed powder and MC powders at 773 K and 1073 K for 1 h. Treatment of the mixed powder at 773 K yielded no major XRD pattern change, but after treatment at 1073 K there was a mixture of a

perovskite phase,  $\text{PbTiO}_3$  phase, and pyrochlore phase. It is known that generally thermal synthesis yields  $\text{PbTiO}_3$ , perovskite, and pyrochlore phases partway through the process, [12, 13] and the above-described results suggest the occurrence of the reactions typical to conventional thermal synthesis. But heat treatment of MC 3.6-ks powder at 773 K sharpened the peaks that were broad before heat treatment, and the diffraction pattern assumed a form close to that of the starting powder. In this consideration, the broadening of diffraction peaks is probably attributable to the strain and decreased crystallinity (amorphization) introduced by mechanical energy, [14, 15] while heat treatment at temperatures under 773 K mitigates that strain. And because no manifest phase change was observed in MC 3.6-ks powder, it was essentially a mixture of oxidized starting powder. For that reason it was a mixture of perovskite and  $\text{PbTiO}_3$  phases even after heat treatment at 1073 K, just as the mixed powder was. On the other hand MC 36-ks powder had two broad diffraction peaks in the  $30^\circ$  locality before heat treatment, but heat treatment at 773 K released strain energy, and the two broad peaks divided into a comparatively sharp  $\text{ZrO}_2$  ( $28^\circ$ ) peak and perovskite phase ( $31^\circ$ ) peak, accompanied by a small  $\text{PbO}$  peak.

**Fig. 4** shows MC powder DSC results in comparison with mixed and calcined powders. At 973 K or below, there were no structural changes or chemical reactions in the calcined powder, so it was neither endothermic nor exothermic at all. For the mixed powder, the exothermic peak from 523 to 573 K and the endothermic peak from 573 to 673 K were caused by, respectively, the decomposition of the polymer entering from the pot, and the dehydration of the

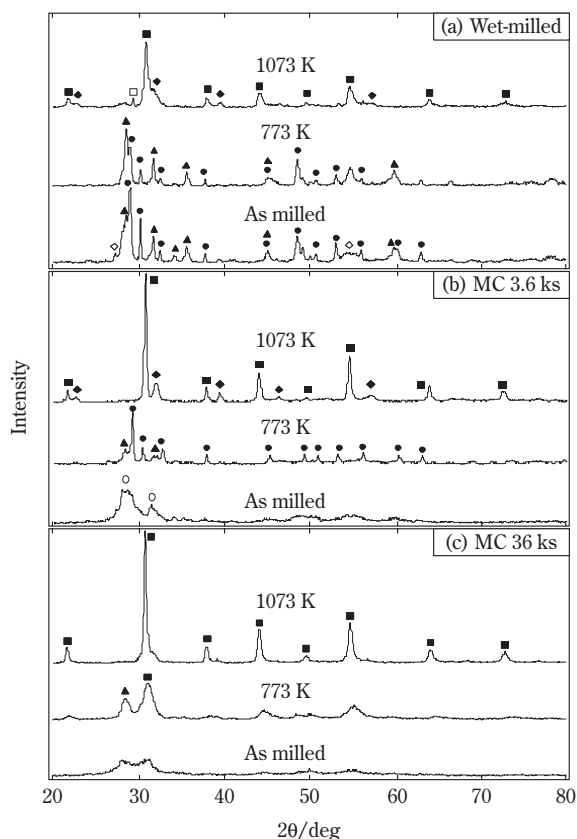


**Fig. 3** Changes in the XRD patterns of the powders after heat treatment at 773 and 1073 K.

(a) wet-milled, and (b) MC 3.6 ks and (c) MC 36 ks at 300 rpm

$\beta\text{-PbO}$ ,  $\alpha\text{-PbO}$ ,  $\text{ZrO}_2$ ,  $\text{TiO}_2$ ,  $\text{PbTiO}_2$ ,  
perovskite PLZT, pyrochlore

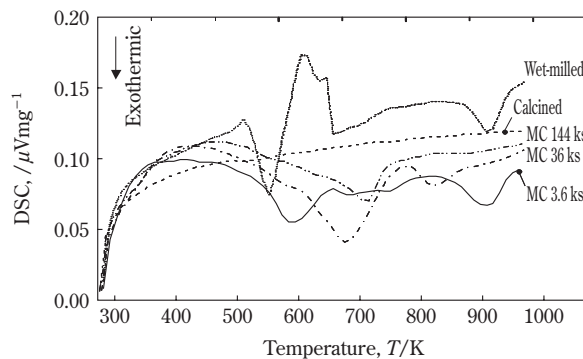


**Fig. 4** DSC traces of MC powders prepared at 300 rpm for various durations, compared with traces of wet-milled and calcined powders. The heating rate was  $0.16 \text{ K s}^{-1}$  in air.

$\text{La}(\text{OH})_3$  in the  $\text{La}_2\text{O}_3$  starting powder, which means that effectively one need consider only the heat generated at around 873 K. The heat generated by  $\text{PbTiO}_3$  formation is reported to appear around the 773 to 873 K range, [16] and the 873 K peak appearing with mixed powder is also attributed to  $\text{PbTiO}_3$  formation. Similarly with MC 3.6-ks powder, there is an exothermic peak accompanying  $\text{PbTiO}_3$  formation. MC 36-ks powder also exhibited an exothermic peak at 793 K, but because we were unable to confirm the presence of  $\text{TiO}_2$  after 773 K heat treatment in **Fig. 3(b)**, it is quite possible the heat was incidental to another reaction. Meanwhile, all MC powders exhibited gentle exothermic peaks between 473 and 723 K, regardless of milling time. Considering that, as seen in **Fig. 3(b)**, MC 3.6-ks powder retained its starting composition even after heat treatment at 773 K, it seems reasonable to suppose that this exothermic peak is related to the release of energy from the strain induced by milling. [14] The probable reason that the exothermic peak temperature differed according to milling time is that constituent phases and induced strain energy were different for each processing time.

**Fig. 5** plots the sinterability of MC powders in comparison with mixed and calcined powders. XRD analyses of all sintered products revealed that all were single-phase perovskite powders. As the graph shows, the sintered density of 3.6-ks to 144-ks MC powder was far higher than that of mixed powder, and rivaled that of calcined powder. In **Fig. 1** a perovskite phase was not completely formed in MC powder whose processing time is 72 ks or less, but that powder had

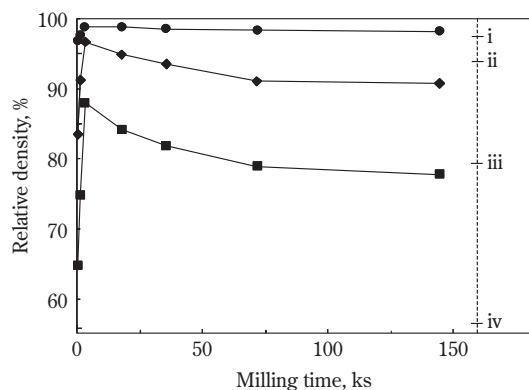


**Fig. 5** Changes in relative sintered density of MC powder at 1273 K (●), 1373 K (○), and 1473 K (◻) compared to the relative sintered density of a calcined powder at 1473 K (i) and a wet-milled powder at 1473 K (ii), 1373 K (iii), and 1273 K (iv).

comparatively high sinterability. As noted above, the constituent phases of 3.6-ks MC powder in particular are about the same as those of mixed powder, yet MC powder's sinterability is far higher.

**Fig. 6** shows the linear dilatation of green compacts from each powder. Mixed powder started expanding at 873 K. At 973 K its expansion rate changed, and at 1123 K it began to shrink. In research reported heretofore, heating  $\text{PbO-ZrO}_2\text{-TiO}_2$  mixed green compacts has resulted in expansion caused by the formation of  $\text{PbTiO}_3$  and PZT at 873 K and 973 K, respectively. [16, 17] The mixed powder expansion in the figure was a combination of these two expansion phenomena, and the expansion in the 873 to 1073 K and the 973 to 1173 K ranges corresponds to the formation of  $\text{PbTiO}_3$  and PLZT phases. In fact, the mixed powder exothermic peak at about 873 K in **Fig. 4** coincides with this expansion. Expansion did not occur in the 144-ks MC powder and the calcined powder because their  $\text{PbTiO}_3$  and PLZT phase formation processes had already finished. Although expansion was observed in the 3.6-ks MC powder, it was far smaller than that of the wet-milled powder, and it finished in the low-temperature range of 873 to 1073 K. Meanwhile, all MC powders had slow shrinkage in the temperature range of 423 to 823 K, and because this coincides closely with the moderate generation of heat in the DSC results, this shrinkage was accompanied by the relaxation of strain and by the crystallization.

**Fig. 7** shows the microstructures of sintered products made from mixed powder and MC powder. Although one can observe differences in the porosity

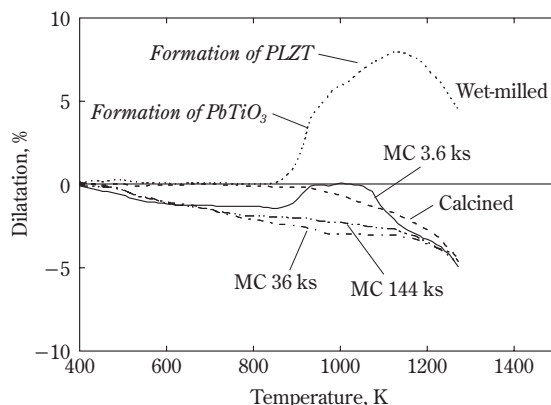


**Fig. 6** Changes in the linear dilatation of green compacts derived from the MC, wet-milled, and calcined powders.



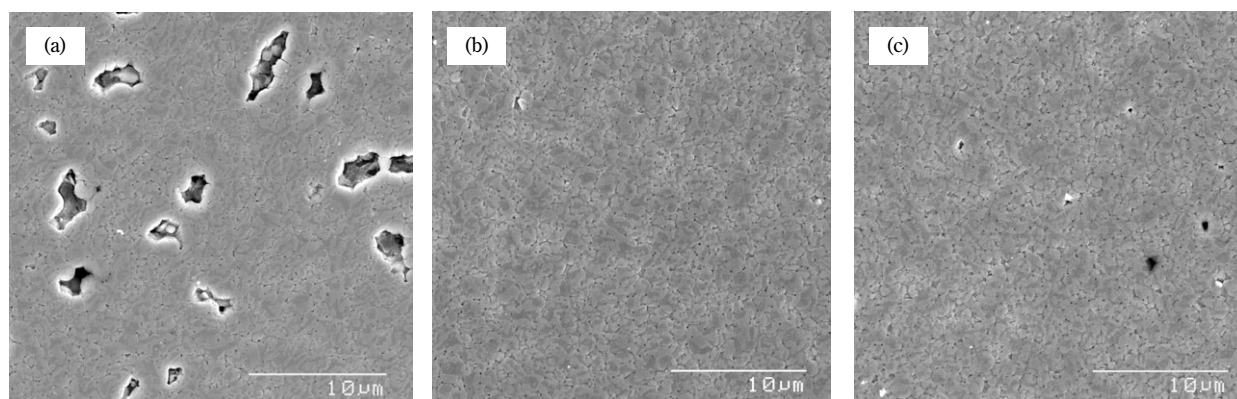


**Fig. 7** Chemically etched microstructures sintered at 1473 K from (a) the wet-milled powder, and from (b) MC 3.6 ks and (c) 144 ks powders at 300 rpm.

corresponding to sintered density, all three are very similar, uniform structures having fine crystal sizes of about 1  $\mu\text{m}$ .

#### 4. Discussion

Our results indicate that MC powders have sinterability equal to that of calcined powders, and our MC powders exhibited high sinterability even after very short MC processing time. Especially 3.6-ks MC powder had remarkably high sinterability despite it having the same constituent phases as the mixed powder. It is evident from **Fig. 6** that the difference in sinterability is attributable to the difference in the amounts of expansion occurring in the formation of  $\text{PbTiO}_3$  and PLZT. Expansion resulting from the formation of  $\text{PbTiO}_3$  is generally attributed to a molar volume difference, in which the  $\text{PbO}$  existing within interparticle space of the  $\text{TiO}_2$  skeletal particles diffuses into  $\text{TiO}_2$  particles, and the molar volume of the  $\text{PbTiO}_3$  which forms as a result is larger than that of the original  $\text{TiO}_2$ . The same holds for expansion by PLZT. We conjecture that after  $\text{PbO}$  diffuses, voids form in particle interstices, resulting in the whole skeleton expansion, and that voids which are not eliminated by sintering act to lower sinterability. If this scenario is correct, then the reason that 3.6-ks MC powder showed high sintering shrinkage and small voids distribution is that in this powder no appreciable phase reactions, which will yield skeletal expansion, occurred. A possible reason that voids were small is that starting powders were finely pulverized in MC processing and mixed very finely. In fact, **Fig. 2** shows that in the 3.6-ks MC powders 20 to 30 nm particles are tightly agglomerated suggesting a fine mixing.

**Fig. 5** reveals something highly interesting about sintering behavior. Conducting MC processing for longer than 3.6 ks actually decreased sinterability as milling time increased. Although there are several instances of research on the MC synthesis of perovskite crystals, they all reported that longer MC processing time increased sintered density, [8, 9] which contradicts our observation of decreased density. There are two conceivable reasons for this density decrease: (1) nonuniform sintering due to the presence of tightly agglomerated coarse powder (**Fig. 2(c)**), and (2) an increase in the amount of impurities from the pot and balls as milling progresses. We investigated (1) by conducting wet milling after MC processing to pulverize coarse particles. After MC processing finished, we put 200 ml of ethanol into the pot and milled for another 90 ks at 200 rpm. Recovering powder that adheres to the balls and pot is easy because this method makes the powder into a slurry. The resulting slurry was dried at 353 K and sintered as described. XRD examination of the powder before and after this wet milling revealed no clear change. **Table 1** gives the changes in specific surface area and sintered density before and after the wet milling.

**Table 1** Specific surface area and sintered density of the wet-milled powder and the dry-milled powders with and without the additional wet-milling process.

	Specific surface area ( $\text{m}^2/\text{g}$ )		Sintered density (%)	
	As milled	Pulverized	As milled	Pulverized
Wet-milled	8.41	—	79.2	—
MC 3.6 ks	1.73	15.60-21.26	94.3	94.9
MC 144 ks	2.58	8.76	86.4	97.7



This wet milling increased the specific surface area of the 144-ks powder about 3.4 times, which indicates that coarse particles were pulverized by the wet milling. Pulverization increased sintered density about 10%, and relative density to 97.7%, a substantial increase. This sinterability surpasses that of 3.6-ks MC powder (relative density 94.9%), meaning that nonuniform sintering caused by the presence of coarse particles strongly affects decreasing sinterability as related to MC processing time. With a simple experiment we also confirmed to a certain extent the influence of (2), but a closer investigation is planned for the future. In any case, MC powders exhibit high sinterability even with short processing times, but single-phase PLZT powders with long processing times have even better sinterability.

This study of MC powder characteristics and MC powder sintering behavior makes it generally possible to discern the mechanism of powder synthesis by MC processing. The initial stage involves starting powder pulverization and reagglomeration, which mixes more finely than conventional wet milling. And as seen in **Fig. 3**, ball impact on starting powder oxides induces strain and decreases crystallinity. Reactions caused by mechanical energy then start among oxide particles. **Fig. 3** indicates that first  $\text{PbTiO}_3$  forms from reactions between  $\text{PbO}$  and  $\text{TiO}_2$ , after which the reaction of  $\text{PbTiO}_3$  with  $\text{ZrO}_2$  and  $\text{PbO}$  leads to gradual PLZT formation, and the ultimate synthesis of single-phase perovskite PLZT powder. Because the small  $\text{La}_2\text{O}_3$  content made it difficult to determine La behavior by XRD.

## 5. Conclusion

We synthesized PLZT powder using the mechanochemical method, and reached the following conclusions from the results of our study of the synthesis process and the sinterability of synthesized powder.

- (1) Dry planetary milling of a mixture of the oxides of elements comprising PLZT succeeded in synthesizing single-phase perovskite PLZT powder in a comparatively short time at a minimum prescribed rotational speed.
- (2) Sinterability improved greatly even in powder dry-milled for a short time, in which a PLZT phase did not form. This was because in dry milling the starting powder of oxides was mixed very finely.
- (3) If dry milling is continued until a single-phase PLZT powder is synthesized, the powder becomes coarse and its sinterability declines, but we found that an additional wet-milling process can make

single-phase PLZT powder which exhibits very high sinterability.

- (4) We conjecture that the synthesis process works like this: As soon as milling begins, the starting powder is mixed by pulverization and reagglomeration, strain is induced, and amorphization occurs.  $\text{PbTiO}_3$  then forms from the reaction between  $\text{PbO}$  and  $\text{TiO}_2$ , after which a perovskite phase forms because of the reaction of  $\text{PbTiO}_3$  with  $\text{ZrO}_2$  and  $\text{PbO}$ .

## Citations

- 1) G. H. Haertling and C. E. Land: "Hot-Pressed (Pb, La)(Zr, Ti) $\text{O}_3$  Ferroelectric Ceramics for Electrooptic Application," *J. Am. Ceram. Soc.*, **54** (1971) 1.
- 2) A. M. Glass, D. von der Linde, D. H. Auston and T. J. Negran: "Excited State Polarization, Bulk Photovoltaic Effect and the Photorefractive Effect in Electrically Polarized Media," *J. Elec. Mater.*, **4** (1975) 915.
- 3) P. Poosanaas, K. Tonooka and K. Uchino: "Photostrictive actuators," *Mechatronics*, **10** (2000) 467.
- 4) G. S. Snow: "Fabrication of Transparent Electrooptic PLZT Ceramics by Atmosphere Sintering," *J. Am. Ceram. Soc.*, **56** (1975) 91.
- 5) S. Shah and M. S. R. Rio: "Preparation and Dielectric Study of High-Quality PLZTx/65/35 (x=6, 7, 8) Ferroelectric Ceramics," *J. Appl. Phys.*, **A71** (2000) 65.
- 6) T. Sada, M. Inoue and K. Uchino: "Photostrictive Effect of PLZT Ceramics," *Journal of the Ceramic Society of Japan*, **95** (1987) 545.
- 7) F. Saito: "Mechanochemical Effect Based on Pulverization," *Ceramics*, **31** (1996) 39.
- 8) S. K. Ang, J. Wang, D. Wan and J. Xue: "Mechanical Activation-assisted Synthesis of  $\text{Pb}(\text{Fe}_{2/3}\text{W}_{1/3})\text{O}_3$ ," *J. Am. Ceram. Soc.*, **83** (2000) 1575.
- 9) S. E. Lee, J. M. Xue, D. M. Wan and J. Wang: "Effect of Mechanical Activation on the Sintering and Dielectric Properties of Oxide-derived PZT," *Actametall.*, **47** (1999) 2633.
- 10) L. B. Kong, J. Ma, W. Zhu and O. K. Tan: "Preparation and Characterization of PLZT Ceramics Using High-energy Ball Milling," *J. Alloy comp.*, **322** (2001) 290.
- 11) F. Dacheille and R. Roy: "High-pressure Phase Transformations in Laboratory Mechanical Mixers and Mortars," *Nature*, **186** (1960) 71.
- 12) Y. Matsuo and H. Sasaki: "Formation of Lead Zirconite-Lead Titanate Solid Solutions," *J. Am. Ceram. Soc.*, **48** (1965) 289.
- 13) B. V. Hiremath, A. I. Kingon and J. V. Biggers: "Reaction Sequence in the Formation of Lead Zirconate-Lead Titanate Solid Solutions," *J. Am. Ceram. Soc.*, **66** (1983) 790.
- 14) H. Kimura and K. Hongo: "Solid-state Amorphization and Spark Sintering of Oxide Ceramics," *J. Japan Inst. Metals*, **63** (1999) 649.
- 15) J. Wang, J. Xue and D. Wan: "How Different Is Mechani-

- cal Activation from Thermal Activation? A Case Study with PZN and PZN-based Relaxors," *Solid State Ionics*, **127** (2000) 169.
- 16) S. S. Chandratreya, R. M. Fulrath and J. A. Pask: "Reaction Mechanisms in the Formation of PZT Solid-state Solution," *J. Am. Ceram. Soc.*, **64** (1981) 422.
- 17) S. Kim, G. S. Lee, T. R. Shrout and S. Venkatamani: "Fabrication of Fine-grain Piezoelectric Ceramics Using Reactive Calcination," *J. Mater. Sci.*, **26** (1991) 4411.

### Author's short biography



#### Kenta Takagi

Kenta Takagi received his BE, ME and Dr. E degrees in materials science and engineering from Tohoku University in 1994, 1996 and 2003, respectively. He was working at NGK ceramics Corp., Nagoya as a research engineer from 1996 to 2000, and is now a research fellow of NEDO project at the Department of Materials Processing, Tohoku University, Sendai, Japan. His research interest is processing and evaluation of functional ceramics.



#### Jing-Feng Li

Jing-Feng Li received his BS in materials science and engineering from Huazhong University of Science and Technology, Wuhan, China in 1984, and MS and PhD degree in materials Science and engineering from Tohoku University, Sendai, Japan in 1988 and 1991, respectively. He was assistant professor from 1992 to 1997 and associate professor from 1997 to 2002 at the Department of Materials Processing, Tohoku University. He is currently professor at the Department of Materials Science and Engineering, Tsinghua University, Beijing, China. His research interests include microfabrication of functional materials, processing and property control of ceramic materials.



#### Ryuzo Watanabe

Ryuzo Watanabe received his BE, ME, and Dr. E degrees in metallurgy from Tohoku University in 1964, 1966 and 1977, respectively. He was an assistant professor from 1996 to 1997, was an associate professor from 1978 to 1986. From 1986 he has been a professor at the Department of Materials Processing, and currently serves as the Dean of the Graduate School of Educational Informatics, Tohoku University, Sendai, Japan. His research interests include functionally graded materials, sintering mechanisms, mechanical alloying and property-microstructure relationship of sintered composites.

## Information Articles

### The 37th Symposium on Powder Technology

The 37th Symposium on Powder Technology was held on August 21, 2003 at the Senri Hankyu Hotel in Osaka under the sponsorship of the Hosokawa Powder Technology Foundation and with the support of Hosokawa Micron Corporation. The symposium in

this year was also very successful with the attendance of 227 including about 30 academic people. The main subject of this year was “Nano-particle Technology”.

#### The 37th Symposium on Powder Technology

Subject: “Nano-particle Technology”

**Session 1** Chairperson: Emeritus Prof. Hitoshi Emi (Kanazawa Univ.)

- |  |   |
|--|---|
| <ul style="list-style-type: none"> <li>• Powder Technology and Evolution/Survival of Technology based Civilization (KONA Award Commemorative Lecture)</li> <li>• Nano Particle Technology towards Nano-bio Technology — Nano-bio Technology with Supercritical Fluid —</li> <li>• Mono and Multicomponent Nanoscale Powders and Process</li> </ul> | <p>Prof. Masayuki Horio<br/>(Tokyo Univ. of Agriculture &amp; Technology)</p> <p>Prof. Tadafumi Adschiri<br/>(Tohoku Univ.)</p> <p>Masayoshi Kawahara<br/>(Hosokawa Powder Technology Research Institute)</p> |
|--|---|

**Session 2** Chairperson: Prof. Kiyoshi Nogi (Osaka Univ.)

- |  |  |
|--|--|
| <ul style="list-style-type: none"> <li>• Application, Control and Characterization of Aggregation and Dispersion Behavior of Nano-particles</li> <li>• Application of Nanoparticles to Pharmaceutical Dosage Forms</li> <li>• Nano Structure Control by Mechano-Chemical Bonding Technique for Fuel Cells</li> </ul> | <p>Prof. Hidehiro Kamiya<br/>(Tokyo Univ. of Agriculture &amp; Technology)</p> <p>Prof. Yoshinobu Fukumori<br/>(Kobe Gakuin Univ.)</p> <p>Takehisa Fukui<br/>(Hosokawa Powder Technology Research Institute)</p> |
|--|--|

**Session 3** Chairperson: Prof. Makio Naito (Osaka Univ.)

- Discussion



---

## The 11th KONA Award

---

As the winner of the KONA Award, which is sponsored by Hosokawa Powder Technology Foundation and given to the scientists or groups who have achieved excellent researches in the field of particle science and technology, Professor Masayuki Horio of Tokyo University of Agriculture & Technology was selected.

Prof. Horio has achieved remarkable results in the field of particle science and technology, especially in the field of fluidization.

On January 30, 2003, Mr. Masuo Hosokawa, President of the Foundation, handed the 11th KONA Award to Prof. Horio at the ceremony of presentation held at the Senri Hankyu Hotel in Osaka, Japan.



---

**Academic publication concerning powder technology in Japan (2002)**

---

**JOURNAL OF THE SOCIETY OF POWDER TECHNOLOGY, JAPAN VOL. 39 (2002)**

● Attrition of High Bulk Density Granules by Blow-Tank-Type Dense Phase Pneumatic Transporter Moriyoshi Konami, Shigeho Tanaka and Kanji Matsumoto	4
● Effects of Dry Grinding of Talc/Mg-Source Mixtures on Formation of Forsterite Mitsuru Nikaido, Shigeru Sano and Fumio Saito	12
● Tensile Fracture Behavior of Fiber-Powder Mixture and Energy Consumption for Pulling out Single Fiber from Powder Bed Akinori Hashimoto, Munetake Satoh, Tomohiro Iwasaki and Masayuki Morita	32
● Effect of Humidity Condition on Tableting Compression Characteristics of Water-soluble Lubricants: Sodium Lauryl Sulfate Yasuyuki Tsumamoto, Kiyoshi Horie, Makoto Otsuka and Yoshihisa Matsuda	90
● Role of Nonionic Surfactants to Adhesive Forces between Surfaces in Moist Cyclohexane Yoichi Kanda, Yoshinori Nishitani and Ko Higashitani	96
● Surface Structure and Photocatalytic Activity of Ti Supported on Alumina Powder Masayoshi Fuji, Yoshio Sugiyama, Takashi Takei, Masatoshi Chikazawa, Katsuyuki Tanabe and Kohei Mitsunashi	102
● Environmental Assessment for Recovery of Copper from Printed Wiring Boards Koji Oka, Tadao Moro, Hitoshi Ohya, Shigeyuki Suzuki, Shigehisa Endoh, Atsushi Inaba and Takahiko Ohkura	154
● Zinc Dust Recycling Technique – Magnetic Separation of Fine Particles – Ruili Liang, Eiji Kikuchi, Hiroshi Sakamoto, Toyohisa Fujita and Yoshiaki Numata	161
● Mutual Separation of Ultra-fine Silica and Hematite Particles from Suspension Using Surface Characteristics Tsuyoshi Takahashi, Wataru Todoroki, Kenji Kazama, Hiroshi Hayashi and Hiroshi Sasaki	169
● Rapid Size Classification of Ultrafine Particles Using Surface Characteristics Kazuya Wakabayashi, Sonoko Sekita, Hiroshi Hayashi and Hiroshi Sasaki	175
● Particle Shape Control of Crushed Glass Particles by Autogenous Grinding with a Stirred Mill Naoya Kotake, Yosuke Sato and Yoshiteru Kanda	183
● Effect of Apparent Volume Fraction of Grinding Media on Characteristics and Catalytic Activity of MoS <sub>2</sub> Comminuted in Dry Air Kazumi Toda, Nobuyuki Koura, Yasushi Idemoto, Kunio Uchida, Yasunori Kuriki, Kazuo Shimada, Hiroshi Hayakawa and Fumikazu Ikazaki	240
● Release Process of Enzymes from Baker's Yeast Accompanied with Inactivation by Disruption in Agitating Bead Mill Shoichi Morohashi, Kazuhito Adachi, Sachiko Nomura, Rieko Hase, Hideaki Hatakeyama and Kazuhiro Hoshino	247
● Evaluation of the Inner Structure of Fiber-Powder Composite Prepared by Different Granulation Processes Using a Drilling Tester Akinori Hashimoto, Munetake Satoh, Tomohiro Iwasaki and Makoto Kawasaki	255
● Application of Violet Laser to Laser Diffraction and Scattering Method Takeshi Kinoshita	334
● Hardness Measurement of Particulate Matter Junichiro Tsubaki, Takamasa Mori, Hiroo Yamakawa, Hidetoshi Mori and Hitoshi Hirose	339
● Dependence of Coordination Number on Particle Diameter for Randomly Packed Bed of Uniform Spheres Mitsuaki Hirota, Syougo Matono, Hitoshi Ozaki, Kenji Iimura and Michitaka Suzuki	346
● Evaluation of Pharmaceutical Powders by Near-Infrared Spectroscopy Keiji Terashita and Ippei Kurimoto	424
● Change in Angle of Repose of Potato Starch during Ball-Milling Toru Suzuki, Yu Jin Kim, Yu Ito and Rikuo Takai	449
● Effect of Freeze-Grinding and Drying Process on the Quality of Fish Oil Extracted from Fish Bone of Yellow-fin Tuna and Bonito Yoshio Hagura, Takahiro Shuto, Makiko Okada and Kanichi Suzuki	454
● Feedback Control of Powder Electrostatic Charge in a Pneumatic Conveying Process Satoru Watano, Seiji Saito and Teruo Suzuki	496
● Effect of Deaeration of Fine Powders on the Discharge Characteristics by a Screw Feeder Hiroshi Nagashima and Toshifumi Ishikura	566



● Fabrication of Composite-Particle Thermistor Having a V-type Electric Resistance Dependence on Temperature Takehiro Dan, Mitsuru Egashira, Kyoko Saito, Junro Kyono, Mikihiro Kobayashi and Norio Shinya	573
● Evaluation at the Circularity of Rounding Effect of Coal Particles in CWM Tetsuo Ono	580
● Configuration of CCA Particles in the Toner Surface and Its Influence on Charging Characteristics Keiki Suganami, Manabu Takeuchi and Toshihiko Oguchi	642
● Influence of Additives on Toner Powder Characteristics and Ghost Images in Electrophotographic Non-Magnetic Mono Component Developers Shougo Sato and Manabu Takeuchi	648
● Effect of Particle Size Distribution on Coordination Number in Randomly Packed System of Spheres Mitsuaki Hirota, Syougo Matono, Tatsumi Kawaguchi, Kenji Iimura and Michitaka Suzuki	656
● Preparation of MoS <sub>2</sub> Catalyst for Ultra-deep Desulfurization of Diesel Oil by a Media Agitation Mill – Effect of Media Filling Ratio – Kunio Uchida, Yasunori Kuriki, Masato Kouzu, Hideo Orita, Kazumi Toda, Naotsugu Itoh and Fumikazu Ikazaki	679
● Mechanical Strength and Drug Release Characteristics of Bioactive Bone Cement Using $\alpha$ -Tricalcium Phosphate and Biopolymer Kunihisa Osasa, Makoto Yoshitomi and Shiho Iwai	685
● Effect of Plug Characteristics on Pressure Drop in Horizontal Conveyance of Fine Powder Yuya Kouzaki, Kenji Iimura, Michitaka Suzuki and Mitsuaki Hirota	730
● Effect of Liquid Additives and Behavior of Alumina Powder in Ultrafine Grinding of Alumina Masahiro Hasegawa, Mitsumasa Kimata and Tomoyuki Shoji	736
● Comparison between Spherical and Non-spherical Particles in Reverse Combustion Processes of Packed Bed Yoshiyuki Yamada, Yuichi Nakamura, Kuniaki Gotoh and Tatsuo Nishimura	743
● Hardness Measurement of Particulate Matter – Comparison between Experimental and Estimation – JunIchiro Tsubaki, Takamasa Mori, Hiroo Yamakawa, Hidetoshi Mori and Hitoshi Hirose	800
● Detection of Particles in Semiconductor Material Gases Using Light Scattering Method Kaoru Kondo, Yuji Imajo, Manabu Shimada and Kikuo Okuyama	806
● Observation of Laminated Particle Layers Vibrated Vertically under Microgravity Yasushi Ohyama, Hiromi Takeuchi, A. T. Pyatenko, Shigeo Chiba and Kunio Shinohara	813
● Development of Air Separator for Pharmaceutical Powder Products Moriyuki Ohkuma, Yasutomi Kato, Keiko Matsumoto and Hisakazu Sunada	864
● Effect of Particle Size Distribution of Filler in Thermosetting Plastics Molding Compound on the Flowability Tatsumi Kawaguchi, Michitaka Suzuki and Mitsuaki Hirota	870

---

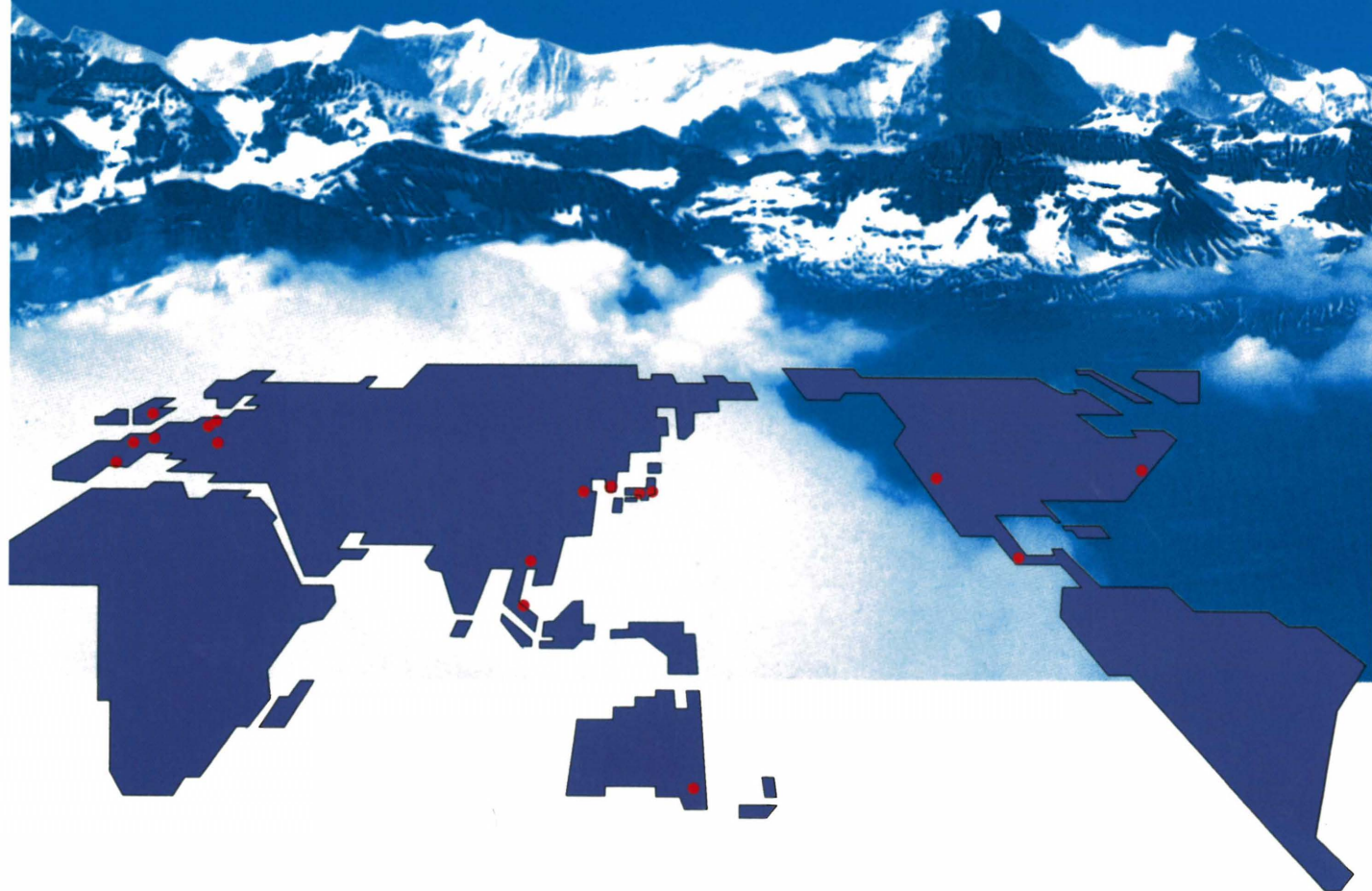
**KAGAKU KOGAKU RONBUNSHU VOL. 28 (2002)**


---

● Study of Stabilizing Conditions for Closed-circuit Pulverization System Eiji Shinoda, Kenji Yoshida, Kunihiro Fukui and Hideto Yoshida	36
● Motion of Splash Particles Released by Bubble Rupture in Fluidized Bed Yuji Tatemoto, Yoshihide Mawatari, Takahiro Saito, Tetsuya Tachi, Takenari Takeshita and Katsuji Noda	43
● Effect of Opening Size Distribution on Separation Characteristics of Test Sieves Satoshi Ishikawa, Atsuko Shimosaka, Yoshiyuki Shirakawa and Jusuke Hidaka	82
● Evaluation of Kneading Result of Kneaded Wet Powder by Compression Test in a Cylinder Tohru Moriwaki	110
● Bubble Characteristics and Fluctuation of Pressure and Particle Bed in Two-Dimensional Pulsated Fluidized Bed Akira Nishimura, Hiroshi Hoshino, Noriyuki Kobayashi and Masanobu Hasatani	121
● Influence of the Behavior of Particles and Dispersion Medium on the Particle Size Measurement with the Sedimentation Balance Method Kunihiro Fukui, Hideto Yoshida and Yuusuke Tokunaga	161
● Unstable Behavior of Electrostatic Particle Deposition Kenichiro Tanoue, Masato Yamamoto, Akihiko Ema and Hiroaki Masuda	196
● Sintering Mechanism of Two Spheres Forming a Homogeneous Solid Solubility Neck Atsuko Shimosaka, Yasushi Ueda, Yoshiyuki Shirakawa and Jusuke Hidaka	202
● Better Control of Flyash Mechanical Properties by Adding Carbon Black Fine Particles Kaori Jono, Takehisa Fukui, Makio Naito, Akira Kimura and Hidehiro Kamiya	224
● Effect of Particle Size on the Combustion Propagation Rate of Counter Combustion in a Packed Bed Yoshiyuki Yamada, Yuichi Nakamura, Kuniaki Gotoh and Tatsuo Nishimura	227
● Analysis of Pressure Drop in a Multi-Compartment Bag Filter Hidenori Ikeno, Yutaka Tada Setsuro Hiraoka and Yusuke Shuto	241
● Behavior of Bubbles and Heat Transfer Characteristics in a Fine Particle Fluidized Bed Equipped with Immersed Vertical Tube Bundles at Lower Gas Velocities Ryohei Yamazaki, Kei Nishibori, Kiyonobu Ogura, Mikio Hotta, Kennichi Yamamoto, Shigenobu Hatano and Shigekatsu Mori	297
● Variation in Electric Conductivity of the Carbon Particle Bed with Gas Velocity and Characterization of the Void Generation Nobuyoshi Nakagawa, Takuya Khomura, Ryoji Fujii and Kunio Kato	317
● Theoretical Study on Particle Size Distribution and Suspension Viscosity Shinichi Ookawara and Kohei Ogawa	322
● In-line Measurement of the Size and Moisture Content of Particles Using an Optical Displacement Gauge and an Infrared Moisture Meter Naohito Yoshikawa, Yumi Makabe, Fumihiko Yamada, Syu Ogawa and Kanji Matsumoto	354
● Application of Particle-Wall Collision to Parallel-Flow-Type Classification Jiangbo Chen and Toshihiko Shakouchi	417
● Analysis of Particle Flow in an Internally Circulating Fluidized Bed Having Several Chambers Seiichiro Toyoda, Yuki Iwadate, Tatsuya Hasegawa, Daisaku Fukuoka, Kimihito Narukawa and Masayuki Horio	424
● Simulation of Solid State Sintering Behavior of Two Spherical Particles with Formation of Eutectic Composition Atsuko Shimosaka, Yasushi Ueda, Yoshiyuki Shirakawa and Jusuke Hidaka	409
● Dispersion and Flocculation Behavior of Rare Earth Oxide Powders in Organic Solvent Junji Shibata, Katsuya Fujii and Hideki Yamamoto	641
● Relation between Suspension Viscosity and Parameters of Representative Particle Size Distribution Shinichi Ookawara and Kohei Ogawa	779

# HOSOKAWA MICRON

Hosokawa Micron Ltd. is a member of the Hosokawa Micron Group, responding to global needs through an emphasis on materials science and engineering. The Group is an international provider of equipment and Technology for powder and particle processing, product recovery, plastics processing and confectionery products. The Group maintains facilities for research, engineering, manufacturing, and service in each of the world's major industrial markets.



Process Technologies for Tomorrow



## HOSOKAWA MICRON

Headquarter Locations;

**HOSOKAWA MICRON CORPORATION**

5-14, 2-chome, Kawaramachi, Chuo-ku,  
Osaka 541-0048, Japan

Tel: 81-6-6233-3968

Fax: 81-6-6229-9267

<http://www.hosokawamicon.com/japan>